Organic Anolyte Materials for Novel Redox Flow Batteries

A thesis submitted to the University of Manchester for the degree of Doctor of Philosophy in the Faculty of Science and Engineering

2022

Alexandra E. Jones

Department of Chemistry

School of Natural Sciences

[blank page]

For Taid

Table of Contents

Word Count: 69,569

List of Figures

List of Tables

Abbreviations

(OFA)₂	Octafluoro-9,10-Anthrone Dimer
[dema][HSO₄]	Diethylmethylammonium Hydrogensulfate
1,5-DAAQ	1,5-Diaminoanthraquinone
2,6-DHAQ	2,6-Dihydroxyanthraquinone
4-OH-TEMPO	4-Hydroxy-2,2,6,6-Tetramethylpiperidin-1-Oyxl
ABS	Aqueous Biphasic Systems
Acac	Acetylacetonate
ACN	Acetonitrile
ADQS	9,10-Anthraquinone-2,6-Disulfonic Acid Disodium
AEM	Anion Exchange Membrane
AFM	Atomic Force Microscopy
AQ	9,10-Anthraquinone
BE	Bulk Electrolysis
BF₄⁻	Tetrafluoroborate
BMIm	1-Butyl-Methyl Imidazolium
BMPyrr	1-Butyl-1-Methylpyrrolidinium
BP	Benzophenone
BQ	1,4-Benzoquinone
BSE	Backscattered Electrons
BTMAP	1,1′-Bis[3-(trimethylammonio)propyl]-4,4′-Bipyridinium
BuPh	*N*-Butylphthalimide
BzNSN	2,1,3-Benzothiadiazole
C	Chemical Reaction Step
CAES	Compressed Air Energy Systems
CE	Coulombic Efficiency
CE	Counter Electrode
CEM	Cation Exchange Membrane
ChCl	Choline Chloride
CV	Cyclic Voltammetry/Voltammogram
DB-1	Tetra-Aminoanthraquinone
DBB	1,4-Di-*Tert*-Butyl-2,5-Dimethyoxybenzene
DBMMB	2,5-Di-*Tert*-Butyl-1-Methoxy-4-[2′-Methoxyethoxy]benzene
DCB	1,2-Dichlorobenzene

DCE	1,2-Dichloroethane
DESs	Deep Eutectic Solvents
DFT	Density Functional Theory
DHAQDMS	Dihydroxyanthraquinone Dimethylsulfonic Acid
DHBQ	2,5-Dihydroxy-1,4-Benzoquinone
DHBS	2,5-Dihydroxybenzenedisulfonate
DHPS	7,8-Dihydroxyphenazine-2-Sulfonic Acid
DI	Double Integral
DME	1,2-Dimethoxyethane
DMF	Dimethylformamide
DMFc	1,1-Dimethylferrocene
DoD	Depth of Discharge
DoE	Department of Energy
E	Electron Transfer Step
e⁻	Electron
EA	Ethyl Acetate
EDG	Electron Donating Group
EDX	Energy Dispersive X-Ray Spectroscopy
EE	Energy Efficiency
EESS	Electrochemical Energy Storage Systems
EG	Ethylene Glycol
EMIm	1-Ethyl-3-Methyl Imidazolium
EPR	Electron Paramagnetic Spectroscopy
EPSRC	Engineering and Physical Science Research Council
ESS	Energy Storage Systems
ESW	Electrochemical Stability Window
EWG	Electron Withdrawing Group
Fc	Ferrocene
FC	Flow Cell
FcNCl	Ferrocenylmethyl)trimethylammonium Chloride
FcNTFSI	(Ferrocenylmethyl)trimethylammonium Bis(trifluoromethanesulfonyl)imide
FEG	Field Emission Gun
FL	Fluorenone

FQH$_2$	2,3,5,6-Tetrakis((dimethylamino)methyl)hydroquinone
FT-IR	Fourier Transformed Infrared Spectroscopy
GC	Glassy Carbon
H$_2$Q	Hydroquinone
HBA	Hydrogen Bond Acceptor
HBD	Hydrogen Bond Donor
HER	Hydrogen Evolution Reaction
HOMO	Highest Occupied Molecular Orbital
IEM	Ion Exchange Membrane
ITIES	Interface Between Two Immiscible Electrolyte Solutions
L/L	Liquid/Liquid
LIB	Lithium Ion Battery
LSV	Linear Sweep Voltammetry
LUMO	Lowest Unoccupied Molecular Orbital
MV	4,4-Dimethyl Bipyridinium Dichloride
NIAFEM	Nanoscale Imagine and Analysis Facility for Environmental Materials
NMePh	N-methyl Phthalimide
NMR	Nuclear Magnetic Resonance
NQ(1,4)H	2-Hydroxy-3-Carboxy-1,4-Napthoquinone
OCV	Open Circuit Voltage
OER	Oxygen Evolution Reaction
OFAQ	Octafluoro-9,10-Anthraquinone
ORAM	Organic Redox Active Material
ORFB	Organic Redox Flow Battery
OA	Oxalic Acid
PAH	Polycyclic Aromatic Hydrocarbons
PC	Polycarbonate
PCET	Proton Coupled Electron Transfer
PF$_6^-$	Hexafluorophosphate
PHS	Pumped Hydroelectric Systems
pKa	Acid Dissociation Constant
PTIO	2-Phenyl-4,4,5,5-Tetramethylimidazoline-1-Oxyl-3-Oxide

Pyrr$_{14}$	*N*-Methylpyrrolidium
Q	Quinone
RAM	Redox Active Material
RDE	Rotating Disk Electrode
RE	Reference Electrode
RFB	Redox Flow Battery
RVC	Reticulated Vitreous Carbon
RPM	Revolutions Per Minute
RTIL	Room-Temperature Ionic Liquid
SCE	Saturated Calomel Electrode
SE	Secondary Electron
SECM	Scanning Electrochemical Microscopy
SEI	Solid Electrolyte Interface
SEM	Scanning Electron Microscope
SHE	Standard Hydrogen Electrode
SoC	State of Charge
T&D	Transmission and Distribution
TABP	3,3'-5,5'-Tetramethylaminmethylene-4,4'-Biphenol
TBABF$_4$	Tetrabutylammonium Tetrafluoroborate
TEA	Tetraethylammonium
TEG	Triethyleneglycol
TEMPO	2,2,6,6-Tetramethylpiperidin-1-Oyxl
TFBQ	Tetrafluoro-1,4-Benzoquinone
TFSI	Bis(trifluoromethane)sulfonamide
TFSI	Bis(trifluoromethylsulfonyl)imide
TFT	α,α,α-Trifluorotoluene
TMA	Trimethylammonium
TMAP	3-(Trimethylammonio)propoxy
TNO	Nederlandse Organisatie voor Toegepast Natuurwetenschappelijk Onderzoek
UHV	Ultra-High Vacuum
UME	Ultramicroelectrode
UPS	Uninterruptible Power Systems
UV-Vis	Ultraviolet-Visible
V/V	Volume Ratio
VE	Voltage Efficiency

VRFB	Vanadium Redox Flow Battery
WE	Working Electrode
WIS	Water-in-Salt
XAFS	X-Ray Absorption Spectroscopy
XPS	X-Ray Photoelectron Spectroscopy

Symbols

Standard Constants

Symbol	Definition	Value
F	Faraday's constant	96485 C mol^{-1}
R	Ideal gas constant	$8.314 \text{ J mol}^{-1} \text{ K}^{-1}$

Symbols

Symbol	Definition	Unit
A	Electrode Surface Area	cm
Abs	Absorbance	
B	Magnetic Field	T
C	Electrolyte Concentration	Mol dm^{-3}
C_{active}	Active Material Concentration	Mol dm^{-3}
CE_{ff}	Coulombic Efficiency	%
D_o	Diffusion Coefficient	$\text{cm}^2 \text{ s}^{-1}$
E	Electrode Potential	V
$E_{1/2}$	Half-Wave Potential	V
E_a	Activation Energy	J mol^{-1}
E_{charge}	Charge Voltage	V
E_d	Energy Density	Wh L^{-1}
$E_{discharge}$	Discharge Voltage	V
EE_{ff}	Energy Efficiency	%
En	Energy	eV
E^o	Standard Electrode Potential	V
E_p	Peak Potential	V
E_{pa}	Anodic Peak Potential	V
E_{pc}	Cathodic Peak Potential	V
f	Frequency	Revolutions Per Minute
g_e	Electron G-Factor	
i	Current	A
I	Quantic Number	
Int_0, Int_{final}	Initial/Final Intensity	
i_c	Capacitive Current	A
i_k	Kinetic Current	A

i_{llim}	Mass Transfer Limited Current	A
i_p	Peak Current	
j	Current Density	mA cm^{-2}
J	Coupling Constant	Hz
k_0	Rate Constant	cm s^{-1}
K_{eq}	Equilibrium Constant	
l	Path Length	cm
m	Mass	g
M	Molar Mass	g mol^{-1}
m_s	Magnetic Component	
n	Number of Electrons	
P	Power Density	W cm^{-2}
Q	Reaction Quotient	
q	Charge	
q_t	Theoretical Cell Capacity	mAh
R_u	Uncompensated Resistance	Ω
S	Intrinsic Spin	
s	Spin Quantum Number	
S	Signal Intensity	
t	Time	s
T	Temperature	K
T_m	Melting Point	K
T_{VF}	Empirical Fitting Parameter	K
V	Volume	L
v	Scan Rate	V s^{-1}
V_{cell}	Open Circuit Voltage	V
VE_{ff}	Voltage Efficiency	%
$v_{kinematic}$	Kinematic Viscosity	m^2 s^{-1}
V_m	Molar Volume	m^3 mol^{-1}
α_M	Activity	
ΔE_p	Peak-to-Peak Separation	V
ΔG	Gibbs Free Energy Change	kJ mol^{-1}
ΔG^o	Standard Gibbs Free Energy Change	kJ mol^{-1}

$\Delta_o^w\varphi$	Equilibrium Potential Difference	V
$\Delta_o^w\varphi_M^0$	Standard Transfer Potential	V
ε	Molar Extinction Coefficient	$M^{-1}\ cm^{-1}$
η	Dynamic Viscosity	Pa s
η^0	Exponential Pre-Factor Constant	
η_0, D	Empirical Material Dependent Parameters	
μ	Magnetic Moment	
μ_M^0	Standard Chemical Potential	$J\ mol^{-1}$
μ_B	Bohr Magnetron	$J\ T^{-1}$
ρ	Density	$g\ cm^{-3}$
σ	Conductivity	$S\ m^{-1}$
Υ	Gyromagnetic Ratio	
φ	Inner Potential	V
$\varphi_{instrument}$	XPS Work Function Correction Factor	
ω	Angular Velocity	$rad\ s^{-1}$

Abstract

The work presented in this thesis focusses on developing a high-energy all-organic membrane-free redox flow battery. Redox flow batteries are promising energy storage devices due to the decoupling of energy capacity and power. Low energy densities owing to using aqueous electrolytes, alongside costly inorganic redox materials and ion-exchange membranes hinder their mass commercialisation.

Organic redox active materials and non-aqueous electrolytes are promising pathways to realising high energy density redox flow batteries at an affordable price. Additionally, manipulation of the liquid/liquid interface that forms between high concentration water-in-salt electrolytes and non-aqueous electrolytes presents a method of removing the expensive, and lifetime limiting membranes.

The main body of this work concentrates on a novel redox active molecule for the negative half-cell, octafluoro-9,10-anthraquinone. Octafluoro-9,10-anthraquinone shows promising redox properties, with a highly negative redox potential, rapid mass transfer, and rapid kinetics. Instability of the highly reactive charged states when in high concentrations leads to rapid decomposition and passivates the electrode. Typical stabilisation techniques, such as hydrogen bonding, protonation, and more strongly supporting electrolytes did not stabilise the reduced states. The instability of the charged states of novel redox materials is a constant challenge in this field, as capacity loss is present in every non-aqueous organic redox material to date.

Low concentrations of the quinone show promising battery performance in a membrane-free device. The membrane-free devices separate the half-cells by a liquid/liquid interface that forms from the spontaneous partitioning of high concentration water-in-salt electrolytes and acetonitrile. Through studying a selection of inorganic and organic catholyte materials, this study demonstrates a novel organic membrane-free water-in-salt based static battery. However, incomplete separation and subsequent reactions of the organic materials limits the system to only static function. Flowing the membrane-free device perturbs the interface and propagates self-discharge reactions, which destroys the promising performance seen in the static systems.

The second focus of this work involves a separate study covering organic redox active, high concentration deep eutectic solvent-based electrolytes. The study discovers a redox active novel benzophenone/(2,2,6,6-tetramethylpiperidin-1-yl)oxyl deep eutectic solvent with a lower viscosity and density than previously reported systems. The work highlights the challenges of using highly concentrated electrolyte solutions for redox flow battery applications.

Declaration

I, the author, Alexandra Emily Jones, declare that no portion of the work referred to in this thesis has been submitted in support of an application for another degree or qualification of this or any other university or other institute of learning.

Copyright Statement

i. The author of this thesis (including any appendixes and/or schedules to this thesis) owns certain copyright or related rights in it (the "Copyright") and she has given the University of Manchester certain rights to use such Copyright, including for administrative purposes.

ii. Copies of this thesis, either in full or in extracts and whether in hard or electronic copy, may be make **only** in accordance with the Copyright, Designs and Patents Act 1988 (as amended) and regulations issued under it or, where appropriate, in accordance with licensing agreements which the University has from time to time. This page must form part of any such copies made.

iii. The ownership of certain Copyright, patents, designs, trademarks and other intellectual property (the "Intellectual Property") and any reproductions of copyright works in the thesis, for example graphs and tables ("Reproductions"), which may be described in this thesis, may not be owned by the author and may be owned by third parties. Such Intellectual Property and Reproductions cannot and must not be made available for use without the prior written permission of the owner(s) of the relevant Intellectual Property and/or Reproductions.

iv. Further information on the conditions under which disclosure, publication and commercialisation of this thesis, the Copyright and any Intellectual Property and/or Reproductions described in it may take place is available in the University IP Policy (see http://documents.manchester.ac.uk/DocuInfo.aspx?DocID=2442 0), in any relevant Thesis restriction declarations deposited in the University Library, the University Library's regulations (see http://www.library.manchester.ac.uk/about/regulations/) and in the University's policy on Presentation of Theses.

Publications

A. E. Jones, A. Ejigu, B. Wang, R. W. Adams, M. A. Bissett and R. A. W. Dryfe, Quinone voltammetry for redox-flow battery applications, *J. Electroanal. Chem.*, 2022, **920**, 116572

Acknowledgements

I would like to express my deepest appreciate to my supervisor Prof. Robert Dryfe. Thank you for accepting me into your group despite my limited electrochemistry knowledge. Your years of mentoring mean that I can now confidently call myself an electrochemist. Thank you for your patience, your guidance, and your understanding over these four years. I count myself very lucky to have had you as my supervisor.

To every member of the Dryfe group, past and present, I thank you for brightening my life on a daily basis and making it a joy to come to the laboratory. These talented individuals deserve far more thanks than I can give here. Such a wonderful group of colleagues are rare and I treasure you all. I would specifically like to mention Dr Andinet Ejigu, who has patiently answered my relentless, and sometimes stupid, questions over the years. My work would not have been possible without your direction and enthusiasm for research. I also thank Dr Mark Bisset for his guidance and incredibly useful second opinions in our weekly meetings.

Special thanks to Dr Ralph Adams for always being up for the task of analysing NMR, and to Dr Bin Wang for his help with the *in-situ* EPR during the challenge of lockdown.

Words cannot express my gratitude to TNO for hosting me during my secondment. The four months spent working with TNO in Delft were a fascinating opportunity to step outside of the world of academia. I extend particular thanks to Dr Ruud Cuypers for taking a chance on me and battling with bureaucracy to get me to the Netherlands. I am also grateful to Dr. Riccardo Zaffaroni for sharing his wealth of electrochemical knowledge, developing my technical understanding, and his fantastic tiramisu.

I also thank the ESPRC and the Graphene NOWNANO CDT for their studentship. Being a member of the CDT program gave me experiences and provided me with friendships that I believe is often lost in some PhD programmes.

I could not have undertaken this journey without the resounding love and support from my wonderful family. Thank you to my mum, you gave me the strongest of roots and the wings to fly. To my dad, the cleverest person I know. Your contagious passion and drive have been my inspiration from day one. To my siblings who lovingly pretend to care when I talk to them about chemistry. Thank you to my friends for the encouragement, the checking in, and the well-needed distractions.

I was lucky enough to have Joshua Godson by side throughout this endeavour. Thank you for being my rock and reminding me to relax and just be. Thank you for the adventures, the long talks, the wonderful dinners, and all of the laughs. You mean a lot to me.

1. Introduction

1.1. Energy Storage Problems

Energy is arguably the most important global commodity, playing a vital role in all international development. Energy storage has many different forms but falls into two categories: primary and secondary energy. Primary energy forms are those that involve only extraction or capture and are not subject to transformation processes. These sources are typically found in nature where the energy is released through heat or mechanical work.[1] Key examples include crude oil, natural gas, coal, biomass, wind, solar, and tidal. Subjecting these primary forms to a conversion process transforms them into secondary energy. Secondary energies, known as energy carriers, are more convenient as they are used directly. These include electricity, biofuels, diesel, ethanol, hydrogen and heat.[1]

Global energy consumption is consistently increasing with time and is set for further growth as the population climbs. The 2021 Key World Energy statistics by the International Energy Agency report a global supply of 606 EJ in 2019. This is 10 % higher than in 2012 and 238 % higher than in 1973.[2]

Traditionally, most of our energy production has come from fossil fuels such as coal, crude oil, and natural gas. The anthropogenic CO_2 emissions from burning fossil fuels correlates with the global warming effects over the last 200 years. Fortunately, the percentage share of global energy consumption from fossil energy sources is decreasing. This is a direct result of renewable energy resource integration. For example, only 13.2 % of the total primary energy supply in 1973 came from renewable resources compared to 19 % in 2019.[2] However, the reduction of fossil fuel utilisation as a primary energy supply does not reflect in a reduction in CO_2 emissions. Fossil fuels contributed 32,840 Mt CO_2 emissions in 2017 compared to only 15,460 Mt in 1973.[3] This is because even though the percentage share has dropped, this effect is outstripped by the overall increase in energy consumption, noted above.

To stem the rising temperatures, it is imperative that we move away from fossil-based energy sources and integrate renewable systems into our existing energy network. Wider utilisation of renewable energy sources would lower the total CO_2 emissions from the burning of primary energy forms. Current goals set by the European Commission have the target of a 32 % renewable energy share by 2030.[4] This is aligned with the EU policy goal to reduce 93 – 99 % of greenhouse gas emissions in the energy sector by 2050.[5]

Renewable energy resources include geothermal, hydroelectricity, solar, and wind. These sources improve upon traditional fossil fuels due to their abundance. Geothermal and

hydroelectricity are disadvantaged by massive ecological impact and are limited to certain geographical conditions.[6] Inherent intermittency hinders energy production from solar and wind. Variations in solar irradiance and wind speed create fluctuations in output power and results in an unstable grid frequency. Full renewable utilisation would therefore lead to an unstable power grid with times of imbalance between supply and demand.

The present electrical grid system transmits energy from the point of production to the end user almost instantaneously and has nearly no storage capability.[7] If the market share of these unpredictable sources surpasses 20 % of the total energy generation capacity then it will destabilise the power grid. Developing large-scale energy storage systems (ESSs) that can deliver stable and flexible electricity is therefore essential in achieving our low carbon goals.[7,8]

ESSs could mitigate the instabilities through load-levelling, where energy is stored in times of overproduction to be accessed in hours of peak demand.[1] For example, solar energy could be stored during the day when production is at a maximum, and then utilised at night when demand is typically highest. Figure 1.1. shows a schematic of the load profile for this process.[9] Further ESS benefits include: improved power quality, reliability, and stability; peak-shaving; power management; and assisting the growth of smart cities.[1]
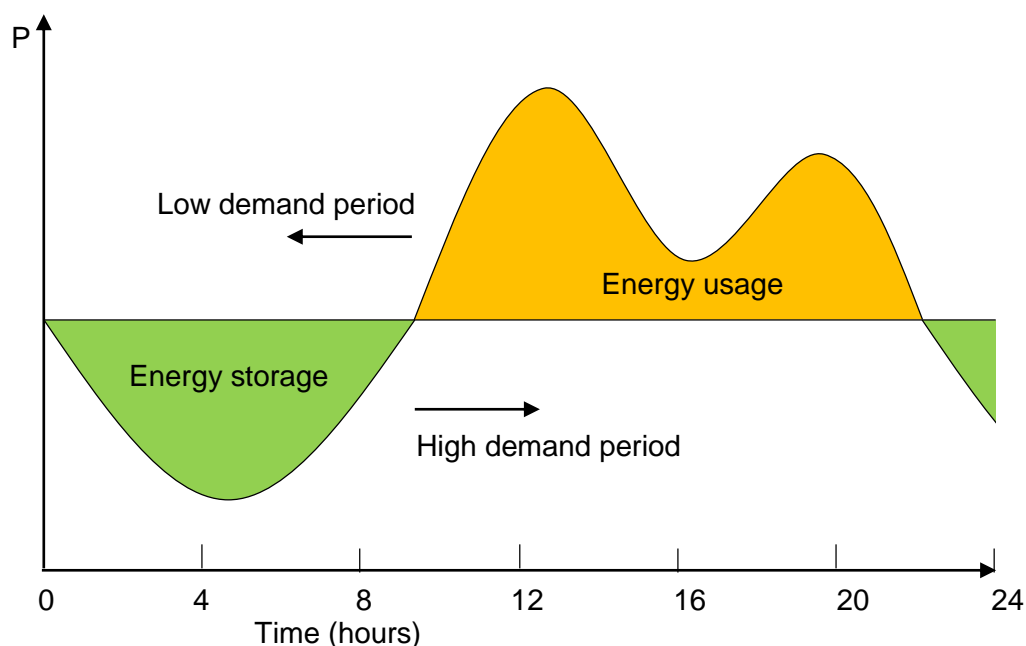
Figure 1.1. Load profile showing load levelling of a large-scale ESS.

To ensure the long-term economic feasibility of an ESS, the U.S. Department of Energy (DoE) have set a system capital cost of \$ 150 kW h^{-1} by 2023, with a target of \$ 100 kW h^{-1} to match the present physical energy storage devices. EU requirements are expected to be analogous.[10]

There are four categories for ESSs viable for large-scale energy storage: mechanical, electrical, chemical, and electrochemical. Mechanical techniques include pumped hydroelectric systems (PHS), compressed air energy storage (CAES), and flywheels. Supercapacitors are an example of electrical storage, and chemical storage is usually via hydrogen. Electrochemical energy storage systems (EESSs) encompass all types of batteries. EESSs are strong candidates for solving the large-scale energy storage conundrum over other ESSs due to several desirable features. These include a) high energy densities, b) pollution-free processes, c) fast response times, d) modularity and scalability, e) low maintenance upkeep, f) wide range of storage times and capacities, g) flexible designs, and h) no geographical restraints.[11]

Figure 1.2. shows a sample of the available EESSs as a function of their power rating. Figure 1.2. displays how EESSs best apply to grid applications from power quality (<100 kW) to energy management (10 – 100 MW).[12,13] The power rating determines their optimal application and duration of discharge. This then determines their suitability for uninterruptible power systems (UPS), transmission and distribution (T&D), or bulk power management.[11] The main characteristics used to compare EESSs are: power density (rated power output divided by volume of device, W kg^{-1} or W L^{-1}); energy density (energy stored divided by volume of the storage device, Wh kg^{-1} or Wh L^{-1}); lifetime; capital and operating costs (kW h or kW h cycle^{-1}); storage capacity and duration (Wh); round trip efficiency; response time; and technological maturity.[1]

A wide variety of EESS technologies are already in demonstration. These include lithium-ion batteries (LIBs), sodium-sulfur (NaS) batteries, lead-acid batteries (PbO_2), and redox flow batteries (RFBs). EESSs fall into 3 groups: primary batteries, secondary batteries and fuel cells.[14] Primary batteries cannot recharge whereas secondary batteries can. Fuel cells supply the energy from an external source, such as hydrogen, whereas batteries store the energy internally as part of the design.[14]

Each EESS has its own performance metrics and characteristics, meaning that no single design can meet the requirements to cover all system applications. Table 1.1. compares the technical characteristics of major EESSs.[15,16] Most battery development has focussed on devices for portable power, intermittent backup power, and transportation applications where a high energy density is key. Large-scale storage applications place less demand on size and volume metrics and more weight on superior performance for low capital cost, durability, lifetime, high round-trip efficiency, and rapid response times.[7] The most ideal batteries for

large-scale applications are external storage devices with deep cycle capabilities, an energy efficiency around 70 – 80 %, and an energy capacity between 17 – 40 MW h.[14]
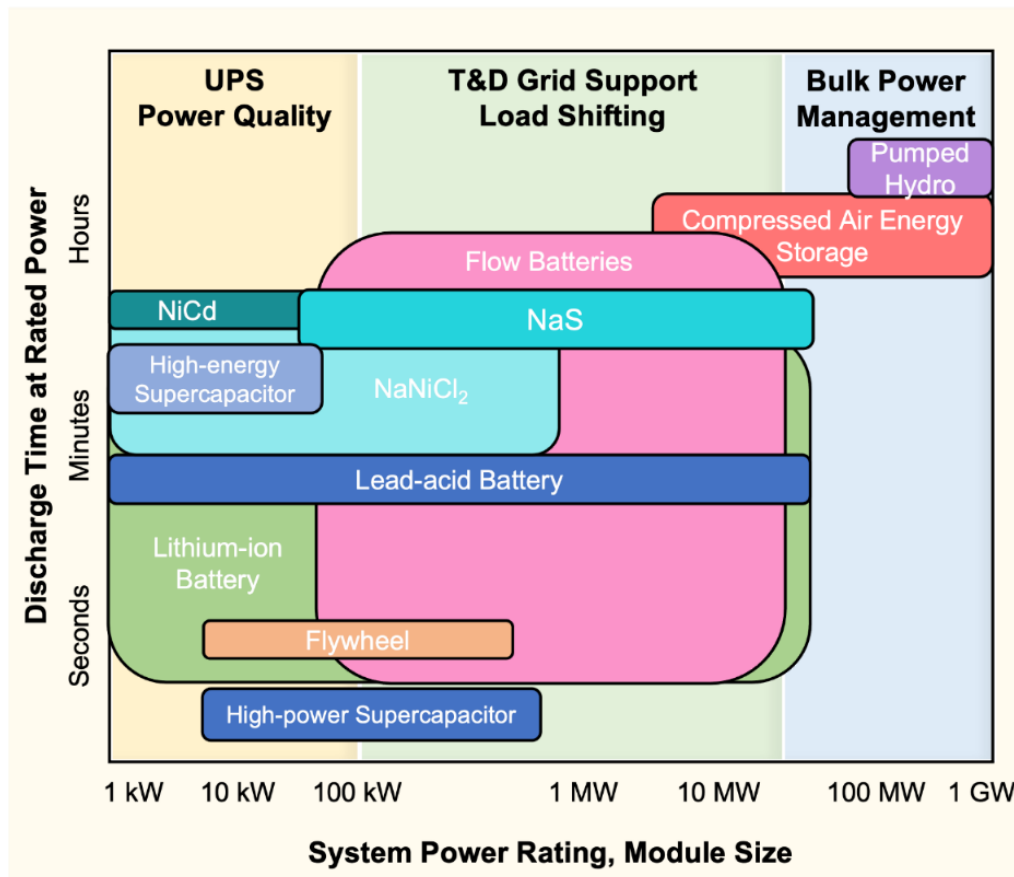
Figure 1.2. Applications of EESSs in terms of power rating and discharge time. Adapted with permission from EPRI,[12] using data from Rahman et al.[13]

LIBs, PbO_2, and NiCd batteries are internal storage systems. They operate via intercalation or plating mechanisms, which means that battery power and capacity are dependent on the electrode surface area. Hence, the capacity can only be improved by increasing the quantity of individual cells.[17] Large numbers of cells bring safety concerns due to different cell deterioration rates and subsequent thermal runaway. This then becomes expensive as each cell requires a battery management system.[17] Internal energy storage systems are therefore not optimal for large-scale ESSs.

NaS, NaNiCl, and RFBs are external storage systems. The active material is stored outside of the battery stack, decoupling energy and power such that each scale independently. This makes them much better suited as large scale ESSs.[15]

Table 1.1. Table comparing the performance metrics of established EESSs. Adapted from refs.[13,15,16,18]

EESS	Power Rating (MW)	Discharge Duration (h)	Energy Efficiency (%)	Capital Cost ($ kW h^{-1})	Durability (cycles)	Rated Energy Capacity (MW h)	Lifetime (years)	Limitation
LIB	0– 50	seconds – 5	65 – 90	400 – 5000	600 – 10,000	0.004 – 10	5 – 20	High energy cost; safety
Nickel-Cadmium Battery (NiCd)	0 – 46	6 – 8	60 – 80	800 – 1500	1500 – 3000	6.75	5 – 20	Toxicity; high cost; memory effect[18]
PbO$_2$	0.001 – 50	0.1 – 4	70 – 80	200 – 400	500 – 1200	0.001 – 40	5 – 15	Limited life cycle; high cost; toxicity
NaS	0.05 – 34	5 – 8	70 – 90	300 – 500	2000 – 5000	0.4 – 244.8	15	Safety; high operating temperature
Sodium Nickel Chloride Battery (NaNiCl)	0.001 – 1	Minutes – 8	60 – 80	100 – 200	2500 – 3000	0.004 – 0.025	8 – 14	High operating temperature
RFB	0.03 – 12	Seconds – 12	60 – 85	150 – 1000	13,000+	2 – 60	10 – 20	Low energy density; high cost

To be suitable for renewable integration, the EESS must span a wide range of power ratings. Generally, photovoltaic power outputs range between 1 kW for small-scale rooftop systems up to 550 MW for large solar farms (for example, Topaz Solar Farm, California, USA).[6] Wind turbines have typical power outputs ranging 2.5 – 7.5 MW.[6] Both Figure 1.2. and Table 1.1. show RFBs are a suitable EESS to cover this range. A $ 15 million investment into VRFB development for the company H_2 demonstrates the industrial and commercial interest in this technology.[19] Section 1.2. covers the technical aspects, advantages, and disadvantages of RFB systems.

1.2. Redox Flow Batteries

When considering economic and safety characteristics, the RFB system is recognised as the most realistic energy storage solution in the several kW/kW h^{-1} to tens of MW/MW h^{-1} range. RFBs cover a wide range of power ratings, can store electricity for several hours, and are able to switch between charge/discharge within a fraction of a second. These characteristics make them ideal for integrating a wide range of renewable resources and responding to fluctuations in output power and consumer demand.

1.2.1. Working Principle

Figure 1.3. shows a typical RFB configuration undergoing discharge. Equations 1.1. and 1.2. give the corresponding equations. The anolyte (A*)* and the catholyte (C), represent the redox-active materials (RAMs), *n* and *m* are the oxidation states, e^- represents an electron, and *x* and *y* are integers.

The overall design is similar to a fuel cell, with the key difference being the reversibility of an RFB. The fuel cell is a galvanic cell that catalytically oxidises an external fuel whilst simultaneously reducing an oxidant. The RFB is a closed system that re-circulates the electrolyte under charge and discharge conditions, and so does not require the constant fuel supply. Fuel cells are not considered for large-scale storage applications due to their low round-trip efficiencies (<40 % compared with up to 85 % for RFBs).[20]

The main RFB components are two external electrolyte tanks, two peristaltic pumps, and an electrochemical cell. The electrochemical cell is made from two half-cells separated by an ion-exchange membrane (IEM) that is permeable to the supporting electrolyte but impermeable to the RAM.[21]
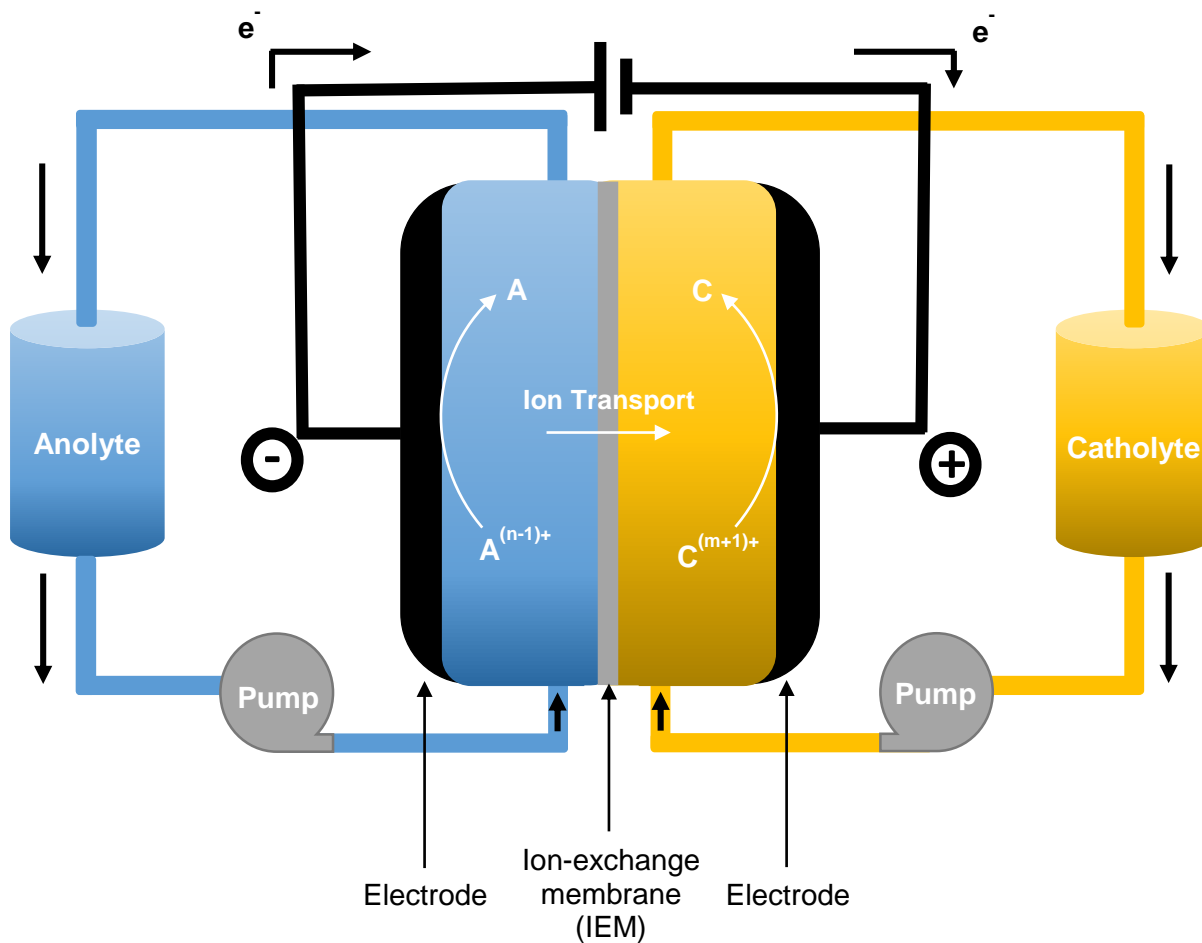
Figure 1.3. Schematic representation of a RFB undergoing discharge.

$$A^{(n-x)+} \xrightarrow{discharge} A^{n+} + xe^-$$

<div align="right">1.1.</div>

$$C^{(m+y)+} \xrightarrow{discharge} C^{m+} - ye^-$$

<div align="right">1.2.</div>
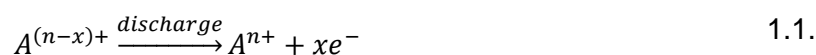
Each half-cell carries an electrode connected to a bipolar plate and a current collector. Redox couples dissolved in electrolytes are stored in the external reservoirs and are termed the 'anolyte' and 'catholyte' when used on the anode and cathode side, respectively.[22] Pumps continuously carry the electrolytes into the electrochemical cell where charge/discharge reactions occur. Anions or cations of the supporting electrolyte or counter-ions of the RAMs act as charge carriers through the IEM to balance the charge of the cell.

The IEM plays a major role in the RFB function. The IEM selectively transports charge-carrying ions across the cell whilst preventing cross-contamination of the electrolytes into the adjacent half-cell. This cross-contamination can be a major source of capacity loss.[21] The ideal IEM

has high ion conductivity for the charge carrier but is impermeable to the RAMs. Typical RFBs use Nafion, a perfluorosulfonated cation-exchange membrane (CEM) that was originally designed for proton-exchange membrane fuel cells.[21] These perfluorinated IEMs come with a high price. Additionally, poor selectivity and high degradation rates due to the concentrated acidic and highly oxidising conventional RFB environment lead to sub-optimal activity.[21] The RFB life cycle closely relates to the chemical stability of the membrane. Much research is directed to finding low-cost non-fluorinated IEMs with high mechanical strength and chemical stability.[23–25] Developing a low-cost alternative to Nafion is a priority, as current IEMs can account for up to 40 % of the total battery cost.[10]

RFBs have a particularly flexible battery design. The RAMs can range from any combination of redox active metallic or organic material and the electrolyte can comprise either aqueous or non-aqueous media.[21] This allows for a wide range of possible battery compositions and hence a wide range power and energy capabilities.

The RFB external storage system decouples power generation and energy density such that they scale independently. Increasing the size of the active area, number of battery stacks, and number of stacks in the system increases the power output. Increasing the volume or concentration of the externally held electrolyte improves the energy capacity. RFBs are therefore scalable without incurring the power losses seen in conventional battery designs. This makes them more economically viable than other battery technologies.[10]

The modular RFB design means RFBs can find use as "mobile" energy storage devices in the form of shipping containers and placed as an electricity supply to decentralised regions.[6] Further RFB advantages comprise their low environmental impact, safety, long-storage times, large storage capacities, low maintenance costs, tolerance to overcharging, high overall energy efficiencies, millisecond response-times, operational ability at high depth-of-discharge (DoD), and site-independence.[20]

The low volumetric energy density of the RFB hinders its utility.[26] Storing energy in liquids is inherently less energy dense than in solids. For example, the leading commercial RFB design, the vanadium RFB (VRFB), has an energy density of 35 Wh L^{-1}, whereas typical LIBs have energy densities of 240 Wh L^{-1}.[10] Approaches to improve the energy density involve using highly concentrated RAMs with multi-electron transfer processes.[10]

Further drawbacks include the large size of the electrolyte tanks, as it reduces RFB usefulness in space-limited applications such as in commercial buildings or cars. Electrolyte toxicity is another point of concern, for example the 2 M H_2SO_4 and highly oxidising VO^{2+} in conventional VRFBs.

There are some deviations from the standard all-liquid RFB design, such as the soluble lead-acid battery, which utilises a mixed electrolyte in an undivided cell with one reservoir. Such designs are termed 'hybrid RFBs' and function with one half-cell reaction being the deposition of solid active species during cycling. Other examples include the hybrid-lithium-RFB which uses a lithium metal anode in an organic electrolyte and an aqueous redox active catholyte, such as Br_2/Br^-, separated by a ceramic solid separator.[27] The intercalation/dissolution operating mechanism of hybrid RFBs means the energy and power are not decoupled. This allows for higher energy density than the all-liquid designs, but at the expense of the scalability/modularity that is pivotal for large-scale EESS. Therefore, this report does not discuss hybrid-systems.

Another, more recent, unconventional RFB design is the membrane-free approach. These designs separate the half-cells through rational design of immiscible electrolyte solutions. Section 1.5. discusses how this concept overcomes the cost and lifetime limitations of the IEM, and Chapter 5. investigates the applicability of a membrane-free design in the present research.

1.2.2. Redox Flow Battery Performance Metrics, Cell Attributes and Decay Mechanisms

The wide expanse of RFB chemistry and designs requires a strict set of performance parameters and cell attributes to accurately assess and compare the systems. This allows us to identify how metrics such as cell component cost and the molar mass of corresponding RAMs affects the overall cost per kW h. The overall battery performance is dependent on the chemistries chosen for the RAMs. The solubility, chemical stability, redox potential, and material cost directly influence the energy density, lifecycle, cell potential, and price of the RFB system.[28] This section briefly discusses the parameters and cell attributes that rate the electrical performance.

Equation 1.3. calculates the energy density (E_d) in Wh L^{-1}. The E_d is a measure of how much energy a device contains. n is the number of electrons, F is the Faraday constant in Ah L^{-1}, V_{cell} is the open circuit voltage (OCV), and C is the RAM concentration.[29] The theoretical E_d is the product of capacity and OCV with reference to the overall electrolyte volume. One increases the E_d by increasing the RAM solubility, the OCV, or the number of electrons in the redox process.

$$E_d = nFV_{cell}C \qquad\qquad 1.3.$$

Theoretical cell capacity (q_t) of an anolyte or catholyte (Equation 1.4.) is amount of electric charge stored in the cell in Coulombs, or more commonly in mA h. Expressing this as the volumetric specific capacity ($q_{t,v}$) is most suitable for RFBs, as the active materials are liquid electrolytes.[30] The $q_{t,v}$ depends on the number of electrons transferred, electrolyte concentration, and electrolyte volume (V). The volumetric cell capacity is critical in projecting the size of the RFB tank for large-scale purposes. By integrating $q_{t,v}$ with the discharge curves of cell voltage one obtains the volumetric energy density of the cell.

$$q_t = nCVF \hspace{4cm} 1.4.$$

Equation 1.5. defines the current density (j), which is the current (i) applied by membrane area (A) in mA cm^{-2} and has direct influence over the battery's charge/discharge time. It becomes particularly relevant when comparing different membranes and solvent systems.

$$j = \frac{i}{A} \hspace{4cm} 1.5.$$

When also considering voltage, one obtains the power density (P) in mW cm^{-2}, which is the measure of how quickly the device discharges per membrane area (Equation 1.6).

$$P = \frac{i \times V_{cell}}{A} \hspace{4cm} 1.6.$$

Equation 1.7. shows the state of Charge (SoC), which is the charged capacity stored, q_{charge}, over the theoretical capacity.

$$SoC = \frac{q_{charge}}{q_t} \hspace{4cm} 1.7.$$

The capacity decay rate is the loss in capacity over the total duration of the test and is typically a percentage loss per day or per cycle number. This metric is significant in determining the long-term stability of RAMs.

Coulombic efficiency (CE_{ff}) is the ratio of discharge capacity over charge capacity as a percentage (Equation 1.8.). Ion crossover through the membrane and/or irreversible side reactions results in a CE_{ff} of <99 %.

$$CE_{ff} = \frac{q_{discharge}}{q_{charge}} \hspace{4cm} 1.8.$$

Alongside the CE_{ff}, reports often state the voltage efficiency (VE_{ff}, Equation 1.9.) and energy efficiency (EE_{ff}, Equation 1.10.). VE_{ff} is the average ratio between charge and discharge voltages (E_{charge}, $E_{discharge}$) at constant current as a percentage. Voltage losses are caused by a mixture of overpotentials such as diffusion, polarisation, and ohmic overpotentials during charge and discharge processes.[6] Hence, VE_{ff} typically decreases with increasing current density.

$$VE_{ff} = \frac{E_{discharge}}{E_{charge}} \qquad\qquad 1.9.$$

The product of CE_{ff} and VE_{ff} yield the EE_{ff}, which gauges the applied and retained energy in percentage form.

$$EE_{ff} = CE_{ff} \times VE_{ff} \qquad\qquad 1.10.$$

It is important to report a range of performance metrics and cell attributes when discussing RFB systems to enable comprehensive electrochemical evaluations. It is through these features that we learn the causes of capacity loss and energy inefficiencies and take educated steps towards improvement. For example, to achieve high-energy-density RFBs it is important to prove a stable cycling stability through a capacity decay rate of <0.01 % per day (around 80 % capacity retention over five years) and a volumetric capacity of 80.4 Ah L^{-1}.[31]

The performance metrics and cell attributes give useful quantitative information over the cell, but it is important to extrapolate the physical origins of deviations in each. Reduction in performance is normally due to one of the key decay mechanisms: crossover, self-decomposition of active materials, or electrolyte side reactions.

Crossover refers to the transfer of RAMs across the IEM and subsequent self-discharge and/or irreversible side reaction resulting in a lower CE_{ff} and/or capacity decay.[31] Appropriate membrane design can reduce the effects of crossover through the Donnan effect and size exclusion techniques.[32–34] The extent to which crossover destroys the battery depends on whether the crossover species is irreversibly destroyed or if side products are damaging to the system. One of the key attributes of the VRFB system is the lack of damage from vanadium crossing into the alternate half-cell. This is because rebalancing the electrolyte recovers the capacity and gives the VRFB a tolerance of up to 97 % CE_{ff}. If the active species are permanently destroyed after crossover then practical applications require a CE_{ff} of 99.99 %.[35] The rate of crossover varies significantly at different SoC, RAM concentration, and can be influenced by migrating water or supporting ions due to pH fluctuations or volume imbalances from osmotic pressure.[31,36] If crossover is the major degradation mechanism then understanding the time-dependent capacity decay over a given period with respect to both redox cycles is critical.

It is challenging to compare the crossover rate between two different cell compositions due to the array of other cell testing parameters that also affect capacity decay rate. For example, thicker membranes, higher current densities, and smaller cell areas all lead to a decreased capacity decay rate even if the intrinsic rate of crossover remains high.[31]

Another primary route of capacity loss is self-decomposition of the RAMs.[37] This stems from their intrinsic instability and is the prominent decay mechanism in organic redox active material

(ORAM) based RFBs.[38–42] There are five major decay routes for organic systems: nucleophilic substitution, nucleophilic addition, disproportionation, dimerization/polymerisation, and tautomerisation.[38,41,43–45] Inorganic systems suffer similar losses through disproportionation, hydrolysis, or irreversible chemical reaction mechanisms leading to precipitation of the active materials.[46–48] As above, the time-dependent capacity fade rate is key to understanding the time-sensitivity of the decomposition process. Self-decomposition accelerates with RAM concentration, and so the amount of RAM present alongside the SoC should be taken into account when studying these systems.[31,49]

Electrolyte side reactions are a common cause of capacity decay in aqueous systems due to the water-splitting reactions of the hydrogen evolution reaction (HER) and the oxygen evolution reaction (OER). Non-aqueous solvent systems also undergo decomposition reactions but the wider electrochemical stability windows (ESWs) make this less common. Keeping the cell potential to values within the systems ESW avoids these side reactions. However, this is problematic when the RAMs are active beyond the potential of the window, and leads to low CE_{ff}, capacity loss, and pH fluctuations. This can in turn cause nucleophilic attack of OH^- on organic molecules and subsequent capacity decay.[31,43] The next section discusses the advantages and disadvantages of aqueous and non-aqueous organic-RFBs (ORFBs) in more detail.

1.3. Organic Redox Flow Batteries

'Traditional' RFBs exploit the multiple available oxidation states within inorganic RAMs. The scarcity and rising prices of mineral resources hinder their commercialisation, a problem that will only amplify as demand increases.

The VRFB is the RFB technology with the largest market presence. This is primarily due to its high reversibility, aqueous solvent, relatively large power output, and limited capacity loss. The low crossover capacity loss stems from utilising the same active element in each half-cell (V^{2+}/V^{3+} anolyte and VO^{2+}/VO_2^+ catholyte). These attributes lead to longer lifespans (around 20,000 charge/discharge cycles) than other flow systems (5,000 cycles).[50] Equations 1.11. and 1.12. show the VRFB charge reactions, with the full cell reaction in Equation 1.13.

Positive electrode reaction:

$$VO^{2+} + H_2O \xrightarrow{charge} VO_2^+ + 2H^+ + e^- \qquad E^o = +1.00\,V\;vs\;NHE \qquad 1.11.$$

Negative electrode reaction:

$$V^{3+} + e^- \xrightarrow{charge} V^{2+} \qquad E^o = -0.25\,V\;vs\;NHE \qquad 1.12.$$

Full cell:

$$VO^{2+} + V^{3+} + H_2O \xrightarrow{charge} VO_2^+ + V^{2+} + 2H^+ \qquad E^o = +1.25\,V\;vs\;NHE \qquad 1.13.$$
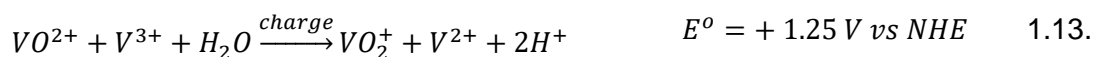
The overall energy of installed storage by RFBs was only 0.25 GW h in 2019, compared to 8.8 GW h of LIB capacity.[50] The high capital cost of the VRFB (\$ 300 – 800 kW h^{-1})[10] stems from the expensive vanadium electrolytes (\$ 80 kW h^{-1}) and the IEM (up to 40 % of the total battery cost).[51] This places them far out of reach of the DoE's 2023 goals. Despite the economic downsides, the VRFB and other inorganic RFB designs have received significant investment and reached commercialisation stage. The largest VRFB installation is in Dalian, China, rated at 200 MW/800 MW h.[37] The low energy densities of the systems means most RFB deployments are at grid-scale. Table 1.2. compares the performance metrics of the VRFB against a conventional LIB system. The table shows that energy density and cell potential limit the RFB performance against the LIB. Improving the benchmark VRFB's low energy density of <35 Wh L^{-1} is not easy as the system is at the maximum solubility limit and wider potentials are not possible without promoting HER or OER.[52]

Table 1.2. Conventional VRFB vs LIB performance metric comparison. Adapted from ref.[10]

Metric	VRFB	LIB
Electron Stoichiometry	1	1
Cell Potential (V)	1.25 – 1.8	3.6
Energy Density (Wh L^{-1})	35	240
Energy Efficiency (%)	75	90
Charge capacity (Ah L^{-1})	54	170
Specific Energy (Wh kg^{-1})	31	120

These inorganic technologies face limitations including high price, hazardousness, toxicity, slow electrode kinetics, and crossover. Recent research overcomes these difficulties by moving to ORAMs, wherein the redox couples comprise the earth abundant elements C, H, O, and N. Successful ORAMs may produce sustainable, environmentally benign, scalable, cost-effective, and high energy density RFBs.[53] Ideally, the organic species will be less toxic and corrosive than the current metal designs, improving both the environmental safety and ecological sustainability of the RFB.[54] Other devices already demonstrate the benefits of moving to organic materials, such as with radical organic polymers in solid state batteries, organic fuel cells and regenerative fuel cells.[55]

Projected ORAM costs are as low as $ 3 – 7 kg^{-1} with an electrolyte cost of less than $ 35 kW h^{-1} (based on half-cell estimates). This is an improvement over the predicted VRFB cost of $ 7 – 37 kg^{-1} (the wide range is representative of the uncertainty in supply for inorganic materials) and $ 80 kW h^{-1}.[56] The DoE cost targets of $ 4 kg^{-1} ($ 15 kA h^{-1}) and $7 kg^{-1} ($ 26 kA h^{-1}) are not unrealistic for ORAMs, given the base chemical cost of unsubstituted 9,10-anthraquinone (AQ) is only $ 3 kg^{-1} ($ 11.6 kA h^{-1}).[57]

The financial benefits from ORAMs stem from their abundance from a diverse range of natural sources. They therefore avoid the geopolitics and rarity concerns of their metallic counterparts. The first ORFB was reported only a few years ago, in 2011, and so the full potential of ORFBs is yet to be discovered.[58]

A key attribute of ORAMs lies their chemical tailorability, something that is not facile with metallic equivalents. The extensive structural database of organic molecules allows the design of the materials' characteristics through substituent modifications to give desirable properties. Tuneable properties include fast kinetics, high solubility, high stability, and high (for catholyte) and low (for anolyte) redox potentials.[53]

Low molar masses and high solubility of RAMs improve the energy density of a given amount of electrolyte and hence the overall capacity of the system. This reduces the overall cost per kW h and makes the technology more economically viable. For example, in a two-electron reduction 1,4-benzoquinone (BQ) has a molar mass of 108 g mol^{-1} and a capacity of ca. 496 A h kg^{-1}, whereas 9,10-anthraquinone-2,6-disulfonic acid disodium (AQDS) has a molar mass of 412 g mol^{-1} and a specific capacity of ca. 129 A h kg^{-1}.[10] Lower molecular weight organic RAMs also have higher diffusion coefficients (D_o, cm^2 s^{-1}), higher specific capacities, and lower costs, but are more likely to cross through the IEM.[57] Tuning molecular size and net charge minimises ion crossover.[40] Maximising the discharge voltage, valence number, and concentration of the ORAM maximises the electrolyte energy density. Ideally, the redox processes at the electrode occur under charge transfer control in low viscosity solutions.[10]

High solubility of the active species maintains high current flow whilst minimising mass transport losses. The inherent tuneability means ORAMs can have higher solubilities than metallic counterparts in both aqueous and non-aqueous electrolytes. For example, quinoxaline is soluble up to 4 M in KOH solution (0.9 M KCl, 0.1 M KOH, pH 12.9) with a reduction potential of −0.7 V (*vs* the standard hydrogen electrode (SHE)), and methyl-parabenzoquinone (Mr = 122.12 g mol^{-1}) is soluble to 6 M in ACN.[59] In comparison, the standard VRFB has a V concentration of 1.6 M in H_2SO_4.[60]

The main ORAM families are carbonyls (including quinones),[43,61–63] dialkoxybenzenes,[40] nitroxide radicals,[64,65] and heterocyclic aromatics.[44,66] Figure 1.4. depicts their general electrochemical processes.[28] Some families, such as quinones and nitroxide radicals, allow for multi-electron transfers. This means they are able to store more than twice the energy in a given concentration, and is a key method to improving the energy density.
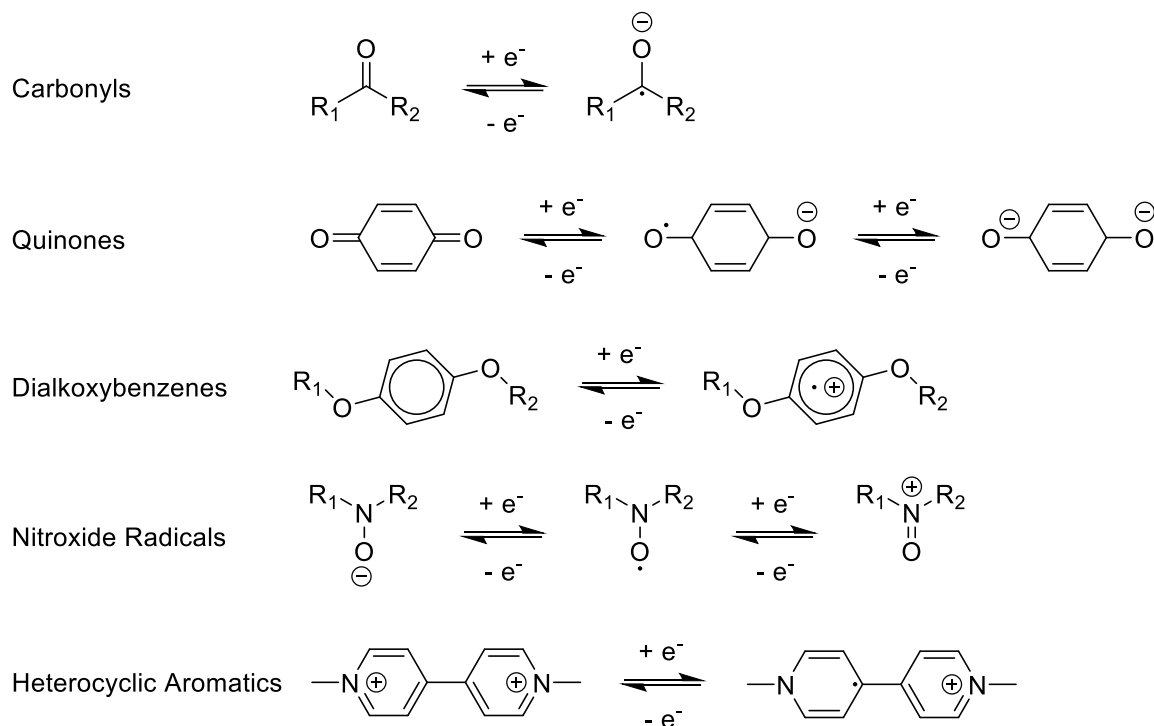
Figure 1.4. Electrochemical reactions of ORAMs typically used in ORFB literature.[28]

Metallic redox species form stable ions whereas organic molecules tend to undergo electron-transfer to form radical anions/cations and dianions/dications. These 'persistent' radical states are at the core of ORFB function. The high electron density at these sites renders them unstable, which is a major cause of irreversibility during cycling.[21] Overcoming this instability is the main challenge in ORFB development and spurs research into fine-tuning the peripheral substituents to improve stability.

The structural diversity, tuneabilty, and relatively stable redox mechanism of quinoyl species mean they are most widely investigated family. The redox square in Figure 1.5. demonstrates the different electrochemical pathways of quinones when in either protic or aprotic media. If protons are freely available, as in acidic or neutral aqueous media (typically between pH 0.5 – 10), they balance the charges of the reduced quinones. The quinone (Q) undergoes a proton-coupled electron transfer (PCET) to produce hydroquinone (H_2Q) via a process involving two protons and two electrons ($2H^+/2e^-$) which shows as one peak in the cyclic voltammogram (CV). The cationic species in Figure 1.5. are in grey because they are thermodynamically too high in energy to be involved in the PCET.
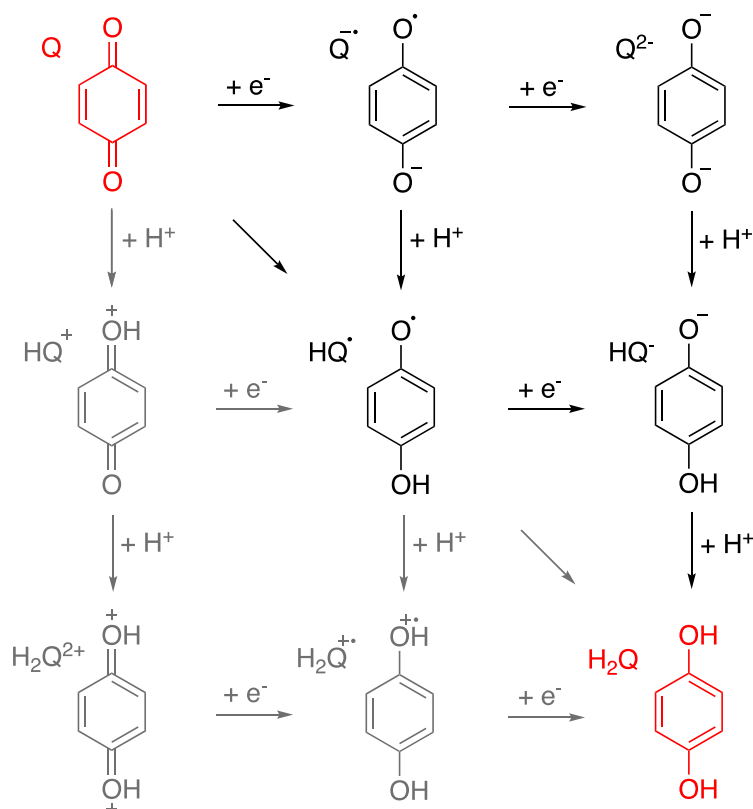
Figure 1.5. Quinone electron transfer and proton coupled electron transfer process.[68]

PCET is thermodynamically unlikely to occur at high pH. In highly basic conditions, as well as in non-aqueous media, the charge-containing radicals and dianions form through successive one-electron reduction steps ($2 \times 1e^-$). This corresponds to the top row of Figure 1.5. where the transitions between Q/Q^{-} and Q^{-}/Q^{2-} show as two separate redox waves in the CV.

The pH environment defines the ORFB as acid, alkaline, or neutral. Figure 1.5. shows how the electrochemical pathway and behaviour changes, depending on the local pH. It is therefore important to select an appropriate pH for each molecule. For example, the redox potential of quinones shifts from 0.21 to −0.30 V as pH increases from 0 – 11 due to the PCET.[38] Quinones tend to have low solubility at neutral pH, so acidic or alkaline environments are preferable. In

non-aqueous systems, the redox waves shift in the positive direction with stronger Lewis acid cations.[68]

Substituting quinones (and all ORAMs) lets us design their electrochemical properties. The computational study by Er *et al.* demonstrates how aromatic rings lower the redox potential from +0.7 V (*vs* SHE) for BQ to + 0.10 V (*vs* SHE) for AQ.[69] Through substituting AQ with electron-donating groups (EDGs) and pairing with a H_2Q catholyte, one forms an RFB with a cell potential >1 V. Wedege *et a*l.[57] show the position of the side groups on quinone species plays a more dominant role than the number of side groups in both solubility and redox potential. Recently, the Guzik group used high-throughput density functional theory (DFT) calculations to screen 300 quinone derivatives, predicting their redox potentials, substitution effects and structure-property relationships.[70] The team found carboxylic and sulfonic acid functionalising result in higher reduction potentials. The screening demonstrated the rarity of high reduction potential molecules stable to nucleophilic addition, but that bulk substitutions and pKa modulation can improve the aqueous stability. Gerhardt *et al.* reinforced this by showing that the position and hydrophilicity of functional groups vastly affects the reduction potentials of AQ derivatives, with a 200 mV difference between AQDS and dihydroxyanthraquinone dimethylsulfonic acid (DHAQDMS).[71] Similar computational studies have shown trends in other viable ORAM moieties, such as the work by de la Cruz *et al.* on phenanzines.[72]

Other than the ORAMs, the electrodes and membranes are also important battery components. The electrode surface provides the reaction site, and so they must have high specific surface area, electrical conductivity (σ), and stability. High ionic conductivity and high selectivity membranes reduce ohmic overpotentials and enhance the overall CE_{ff} and power density. The large molecular size of some ORAMs means ORFBs can avoid the conventional, expensive IEMs as the cheaper, more flexible, high ionic conductivity, porous polymer-composite membranes are able to prevent cross-over by the size exclusion effect.[73] Traditional membranes may also benefit from reduced ion-crossover due to the dense membrane structure and the Donnan exclusion effect.[22] Research is still yet to uncover a suitable membrane for non-aqueous systems, as these membranes typically suffer from low ion conductivity and limited stability. A key downside to ORAMs is that they may irreversibly adsorb onto the membrane during cycling, which increases resistance and decreases the output efficiency.[74]

ORFBs divide into 2 main categories: aqueous and non-aqueous systems. Aqueous ORFBs further divide by the pH of the electrolyte. Section 1.3.1. discusses existing literature surrounding these devices.

1.3.1. Aqueous *vs* Non-Aqueous Electrolytes

The wide range of redox potentials of ORAMs makes them exploitable as both anolyte and catholyte materials in both aqueous and non-aqueous RFBs. Tables 1.3. – 1.6. show the variety of structures used in key ORAMs in aqueous (Tables 1.3. – 1.5.) and non-aqueous (Table 1.6.) systems. Catholyte and anolyte molecules are in red and blue, respectively.

Most commercial units utilise aqueous electrolytes because of their inherent safety, abundance, low cost, and environmental neutrality. Techno-economic analysis estimates that an aqueous ORFB with a $ 5 kg^{-1} active material cost, 150 g mol^{-1} of transferable electrons and a 1.5 V OCV should equate to $ 120 kW h^{-1} at the system level. Cheaper electrolytes and economies of scale in volume productions will further reduce costs.[37]

For maximum electrolyte energy density, the discharge voltage, valence number and concentration of RAM must be maximised. A key disadvantage of aqueous ORFBs is that many ORAMs are insoluble in water. Simultaneously obtaining high solubility and high cell voltage in aqueous systems is a major challenge. The thermodynamic ESW of water (1.23 V) also limits the energy density and limits commercialisation.

Non-aqueous solvents provide wider ESWs (Acetonitrile (ACN) = 6 V, propylene carbonate (PC) = 4.5 V) and working temperature ranges which produces batteries with higher energy densities that are useful in more environments. This is an advantage over the VRFB, which is limited to between 10 – 45 °C due to V precipitation, and other water-based RFBs that cannot function below the freezing point of 0 °C.[60] The wider ESW means one can use ORAMs with higher potentials. There are also a wider pool of ORAMs soluble in non-aqueous media, making these systems a more versatile option. Additionally, radicals are often more stable in non-aqueous media. Computational work shows asymmetric charge distribution improves organic solubility.[75] If these high voltage systems can operate using highly soluble ORAMs (>1 mol dm^{-3}), then fewer ancillary parts and unit cells will be required for a given energy output.[10]

Nevertheless, non-aqueous electrolytes are more flammable, toxic and costly, which may counteract the improvements in energy density. Water-based electrolytes are low cost, around $ 0.1 kg^{-1}, and are unlikely to increase in price due to natural abundance and high-volume production.[56] Increasing the cell voltage lowers the expense for both the reactor and electrolyte and is the most effective cost reduction method in non-aqueous batteries. Further cost-saving tactics involve reducing RAM molar mass and utilising multi-electron transfers.[10]

An additional challenge of non-aqueous electrolytes is the low ionic conductivity (10^{-8} – 10^{-10} S cm^{-1}), which is about 100 times lower than aqueous systems (6×10^{-8} S cm^{-1} for pure water)

without salts.[10] This causes a large ohmic drop and decreases the VE_{ff}. The inherent low ionic conductivity necessitates costly conducting salts. Typical salts are tetrafluoroborates which have a predicted future cost of \$ 20 kg^{-1}.[56] This improves the non-aqueous conductivities to values comparable with salt water (5.6 × 10^{-2} S cm^{-1} for ACN with 1 M TEABF$_4$, 0.11 S cm^{-1} for 1.05 M KCl$_{(aq)}$).[10] Adding supporting salts also reduces the maximum ORAM solubility by the theory of partial molar volume for solvents. The cost and competing solute nature must be taken into consideration when deciding on the identity and concentration of the supporting electrolytes.[10]

A lack of optimised IEMs for non-aqueous systems leads to high cell resistances, low cost-effectiveness, crossover, and undesirable material-membrane interactions.[76] This results in low operational current densities of <0.5 mA cm^{-2} compared to aqueous RFBs at >100 mA cm^{-2} and is a bottleneck in non-aqueous ORFB research.[76] Approaches to solve this include developments in flow cell design and improvements in membrane permeance.[77,78]

In-depth techno-economic analysis is required to conclude the feasibility of ORAMs and determine the cost-benefit analysis of utilising high-energy organic electrolytes over the cheaper aqueous systems. Several in-depth reviews observe the advances in aqueous and non-aqueous ORFB technology covering the redox chemistries, cell designs, cell components, theoretical modelling, and cost analyses.[7,20,23,79–88] Specific reviews cover the solvent selection, cost evaluation, and molecular engineering aspects of non-aqueous ORFBs.[10,56,84,89,90] The rest of this section compares the existing ORAMs in the aqueous and non-aqueous literature.

1.3.1.1. Acidic Aqueous

The high proton concentration and migration rate (up to 3.62 × 10^{-3} cm^2 V^{-1} s^{-1}) in acidic media yields highly conductive electrolytes.[91] Table 1.3. shows an overview of acidic aqueous ORFBs.

Xu *et al.* report the first use of ORAMs in acidic aqueous RFBs in 2009 using the catholytes 4,5-dihydroxy-1,3-benzendisulfonate (Tiron) (0.72 V (*vs* SHE)) and 2,5-dihydroxybenzenedisulfonate (DHBS) (0.71 V (*vs* SHE)) against a PbSO$_4$ anolyte in 3 M H$_2$SO$_4$. Hydrophilic functionalisation of the quinone moieties with the electron-withdrawing group (EWG) -SO$_3$H improves the solubility and pushes the redox potentials to more positive values. The DHBS battery shows 99 % CE_{ff} over 100 cycles, but Michael addition of H$_2$O causes Tiron capacity fade.[85] A 67 % drop in CE_{ff} occurs in the first cycle due to a similar nucleophilic attack on the BDQS catholyte with an AQDS anolyte.[43] Functionalising the β-

position reduces the probability of Michael addition, as shown in the completely substituted 2,3,5,6-tetrakis((dimethylamino)methyl)hydroquinone (FQH$_2$).[92] FQH$_2$ has good solubility at 1.4 M and a capacity retention of 99.92 % cycle^{-1} when paired in an aqueous hybrid RFB with an Zn/[Zn(OH)$_4$]$^{2-}$ anolyte.[93] Liu *et al.* extend the conjugated FQH$_2$ structure to the biphenol-quinone derivative 3,3'-5,5'-tetramethylaminomethyle-4,4'-biphenol (TABP).[94] Fully occupying the hydroxyl ortho-position results in better stability >1.5 M and higher chemical stability (900 cycles).
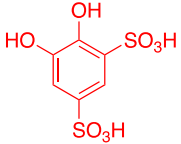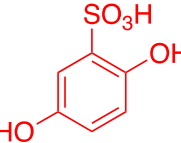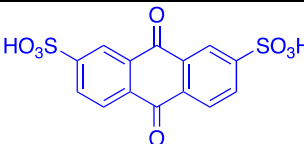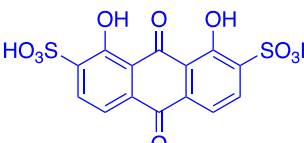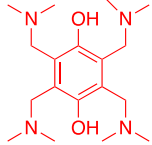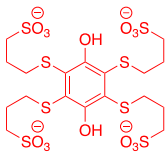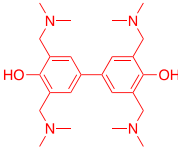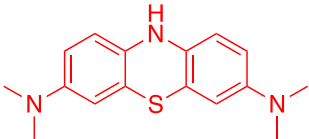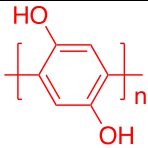
The extended π-system of AQ molecules makes them more stable anolytes than their benzo- and naphthoquinone counterparts, but reduces their solubility. Gerhardt *et al.* improve the water solubility of the AQDS anolyte to 1 M in 1 M H$_2$SO$_4$ by adding -SO$_3$H and -COOH groups.[71] Pairing this with a catholyte of Br$_2$ in 3 M HBr leads to the deterioration of AQ via a side reaction with the cross-contaminated catholyte, resulting in a low *CE$_{ff}$* and capacity decay.[38] Gerkin *et al.* show tetra-substituting the quinones with sulfonated thioethers forms highly soluble polyanionic quinones with inhibited IEM crossover.[95]

Relative stability of the charged and uncharged states also plays a role in battery performance. Lee *et al.* show deterioration of the charged H$_2$AQDS half-cell causes capacity decay, whereas the discharged AQDS shows no obvious chemical degradation against a V catholyte.[36,96] Overall, dimerisation and side reactions are critical in capacity decay, and the stability of functionalised quinones is still not satisfactory for an acidic aqueous RFB device.[92,97,98]

Outside of the quinone family, heteroaromatics phenothiazine derivatives, such as methylene blue, are attractive catholytes due to their low cost, rapid kinetics (0.32 cm s^{-1} in 3 M H$_2$SO$_4$), facile synthetic tuneability, and exceptional chemical stability (no capacity decay in 1200 cycles).[39,99]

Table 1.3. Acidic aqueous ORFBs. Adapted from [91].

RAM	Structure	E^0 (V)	Solubility (M)	Catholyte / Anolyte	j (mA cm^{-2})	Capacity Retention (%)	Cycle No.	E_d (Wh L^{-1}) / P (W cm^{-2})	Ref / Year
Tiron		0.65 *vs* SCE	1	PbSO$_4$	10	>90	10	- / -	[43] / 2016
DHBS		0.47 *vs* SCE	0.8	PbSO$_4$	10	-	-	- / -	[92] / 2017
AQDS		0.21 *vs* SHE	>1	Br$_2$	200	>99 cycle^{-1}	15	50 / 0.6	[38] / 2017
1,8-dihydroxyanthraquinone-2,7-disulfonic acid (DHAQDS)		0.23 *vs* SHE	>1	Br$_2$	200	Low	15	- / 0.7	[71] / 2016

Name	Structure	Potential		Counter					Ref / Year
FQH$_2$		0.7 vs SHE	1.4	Zn	20	>99.92 cycle^{-1}	50	Theoretical: 136 / 0.15	[93] / 2019
2,3,5,6-tetrakis(ethylsulfanyl-2'-sulfonate)-1,4-hydroquinone		0.61 vs NHE	1.0	AQDS	-	High	150	- / 0.18	[95] / 2020
TABP		0.91 vs SHE	>1.5	silicotungstic acid	40	High	900	- / 0.14	[94] / 2021
Methylene blue		0.57 vs NHE	>2	V^{2+}	60 – 140	High	900	- / -	[99] / 2019
Polyhydroquinone		0.69 vs SHE	-	Polyimide	20	70	300	- / -	[100] / 2019

1.3.1.2. Alkaline Aqueous

Hydroxyl ions also have a fast migration rate but their strongly nucleophilic nature is an issue for ORAM stability.[91] The deprotonation of OH$^-$ groups in alkaline media often improves ORAM solubilities, for example 2,5-dihydroxy-1,4-benzoquinone (DHBQ) is soluble to over 8 M in KOH.[101] Despite the high solubility, DHBQ's small size causes significant crossover and hence capacity decay. Wedege *et al.* increase the size to the more rigid 2-hydroxy-1,4-napthoquinone, but this drops the alkaline solubility to 0.5 M and does not prevent Michael addition.[57] Wang *et al.* introduce carboxyl groups to form 2-hydroxy-3-carboxy-1,4-napthoquinone (NQ(1,4)H), wherein the interaction between the carbonyl groups and napthoquinone π-system improve the solubility to 1.2 M and shift the redox potential more negative (-0.53 V (*vs* SHE)).[102] Pairing NQ(1,4)H in an RFB with ferrocyanide (K$_4$[Fe(CN)$_6$]) gives an OCV of 1 V and a high capacity retention of 94.7 % over 100 cycles.
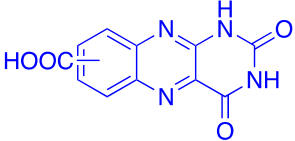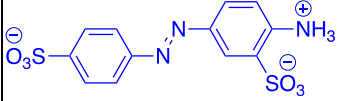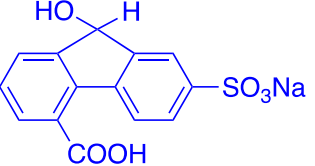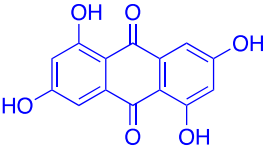
Lin *et al.* improve the cell potential to 1.2 V by increasing the anolyte size to 2,6-dihydroxyanthraquinone (2,6-DHAQ).[62] However, the reduced state of AQ is more fragile than its oxidative form and leads to undesirable side reactions and capacity decay.[36] Molecular engineering techniques of iteratively introducing carboxylic acid and phosphonic acid groups improves cell performance under weaker alkaline conditions (pH 12 and 9), suggesting high OH$^-$ concentration does not improve AQ stability.[63,103]

Other molecular families such as phenazine and alloxazine also show promise in alkaline aqueous ORFBs.[74,99,104] Alloxazines have high electrochemical stability, but need hydrophilic molecular tailoring to prevent π-stacking and precipitation.[40] Feng *et al.* recently uncovered the potential of ketone to alcohol conversion as a player in aqueous ORFB electrochemistry with the reversible ketone hydrogenation/dehydrogenation of fluorenone (FL).[105] Hollas *et al.* use molecular asymmetry and sulfonate groups to combat the limited aqueous solubility of ORAMs (near 0 for phenazine) with 7,8-dihydroxyphenazine-2-sulfonic acid (DHPS), achieving 1.4 M in 1 M NaOH.[74] A DHPS/K$_4$[Fe(CN)$_6$] ORFB has an OCV of 1.4 V with a reversible anolyte capacity of 67 Ah L^{-1} and a capacity retention of 99.98 % per cycle of 500 cycles.

Alkaline ORFB catholytes are limited and studies typically employ K$_4$[Fe(CN)$_6$] (0.36 V (*vs* SHE)).[106] However, the low stability of ferrocyanide in alkaline media means it must be in excessive quantities to limit its impact on capacity retention.[107] Functionalising phenazines with hydrophilic and amino acid groups presents another catholyte option.[108] The expansion of alkaline catholytes is critical for the future success of alkaline ORFBs.

Table 1.4. Alkaline Aqueous ORFBs. Adapted from [91].

RAM	Structure	E^o (V)	Solubility (M)	Catholyte/ Anolyte	j (mA cm^{-2})	Capacity Retention (%)	Cycle No.	E_d (Wh L^{-1}) / P (W cm^{-2})	Ref / Year
DHBQ		−0.72 vs SHE	8.0	K$_4$[Fe(CN)$_6$]	100	>99.96 cycle^{-1}	150	- / 0.3	[101] / 2018
NQ(1,4)H		−0.50 vs SHE	0.5	K$_4$[Fe(CN)$_6$]	-	50	30	- / -	[57] / 2016
2-Hydroxy-3-carboxy-1,4-naphthoquinone		−0.53 vs SHE	1.2	K$_4$[Fe(CN)$_6$]	100	>94.7	100	- / 0.25	[102] / 2018
2,6-DHAQ		−0.68 vs SHE	0.6	K$_4$[Fe(CN)$_6$]	100	>99.9 cycle^{-1}	100	- / -	[36] / 2018
DHPS		−0.86 vs NHE	1.8	K$_4$[Fe(CN)$_6$]	100	>99.8 cycle^{-1}	500	- / -	[74] / 2018

Name	Structure	Potential		Electrolyte		Efficiency			Ref / Year
Alloxazine-7,8-carboxylic acid	(structure)	-0.61 vs SHE	2.0	$K_4[Fe(CN)_6]$	100	91	400	0.35	[40] / 2016
4-amino-1,1′-azobenzene-3,4′-disulfonic acid monosodium salt	(structure)	$-0.79/-0.29$ vs Ag/AgCl	2.0	$K_4[Fe(CN)_6]$	40	>99.95 $cycle^{-1}$	500	- / -	[104] / 2020
4-carboxylic-7-sulfonate fluorenol	(structure)	-1.3 (vs NHE)	2.0	$K_4[Fe(CN)_6]$	100	99.98	700	- / -	[105] / 2021
1,3,5,7-tetrahydroxyanthraquinone	(structure)	-0.68 V (vs Ag/AgCl)	1.88	$K_4[Fe(CN)_6]$	100	95.2	1100	- / 0.36	[109] (2022)

1.3.1.3.   pH Neutral

The environmental benignity, mild conditions, safety, low cost, and stability of pH neutral electrolytes attracts a lot of attention for future EESSs.[91] Neutral pH RFBs avoid acid/base catalysed chemical degradation and thus demonstrate the most stable cycling performances.[42,44,110] Table 1.5. gives the structures of ORAMs used in pH neutral ORFBs.[91]

2,2,6,6-tetramethylpiperidin-1-oyxl (TEMPO) and viologen derivatives are the most recognised neutral aqueous ORFB catholyte and anolyte materials. TEMPO undergoes a single electron redox process at 0.75 V (*vs* SHE).[111] The delocalisation of electrons onto the N and O groups as well as the steric-hindering effect of the methyl groups gives impressive stability.[22] Hydrophilic functionalisation into 4-hydroxy-TEMPO (4-OH-TEMPO) yields high water solubility of 2.1 M (0.81 V (*vs* SHE)).[112]

Liu *et al.* report the first all-organic neutral pH ORFB in 2015. Pairing a 0.1 M 4-OH-TEMPO catholyte with a 4,4-dimethyl bipyridinium dichloride (MV) anolyte gives an OCV of 1.25 V and a CE_{ff} of nearly 100 % at 40 mA cm^{-2}.[39] Higher electrolyte concentrations (0.5 M) improve the EE_{ff} and capacity utilisation but crossover through the anion exchange membrane (AEM) and degradation reactions hinder capacity retention.

Synthetic modifications increase the stability. Substituting the cationic EWGs trimethylammonium (TMA-TEMPO) improves the solubility to 3.2 M and shifts the redox potential positive by 0.15 V. Charge repulsion alleviates crossover through the AEM and results in a stable cycling prformance.[22,113] Liu *et al.* substitute the positively charged 3-(Trimethylammonio)propoxy- (TMAP)-TEMPO with ammonium alkyl groups and improve the redox potential to 0.81 V (*vs* SHE). Pairing TMAP-TEMPO with a 1,1′-bis[3-(trimethylammonio)propyl]-4,4′-bipyridinium tetrachloride (BTMAP)-viologen anolyte yields an OCV of 1.1 V. The resulting ORFB has an impressive capacity retention of >99.974 % h^{-1} over 1000 cycles.[41] Including a different EWG, SO_3^- (SO_3^--TEMPO), yields a high capacity (<20 Ah L^{-1}) hybrid-RFB with Zn and less capacity decay than the parent 4-OH-TEMPO molecule.[114]

Side reactions hamper TEMPO's aqueous ORFB success. These include: disproportionation into oxoammonium and a nitroxyl anion, producing the redox inactive hydroxylamine; dimerization of this hydroxylamine with other TEMPO radicals; intramolecular proton transfer induced ring-opening in acidic media; and deprotonation in alkaline environments.[115,116] Janoschka *et al.* reduce side reactions and lessen crossover via steric hindrance by substituting polymers onto TEMPO- and MV.[73] The battery has 80 % capacity retention in 10,000 cycles at 20 mA cm^{-2}. The same group also show cycling stability of a bifunctional molecule by linking TEMPO and phenazine with triethylene glycol (TEG).[117] Other pH neutral

catelytes that show reasonable cycling stability include ferrocene (Fc) derivatives and triphenylamines.[42,118]

Low cost and high electrochemical reversibility make MV the most popular neutral pH ORFB anolyte material. MV undergoes a $2 \times 1e^-$ transfer. The insolubility of MV^0 in water means the second redox state is only reachable with the aid of hydrophilic substitution (typically with quaternary ammonium or sulfonate groups).[44,66,119]
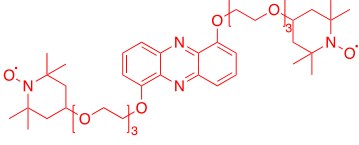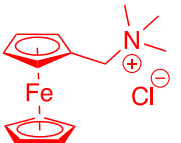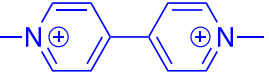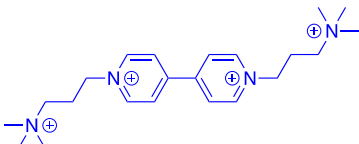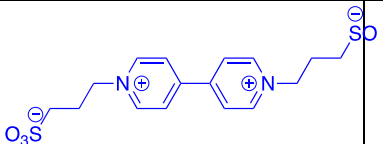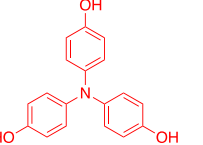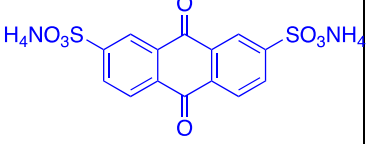
These substitutions improve the solubility and hinder the dimerization of reduced viologens, an effect also seen with hydroxyl-alkyl and phosphono-alkyl side chains.[110,120,121] Pairing ammonium substituted MV with ferrocenyl(methyl)trimethylammonium chloride (FcNCl) achieves an OCV of 1.39 V, theoretical energy and power densities of 75.9 Wh L^{-1} and 130 mW cm^{-2}, and a capacity retention of 99.99% per cycle.[66] Unfortunately, significant toxicity concerns dampen the future of MV in ORFB devices.[123]

Quinones are also alkaline ORFB anolyte candidates, for example the AQDS diammonium salt (AQDS-$(NH_4)_2$) by Hu *et al.*[124] The anolyte shows a 3-fold increase in solubility over the corresponding sodium salt and an energy density of 12.5 Wh L^{-1}. Pairing with an NH_4I catholyte results in stable cycling over 300 cycles.

Overall, many promising organic candidates exist over all pH ranges for aqueous ORFBs. However, the distinct limitation on energy density presented by their small ESW promotes research into non-aqueous electrolytes.

Table 1.5. Table of pH neutral ORFBs. Adapted from [91].

RAM	Structure	E^o (V)	Solubility (M)	Catholyte/ Anolyte	j (mA cm^{-2})	Capacity Retention (%)	Cycle No.	E_d (Wh L^{-1}) / P (W cm^{-2})	Ref / Year
4-OH-TEMPO		0.80 *vs* SHE	2.1	MV	40	99	100	Theoretical: 8.4 / -	[39] / 2016
TMA-TEMPO		0.95 *vs* SHE	2.3	MV	50	>99	100	38 / -	[113] / 2016
SO$_3$$^-$-TEMPO		0.80 *vs* SHE	1	Zn	3	93.6	1100	20.4 / -	[114] / 2017
TMAP-TEMPO		0.81 *vs* SHE	4.62	BTMAP-Viologen	100	99.993	1000	- / 0.13	[41] / 2019
Poly-TEMPO		0.90 *vs* SHE	N/A	Poly(MV)	100	80	10,000	10 / -	[73] / 2015

Name	Structure	Potential		Paired					Ref / Year
Combi-phenazine		0.80 vs SHE	0.01	Combi-phenazine	20	80	1800	- / -	117 / 2016
FcNCl		0.61 vs NHE	2	Viologen	60	90	700	Theoretical: 45.5 / 0.13	42 / 2017
MVCl$_2$		−0.45 vs NHE	3	4-OH-TEMPO	60	89	100	8.4 / 0.12	66 / 2017
BTMAP^{2+}-Vi^{2+}		−0.35 / −0.72 vs NHE	1.8	FcNCl	60	99	100	Theoretical: 79.5 Experimental: 8.04 / 0.13	66 / 2017
(SPr)$_2$−Vi^{2+}		−0.43 vs NHE	2	I$^-$	60	94.1	300	- / 0.07	125 / 2018
TPA(P3)		0.33 / 0.44 vs Ag/AgCl	0.6	Zn	40	80	300	16 / 0.23	118 / 2021
AQDS-(NH$_4$)$_2$		−0.20 vs Ag/AgCl	1.9	NH$_4$I	40	100	300	12.5 / 0.92	53,124 / 2019, 2019

1.3.1.4. Non-Aqueous

Non-aqueous electrolytes provide wider ESWs, temperature ranges, and ORAM possibilities, which culminates in higher energy density ORFBs. Table 1.6. gives a summary of molecules from the non-aqueous ORFB literature. Thus far, the widest OCV in a non-aqueous ORFBs is 2.97 V using a 2,5-di-tert-butyl-1-methoxy-4-[2′-methoxyethoxy]benzene (DBMMB) catholyte and 2-methylbenzophenone anolyte.[126] The low experimental energy density compared to the theoretical for this cell (4 *vs* 223 Wh L^{-1}) demonstrates the challenges in this area of research.

Pyridinium molecules, such as *N*-methyl-4-acetyl-pyridinium tetrafluoroborate, are stable, low molecular mass (111 g mol^{-1} per e$^-$) ORAMs. Substituting with EDGs lowers the potential along with the stability, but adding sterically hindering groups at N improves radical persistence to yield no capacity fade over 200 cycles.[127,128] Antoni *et al.* synthesised three- and four- state redox systems from pyridinium salts and carbenes, however, accessing the more charged states causes capacity decay.[129] The most stable non-aqueous RFB anolyte, developed by Sanford *et al.*, uses perpendicular xylyl substituent groups to protect against the homocoupling of pyridine radicals and C$_2$ and C$_5$ positions in acylpyridinium-based molecules.[127]

Including a bis(trifluoromethane)sulfonimide ([TFSI]$^-$) counter anion to MV makes it into the non-aqueous ORFB anolyte, MVTFSI. Pairing MVTFSI with (Ferrocenylmethyl)trimethylammonium bis(trifluoromethanesulfonyl)imide (FcNTFSI) gives a cell with a theoretical energy density similar to the VRFB at 24.9 Wh L^{-1}, a 88 % capacity retention over 100 cycles at 40 mA cm^{-2}, but an OCV of only 1.5 V.[130]

Benzophenone (BP) has a particularly negative redox potential (−2.16 V (*vs* Ag/AgNO$_3$)) and high solubility (4.3 M in ACN), and hence can yield high OCV's. Substituting methyl groups further lowers the potential to −2.29 V.[126] However, BP's radical stability is sensitive to the supporting salts and solvent environment, showing particular instability with alkali metals and stability with tetraethylammonium (TEA) salts.[126,131,132] FL is similar in structure to BP, but carries a less negative redox potential of −1.64 V (*vs* Ag/Ag$^+$). Studies pairing FL with DBMMB and FL-Phenazine in ACN corroborate the need for careful consideration of the supporting electrolyte and solvent system for radical stability. Fewer side reactions occur with the FL radical in DME with a [TEA][TFSI] supporting electrolyte compared to other systems, making it significantly more chemically stable.[133–135]

The quinone family is also promising for non-aqueous ORAM materials. Quinones capitalise on the oxygen radical anion for non-aqueous electrochemistry. Neutral Q reduces to a dianion via a radical anion semiquinone intermediate, the stability of which arises from high electron

delocalisation (See Figure 1.5.). The presence of two oxygen groups per quinone means they can store twice the number of electrons in any given concentration. Some derivations are able to store even higher electron counts, such as the high potential multi-electron tetra-aminoanthraquinone (DB-1). DB-1 has 4 oxidation states and one of the highest electrode potentials (4.4 V (*vs* Li), 1.35 (*vs* Ag/Ag$^+$)) and almost 100 % capacity retention over 50 cycles.[136]

ORAMs with other heteroatoms, such as S, are also ORFB candidates. For example, 2,1,3-benzothiadiazole (BzNSN) which has a relatively stable radical anion (half-life of 52 h), fast electrochemical kinetics, high solubility (>2 M in ACN), and low redox potential (−1.58 V (*vs* Ag/AgNO$_3$)).[91,137] Pairing BzNSN with DBMMB yields good cyclability, but increasing the ORAM concentration >1 M lowers the cell efficiency due to increasing viscosity and cell polarisation.[137] The radical anion stability also heavily depends on the arene substituent groups and the degree of ion-pairing in the solution, with Li$^+$ pairs providing the least stability.[137,138]

DBMMB's high redox potential (0.74 V (*vs* Ag/AgNO$_3$)), stable radical cation (half-life of 230 h in 0.5 M LiTFSI ACN), compatibility with a range of anolyte materials, and good solubility make it one of the useful non-aqueous catholytes.[138,139] Other catholyte candidates include phenazine and phenothiazine derivatives. These have a similar polyaromatic backbone to AQ, but with N-heteroatoms substituted in place of the carbonyl functional groups. Unfortunately, this does not mean that both electron transfers are accessible like in AQ. For example, in phenanzine only the first redox process at −1.5 V (*vs* Ag/AgNO$_3$) is reversible.[140] Substituting oligomeric ethylene glycol ether groups shifts this more negative to −1.72 V (*vs* Ag/AgNO$_3$). A cell of the substituted phenazine anolyte against a substituted triarylamine catholyte gives a *CE$_{ff}$* of >95 %.[141] Further iterations by Kwon *et al.* result in dimethyoxy- and dimethoxyethyl-phenazine derivatives.[135] The latter holds a redox potential of 0.5 V (*vs* Fc/Fc$^+$) and an OCV of 2.0 V when paired with FL, with a 99.3 % capacity retention per cycle over 200 cycles.[134,135] The energy density of 17 Wh L^{-1} is among the highest of all reported non-aqueous ORFBs.

N-methyl phthalimide (NMePh) has a particularly negative redox potential at −1.79 V (*vs* Ag/Ag$^+$). Wei *et al.* report an NMePh/DBMMB ORFB with an OCV of 2.30 V that operates up to 50 mA cm^{-2} with constant capacity for 50 cycles.[76] Zhang *et al.* overcome the low solubility (<0.7M in DME) by using the eutectic electrolyte NMePh: LiTFSI:Urea, yielding a 6-fold improvement.[142] Section 1.4. and Chapter 6. discuss the opportunities of this eutectic concept in more detail.

Azobenzenes are ORAM anolytes based on the π-conjugated structure of an N=N bond linking two phenyl rings. They have high solubility (4 – 5 M) in organic electrolytes, and when paired

with DBMMB exhibit an EE_{ff} of 63.5 % at a current density of 100 mA cm^{-2}.[143] Cyclopropenium has a high oxidation potential of >0.8 V (*vs* Fc/Fc$^+$), with the tris(disubstituted-amino) cyclopropenium cations only showing a <3 % capacity fade over 200 cycles.[144] Further substitutions, such as with meththio- groups, raise the redox potential to 1.33 V (*vs* Fc/Fc$^+$) but the higher energy radical dications lower cycling stability.[145] Shrestha *et al.* demonstrate a battery with >95 % capacity retention with an OCV of 1.57 V by pairing cyclopropenium with a pyridinium anolyte.[146]

1.3.2. Perspectives on Organic Redox Flow Batteries
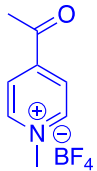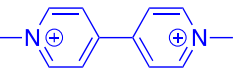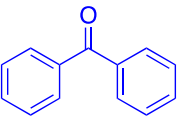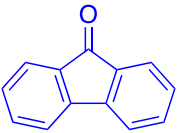
RFBs are one of the most promising electrochemical technologies for large-scale stationary ESS due to their low cost, chemical diversity, tailorable designs, and high safety. However, there remain significant challenges to overcome before widespread deployment is possible. These include low energy density, electrochemical stability, membrane lifetime and permeability, and capital cost.
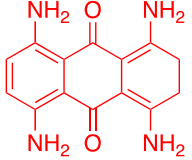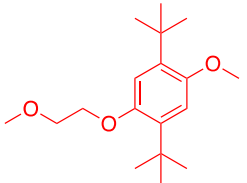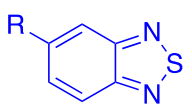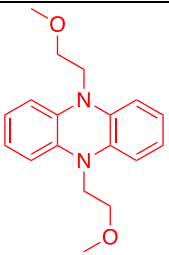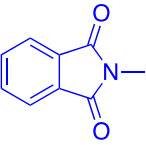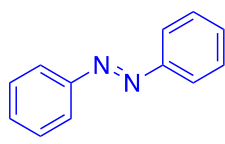
To be economically competitive, the DoE states the RFB system must have a system capital cost of <\$ 150 Wh kg^{-1} or an energy density of 240 Wh L^{-1}. To be technologically competitive it must equal or improve upon the conventional LIB, which operates at 120 Wh kg^{-1} and 240 Wh L^{-1}. The relatively high cost of transition metals limits their energy density and make ORAMs attractive. However, the search for an appropriate ORAM and electrolyte composition is still a long way from reaching the DoE targets.
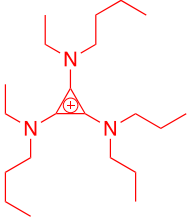
ORAMs benefit from flexible chemistry, adaptable electrochemistry, and cost-effectiveness, which befit them to the future RFB rollout. Molecular degradation is the main roadblock to developing successful ORFB electrolytes.[36] Thorough knowledge of the degradation pathways of newly proposed ORAMs is critical to developing mitigation strategies and improving longevity.

Electrolytes can be either aqueous or non-aqueous. Aqueous systems currently dominate the market due to their high ionic conductivity, good stability, low operational cost, and high safety. However, the low ESW limits the energy density and hinders mass commercialisation. On the other hand, non-aqueous RFBs have intrinsically wider operating temperatures and ESWs, alongside a wider library of ORAMs with more opportunity for chemical tuning. These metrics can create much higher energy density ORFBs. Low ionic conductivities, side reactions, higher costs, flammability, toxicity, and poor cycling performance due to un-optimised IEMs limit their wide-scale development and demand further research.

Table 1.6. Overview of non-aqueous ORAMs. Adapted from [91].

RAM	Structure	E^o (V)	Solubility (M)	Catholyte/Anolyte	j (mA cm^{-2})	Capacity Retention (%)	Cycle No.	E_d (Wh L^{-1}) / P (W cm^{-2})	Ref / Year
Pyridinium		−2.20 vs Ag/Ag$^+$	1.5	Fc/Fc$^+$	5	100	200	- / -	[127–129] / 2015, 2017, 2019
MVTFSI		−1.20 vs Fc/Fc$^+$	0.98	FcNTFSI	40	88	100	Theoretical: 24.9 Experimental 5.66 / -	[130] / 2018
BP		−2.97 vs Ag/Ag$^+$	5.6	DBMMB	7.5	~80	50	Theoretical: 223 Experimental : 4 / -	[126,131] / 2017, 2019
FL		−1.64 vs Ag/Ag$^+$	0.9	DBMMB	15	90	50	15 / -	[133–135] / 2015, 2019, 2018

Name	Structure	Potential		Pair					Ref / Year
DB-1		1.35 *vs* Ag/Ag+	1	Li	20	100	50	22 / -	[136] / 2021
DBMMB		0.82 *vs* Ag/Ag+	0.9	FL	15	20	10	15 / -	[133,137,138] / 2015, 2018, 2017
BzNSN		−1.58 *vs* Ag/Ag+	>5	DBMMB	60	80	150	- / -	[137,138] / 2018, 2017
Phenazine derivatives		0.50 V *vs* Fc/Fc+	0.5	FL	20	99.94	200	17 / -	[134,135,140] / 2020, 2021, 2019
N-MePh		−1.77 *vs* Ag/Ag+	0.7 (DME), 4 (DES)	DBMMB	35	100	50	9.3 / -	[76] / 2016
Azobenzene		−1.76 *vs* Ag/AgNO3	5	DBMMB	80	-	50	Theoretical: 40.1 / 0.34	[143] / 2021

66

Cyclopropenium		0.87 - 1.56 V *vs* Fc/Fc⁺	1.7	Pyridinium-derivative		95 %	200	- / -	146 / 2020

1.4. Room-Temperature Ionic Liquids and Deep Eutectic Solvents

1.4.1. Room-Temperature Ionic Liquids

Aqueous systems have high power density (10 – 700 mW cm^{-2}) and safety, but low energy density (<38 Wh L^{-1}) as they are limited by the ESW of water (1.23 V). Methods of improving the energy density lie in multi-electron redox processes and additives to improve solubility. Non-aqueous systems offer wider operational ranges but suffer from low RAM solubility (<0.1 M) and poor cycling stability which causes low experimental energy density (<22 Wh L^{-1}) and power density (1 – 10 mW cm^{-2}). The most effective mitigation strategy is molecular engineering, which can be complex with expensive synthetic steps.[147]

Room-temperature ionic liquids (RTILs) and deep eutectic solvents (DESs) propose an alternate class of non-aqueous electrolytes that overcome some of the limitations in conventional systems. RTILs are room temperature molten salts that are liquid <100 °C and typically comprise an organic component and an ionic salt. At least one of the molecular structures present a delocalised charge or charge shielding. This prevents a stable crystal lattice from forming and causes the low melting point.[148]

RTILs are characterised by low vapour pressure, non-flammability, high thermal and chemical stability, high density (ρ) and intrinsic conductivity, and wide electrochemical stability windows (> 4 V).[149] These attributes have led to their use in sensors, electrochemical capacitors, LIBs, Pb-acid batteries, dye-sensitised solar cells, fuel cells, and RFBs.[150–156] Another interesting application of RTILs in RFBs lies in membrane-free configurations.[157] Section 1.5. covers this concept in more detail.

These characteristics pique an interest for RTILs in RFBs. Li *et al.* pioneered RTIL-RFBs in 2012 with a 1-ethyl-3-methyl imidazolium hexafluorophosphate ([EMIm][PF$_6$]) additive (0.2 M) to a non-aqueous vanadium acetylacetonate (V(acac)$_3$) RFB.[158] The cell boasts an OCV of 2.4 V but low *CE$_{ff}$*'s of 57 %. Ejigu *et al.* studied a range of metal acac complexes in RTILs in 2015, employing an [EMIm][TFSI] electrolyte. The relatively low viscosity (27 mPa s) and high ionic conductivity of [EMIm][TFSI] presents it as a favourable electrolyte, achieving a *CE$_{ff}$* of 72 % with V(acac)$_3$.[159] The D_o values are an order of magnitude lower than in ACN systems, meaning sluggish mass transport will be an issue.

RTILs also extend to ORFBs. In ORFBs one must also consider possible reactions between the supporting anions and the ORAMs that may lead to instability.[132] Wei *et al.* show the inherent stability of the [TEA][TFSI] RTIL and the DME solvent in a FL/DBMMB cell, resulting in the highest capacity retention (>90 % over 50 cycles) of all RTILs in the study.[133]

Wang *et al.* demonstrate a stable cycling performance over 50 cycles using [TEA][TFSI] in ACN for BP/1,4-di-*tert*-butyl-2,5-dimethyoxybenzene (DBB), resulting in a high OCV of 2.95 V and a CE_{ff} of 97 %, but a low EE_{ff} of 44 %.[132] [TEA][TFSI] has superior performance over all the salts and RTILs in the report, with the BF_4^-, PF_6^-, and $[EMIm]^+$ likely interacting with the free radicals of the active species.[132] The $[TFSI]^-$ anion is, however, much more costly than the other anions.

Wylie *et al.* show RTIL electrolytes improve the reversibility of nitroxide radicals over conventional electrolytes whilst increasing the redox potential to 5.5 V against the 2.2 V theoretically possible in aqueous systems. The cell did however, only achieve a CE_{ff} of 61 %, indicating there is still significant capacity loss.[160]

High CE_{ff}'s of 99.5 % and 99.7 % are possible by pairing 4-OH-TEMPO (0.6 M) and MV (0.6 M) in 3 mM 1-butyl-methylimidazolium chloride ([BMIm]Cl) and [EMIm]Cl, respectively, in an aqueous RFB. Cycling the systems >150 times achieves capacity retentions >91 %, but the small cell voltage of 1.2 V limits the energy density to around 25 Wh kg^{-1}.[161]

1.4.2. Deep Eutectic Solvents

Whilst RTILs display many advantages for battery electrolytes, they come with high costs, complex and non-environmentally friendly synthetic routes, hazardous toxicity and poor biodegradability.[162,163] The physical properties of RTILs is heavily dependent on their purity. The expensive and sometimes challenging purification pathways only adds to their already high cost.

A simpler and more affordable solvent system is the DES. The first DES was coined by Abbot *et al.* in 2003.[164] A DES is a eutectic mixture typically formed from Lewis or Brønsted acids and bases. Table 1.7. gives the general classifications of DES systems, where Cat$^+$ is generally an ammonium, sulfonium, or phosphonium cation and X$^-$ is a halide anion.[165]

Table 1.7. General classification of DES systems. Reprinted with permission from ref [165]. Copyright (2014) American Chemical Society.

Type	General Formula	Terms
Type I	$Cat^+X^-zMCl_x$	M = Zn, Sn, Fe, Al, Ga, In
Type II	$Cat^+X^-zMCl_x \cdot yH_2O$	M = Cr, Co, Cu, Ni, Fe
Type III	Cat^+X^-zRZ	Z = CONH$_2$, COOH, OH
Type IV	$MCl_x + RZ = MCl^+_{x-1} \cdot$ $RZ + MCl^-_{x+1}$	M = Al, Zn and Z = CONH$_2$, OH

Type III DESs usually comprise an organic salt that is a hydrogen bond acceptor (HBA), typically an ammonium or phosphonium cation, and a hydrogen bond donor (HBD) that can be a wide range of components involving: amides, metallic salts, alcohols, carboxylic acids and amines.[166] They can therefore be completely organic. These are often binary mixtures but can have ternary or even quaternary compositions. Figure 1.6. shows a sample of the wide variety of HBA and HBD combinations that can form Type III DESs. Many of these molecules come from biomass, increasing the DES sustainability credentials.
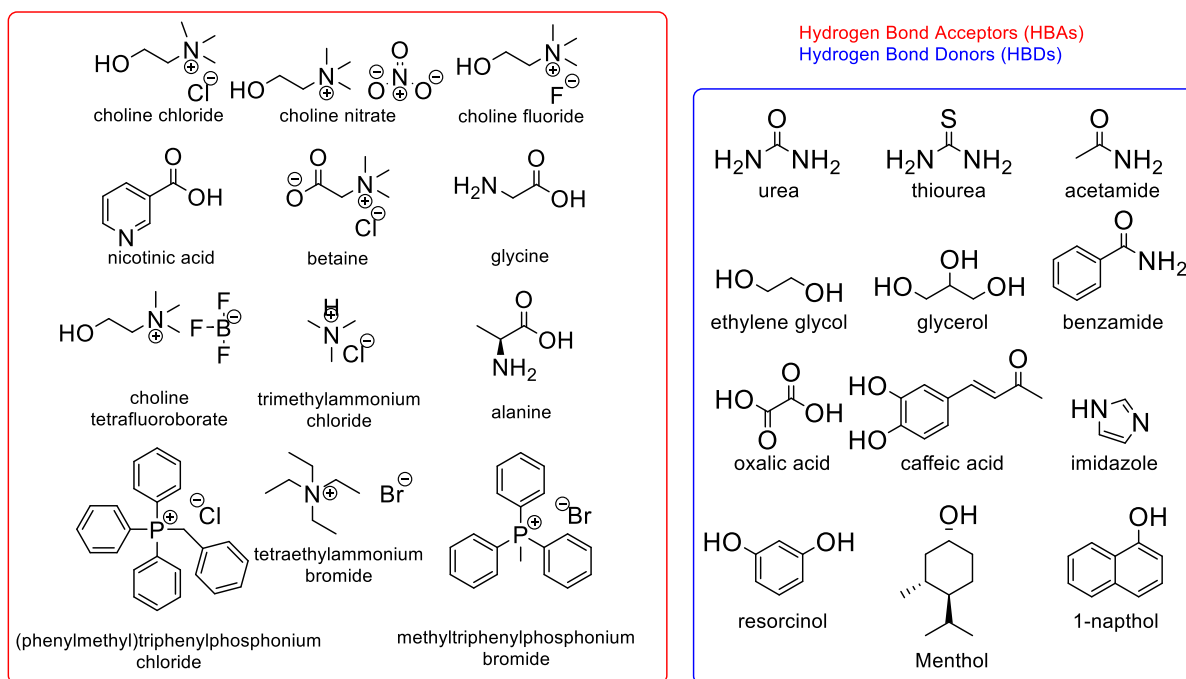
Figure 1.6. Molecular structures of some possible hydrogen bond acceptor and donor molecules that could form DESs.

DESs have melting points (T_m) far lower than their constituent parts and can even be liquid at room temperature. This physical phenomenon is due to a reduction in lattice energy. The interactions between the components lead to a depression in the T_m of the mixture (Figure 1.7.). The depression in T_m relates to the magnitude of HBD and HBA interactions, which depends on the nature and the mole ratio of the species involved.[167] If one or more of the constituent parts are redox active, then these electrolytes could possible form highly concentrated electrolyte solutions.

An advantage of DESs is their simple synthesis and biodegradable nature. DES synthesis comprises simply mixing the parent compounds until a homogenous liquid forms, with no additional purification steps. Thus, the atom economy for the final DES is the highest possible. Additionally, DESs are non-reactive with water, and the addition of water or other co-solvents can even improve their physicochemical properties.[169,170]
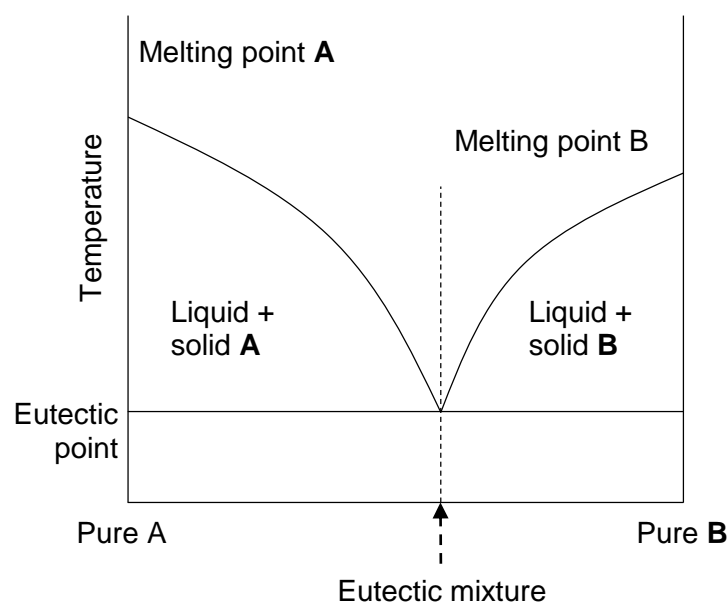
Figure 1.7. Binary phase diagram for eutectic mixtures.[189]

DESs share many characteristics with RTILs, including low-volatility, compositional tuneability, high thermal and chemical stability, good electrochemical stability and non-flammability. These favourable attributes make DESs applicable in electrodeposition, electropolishing, electrochemistry, separation processes, chemical and biochemical reactions, and organic and inorganic synthesis.[163,171–177] The low cost and high energy density make DESs an interesting candidate for ESS, however there are few patents on the topic.[178–180]

The identity of the HBD and the salt tunes the DES properties. High-throughput techniques are in development to streamline the research on the over 10^{18} possible DES structures.[181] Amide HBDs exhibit the lowest viscosities (η) amongst ammonium-based DESs, but nitrite HBDs have lower η than acidic- and amine-based, which results in higher conductivities.[182]

Approaches to improving conductivity involve altering the intrinsic components, adding co-solvents, or including functional additives. These ternary mixtures also tend to have a positive impact on η and ρ. The typically high surface tension and viscosity of eutectic electrolytes means one must pay special attention to the electrolyte/electrode interface, as these properties can lead to insufficient contact between the two.[183]

It is facile to map the significance of intermolecular interactions on the DES and its resulting phase behaviour. However, a systematic expansion of the methodology into thermodynamic models and correlation to new ORAM systems remains unclear. This is primarily because no existing models can account for the complicated effects from the many different HBA/HBD interactions, ionic interactions, and steric effects created by molecular geometries.[184]

Table 1.8. shows how the physicochemical limitations of some of the most well-known DES systems compare with pure water and ACN.[185,186] The fluid properties depend on the

molecular size and the availability of holes of appropriate dimensions to allow mobility.[187] The most widely studied DES system, ethaline, comprises choline chloride (ChCl) and ethylene glycol (EG) in a 1:2 ratio. ChCl is commonly chosen as the HBA due to its low cost, low toxicity, biodegradability, and biocompatibility.[167] Ethaline has the most favourable fluid properties of the room-temperature DESs, making it a popular choice for DES-based electrolytes. The viscosities and densities are significantly higher than typical aqueous and non-aqueous electrolytes. This compounds into low D_o values alongside the insufficient conductivities and reveals the chemical engineering challenge posed by DES-based RFBs.

Table 1.8. The physicochemical properties of the most common DES systems. Data from [185], [186] and [10] for (a) and (b), and (c) respectively.

DES	Molar Ratio	T_m (°C)	ρ (g cm^{-3})	η at 298 K (mPa s)	σ at 298 K (mS cm^{-1})	ESW (V)
Ethaline (ChCl/ethylene glycol)[a]	1:2	−66	1.11	42	7.61	3.61
Reline (ChCl/urea)[a]	1:2	12	1.20	750	0.20	4.29
Maline (ChCl/malonic acid)[a]	1:2	10	1.4	1124	0.88	4.25
ChCl/glycerol[a]	1:2	−40	1.25	315	1.05	3.59
Pure H$_2$O	-	0	0.997	0.890	1×10^{-5} [c] (110 with 1.05 M KCl)[b]	1.23
Pure ACN	-	−43	0.79	0.37	1×10^{-7} [c] (56 with 1 M TEABF$_4$)[b]	5.5

DES systems benefit from wider ESWs than aqueous counterparts due to a lack of HER and OER. The ESW is mainly dictated by the salt identity and water content.[188] DESs tend to be hygroscopic and water traces are unavoidable on a commercial scale.[189] Fortunately, small quantities of water do not affect the ESW as the H$_2$O molecules are confined in the hydrogen-

bonding network. Water inclusion actually serves to decrease the density and viscosity whilst increasing conductivity. Adding up to 17 wt% water or ACN to the 'solvated ionic liquid' MeO-TEMPO-LiTFSI battery disrupts the ion pairs and decreases the viscosity and improves battery performance.[190] Larger quantities of water weaken the hydrogen bonding network and eventually the ESW decreases with increasing water content. For example reline (ChCl/urea) can tolerate up to 51 wt% of water before any major structural changes.[191]

DES system can be metal- or organic-based. Table 1.9. shows the characteristics of both types of DES systems used as RFB electrolytes. Inorganic systems are typically alkali metal salts and organic systems tend to utilise carbonyl, nitroxyl radical, or methoxy functional groups as a DES driving force.[192]

Techno-economic analyses suggests non-aqueous RFBs require 1-2 M RAM to be competitive with other battery types.[193] The high concentrations in Table 1.9. show how the DES electrolytes can be competitive. However, alongside high active material concentrations, the systems also need sufficient ionic conductivity (>5 mS cm^{-1}) and low viscosity (<10 mPa s) to minimise hydrodynamic resistance for battery applications.[193]

Many DES electrolytes have inherent conductivity provided by the salt component, such as ChCl or LiTFSI. However, some systems comprise only non-ionic components and hence have no conductivity, meaning supporting salts are necessary to create a functional electrolyte. Ionic conductivity increases with increasing supporting salt concentration until it peaks and falls due to ion aggregation and reductions in ionic mobility.[187] One must therefore also consider the identity, solubility, and cost of the supporting salt.

Little literature covers completely organic-based RFBs, and there is yet to be a flowing fully organic DES-RFB. This is unsurprising given the relative infancy of both the ORFB and DES fields. A further issue is that even though studies quote high RAM solubilities, demonstration units rarely use such concentrations, or do so but with miniscule volumes. For example, Zhang *et al.* discuss a redox active DES based on a 2:2:1.6 ratio of NMePh-LiTFSI-Urea in DCE with an active ORAM concentration of 4 M and a low viscosity of 15 mPa s.[142] The full demonstration cell however, only uses an ORAM concentration of 0.5 M. Similar adaptations occur in the "solvated ionic liquid" study on MeO-TEMPO:LiTFSI.[190] The report discusses an electrolyte with >2 M concentration with an energy density of 200 Wh L^{-1}. However, the high viscosity (72 mPa s) means the cell is only tested at low current densities (0.1 mA cm^{-2}) and low electrolyte volumes (20 – 50 µL).[190]

Table 1.9. Characteristics of metal- and organic-based RTIL and DES electrolytes.[184]

DES	Composition	Ternary Component/Additive	Molar Ratio	RAM Concentration (M)	η at 298 K (mPa s)	σ at 298 K (mS cm^{-1})	Ref / Year
Fe-DES	FeCl$_3$.6H$_2$O-Urea	EG	1:2:0	3.9	70	10	194,195 / 2017, 2016
			2:1:0	5.4	50	30	
			1:2:1	3.3	140	9	
			1:2:6	1.8	55	10	
			2:1:2	4.2	80	12	
Al-DES	AlCl$_3$-Urea	DCE	1:1.3:0	4.8	-	1.9	189,194,196,197 / 2017, 2017, 2014, 2021
			1:1:0		133.2	1.02	
			1:1.2:0		87.6	1.18	
			1:1.5:0		77.7	1.21	
			1:1.3:1.5		-	-	
Li-DES	LiClO$_4$-Acetamide	H$_2$O	1:4.3:0.5	3.2	157.8	1.3	188,189 / 2021, 2021
			1:4.3:1		98.7	2.5	
			1:4.3:1.5		6	3.3	
			1:4.3:5		14	12.3	
		H$_2$O + ACN	1:4.3:1:3.3		9.1	13.3	
			1:4.3:1:6		5.8	15.6	
			1:4.3:1:4.4		4.4	19.3	
			1:4.2:1:18.1		1.1	25.6	

	LiTFSI-Trifluoroacetamide (303 K)	EC	1:2:0		134	0.26	[198] / 2020
			1:4:0		59.2	1.53	
			1:4 + 10 wt%		30.5	1.86	
			1:4 + 12 wt%		28.6	2.59	
			1:4 + 30 wt%		-	3.49	
Zn-DES	ZnCl$_2$-Acetamide		1:2	4.5 – 6.5	10 – 25	1	[199,200] / 2012, 2018
	ZnCl$_2$-EG		1:3		274.75	0.36	
	Zn(TFSI)$_2$-Acetamide		1:4		2130	0.16	
			1:5		1890	0.19	
			1:7		789	0.31	
Pthalimide-based	NMePh-LiTFSI	Urea	2:1:0	4.0	5	1-2	[142] / 2018
			2:1:3	2	-	4-5	
BQ-based	BQ-LiTFSI		1:1	-	-	-	[192] / 2021
Fc-based	Fc-LiTFSI	EC	2:1:0	3.7	-	-	
			2:2:3	2.8	-	-	
Viologen-based	EG-malonic-viologen		4:1	4.2	-	-	[201] / 2017
MeO-TEMPO-based	EC-LiTFSI-Fc		-	2.0	-	2.4	[190] 2015
BuPh-DMFc				3.5	4.5	1×10^{-4}	[202] / 2019
		0.1 M TEABF$_4$, ACN		2.0	16.1	3.3	
PTIO-based	1:4 ChCl:EG		1:4	0.1			[203] / 2021

Another reason for using lower concentrations is that the high concentration electrolytes require a significantly long charge time to reach a reasonable SoC. This experimental limitation is a fundamental challenge in researching high concentration electrolytes. For example, it would take over 133 days to reach 100 % SoC in a static 15 mL cell with a 4 M active concentration at a current of 0.005 A. Incorporating flow, however, will improve these metrics. Additionally, viscosity increases with increasing RAM concentration whilst the ionic conductivity drops rapidly. This leads to high resistances which require low charging currents (~0.1 mA cm^{-2}) to limit excess ohmic loss.[160] This substantially deteriorates the rate performance of the batteries.[22] Researchers therefore either lower the concentration and/or the electrolyte volume to combat these restrictions. This makes it difficult to extrapolate literature into full-scale industrially applicable RFB systems.

Zhang *et al.* demonstrate a flow cell with an OCV of 1.8 V based on a biredox eutectic electrolyte of *N*-butylphthalimide (BuPh) and 1,1-dimethylferrocene (DMFc).[202] The eutectic electrolyte has active material concentrations of 3.5 M, but the demonstration cell only uses 1 M electrolyte at 5 mL and 40 µL under flow and static modes, respectively. Additionally, 1 M TEABF$_4$ is necessary for sufficient ionic conductivity (3.3 mS cm^{-1}). The final cell achieves a power density of 192 mW cm^{-2} but an EE_{ff} of only 45 % over 20 cycles due to crossover. In a move away from metallic components, the team also produce a room temperature DES with a BuPh-TEMPO mixture; however, they give no further information.

The hybrid flowing system by Ding *et al.* utilises hydrotropic solubilisation of H$_2$Q with urea to yield a high energy density catholyte against Al- and Zn-DES based anolytes.[204] Adding 4 M urea to aqueous H$_2$Q leads to a 3-fold increase in solubility to 1.5 M. This hydrotropic effect extends to other organic molecules, with catechol soluble up to almost 16 M with 4 M urea. The team discuss a 5.6 M Al-DES anolyte, but only use 0.5 M in the demonstration battery due to viscosity issues. The demonstration battery's power density (1.5 mW cm^{-2} at 2 mA cm^{-2}) is comparable with reported non-aqueous RFBs, but inferior to aqueous systems. The team extend the study to an all-organic system by pairing the organic catholyte with aqueous organic anolyte 0.4 M anthraflavic acid; however, the latter half-cell is not a DES electrolyte.

ORAMs still face instability issues in DES electrolytes. For example, the nitroxide radical 2-phenyl-4,4,5,5-tetramethylimidazoline-1-oxyl-3-oxide (PTIO) only has a 50 % round-trip efficiency in a 1:4 ChCl:EG DES RFB system.[203] The low performance is due to the instability of oxidised PTIO states. PTIO, which dissolves up to 2.6 M in ACN, shows limited solubility (0.5 M) in the electrolyte at 30 °C and crystallises below this temperature.

Although most of the progress in the DES RFB field covers metallic systems, the possible improvements in both energy density and cost from developing a DES-ORFB are significant.

Chapter 6. of this thesis investigates DES-ORFB systems for high energy, low-cost, and scalable flow batteries. Researching these systems is not facile. The inherent ORAM instability paired with the challenging physicochemical DES properties alongside the long charging times such high concentration electrolytes demand are challenges. However, the possible step-change that DES-ORFBs could afford make this work worth the challenge.

1.5.   Membrane-Free Redox Flow Batteries

The RFB design carries many technical merits. However, low energy densities and high component costs limit mass commercialisation. As discussed above, moving away from scarce metallic active compounds to affordable, tailorable, and abundant ORAMs can improve the energy density and lower the cost. Regardless of the ORAM and electrolyte chemistry, the dependence on the expensive and lifetime limiting IEMs still hampers maketability.[50] The IEM separating the half-cells is typically Nafion-based and is a costly, and lifetime limiting component. Cost analyses show the IEM and electrolyte account for 20 – 40 % and 62 % of a 300 kW h VRFB, respectively.[50,81,205]

IEMs prevent electrolyte cross mixing. Employing sub-optimal IEMs results in RFBs with low chemical stabilities and poor performances, especially in terms of conductivity and reactivity in non-aqueous media. There has been important progress in membrane development over recent decades, with significant advances in non-fluorinated CEMs, AEMs, amphoteric polymers, and non-ionic separators.[25,206–209] Inorganic/Nafion composite membranes carry the best performances, but are yet to match conventional Nafion CEMs and cost improvements are minimal.[206] Low-cost, non-ionic porous separators improve the power density.[73] However, these designs must use mixed electrolytes to mitigate detrimental amounts of electrolyte crossover. This decreases the amount of usable electrolyte in each half-cell and hence lowers the energy density.

Another method of improving durability, performance, and cost-effectiveness is through a membrane-free design. This is where the two half-cells are separated by a liquid-liquid (L/L) interface instead of a physical membrane barrier. Two strategies for this include a) laminar flow of electrolytes in a microfluidic device and b) biphasic batteries based on immiscible electrolyte solutions.[111,157,210–216]

Self-discharge at the L/L interface is inherent in membrane-free designs. This is where a chemical reaction between the oxidised and reduce species generated during the charging step diffuse to the interphase. Upon encountering each other, they react and transfer electrons to return to their original states. No active materials cross the interface during self-discharge, and so there is constant ORAM concentration in each half-cell, but the cell does not hold

charge. This results in atypical battery behaviour wherein applying lower current densities leads to lower capacities. Flowing the electrolytes minimises the residence time for the active species in the cell and hence minimises the interfacial self-discharge.[216]

The laminar flow of electrolytes through parallel micro-channels produces flow batteries with power densities up to 750 mW cm^{-3}.[217] The process requires low flow rates to minimise electrolyte mixing, but even this cannot prevent some self-discharge, resulting in low CE_{ff} (<40 %) and reactant conversions (<20 %).[211] These microfluidic devices do not behave the same upon scale-up, limiting the practical application to small power utilities and fundamental studies rather than large scale EESSs.[210]

The second technique of immiscible electrolyte solutions has more potential for industrially sized systems. It is thermodynamics (i.e. the partition coefficients) that governs electrolyte cross over rather than the effectiveness of the IEM as in traditional RFBs. The catholyte and the anolyte are immiscible, thus, upon contact they spontaneously form an interface between two immiscible electrolyte solutions (ITIES).

The first proof-of-concept biphasic organic battery by Navalpotro *et al.* was in 2017 and employs the RTIL *N*-butyl-*N*-methylpyrrolidium TFSI ([Pyrr$_{14}$][TFSI]) with BQ against H$_2$Q in an acidic solution.[157] The static system has a 1.4 V OCV and a power density of 1.98 mW cm^{-2}. The wide array of different ORAMs in a range of immiscible aqueous/non-aqueous systems shows the versatility of the concept.[111] The substituted AQ Oilblue N in a PC/[Pyrr$_{14}$][TFSI] (75/25 wt%) electrolyte against OH-TEMPO in 0.5 M NaCl$_{(aq)}$ gives a 1.8 V operating voltage and a 35 % increase in power density over the original proof-of-concept design.

The membrane-free design can also include metallic redox centres.[218,219] For example, Bamgbopa *et al.* create the first ever flowing membrane-free RFB with a hydrophobic RTIL (1-butyl-1-methylpyrrolidinium [TFSI]$^-$ ([BmPyrr][TFSI]) with Fe(acac)$_3$ as an immiscible catholyte against aqueous FeSO$_4$.[219] The battery retains over 60 % of initial discharge capacity and over 80 % of CE_{ff} after 25 cycles.

More recently, the discussion opens to aqueous biphasic systems (ABS). These are immiscible fully aqueous systems wherein separate layers form from certain concentrations of two water soluble compounds (either two polymers, one polymer/one salt, one ionic liquid/one salt).[216] ABS systems are less toxic, more affordable, and more sustainable than existing chemistries. Optimising the partition coefficients of ORAMs and electrolytes leads to a MV/TEMPO battery based on a 1000 g mol^{-1} poly(ethylene glycol)/Na$_2$SO$_{4(aq)}$ ABS with an OCV of 1.23 V, a 99.9 % capacity retention over 550 cycles under static testing, and a peak power density of 23 mW cm^{-2}.

Most of the research in this area studies 'static systems' because the filter-press electrochemical reactors in conventional RFB designs are not easily adapted to the membrane-free concept. There are several proposals for membrane-less flow reactors, with most recent examples including a patent by Montes Gutierrez *et al.* for their immiscible electrolyte RFB design with a flow through electrode, and the hybrid system by Wang *et al.*[211,219–223] The above concepts cover both aqueous/non-aqueous biphasic and ABS electrolyte systems. Their recent conception means volume the work surrounding membrane-free RFBs is low. However, the topic is expected to receive a vast amount of attention in coming years as the separator is considered the major obstacle for large scale implementation.[148]

1.6.   Thesis Outline

Increasing demand for renewable energy resources solidifies our need for large-scale ESSs. The most appropriate technology for this task is the RFB. Low energy densities, expensive metallic components, and sub-optimal IEMs hinder these systems from commercialisation. Methods to combat this lie in non-aqueous electrolytes, ORAMs, and new cell designs. This research intends to investigate these areas in the interest of furthering cost-effective, energy dense ORFBs.

Chapter 1. includes a critical review of the relevant literature surrounding the thesis topics, beginning with the overarching motivation of large-scale stationary energy storage technologies and ORFBs as the potential solution. Section 1.1. discusses the global need for an energy storage solution, and Section 1.2. highlights the benefits and working principles of RFBs for this task. A review of the existing literature on aqueous and non-aqueous ORFBs is in Section 1.3. and Section 1.4. covers the prospects of the alternate electrolytes of RTILs and DESs. Section 1.5. introduces the opportunities and challenges offered by membrane-free devices and discusses the recent literature.

Chapter 2. summarises the theoretical framework and experimental techniques behind the methods employed throughout the experimental work, namely physical characterisation, and electrochemical testing.

Chapter 3. is the first results chapter, focusing on the selection of organic RAMs with an investigation into various solvent systems and the effects of supporting electrolytes. The Chapter finds octafluoro-9,10-anthraquinone (OFAQ) to be a molecule of interest. Optimising the OFAQ electrochemistry for an ORFB anolyte half-cell is the focus of this chapter.

Chapter 4. comprises an in-depth study of the fundamental electrochemistry of OFAQ to determine its viability as a redox couple for an ORFB. The electrochemical attributes studied include redox potential, redox reactivity, and non-aqueous solubility. The Chapter investigates the OFAQ degradation processes when under high potentials at high concentrations, and focusses on mitigation and stabilisation techniques. The results from this Chapter are published in 'Quinone voltammetry for redox-flow battery applications', *J. Electroanal. Chem.*, 2022, **920**, 116572.[224]

Chapter 5. discusses the applicability of the OFAQ anolyte from Chapters 3. and 4. for a membrane-free RFB. This chapter demonstrates a novel membrane-free battery based on a water-in-salt (WIS)-electrolyte aqueous and ACN non-aqueous phase. Three different cell chemistries are tested, and the study presents the first fully organic WIS/ACN-based static battery using a 4-OH-TEMPO catholyte and OFAQ anolyte. The chapter ends by demonstrating stability of the interface under flow conditions for a VOSO$_4$/OFAQ WIS/ACN membrane-free battery.

Chapter 6. details a separate study as part of an industrial secondment placement with Nederlandse Organisatie voor Toegepast Natuurwetenschappelijk Onderzoek (TNO). This section involves the research and development of a highly concentrated DES ORFB.

Chapter 7. concludes the work in this report with a summary of the results and proposals for future work.

1.7. References

1   M. Aneke and M. Wang, Energy storage technologies and real life applications – A state of the art review, *Appl. Energy*, 2016, **179**, 350–377.

2   IEA, *Key World Energy Statistics*, Paris, 2021.

3   IEA, *Key World Energy Statistics*, Paris, 2019.

4   M. Papież, S. Śmiech and K. Frodyma, Effects of renewable energy sector development on electricity consumption – Growth nexus in the European Union, *Renew. Sustain. Energy Rev.*, 2019, **113**, 109276.

5   A. Pfeifer, G. Krajačić, D. Ljubas and N. Duić, Increasing the integration of solar photovoltaics in energy mix on the road to low emissions energy system – Economic and environmental implications, *Renew. Energy*, 2019, **143**, 1310–1317.

6   J. Winsberg, T. Hagemann, T. Janoschka, M. D. Hager and U. S. Schubert, Redox-flow

batteries: From metals to organic redox-active materials, *Angew. Chemie - Int. Ed.*, 2017, **56**, 686–711.

7   A. Z. Weber, M. M. Mench, J. P. Meyers, P. N. Ross, J. T. Gostick and Q. Liu, Redox flow batteries: A review, *J. Appl. Electrochem.*, 2011, **41**, 1137–1164.

8   National Research Council of the National Academies, *America's Energy Future*, The National Academies Press., Washington, DC, 2008.

9   H. Chen, T. N. Cong, W. Yang, C. Tan, Y. Li and Y. Ding, Progress in electrical energy storage system: A critical review, *Prog. Nat. Sci.*, 2009, **19**, 291–312.

10   P. Leung, A. A. Shah, L. Sanz, C. Flox, J. R. Morante, Q. Xu, M. R. Mohamed, C. Ponce de León and F. C. Walsh, Recent developments in organic redox flow batteries: A critical review, *J. Power Sources*, 2017, **360**, 243–283.

11   B. Dunn, H. Kamath, J. M. Tarascon, D. Bruce, K. Haresh and T. Jean-Marie, Electrical energy storage for the grid: a battery of choices, *Science*, 2011, **334**, 928–935.

12   Electric Power Research Institute, *Electric energy storage technology options - a primer on applications, costs & benefits*, Palo Alto, CA, 2010.

13   M. M. Rahman, A. O. Oni, E. Gemechu and A. Kumar, Assessment of energy storage technologies: A review, *Energy Convers. Manag.*, 2020, **223**, 113295.

14   S. Koohi-kamali, V. V. Tyagi, N. A. Rahim, N. L. Panwar and H. Mokhlis, Emergence of energy storage technologies as the solution for reliable operation of smart power systems: A review, *Renew. Sustain. Energy Rev.*, 2013, **25**, 135–165.

15   H. L. Ferreira, R. Garde, G. Fulli, W. Kling and J. P. Lopes, Characterisation of electrical energy storage technologies, *Energy*, 2013, **53**, 288–298.

16   X. Luo, J. Wang, M. Dooner and J. Clarke, Overview of current development in electrical energy storage technologies and the application potential in power system operation, *Appl. Energy*, 2015, **137**, 511–536.

17   M. Yekini Suberu, M. Wazir Mustafa and N. Bashir, Energy storage systems for renewable energy power sector integration and mitigation of intermittency, *Renew. Sustain. Energy Rev.*, 2014, **35**, 499–514.

18   F. Nadeem, S. M. S. Hussain, P. K. Tiwari, A. K. Goswami and T. S. Ustun, Comparative review of energy storage systems, their roles, and impacts on future power systems, *IEEE Access*, 2019, **7**, 4555–4585.

19   A. Holland and X. He, *Advanced Li-ion and beyond lithium batteries 2022-2032: Technologies, players, trends, markets*, 2021.

20   M. Skyllas-Kazacos, M. H. Chakrabarti, S. A. Hajimolana, F. S. Mjalli and M. Saleem, Progress in flow battery research and development, *J. Electrochem. Soc.*, 2011, **158**, R55–R79.

21   M. Park, J. Ryu, W. Wang and J. Cho, Material design and engineering of next-generation flow-battery technologies, *Nat. Rev. Mater.*, 2016, **2**, 1–17.

22   J. Luo, B. Hu, M. Hu, Y. Zhao and T. L. Liu, Status and prospects of organic redox flow batteries toward sustainable energy storage, *ACS Energy Lett.*, 2019, **4**, 2220–2240.

23   S. Maurya, S.-H. H. Shin, Y. Kim and S. H. Moon, A review on recent developments of anion exchange membranes for fuel cells and redox flow batteries, *RSC Adv.*, 2015, **5**, 37206–37230.

24   X. Li, H. Zhang, Z. Mai, H. Zhang and I. Vankelecom, Ion exchange membranes for vanadium redox flow battery (VRB) applications, *Energy Environ. Sci.*, 2011, **4**, 1147–1160.

25   B. Schwenzer, J. Zhang, S. Kim, L. Li, J. Liu and Z. Yang, Membrane development for vanadium redox flow batteries, *ChemSusChem*, 2011, **4**, 1388–1406.

26   M. Bartolozzi, Development of redox flow batteries. A historical bibliography, *J. Power Sources*, 1989, **27**, 219–234.

27   Y. Zhao, Y. Ding, J. Song, L. Peng, J. B. Goodenough and G. Yu, A reversible Br2/Br- redox couple in the aqueous phase as a high-performance catholyte for alkali-ion batteries, *Energy Environ. Sci.*, 2014, **7**, 1990–1995.

28   X. Wei, W. Pan, W. Duan, A. Hollas, Z. Yang, B. Li, Z. Nie, J. Liu, D. Reed, W. Wang and V. Sprenkle, Materials and systems for organic redox flow batteries: status and challenges, *ACS Energy Lett.*, 2017, **2**, 2187–2204.

29   J. Moutet, D. Mills, M. M. Hossain and T. L. Gianetti, Increased performance of an all-organic redox flow battery model: Via nitration of the [4]helicenium DMQA ion electrolyte, *Mater. Adv.*, 2022, **3**, 216–223.

30   W. Wang, X. Wei, D. Choi, X. Lu, G. Yang and C. Sun, Electrochemical cells for medium-and large-scale energy storage: Fundamentals, *Adv. Batter. Mediu. Large-Scale Energy Storage Types Appl.*, 2014, 3–28.

31   Y. Yao, J. Lei, Y. Shi, F. Ai and Y. C. Lu, Assessment methods and performance metrics

for redox flow batteries, *Nat. Energy*, 2021, **6**, 582–588.

32 L. Zeng, T. S. Zhao, L. Wei, H. R. Jiang and M. C. Wu, Anion exchange membranes for aqueous acid-based redox flow batteries: Current status and challenges, *Appl. Energy*, 2019, **233**–**234**, 622–643.

33 Y. Shi, C. Eze, B. Xiong, W. He, H. Zhang, T. M. Lim, A. Ukil and J. Zhao, Recent development of membrane for vanadium redox flow battery applications: A review, *Appl. Energy*, 2019, **238**, 202–224.

34 R. Tan, A. Wang, R. Malpass-Evans, R. Williams, E. W. Zhao, T. Liu, C. Ye, X. Zhou, B. P. Darwich, Z. Fan, L. Turcani, E. Jackson, L. Chen, S. Y. Chong, T. Li, K. E. Jelfs, A. I. Cooper, N. P. Brandon, C. P. Grey, N. B. McKeown and Q. Song, Hydrophilic microporous membranes for selective ion separation and flow-battery energy storage, *Nat. Mater.*, 2020, **19**, 195–202.

35 M. L. Perry, J. D. Saraidaridis and R. M. Darling, Crossover mitigation strategies for redox-flow batteries, *Curr. Opin. Electrochem.*, 2020, **21**, 311–318.

36 M. A. Goulet and M. J. Aziz, Flow Battery Molecular Reactant Stability Determined by Symmetric Cell Cycling Methods, *J. Electrochem. Soc.*, 2018, **165**, A1466–A1477.

37 D. G. Kwabi, Y. Ji and M. J. Aziz, Electrolyte lifetime in aqueous organic redox flow batteries: A critical review, *Chem. Rev.*, 2020, **120**, 6467–6489.

38 B. Huskinson, M. P. Marshak, C. Suh, S. Er, M. R. Gerhardt, C. J. Galvin, X. Chen, A. Aspuru-Guzik, R. G. Gordon and M. J. Aziz, A metal-free organic-inorganic aqueous flow battery, *Nature*, 2014, **505**, 195–8.

39 T. Liu, X. Wei, Z. Nie, V. Sprenkle and W. Wang, A total organic aqueous redox flow battery employing a low cost and sustainable methyl viologen anolyte and 4-HO-TEMPO catholyte, *Adv. Energy Mater.*, 2016, **6**, 1501449.

40 K. Lin, R. Gómez-Bombarelli, E. S. Beh, L. Tong, Q. Chen, A. Valle, A. Aspuru-Guzik, M. J. Aziz and R. G. Gordon, A redox-flow battery with an alloxazine-based organic electrolyte, *Nat. Energy*, 2016, **1**, 1–8.

41 Y. Liu, M. A. Goulet, L. Tong, Y. Liu, Y. Ji, L. Wu, R. G. Gordon, M. J. Aziz, Z. Yang and T. Xu, A long-lifetime all-organic aqueous flow battery utilizing TMAP-TEMPO radical, *Chem*, 2019, **5**, 1861–1870.

42 B. Hu, C. DeBruler, Z. Rhodes and T. L. Liu, Long-cycling aqueous organic redox flow battery (AORFB) toward sustainable and safe energy storage, *J. Am. Chem. Soc.*,

2017, **139**, 1207–1214.

43   B. Yang, L. Hoober-Burkhardt, S. Krishnamoorthy, A. Murali, G. K. S. Prakash and S. R. Narayanan, High-performance aqueous organic flow battery with quinone-based redox couples at both electrodes, *J. Electrochem. Soc.*, 2016, **163**, A1442–A1449.

44   E. S. Beh, D. De Porcellinis, R. L. Gracia, K. T. Xia, R. G. Gordon and M. J. Aziz, A neutral pH aqueous organic-organometallic redox flow battery with extremely high capacity retention, *ACS Energy Lett.*, 2017, **2**, 639–644.

45   L. Tong, M. A. Goulet, D. P. Tabor, E. F. Kerr, D. De Porcellinis, E. M. Fell, A. Aspuru-Guzik, R. G. Gordon and M. J. Aziz, Molecular engineering of an alkaline naphthoquinone flow battery, *ACS Energy Lett.*, 2019, **4**, 1880–1887.

46   Y. R. Dong, H. Kaku, K. Hanafusa, K. Moriuchi and T. Shigematsu, A novel titanium/manganese redox flow battery, *ECS Trans.*, 2015, **69**, 59–67.

47   C. Xie, Y. Duan, W. Xu, H. Zhang and X. Li, A low-cost neutral zinc–iron flow battery with high energy density for stationary energy storage, *Angew. Chemie - Int. Ed.*, 2017, **56**, 14953–14957.

48   S. Roe, C. Menictas and M. Skyllas-Kazacos, A high energy density vanadium redox flow battery with 3 M vanadium electrolyte, *J. Electrochem. Soc.*, 2016, **163**, A5023–A5028.

49   M. A. Goulet, L. Tong, D. A. Pollack, D. P. Tabor, S. A. Odom, A. Aspuru-Guzik, E. E. Kwan, R. G. Gordon and M. J. Aziz, Extending the lifetime of organic flow batteries via redox state management, *J. Am. Chem. Soc.*, 2020, **141**, 8014–8019.

50   E. Sánchez-Díez, E. Ventosa, M. Guarnieri, A. Trovò, C. Flox, R. Marcilla, F. Soavi, P. Mazur, E. Aranzabe and R. Ferret, Redox flow batteries: Status and perspective towards sustainable stationary energy storage, *J. Power Sources*, 2021, **481**, 228804.

51   B. Huskinson, M. P. Marshak, M. R. Gerhardt and M. J. Aziz, Cycling of a quinone-bromide flow battery for large-scale electrochemical energy storage, *ECS Trans.*, 2014, **61**, 27–30.

52   M. Li, Z. Rhodes, J. R. Cabrera-Pardo and S. D. Minteer, Recent advancements in rational design of non-aqueous organic redox flow batteries, *Sustain. Energy Fuels*, 2020, **4**, 4370–4389.

53   S. Jin, Y. Jing, D. G. Kwabi, Y. Ji, L. Tong, D. De Porcellinis, M. A. Goulet, D. A. Pollack, R. G. Gordon, M. J. Aziz and J. A. Paulson, A water-miscible quinone flow battery with

high volumetric capacity and energy density, *ACS Energy Lett.*, 2019, **4**, 1342–1348.

54   S. Bauer, J. C. Namyslo, D. E. Kaufmann and T. Turek, Evaluation of options and limits of aqueous all-quinone-based organic redox flow batteries, *J. Electrochem. Soc.*, 2020, **167**, 110522.

55   T. Janoschka, M. D. Hager and U. S. Schubert, Powering up the future: Radical polymers for battery applications, *Adv. Mater.*, 2012, **24**, 6397–6409.

56   R. Dmello, J. D. Milshtein, F. R. Brushett and K. C. Smith, Cost-driven materials selection criteria for redox flow battery electrolytes, *J. Power Sources*, 2016, **330**, 261–272.

57   K. Wedege, E. Dražević, D. Konya and A. Bentien, Organic redox species in aqueous flow batteries: Redox potentials, solubility and chemical stability, *Sci. Rep.*, 2016, **6**, 1–13.

58   Z. Li, S. Li, S. Liu, K. Huang, D. Fang, F. Wang and S. Peng, Electrochemical properties of an all-organic redox flow battery using 2,2,6,6-tetramethyl-1-piperidinyloxy and N-methylphthalimide, *Electrochem. Solid-State Lett.*, 2011, **14**, 171–173.

59   D. R. Garcia, *Design of new electroactive fluids for redox flow batteries based on quinones*, Barcelona, 2014.

60   X. Wu, J. Liu, X. Xiang, J. Zhang, J. Hu and Y. Wu, Electrolytes for vanadium redox flow batteries, *Pure Appl. Chem.*, 2014, **86**, 661–669.

61   P. Geysens, Y. Li, I. Vankelecom, J. Fransaer and K. Binnemans, Highly soluble 1,4-diaminoanthraquinone derivative for nonaqueous symmetric redox flow batteries, *ACS Sustain. Chem. Eng.*, 2020, **8**, 3832–3843.

62   K. Lin, Q. Chen, M. R. Gerhardt, L. Tong, S. B. Kim, L. Eisenach, A. W. Valle, D. Hardee, R. G. Gordon, M. J. Aziz and M. P. Marshak, Alkaline quinone flow battery, *Science*, 2015, **349**, 1529–1532.

63   D. G. Kwabi, K. Lin, Y. Ji, E. F. Kerr, M. A. Goulet, D. De Porcellinis, D. P. Tabor, D. A. Pollack, A. Aspuru-Guzik, R. G. Gordon and M. J. Aziz, Alkaline quinone flow battery with long lifetime at pH 12, *Joule*, 2018, **2**, 1894–1906.

64   S. K. Park, J. Shim, J. H. Yang, K. H. Shin, C. S. Jin, B. S. Lee, Y. S. Lee, J. D. Jeon, B. Suk, Y. S. Lee and J. D. Jeon, Electrochemical properties of a non-aqueous redox battery with all-organic redox couples, *Electrochem. commun.*, 2015, **59**, 68–71.

65   X. Wei, W. Xu, M. Vijayakumar, L. Cosimbescu, T. Liu, V. Sprenkle and W. Wang,

TEMPO-based catholyte for high-energy density nonaqueous redox flow batteries, *Adv. Mater.*, 2014, **26**, 7649–7653.

66   C. DeBruler, B. Hu, J. Moss, X. Liu, J. Luo, Y. Sun and T. L. Liu, Designer two-electron storage viologen anolyte materials for neutral aqueous organic redox flow batteries, *Chem*, 2017, **3**, 961–978.

67   M. T. Huynh, C. W. Anson, A. C. Cavell, S. S. Stahl and S. Hammes-Schiffer, Quinone 1e- and 2e-/2H+ reduction potentials: Identification and analysis of deviations from systematic scaling relationships, *J. Am. Chem. Soc.*, 2016, **138**, 15903–15910.

68   K. H. Hendriks, C. S. Sevov, M. E. Cook and M. S. Sanford, Multielectron cycling of a low-potential anolyte in alkali metal electrolytes for nonaqueous redox flow batteries, *ACS Energy Lett.*, 2017, **2**, 2430–2435.

69   S. Er, C. Suh, M. P. Marshak and A. Aspuru-Guzik, Computational design of molecules for an all-quinone redox flow battery, *Chem. Sci.*, 2015, **6**, 885–893.

70   D. P. Tabor, R. Gómez-Bombarelli, L. Tong, R. G. Gordon, M. J. Aziz and A. Aspuru-Guzik, Mapping the frontiers of quinone stability in aqueous media: implications for organic aqueous redox flow batteries, *J. Mater. Chem. A*, 2019, **7**, 12833–12841.

71   M. R. Gerhardt, L. Tong, R. Gómez-Bombarelli, Q. Chen, M. P. Marshak, C. J. Galvin, A. Aspuru-Guzik, R. G. Gordon and M. J. Aziz, Anthraquinone derivatives in aqueous flow batteries, *Adv. Energy Mater.*, 2017, **7**, 1601488.

72   C. De La Cruz, A. Molina, N. Patil, E. Ventosa, R. Marcilla and A. Mavrandonakis, New insights into phenazine-based organic redox flow batteries by using high-throughput DFT modelling, *Sustain. Energy Fuels*, 2020, **4**, 5513–5521.

73   T. Janoschka, N. Martin, U. Martin, C. Friebe, S. Morgenstern, H. Hiller, M. D. Hager and U. S. Schubert, An aqueous, polymer-based redox-flow battery using non-corrosive, safe, and low-cost materials, *Nature*, 2015, **527**, 78–81.

74   A. Hollas, X. Wei, V. Murugesan, Z. Nie, B. Li, D. Reed, J. Liu, V. Sprenkle and W. Wang, A biomimetic high-capacity phenazine-based anolyte for aqueous organic redox flow batteries, *Nat. Energy*, 2018, **3**, 508–514.

75   K. S. Han, N. N. Rajput, M. Vijayakumar, X. Wei, W. Wang, J. Hu, K. A. Persson and K. T. Mueller, Preferential solvation of an asymmetric redox molecule, *J. Phys. Chem. C*, 2016, **120**, 27834–27839.

76   X. Wei, W. Duan, J. Huang, L. Zhang, B. Li, D. Reed, W. Xu, V. Sprenkle and W. Wang,

A high-current, stable nonaqueous organic redox flow battery, *ACS Energy Lett.*, 2016, **1**, 705–711.

77 W. Duan, R. S. Vemuri, J. D. Milshtein, S. Laramie, R. Dmello, J. Huang, L. Zhang, D. Hu, M. Vijayakumar, W. Wang, J. Liu, R. M. Darling, L. Thompson, K. Smith, J. S. Moore, F. R. Brushett and X. Wei, A symmetric organic-based nonaqueous redox flow battery and its state of charge diagnostics by FTIR, *J. Mater. Chem. A*, 2016, **4**, 5448–5456.

78 E. Pérez-Gallent, C. Sánchez-Martínez, L. F. G. Geers, S. Turk, R. Latsuzbaia and E. L. V. Goetheer, Overcoming mass transport limitations in electrochemical reactors with a pulsating flow electrolyzer, *Ind. Eng. Chem. Res.*, 2020, **59**, 5648–5656.

79 Q. Xu and T. S. Zhao, Fundamental models for flow batteries, *Prog. Energy Combust. Sci.*, 2015, **49**, 40–58.

80 R. M. Darling, K. G. Gallagher, J. A. Kowalski, S. Ha and F. R. Brushett, Pathways to low-cost electrochemical energy storage: A comparison of aqueous and nonaqueous flow batteries, *Energy Environ. Sci.*, 2014, **7**, 3459–3477.

81 G. Kear, A. A. Shah and F. C. Walsh, Development of the all-vanadium redox flow battery for energy storage: a review of technological, financial and policy aspects, *Int. J. energy Res.*, 2012, **36**, 1105–1120.

82 P. Leung, X. Li, C. Ponce De León, L. Berlouis, C. T. J. Low, F. C. Walsh, P. De Leo, L. Berlouis, C. T. John, F. C. Walsh, C. Ponce De León, L. Berlouis, C. T. J. Low and F. C. Walsh, Progress in redox flow batteries, remaining challenges and their applications in energy storage, *RSC Adv.*, 2012, **2**, 10125–10156.

83 C. Ponce de León, A. Frías-Ferrer, J. González-García, D. A. Szánto and F. C. Walsh, Redox flow cells for energy conversion, *J. Power Sources*, 2006, **160**, 716–732.

84 K. Gong, Q. Fang, S. Gu, S. F. Y. Li and Y. Yan, Nonaqueous redox-flow batteries: Organic solvents, supporting electrolytes, and redox pairs, *Energy Environ. Sci.*, 2015, **8**, 3515–3530.

85 Y. Xu, Y. H. Wen, J. Cheng, G. P. Cao and Y. S. Yang, A study of tiron in aqueous solutions for redox flow battery application, *Electrochim. Acta*, 2010, **55**, 715–720.

86 Q. Huang and Q. Wang, Next-generation, high-energy-density redox flow batteries, *Chempluschem*, 2015, **80**, 312–322.

87 A. Parasuraman, T. M. Lim, C. Menictas and M. Skyllas-Kazacos, Review of material

research and development for vanadium redox flow battery applications, *Electrochim. Acta*, 2013, **101**, 27–40.

88   P. Alotto, M. Guarnieri and F. Moro, Redox flow batteries for the storage of renewable energy: A review, *Renew. Sustain. Energy Rev.*, 2014, **29**, 325–335.

89   S. M. Laramie, J. D. Milshtein, T. M. Breault, F. R. Brushett and L. T. Thompson, Performance and cost characteristics of multi-electron transfer, common ion exchange non-aqueous redox flow batteries, *J. Power Sources*, 2016, **327**, 681–692.

90   J. A. Kowalski, L. Su, J. D. Milshtein and F. R. Brushett, Recent advances in molecular engineering of redox active organic molecules for nonaqueous flow batteries, *Curr. Opin. Chem. Eng.*, 2016, **13**, 45–52.

91   Z. Zhao, C. Zhang and X. Li, Opportunities and challenges of organic flow battery for electrochemical energy storage technology, *J. Energy Chem.*, 2022, **67**, 621–639.

92   L. Hoober-Burkhardt, S. Krishnamoorthy, B. Yang, A. Murali, A. Nirmalchandar, G. K. S. Prakash and S. R. Narayanan, A new michael-reaction-resistant benzoquinone for aqueous organic redox flow batteries, *J. Electrochem. Soc.*, 2017, **164**, A600–A607.

93   M. Park, E. S. Beh, E. M. Fell, Y. Jing, E. F. Kerr, D. De Porcellinis, M. A. Goulet, J. Ryu, A. A. Wong, R. G. Gordon, J. Cho and M. J. Aziz, A high voltage aqueous zinc–organic hybrid flow battery, *Adv. Energy Mater.*, 2019, **9**, 1–8.

94   W. Liu, Z. Zhao, T. Li, S. Li, H. Zhang and X. Li, A high potential biphenol derivative cathode: toward a highly stable air-insensitive aqueous organic flow battery, *Sci. Bull.*, 2021, **66**, 457–463.

95   J. B. Gerken, C. W. Anson, Y. Preger, P. G. Symons, J. D. Genders, Y. Qiu, W. Li, T. W. Root and S. S. Stahl, Comparison of quinone-based catholytes for aqueous redox flow batteries and demonstration of long-term stability with tetrasubstituted quinones, *Adv. Energy Mater.*, 2020, **10**, 1–7.

96   W. Lee, G. Park, Y. Kim, D. Chang and Y. Kwon, Nine watt – Level aqueous organic redox flow battery stack using anthraquinone and vanadium as redox couple, *Chem. Eng. J.*, 2020, **398**, 125610.

97   T. J. Carney, S. J. Collins, J. S. Moore and F. R. Brushett, Concentration-dependent dimerization of anthraquinone disulfonic acid and its impact on charge storage, *Chem. Mater.*, 2017, **29**, 4801–4810.

98   B. Yang, L. Hoober-Burkhardt, F. Wang, G. K. Surya Prakash and S. R. Narayanan, An

inexpensive aqueous flow battery for large-scale electrical energy storage based on water-soluble organic redox couples, *J. Electrochem. Soc.*, 2014, **161**, A1371–A1380.

99   C. Zhang, Z. Niu, S. Peng, Y. Ding, L. Zhang, X. Guo, Y. Zhao and G. Yu, Phenothiazine-based organic catholyte for high-capacity and long-life aqueous redox flow batteries, *Adv. Mater.*, 2019, **31**, 1901052.

100   W. Yan, C. Wang, J. Tian, G. Zhu, L. Ma, Y. Wang, R. Chen, Y. Hu, L. Wang, T. Chen, J. Ma and Z. Jin, All-polymer particulate slurry batteries, *Nat. Commun.*, 2019, **10**, 1–11.

101   Z. Yang, L. Tong, D. P. Tabor, E. S. Beh, M. A. Goulet, D. De Porcellinis, A. Aspuru-Guzik, R. G. Gordon and M. J. Aziz, Alkaline benzoquinone aqueous flow battery for large-scale storage of electrical energy, *Adv. Energy Mater.*, 2018, **8**, 1–9.

102   C. Wang, Z. Yang, Y. Wang, P. Zhao, W. Yan, G. Zhu, L. Ma, B. Yu, L. Wang, G. Li, J. Liu and Z. Jin, High-performance alkaline organic redox flow batteries based on 2-hydroxy-3-carboxy-1,4-naphthoquinone, *ACS Energy Lett.*, 2018, **3**, 2404–2409.

103   Y. Ji, M. A. Goulet, D. A. Pollack, D. G. Kwabi, S. Jin, D. De Porcellinis, E. F. Kerr, R. G. Gordon and M. J. Aziz, A phosphonate-functionalized quinone redox flow battery at near-neutral pH with record capacity retention rate, *Adv. Energy Mater.*, 2019, **9**, 1–7.

104   X. Zu, L. Zhang, Y. Qian, C. Zhang and G. Yu, Molecular engineering of azobenzene-based anolytes towards high-capacity aqueous redox flow batteries, *Angew. Chemie Int. Ed.*, 2020, **59**, 22163–22170.

105   R. Feng, X. Zhang, V. Murugesan, A. Hollas, Y. Chen, Y. Shao, E. Walter, N. P. N. Wellala, L. Yan, K. M. Rosso and W. Wang, Reversible ketone hydrogenation and dehydrogenation for aqueous organic redox flow batteries, *Science*, 2021, **372**, 836–840.

106   A. J. Bard and L. R. Faulkner, *Electrochemical Methods: Fundamentals and Applications*, John Wiley and Sons, Inc., Austin, Texas, 2nd edn., 2001.

107   J. Luo, A. Sam, B. Hu, C. DeBruler, X. Wei, W. Wang and T. L. Liu, Unraveling pH dependent cycling stability of ferricyanide/ferrocyanide in redox flow batteries, *Nano Energy*, 2017, **42**, 215–221.

108   S. Pang, X. Wang, P. Wang and Y. Ji, Biomimetic amino acid functionalized phenazine flow batteries with long lifetime at near-neutral pH, *Angew. Chemie Int. Ed.*, 2021, **60**, 5289–5298.

109 C. Wang, Z. Yang, B. Yu, H. Wang, K. Zhang, G. Li, Z. Tie and Z. Jin, Alkaline soluble 1,3,5,7-tetrahydroxyanthraquinone with high reversibility as anolyte for aqueous redox flow battery, *J. Power Sources*, 2022, **524**, 3–9.

110 B. Hu, Y. Tang, J. Luo, G. Grove, Y. Guo and T. L. Liu, Improved radical stability of viologen anolytes in aqueous organic redox flow batteries, *Chem. Commun.*, 2018, **54**, 6871–6874.

111 P. Navalpotro, N. Sierra, C. Trujillo, I. Montes, J. Palma and R. Marcilla, Exploring the versatility of membrane-free battery concept using different combinations of immiscible redox electrolytes, *ACS Appl. Mater. Interfaces*, 2018, **10**, 41246–41256.

112 W. Zhou, W. Liu, M. Qin, Z. Chen, J. Xu, J. Cao and J. Li, Fundamental properties of TEMPO-based catholytes for aqueous redox flow batteries: Effects of substituent groups and electrolytes on electrochemical properties, solubilities and battery performance, *RSC Adv.*, 2020, **10**, 21839–21844.

113 T. Janoschka, N. Martin, M. D. Hager and U. S. Schubert, An aqueous redox-flow battery with high capacity and power: The TEMPTMA/MV system, *Angew. Chemie Int. Ed.*, 2016, **55**, 14427–14430.

114 J. Winsberg, C. Stolze, A. Schwenke, S. Muench, M. D. Hager and U. S. Schubert, Aqueous 2,2,6,6-tetramethylpiperidine-N-oxyl catholytes for a high-capacity and high current density oxygen-insensitive hybrid-flow battery, *ACS Energy Lett.*, 2017, **2**, 411–416.

115 A. M. Janiszewska and M. Grzeszczuk, Mechanistic-kinetic scheme of oxidation/reduction of TEMPO involving hydrogen bonded dimer. RDE probe for availability of protons in reaction environment, *Electroanalysis*, 2004, **16**, 1673–1681.

116 J. R. Fish, S. G. Swarts, M. D. Sevilla and T. Malinski, Electrochemistry and spectroelectrochemistry of nitroxyl free radicals, *J. Phys. Chem.*, 1988, **92**, 3745–3751.

117 J. Winsberg, C. Stolze, S. Muench, F. Liedl, M. D. Hager and U. S. Schubert, TEMPO/Phenazine Combi-Molecule: A Redox-Active Material for Symmetric Aqueous Redox-Flow Batteries, *ACS Energy Lett.*, 2016, **1**, 976–980.

118 X. Wang, W. Tang and K. P. Loh, Para-Substituted Triphenylamine as a Catholyte for Zinc-Organic Aqueous Redox Flow Batteries, *ACS Appl. Energy Mater.*, 2021, **4**, 3612–3621.

119 J. Luo, B. Hu, C. Debruler, Y. Bi, Y. Zhao, B. Yuan, M. Hu, W. Wu and T. L. Liu,

Unprecedented capacity and stability of ammonium ferrocyanide catholyte in pH neutral aqueous redox flow batteries, *Joule*, 2019, **3**, 149–163.

120   Q. Liu, X. Li, C. Yan and A. Tang, A dopamine-based high redox potential catholyte for aqueous organic redox flow battery, *J. Power Sources*, 2020, **460**, 228124.

121   S. Jin, E. M. Fell, L. Vina-Lopez, Y. Jing, P. W. Michalak, R. G. Gordon and M. J. Aziz, Near neutral pH redox flow battery with low permeability and long-lifetime phosphonated viologen active species, *Adv. Energy Mater.*, 2020, **10**, 1–10.

122   J. Luo, B. Hu, C. Debruler and T. L. Liu, A π-conjugation extended viologen as a two-electron storage anolyte for total organic aqueous redox flow batteries, *Angew. Chemie Int. Ed.*, 2018, **57**, 231–235.

123   J. S. Bus, S. D. Aust and J. E. Gibson, Superoxide- and singlet oxygen-catalyzed lipid peroxidation as a possible mechanism for paraquat (methyl viologen) toxicity, *Biochem. Biophys. Res. Commun.*, 1974, **58**, 749–755.

124   B. Hu, J. Luo, M. Hu, B. Yuan and T. L. Liu, A pH-neutral, metal-free aqueous organic redox flow battery employing an ammonium anthraquinone anolyte, *Angew. Chemie*, 2019, **131**, 16782–16789.

125   C. Debruler, B. Hu, J. Moss, J. Luo and T. L. Liu, A sulfonate-functionalized viologen enabling neutral cation exchange, aqueous organic redox flow batteries toward renewable energy storage, *ACS Energy Lett.*, 2018, **3**, 663–668.

126   X. Xing, Q. Liu, W. Xu, W. Liang, J. Liu, B. Wang and J. P. Lemmon, All-liquid electroactive materials for high energy density organic flow battery, *ACS Appl. Energy Mater.*, 2019, **2**, 2364–2369.

127   C. S. Sevov, R. E. M. Brooner, E. Chénard, R. S. Assary, J. S. Moore, J. Rodríguez-López and M. S. Sanford, Evolutionary design of low molecular weight organic anolyte materials for applications in nonaqueous redox flow batteries, *J. Am. Chem. Soc.*, 2015, **137**, 14465–14472.

128   C. S. Sevov, D. P. Hickey, M. E. Cook, S. G. Robinson, S. Barnett, S. D. Minteer, M. S. Sigman and M. S. Sanford, Physical organic approach to persistent, cyclable, low-potential electrolytes for flow battery applications, *J. Am. Chem. Soc.*, 2017, **139**, 2924–2927.

129   P. W. Antoni, T. Bruckhoff and M. M. Hansmann, Organic redox systems based on pyridinium-carbene hybrids, *J. Am. Chem. Soc.*, 2019, **141**, 9701–9711.

130   B. Hu and T. L. Liu, Two electron utilization of methyl viologen anolyte in nonaqueous organic redox flow battery, *J. Energy Chem.*, 2018, **27**, 1326–1332.

131   X. Xing, Y. Huo, X. Wang, Y. Zhao and Y. Li, A benzophenone-based anolyte for high energy density all-organic redox flow battery, *Int. J. Hydrogen Energy*, 2017, **42**, 17488–17494.

132   X. Wang, X. Xing, Y. Huo, Y. Zhao, Y. Li and H. Chen, Study of tetraethylammonium bis(trifluoromethylsulfonyl)imide as a supporting electrolyte for an all-organic redox flow battery using Benzophenone and 1,4-di-tert-butyl-2,5-dimethoxybenzene as active species, *Int. J. Electrochem. Sci.*, 2018, **13**, 6676–6683.

133   X. Wei, W. Xu, J. Huang, L. Zhang, E. Walter, C. Lawrence, M. Vijayakumar, W. A. Henderson, T. Liu, L. Cosimbescu, B. Li, V. Sprenkle and W. Wang, Radical compatibility with nonaqueous electrolytes and its impact on an all-organic redox flow battery, *Angew. Chemie Int. Ed.*, 2015, **54**, 8684–8687.

134   G. Kwon, K. Lee, M. H. Lee, B. Lee, S. Lee, S. K. Jung, K. Ku, J. Kim, S. Y. Park, J. E. Kwon and K. Kang, Bio-inspired molecular redesign of a multi-redox catholyte for high-energy non-aqueous organic redox flow batteries, *Chem*, 2019, **5**, 2642–2656.

135   G. Kwon, S. Lee, J. Hwang, H. S. Shim, B. Lee, M. H. Lee, Y. Ko, S. K. Jung, K. Ku, J. Hong and K. Kang, Multi-redox molecule for high-energy redox flow batteries, *Joule*, 2018, **2**, 1771–1782.

136   M. Pahlevaninezhad, P. Leung, P. Q. Velasco, M. Pahlevani, F. C. Walsh, E. P. L. Roberts and C. Ponce de León, A nonaqueous organic redox flow battery using multi-electron quinone molecules, *J. Power Sources*, 2021, **500**, 1–9.

137   W. Duan, J. Huang, J. A. Kowalski, I. A. Shkrob, M. Vijayakumar, E. Walter, B. Pan, Z. Yang, J. D. Milshtein, B. Li, C. Liao, Z. Zhang, W. Wang, J. Liu, J. S. Moore, F. R. Brushett, L. Zhang and X. Wei, 'wine-dark sea' in an organic flow battery: Storing negative charge in 2,1,3-benzothiadiazole radicals leads to improved cyclability, *ACS Energy Lett.*, 2017, **2**, 1156–1161.

138   J. Huang, W. Duan, J. Zhang, I. A. Shkrob, R. S. Assary, B. Pan, C. Liao, Z. Zhang, X. Wei and L. Zhang, Substituted thiadiazoles as energy-rich anolytes for nonaqueous redox flow cells, *J. Mater. Chem. A*, 2018, **6**, 6251–6254.

139   J. Huang, L. Cheng, R. S. Assary, P. Wang, Z. Xue, A. K. Burrell, L. A. Curtiss and L. Zhang, Liquid catholyte molecules for nonaqueous redox flow batteries, *Adv. Energy Mater.*, 2015, **5**, 1–6.

140   C. N. Gannett, B. M. Peterson, L. Shen, J. Seok, B. P. Fors and H. D. Abruña, Cross-linking effects on performance metrics of phenazine-based polymer cathodes, *ChemSusChem*, 2020, **13**, 2428–2435.

141   E. I. Romadina, D. S. Komarov, K. J. Stevenson and P. A. Troshin, New phenazine based anolyte material for high voltage organic redox flow batteries, *Chem. Commun.*, 2021, **57**, 2986–2989.

142   C. Zhang, Z. Niu, Y. Ding, L. Zhang, Y. Zhou, X. Guo, X. Zhang, Y. Zhao and G. Yu, Highly concentrated phthalimide-based anolytes for organic redox flow batteries with enhanced reversibility, *Chem*, 2018, **4**, 2814–2825.

143   D. Xu, C. Zhang, Y. Zhen, Y. Zhao and Y. Li, A high-rate nonaqueous organic redox flow battery, *J. Power Sources*, 2021, **495**, 229819.

144   C. S. Sevov, S. K. Samaroo and M. S. Sanford, Cyclopropenium salts as cyclable, high-potential catholytes in nonaqueous media, *Adv. Energy Mater.*, 2017, **7**, 1602027.

145   Y. Yan, S. G. Robinson, M. S. Sigman and M. S. Sanford, Mechanism-based design of a high-potential catholyte enables a 3.2 V all-organic nonaqueous redox flow battery, *J. Am. Chem. Soc.*, 2019, **141**, 15301–15306.

146   A. Shrestha, K. H. Hendriks, M. S. Sigman, S. D. Minteer and M. S. Sanford, Realization of an asymmetric non-aqueous redox flow battery through molecular design to minimize active species crossover and decomposition, *Chem. Eur. J.*, 2020, **26**, 5369–5373.

147   C. Zhang, L. Zhang, Y. Ding, X. Guo and G. Yu, Eutectic electrolytes for high-energy-density redox flow batteries, *ACS Energy Lett.*, 2018, **3**, 2875–2883.

148   V. M. Ortiz-Martínez, L. Gómez-Coma, G. Pérez, A. Ortiz and I. Ortiz, The roles of ionic liquids as new electrolytes in redox flow batteries, *Sep. Purif. Technol.*, 2020, **252**, 117436.

149   M. H. Chakrabarti, F. S. Mjalli, I. M. Alnashef, M. A. Hashim, M. A. Hussain, L. Bahadori, C. T. J. Low, M. Harun, F. Sabri, I. Muen, M. Ali, M. Azlan, L. Bahadori, C. Tong and J. Low, Prospects of applying ionic liquids and deep eutectic solvents for renewable energy storage by means of redox flow batteries, *Renew. Sustain. Energy Rev.*, 2014, **30**, 254–270.

150   D. Wei and A. Ivaska, Applications of ionic liquids in electrochemical sensors, *Anal. Chim. Acta*, 2008, **607**, 126–135.

151   W. Lu, L. Qu, K. Henry and L. Dai, High performance electrochemical capacitors from

aligned carbon nanotube electrodes and ionic liquid electrolytes, *J. Power Sources*, 2009, **189**, 1270–1277.

152   A. Lewandowski and A. Świderska-Mocek, Ionic liquids as electrolytes for Li-ion batteries-An overview of electrochemical studies, *J. Power Sources*, 2009, **194**, 601–609.

153   B. Rezaei, S. Mallakpour and M. Taki, Application of ionic liquids as an electrolyte additive on the electrochemical behavior of lead acid battery, *J. Power Sources*, 2009, **187**, 605–612.

154   H. R. Jhong, D. S. H. Wong, C. C. Wan, Y. Y. Wang and T. C. Wei, A novel deep eutectic solvent-based ionic liquid used as electrolyte for dye-sensitized solar cells, *Electrochem. commun.*, 2009, **11**, 209–211.

155   R. F. De Souza, J. C. Padilha, R. S. Gonçalves and J. Dupont, Room temperature dialkylimidazolium ionic liquid-based fuel cells, *Electrochem. commun.*, 2003, **5**, 728–731.

156   R. Chen and R. Hempelmann, Ionic liquid-mediated aqueous redox flow batteries for high voltage applications, *Electrochem. commun.*, 2016, **70**, 56–59.

157   P. Navalpotro, J. Palma, M. A. Anderson and R. Marcilla, A membrane-free redox flow battery with two immiscible redox electrolytes, *Angew. Chemie Int. Ed.*, 2017, **56**, 12460–12465.

158   H. Wang, R. Emanuelsson, A. Banerjee, R. Ahuja, M. Strømme and M. Sjödin, Effect of cycling ion and solvent on the redox chemistry of substituted quinones and solvent-induced breakdown of the correlation between redox potential and electron-withdrawing power of substituents, *J. Phys. Chem. C*, 2020, **124**, 13609–13617.

159   A. Ejigu, P. A. Greatorex-Davies and D. A. Walsh, Room temperature ionic liquid electrolytes for redox flow batteries, *Electrochem. commun.*, 2015, **54**, 55–59.

160   L. Wylie, T. Blesch, R. Freeman, K. Hatakeyama-Sato, K. Oyaizu, M. Yoshizawa-Fujita and E. I. Izgorodina, Reversible reduction of the TEMPO radical: One step closer to an all-organic redox flow battery, *ACS Sustain. Chem. Eng.*, 2020, **8**, 17988–17996.

161   Z. Huang, C. W. M. Kay, B. Kuttich, D. Rauber, T. Kraus, H. Li, S. Kim and R. Chen, An "interaction-mediating" strategy towards enhanced solubility and redox properties of organics for aqueous flow batteries, *Nano Energy*, 2020, **69**, 104464.

162   Y. Katayama, I. Konishiike, T. Miura and T. Kishi, Redox reaction in 1-ethyl-3-

methylimidazolium-iron chlorides molten salt system for battery application, *J. Power Sources*, 2002, **109**, 327–332.

163 C. A. Nkuku and R. J. LeSuer, Electrochemistry in deep eutectic solvents, *J. Phys. Chem. B*, 2007, **111**, 13271–13277.

164 A. P. Abbott, G. Capper, D. L. Davies, R. K. Rasheed and V. Tambyrajah, Novel solvent properties of choline chloride/urea mixtures, *Chem. Commun.*, 2003, 70–71.

165 E. L. Smith, A. P. Abbott and K. S. Ryder, Deep eutectic solvents (DESs) and their applications, *Chem. Rev.*, 2014, **114**, 11060–11082.

166 B. Chakrabarti, J. Rubio-Garcia, E. Kalamaras, V. Yufit, F. Tariq, C. T. J. Low, A. Kucernak and N. P. Brandon, Evaluation of a non-aqueous vanadium redox flow battery using a deep eutectic solvent and graphene modified carbon electrodes via electrophoretic deposition, *Batteries*, 2020, **6**, 38.

167 H. Qin, X. Hu, J. Wang, H. Cheng, L. Chen and Z. Qi, Overview of acidic deep eutectic solvents on synthesis, properties and applications, *Green Energy Environ.*, 2020, **5**, 8–21.

168 G. Di Carmine, A. P. Abbott and C. D'Agostino, Deep eutectic solvents: Alternative reaction media for organic oxidation reactions, *React. Chem. Eng.*, 2021, **6**, 582–598.

169 T. Zhekenov, N. Toksanbayev, Z. Kazakbayeva, D. Shah and F. S. Mjalli, Formation of type III deep eutectic solvents and effect of water on their intermolecular interactions, *Fluid Phase Equilib.*, 2017, **441**, 43–48.

170 F. S. Mjalli and H. Mousa, Viscosity of aqueous ionic liquids analogues as a function of water content and temperature, *Chinese J. Chem. Eng.*, 2017, **25**, 1877–1883.

171 M. Steichen, M. Thomassey, S. Siebentritt and P. J. Dale, Controlled electrodeposition of Cu-Ga from a deep eutectic solvent for low cost fabrication of CuGaSe2 thin film solar cells, *Phys. Chem. Chem. Phys.*, 2011, **13**, 4292–4302.

172 A. P. Abbott, G. Capper, K. J. McKenzie and K. S. Ryder, Voltammetric and impedance studies of the electropolishing of type 316 stainless steel in a choline chloride based ionic liquid, *Electrochim. Acta*, 2006, **51**, 4420–4425.

173 K. Pang, Y. Hou, W. Wu, W. Guo, W. Peng and K. N. Marsh, Efficient separation of phenols from oils via forming deep eutectic solvents, *Green Chem.*, 2012, **14**, 2398–2401.

174 Y. Dai, J. van Spronsen, G. J. Witkamp, R. Verpoorte and Y. H. Choi, Natural deep

eutectic solvents as new potential media for green technology, *Anal. Chim. Acta*, 2013, **766**, 61–68.

175   D. Lindberg, M. de la Fuente Revenga and M. Widersten, Deep eutectic solvents (DESs) are viable cosolvents for enzyme-catalyzed epoxide hydrolysis, *J. Biotechnol.*, 2010, **147**, 169–171.

176   A. P. Abbott, T. J. Bell, S. Handa and B. Stoddart, O-Acetylation of cellulose and monosaccharides using a zinc based ionic liquid, *Green Chem.*, 2005, **7**, 705–707.

177   A. P. Abbott, G. Capper, D. L. Davies, K. J. McKenzie and S. U. Obi, Solubility of metal oxides in deep eutectic solvents based on choline chloride, *J. Chem. Eng. Data*, 2006, **51**, 1280–1282.

178   US20200243912A1, 2020, 1–12.

179   US20210104772A1, 2020, 1–12.

180   WO2020221918A3, 2020, 1–6.

181   J. Rodriguez, M. Politi, S. Adler, D. Beck and L. Pozzo, High-throughput and data driven strategies for the design of deep-eutectic solvent electrolytes, *Mol. Syst. Des. Eng.*, 2022, **7**, 933–949.

182   L. Bahadori, M. H. Chakrabarti, F. S. Mjalli, I. M. Alnashef, N. S. A. Manan and M. A. Hashim, Physicochemical properties of ammonium-based deep eutectic solvents and their electrochemical evaluation using organometallic reference redox systems, *Electrochim. Acta*, 2013, **113**, 205–211.

183   T. Xuan and L. Wang, Eutectic electrolyte and interface engineering for redox flow batteries, *Energy Storage Mater.*, 2022, **48**, 263–282.

184   B. B. Hansen, S. Spittle, B. Chen, D. Poe, Y. Zhang, J. M. Klein, A. Horton, L. Adhikari, T. Zelovich, B. W. Doherty, B. Gurkan, E. J. Maginn, A. Ragauskas, M. Dadmun, T. A. Zawodzinski, G. A. Baker, M. E. Tuckerman, R. F. Savinell and J. R. Sangoro, Deep eutectic solvents: A review of fundamentals and applications, *Chem. Rev.*, 2021, **121**, 1232–1285.

185   Y. Marcus, *Deep Eutectic Solvents*, 2019.

186   S. Creager, in *Handbook of Electrochemistry*, ed. C. G. Zoski, Elsevier B.V., Las Cruces, 1st Ed., 2007, pp. 57–72.

187   A. P. Abbott, D. Boothby, G. Capper, D. L. Davies and R. K. Rasheed, Deep Eutectic

Solvents formed between choline chloride and carboxylic acids: Versatile alternatives to ionic liquids, *J. Am. Chem. Soc.*, 2004, **126**, 9142–9147.

188 C. W. Lien, B. Vedhanarayanan, J. H. Chen, J. Y. Lin, H. H. Tsai, L. D. Shao and T. W. Lin, Optimization of acetonitrile/water content in hybrid deep eutectic solvent for graphene/MoS2 hydrogel-based supercapacitors, *Chem. Eng. J.*, 2021, **405**, 126706.

189 M. E. Di Pietro and A. Mele, Deep eutectics and analogues as electrolytes in batteries, *J. Mol. Liq.*, 2021, **338**, 116597.

190 K. Takechi, Y. Kato and Y. Hase, A highly concentrated catholyte based on a solvate ionic liquid for rechargeable flow batteries, *Adv. Mater.*, 2015, **27**, 2501–2506.

191 S. Kaur, M. Kumari and H. K. Kashyap, Microstructure of deep eutectic solvents: Current understanding and challenges, *J. Phys. Chem. B*, 2020, **124**, 10601–10616.

192 C. Zhang, H. Chen, Y. Qian, G. Dai, Y. Zhao and G. Yu, General design methodology for organic eutectic electrolytes toward high-energy-density redox flow batteries, *Adv. Mater.*, 2021, **33**, 1–8.

193 J. Zhang, R. E. Corman, J. K. Schuh, R. H. Ewoldt, I. A. Shkrob and L. Zhang, Solution properties and practical limits of concentrated electrolytes for nonaqueous redox flow batteries, *J. Phys. Chem. C*, 2018, **122**, 8159–8172.

194 L. Zhang, C. Zhang, Y. Ding, K. Ramirez-Meyers and G. Yu, A low-cost and high-energy hybrid iron-aluminum liquid battery achieved by deep eutectic solvents, *Joule*, 2017, **1**, 623–633.

195 Y. Wang and H. Zhou, A green and cost-effective rechargeable battery with high energy density based on a deep eutectic catholyte, *Energy Environ. Sci.*, 2016, **9**, 2267–2272.

196 C. Zhang, Y. Ding, L. Zhang, X. Wang, Y. Zhao, X. Zhang and G. Yu, A sustainable redox-flow battery with an aluminum-based, deep-eutectic-solvent anolyte, *Angew. Chemie Int. Ed.*, 2017, **56**, 7454–7459.

197 D. R. Macfarlane, N. Tachikawa, M. Forsyth, J. M. Pringle, P. C. Howlett, G. D. Elliott, J. H. Davis, M. Watanabe, P. Simon and C. A. Angell, Energy applications of ionic liquids, *Energy Environ. Sci.*, 2014, **7**, 232–250.

198 T. T. A. Dinh, T. T. K. Huynh, L. T. M. Le, T. T. T. Truong, O. H. Nguyen, K. T. T. Tran, M. V. Tran, P. H. Tran, W. Kaveevivitchai and P. M. L. Le, Deep eutectic solvent based on lithium bis[(trifluoromethyl)sulfonyl] imide (LiTFSI) and 2,2,2-trifluoroacetamide (TFA) as a promising electrolyte for a high voltage lithium-ion battery with a LiMn2O4

cathode, *ACS Omega*, 2020, **5**, 23843–23853.

199 Q. Zhang, K. De Oliveira Vigier, S. Royer and F. Jérôme, Deep eutectic solvents: Syntheses, properties and applications, *Chem. Soc. Rev.*, 2012, **41**, 7108–7146.

200 Y. Wang, Z. Niu, Q. Zheng, C. Zhang, J. Ye, G. Dai, Y. Zhao and X. Zhang, Zn-based eutectic mixture as anolyte for hybrid redox flow batteries, *Sci. Rep.*, 2018, **8**, 8–15.

201 J. C. Goeltz and L. N. Matsushima, Metal-free redox active deep eutectic solvents, *Chem. Commun.*, 2017, **53**, 9983–9985.

202 C. Zhang, Y. Qian, Y. Ding, L. Zhang, X. Guo, Y. Zhao and G. Yu, Biredox eutectic electrolytes derived from organic redox-active molecules: High-energy storage systems, *Angew. Chemie Int. Ed.*, 2019, **58**, 7045–7050.

203 N. S. Sinclair, D. Poe, R. F. Savinell, E. J. Maginn and J. S. Wainright, A nitroxide containing organic molecule in a deep eutectic solvent for flow battery applications, *J. Electrochem. Soc.*, 2021, **168**, 020527.

204 Y. Ding, C. Zhang, L. Zhang, H. Wei, Y. Li and G. Yu, Insights into hydrotropic solubilization for hybrid ion redox flow batteries, *ACS Energy Lett.*, 2018, **3**, 2641–2648.

205 V. Viswanathan, A. Crawford, D. Stephenson, S. Kim, W. Wang, B. Li, G. Coffey, E. Thomsen, G. Graff, P. Balducci, M. Kintner-Meyer and V. Sprenkle, Cost and performance model for redox flow batteries, *J. Power Sources*, 2014, **247**, 1040–1051.

206 Q. Luo, H. Zhang, J. Chen, D. You, C. Sun and Y. Zhang, Preparation and characterization of Nafion/SPEEK layered composite membrane and its application in vanadium redox flow battery, *J. Memb. Sci.*, 2008, **325**, 553–558.

207 D. Xing, S. Zhang, C. Yin, B. Zhang and X. Jian, Effect of amination agent on the properties of quaternized poly(phthalazinone ether sulfone) anion exchange membrane for vanadium redox flow battery application, *J. Memb. Sci.*, 2010, **354**, 68–73.

208 J. Xi, Z. Wu, X. Teng, Y. Zhao, L. Chen and X. Qiu, Self-assembled polyelectrolyte multilayer modified Nafion membrane with suppressed vanadium ion crossover for vanadium redox flow batteries, *J. Mater. Chem.*, 2008, **18**, 1232–1238.

209 S. C. Chieng, M. Kazacos and M. Skyllas-Kazacos, Modification of Daramic, microporous separator, for redox flow battery applications, *J. Memb. Sci.*, 1992, **75**, 81–91.

210 H. Park, G. Kwon, H. Lee, K. Lee, S. Y. Park, J. E. Kwon, K. Kang and S. J. Kim, In operando visualization of redox flow battery in membrane-free microfluidic platform,

Proc. Natl. Acad. Sci. U. S. A., 2022, **119**, 1–9.

211   M. O. Bamgbopa, S. Almheiri and H. Sun, Prospects of recently developed membraneless cell designs for redox flow batteries, *Renew. Sustain. Energy Rev.*, 2017, **70**, 506–518.

212   S. Yin, W. Liu, S. Yao, X. Du, P. Song and Z. Wang, A simply designed galvanic device with an electrocatalytic reaction, *New J. Chem.*, 2019, **43**, 6279–6287.

213   P. Navalpotro, C. M. S. S. Nevers, J. Palma, R. Marcilla, M. G. Freire, J. A. P. Coutinho and R. Marcilla, Pioneering use of ionic liquid-based aqueous biphasic systems as membrane-free batteries, *Adv. Sci.*, 2018, **5**, 1800576.

214   P. Xu, C. Xie, C. Wang, Q. Lai, W. Wang, H. Zhang and X. Li, A membrane-free interfacial battery with high energy density, *Chem. Commun.*, 2018, **54**, 11626–11629.

215   G. Li, W. Chen, H. Zhang, Y. Gong, F. Shi, J. Wang, R. Zhang, G. Chen, Y. Jin, T. Wu, Z. Tang and Y. Cui, Membrane-free Zn/MnO2 flow battery for large-scale energy storage, *Adv. Energy Mater.*, 2020, **10**, 1–10.

216   P. Navalpotro, C. Trujillo, I. Montes, C. M. S. S. Neves, J. Palma, M. G. Freire, J. A. P. Coutinho and R. Marcilla, Critical aspects of membrane-free aqueous battery based on two immiscible neutral electrolytes, *Energy Storage Mater.*, 2020, **26**, 400–407.

217   O. A. Ibrahim, M. A. Goulet and E. Kjeang, In-situ characterization of symmetric dual-pass architecture of micro fluidic co-laminar flow cells, *Electrochim. Acta*, 2016, **187**, 277–285.

218   K. Gong, F. Xu, M. G. Lehrich, X. Ma, S. Gu and Y. Yan, Exploiting immiscible aqueous-nonaqueous electrolyte interface toward a membraneless redox-flow battery concept, *J. Electrochem. Soc.*, 2017, **164**, A2590–A2593.

219   M. O. Bamgbopa, Y. Shao-Horn, R. Hashaikeh and S. Almheiri, Cyclable membraneless redox flow batteries based on immiscible liquid electrolytes: Demonstration with all-iron redox chemistry, *Electrochim. Acta*, 2018, **267**, 41–50.

220   S. A. M. Shaegh, N. T. Nguyen and S. H. Chan, A review on membraneless laminar flow-based fuel cells, *Int. J. Hydrogen Energy*, 2011, **36**, 5675–5694.

221   ES2633601A1, 2016.

222   WO2021209585A1, 2021.

223   X. Wang, A. Lashgari, J. Chai and J. Jiang, A membrane-free, aqueous/nonaqueous

hybrid redox flow battery, *Energy Storage Mater.*, 2022, **45**, 1100–1108.

224   A. E. Jones, A. Ejigu, B. Wang, R. W. Adams, M. A. Bissett and R. A. W. Dryfe, Quinone voltammetry for redox-flow battery applications, *J. Electroanal. Chem.*, 2022, **920**, 116572.

2. Experimental Methods and Theory

2.1. Materials

2.1.1. Chemicals

All chemical reagents, solvents and supporting salts were analytical or reagent grade and used as received without further purification.

Sigma-Aldrich, UK; acetonitrile (HPLC grade), ethyl acetate (>99.5 %), 1,2-dichlorobenzene (HPLC grade, >98%), 5-nonanone (98 %), trifluoromethanesulfonic acid (98 %), 2,2,6,6-tetramethylpiperidin-1-yl)oxyl (98 %), choline chloride (>98 %), ethylene glycol (99.8 %), $VOSO_4$ (>97 %), H_2SO_4 (99.99 %), KCl (99 %), KOH (>85 % pellets), D_2O (99.9%), CF_3CO_2D (>99 %), TFT (>99 %), valeronitrile (99.5 %), heptanenitrile (98 %), tetrabutylammonium perchlorate (>99 %), catechol (>99 %), 1,5-diaminoanthraquinone (97 %), *N*-methyl phthalimide (98 %), phenazine (98 %), benzophenone (99 %), 2,3-diaminophenazine (90 %), oxalic acid (98 %), glycerol (>99.5 %), urea (>99 %). Acros Organics; anhydrous acetonitrile (Acroseal®, anhydrous, extra-dry over molecular sieves, 99.99%). [BMPyrr][TFSI] (98 %). Merck Life Science UK, Ltd.; tetrafluorobenzoquinone (98 %), octafluoro-9,10-anthraquinone (98 %). Fisher Scientific UK, Ltd; tetra-*N*-butylammonium tetrafluoroborate (99.9 %), lithium perchlorate (99.99 %), LiCl (>99 %), LiTFSI (>99.99 %), heptanenitrile (98 %), tetrabutylammonium hexafluorophosphate (>99.9 %), tetraethylammonium chloride (<99.9 %). Fluorochem Ltd.; 4-hydroxy-2,2,6,6-tetramethylpiperidin-1-oxyl, 2,1,3-benzothiadiazole, $LiBF_4$, [BMPyrr][TFSI], [EMIM][TFSI]. Scientific Laboratory Supplies Ltd.; heptyl cyanide (97 %).

2.2. Electrochemical Methods

All electrochemical measurements were performed using a PGSTAT100 interface potentiostat and galvanostat, with NOVA (version 2.1.4.) software, as supplied by Metrohm Autolab B. V., the Netherlands.

The field of electrochemistry focusses on the relationship of electrical and chemical processes. At the heart of electrochemistry is the study of electron transfer at the electrolyte/electrode interface. The field covers a vast array of scientific fields, such as fundamental phenomena and thermodynamics, application-based devices, and large-scale technologies.[1]

Fundamentally, electrochemical systems comprise an ionic conductor, the electrolyte, and electronic conductors (the electrodes), with charge passing between the components when processes occur. The electrolyte phase carries charge by the movement of ions and must have sufficiently high conductivity to yield low resistance in the electrochemical system.

Electrolytes are typically solutions with free ionic species (e.g. H^+, Na^+, Cl^-) and can be either aqueous or non-aqueous. They can also consist of ionically conductive polymers (e.g. Nafion) or solid electrolytes (e.g. Na β-alumina).[1] The electrodes pass charge through movement of electrons and holes. The materials are usually solid metals (e.g. Pt, Au), liquid metals (e.g. Hg), carbon-based (e.g. graphite), or semiconductors (e.g. Si).

Two half-reactions make up each electrochemical reaction and occur independently at the electrolyte/electrode interface. The oxidation/reduction processes of these half-reactions alter the chemical composition at the interface, which in turn alters the interfacial potential difference. From this process, one can obtain qualitative and quantitative information over the reaction kinetics, thermodynamics and concentrations of the species involved.

This is possible because each half-cell reaction has a specific standard potential quoted. Usually, only one of the half-cell reactions is of interest, and the electrode corresponding to this reaction is the working electrode (WE). The generated current is then measured between the WE and a counter electrode (CE), which is typically a Pt mesh due to its low reactivity and high conductivity. A third electrode, termed the reference electrode (RE), comprises phases with essentially constant composition. The potentials recorded at the WE are reported *vs* the RE, which has a fixed potential compared to the internationally accepted primary RE: the standard hydrogen electrode (SHE). Equation 2.1. shows the half-equation that occurs at the SHE, which has a fixed potential of 0.0 V.

$$2H^+_{(aq)} + 2e^- \rightarrow H_{2(g)} \qquad\qquad 2.1.$$

This process means any changes in current potential response are ascribed to the process occurring at the WE. The SHE experimental set-up is inconvenient for everyday laboratory use, and so electrode potentials are often reported against other REs such as silver-silver chloride (Ag/AgCl, 0.197 V (*vs* SHE)) for aqueous, or silver-silver nitrate (Ag/Ag$^+$) for non-aqueous systems.[2]

This section explains the theory and procedures of the techniques used to build this thesis. Some methods work to calculate the D_o of a process. This is important for battery performance because it determines the rate of transport of active material through the electrolyte and to the electrode surface. A suitable redox-active material should have a high reaction speed as this contributes to lower overpotentials at a given current density. Either or both the electrochemical kinetics (electrochemical polarisation) and ORAM diffusion (concentration polarisation) control the electrochemical rate of reaction on the electrode surface.[3] The D_o is indicative of a molecule's ability to diffuse. A high D_o is necessary for high power output as it ensures the RAMs can get to and away from the electrode as fast as possible to undergo

charge transfer.[4] For reference, reported D_o values for VRFBs are (V^{2+}/V^{3+} = 1.41 × 10^{-6} cm^2 s^{-1}, V^{4+}/V^{5+} = 2.14 × 10^{-6} cm^2 s^{-1} in H_2SO_4 on carbon electrodes).[5,6]

2.2.1. Cyclic Voltammetry

Cyclic voltammetry (CV) is a technique used to study the reduction and oxidation processes of molecular species by cycling the potential (E, V) of the WE and measuring the resulting i. CV is a simple and direct technique for measuring the standard reduction potential (E^o) of RAMs. This is a popular electrochemical technique due to its non-destructive nature, versatility, fast rate of data collection, and relatively ease.

CV works by applying a potential to the WE (where the oxidation/reduction reactions occur) relative to the RE and varying E linearly with time (t). Figure 2.1.(a) gives an example waveform and (b) its corresponding voltammogram.[1] Significant features of the voltammogram are the number of peaks, the peak shapes, peak potentials (E_p), peak currents (i_p, A), and the current density (j, mA cm^{-2}). Key information on the kinetics and overall reaction come from studying the changes in these features with respect to increased cycling or scan rate (v, V s^{-1}). The exact value of E_p changes in different cell conditions due to factors such as the solvating power of the solvent.[7] Generally, increasing solvent permittivity or acidity increases solvation of X^- and a shift to more positive values for the X/X^- pair.
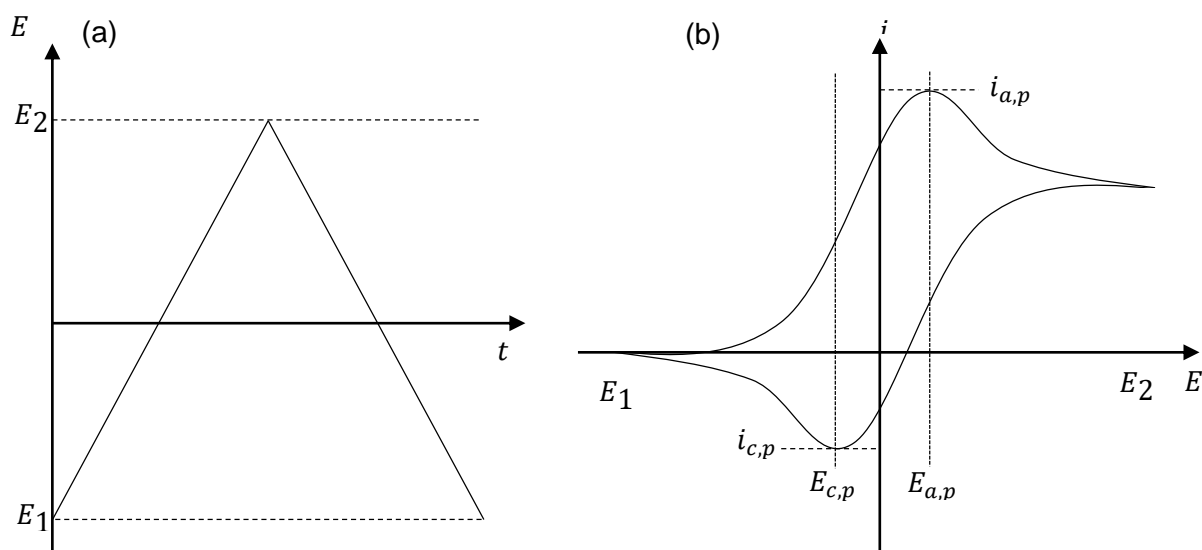
Figure 2.1. (a) Waveform for a cyclic voltammetry experiment and (b) the resulting voltammogram from a reversible redox reaction.[1]

The RAM undergoes reduction when the potential energy of the electrons in the WE are above that of the RAM's lowest unoccupied molecular orbital (LUMO). When the potential energy of the highest occupied molecular orbital (HOMO) of the RAM is higher than that of the WE, it is

energetically more favourable to undergo oxidation and transfer the electron to the electrode. The generated current is then measured between the WE and the CE. Placing the RE tip as close as possible to the WE minimises uncompensated solution resistance (R_u). This configuration only includes a single electrolyte phase and is known as the three-electrode cell.[1]

The experiments are controlled by altering the upper and lower potential limits, v, the number of cycles, the direction of the initial scan, the temperature (T, K), gas presence, the nature of the electrolyte, or the electrode materials. The starting potential is where j is zero, and positive and negative scans study oxidative and reductive processes, respectively.

The Nernst equation predicts how a system will respond to changes in electrode potential or species concentration. Equations 2.2. – 2.6. show how the Nernst equation governs electron-transfer reactions. The Nernst equation is derived from the standard Gibbs free energy change, ΔG^o (kJ mol^{-1}), under standard conditions which is related to the E^o, under standard conditions. All symbols are as before.

$$E^o = E^o_{reduction} - E^o_{oxidation} \qquad\qquad 2.2.$$
$$\Delta G^o = -nFE^o \qquad\qquad 2.3.$$

The Gibb's energy change under non-standard conditions (ΔG) relates to ΔG^o by Equation 2.4., where R is the ideal gas constant (J K^{-1} mol^{-1}), and Q the reaction quotient, which is equivalent to the equilibrium constant (K_{eq}) at equilibrium.

$$\Delta G = \Delta G^o + RTlnQ \qquad\qquad 2.4.$$

Substituting Equation 2.3. into Equation 2.4. yields Equation 2.5., the Nernst equation. Equation 2.6. gives a more experimentally accessible version of the Nernst equation, where $E^{o'}$ represents the formal potential, which is specific to the experimental conditions and is the correction for the non-standard potential for non-ideal conditions. Q is the ratio of the concentration of reduced ([X$^-$]) and oxidised ([X]) species in the one electron reversible reaction in Equation 2.7.

$$E = E^o - \frac{RT}{nF}\ln Q \qquad\qquad 2.5.$$
$$E = E^{o'} + 2.3026\frac{RT}{nF}\log_{10}\frac{[X^-]}{[X]} \qquad\qquad 2.6.$$
$$X + e^- \leftrightarrow X^- \qquad\qquad 2.7.$$

At standard conditions (T = 298 K), this becomes Equation 2.8. This shows how an ideal chemically and electrochemically reversible reaction should have a peak-to-peak separation

(ΔE_p), that is the potential difference between the anodic (E_{pa}) and cathodic peaks (E_{pc}), of 59 mV. Reactions that follow this are considered 'Nernstian processes' and produce the typical CV shape in Figure 2.1. Experimentally, CVs vary from the ideal curve due to a combination of polarisation and diffusion effects. Figure 2.1. also shows another important element of CV analysis, the half wave potential ($E_{1/2}$), which is the difference between E_{pa} and E_{pc}.

$$E = E^o + \frac{0.0592}{n}\log_{10}\frac{[X^-]}{[X]} \qquad \text{2.8.}$$

Chemical reversibility refers to the ability of the RAM to undergo reduction and subsequent re-oxidation without decomposition. Electrochemical reversibility relates to the electron transfer kinetics between the electrode and the RAM. The ΔE_p will not change in a reversible process because the electron transfer rate constant (k_0, cm s^{-1}) is high enough that concentrations of both the oxidised and reduced species at the electrode change instantly with every small variation in electrode potential.[8]

Irreversible electron transfer processes have a lower k_0, and so require more extreme potentials to induce electron transfer and cause current to flow. This culminates in an increase in ΔE_p with v. For most irreversible electron transfer processes, a plot of E_p vs $\log_{10}v$ gives a slope of 60 mV per logarithmic integer. Quasi-reversible electron transfers are those with an intermediate k_0, and hence also experience an increase in ΔE_p with v. Chemical irreversibility also contributes to quasi-reversible or irreversible redox processes. Termed EC processes, these are attributable to a chemical reaction step (C) that is triggered by the electron transfer step (E). An ECE reaction is another possible pathway. In this process the first E step leads to a C step that produces an intermediate which is easier to reduce/oxidise than the starting compound.

A plot of the cathodic and anodic maximum currents (i_{pc} and i_{pa}, respectively) against the square root of v ($v^{1/2}$) calculates D_o using the Randles-Ševčík equation in Equation 2.9.:

$$i_p = 0.446nFAC^0(\frac{nFvD_0}{RT})^{\frac{1}{2}} \qquad \text{2.9.}$$

Where all symbols are the same as above, A is the surface area of the working electrode (cm^2), and C the molar concentration (mol cm^{-3}).

Equation 2.9. describes the dependence of i_p on v. Faster v leads to a thinner diffusion layer which results in higher measured i. A fast D_o of $>10^{-7}$ cm^2 s^{-1} is essential for battery applications.[9] For an electron transfer process including freely diffusing redox species to be

electrochemically reversible ($\Delta E_{p,rev} = 59/n$ mV), i_p must increase linearly with $v^{1/2}$. Deviations from linearity suggest either electrochemical quasi-reversibility ($\Delta E_{p,rev} < \Delta E_{p,qrev} < 200/n$ mV), electrochemical irreversibility ($\Delta E_{p,irrev} > 200/n$ mV), or that the electron transfer step involves a surface-adsorbed species. An anodic to cathodic peak current ratio (i_{pa}/i_{pc}) of 1 indicates a reversible, diffusion-controlled reaction. Electrochemically quasi-reversible systems are identifiable as ΔE_p shifts with v, which does not occur with surface-adsorbed species. Furthermore, surface adsorbed species should give linear plots of i_p *vs* v and have a peak width of 90 mV.[8]

In this report, CV is conducted over scan rates of $25 \leq v \leq 1000$ mV s^{-1}. Solutions are de-aerated by bubbling Ar$_{(g)}$ through the solution for 20 minutes before experiments, and the headspace purged with Ar$_{(g)}$ during testing. All CV experiments utilise a bespoke three-electrode cell designed to exclude oxygen. A glassy carbon (GC) WE of surface area 0.196 cm^2 (unless otherwise specified) was polished to a mirror shine with 0.05 μm alumina slurry then rinsed with *iso*-propanol and deionised water prior to use. The platinum CE was annealed prior to each test. A saturated calomel electrode (SCE, −0.244 V (*vs* SHE)) or Ag/AgCl RE was used for aqueous tests, and either a silver wire quasi-reference electrode or commercial Ag/AgNO$_3$ (Ag/Ag$^+$) RE were used in non-aqueous studies.

Aqueous experiments used 10 mM concentrations of RAM. Non-aqueous experiments used concentrations of 1 mM RAM and 100 mM supporting electrolyte. Tetrabutylammonium tetrafluoroborate (TBABF$_4$) was used as a supporting electrolyte in non-aqueous solvents due to its high stability and wide electrochemical potential window. A background CV was recorded before each CV experiment to exclude background contaminations.

2.2.2. Hydrodynamic Voltammetry

CV experiments occur under static conditions thus the steady-state current is limited by the diffusion-controlled mass-transfer of the RAM to the electrode. Under these conditions, the diffusion layer thickness is equal to the boundary layer, which is easily perturbed by external disturbances. Hydrodynamic voltammetry differs from this by changing the WE to a rotating disk electrode (RDE).

The RDE rotates at a particular frequency, f (revolutions per minute (RPM)), but the rate is often described in terms of the angular velocity, ω (rad s^{-1}), where $\omega = 2\pi f$. This thesis expresses rotation speeds in terms of f. Figure 2.2.(a) shows how rotating the RDE creates a laminar flow of solution across the electrode surface and (b) the typical resulting i vs E voltammogram from a linear sweep voltammetry (LSV) experiment. The rotation ensures a constant flow of fresh reactant to the electrode surface. As f increases, the distance that material can diffuse from the surface before removal by convection decreases. Increased rotation rates lead to a higher flux of reactant to the electrode, resulting in increased reaction rates, higher currents, improved sensitivity, and insight into mechanistic analysis.[1]
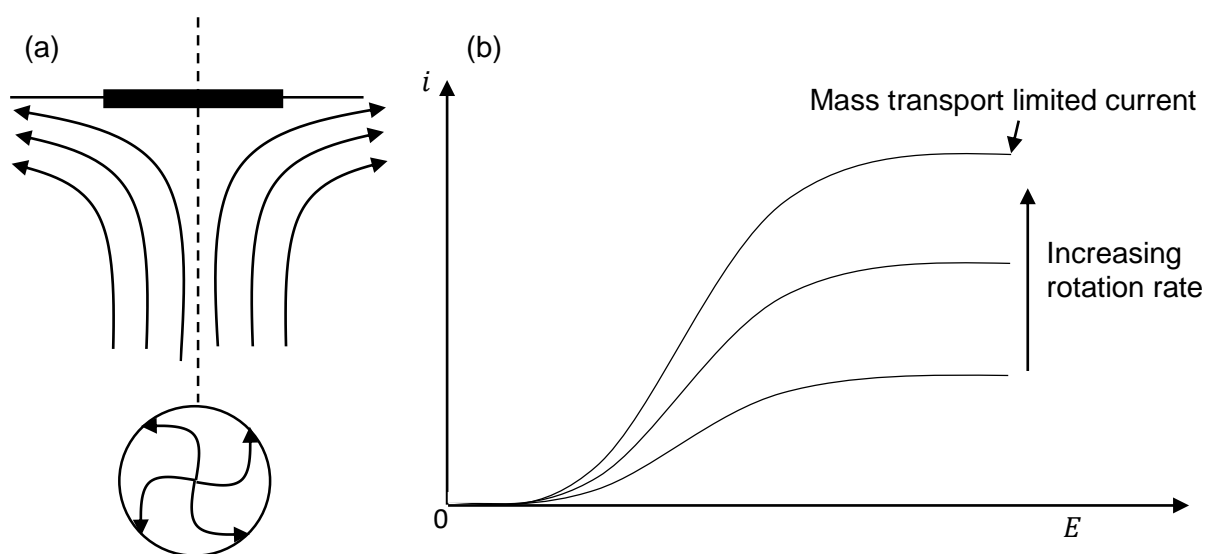
Figure 2.2. (a) Schematic of the laminar flow that occurs with a rotating disk electrode. (b) The resulting voltammogram from a linear sweep voltammetry experiment under a variety of rotation rates.[1]

LSV experiments study the hydrodynamic electrochemistry. LSV is similar to CV in that the potential is swept between two given potential values, except LSV is not reversed and so the waveform and resulting voltammogram appears as half of the CV. When in rotating conditions, the system quickly attains a steady state that results in a mass transfer limited current (i_{lim}), also known as the diffusion limited current. At this point, the potential is so far past the $E_{1/2}$ that the electron transfer equilibrium drives completely to the products. At this point, the rate of electron transfer is dependent on the rate of RAM diffusion to the electrode surface. This registers as a current plateau in the plot. The steady-state current means the response in both halves of the cycle should be the same. Therefore, no new information is gathered upon reversing the scan and hence, the LSV is only performed in one direction.

Reversible reactions produce a straight-line plot of i_{lim} vs $\omega^{1/2}$ from which one applies the Levich equation in Equation 2.10. to calculate the D_o. Deviations from a straight line intersecting the origin suggest a kinetic limitation in the electron-transfer reaction.

$$i_{lim} = 0.62nFAC_{bulk}D_o^{\frac{2}{3}}v^{\frac{-1}{6}}\omega^{\frac{1}{2}} \qquad\qquad 2.10.$$

Hydrodynamic analysis also uncovers information on the reaction kinetics and k_0. If the electron transfer process at the electrode surface is fast, then the voltammogram carries the sigmoidal shape from Figure 2.2.(b). Slow kinetics require a larger overpotential to reach i_{lim}, so the plateau shifts further from E^o and the voltammogram appears stretched along the potential axis.

By sampling i at specific E values along the rising portion of the voltammogram and subsequently plotting $1/i_{lim}$ against $\omega^{-1/2}$, one obtains a linear Koutecký–Levich plot. Extrapolating this linear relationship to the vertical axis yields a non-zero intercept equal to the reciprocal kinetic current ($1/i_K$) by Equation 2.11. i_K is the current when there is an absence of any mass transfer limitations, and thus indicates a kinetic limitation on the process. Applying i_K in the Koutecký–Levich equation in Equation 2.12. gives k_0.

$$intercept = \frac{1}{nFk_0C} \qquad\qquad 2.11.$$

$$\frac{1}{i_{lim}} = \frac{1}{i_{k0}} + (\frac{1}{0.62nFAD^{2/3}v^{-1/6}C})\omega^{-1/2} \qquad\qquad 2.12.$$

RDE experiments were carried out in the same three-electrode cell as CV. The WE consisted of a GC RDE of surface area 0.196 cm^2, and the CE and RE were the same as employed in CV characterisation (see section 2.2.1.). LSV was performed at a scan rate of 2 mV s^{-1} over a range of rotational frequencies from $200 \leq f \leq 3600$ RPM. All electrolytes were purged with $Ar_{(g)}$ for 20 minutes prior to experimentation and the headspace continuously gassed throughout to guarantee de-aeration.

2.2.3. Chronoamperometry

Chronoamperometry is a method of determining thermodynamic or kinetic information from a system (e.g. D_o), driving reactions within a given set of conditions (e.g. electrodeposition), or studying spontaneous processes under zero applied potential. Using the reversible reaction in Equation 2.7. as an example, chronoamperometry involves applying a potential step to the WE from a value where no faradaic processes occur (E_1) to a potential where X is reduced at a diffusion-limited rate to X$^-$ whilst recording i as a function of time (t). Figures 2.3.(a) and 2.3(b) show the waveform and respective plot from this test.[1]

The magnitude of the initial current is significantly high because as the potential steps from V_1 to V_2 all of X at the WE surface instantly reduces to X⁻. The resulting concentration gradient leads to flux of X to the WE surface, where it immediately reduces. The flux of X, and hence resulting i, is proportional to the concentration gradient at the surface. The magnitude of i decays with respect to t because the continued flux leads to an increase in the depletion layer thickness, and thus a decrease in the concentration gradient at the WE surface over time.[1]
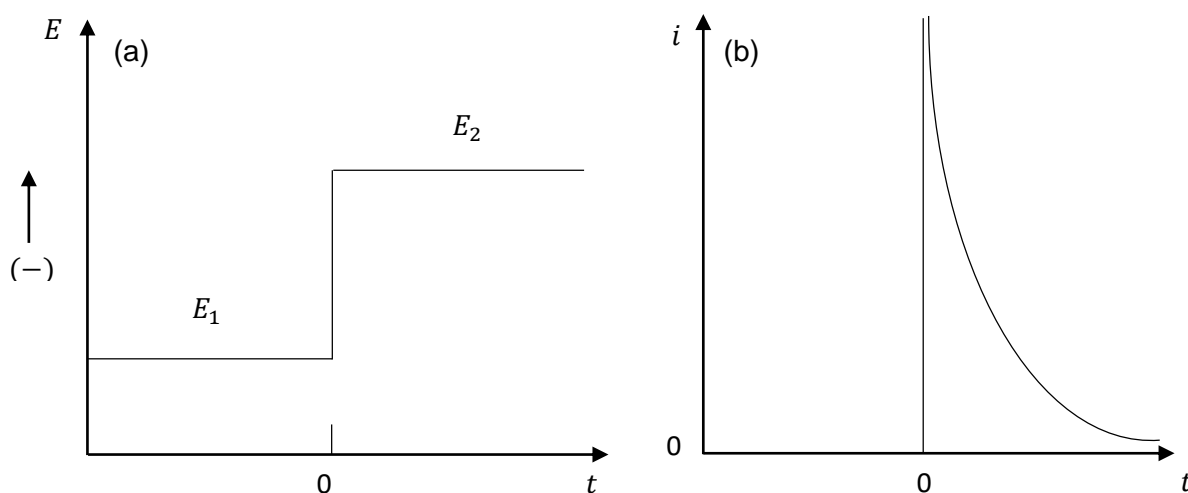
Figure 2.3. (a) Waveform of the step experiment from a region where X is electro-inactive (E_1) to a potential where X reduces to X⁻ at a diffusion-limited rate (E_2). (b) The resulting current vs time plot of (a).[1]

The Cottrell equation in Equation 2.13. describes the i at any time following this potential step in the reversible redox reaction as a function of $t^{-1/2}$.

$$i_t = \frac{nFACD_o^{1/2}}{\pi^{1/2}t^{1/2}}$$

2.13.

The electrical double layer effect causes a capacitive current (i_c) that contributes to the overall current. The i_c decays as a function of $1/t$ and so is only significant during the first few ms after the potential step. Its contribution can either be digitally subtracted using a blank electrolyte test, or through ignoring the first 10 % of the $i - t$ data.

2.2.4. Electrochemistry at Liquid/Liquid Interfaces

Charge transfer at L/L interfaces is one of the most fundamental physical processes. This field of electrochemistry studies electron or ion transfer over a L/L, or oil/water (o/w) interface, or at an ITIES. L/L studies are key in understanding the mechanisms in phase transfer catalysis, extraction process and chemical sensing, exploring solar energy conversion processes, drug delivery, and in understanding biological membranes.[10]

There are two types of charge transfer reactions at L/L interfaces:

1) Ion transfer (Equation 2.14.): Transfer of an ion, M^z, where z is the charge number, from the water phase (w) to the oil phase (o) and *vice versa*.

$$M_w^z \leftrightarrow M_o^z \tag{2.14.}$$

2) Electron transfer (Equation 2.15.): Transfer between a redox couple, O_1/R_1, in phase w and another, O_2R_2, in phase o.

$$O_{1,w} + R_{2,o} \leftrightarrow R_{1,w} + O_{2,o} \tag{2.15.}$$

The heterogeneous charge transfer reactions are sometimes more complex as they can couple to homogeneous chemical reactions in each phase or to heterogeneous reaction at the interfacial region (for example, ion-pair formation or adsorption).

The electrochemical potentials for the ion M^z in both phases must be equal for equilibrium. Equation 2.16. shows the equilibrium and Equation 2.17. and 2.18. the expanded w and o forms, where μ^0_M is the standard chemical potential, α_M the activity, and φ the inner potential of M^z in w and o phases.

$$\bar{\mu}_M^w = \bar{\mu}_M^o \tag{2.16.}$$
$$\bar{\mu}_M^w = \bar{\mu}_M^{0,w} + RT \ln \alpha_M^w + zF\varphi^w \tag{2.17.}$$
$$\bar{\mu}_M^o = \bar{\mu}_M^{0,o} + RT \ln \alpha_M^o + zF\varphi^o \tag{2.18.}$$

By combining Equations 2.17. and 2.18. one achieves the equilibrium potential difference, $\Delta^w_o\varphi$. This results in Equation 2.20. and is analogous to the Nernst equation (Equation 2.5.) for electrode potential, where $\Delta^w_o\varphi^0_M$ is the standard transfer potential.

$$\Delta_o^w \varphi = \varphi^w - \varphi^o \tag{2.19.}$$
$$\Delta_o^w \varphi = \Delta_o^w \varphi_M^0 = \left(\frac{RT}{zF}\right) \ln\left(\frac{\alpha_M^o}{\alpha_M^w}\right) \tag{2.20.}$$

The resemblance of Equation 2.20. for ion transfer reactions at equilibrium to the classical Nernst equation for redox reactions implies that the same electrochemical methods used for reversible reactions are equally relevant in the L/L case.

Charge-discharge experiments on L/L devices were recorded using two defined conditions:

(a) Galvanostatic conditions of a charge and discharge current equal to that in the two-electrode cell CV set for an arbitrary time of 3600 s.

(b) Potentiostatic conditions using cut-off voltages determined by the separation of redox events between the separate three-electrode cell CVs.

Charge was initiated under galvanostatic conditions. If the cut-off voltage was reached before the time limit, the system switched to discharging. This process was repeated for several cycles to study the charge-discharge characteristics of the system.

2.3.   Electrochemical Cell Designs

Chapter 1.2.1. discusses the conventional RFB design of an all solution-phase ESS wherein liquid electrolytes containing RAMs cycle through a central stack and undergo charge-discharge. The electrochemical processes take place on the surface of the electrodes. Therefore, it is solely the fundamental electrochemistry of the RAMs that governs the redox kinetics of the battery. This simplifies the RFB system in such a way that conventional voltammetry or bulk electrolysis (BE) apparatus are useful in studying the electrochemical processes. Developing a full RFB-system requires much more detailed chemical engineering considerations. This is because optimising the characteristics of each flow-cell component is critical in the final battery performance.

For example, to optimise the power density one must improve mass transport; reduce ohmic resistance; and optimise the redox kinetics. Higher electrolyte flow rates and even flow distributions reduce electrolyte convection and facilitate material diffusion, improving the mass transport. Increasing electrolyte and membrane conductivity, for example by reducing the inter-electrode separation, reduces the ohmic resistance. To improve the kinetics, one can surface treat electrode materials or employ electrocatalysts. It is therefore clear that optimal cell design is a critical factor in the overall performance of the RFB.

Commercial RFBs require large electrolyte volumes. For example, a 400 kW h VRFB ESS with an electrolyte energy density of 30 Wh L^{-1} requires 26,000 L of electrolyte.[13] The same VRFB also requires 715 minutes at 100 kW cycle power for a full charge-discharge cycle.[13] Minimising electrolyte volumes reduces these experimental timescales and allows for higher numbers of cell cycles in a given timeframe. This not only yields more accessible long-term stability data, but also minimises the quantities and costs of redox material, supporting electrolyte, and solvent used per experiment. This explains why cells in academic research hold different designs than life-size RFB systems.

This thesis focusses solely on the electrolyte component of the RFB system, which as discussed above, is independent of the flow-cell construction. Therefore, most of the tests over Chapter 3. to Chapter 6. use homemade electrochemical cells with total electrolyte volumes <100 cm^3 to study the ORAM electrochemistry. At the onset of this work, our research group did not possess suitable electrochemical redox-flow cells to enable cell cycling. Towards

the end of the study, H-cells and flow cells became accessible and are used to probe ORAM stability in Chapter 4. and the membrane-free battery under flow in Chapter 5.

2.3.1. Three-Electrode Cells

All CV and LSV experiments in this thesis utilise the standard three-electrode cell described in Section 2.2.1. to study the ORAM electrochemistry. Figure 2.4. gives a schematic of the cell, which includes a GC WE that is also an RDE. The cell comprises two side-arms, one for the Pt mesh CE and one for the $Ar_{(g)}$ flow.
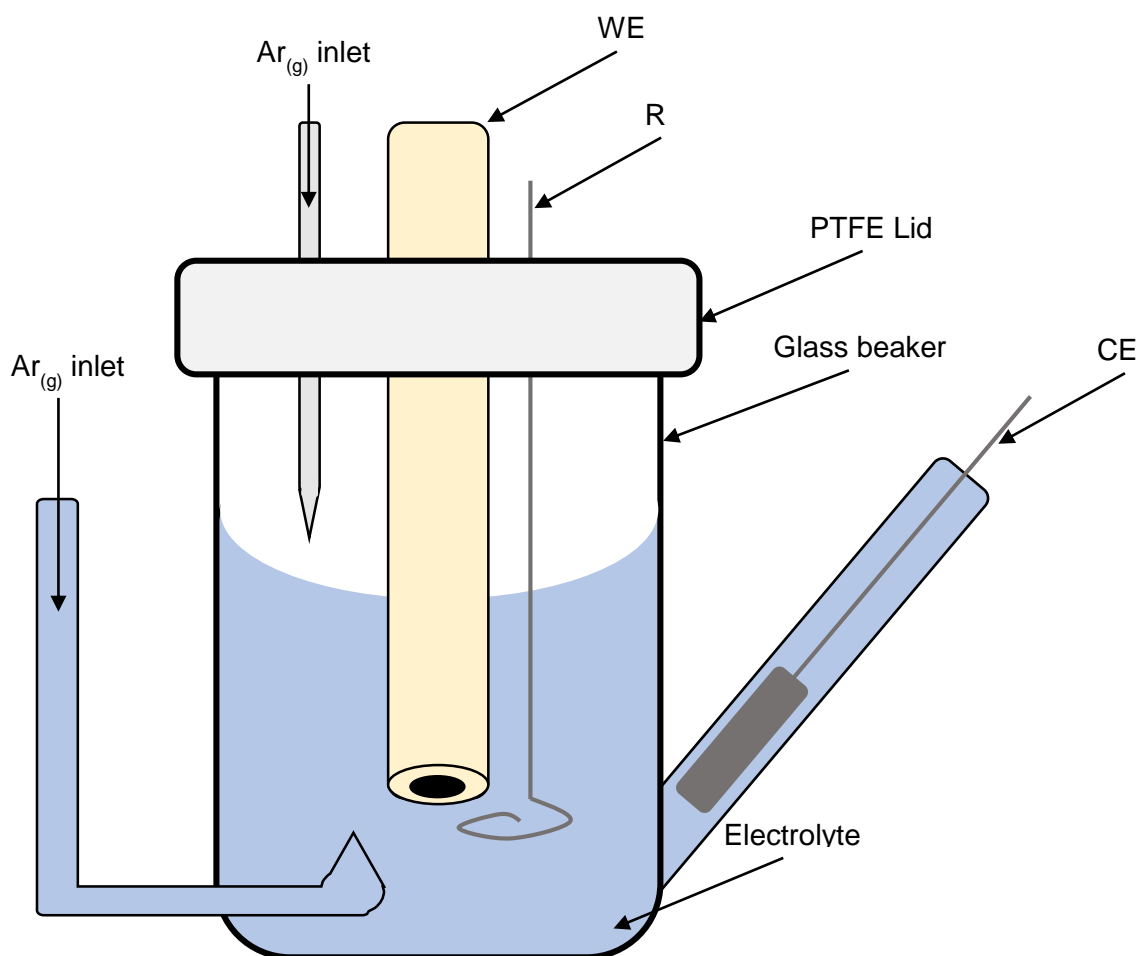
Figure 2.4. Schematic of the three-electrode cell used for electrochemical analysis.

The outlet of the gas flow is small and offset from the WE, so only small bubbles release into the electrolyte to minimise noise. Separating the CE from the rest of the cell allows observations of any colour changes in solution around the CE that may indicate side reactions. A gas-tight lid fits the top of the beaker with holes for the WE, RE, and an additional gas flow inlet constantly degasses the headspace.

2.3.2. Bulk Electrolysis

Schematic of bulk electrolysis glass H-cell.BE was performed using the homemade glass H-Cell with a PVDF separator in Figure 2.5. The left-hand compartment carries out electrolysis by use of a reticulated vitreous carbon (RVC) felt WE and a commercial Ag/Ag$^+$ RE. The right-hand compartment contains the sacrificial electrolysis material with an RVC CE. A porous PVDF membrane separates the half-cells and inhibits excessive solution crossover but allows counter-ion migration.
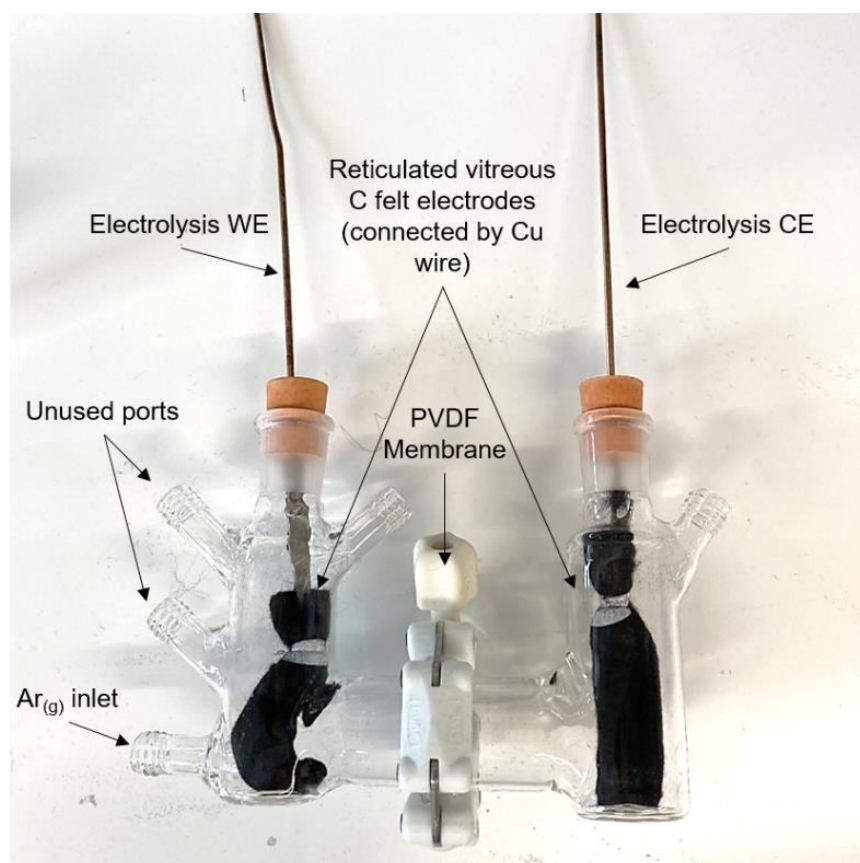
Figure 2.5. Schematic of bulk electrolysis glass H-cell.

Applying a potential sufficiently negative of the E^o will reduce and electrolyse the ORAM. The endpoint of the experiment is when the current drops to near 0 A, indicating no more neutral ORAM remains in the solution for reduction. Constant $Ar_{(g)}$ bubbling maintains the de-aerated atmosphere for the BE experiments and agitates the solution to ensure adequate mixing of the electrolyte in the WE compartment.

2.3.3. Symmetric Cell Cycling

Battery-like experiments on a singular ORAM are possible by coupling both the re-oxidation of the BE product and reductive processes of the same neutral molecule in one full cell system. The cell can undergo 'charge' and 'discharge' such that each electrolyte converts between 0

and 100 % SoC. These are, however, arbitrary definitions merely to define the passing of positive and negative current until reaching a positive or negative potential. This simplifies the full-cell RFB experiment to studying properties such as overpotentials and ORAM stability of just one ORAM over its range of oxidation states.[14] As the overall cell potential is 0 V, this is not a battery and it stores no energy.

Symmetric flow-cell tests were conducted using the H-cell in Figure 2.5. at a constant charging current of 0.75 mA with the time constraint of 120 s per charge and discharge cycle. Symmetric redox couple cell cycling experiments take place by performing BE on 1 mM OFAQ, 0.1 M TBABF$_4$, ACN, to produce one fully charged half-cell of OFAQ^{2-}. Then disposing of the opposite half-cell electrolyte and replacing it with fresh OFAQ solution.

2.3.4. Membrane-Free Working Principle and Cell Design

Typical L/L electrochemical studies adopt the four-electrode system in Figure 2.6. A four-electrode potentiostat compensates for the *iR*-drop over both phases. The cell comprises two REs and two CEs, wherein the WE and the sense electrode are connected to the aqueous half-cell CE and RE, respectively. Placing the Luggin capillaries for the REs, typically Ag/AgCl, in each phase as close to the interface as possible minimises the R_u. A reference phase containing a common ion is necessary for referencing the organic phase electrochemistry against the same RE as the aqueous phase. The current passes through the two Pt CEs to complete the circuit.
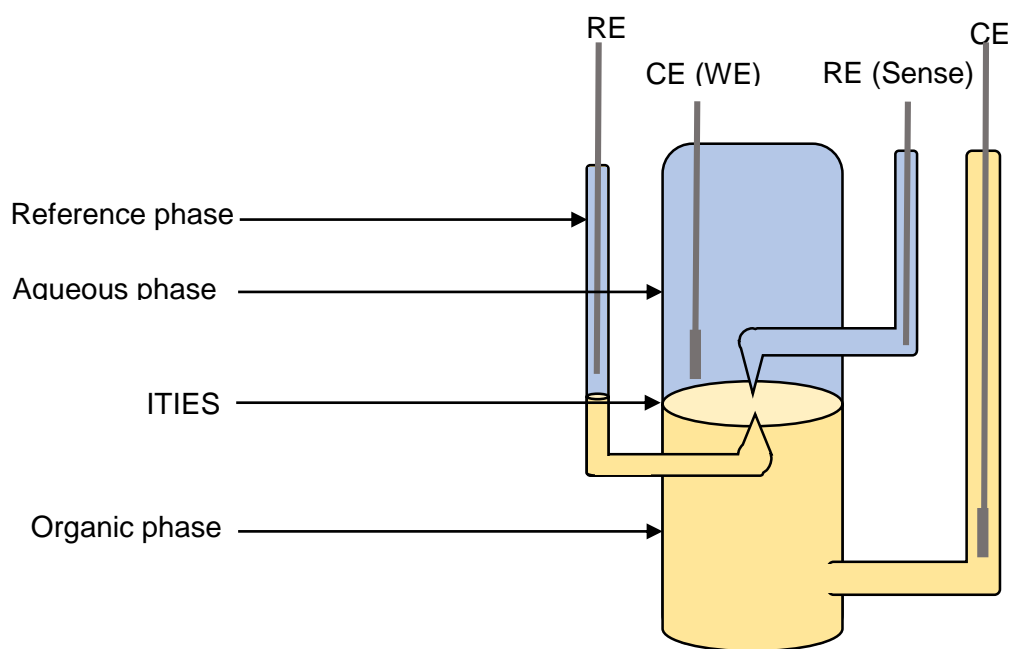
Figure 2.6. Schematic of typical four-electrode cell for liquid-liquid electrochemistry.

This electrochemical set-up allows direct access to the lower (organic) phase for a CE without disrupting the L/L interface. However, this is only practical when the organic phase is more dense than the aqueous. If the organic phase is less dense than the aqueous phase it becomes the upper layer, and the standard four-electrode cell is not useful.
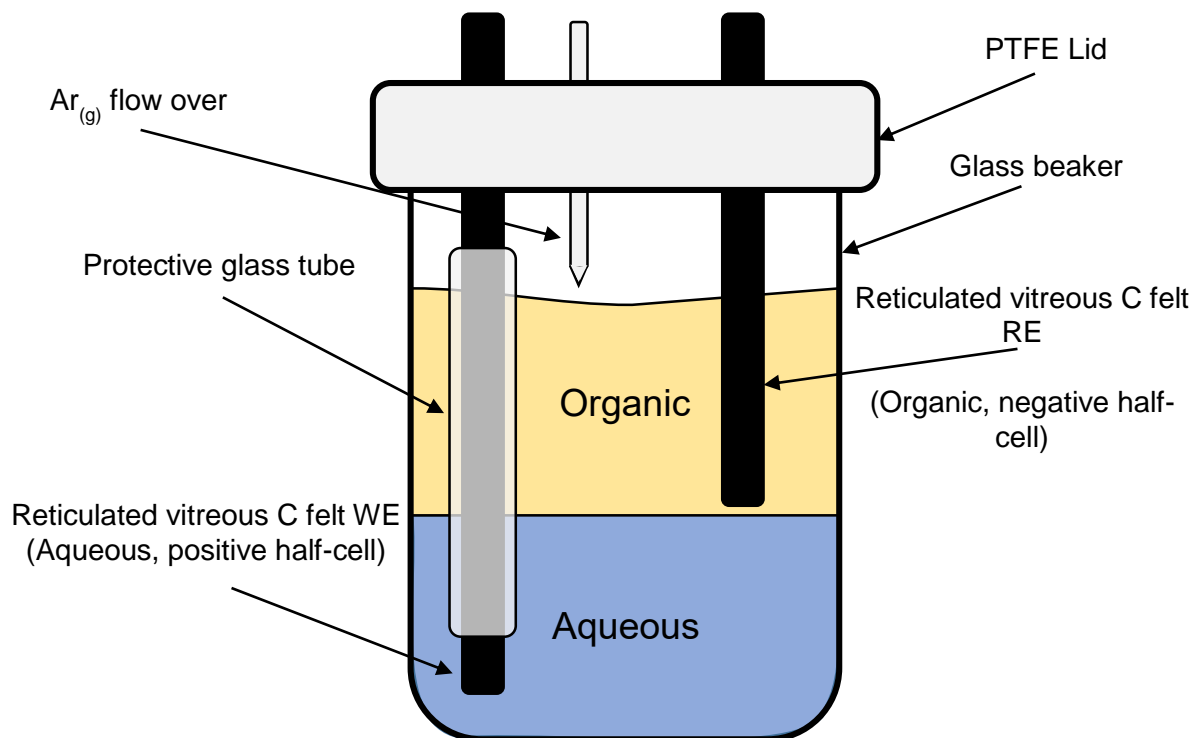
Figure 2.7. Schematic of the cell used in liquid-liquid membrane-free cell tests.

In this scenario, one can use a two-electrode cell. The schematic in Figure 2.7. shows the two-electrode cell used in this study. Membrane-free battery testing was conducted using a 25 cm^3 glass beaker with a PTFE lid with inlet ports for the electrodes and Ar$_{(g)}$ flow. The cell comprises two rectangular RVC felt electrodes for the WE and the RE in the positive and negative half-cells, respectively. A glass tube covers the WE to protect it from contacting the organic electrolyte and shorting the battery. Each phase contains the same volume of electrolyte (10 mL) and the surface area of the interface is 6.51 cm^2.

The membrane-free systems use the same three-electrode cell set-up described in Section 2.2.1. for CV studies, which comprises a GC WE, an Ag/Ag$^+$ RE, and a Pt CE under constant Ar$_{(g)}$ flow. Charge-discharge profiles were obtained using the method described in 2.2.4. and the cell in Figure 2.7. The gas inlet maintains Ar$_{(g)}$ flow in the headspace to prevent anion degradation in the organic phase and reduce the propensity for ACN solvent evaporation. For each ORAM L/L system a CV scan was run prior to battery testing to ensure that charge passes the interface, and the interface is stable over the course of the scan.

The nature of the ORAMs in this work mean the aqueous half-cell is the positive side and the organic the negative counterpart. Aqueous half-cells comprise 2 – 20 mM ORAM in a 10 m LiCl WIS electrolyte. The high concentration of LiCl is necessary to obtain a stable L/L interface with the organic electrolyte, ACN. Systematic tests on increasing molalities of LiCl show 5 m is the minimum concentration LiCl sufficient to produce a biphasic system with ACN. 10 m LiCl was used to ensure complete and stable phase separation. At such high WIS concentrations, the aqueous phase is denser than the organic phase and thus lies underneath the ACN.

Organic electrolytes comprise a negative ORAM in 0.1 M $LiBF_4$, ACN. The $LiBF_4$ supporting electrolyte is necessary to ensure there is a common ion (Li^+) in both the aqueous and non-aqueous half-cells to conduct charge across the interface.

Galvanostatic charge-discharge experiments were performed on the membrane-free battery under flow conditions using the bespoke cell in Figure 2.8. Norprene peristaltic pump tubing (Cole-Parmer, Masterflex L/S 14) connects the flow cell to a peristaltic pump. The cell is analogous to the static cell in Figure 2.7. in using an RVC Felt WE and RE. The surface area of the interface is 3.14 cm^2. This is slightly lower than for the static cell, which may influence the charge-transfer performance. Additionally, the top of the cell is open to air, which causes issues in long-term cycling due to solvent evaporation.
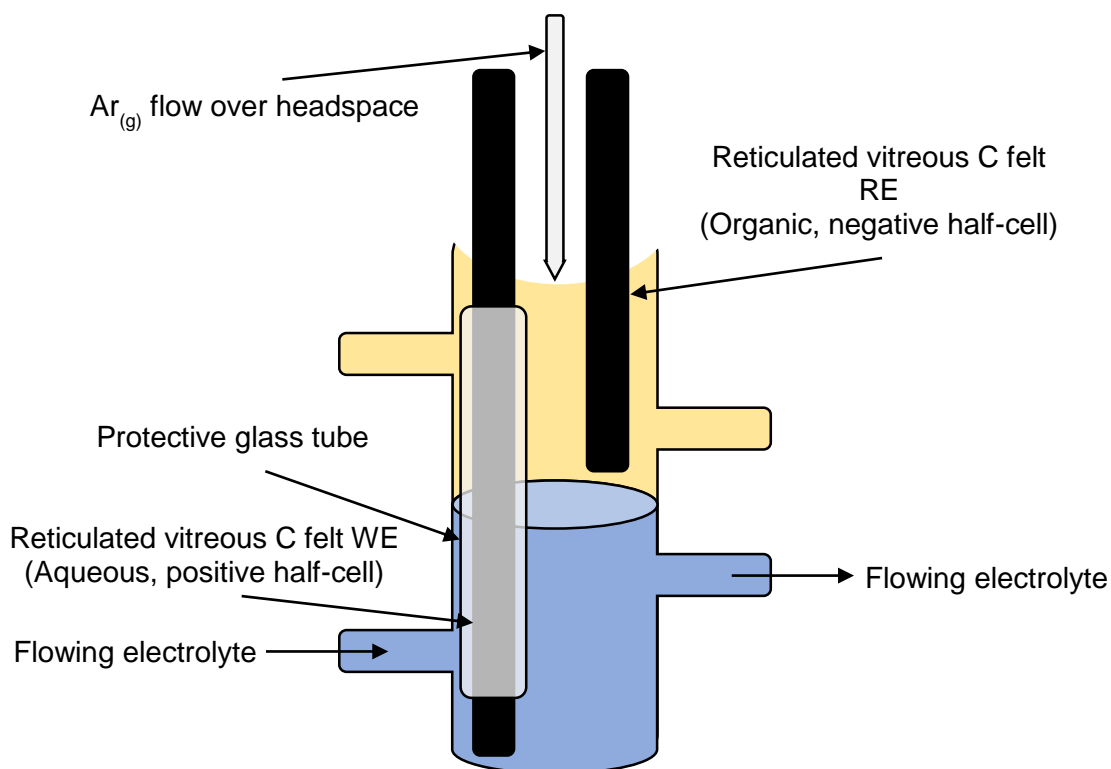
Figure 2.8. Schematic of the cell used in flowing liquid-liquid membrane-free cell tests.

Battery experiments use 1 mM OFAQ in 0.1 M LiBF$_4$, ACN as the upper, non-aqueous phase, and 20 mM VOSO$_4$, 2 M HCl, 10 m LiCl as the lower, aqueous phase. Only the aqueous phase was tested under flow, over the range of flow rates 16.8 to 37.2 mL min^{-1}. The poor performance after flowing just one half-cell in Chapter 5.3. meant the study did not extend to flowing both.

2.4. Physical Characterisation Methods

2.4.1. Ultraviolet-Visible Spectroscopy

Ultraviolet-visible (UV-Vis) spectroscopy was performed with a Mikropack DH-2000-BAL spectrometer with deuterium-halogen light sources and operated with OOIBase32 (version 2.0.6.5.) software (Ocean Optics, Germany).
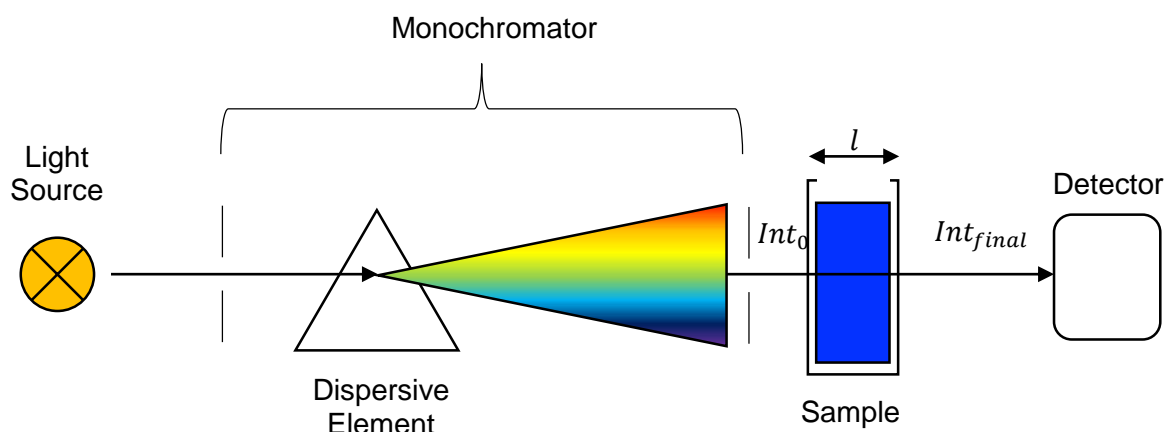
Figure 2.9. Schematic of the ultraviolet-visible spectrometer.

UV-Vis spectroscopy is a qualitative and quantitative absorption spectroscopy technique performed by irradiating a sample with electromagnetic waves in the UV-Vis region (800-200 nm or 6.2-1.5 eV) and recording the change in light intensity. Figure 2.9. shows a schematic of the process and the component parts of the spectrometer.

The change from the initial intensity (Int_0) to the final intensity (Int_{final}) occurs because molecules in the sample absorb photons and excite electrons from the ground to the excited state. Every molecule absorbs photons of a specific wavelength, and thus yields a characteristic absorbance peak. The total absorbance (Abs) is related to the intensity of light by Equation 2.21.

$$Abs = \log_{10}[\frac{Int_0}{Int_{final}}]$$

2.21.

Applying an accurate calibration curve in conjunction with the Beer-Lambert law (Equation 2.22.) gives quantitative information on the concentration of the molecules in the sample.

$$Abs = \varepsilon Cl \hspace{4cm} 2.22.$$

Where *l* is the path length of the cuvette (cm), and ε is the molar extinction coefficient (M^{-1} cm^{-1}).

2.4.2. Scanning Electron Microscopy with Energy Dispersive X-ray Spectroscopy

Scanning electron microscope (SEM) images were gathered using an FEI Quanta 650 FEG ESEM equipped with a field emission gun (FEG), Everhart-Thornley secondary electron (SE) detector, concentric backscattered electron (BSE) detector, Bruker XFlash6, energy dispersive X-ray spectroscopy (EDX) detector and QUANTAX µ-XRF source. SEM images were acquired using an accelerating voltage of 15 or 10 kV under low vacuum conditions using either BSE or SE detection. The experiments were performed at the Nanoscale Imaging and Analysis Facility for Environmental Materials (NIAFEM) Facility in the Williamson Research Centre for Environmental Science, University of Manchester, funded by NERC (NERC CC042).
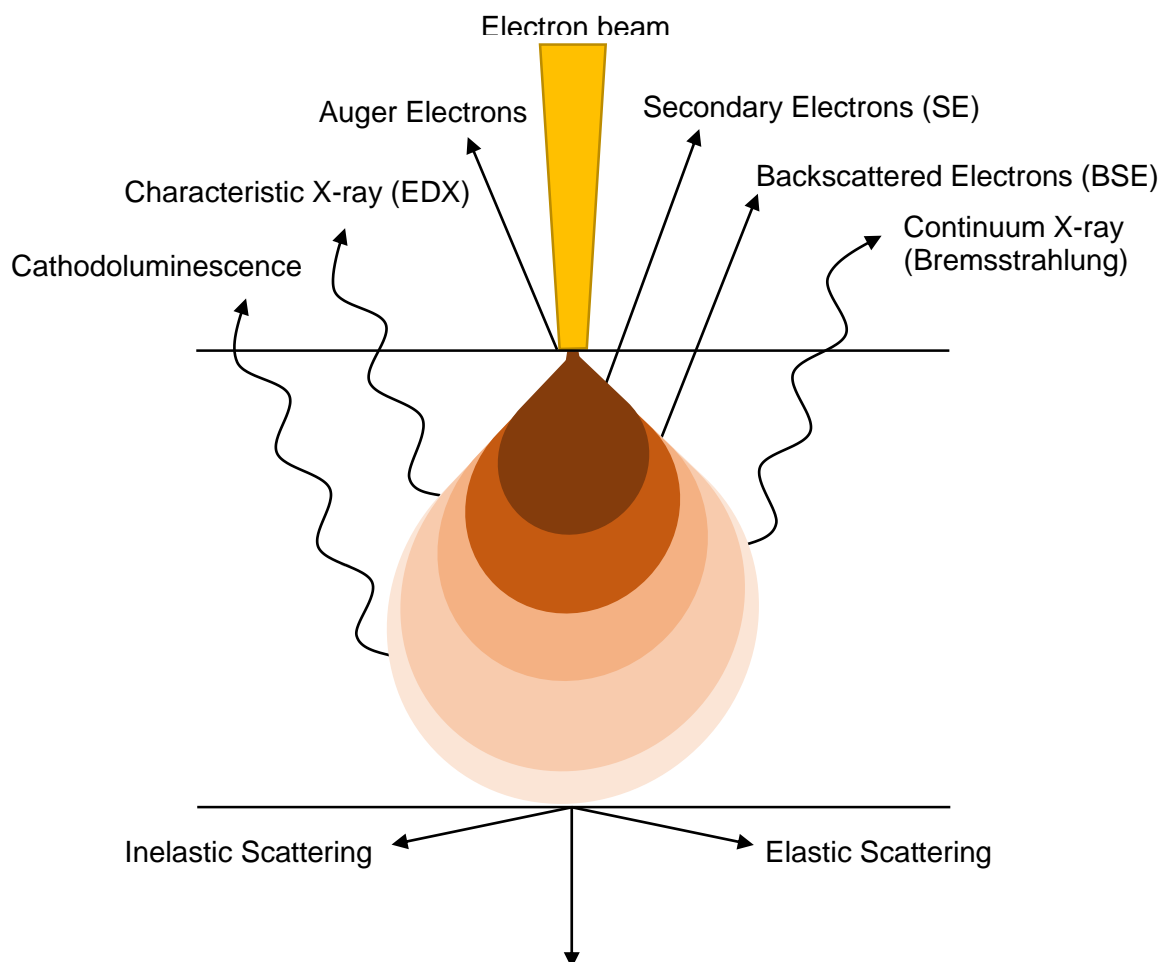
Figure 2.10. Signals produced after the electrons interact with matter in the scanning electron microscope.

The SEM uses an electron beam to image the surface structure and composition of samples at nanometre resolutions. A filament emits electrons, which collimate into a beam that focusses on the sample surface through a series of lenses in the electron column. Upon interacting with the surface, the electrons produce the variety of different signals in Figure 2.10. These are BSE, SE, Auger electrons, characteristic X-rays, continuum X-rays, and cathodoluminescence, and are each detected by the various detectors located within the chamber.

BSEs are high-energy electrons that originate from deep within the sample (a few µm deep) and provide compositional information and lower resolution images. BSEs reflect after elastic interactions and so only lose a small amount of energy upon scattering out of the sample. Higher atomic numbers make the material appear brighter in the BSE image.

SEs on the other hand, are the result of inelastic interactions with the atoms and so come from a shallower part of the sample (a few nm). The shallow depth means they provide information on the surface structure and topographic information and carry a lower energy compared to the BSE.

Electrons hitting the sample surface produce characteristic X-rays that give information on the elemental composition of the sample. Performing EDX on these X-rays garners both qualitative and quantitative data over the samples' bulk elemental composition.
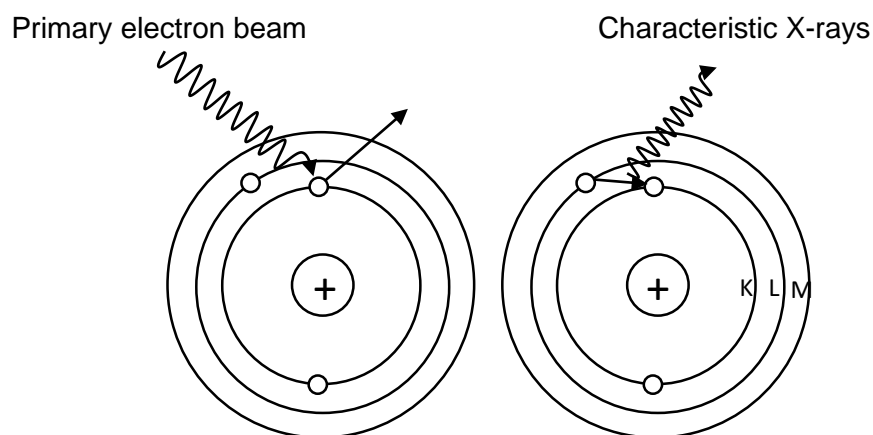
Figure 2.11. Simplified schematic of the electronic process of X-ray photoelectron emission studied by energy dispersive X-ray spectroscopy.

The primary electron beam interacts with an inner electron shell of the atom and ejects an electron. An outer shell electron drops into the vacancy left behind in the core shell. The difference in binding energy between the two shells is released as a sharply defined X-ray photon. Measuring the characteristic energetic value of these X-rays determines the elemental

composition of the sample. Figure 2.11. shows a simplified schematic of this process, where K, L, and M are the electron shells.

These characteristic X-rays and the background continuum (Bremsstrahlung) X-rays make up the EDX spectrum. Continuum X-rays occur because the electron slows when its path deflects from passing near the nucleus of an atom. The resulting electromagnetic continuum occurs over the entire energy range as background in the spectrum.

2.4.3. Nuclear Magnetic Resonance Spectroscopy

^{1}H- and ^{19}F-nuclear magnetic resonance (NMR) were used in this thesis to identify structural changes, determine protonation states, and understand neutral stabilities of the RAMs in different environments. ^{1}H- and ^{19}F-NMR spectroscopy were performed with a Bruker AV III 400 spectrometer (^{1}H at 400.13 MHz). All samples were tested in standard NMR tubes or with an NMR tube with inserted coaxial reference tube, as in Figure 2.12. For ^{1}H spectra the internal capillary was filled with a D_2O reference and ^{19}F-NMR used a CF_3CO_2D reference solution. The external standard ensures the solution under study does not undergo any reaction with the standard, which an internal standard cannot confirm.

Reference inside insert

Sample inside annular space
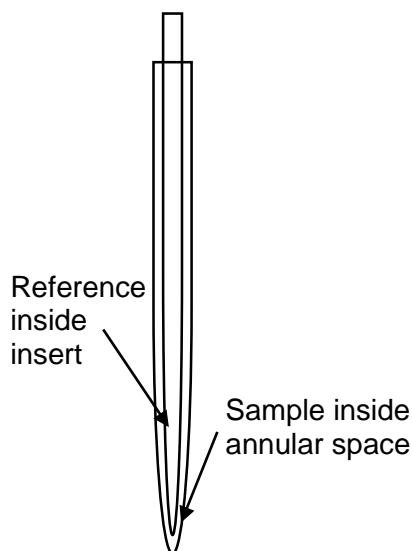
Figure 2.12. Diagram of nuclear magnetic resonance tube with inserted coaxial reference insert.

NMR spectroscopy is a physicochemical analysis technique that provides structural information from the magnetic properties of nuclei. An externally applied radiofrequency radiation interacts with atomic nuclei causing a net exchange of energy that changes the nuclear spin. Nuclear spin is an intrinsic atomic property defined by a quantic number (I) that varies depending on the isotope, and nuclei are only detectable by NMR spectroscopy if $I \neq 0$.

Equation 2.23. shows how the underpinning theory of NMR relies on the intrinsic spin (S) of the nucleus involved, where μ is the magnetic moment and γ the gyromagnetic ratio, which is always non-zero.

$$\mu = \gamma \cdot S \qquad\qquad 2.23.$$

Two spin states exist for a nucleus with the spin $I = \frac{1}{2}$ in the presence of an external magnetic field (B); these are +1/2 and −1/2. At a specific external magnetic field (B_x) these states are split by a small energy (En). Equation 2.24. describes this relationship and Figure 2.13. shows the splitting.

$$En = \mu \cdot \frac{B_x}{I} \qquad\qquad 2.24.$$

Specific nuclides absorb at specific frequencies, allowing NMR to differentiate between different elements and isotopes. This specificity means that NMR can generally only detect one isotope at a time, resulting in a range of different types of NMR such as ^{1}H, ^{13}C, and ^{19}F.

The specific local environment around a particular nucleus causes greater or lesser shielding. Generally, electronic shielding reduces the magnetic field at the nucleus, resulting in a lower NMR frequency. This shift in frequency due to the electronic molecular orbital coupling because of B_x is known as the chemical shift. An increase in electron density surrounding a molecular orbital causes the chemical shift to move "up-field" to a lower value. A decrease in electron density shifts the chemical shift "downfield" to a higher value.

The spin-spin coupling phenomena also gleams structural information. This is where the spins of non-chemically identical nuclei interact through the chemical bonds and couple, resulting in
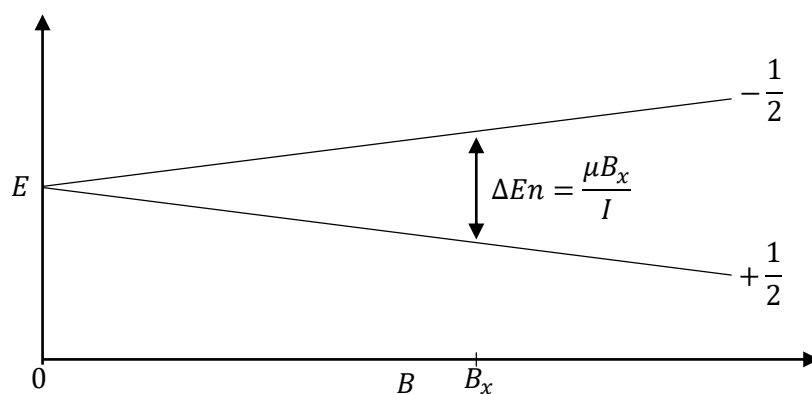
Figure 2.13. Difference in energy between two spin states over a varying magnetic field (B).

peak splitting in the NMR spectra. The splitting pattern and the magnitude of the resulting coupling constant, J, gives direct information on the connectivity of atoms in a molecule. Typically, this splitting only covers neighbouring NMR active nuclei three or fewer bonds away. However, due to the sensitivity of ^{19}F-NMR the spin-spin coupling can traverse a much wider

distance. This can complicate the spectra and make accurate structural determination challenging.[15]

2.4.4. *In-situ* Electron Paramagnetic Spectroscopy

Electron paramagnetic (EPR) spectra were recorded at room temperature using a continuous-wave (CW) Bruker EMX Micro spectrometer with the microwave frequency around 9.8 GHz, the modulation amplitude 1 G, the sweep width of 100 G, a scan time of 5 s, and a microwave power of 2 mW. The potential waveform was applied with an Autolab potentiostat. The *in-situ* EPR spectra were recorded using CV from −1.8 V to 0.5 V (*vs.* Ag/Ag⁺). Spectral simulations were performed using the EasySpin 5.2.25 simulation software by the MATLAB. EPR spectroscopy is a sensitive method for studying chemical species with unpaired electrons.[15] It is important in our understanding of organic and inorganic radicals, transition metal complexes, and some biomolecules. The general theory of EPR is similar to NMR, but the excited spin states are those of the electrons as opposed to the atomic nuclei. Every electron has a magnetic moment and a spin quantum number $s = 1/2$, with magnetic components m_s = +1/2 or m_s = −1/2. In the presence of B_x, the magnetic moment aligns either parallel or antiparallel to the field according to a specific energy defined by the Zeeman effect. Equation 2.25. describes this phenomenon, where g_e is the electrons' g-factor (2.0023 for the free electron) and μ_B is the Bohr magneton.[16]

$$En = m_s g_e \mu_B B_x \qquad \qquad 2.25.$$

The Δ*En* between the two spin states is therefore directly proportional to the strength of B_x. The change in electron spin occurs via either the absorption or emission of a photon of energy (*hv*). This leads to the fundamental EPR equation in Equation 2.26.

$$hv = g_e \mu_B B_x \qquad \qquad 2.26.$$

Equation 2.26. permits a variety of frequency and magnetic field values, but studies typically use a fixed frequency with microwaves in the 9 to 10 GHz region, with fields of around 3500 G. Experimentally, a paramagnetic material is exposed to an increasing B_x until the gap between the two m_s states is equal to the energy of the microwaves. At this value, the unpaired electrons can move between the two spin states leading to a net absorption of energy due to the Maxwell-Boltzmann distribution. This absorption is measured and converted into a spectrum, which is commonly reported in the first derivative form.

The spectrum gives rise to a plethora of information. Systems with multiple unpaired electrons have electron-electron interactions that lead to "fine" structure in the spectra. Additionally, the magnetic moment of a nucleus with a non-zero nuclear spin will affect any associated unpaired

electrons and give rise to hyperfine coupling, which is analogous to the *J*-coupling in NMR (See Section 2.4.3.). Furthermore, the line shape can give information on the rates of chemical reactions. All of these affects can differ depending on the orientation of the unpaired electron in the presence of B_x, which can give further information over the atomic or molecular orbital where the unpaired electron is situated.[15]

This thesis uses simulated and experimental *in-situ* EPR spectroscopy to study the generation and elimination of radical anions. The *in-situ* set-up is necessary as the radicals form via an electrochemical reaction that occurs within the electrochemical cell. The stability of the radicals is unknown, and so *ex-situ* analysis does not present adequate information.

2.4.5. Mass Spectrometry

Mass spectrometry analysis was performed using Agilent 6120 Quadrupole mass spectrometer, electrospray/atmospheric pressure chemical ionisation ion source at low resolution.[15]

Mass spectrometry is a characterisation technique that determines the exact molecular weight of chemical species in a sample by measuring the mass-to-charge ratio (m/z). Typical uses are chemical identification, compound quantification, and structural and chemical property determination.

Figure 2.14. shows the key components of a mass spectrometer. A beam of electrons ionises the gas phase sample, which passes through a magnetic field or electric field. This field deflects ions into a curved trajectory, with the angle dependant on the specific m/z ratio. Heavier ions will have more momentum and thus experience less deflection. By varying the field strength linearly or exponentially, the ions focus on the detector slit which generates a mass spectrum. Each peak in the mass spectrum represents a component with a unique m/z, and the peak heights represent the relative abundance of each component.
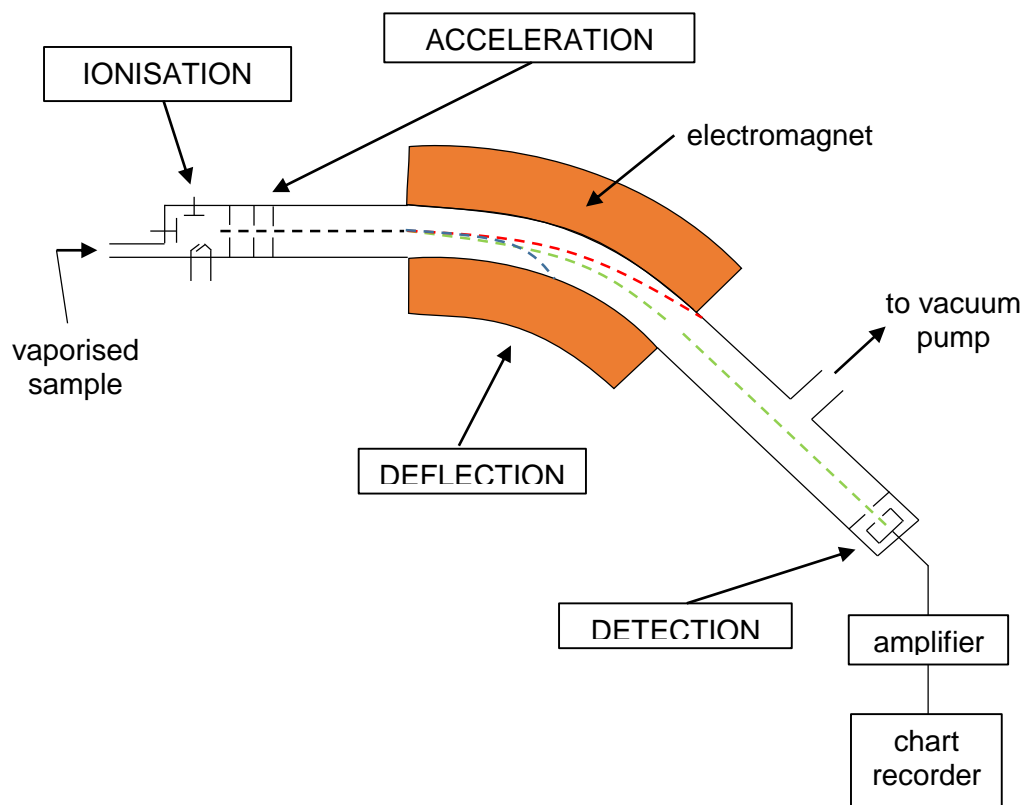
Figure 2.14. Schematic of the mass spectrometer.

2.4.6. Density

Density was measured using an Anton Paar DMA 4100 M vibrating tube densimeter in the temperature range of 293.15 – 323.15 K. The instrument was calibrated with degassed Millipore Milli Q water and air using the built-in calibration routine. The temperature uncertainty is ±0.02 K and the absolute uncertainty of the density is ±0.0005 g cm^{-3} (accounting for the purity and handling of the samples).

The ρ of a substance describes its mass per unit volume, with SI units of kg m^{-3}. Different materials have different densities, and the specific values vary with respect to temperature and pressure. Increasing the pressure on an object will usually decrease its volume and result in a net increase in density. Increasing the temperature typically increases the volume and decreases the density. Equation 2.27. defines the ρ of a material, where m is the mass and V the volume.

$$\rho = \frac{m}{V}$$

2.27.

Density is a vital component of fluid properties and so it is important to understand the ρ of liquids in applications that depend on accurate and reliable flow. The direct measurement of a material with the oscillating U-tube method in a densimeter gives the ρ. The sample is introduced into a U-shaped borosilicate glass tube that is excited to vibrate at its characteristic

124

frequency. This characteristic frequency changes depending on the ρ of the sample residing inside. Through measuring changes in the characteristic frequency from the quotient of the period of oscillations of the tube against a reference oscillator, one computes the sample's ρ.[17]

Using the ρ, one calculates the molar volume (V_m) where M is the molar mass (g mol^{-1}) (Equation 2.28). V_m is useful in understanding changes in a fluid's ρ and viscosity with respect to molecular size.

$$V_m = \frac{M}{\rho}$$

<div align="right">2.28.</div>

2.4.7. Viscosity

Viscosity is the measure of the resistance of a fluid to deformation under shear stress and comprises dynamic (η, Pa s) and kinematic viscosity ($v_{kinematic}$) (m^2 s^{-1}). The shear resistance is a result of attractive forces between molecules and intermolecular friction between layers in the fluid sliding over one another. Viscosity is an important fluid property in the analysis of liquid behaviour and fluid motion near solid boundaries.

The η is the measure of internal resistance. It is the tangential force per unit area required to move a horizontal plane with respect to an adjacent plane whilst maintaining a unit distance apart in the fluid. Equation 2.29. calculates the $v_{kinematic}$, which is the ratio of η to ρ.

$$v = \frac{\eta}{\rho}$$

<div align="right">2.29.</div>

The Arrhenius-type Equation in Equation 2.30. describes the relationship of η with respect to T.

$$\eta = \eta^o e^{\frac{E_a}{RT}}$$

<div align="right">2.30.</div>

Where η^0 is the exponential pre-factor constant, E_a is the activation energy of shear stress (J mol^{-1}).

The rolling-ball viscometer applies Hoeppler's falling ball principle for a simple and precise method of determining both the dynamic and kinematic viscosities of Newtonian fluids. The basic concept is to measure the rolling time of a ball of known diameter and density through an almost vertical glass tube of known diameter and length after filling it with the sample fluid. The time taken for the ball to pass through a specified distance is related to the viscosity of the sample.[18]

Viscosity is a key metric within RFB development. It affects the electrolyte viscosity, which determines the operating pumping energy requirements and can lead to power-efficiency

losses. Additionally, increased viscosity can reduce ion mobility within the solution, which will decrease the conductivity. Viscosity values can vary widely, for example at 208 K ACN, water, and the common deep eutectic solvent 'reline' have dynamic viscosities of 0.38, 1.1, and around 1000 mPa s, respectively.[19,20]

2.4.8. Conductivity

Conductivity (σ) was measured with a Metrohm 914 pH/Conductometer over the temperature range 293.15 – 333.15 K using a thermostated water bath. The probe was calibrated before use with a Mettler Toledo AG Analytical Conductivity standard.

Conductivity is the measure of a material's ability to pass an electric current. It is the reciprocal of the fundamental property of electrical resistivity, which is the measure of how strongly a material resists electric current. Good conductors will give little resistance to the electrical current flow. In liquid electrolytes, the electrical conduction occurs by ions travelling through the solution and is heavily dependent on their concentration. The conductivity meter measures the resistance of the solution by applying an alternating voltage between two electrodes separated at a known distance.

Ionic conductivity is a key parameter in EESSs. Conductivity increases with temperature due to the decreasing viscosity, as explained in Equation 2.30., which yields an increase in ion mobility. The Arrhenius equation in Equation 2.31. uses this relation to predict the conductivity behaviour of a given system.

$$\sigma = \sigma^o e^{\frac{E_\sigma}{RT}}$$
2.31.

Where σ is the conductivity (μS cm^{-1}), σ^o is the exponential pre-factor constant, E_σ is the activation energy of conductivity.

2.4.9. Karl-Fischer Titration

The water content of DES systems was measured by Karl-Fischer titration using a Mettler Toledo Titrator Compact C30SD.

The Karl-Fischer titrator quantifies water using the oxidation of sulfur dioxide with iodine in the elementary reaction in Equation 2.32.

$$H_2O + SO_2 + I_2 \rightarrow SO_3 + 2HI$$
2.32.

The titration cell includes a Pt anode, and an anode solution of SO_2, KI, plus an alcohol and a base. The latter two components, typically ethanol and imidazole, are necessary to consume

the titration products. Inside the titration cell is a cathode-containing compartment immersed in the anode solution and separated by an IEM. An electrical circuit provides current which generates I_2 from the KI at the Pt anode. Adding the anolyte to the sample leads to the consumption of one mole of I_2 per mole of added H_2O. An excess of I_2 in the solution marks the titration endpoint, which is detected using bipotentiometry. A detector circuit maintains a constant current between a pair of Pt electrodes immersed in the anode solution, which measures the voltage drop caused by the excess I_2 at the equivalence point. As two moles of electrons are consumed per mole of water, the amount of charge required to generate the I_2 calculates the amount of water in the original analyte solution.[21]

2.5.   References

1   A. J. Bard and L. R. Faulkner, *Electrochemical Methods: Fundamentals and Applications*, John Wiley and Sons, Inc., Austin, Texas, 2nd edn., 2001.

2   M. Ciobanu, J. P. Wilburn, M. L. Krim and D. E. Cliffel, in *Handbook of Electrochemistry*, ed. C. Zoski, Elsevier B.V., Las Cruces, 2007, pp. 3–30.

3   G. Wang, B. Huang, D. Liu, D. Zheng, J. Harris, J. Xue and D. Qu, Exploring polycyclic aromatic hydrocarbons as an anolyte for nonaqueous redox flow batteries, *J. Mater. Chem. A*, 2018, **6**, 13286–13293.

4   J. D. Hofmann and D. Schröder, Which Parameter is Governing for Aqueous Redox Flow Batteries with Organic Active Material?, *Chemie-Ingenieur-Technik*, 2019, **91**, 786–794.

5   E. Sum and M. Skyllas-Kazacos, A study of the V(II)/V(III) redox couple for redox flow cell applications, *J. Power Sources*, 1985, **15**, 179–190.

6   S. Zhong and M. Skyllas-Kazacos, Electrochemical behaviour of vanadium(V)/vanadium(IV) redox couple at graphite electrodes, *J. Power Sources*, 1992, **39**, 1–9.

7   K. Izutsu, in *Electrochemistry in Nonaqueous Solutions*, Wiley Online Library, 2002, pp. 89–110.

8   N. Elgrishi, K. J. Rountree, B. D. McCarthy, E. S. Rountree, T. T. Eisenhart and J. L. Dempsey, A practical beginner's guide to cyclic voltammetry, *J. Chem. Educ.*, 2018, **95**, 197–206.

9   M. Li, S. A. Odom, A. R. Pancoast, L. A. Robertson, T. P. Vaid, G. Agarwal, H. A. Doan, Y. Wang, T. M. Suduwella, S. R. Bheemireddy, R. H. Ewoldt, R. S. Assary, L. Zhang, M. S. Sigman and S. D. Minteer, Experimental protocols for studying organic non-aqueous redox flow batteries, *ACS Energy Lett.*, 2021, **6**, 3932–3943.

10   Y. Shao, *Electrochemistry at liquid/liquid interfaces*, Elsevier B.V., Austin, Texas, 1st Editio., 2007.

11   A. J. Bard, F. R. F. Fan, J. Kwak and O. Lev, Scanning electrochemical microscopy. Introduction and principles, *Anal. Chem.*, 1989, **61**, 132–138.

12   Y. Shao and M. V. Mirkin, Probing ion transfer at the liquid/liquid interface by scanning electrochemical microscopy (SECM), *J. Phys. Chem. B*, 1998, **102**, 9915–9921.

13   D. Bryans, V. Amstutz, H. H. Girault and L. E. A. Berlouis, Characterisation of a 200 kw/400 kwh vanadium redox flow battery, *Batteries*, , DOI:10.3390/batteries4040054.

14   C. G. Armstrong, R. W. Hogue and K. E. Toghill, Application of the dianion croconate violet for symmetric organic non-aqueous redox flow battery electrolytes, *J. Power Sources*, 2019, **440**, 227037.

15   P. M. V Raja and A. R. Barron, *Physical Methods in Chemistry and Nano Science*, Rice University, 2019.

16   V. Chechik, E. Carter, D. Murphy, E. Corter and D. Murphy, *Electron Paramagnetic Resonance*, Oxford Chemistry Primers, Oxford, 1st Editio., 2016.

17   A. Paar, Instruction Manual DMA 4100 M DMA 4500 M DMA 5000 M, 2012, 152.

18   A. Paar, *Instruction Manual Lovis 2000 M/ME*, 2012.

19   S. Creager, in *Handbook of Electrochemistry*, ed. C. G. Zoski, Elsevier B.V., Las Cruces, 1st Ed., 2007, pp. 57–72.

20   Y. Marcus, *Deep Eutectic Solvents*, 2019.

21   K. Fischer, Neues Verfahren zur maBanalytischen Bestimmung des Wassergehaltes von Fllissigkeiten und festen Korpern, *Angew. Chemie*, 1935, **48**, 394–396.

3. Anolyte Half-Cell Design

3.1. **Organic Redox Active Molecule Selection**

The wide scope of ORFB literature demonstrates the necessity of rational design of the ORAM, electrolyte, and solvent in achieving a successful system. The ideal RFB system must have high solubility; fast redox kinetics on cheap electrode materials; chemical and electrochemical stability of neutral and active species; stability of the supporting electrolyte-electrolyte-electrode interphase; high ionic conductivity; low dynamic viscosity; low toxicity; and low membrane permeability. Additionally, all components must be abundant or facile to produce.

The most challenging part of developing an ORFB lies in tackling the instability of the high energy ions formed after electron transfer. Molecular tailoring to shield or decrease electron density in reactive areas alongside careful selection of both solvent and electrolyte can limit molecular attack and improve stability.

The high potential molecules originally designed as redox shuttles for overcharge protection in LIBs are a good starting point for ORFB catholytes.[1] Thus, there exists already a wide range of ORAMs for the positive half-cell. These include TEMPO, 4-oxo-TEMPO, DBBB, and DBMMB.[2–5] Identifying negative potential materials for the anolyte half-cell is more challenging due to the lack of research in other applications.

There are many factors to consider when developing an ORFB. It is therefore useful to focus on one aspect of the system. Chapters 3. and 4. of this work focus on the negative half-cell electrolyte. Chapter 5. carries the anolyte into a membrane-free concept against a range of positive redox couples. A competitive anolyte half-cell must have a significantly negative redox potential. The ORAMs 4-carboxylic-7-sulfonate fluorenol (−1.3 V (*vs* NHE)) and BP (−2.11 V (*vs* Ag/Ag$^+$)) have the most negative potentials in the aqueous and non-aqueous literature, respectively.[6–8] The most positive aqueous and non-aqueous catholytes are TMA-TEMPO (0.95 V (*vs* SHE)) and cyclopropenium (1.56 V (*vs* Fc/Fc$^+$)).[9,10]

The present research aims to exploit the favourable chemical and electrochemical characteristics of the quinone molecular family tree. These include the structural diversity, tuneability, and relatively stable redox mechanisms. The quinone scaffold can store two electrons per molecule. Therefore, they store twice the energy density in a given concentration compared to single electron transferring ORAMs. The wide library of commercially available quinones makes them both affordable and accessible for testing a wide range of compounds.

3.1.1. Tetrafluoro-1,4-Benzoquinone

Quinone derivatives can be naturally occurring, and are present in plants and crude oil. They typically have high k_0 values which lends to small overpotentials, high efficiencies, and high power densities.[11–13] The low molecular weight of the BQ parent molecule provides a higher volumetric energy density than its multi-cyclic derivatives; hence, it is the starting point for this research.

Stabilising the reduced quinone is key to success in this field. EWGs draw electron density away from the charged oxygen atoms through inductive effects and improve the reduced state stability. Fluorine, as the most electronegative element, should inductively stabilise the quinone anionic states. Fluorine creates a net positive charge on the carbon atoms in the ring and draws electron density away from the oxygen groups. This decreases the propensity for undesirable side-reactions. The lone-pairs on F work mesomerically against this inductive stabilising effect and donate some electron density to the aromatic ring through π-donation. The relative magnitude of each effect determines the stability of the reduced quinone. Adding four F groups to BQ in aqueous media has little effect on its reduction potential, demonstrating the competing nature of these two effects.[14] Wei *et al.* show that the EWG effect of F groups improves the stability of FL.$^-$ and yields better capacity retention.[2] De la Cruz *et al.* demonstrate the opposite effect in phenazine, where adding CF_3 groups increases the reduction potential.[15] Other halogens, such as chlorine, also provide these inductive effects. However, the similarity in size of the valence 2p orbitals in F and C mean they are closer in energy and have a more favourable orbital overlap. This leads to more electron donation in fluorobenzene than in chlorobenzene and thus better stabilisation.
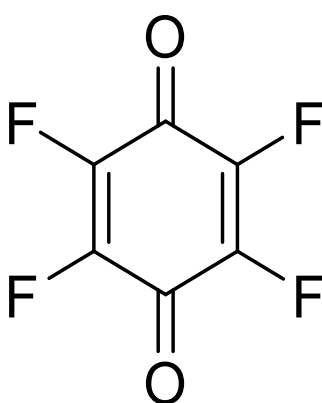
Figure 3.1. Tetrafluoro-1,4-benzoquinone (TFBQ).

Figure 3.1. displays the chemical structure of tetrafluoro-1,4-benzoquinone (TBFQ), a relatively unstudied molecule. The few reports involving TBFQ and closely related structures comment on chemical instability in aqueous media because of nucleophilic attack and substitution reactions.[14,16,17] This may indicate that it could, in fact, be a poor choice for an

aqueous RFB ORAM. Surprisingly, there is little literature over its non-aqueous electrochemistry.[18] When considering TFBQ's ORFB applicability, one should note the increasing restrictions on perfluoroalkyl substances due to their toxicity.

Quinones generally undergo a reversible two-electron reduction/oxidation in aqueous media. As Chapter 1.3. discusses, the redox potential and mechanism is strongly pH dependent. This is because the H^+ availability in the electrolyte determines whether the reaction is a PCET. TFBQ is soluble in aqueous and non-aqueous media. This allows the study of both the aqueous PCET ($2H^+/2e^-$) and the non-aqueous electron transfer ($2 \times 1e^-$) redox chemistries.

Figure 3.2. shows the CV data of TFBQ (10 mM) at 100 mV s^{-1} in unbuffered aqueous solutions comprising 1 M H_2SO_4 (red line), 0.1 M KCl (green line), and 1 M KOH (blue line), which have pH values of 0, 7, and 14, respectively. Table 3.1. gives the corresponding electrochemical data, where the Randles–Ševčík equation, given as Equation 2.9. in Chapter 2.2.1. to calculate the D_o. The wide pH range enables the study of both electron transfer mechanisms and allows us to understand the relative stability of TFBQ over a range of aqueous conditions.
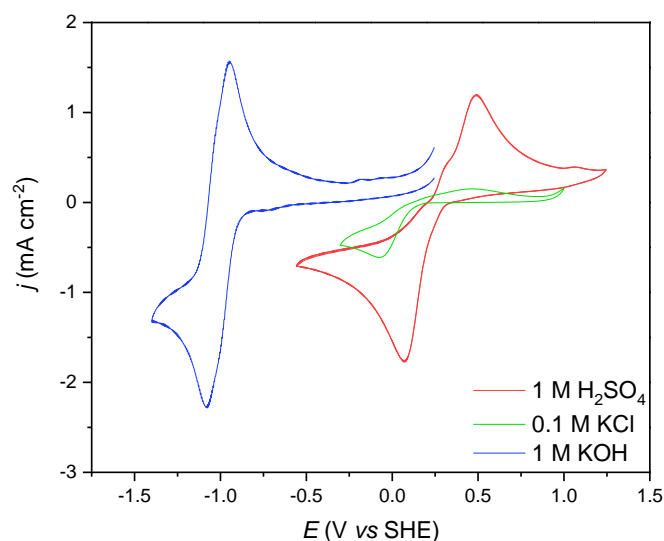
Figure 3.2. CV data of 10 mM TFBQ in unbuffered 1 M H_2SO_4 (red line), (b) 0.1 M KCl (green line), and 1 M KOH (blue line) at scan rate 100 mV s^{-1} using a GC WE, a SCE RE, and a Pt CE.

TFBQ reduction is quasi-reversible in both pH 0 and pH 14, with differing $E_{1/2}$ values of 0.29 V and −1.08 V (*vs* SHE) and ΔE_p values of 0.42 V and 0.14 V, respectively. The similar currents indicate the similar electron stoichiometry, but the larger ΔE_p in the lower pH shows the slower kinetics of PCET compared to the process involving only electron transfer. There are no protons at pH 14, so the electron transfer step is purely electron-based. This lack of

bond breaking/making leads to more facile redox kinetics. These fast kinetics result in such rapid electron transfer steps that the pH 14 CV (blue line) only shows as one peak.

Table 3.1. Electrochemical data for 10 mM TFBQ in aqueous media over pH range 0 – 14 at 100 mV s^{-1}.

pH	E_{pa} (V vs SHE)	E_{pc} (V vs SHE)	ΔE_p (V vs SHE)	$E_{1/2}$ (V vs SHE)	i_{pa} (mA)	i_{pc} (mA)	i_{pa}/i_{pc}	$D_{o(n=2)}$ (cm^2 s^{-1})
0	0.49	−0.07	0.41	0.28	1.01×10^{-4}	-1.22×10^{-4}	0.83	3.91×10^{-7}
7	0.46	−0.07	0.53	0.20	9.68×10^{-7}	-4.35×10^{-5}	0.02	-
14	−0.94	−1.08	0.14	−1.01	-1.50×10^{-4}	-1.51×10^{-4}	0.99	4.72×10^{-5}

The green line in Figure 3.2. shows a greater magnitude of i_{pc} compared to i_{pa} (i_{pa}/i_{pc} = 0.02) alongside the wide ΔE_p of 0.53 V. This indicates TFBQ reduction is chemically and electrochemically irreversible in unbuffered neutral pH. This is likely due to nucleophilic and substitution reactions on the reduced product. The irreversible CV means Randles–Ševčík analysis cannot accurately calculate a D_o value for the pH neutral electrolyte. However, the D_o for the acidic and alkali media indicate rapid diffusion in a similar range to other ORAMs in aqueous conditions.[19] Previous studies report electrochemical irreversibility in alkaline conditions and a better reversibility under neutral conditions with an i_{pa}/i_{pc} greater than one. The discrepancy between the two data sets is possibly due to the unbuffered nature of the electrolyte in this study.[14]

One comprehends the aqueous instability of TFBQ through the colour changes in the solutions. The images of TFBQ at different t after formation of (a) t = 0, (b) t = 5 hours, (c) t = 9 days, and (d) t = 16 days are in Figure 3.3. Each pH solution has a distinct initial colour, ranging from yellow to deep purple with increasing pH. As t increases the solutions become more similar in colour, and all three environments are yellow after 9 days. No further colour changes occur after this point, but a small amount of precipitate forms in the neutral environment. A likely pathway is the nucleophilic attack by water on the halogen subsitutents.[14] Degassing the solutions does not affect the process, but a slower colour change upon storing solutions in the dark suggests a partially photo-catalysed decomposition mechanism.
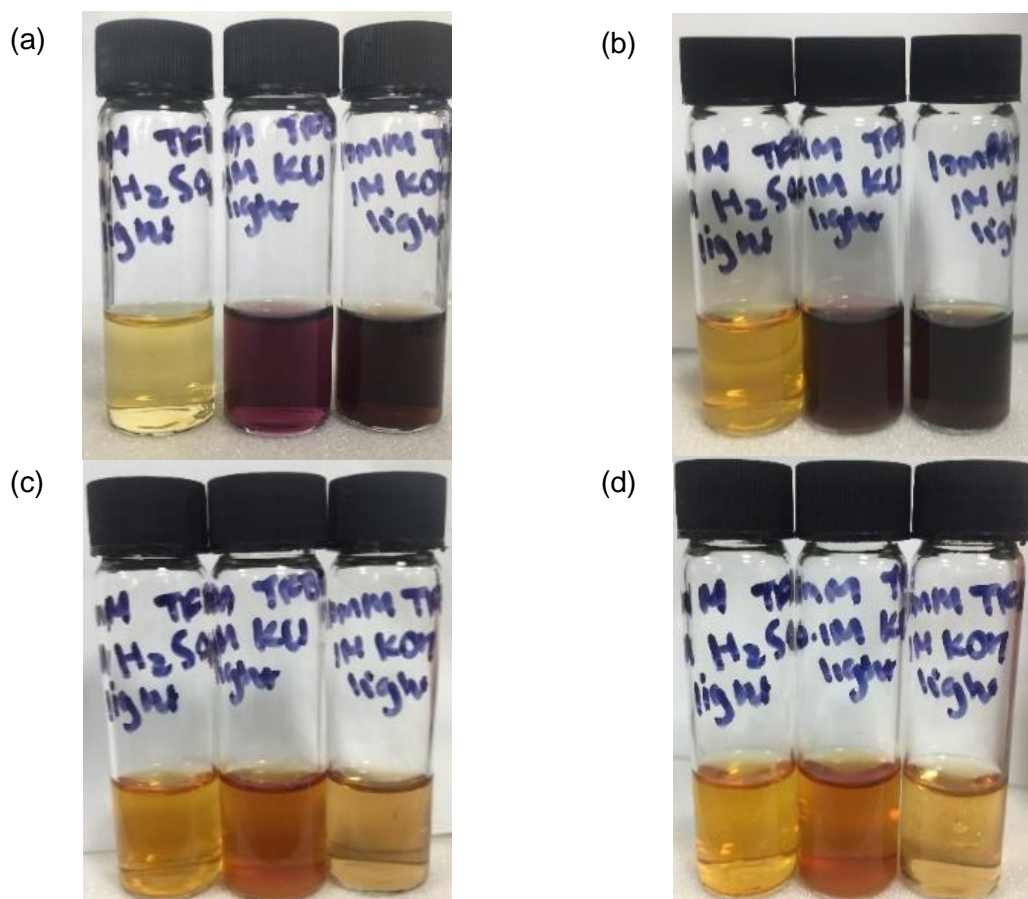
Figure 3.3. Photographs of 10 mM TFBQ in (from left to right) 1 M H_2SO_4, unbuffered H_2O, and 1 M KOH at t = (a) 0, (b) 5 hours, (c) 9 days, and (d) 16 days.

Figure 3.4. shows the CV curves of fresh (solid line) and week-old (darker, dashed line) samples of 10 mM TFBQ in (a) 1 M H_2SO_4, (b) 0.1 M KCl, and (c) 1 M KOH. Each pH records a lower *j* after 9 days and prove TFBQ is too unstable for an aqueous anolyte. The ^{19}F-NMR in Figure 3.5. shows the spectra for (a) fresh, (b) four days, and (c) week-old TFBQ in D_2O. Appendix 3.A. tabulates the chemical shifts. The long-range coupling in ^{19}F-NMR causes multiple peaks in the spectra despite TFBQ only having one F environment.

The fresh sample shows TBFQ peaks at −79.20, −130.17, −139.95, and −144.68 ppm. The −130.17, −139.95, and −144 ppm peaks are indicative of aromatic fluorine.[20] The −79 ppm peak remains stable over all tests. As *t* increases the −139.95 and −144.68 ppm peaks disappear and new peaks grow at −129.35 and −130.18 ppm. These are attributed to the degradation products. Unfortunately, solubility limit of TFBQ is too low for reasonable signal:noise in ^{13}C-NMR and prevents further structural analysis.

One should note spectrum 3.5.(a) uses a lower number of scans so only the relative intensities between Figure 3.5.(b) and (c) are comparable, but this does not affect the chemical shifts. The increasing −130 ppm peak intensities with *t* (Figure 3.5.(c)) indicates the continuing nature of the degradation with time. The presence of the −130 ppm peak in the fresh samples may

indicate some TFBQ instantly degrades. Overall, the lack of strong colour change and less change in the CV indicates TFBQ is most stable in acidic media, despite the high initial alkaline reversibility. However, the lower i_p values in the 7-day old pH 0 sample suggest that the stability in this media is still insufficient for an RFB.
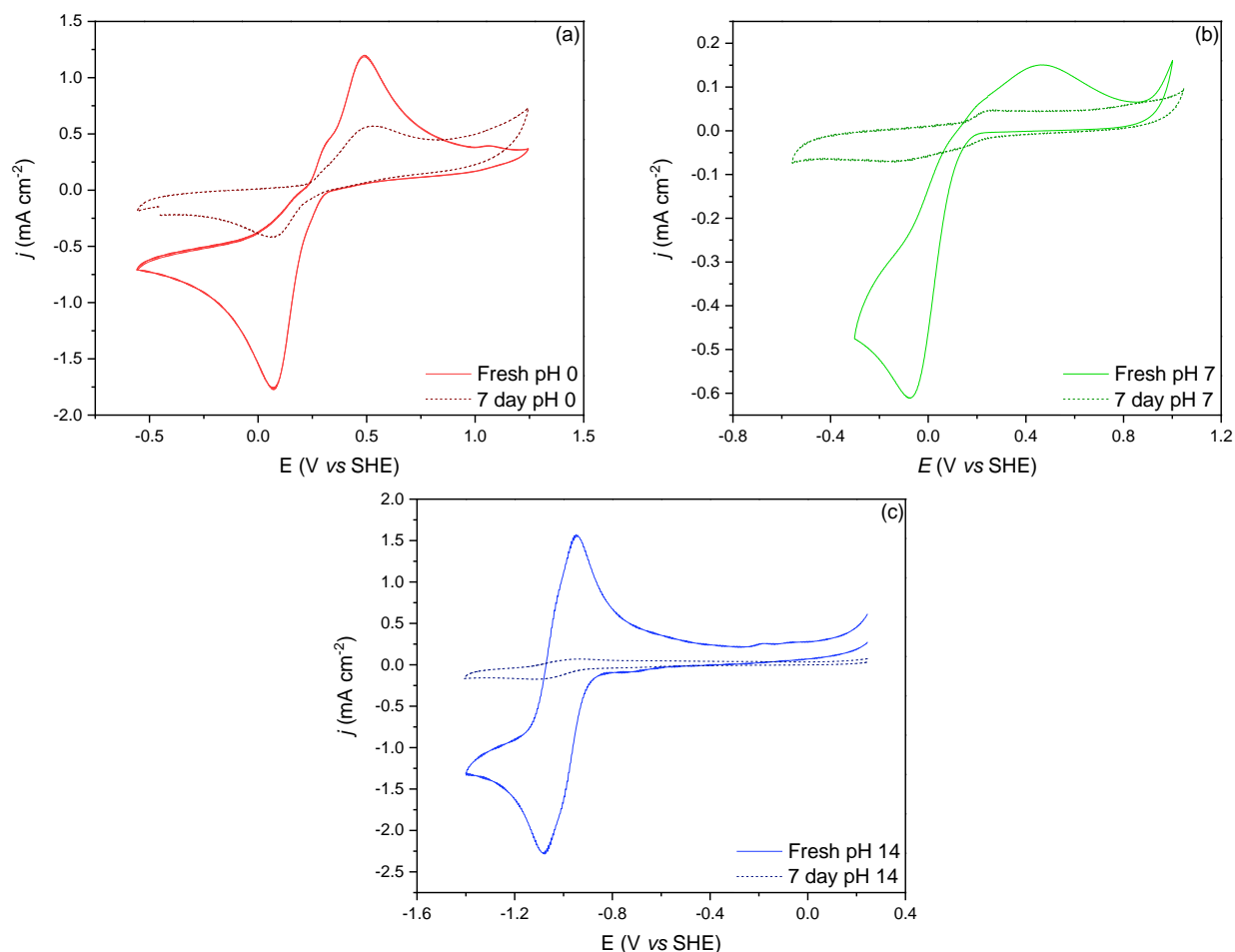
Figure 3.4. CV data of fresh (solid line) and week-old (darker, dashed line) 10 mM TFBQ in unbuffered (a) 1 M H$_2$SO$_4$, (b) 0.1 M KCl, and (c) 1 M KOH at 100 mV s^{-1} on a GC WE, a SCE RE, and a Pt CE.

Non-aqueous electrolytes do not contain the H$^+$ or H$_2$O that facilitate nucleophilic attack of TFBQ. Figure 3.6. gives the fresh and week-old ^{19}F-NMR spectra for 20 mM TFBQ in a non-aqueous CF$_3$CO$_2$D reference solvent. Appendix 3.B. tabulates the chemical shifts. The CF$_3$CO$_2$D solvent peak dominates the spectra over −77 − −78 ppm. The presence of the aromatic F peak at−144.30 ppm in both samples indicates TFBQ does not undergo the same degradation in non-aqueous media. The lack of peaks around −130 ppm confirm the immediate degradation of TFBQ in aqueous media in Figure 3.5.(a).
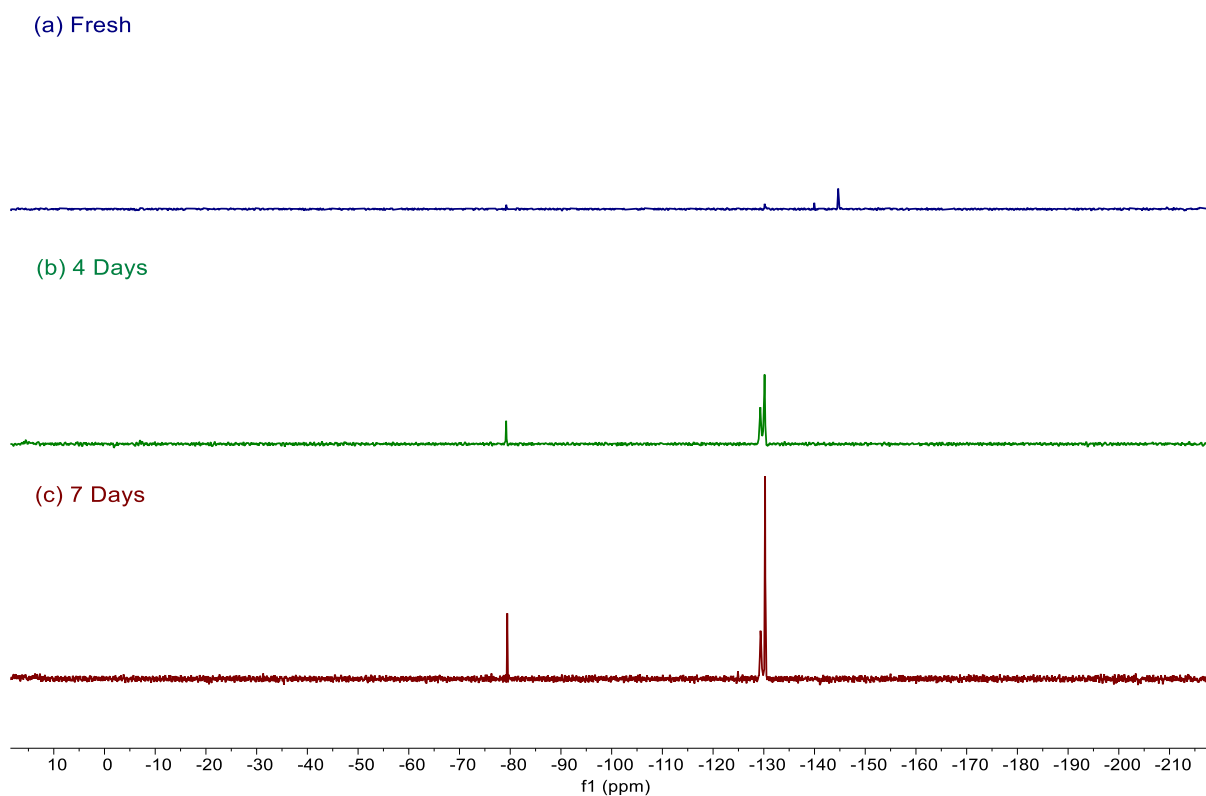
Figure 3.5. ^{19}F-NMR of (a) fresh and (b) four days old, and (c) week-old TFBQ in D$_2$O.
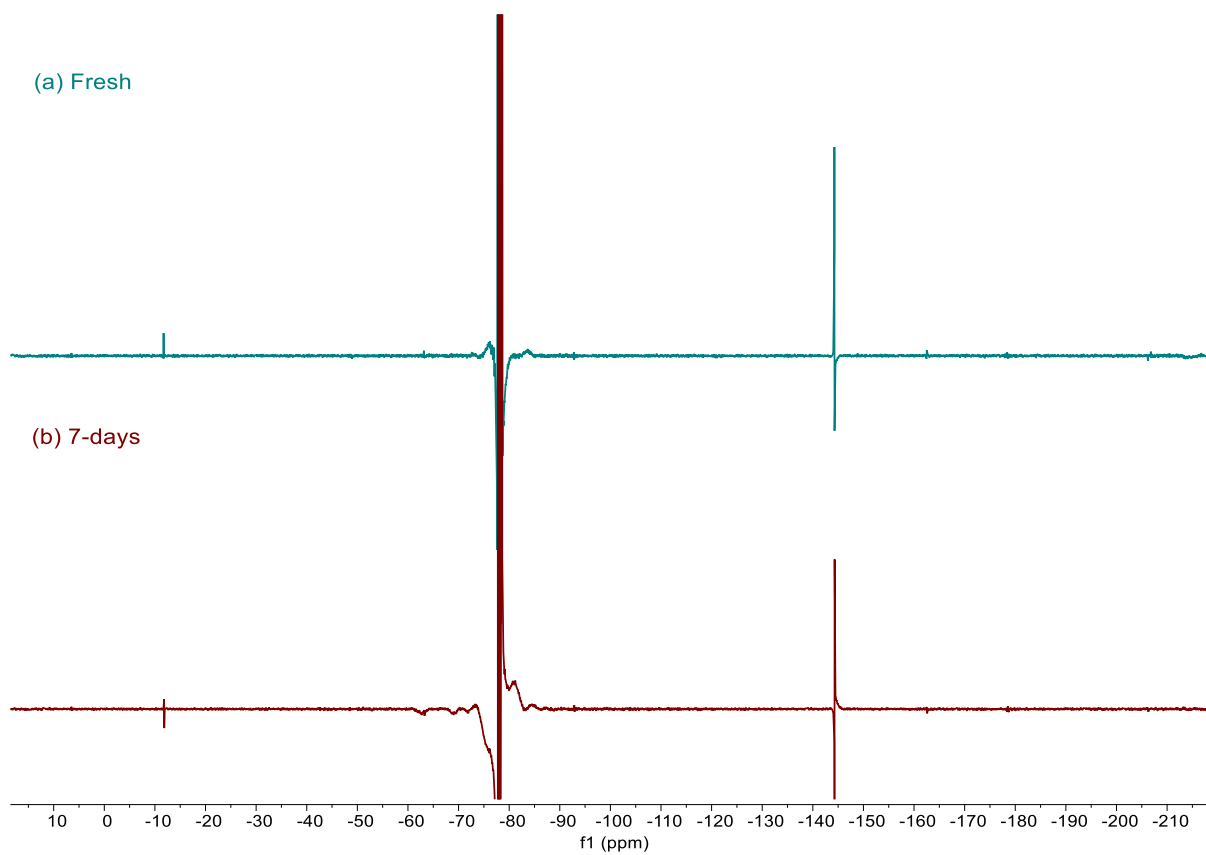
Figure 3.6. ^{19}F-NMR spectra showing non-aqueous stability of (a) fresh and (b) 7 day-old 20 mM TBQ in CF$_3$CO$_2$D.

The low viscosity (0.038 mPa s) and excellent solvating power for a wide range of organic compounds makes α,α,α-trifluorotoluene (TFT) a suitable starting point for studying the non-aqueous electrochemistry.[21,22] Additionally, TFT is a prominent solvent in L/L interface studies which is useful in the prospect of a membrane-free device.[21]

Figure 3.7.(a) gives the CVs for 1 mM TFBQ, 0.1 M TBABF$_4$ in TFT and provide a non-aqueous comparison to the aqueous TFBQ electrochemistry in Figure 3.2. The corresponding i_p vs $v^{1/2}$ plots are in Figure 3.7.(b). The details and discussion over the D_o values is below in Section 3.1.2., Table 3.2.

Figure 3.7.(a) shows a 2 × 1 e$^-$ process with $E_{1/2}$ values for the first ($E_{1,1/2}$) and second ($E_{2,1/2}$) redox processes at $E_{1,1/2}$ = 0.08 V and $E_{2,1/2}$ = −1.02 V (vs Ag/Ag$^+$) with ΔE_p = 0.29 V at 100 mV s^{-1} for both waves. Equations 3.1. and 3.2. give the reaction steps for each reductive wave. The increase in ΔE_p with v and the linear increase of i_p with $v^{1/2}$ indicates an electrochemically quasi-reversible diffusion-controlled redox process.

$$TFBQ \xrightarrow{e^-} TFBQ^{\cdot -} \qquad \text{3.1.}$$

$$TFBQ^{\cdot -} \xrightarrow{e^-} TFBQ^{2-} \qquad \text{3.2.}$$

An i_{pa}/i_{pc} of almost unity over all v indicates the chemical reversibility of E_1. The reduction of E_2 becomes unobservable when v < 100 mV s^{-1}. This suggests chemical irreversibility via an EC mechanism involving a slow chemical step with TFBQ^{2-}. This is not good for charge storage applications as ORAMs must be stable in their charged state for extended periods.
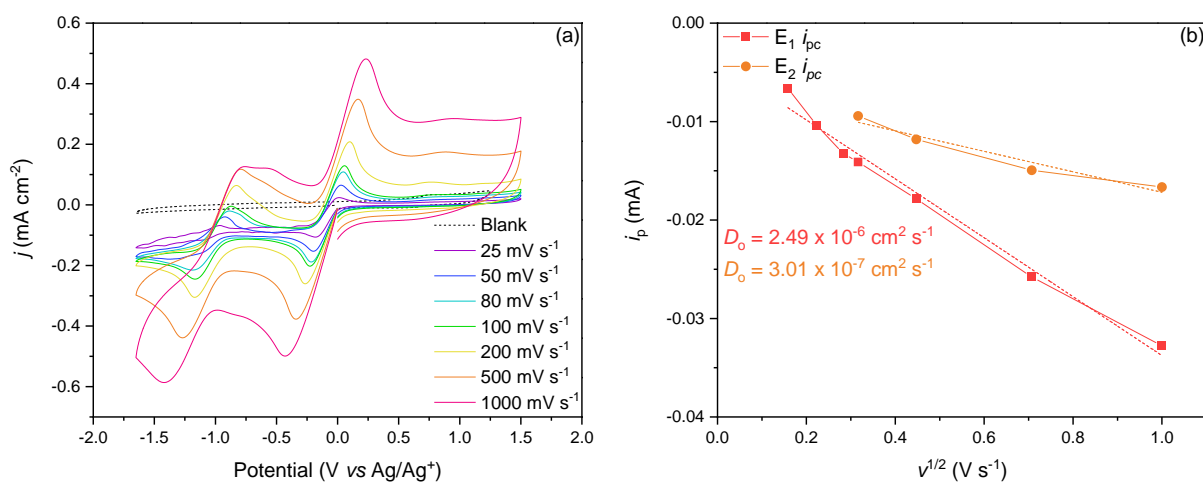
Figure 3.7. (a) CV data for 1 mM TFBQ, 0.1 M TBABF$_4$, TFT over scan rates 25 ≤ v ≤ 1000 mV s^{-1} and (b) corresponding i_p vs $v^{1/2}$ plot.

It is likely that the high electron density around the reduced O atoms in the carbonyl moieties lead to molecular degradation reactions. Protonating the O^- ions may reduce the chance of reaction. Figure 3.8. shows how adding 2 mM of the strong acid trifluoromethanesulfonic acid (CF_3SO_3H) changes the redox process from a 2 × $1e^-$ reduction process into a $2H^+/2e^-$ PCET, with only one widely separated redox wave. The ΔE_p increases to 1.34 V with $E_{1/2} = 0.20$ V (*vs* Ag/Ag$^+$) and i_{pa}/i_{pc} of 0.76 at 100 mV s^{-1}. The lower supporting electrolyte concentration in Figure 3.8. to Figure 3.7.(a) will cause slightly larger ΔE_p values. This means the ΔE_p are not directly comparable, but the difference should not affect the conclusions.
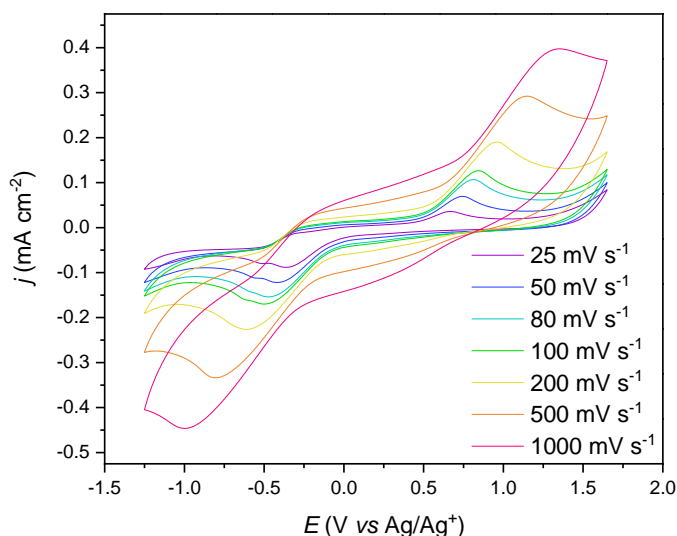
Figure 3.8. CV data for 1 mM TFBQ, 2 mM CF$_3$SO$_3$H, 0.05 M TBABF$_4$, TFT, using a GC WE, Ag/Ag$^+$ RE, and a Pt CE over scan rates 25 ≤ *v* ≤ 1000 mV s^{-1}.

The presence of both reductive and oxidative waves at *v* < 100 mV s^{-1} implies H$^+$ is stabilising the TFBQ^{2-}, but the larger ΔE_p indicates the PCET process is less kinetically facile than the process without acid. A small ΔE_p is most desirable as it leads to lower overpotentials. Therefore, acidification is not useful for stabilising reduced states of TFBQ.

Concerns regarding the low vapour pressure and high toxicity of TFT limit its applicability in RFBs and so this study moves to focus on alternate solvent systems. Furthermore, TFBQ is too unstable in both in aqueous and non-aqueous media to be useful in an ORFB. The investigation therefore moves on to other quinone derivatives.

3.1.2. Octafluoro-9,10-Anthraquinone

The BQ backbone yields the most positive E^o of all the quinone systems. Larger quinone backbones result in ORAMs with more negative reduction potentials. This is because the C-

O bonds have a large effect on the LUMO energies. By increasing the number of conjugated rings, one increases the resonance effect. This raises the LUMO energy by decreasing the effect of the C-O bond on the molecule. Electron insertion is therefore less facile at higher ring numbers, which moves the reduction potential more negative.[23] This in in contrast to the trend in polycyclic aromatics, which contain no C-O moieties.[23] Without any functional group modifications the reduction potentials decrease from 0.70 V to 0.10 V (*vs* SHE) between BQ and AQ.[24] AQs are therefore more desirable anolyte half-cell ORAMs than BQs. AQs are available in nature from a variety of biological sources, including bacteria, marine sponges, fungi, lichen and higher plants, and so are an environmentally favourable option for an ORFB ORAM.[25]

The AQ backbone is responsible for some of the most positive and negative anolyte and catholyte ORAMs, with DB-1 E^o = 1.35 (*vs* Ag/Ag$^+$) and DB-134 with E^o = −1.98 V (*vs* Ag/Ag$^+$).[26,13] Molecules that undergo reduction at more negative potentials tend to be less stable, but the increased number of electron-withdrawing fluorine moieties may work improve the reduced state stability.

The higher molecular weight of the AQ skeleton leads to lower specific capacities, (AQDS: 412 g mol^{-1}; 129 A h kg^{-1} *vs* BQ: 108 g mol^{-1}; 496 A h kg^{-1}) as discussed in Chapter 1.3.[24] On the contary, the larger size may be beneficial by causing lower permeation through the IEM and lower solubility in an adjacent aqueous phase. Additionally, the extra conjugated rings should also give AQ a more disperse electron cloud that will help stabilise reduced states.

Continuing with theory of stabilising F functional groups in Section 3.1.1., this study investigates the AQ derivative OFAQ (Figure 3.9.). As for TFBQ, OFAQ is a relatively unstudied molecule. Of the few studies that cover OFAQ, Matsui *et* al. encouragingly demonstrate the higher non-aqueous solubility of perfluoroalkyl derivatives of AQ dyes over their non-fluorinated counterparts.[27]
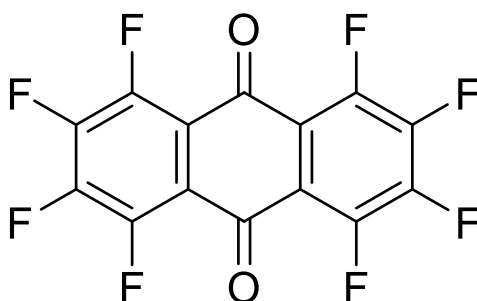
Figure 3.9. Octafluoro-9,10-anthraquinone (OFAQ).

Nagamura *et al.* use DFT methods and X-ray absorption spectroscopy (XAFS) to study the battery characteristics of the quinone family in organic cathode devices.[23] The F groups in OFAQ improve its stability but also give a significantly higher reduction potential than the

parent non-fluorinated molecule.[28] The fully saturated OFAQ has lower energy LUMO electronic states as a direct result of the π-bonding electrons of the aromatic F substituents. This improves the stability but the C-F antibonding overlap population at the LUMO level risks electrochemically reductive decomposition. Matsui *et al.* show that F groups in the aromatic moiety can act as leaving groups when the conditions are sufficient for nucleophilic substitution.[29] For example, 1,2,3,4-tetrafluoro-9,10-anthraquinone reacts with nucleophiles (amines, methoxide ions) to give 1- and 2- substituted derivatives, depending on the kinds of nucleophiles, solvents, and reaction temperature.[29] Despite these negative attributes, the relative little literature surrounding OFAQ and its possible success in ORFBs make it of keen interest to study

Equations 3.3. and 3.4. and Figure 3.10. give the $2 \times 1e^-$ transfer pathway for OFAQ. Figure 3.11. shows the (a) CV and (b) i_p *vs* $v^{1/2}$ plots for 1 mM OFAQ, 0.1 M TBABF$_4$ in TFT. Table 3.2. gives the $E_{1/2}$, D_o and i_{pa}/i_{pc} values for both TFBQ (using data from Figure 3.7.) and OFAQ in TFT at 100 mV s^{-1}. This directly compares the effect of increased conjugation on the electrochemistry, transfer properties, and reversibility.

$$OFAQ \xrightarrow{e^-} OFAQ^{\cdot -} \qquad\qquad 3.3.$$

$$OFAQ^{\cdot -} \xrightarrow{e^-} OFAQ^{2-} \qquad\qquad 3.4.$$
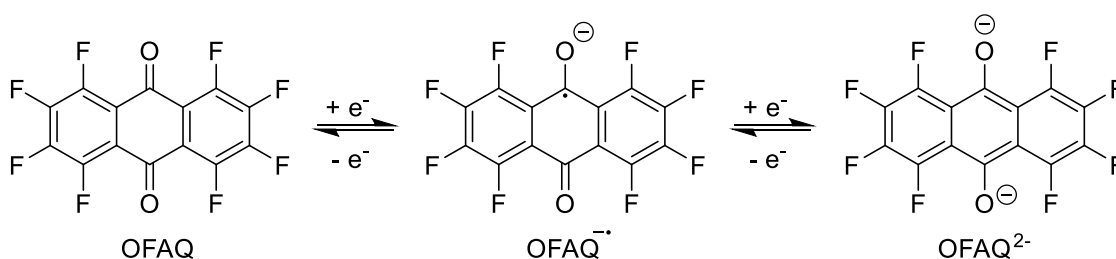
Figure 3.10. The two-step one-electron reduction process for OFAQ in non-aqueous media.

The concurrent contesting effects of increasing aromaticity and F moieties between TFBQ and OFAQ result in similar $E_{2,1/2}$ values. In the AQ derivative, the extra rings move the potential more negative whilst the extra fluorine EWGs move the potential more positive. This culminates in a similar $E_{2,1/2}$ for both quinones.

The i_{pa}/i_{pc} of 1 when $v < 100$ mV s^{-1} in OFAQ shows it has better dianionic chemical reversibility and hence better stability than TFBQ, where E_2 is completely irreversible. The linearity in Figure 3.10.(b) further indicates a reversible, diffusion-controlled process. Table 3.2. shows the D_o values for E_1 are similar over both molecules and in the range of 1×10^{-6} cm^2 s^{-1}.
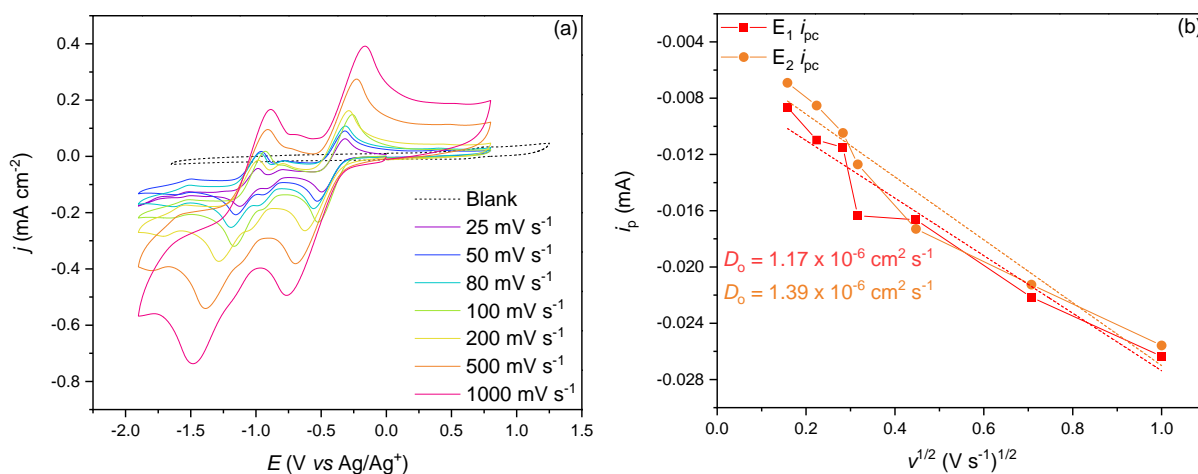
Figure 3.11. (a) CV data for 1 mM OFAQ, 0.1 M TBABF₄, TFT, using a GC WE, Ag/Ag⁺ RE, and Pt CE over the range 25 ≤ v ≤ 1000 mV s⁻¹. (b) The i_p vs $v^{1/2}$ graphs for the first (E₁) and second (E₂) reduction processes, respectively.

Table 3.2. Table of electrochemical data from TFBQ and OFAQ in 0.1 M TBABF₄, TFT at 100 mV s⁻¹.

	E_1				E_2			
	$E_{1,1/2}$ (V vs Ag/Ag⁺)	ΔE_p (V vs Ag/Ag⁺)	D_o (cm² s⁻¹)	i_{pa}/i_{pc}	$E_{2,1/2}$ (V vs Ag/Ag⁺)	ΔE_p (V vs Ag/Ag⁺)	D_o (cm² s⁻¹)	i_{pa}/i_{pc}
TFBQ	0.08	0.286	2.49 × 10⁻⁶	1.04	−1.02	0.286	3.01 × 10⁻⁷	0.97 (irreversible if v < 100 mV s⁻¹)
OFAQ	−0.39	0.265	1.17 × 10⁻⁶	0.90	−1.05	0.236	1.39 × 10⁻⁶	0.94

The D_o for E_2 for TFBQ is an order of magnitude lower than for OFAQ (3.01 × 10⁻⁷ cm² s⁻¹ against 1.39 × 10⁻⁶ cm² s⁻¹). This is counter intuitive as the increased molecular size of OFAQ should decrease the mass transport rate and give a lower D_o. The slower rate may be due inaccuracies in the D_o calculation stemming from the interrelation of E_2 and decomposition with TFBQ.

The D_o for OFAQ are similar to those for the benchmark VRFB (V^{2+}/V^{3+} = 1.41 × 10⁻⁶ cm² s⁻¹, V^{4+}/V^{5+} = 2.14 × 10⁻⁶ cm² s⁻¹ in H_2SO_4 on carbon electrodes)[30,31] and the reduction potentials are significantly more negative (OFAQ $E_{2,1/2}$ = −1.05 V (vs Ag/Ag⁺) and V^{2+}/V^{3+} E^o = −0.26 V (vs SHE)).[3,32] The chemical and electrochemical stability, fast mass transfer, and favourably negative reduction potential make OFAQ appealing for competitive ORFBs. The next sections of this work aims to optimise the electrochemistry of OFAQ by investigating a range of non-aqueous electrolytes and supporting salts.

3.2. Solvent Selection

3.2.1. Organic Solvents

OFAQ is insoluble in aqueous media, thus non-aqueous electrolytes are the focus point. The charge delocalisation over the AQ rings stabilises the reduced states but this is insufficient if the environment is reactive. Therefore, determining a solvent environment that is not reactive to OFAQ$^{.-}$ or OFAQ^{2-} is critical for developing OFAQ into an ORFB.

Key characteristics for an appropriate non-aqueous solvent include: a) sufficient solubility and electro-activity of the ORAM and the reaction products in the solvent; b) sufficient supporting electrolyte solubility; c) easy purification; d) low toxicity; e) environmental benignity; f) low cost; and g) wide ESW. Membrane-free devices require further considerations of mutual immiscibility and solvent polarity. The solvent must be polar enough to stabilise the reduced states, but apolar enough to be immiscible with an aqueous half-cell, all whilst maintaining a sufficiently wide L/L ESW.

Figure 3.11.(a) shows OFAQ has quasi-reversible voltammetry in TFT. The high toxicity and low vapour pressure of TFT discourage its use. These factors move the investigation to study other common non-aqueous and L/L solvents. These are 1,2-dichlorobenzene (DCB), ACN, ethyl acetate (EA), 5-nonanone, valeronitrile, caprylonitrile, and heptanenitrile.

DCB and ACN are widely used in non-aqueous electrochemical systems due to their relatively high polarity and wide ESWs.[33] DCB and 5-nonanone are common in L/L electrochemistry. 5-nonanone has one of the widest L/L ESWs of organic solvents against water.[34] Additionally, the low toxicity, non-halogenated, and non-aromatic nature of 5-nonanone are attractive features. EA is a water immiscible solvent that is less toxic and cheaper than DCB.[35] ACN, 5-nonanone, and EA have densities lower than water at 0.786, 0.826, and 0.902 g cm^{-3}, respectively.[34,36] A solvent with lower ρ than water will likely have better mass transport characteristics and lower pumping losses in a flow system. ACN is miscible with water, however, the system partitions into two immiscible phases when the aqueous phase comprises a highly concentrated WIS.[37,38] It is therefore possible to use an ACN electrolyte against an aqueous phase in a membrane-free device. Chapter 5. investigates this concept further.

Straight chain nitriles have structures that lend well to membrane-free systems. The nitrile functional group is polar and the aliphatic chain is non-polar. This should stabilise the reduced states whilst providing immiscibility with an adjacent aqueous phase. Increasing the aliphatic chain length from valeronitrile (C$_4$) through heptanenitrile (C$_6$) to caprylonitrile (C$_7$) studies effect of the chain length on the anionic stability.

Figure 3.12. gives the CV data of 1 mM OFAQ, 0.1 M TBABF$_4$ in a range of non-aqueous solvents over scan rates $25 \leq v \leq 1000$ mV s^{-1}. Only DCB, ACN, EA and heptanenitrile give reversible 2 ×1e$^-$ transfers, all other solvents are irreversible.

The reversible 2 × 1e$^-$ process in DCB, ACN, EA and heptanenitrile in Figures 3.12.(a), (b), (c), and (f) make these solvents of most interest. Both waves in EA have a wider ΔE_p and a more positive $E_{1/2}$ ($E_{1,p}$ = 0.25 V, $E_{2,p}$ = 0.31 V, $E_{1,1/2}$ = −0.29 V, $E_{2,1/2}$ = −0.96 V (vs Ag/Ag$^+$)) than for DCB or ACN, making it a less attractive solvent. Heptanenitrile also shows more positive $E_{1/2}$ values ($E_{1,1/2}$ = −0.19 V, $E_{2,1/2}$ = 0.96 V (vs Ag/Ag$^+$)). The additional oxidation wave at −0.44 V in Figure 3.12.(f) is likely oxygen contamination.

Figure 3.13. shows the corresponding i_p vs $v^{1/2}$ plots for the OFAQ scan rate dependant voltammograms in (a) DCB and (b) ACN. The linear relationships of i_p with $v^{1/2}$ indicate a diffusion-controlled process in both solvents. Interestingly, Figure 3.12.(a) shows E_2 ($E_{2,1/2}$ = −0.89 V, $\Delta E_{2,p}$ = 0.19 V, i_{pa}/i_{pc} = 1.06) as more chemically reversible than E_1 ($E_{1,1/2}$ = −0.26 V, $\Delta E_{1,p}$ = 0.21 V, i_{pa}/i_{pc} = 0.84) in DCB at 100 mV s^{-1} despite the higher charge density on OFAQ^{2-}. The ΔE_p values are wider than the theoretical 0.059 V for a Nernstian reversible electrochemical process, indicating the electrochemical quasi-reversibility or irreversibility of OFAQ reduction in DCB. The ΔE_p values increase from 0.142 V to 0.391 V for E_1 and 0.145 V to 0.391 V for E_2 over $25 \leq v \leq 1000$ mV s^{-1}.

OFAQ in DCB has D_o values of 1.00×10^{-6} cm^2 s^{-1} and 5.07×10^{-7} cm^2 s^{-1} for E_1 and E_2, respectively, indicating slower diffusion in the E_2 process in DCB than in TFT. This is likely due to the higher viscosity of DCB (1.324 mPa s)[39].

The lower viscosity of ACN (0.34 mPa s)[40] causes the improvements in transport properties in Figures 3.12.(b) and 3.13.(b). This shows through better chemical and electrochemical reversibility's and faster D_o values (1.13×10^{-5} cm^2 s^{-1} and 1.09×10^{-5} cm^2 s^{-1} for E_1 and E_2, respectively). Figure 3.14. plots the electrochemical characteristics of OFAQ in ACN. Figure 3.14.(a) and (b) show the variation of E_p and ΔE_p as a function of scan rate for the E_1 (OFAQ/OFAQ$^-$) and E_2 (OFAQ$^-$/OFAQ^{2-}) redox couples, respectively. Figures 3.14.(c) and (d) show the variation of i_p and i_{pa}/i_{pc} as a function of scan rate for the E_1 and E_2 redox couples, respectively.

The i_{pa}/i_{pc} values are 1.02 and 0.94 for E_1 ($E_{1,1/2}$ = −0.89 V) and E_2 ($E_{2,1/2}$ = −1.49 V) at 100 mV s^{-1}, respectively. The D_o values are over an order of magnitude faster than for DCB and TFT, as well as the benchmark VRFB system. The ΔE_p values are close to an electrochemically reversible Nernstian process (0.065 V and 0.071 V for E_1 and E_2, respectively). These results indicate ACN as the best solvent for OFAQ reduction of those in the screening.
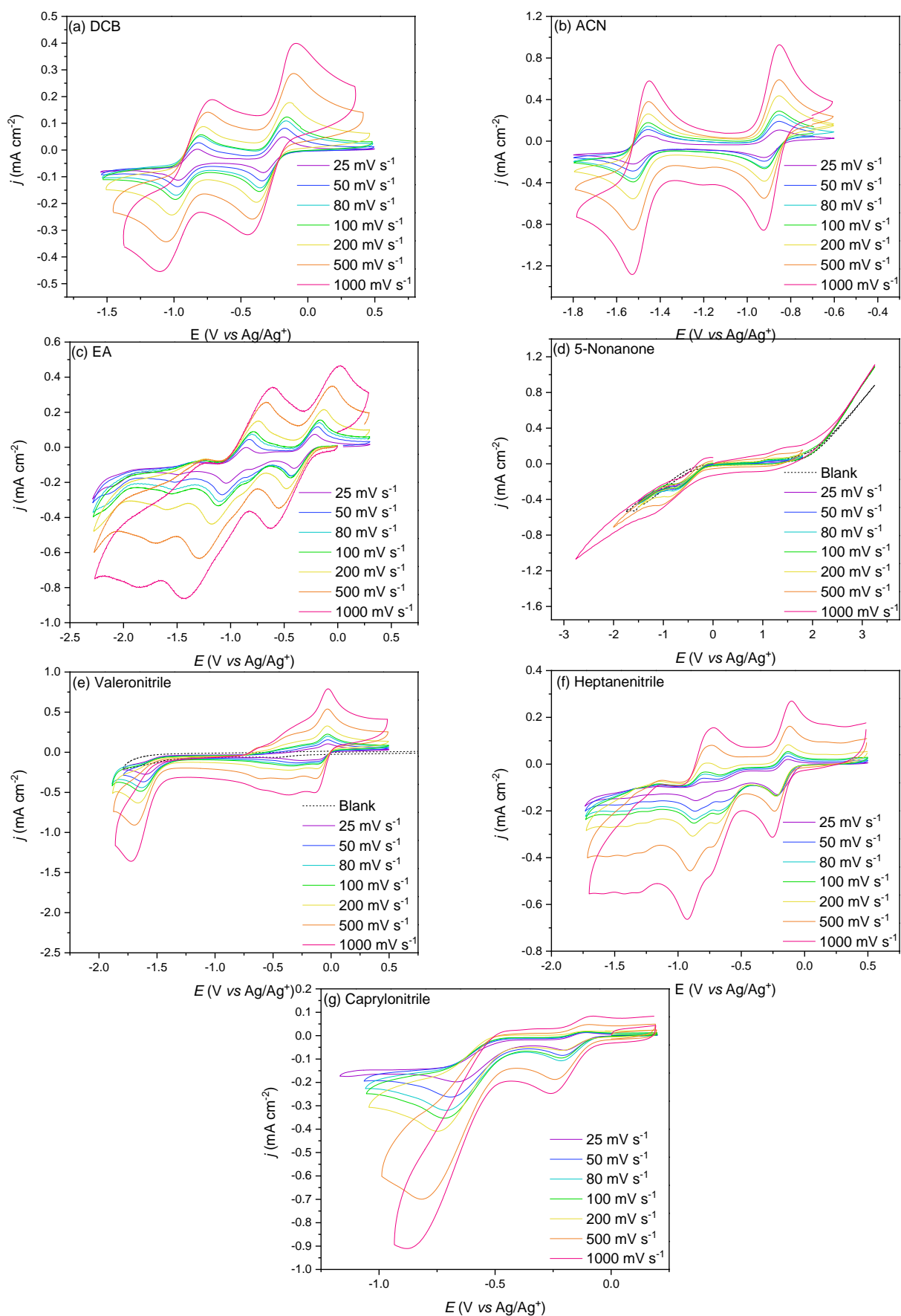
Figure 3.12. CV data of 1 mM OFAQ, 0.1 M TBABF₄ over 25 ≤ v ≤ 1000 mV s⁻¹ in (a) DCB, (b), ACN, (c) EA, (d) 5-nonanone, (e) valeronitrile, (f) heptanenitrile, and (g) caprylonitrile using a GC WE, Ag/Ag⁺ RE, and Pt CE.
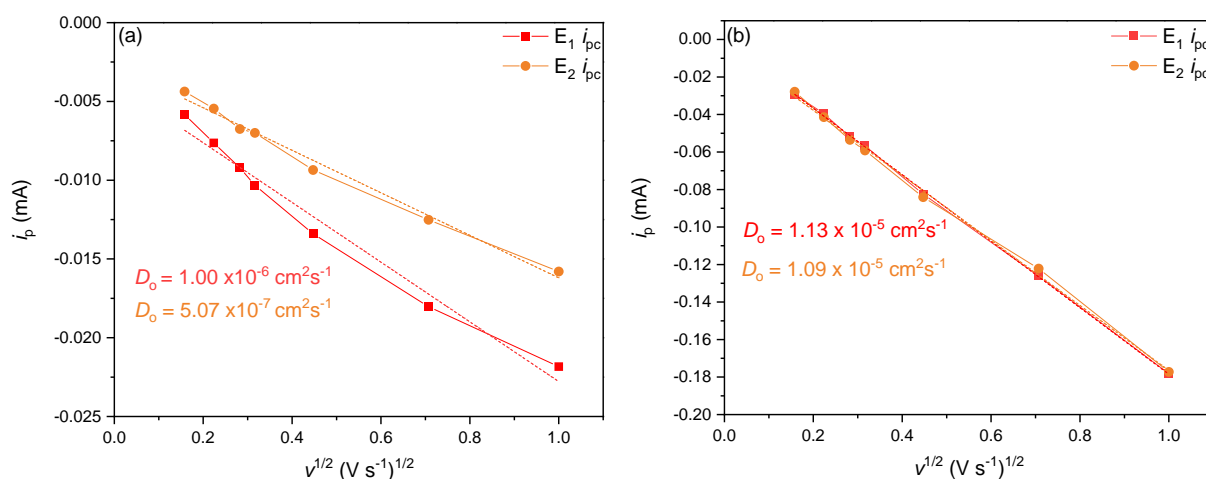
Figure 3.13. i_p vs $v^{1/2}$ plots and Randles–Ševčík D_o values for 1 mM OFAQ, 0.1 M TBABF$_4$ in (a) DCB and (b) ACN.
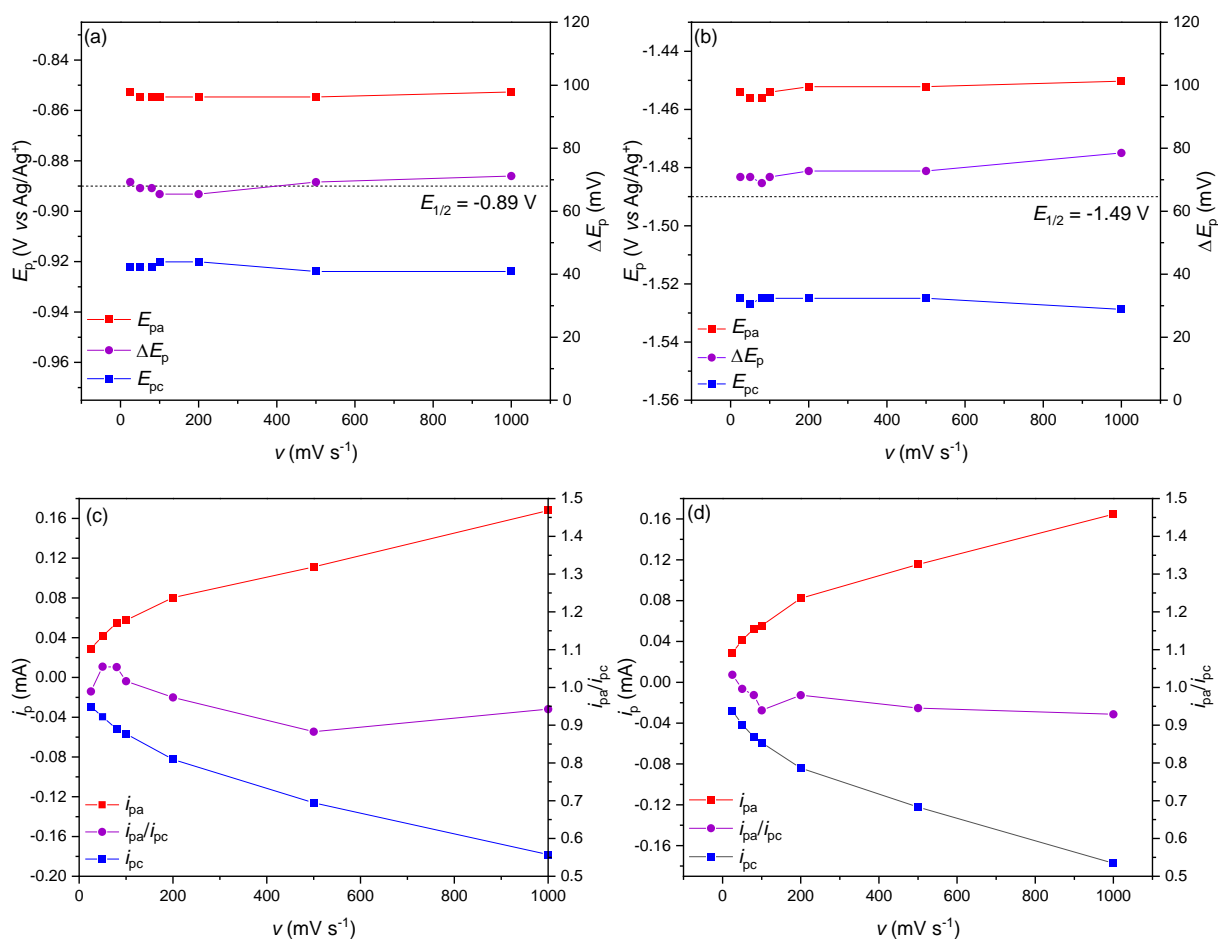
Figure 3.14. (a) and (b) Plot of E_p and ΔE_p as a function of scan rate for the (a) OFAQ/OFAQ$^-$ and (b) OFAQ$^-$/OFAQ^{2-} redox couples. (c) and (d) The variation of i_p and i_{pa}/i_{pc} as a function of scan rate for the (c) OFAQ/OFAQ$^-$ and (b) OFAQ$^-$/OFAQ^{2-} redox couples in ACN.

144

The 5-nonanone CV (Figure 3.12.(d)) only shows one irreversible reduction around $E_{pc} = -0.89$ V (*vs* Ag/Ag$^+$). The ESW of 5-nonanone is $-1 - 2$ V (Figure 3.12.(d), grey dashed line). The small ESW confines the system to irreversibly reducing the solvent ketone group before forming the dianion. The low ESW renders it not useful for an OFAQ-containing electrolyte.

The nitrile chain length plays a significant role in OFAQ reversibility between the C_4, C_7, and C_8 nitriles. Figures 3.12.(e) – (g) show a reversible E_1 in the valero- and heptanenitriles and an irreversible E_2 in valero- and caprylonitrile. The lesser polarity in the longer chain length likely means it is less able to stabilise the reduced quinones, resulting in no return oxidation. The irreversible E_2 in valeronitrile is likely due to proximity with the cathodic end of the ESW.

The median chain length, heptanenitrile, gives the best reversibility for E_1 and E_2. In heptanenitrile, fast scan rates yield an E_1 with a linear increase of i_p with v with a rapid D_o of 5.24×10^{-5} cm^2 s^{-1}. An extra reductive peak appears in Figure 3.12.(f) at $E_{pc} = -0.68$ V at 100 mV s^{-1}, and both E_1 and E_2 become irreversible when $v < 50$ mV s^{-1}. This indicates that both OFAQ$^{\cdot-}$ and OFAQ^{2-} are only stable in heptanenitrile at short timescales and thus it is not a useful solvent.

The UV-Vis spectroscopy data in Figure 3.15. shows even neutral OFAQ is not stable in nitrile solvents. Each solution turns from light pink to dark red with increasing t, with the time taken for colour change decreasing with increasing chain length. All three nitriles experience a hypsochromic shift of the 331 nm peak to 300 nm and the emergence of a new peak at 488 nm, the intensity of which increases with t. The neutral molecule shows least stability in caprylonitrile, with the 488 nm peak only appearing at small absorptions in valeronitrile and heptanenitrile by the second day, but at much larger absorptions in caprylonitrile at the same t.

Mass spectrometry data (Appendix 3.C.) taken after 10 months in each nitrile all show the same major m/z peak at 416. This is higher than the OFAQ molecular ion m/z (molecular weight of 352.14 g mol^{-1}) and indicates a chemical change to a larger molecule. The identity of the 416 m/z molecule is unknown. The colour change and absorption spectra have a similar trend with t. This, alongside the same major peaks in the mass spectrum suggests a similar degradation process over all nitrile chain lengths. Furthermore, this process occurs at a faster rate with longer aliphatic chains.

The chemical and electrochemical instability of OFAQ in the longer chain nitrile solvents makes them unsuitable solvents for this ORFB. Of the non-aqueous solvents in this section, OFAQ shows the best electrochemical and chemical reversibility in EA, DCB and ACN. The ACN solvent gives the most negative reduction potential and fastest D_o and so is the most favourable non-aqueous solvent thus far.
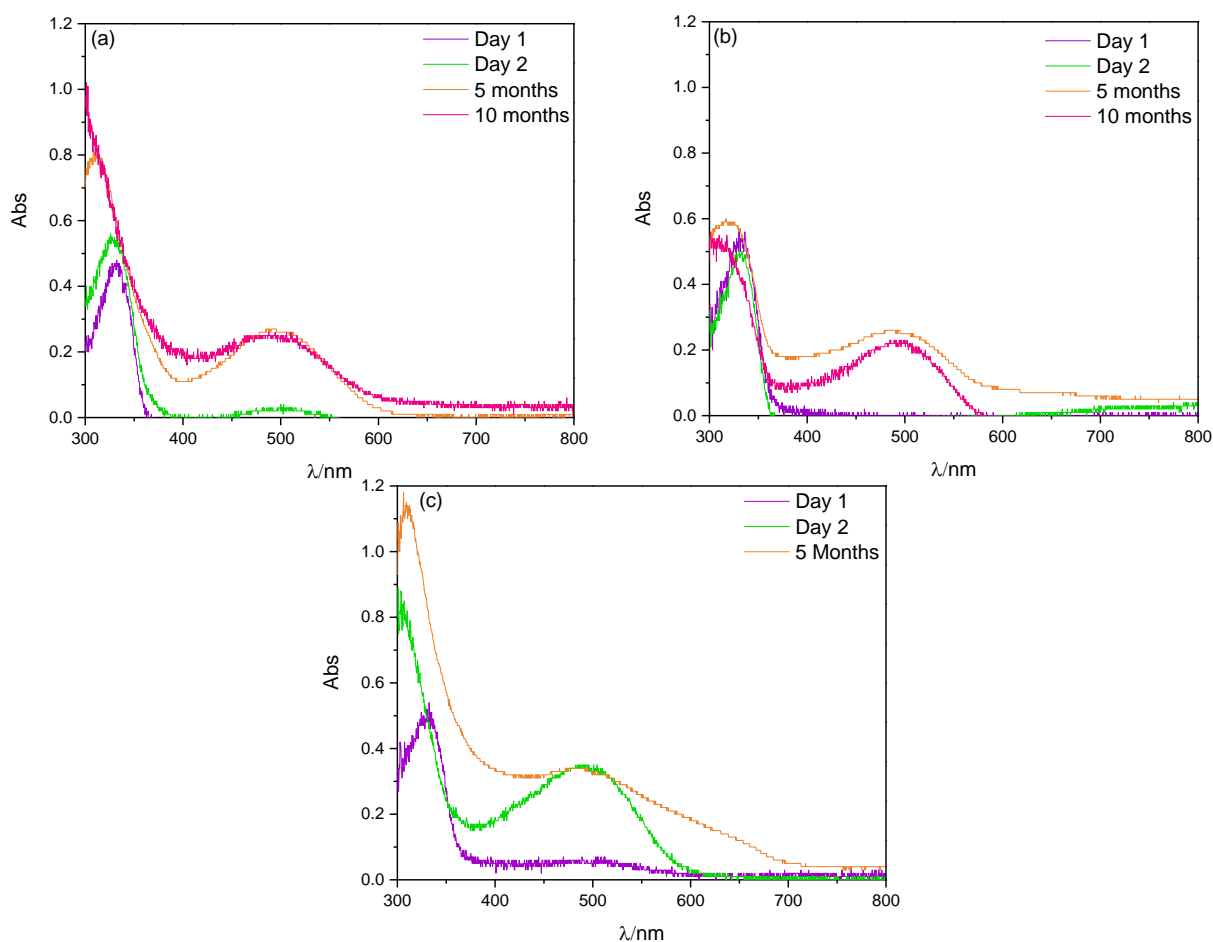
Figure 3.15. UV-visible spectroscopy data for 1 mM OFAQ in (a) valeronitrile, (b) heptanenitrile, and (c) caprylonitrile over 10 months.

Section 3.1. determines nucleophilic attack on quinones by water to be detrimental to the TFBQ system in aqueous media. The quinone reduction pathway is different in non-aqueous media, but the issue of side reactions with water or dissolved protons remains critical. This is because the second reduction product, $OFAQ^{2-}$, is a much stronger base than $OFAQ^{\cdot-}$ and neutral OFAQ, and can easily react with protons in the solution via Equations 3.5. and 3.6.[41]

$$OFAQ^{2-} + H^+ \rightarrow OFAQH^- \qquad\qquad 3.5.$$

$$OFAQH^- + H^+ \rightarrow OFAQH_2 \qquad\qquad 3.6.$$

The protons can originate either from H_2O impurities or from the solvent itself. It is therefore useful to understand the effect of water on the OFAQ reduction process and to comprehend the water tolerance level of the system. The solvents in this section are between 97 – 99.99 % pure, and it is likely that the impurities include water. Water is a weak Brønsted acid, so hydrogen-bonding interactions are more likely to occur than the above protonation processes.

CV studies with successive additions of H_2O give an indication of the stability of OFAQ against dissolved water. Figure 3.16.(a) gives the 100 mV s^{-1} CV plots for 1 mM OFAQ, 0.1 M TBABF$_4$,

in extra-dry anhydrous ACN with successive additions of H_2O from 1 mM to 20 % by volume/volume ratio (v/v). The smaller values are given in concentration rather than percentage for ease of understanding, but for clarity, the 1 mM and 100 mM H_2O contaminations correspond to 1.5×10^{-4} % and 0.15 %, respectively. Figure 3.16.(b) displays the relationship between H_2O v/v and i_p.
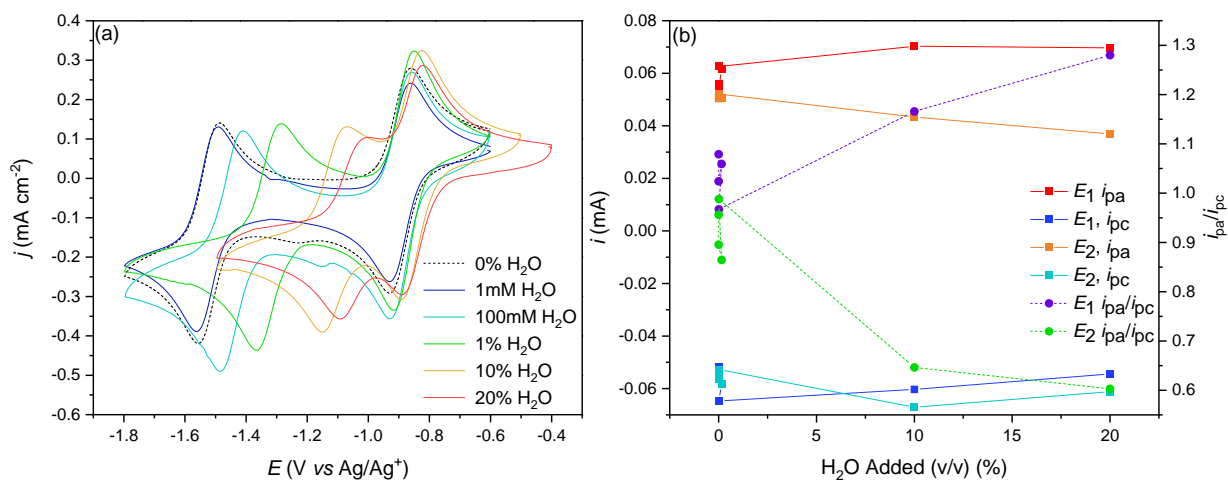
Figure 3.16. (a) CVs of 1 mM OFAQ, 0.1 M TBABF₄, extra-dry anhydrous ACN at scan rates 25 ≤ v ≤ 1000 mV s⁻¹ with successive additions of H₂O by volume. (b) Plot comparing the i_p and i_pa/i_pc values against H₂O v/v.

Figure 3.16.(a) shows no change in the CV between 0 and 1 mM H_2O contamination, suggesting OFAQ needs a much larger than equal quantity of water to change from a $2 \times 1e^-$ to a $2H^+/2e^-$ PCET. This suggests that water contamination is unlikely causing the molecular degradation in the solvent screening, and any loss in reversibility is due to the nature of the solvents themselves. This is interesting as it suggests that both $OFAQ^{2-}$ and $OFAQ^{-}$ are stable in the presence of small quantities of water over CV timescales.

Larger water contaminations do cause electrochemical changes. Increasing the H_2O fraction above 100 mM shifts E_2 positive from $E_{2,1/2} = -1.49$ V to $E_{2,1/2} = -1.45$ V (vs Ag/Ag⁺) but the ΔE_p remains that of an electrochemically reversible process at $\Delta E_{2,p} = 0.073$ V. E_1 remains at the same $E_{1/2}$ independent of the H_2O quantity. The proximity of E_1 and E_2 at higher H_2O v/v makes it challenging to accurately baseline the peaks for analysis. This causes the apparent worsening reversibility in the i_{pa}/i_{pc} values with increasing H_2O content in Figure 3.16.(b). The lowering i_{pa}/i_{pc} are therefore an artefact of the measurement and analysis rather than a result of the electrochemistry.

The electrochemical and chemical reversibility of the E_2 process suggests there is no chemical reaction of the dianion with water. Interactions between the $OFAQ^{-}$ and $OFAQ^{2-}$ with H_2O molecules must therefore be via molecular associations, such as hydrogen bonding, such that

the same EE process can occur. The H_2O-OFAQ complexes facilitate the reduction of OFAQ$^{.-}$ to OFAQ^{2-} and result in the positive E_2 shift.[42]

As the system maintains a reversible 2 × 1e$^-$ at relatively high water concentrations, the use of expensive extra-dry solvents is unnecessary. The CVs of OFAQ reduction in standard laboratory-grade ACN *vs* extra-dry ACN exactly overlay, corroborating that miniscule water contaminations do not affect the OFAQ/OFAQ^{2-} redox process. This is beneficial as it reduces the solvent cost and means that an adjacent aqueous half-cell in a membrane-free device would not destroy the OFAQ.

3.2.2. Room-Temperature Ionic Liquids

Section 1.4. discusses how the non-flammability, low volatility, thermal and chemical stability, wide ESW of RTILs make them promising RFB electrolytes. Their intrinsic conductivity negates the need for additional supporting salts, which improves ORAM solubility and reduces additional system costs. Previous literature employs the aprotic RTIL [EMIm][TFSI] due to its high electrochemical stability (4.35 V on GC), relatively low viscosity (32 mPa s) and high ionic conductivity (9.2 mS cm^{-1}).[43] Another promising RTIL is the hydrophobic ([BMPyrr][TFSI]) due to its wide ESW (5.5 V) and high ionic conductivity (1 mS cm^{-1}).[35] The high viscosity (84.33 mPa s) remains an issue for flow, but methods such as adding co-solvents can reduce this. Both RTILs are immiscible with water which is promising for membrane-free devices.[35,44]

Figure 3.17. gives the CV's over scan rates 25 ≤ v ≤ 1000 mV s^{-1} for 1 mM OFAQ in (a) [EMIm][TFSI], (b) [BMPyrr][TFSI], (c) [EMIm][TFSI] with 2 mM CF_3SO_3H, and (d) diethylmethylammonium hydrogensulfate ([dema][HSO$_4$]). Figures 3.18.(a) and (b) give the corresponding the i_p and $v^{1/2}$ plots for Figures 3.17.(a) and (b).

Figures 3.17.(a) and 3.18.(a) show OFAQ undergoes a quasi-reversible E_1 ($E_{1,1/2}$ = −0.45 V (*vs* Ag/Ag$^+$), i_{pa}/i_{pc} = 0.63) in a [EMIm][TFSI] solvent, with a linear relationship between i_p and $v^{1/2}$. The reversibility of the first step is due to favourable π-π interactions and hydrogen bonding between OFAQ$^{.-}$ and the [EMIm]$^+$ cation. This should also stabilise the dianion, but E_2 is irreversible ($E_{2,pc}$ = −1.75 V (*vs* Ag/Ag$^+$)). The continuously increasing i at −2 V (*vs* Ag/Ag$^+$) marks the cathodic end of the ESW for [EMIm][TFSI]. The ESW for [EMIm][TFSI] ranges between 2 − −2 V (*vs* Ag/AgCl), and so it is possible that some [EMIM]$^+$ begins to degrade at the same potential for OFAQ^{2-} formation.[45] The OFAQ^{2-} may react with the degradation product in a kinetically fast irreversible chemical step (EC mechanism) to yield an electrochemically irreversible product. Figure 3.17.(a) shows this problem exacerbates at faster scan rates, with OFAQ^{2-} reduction completely hidden by [EMIm][TFSI] degradation at

1000 mV s^{-1}. Despite the encouraging stability of the E_1 step, the slower D_o of 6.22×10^{-8} cm^2 s^{-1} reflects the issues from the higher viscosity of RTILs over conventional non-aqueous solvents.
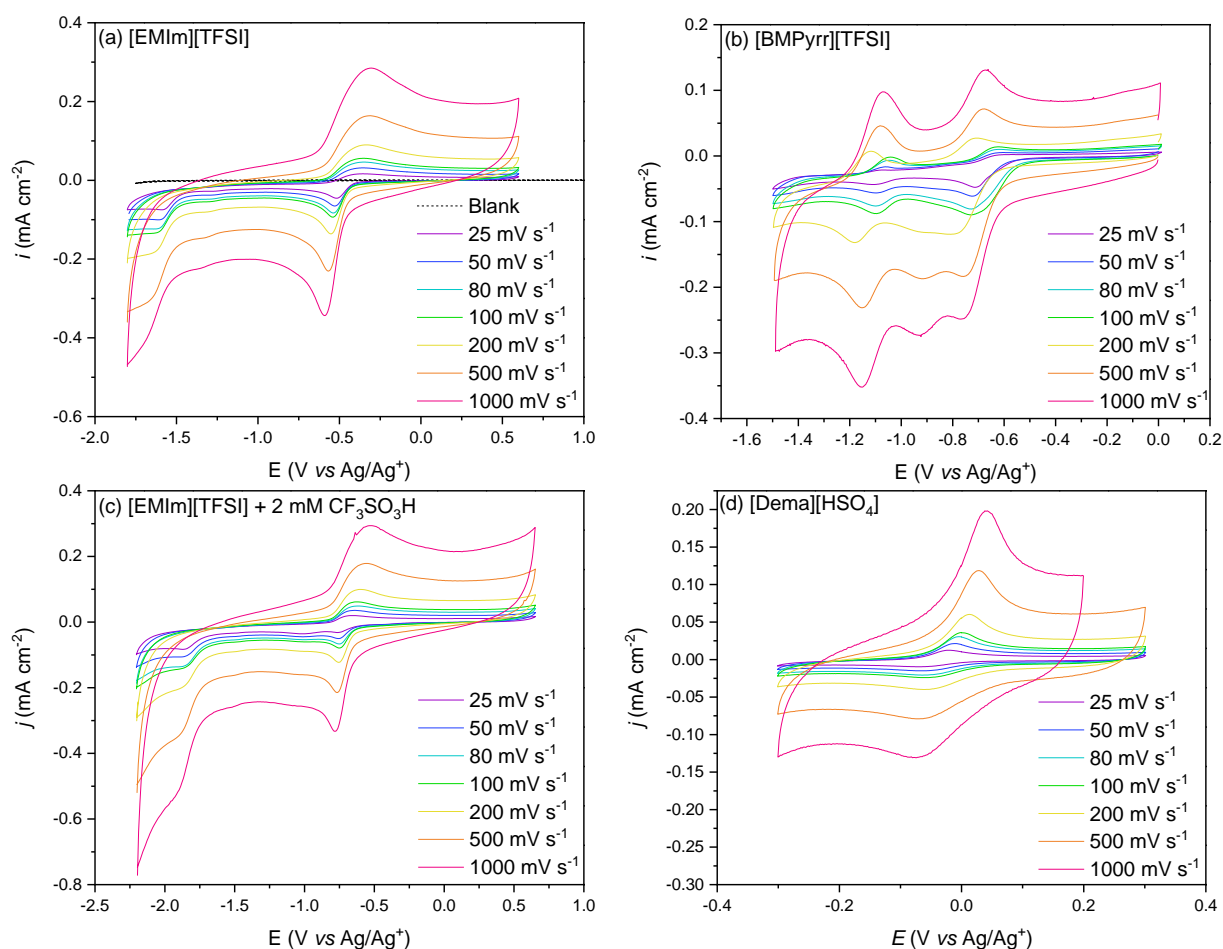
Figure 3.17. CV plots of 1 mM OFAQ in RTILs: (a) [EMIm][TFSI], (b) [BMPyrr][TFSI], (c) [EMIm][TFSI] + 2 mM CF₃SO₃H, (d) [dema][HSO₄] over scan rates 25 ≤ v ≤ 1000 mV s⁻¹ using a GC WE, Ag/Ag⁺ RE, and Pt CE.
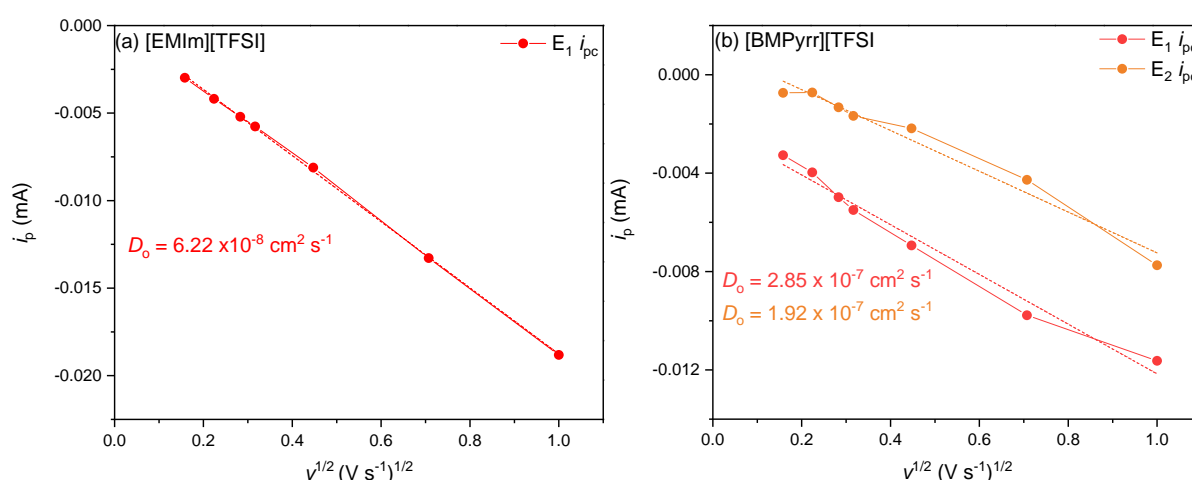
Figure 3.18. i$_p$ vs v$^{1/2}$ plots for 1 mM OFAQ in (a) [EMIm][TFSI] and (b) [BMPyrr][TFSI] over scan rates 25 ≤ v ≤ 1000 mV s⁻¹.

149

Adding a stoichiometric amount of the strong acid CF_3SO_3H alters the reaction pathway of TFBQ in TFT (Figure 3.8.). Figure 3.17.(c) shows an almost identical CV after including 2 mM CF_3SO_3H to the electrolyte without any acid (Figure 3.17.(a)). The point of adding the acid is to study whether H^+ stabilises the high charge density on the reduced carbonyl moieties in $OFAQ^{2-}$, as in Section 3.1.1. for TFBQ. If H^+ stabilises the $OFAQ^{2-}$ it may positively shift the $E_{2,pc}$ enough such that the end of the ESW is no longer an issue. Therefore, acidification does not overcome the reversibility issues stemming from the proximity of E_2 for OFAQ and the end of the ESW for $[EMIm][TFSI]^+$.

Figure 3.17.(d) investigates whether a further increase of the H^+ concentration stabilises reduced forms by employing a protic RTIL ($[dema][HSO_4]$) as the electrolyte. The higher magnitude for i_{pa} than i_{pc} in the CV indicate a reduction in the mono-anionic reversibility despite $OFAQ^{.-}$ showing good stability in the aprotic RTILS. Strong acids can have a pK_a of less than zero, and CF_3SO_3H has a pK_a of 0.7 in ACN.[46] The pK_a of $[dema][HSO_4]$ is only 13.7 in water, suggesting that even though the proton concentration in the RTIL is high, its ability to donate these protons is low.[47] Especially given that H_2O, with a pK_a of 14, fails to protonate the dianion in ACN (Figure 3.16.).

Given the lack of change upon adding the strong proton donor in Figure 3.17.(c), the lack of stabilisation from $[dema][HSO_4]$ is not surprising. Additionally, the ESW of $[dema][HSO_4]$ is not sufficiently negative to access the second reduction process in OFAQ rendering it not useful.

$[BMPyrr][TFSI]$ has a wider ESW (2.28 – −2.92 V (*vs* Ag/AgCl)) and should not suffer from the same side reactions as $[EMIm]^+$ or $[dema]^+$.[48] Figure 3.17.(b) shows a quasi-reversible E_1 and reversible E_2 in $[BMPyrr][TFSI]$ at $E_{1,1/2}$ = −0.67 V and $E_{2,1/2}$ = −1.07 V at 100 mV s^{-1} with ΔE_p values of 0.110 V and 0.057 V (*vs* Ag/Ag$^+$), for E_1 and E_2, respectively. The extra reductive wave at −0.90 V is likely ORR from atmospheric O_2 and not part of the OFAQ redox process.

E_2 is more electrochemically and chemically reversible than E_1 because it shows the same ΔE_p as an electrochemically reversible reaction and an i_{pa}/i_{pc} of 1.10, whereas E_1 has i_{pa}/i_{pc} of 0.37. The low i_{pa}/i_{pc} of E_1 is likely due to the ORR peak affecting the baseline. Therefore, for Randles–Ševčík analysis the baseline is taken as the slope of the 0 – −0.4 V section of the cathodic potential sweep.

Figure 3.17.(b) and 3.18.(b) show the reversibility of E_1 and E_2 in $[BMPyrr][TFSI]$ lessens with decreasing *v*. The slow D_o values of 2.85×10^{-7} cm^2 s^{-1} and 1.92×10^{-7} cm^2 s^{-1} are a result of the higher viscosity of $[BMPyrr][TFSI]$ (84.33 mPa s).[35] Bamgbopa *et al.* improve the electrochemical characteristics of $[BMPyrr][TFSI]$ by reducing the viscosity and optimising the ionic conductivity with 60/40 v/v of $[BMPyrr][TFSI]$/EA.[35] The team use 25/75 v/v in their experiments as a higher RTIL content makes the system denser than water. $[BMPyrr][TFSI]$

is expensive, and so reducing its content in the electrolyte is beneficial as long as it retains the promising electrochemical characteristics.

Figure 3.19. takes the mixed electrolyte concept from this study and applies it to OFAQ with ACN. Section 3.2.1. shows ACN provides most reversible electrochemistry for OFAQ redox and so is the organic co-solvent of choice. Figure 3.19.(a) shows the CV for 1 mM OFAQ in 25/75 [BMPyrr][TFSI]/ACN with the corresponding i_p vs $v^{1/2}$ plot in Figure 3.19.(b). Table 3.3. compares the electrochemical data at 100 mV s^{-1} for ACN (Figure 3.12.(b)), [BMPyrr][TFSI] (Figure 3.17.(b)), and [BMPyrr][TFSI]/ACN 25/75 v/v (Figure 3.19.(a)).

At fast scan rates in [BMPyrr][TFSI]/ACN, E_1 is electrochemically and chemically reversible whereas E_2 is quasi reversible. ($\Delta E_{1,p}$ = 0.065 V, i_{pa}/i_{pc} = 1, $E_{1,1/2}$ = −0.29 V and $\Delta E_{2,p}$ = 0.103 V, i_{pa}/i_{pc} = 0.71, $E_{2,1/2}$ = −0.77 V at 1000 mV s^{-1}). E_1 becomes less reversible, and E_2 completely irreversible when v < 200 mV s^{-1}. OFAQ in ACN without the RTIL gives more reversible electrochemistry with higher chemical stability. This, alongside the high cost of the RTIL means mixing RTILs and organics does not improve upon the previous data. Optimising the RTIL/ACN v/v ratio may improve the reversibility and make the solvent immiscible. However, the high cost and unstable supply chain of [BMPyrr][TFSI] hinders this branch of the research.
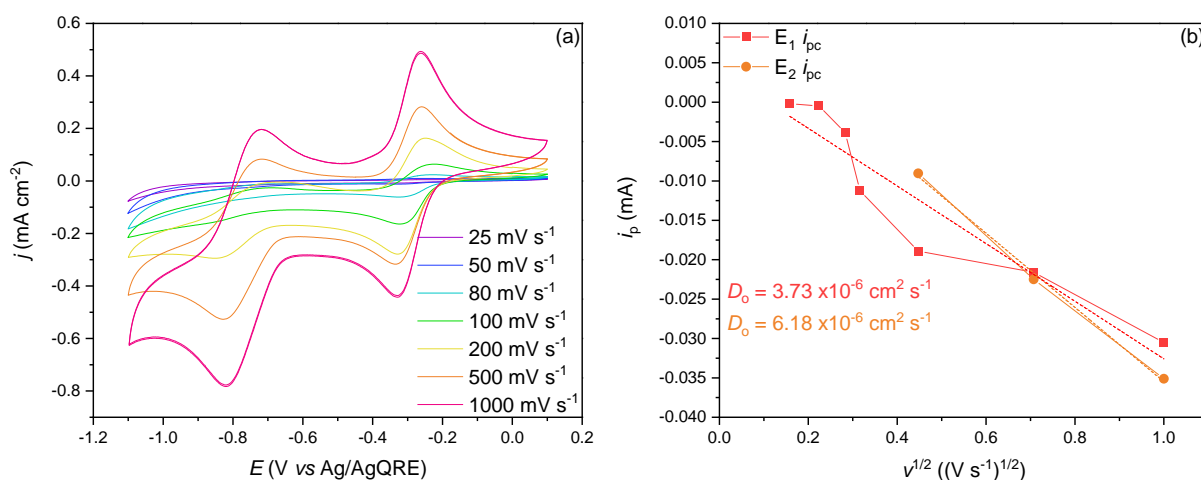
Figure 3.19. CV plots for 1 mM OFAQ in 25/75 v/v (a) [BMPyrr][TFSI]/ACN over scan rates 25 ≤ v ≤ 100 mV s⁻¹ and (b) the corresponding i_p vs v^1/2 plot.

Combining RTILs and co-solvents could be a route to a membrane-free device, as the hydrophobic RTIL may provide immiscibility whilst the non-aqueous co-solvent would improve the electrochemical properties. Unfortunately, at these ratios the [BMPyrr][TFSI]/ACN electrolyte is miscible with water and a much larger quantity of RTIL is necessary for separation. This is expensive and not ideal for the proposed membrane-free device.

Table 3.3. Electrochemical data for 1 mM OFAQ in ACN, [BMPyrr][TFSI], and [BMPyrr][TFSI]/ACN 25/75 v/v at 100 mV s^{-1}.

Solvent	E_1				E_2			
	$E_{1/2}$ (V)	i_{pa} (mA)	i_{pc} (mA)	D_o (cm^2 s^{-1})	$E_{1/2}$ (V)	i_{pa} (mA)	i_{pc} (mA)	D_o (cm^2 s^{-1})
ACN	−0.89	5.76×10^{-2}	$−5.66 \times 10^{-3}$	1.13×10^{-5}	−1.49	5.56×10^{-2}	$−5.91 \times 10^{-3}$	1.09×10^{-5}
[BMPyy][TFSI]	−0.62	2.06×10^{-3}	$−5.50 \times 10^{-3}$	2.85×10^{-7}	−1.07	1.84×10^{-3}	$−1.67 \times 10^{-3}$	1.92×10^{-7}
[BMPyy][TFSI]ACN 25/75 v/v	−0.27	7.14×10^{-3}	$−1.12 \times 10^{-2}$	3.73×10^{-6}	-	-	-	6.18×10^{-6}

Overall, of the RTILs in this section only [BMPyrr][TFSI] shows reversible electrochemistry for both OFAQ electron transfer processes. The reversibility lessens with decreasing v due to the increasing residence time for charge states of OFAQ. This solvent is therefore not suitable in its pure form for an OFAQ-based ORFB. Additionally, the RTIL is expensive and has an unstable supply chain. These factors may improve with economies of scale but currently make the RTIL difficult to study. Furthermore, applying the [BMPyrr][TFSI] as a supporting electrolyte in ACN also impairs the electrochemical and chemical properties of the system. Even if electrochemical and chemical reversibility were apparent, it is unlikely the cost savings made from the lack of necessary supporting salts would overcome the vast price of the RTIL itself. Therefore, the data in this section deems RTILs as unsuitable electrolytes for this ORFB system, and ACN remains as the most viable solvent in this thesis so far.

3.3. Supporting Electrolyte Selection

Section 3.2. shows an ACN solvent provides the most electrochemically and chemically reversible OFAQ redox process. Appropriate supporting electrolyte selection is of equal importance to the solvent. The role of the supporting electrolyte is to make the electrolytic solution conductive; eliminate migrations currents; and to control the reaction conditions by varying the acid-base characteristics and complexing ability of the solvent.[41]

Aqueous solutions usually employ inorganic electrolytes (salts, acids and bases) but these often suffer from low solubility, insufficient dissociation, or have undesirable effects on the electrode reactions in non-aqueous media. Non-aqueous solvents have a smaller selection of supporting salts available. Typically, studies use tetraalkylammonium salts. An effective supporting electrolyte should a) give a wide ESW and be resistant of oxidation and reduction, b) have no unfavourable electrode reactions, c) be commercially available in high purities and of low cost.[41]

The tests in Section 3.2. utilise 0.1 M TBABF$_4$ as the supporting electrolyte. TBABF$_4$ has a wide potential window and good solvating power for a wide range of molecules.[43] The high molecular weight of TBABF$_4$ (329.27 g mol^{-1}) and price (£ 2,120 kg^{-1}) are undesirable for an ORFB. Cheaper supporting electrolytes with lower molecular weights, such as LiClO$_4$ (106 g mol^{-1}, £ 534 kg^{-1}), will make it easier to meet cost ($ 120 kW h^{-1}) and active molecule-electrolyte pair equivalent weight (150 g mol^{-1} e^{-1}) targets.[49] Even discounting the supporting electrolyte, OFAQ lies above this target at 176 g mol^{-1} e^{-1}. This is where RTIL- and DES-based electrolytes have their benefits as they negate the need for additional supporting salts. Including TBABF$_4$ in this calculation records 505 mol^{-1} e^{-1}, a value far above the target. It is therefore critical to reduce the additional supporting electrolyte weight.

This section investigates whether alternate, lower molecular weight supporting electrolytes can compete with the superior electrochemical reversibility, chemical stability, and negative reduction potential of OFAQ with TBABF$_4$ in ACN.

The nature of the supporting electrolyte vastly affects the electrochemical outcome.[2,49] More strongly coordinating supporting ions can improve the anionic stability of organic radicals.[50] Figure 3.20. shows the CVs plots over $25 \leq v \leq 1000$ mV s^{-1} for 1 mM OFAQ with 0.1 M of supporting electrolyte: (a) TBABF$_4$, (b) LiBF$_4$, (c) LiClO$_4$, (d) TBAClO$_4$, (e) [EMIm][TFSI], and (f) LiTFSI in ACN. The corresponding i_p vs $v^{1/2}$ plots and D_o values from Randles–Ševčík analyses are in Figure 3.20.(i) – (v). Supporting salts with one redox wave in the CV show the D_o values for both $n = 1$ and $n = 2$. This is to account for the possible change in electron transfer mechanism from 2 × 1e$^-$ to 1 × 2e$^-$. The data for TBABF$_4$ electrolyte is reiterated in Figure 3.20.(a) and (i) from Figures 3.12.(b) and 3.13.(b) for easier comparison.
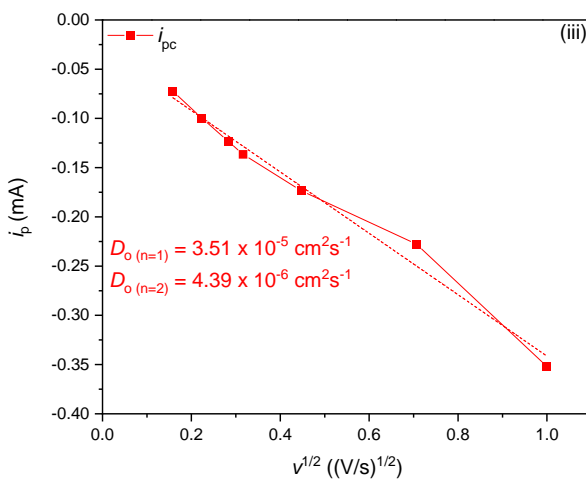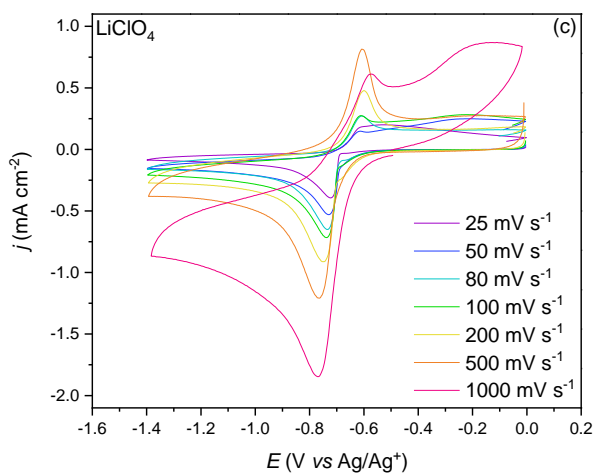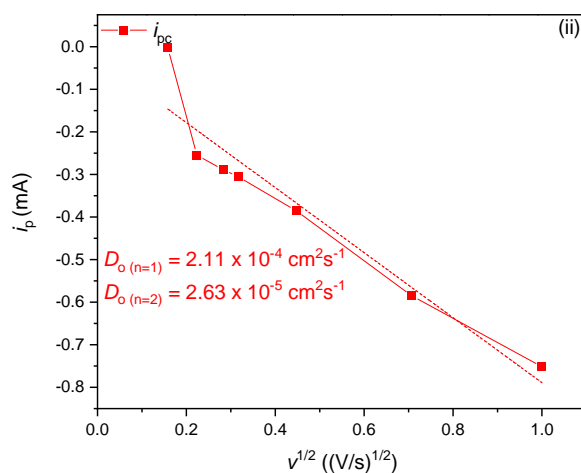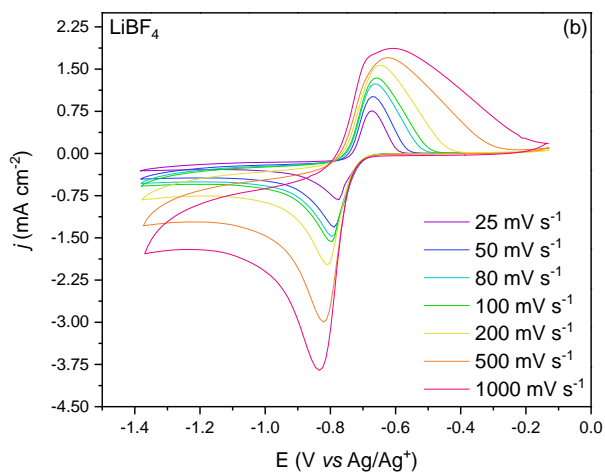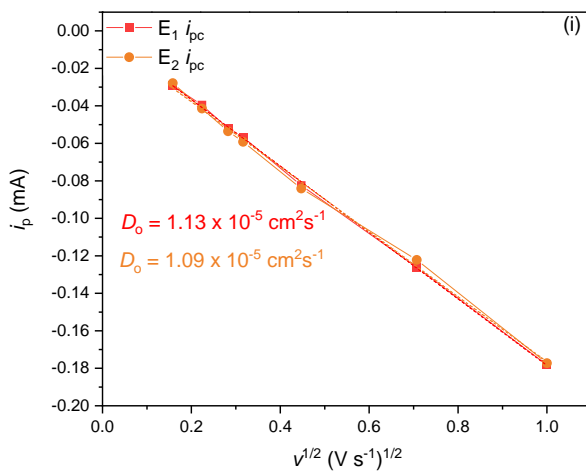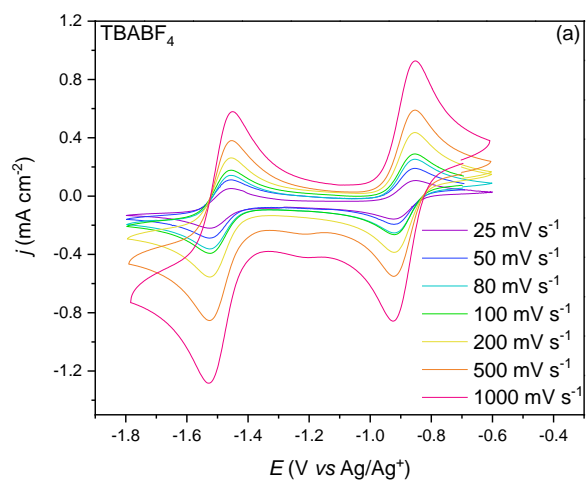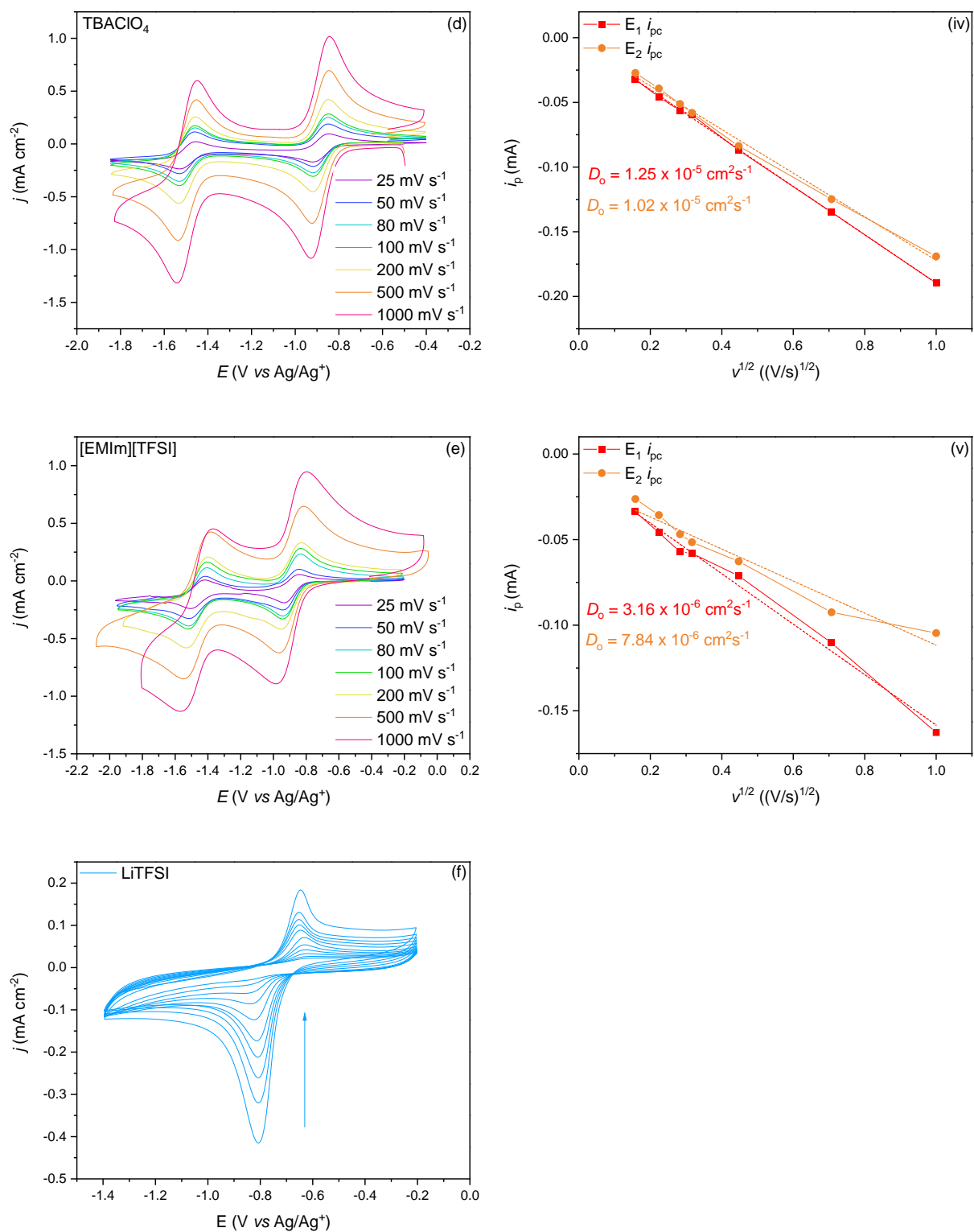
Figure 3.20. CVs of 1 mM OFAQ in 0.1 M of the supporting electrolytes (a) TBABF₄, (b) LiBF₄, (c) TBAClO₄, (d) LiClO₄, (e) [EMIm][TFSI] over scan rates 25 ≤ v ≤ 1000 mV s⁻¹ and (f) LiTFSI in ACN at 100 mV s⁻¹. (i) – (v) The corresponding i_p vs $v^{1/2}$ plots and subsequent D_o values from Randles–Ševčík analyses. CVs taken using a GC WE, Ag/Ag⁺ RE, and Pt CE.

Figures 3.20.(a), (d), and (e) show TBABF$_4$, TBAClO$_4$, and [EMIm][TFSI] give two diffusion-controlled reversible redox waves that overlay exactly. Both TBA$^+$ and [EMIm]$^+$ are large cations (cationic crystallographic radii: TBA$^+$ = 4.94 Å, [EMIm]$^+$ = 4.13 Å) with disperse electron clouds meaning they only coordinate weakly to OFAQ.[45,51] Their low surface charge density means the cations are essentially unsolvated in ACN.[40] Due to this, TBA$^+$ and [EMIm]$^+$ are able to provide steric protection to OFAQ$^{.-}$ and OFAQ^{2-} and hinder degradation reactions. These salts provide enough support to the reduced species such that they are stable on the timescale of the CV.

These weakly coordinating cations facilitate the 2 × 1e$^-$ transfer process at particularly negative reduction potentials of $E_{1,1/2}$ = −0.89 V and $E_{2,1/2}$ = −1.49 V (vs Ag/Ag$^+$) at 100 mV s^{-1}. Interestingly, the negative end of the ESW for [EMIm][TFSI] does not hinder the OFAQ^{2-} redox process when in supporting electrolyte quantities, with Figure 3.20.(e) showing no evidence at any scan rate of dianionic instability or [EMIm][TFSI] degradation. This contrasts to the irreversible chemical reaction with OFAQ^{2-} when the RTIL comprises the entire solvent (Figure 3.17.(a)).

The smaller, more strongly coordinating, Lewis acidic Li$^+$ cation (cationic crystollagraphic radii Li$^+$ = 0.6 Å) forms strong ion-pairs with OFAQ$^{.-}$ and OFAQ^{2-}.[51] The protophobic ACN only weakly solvates the Li$^+$, drastically changing the CV to an electrochemically irreversible single-wave process (Figures 3.20.(b), (c), and (f)) with a positively shifted $E_{1/2}$ ($E_{1/2}$ = −0.73 V, −0.67 V and −0.72 V (vs Ag/Ag$^+$) for LiBF$_4$, LiClO$_4$ and LiTFSI, respectively).

Successive scanning with LiTFSI leads to a lower j with each scan (Figure 3.20.(f)). The irreversibility means the Randles–Ševčík equation does not apply and thus there is no i_p vs $v^{1/2}$ plot for LiTFSI. When using LiTFSI, a reaction occurs during the cathodic scan after the reduction step that forms an electro-inactive product that blocks the WE surface. Each successive scan produces more of this degradation product, thus causing the steady drop in j. LiTFSI is therefore not a useful supporting electrolyte for this system.

The passivation does not occur when pairing Li$^+$ with the other anions (ClO$_4^-$, BF$_4^-$) or when pairing [TFSI]$^-$ with the larger [EMIm]$^+$ cation. LiBF$_4$ and LiClO$_4$ (Figures 3.20.(b) and (c)) both give a similar single-wave CV shape as with LiTFSI, but the CVs are stable over successive scans. Interestingly, OFAQ is more stable with Li$^+$ than existing literature on related quinones. Studies suggest Li-based supporting electrolytes rarely show stable anolyte cycling.[49]

Comparing the i_p and D_o values are methods of investigating the electron stoichiometry and determining whether the process becomes a 2 × 1e$^-$ electron transfer with Li$^+$. The mass transport, and hence D_o values, between the systems with TBA$^+$ and Li$^+$ should not differ greatly as the majority of the electrolyte, i.e. the ORAM and the solvent, is the same. Therefore,

n values that yield similar D_o values are indicative of a similar relative electron stoichiometry for the transfer process.

The Randles–Ševčík equation is only applicable if the CV meets the reversibility criterion: i_{pa}/i_{pc} of 1 at all v, i_p vs $v^{1/2}$ is independent of v, and ΔE_p near $59/n$ mV. This technique is therefore not reliable for analysing the Li$^+$ data in Figures 3.20.(b) and (c) as even though i_p vs $v^{1/2}$ is linear for both tests (Figures 3.20.(ii) and (iii)); the i_{pa}/i_{pc} values are far from 1. With LiBF$_4$, the process is reversible at slower scan rates with an i_{pa}/i_{pc} of almost unity over $25 \leq v \leq 100$ mV s^{-1}. As v increases above 200 mV s^{-1} the reversibility decreases with a larger cathodic wave than anodic, reducing the i_{pa}/i_{pc} from 0.89 at 200 mV s^{-1} to 0.54 at 1000 mV s^{-1}.

LiClO$_4$ suffers from worse reversibility, with the much greater i_{pc} leading to an i_{pa}/i_{pc} of only 0.45 at 100 mV s^{-1}. The sharpness of the reduction peaks with Li$^+$ containing supporting salts in Figures 3.20.(b), (c), and (f) may indicate nucleation, possibly associated with a phase-change due to a passivating film formation. A film is visible by eye on the WE after using LiTFSI, evidencing the deposition is irreversible with LiTFSI and explains the decreasing j with each scan.

The i_p correlates with the number of electrons passing through the electrode; a similar i_p indicates a similar electron stoichiometry. Figure 3.21. compares the change in i_p with respect to $v^{1/2}$ over scan rates $25 \leq v \leq 1000$ mV s^{-1} for LiBF$_4$ and TBABF$_4$ supporting salts. Table 3.4. compares the i_p and E data at 100 mV s^{-1} for OFAQ reduction with TBABF$_4$, LiBF$_4$, and LiClO$_4$ supporting salts.
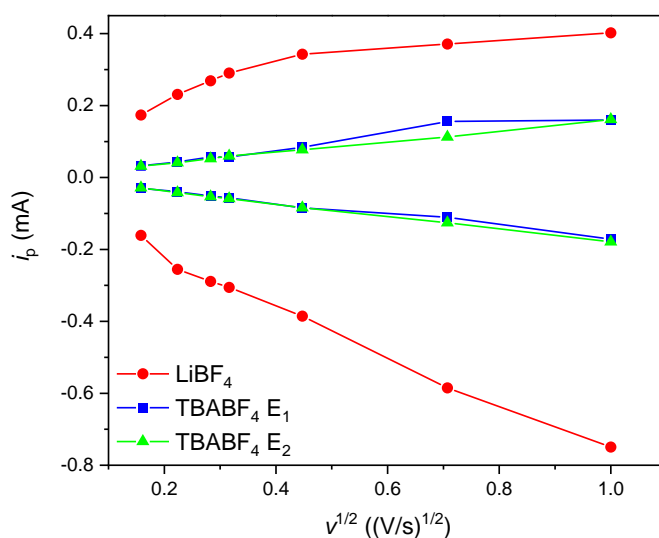
Figure 3.21. i_p vs $v^{1/2}$ for 1 mM OFAQ in ACN with 0.1 M LiBF$_4$ (red circle) and TBABF$_4$ (blue square and green triangle for E$_1$ and E$_2$, respectively) using a GC WE, Pt CE, and Ag/Ag$^+$ RE.

Table 3.4. Comparison of i_p and E data for OFAQ reduction in TBABF$_4$, LiBF$_4$, and LiClO$_4$ at 100 mV s^{-1}.

Supporting Salt	i_{pa} (mA)	i_{pc} (mA)	$E_{1/2}$ (V *vs* Ag/Ag$^+$)	ΔE_p (V *vs* Ag/Ag$^+$)
TBABF$_4$	$E_1 = 0.06$ $E_2 = 0.06$	$E_1 = 0.06$ $E_2 = 0.06$	$E_1 = -0.89$ $E_2 = -1.49$	$E_1 = 0.07$ $E_2 = 0.07$
LiBF$_4$	0.29	−0.31	−0.73	−0.14
LiClO$_4$	0.06	−0.14	−0.67	−0.13

The oxidation and reduction waves in LiBF$_4$ are 5-times greater in magnitude than TBABF$_4$ at 100 mV s^{-1}. This changes as *v* increases, recording an increase of 2.4-factor for i_{pa} and 4.2-factor for i_{pc} in LiBF$_4$ over TBABF$_4$ at 1000 mV s^{-1}. If the process from were changing from a 2 × 1e$^-$ reaction to a 1 × 2e$^-$ it would show as a 2.83-fold change in i_p, as indicated by the dependence of i_p on $n^{3/2}$ in the Randles–Ševčík equation. The current with LiBF$_4$ does not match this trend, confirming that a pathway other than a 1 × 2e$^-$ process is occurring. A more likely pathway involves the stripping and deposition mechanism discussed above, rather than the outer-sphere OFAQ redox reaction.

LiClO$_4$ has an equal i_{pa} and a 2.3-fold increase in i_{pc} compared to TBABF$_4$ at 100 mV s^{-1}. There is less change in i_p with *v* in LiClO$_4$ than with LiBF$_4$. LiClO$_4$ records a ratio of change against TBABF$_4$ of 0.90 and 1.99 at 1000 mV s^{-1} for i_{pa} and i_{pc}, respectively. The difference between all three electrolytes further evidences a more complex Li$^+$ deposition/stripping process is occurring than simple electron transfer.

Using Li$^+$ salts shifts the $E_{1/2}$ shifts to more positive potentials (−0.73 V and −0.67 V (*vs* Ag/Ag$^+$) for LiBF$_4$ and LiClO$_4$, respectively) than the $E_{1,1/2}$ with TBA$^+$ (−0.89 V). The strong Lewis acidity of Li$^+$ causes it to coordinate to, and stabilise, the Lewis basic OFAQ anions. This lowers the LUMO level and shift the reduction potential positive. Zhao *et al.* reveal similar results with BzNSN in molecular dynamics and DFT simulations.[52] A more positive $E_{1/2}$ means a lower OCV in a full battery and a lower energy density. Therefore, Li$^+$ supporting salts are not beneficial for this ORFB.

Figure 3.20. shows the cation plays the dominate role in supporting the OFAQ electron transfer process. Pairing TBA$^+$ with either BF$_4{}^-$ or ClO$_4{}^-$ yields an identical CV. A similar trend is seen with Li$^+$ upon pairing with either BF$_4{}^-$, ClO$_4{}^-$, or [TFSI]$^-$. This is predictable as the supporting cation is interacting with the OFAQ anions and not the supporting anions. Therefore, one should aim to reduce the molecular weight and price of the supporting anion as much as possible. This should make it easier to meet the cost targets whilst maintaining the favourable

2 × 1e⁻ transfer at the more negative reduction potentials. The cost advantages made from moving to a lower molecular weight and cheaper supporting cation (such as Li⁺) are likely lost in the severe positive attenuation of the reduction potential. Thus, the larger, more weakly coordinating supporting salts (such as TBA⁺) are a better choice due to the higher anionic stability and theoretical energy density. Reducing the tetraalkyl chain length to TMA⁺ demonstrates an unstable E_2 process and indicates the larger alkyl chains are necessary for electrochemical and chemical reversibility.

3.4. Conclusions

In summary, this chapter explores the quinone family tree in search of a novel anolyte ORAM. The work focusses on perfluorinated quinones due to their little existing literature and the possible stabilising effects of the F EWGs.

Section 3.1.1. studies the aqueous and non-aqueous electrochemistry of TFBQ. TFBQ shows low stability for both neutral and charged states in aqueous media. Electrochemical testing, ¹⁹F-NMR, and optical analysis confirm that TFBQ begins degrading instantly in aqueous conditions. The degradation takes place over 9 days across all aqueous pH environments. The propensity of nucleophilic attack from OH⁻ ions in high pH media means TFBQ is most stable in acidic environments, but not to a degree satisfactory for an ORFB.

In the non-aqueous TFT environment, the electron transfer expectedly shifts from a 1 × 2e⁻ to a 2 × 1e⁻ process. The relatively positive reduction potentials of $E_{1,1/2}$ = 0.08 V and $E_{2,1/2}$ = −1.02 V (vs Ag/Ag⁺) alongside the chemical irreversibility of E_2 at slow scan rates (v < 100 mV s⁻¹) deems TFBQ as an unsuitable non-aqueous ORAM.

Section 3.2. studies the AQ derivative of TFBQ, OFAQ. The additional F groups and increased number of conjugated rings improve the stability of reduced states at slow scan rates in TFT (i_{pa}/i_{pc} = 0.96 at 25 mV s⁻¹). Additionally, the reduction potentials are at the more negative values of $E_{1,1/2}$ = −0.39 V and $E_{2,1/2}$ = −1.05 V (vs Ag/Ag⁺).

The high toxicity and low vapour pressure of TFT leads Section 3.2.1. of the investigation into exploring alternative organic solvents. OFAQ shows electrochemically and chemically reversible 2 × 1e⁻ processes at 100 mV s⁻¹ in TFT, DCB, ACN and EA. The redox process is irreversible in 5-nonanone, and longer-chain nitrile-based solvents due to proximity of E_2 with the cathodic ends of the ESWs.

Successive additions of water in Section 3.2.1. show how hydrogen-bonding between H_2O and the reduced quinones stabilises the system and shifts E_2 positive. The evidence of

hydrogen bonding rather than protonation indicates that all OFAQ forms must have a pK$_a$ beneath that of H$_2$O (pK$_a$ = 14). The redox process remains a reversible EE transfer even after adding 20 % H$_2$O by volume. This indicates good stability of reduced OFAQ against nucleophilic attack by water.

Section 3.2.2. expands into RTIL electrolytes. OFAQ redox is a reversible 2 x 1e$^-$ process in [BMPyrr][TFSI]. The E_2 is irreversible in [EMIm][TFSI] due to the proximity of E_2 and the cathodic end of the [EMim]$^+$ ESW. Adding a strong proton donor (CF$_3$SO$_3$H) did not stabilise the E_2 and shift it positive. Furthermore, the protic RTIL, [dema][HSO$_4$] has too high a pK$_a$ to donate protons to OFAQ and thus does not improve the system.

Despite the promising electrochemistry, the high cost and unstable supply chain of [BMPyrr][TFSI] make it unsuitable as a bulk solvent. Combining the RTIL with an ACN co-solvent in a 25/75 v/v ratio yields a less reversible system (irreversible when v < 200 mV s^{-1}) than the two solvents separately. Additionally, the high viscosity of the RTIL slows the mass transfer dramatically (D_o = 1.09 × 10^{-5} cm^2 s^{-1} ACN, D_o = 6.18 × 10^{-6} cm^2 s^{-1} [BMPyy][TFSI]/ACN 25/75). This would lead to larger overpotentials and subsequently lower energy efficiencies in a full-RFB system.

Section 3.3. finds large, weakly coordinating supporting salts (TBA$^+$, [EMIm]$^+$) result in a 2 × 1e$^-$ at more favourably negative reduction potentials than smaller, more strongly coordinating salts (Li$^+$). Li$^+$ cations alter the process into a more complex mechanism with inconclusive electron stoichiometry and possible metal electrodeposition. This results in electrode passivation in the case of LiTFSI. The system shows better stability with Li$^+$ cations than literature predicts but the positive attenuation in reduction potential ($E_{1/2}$ = −0.73 V (vs Ag/Ag$^+$)) due to the strong Lewis acidity of Li$^+$ make the larger cations more desirable.

The cation plays the dominant role in the electrochemical process, with the anion acting as a spectator. The wide ESW and high solubility make TBABF$_4$ the best supporting electrolyte of those in the screening. Therefore, future work should consider a wider range of supporting anions to the TBA$^+$ cation with lower molecular weights. Reducing the molecular weight of the anionic component will reduce the overall system cost without affecting the electrochemistry.

The most electrochemically and chemically reversible system over all tests in Chapter 3. is the 1 mM OFAQ, 0.1 M TBABF$_4$, ACN. This systems yields $E_{1,1/2}$ and $E_{2,1/2}$ values of −0.89 V and −1.49 V (vs Ag/Ag$^+$) with respective i_{pa}/i_{pc} values of 1.02 and 0.94, and D_o values of 1.13 × 10^{-5} cm^2 s^{-1} and 1.09 × 10^{-5} cm^2 s^{-1}. These reduction potentials are more negative than the commercial VRFB and are competitive against literature non-aqueous ORFBs. The D_o values are an order of magnitude faster than those in the VRFB (V^{2+}/V^{3+} = 1.41 × 10^{-6} cm^2 s^{-1}, V^{4+}/V^{5+}

= 2.14 × 10^{-6} cm^2 s^{-1} in H_2SO_4 on carbon electrodes)[30,31] which gives promise for a kinetically efficient ORFB.

3.5. References

1   Z. Chen, Y. Qin and K. Amine, Redox shuttles for safer lithium-ion batteries, *Electrochim. Acta*, 2009, **54**, 5605–5613.

2   X. Wei, W. Xu, J. Huang, L. Zhang, E. Walter, C. Lawrence, M. Vijayakumar, W. A. Henderson, T. Liu, L. Cosimbescu, B. Li, V. Sprenkle and W. Wang, Radical compatibility with nonaqueous electrolytes and its impact on an all-organic redox flow battery, *Angew. Chemie Int. Ed.*, 2015, **54**, 8684–8687.

3   Z. Li, S. Li, S. Liu, K. Huang, D. Fang, F. Wang and S. Peng, Electrochemical properties of an all-organic redox flow battery using 2,2,6,6-tetramethyl-1-piperidinyloxy and N-methylphthalimide, *Electrochem. Solid-State Lett.*, 2011, **14**, 171–173.

4   S. K. Park, J. Shim, J. H. Yang, K. H. Shin, C. S. Jin, B. S. Lee, Y. S. Lee, J. D. Jeon, B. Suk, Y. S. Lee and J. D. Jeon, Electrochemical properties of a non-aqueous redox battery with all-organic redox couples, *Electrochem. commun.*, 2015, **59**, 68–71.

5   F. R. Brushett, J. T. Vaughey and A. N. Jansen, An all-organic non-aqueous lithium-ion redox flow battery, *Adv. Energy Mater.*, 2012, **2**, 1390–1396.

6   X. Xing, Y. Huo, X. Wang, Y. Zhao and Y. Li, A benzophenone-based anolyte for high energy density all-organic redox flow battery, *Int. J. Hydrogen Energy*, 2017, **42**, 17488–17494.

7   X. Xing, Q. Liu, W. Xu, W. Liang, J. Liu, B. Wang and J. P. Lemmon, All-liquid electroactive materials for high energy density organic flow battery, *ACS Appl. Energy Mater.*, 2019, **2**, 2364–2369.

8   R. Feng, X. Zhang, V. Murugesan, A. Hollas, Y. Chen, Y. Shao, E. Walter, N. P. N. Wellala, L. Yan, K. M. Rosso and W. Wang, Reversible ketone hydrogenation and dehydrogenation for aqueous organic redox flow batteries, *Science*, 2021, **372**, 836–840.

9   T. Janoschka, N. Martin, M. D. Hager and U. S. Schubert, An aqueous redox-flow battery with high capacity and power: The TEMPTMA/MV system, *Angew. Chemie Int. Ed.*, 2016, **55**, 14427–14430.

10   A. Shrestha, K. H. Hendriks, M. S. Sigman, S. D. Minteer and M. S. Sanford, Realization of an asymmetric non-aqueous redox flow battery through molecular design to minimize active species crossover and decomposition, *Chem. Eur. J.*, 2020, **26**, 5369–5373.

11 M. Pahlevaninezhad, P. Leung, P. Q. Velasco, M. Pahlevani, F. C. Walsh, E. P. L. Roberts and C. Ponce de León, A nonaqueous organic redox flow battery using multi-electron quinone molecules, *J. Power Sources*, 2021, **500**, 1–9.

12 P. Fischer, P. Mazúr and J. Krakowiak, Family tree for aqueous organic redox couples for redox flow battery electrolytes: A conceptual review, *Molecules*, 2022, **27**, 1–39.

13 R. A. Potash, J. R. McKone, S. Conte and H. D. Abruña, On the benefits of a symmetric redox flow battery, *J. Electrochem. Soc.*, 2016, **163**, A338–A344.

14 K. Wedege, E. Dražević, D. Konya and A. Bentien, Organic redox species in aqueous flow batteries: Redox potentials, solubility and chemical stability, *Sci. Rep.*, 2016, **6**, 1–13.

15 C. De La Cruz, A. Molina, N. Patil, E. Ventosa, R. Marcilla and A. Mavrandonakis, New insights into phenazine-based organic redox flow batteries by using high-throughput DFT modelling, *Sustain. Energy Fuels*, 2020, **4**, 5513–5521.

16 S. Er, C. Suh, M. P. Marshak and A. Aspuru-Guzik, Computational design of molecules for an all-quinone redox flow battery, *Chem. Sci.*, 2015, **6**, 885–893.

17 C. den Besten, P. J. van Bladeren, E. Duizer, J. Vervoort and I. M. C. M. Rietjens, Cytochrome P450-mediated oxidation of pentafluorophenol to tetrafluorobenzoquinone as the primary reaction product, *Chem. Res. Toxicol.*, 1993, **6**, 674–680.

18 K. H. Jung, G. S. Jeong, J. B. Joo and K. C. Kim, Improving the understanding of the redox properties of fluoranil derivatives for cathodes in sodium-ion batteries, *ChemSusChem*, 2019, **12**, 4968–4975.

19 M. Wu, Y. Jing, A. A. Wong, E. M. Fell, S. Jin, Z. Tang, R. G. Gordon and M. J. Aziz, Extremely stable anthraquinone negolytes synthesized from common precursors, *Chem*, 2020, **6**, 1432–1442.

20 F. J. Weigert and K. J. Karel, A fluorine NMR database, *J. Fluor. Chem.*, 1987, **37**, 125–149.

21 A. J. Olaya, P. Ge and H. H. Girault, Ion transfer across the water|trifluorotoluene interface, *Electrochem. commun.*, 2012, **19**, 101–104.

22 S. Creager, in *Handbook of Electrochemistry*, ed. C. G. Zoski, Elsevier B.V., Las Cruces, 1st Ed., 2007, pp. 57–72.

23 N. Nagamura, R. Taniki, Y. Kitada, A. Masuda, H. Kobayashi, N. Oka and I. Honma, Electronic states of quinones for organic energy devices: The effect of molecular structure on electrochemical characteristics, *ACS Appl. Energy Mater.*, 2018, **1**, 3084–3092.

24 P. Leung, A. A. Shah, L. Sanz, C. Flox, J. R. Morante, Q. Xu, M. R. Mohamed, C. Ponce

de León and F. C. Walsh, Recent developments in organic redox flow batteries: A critical review, *J. Power Sources*, 2017, **360**, 243–283.

25 E. H. Anouar, C. P. Osman, J. F. F. Weber and N. H. Ismail, UV/Visible spectra of a series of natural and synthesised anthraquinones: Experimental and quantum chemical approaches, *Springerplus*, 2014, **3**, 1–12.

26 Y. Y. Lai, X. Li, K. Liu, W. Y. Tung, C. F. Cheng and Y. Zhu, Stable low-cost organic dye anolyte for aqueous organic redox flow battery, *ACS Appl. Energy Mater.*, 2020, **3**, 2290–2295.

27 M. Matsui, Fluorine-containing dyes, *Funct. Dye.*, 2006, **96**, 257–266.

28 A. T. Bui, N. A. Hartley, A. J. W. Thom and A. C. Forse, Trade-off between redox potential and the strength of electrochemical CO2 capture in quinones, *J. Phys. Chem. C*, 2022, **126**, 14163–14172.

29 M. Matsui, S. Taniguchi, M. Suzuki, M. Wang, K. Funabiki and H. Shiozaki, Dyes produced by the reaction of 1,2,3,4-tetrafluoro-9,10-anthraquinones with bifunctional nucleophiles, *Dye. Pigment.*, 2005, **65**, 211–220.

30 E. Sum and M. Skyllas-Kazacos, A study of the V(II)/V(III) redox couple for redox flow cell applications, *J. Power Sources*, 1985, **15**, 179–190.

31 S. Zhong and M. Skyllas-Kazacos, Electrochemical behaviour of vanadium(V)/vanadium(IV) redox couple at graphite electrodes, *J. Power Sources*, 1992, **39**, 1–9.

32 A. Z. Weber, M. M. Mench, J. P. Meyers, P. N. Ross, J. T. Gostick and Q. Liu, Redox flow batteries: A review, *J. Appl. Electrochem.*, 2011, **41**, 1137–1164.

33 J. Zhang, R. E. Corman, J. K. Schuh, R. H. Ewoldt, I. A. Shkrob and L. Zhang, Solution properties and practical limits of concentrated electrolytes for nonaqueous redox flow batteries, *J. Phys. Chem. C*, 2018, **122**, 8159–8172.

34 P. S. Toth and R. A. W. Dryfe, Novel organic solvents for electrochemistry at the liquid/liquid interface, *Analyst*, 2015, **140**, 1947–1954.

35 M. O. Bamgbopa, Y. Shao-Horn, R. Hashaikeh and S. Almheiri, Cyclable membraneless redox flow batteries based on immiscible liquid electrolytes: Demonstration with all-iron redox chemistry, *Electrochim. Acta*, 2018, **267**, 41–50.

36 M. D. C. Grande, H. L. Bianchi and C. M. Marschoff, On the density of pure acetonitrile, *An. des la Asoc. Quim. Argentina*, 2004, **92**, 109–114.

37 J. A. Renard and H. R. Heichelheim, Ternary systems, *J. Chem. Eng. Data*, 1965, **10**, 485–488.

38 M. Li, B. Zhuang, Y. Lu, L. An and Z. G. Wang, Salt-induced liquid-liquid phase

separation: Combined experimental and theoretical investigation of water-acetonitrile-salt mixtures, *J. Am. Chem. Soc.*, 2021, **143**, 773–784.

39   D. R. Lide, *CRC Handbook of Chemistry and Physics*, CRC Press, Boca Raton, 102nd Ed., 2004.

40   C. G. Armstrong, R. W. Hogue and K. E. Toghill, Application of the dianion croconate violet for symmetric organic non-aqueous redox flow battery electrolytes, *J. Power Sources*, 2019, **440**, 227037.

41   K. Izutsu, *Electrochemistry in nonaqueous solutions*, Wiley-VCH Verlag, Musashino, 2nd Ed., 2002.

42   D. Zarzeczańska, P. Niedziałkowski, A. Wcisło, L. Chomicz, J. Rak and T. Ossowski, Synthesis, redox properties, and basicity of substituted 1-aminoanthraquinones: Spectroscopic, electrochemical, and computational studies in acetonitrile solutions, *Struct. Chem.*, 2014, **25**, 625–634.

43   V. M. Ortiz-Martínez, L. Gómez-Coma, G. Pérez, A. Ortiz and I. Ortiz, The roles of ionic liquids as new electrolytes in redox flow batteries, *Sep. Purif. Technol.*, 2020, **252**, 117436.

44   P. Navalpotro, J. Palma, M. A. Anderson and R. Marcilla, A membrane-free redox flow battery with two immiscible redox electrolytes, *Angew. Chemie Int. Ed.*, 2017, **56**, 12460–12465.

45   S. Kazemiabnavi, Z. Zhang, K. Thornton and S. Banerjee, Electrochemical stability window of imidazolium-based ionic liquids as electrolytes for lithium batteries, *J. Phys. Chem. B*, 2016, **120**, 5691–5702.

46   E. Raamat, K. Kaupmees, G. Ovsjannikov, A. Trummal, A. Kütt, J. Saame, I. Koppel, I. Kaljurand, L. Lipping, T. Rodima, V. Pihl, I. A. Koppel and I. Leito, Acidities of strong neutral Brønsted acids in different media, *J. Phys. Org. Chem.*, 2013, **26**, 162–170.

47   M. Shahriar Hasan Saikat, M. Mominul Islam, M. Y. A Mollah, M. Abu Bin Hasan Susan and M. S. Miran, Thermal and electrochemical properties of protic ionic liquids and their binary mixtures with water, *Mater. Today Proc.*, 2019, **15**, 498–503.

48   M. Hayyan, F. S. Mjalli, M. A. Hashim, I. M. AlNashef and T. X. Mei, Investigating the electrochemical windows of ionic liquids, *J. Ind. Eng. Chem.*, 2013, **19**, 106–112.

49   K. H. Hendriks, C. S. Sevov, M. E. Cook and M. S. Sanford, Multielectron cycling of a low-potential anolyte in alkali metal electrolytes for nonaqueous redox flow batteries, *ACS Energy Lett.*, 2017, **2**, 2430–2435.

50   H. Wang, R. Emanuelsson, A. Banerjee, R. Ahuja, M. Strømme and M. Sjödin, Effect of cycling ion and solvent on the redox chemistry of substituted quinones and solvent-

induced breakdown of the correlation between redox potential and electron-withdrawing power of substituents, *J. Phys. Chem. C*, 2020, **124**, 13609–13617.

51   J. S. Banait, K. S. Sidhu and J. S. Walia, Transference numbers and solvation studies in n-butanol, *Can. J. Chem.*, 1984, **62**, 303–305.

52   Y. Zhao, Z. Yu, L. A. Robertson, J. Zhang, Z. Shi, S. R. Bheemireddy, I. A. Shkrob, Y Z, T. Li, Z. Zhang, L. Cheng and L. Zhang, Unexpected electrochemical behavior of an anolyte redoxmer in flow battery electrolytes: Solvating cations help to fight against the thermodynamic-kinetic dilemma, *J. Mater. Chem. A*, 2020, **8**, 13470–13479.

4. Long-Term Stability and Fundamental Electrochemistry of Octafluoro-9,10-Anthraquinone

The tests in Chapter 3. show that the most suitable system for a non-aqueous OFAQ-based ORFB uses a 0.1 M TBABF$_4$ supporting salt in an ACN electrolyte. The experiments throughout Chapter 3. utilise 1 mM active material, which is a typical concentration for electrochemical screening. EESSs require much higher active material concentrations to store an adequate quantity of charge. Techno-economic studies suggest the ORAM concentration must be 1 – 2 M for a feasible ORFB.[1]

Placing a solute into a solvent in successive additions until observing a precipitate determines the maximum solubility. Using this method, OFAQ shows a maximum solubility of 10 mM in pure ACN. This reduces to 8 mM after adding the supporting electrolyte. The solubility is too low for a viable ORFB system, but a key characteristic of ORAMs is their tailorability and leeway for optimisation. Reports show introducing solubilising groups can improve the notoriously low solubilities of AQ ORAMs.[2,3] Further work beyond the scope of this project should consider functional group substitution to improve OFAQ's solubility.

Detailed studies of OFAQ chemistry are almost non-existent in the literature, thus its electrochemical behaviour is unknown.[4] The data in Chapter 3. demonstrates it has a particularly negative reduction potential ($E_{2,1/2}$ = −1.49 V (*vs* Ag/Ag$^+$)) in ACN as well as fast mass transfer. This postures OFAQ as a good anolyte material. Full understanding of the fundamental electrochemistry of OFAQ is critical if one is to work on molecular tailoring to improve the solubility. This will allow for easy comparison as to whether future chemical substitutions improve or hinder the molecules' capabilities. Therefore, this chapter serves to uncover the fundamental electrochemistry and kinetics of OFAQ. Studies cover the effects of concentration, long-term stability, relative stability of charged forms, and the effects of additives on the system.

4.1. Effect of Concentration

4.1.1. Electrochemistry

At 1 mM, OFAQ shows good reversibility in Section 3.2.1. with a 0.1 M TBABF$_4$ supporting electrolyte in an ACN solvent upon degassing with Ar$_{(g)}$. Figure 4.1. (blue line) shows how without rigorous O$_{2(g)}$ exclusion, the oxygen reduction reaction (ORR) dominates the CV and masks the OFAQ electrochemical process. Upon re-degassing the solution, the ORR wave disappears and the OFAQ reduction becomes visible again (red line). This indicates the exclusion of O$_{2(g)}$ is essential to access OFAQ redox, but that the molecule itself is not

destroyed by the presence of oxygen. This is beneficial in terms of RFB applicability, as any faults in an industrial system that may allow oxygen to enter, for example a faulty seal, will not permanently destroy the device. The performance will diminish temporarily until the system is de-oxygenated again, but the electrochemistry is restorable.
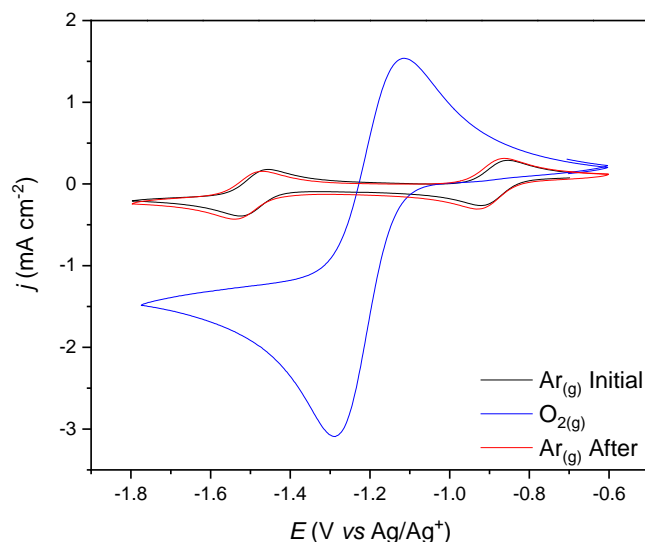
Figure 4.1. CV data for 1 mM OFAQ 0.1 M TBABF$_4$ ACN, 100 mV s^{-1}, after fully degassing with Ar$_{(g)}$ (black line) followed by saturation with O$_{2(g)}$ (blue line), and subsequent Ar$_{(g)}$ saturation (red line).

A particular challenge with ORAMs is their tendency to degrade after charging. This problem exacerbates with increasing ORAM concentration. Studies show ORAM concentration has a large effect on the electrochemical behaviour of the solution.[5] When present in higher concentrations, the reduced ORAM forms have a higher propensity to interact with each other and undergo side reactions.

Figure 4.2. shows the CV data for 1 mM (black line), 2.5 mM (red line), and 5 mM (blue line) OFAQ in 0.1 M TBABF$_4$, ACN at 100 mV s^{-1} with normalised currents. The overlapping data indicates the same electrochemically and chemically reversible process occurs in each concentration. This trend holds even for the lowest CV scan rate, 25 mV s^{-1} and evidences the relative permanence of the highly charged dianionic state.

Hydrodynamic voltammetry tests use LSV run at a slower *v* than CV (2 mV s^{-1} *vs* 25 mV s^{-1}) and potential scans in one direction without reversal. This approach probes the longer-term stability of the reduced states, as they are not immediately re-oxidised after formation.

Figure 4.3. gives the scan rate dependent CVs, and rotation rate dependent LSVs for ((a) and (i)) 1 mM, ((b) and (ii)) 2.5 mM, and ((c) and (iii)) 5 mM OFAQ, 0.1 M TBABF$_4$, ACN at 2 mV s^{-1} over scan rates 25 ≤ *v* ≤ 1000 mV s^{-1} and rotation rates 200 ≤ *f* ≤ 3600 RPM. Table 4.1. compares the currents of the first i_{lim} of each OFAQ concentration and their relative increase

ratios. Figure 4.4. gives the (a) Randles–Ševčík and (b) Levich plots for each concentration and (c) and (d) the Koutecký–Levich plots for E_1 and E_2, respectively, for the 1 mM OFAQ electrolyte. Table 4.2. gives the D_o values of each concentration from Figure 4.4.(a) and (b) and Table 4.3. the k_0 values from the Koutecký–Levich analysis. The D_o values for i_{lim2} in Figure 4.3.(ii) and 4.3.(iii) are not calculable as the Levich plots are not linear.
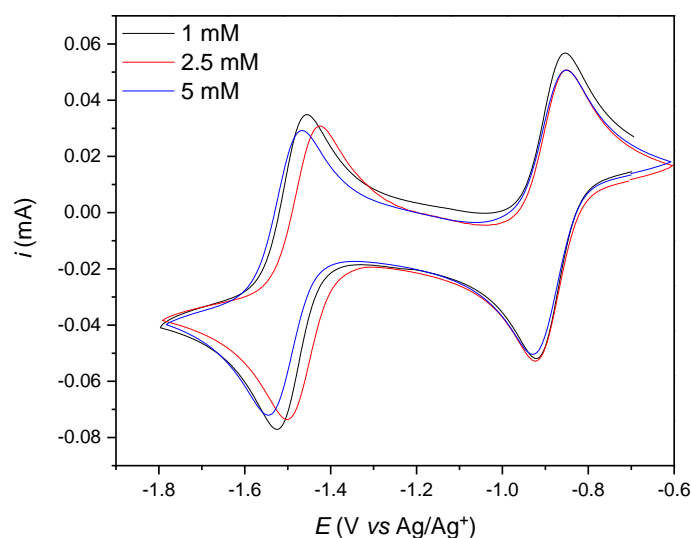
Figure 4.2. CV data normalised to 1 mM OFAQ for 1 (black line), 2.5 (red line), and 5 (blue line) mM OFAQ in 0.1 M TBABF₄ ACN at 100 mV s⁻¹ with a GC WE and Ag/Ag⁺ RE.

The CVs for each concentration in Figures 4.3.(a) to (c) show the same symmetric diffusion-limited, electrochemically and chemically reversible redox responses. Peak separations of the redox couples are small (ΔE_p of approximately 70 mV at 100 mV s⁻¹) and show minimal increase with scan rate, with approximately 25 mV s⁻¹ increase from 25 to 1000 mV s⁻¹. In addition, i_{pa}/i_{pc} values are close to unity ($0.9 \leq i_{pa}/i_{pc} \leq 1.0$) and the i_{pa} and i_{pc} have linear dependencies on $v^{1/2}$, allowing application of the Randles–Ševčík equation. The Randles–Ševčík D_o values for the OFAQ species from the i_{pc} on the first scan range over 1.09×10^{-5} cm² s⁻¹ to 8.53×10^{-6} cm² s⁻¹. These D_o values are similar to, or faster than, previously reported aqueous and non-aqueous ORAMs.[6,7] Additionally, they exceed the D_o values of the archetypal VRFB.[8]

The LSV curves for 1 mM OFAQ display an i_{lim} at low overpotentials, indicating the redox reactions have fast electrochemical kinetics. Kinetic analysis for the OFAQ/OFAQ·⁻ and OFAQ·⁻/OFAQ²⁻ conversions gives k_0 values of 3.33×10^{-2} cm s⁻¹ and 2.20×10^{-3} cm s⁻¹. These values are similar to state-of-the-art ORAMs, for example DB-134 and 4-OH-TEMPO in ACN which have k_0 values of 1.60×10^{-2} cm s⁻¹ and 2.6×10^{-4} cm s⁻¹, respectively.[6,9] Additionally, the k_0 for both OFAQ conversions are greater than those for the VO₂⁺/VO²⁺ (3 ×

10^{-6} cm s^{-1} in 1 M H$_2$SO$_4$ on carbon electrodes) and similar to the V^{3+}/V^{2+} (4×10^{-3} cm s^{-1} in 1 M H$_2$SO$_4$ on Hg) inorganic redox couples.[10]
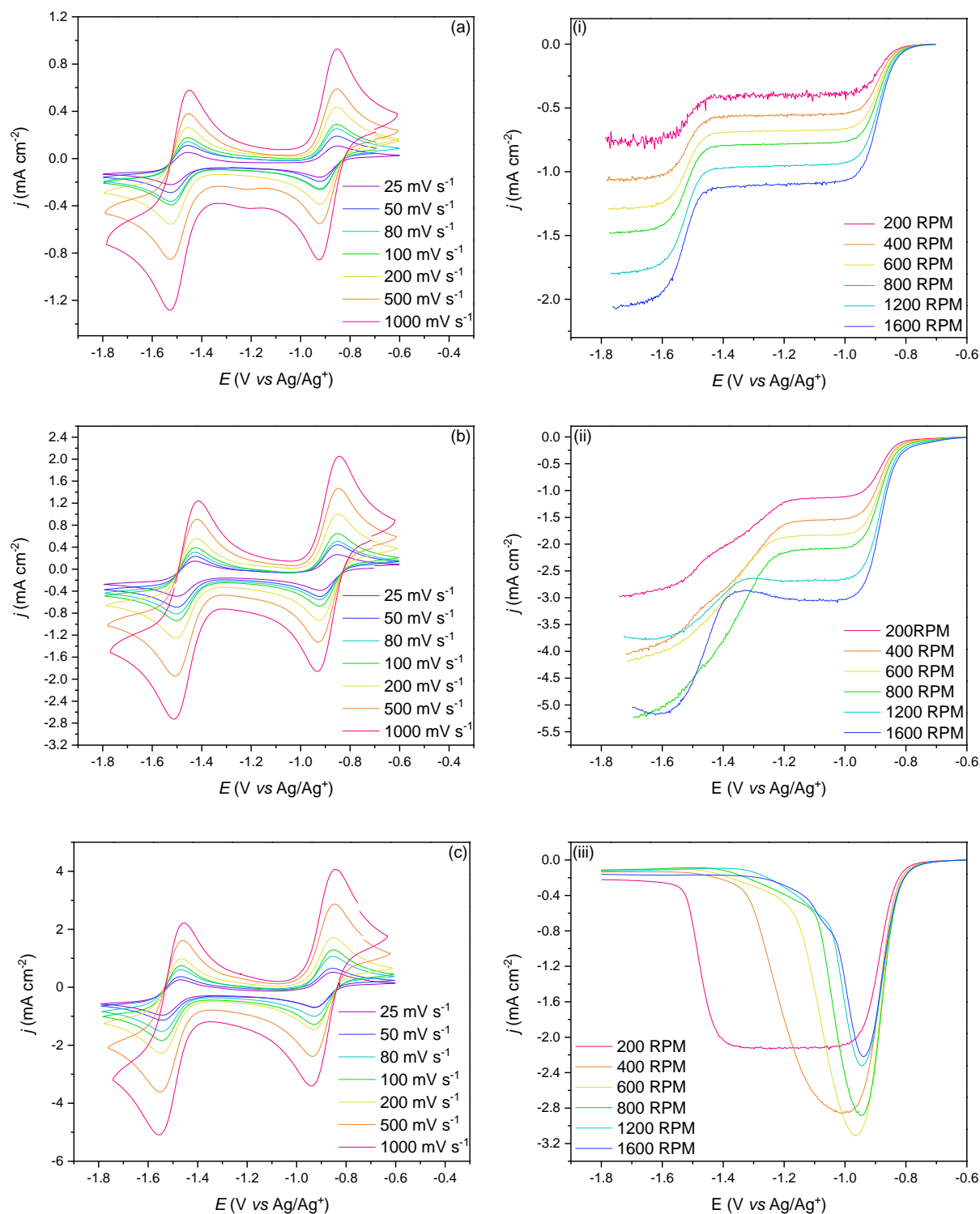
Figure 4.3. (a)-(c) Cyclic voltammograms over scan rates 25 ≤ v ≤ 1000 mV s^{-1} and (i)-(iii) linear sweep voltammograms over rotation rates 200 ≤ f ≤ 1600 s^{-1} at 2 mV s^{-1} of 1 mM ((a) and (i)), 2.5 mM ((b) and (ii)) and 5 mM ((c) and (iii)) OFAQ in 0.1 M TBABF$_4$, ACN.

Table 4.1. Current comparison of first i$_{lim}$ (i$_{lim1}$) of 1, 2.5, and 5 mM OFAQ and their relative increase ratios.

f (RPM)	i_{lim} (mA) at OFAQ (mM)			Normalised i (relative to 1 mM)	
	1	**2.5**	**5**	**1 → 2.5 (mM)**	**1 → 5 (mM)**
200	−78	−224	−418	2.9	5.3
400	−110	−307	−561	2.8	5.1
600	−132	−358	−610	2.7	4.6
800	−152	−415	−566	2.7	3.7
1200	−186	−527	−456	2.5	2.5
1600	−212	−600	−437	2.1	2.1
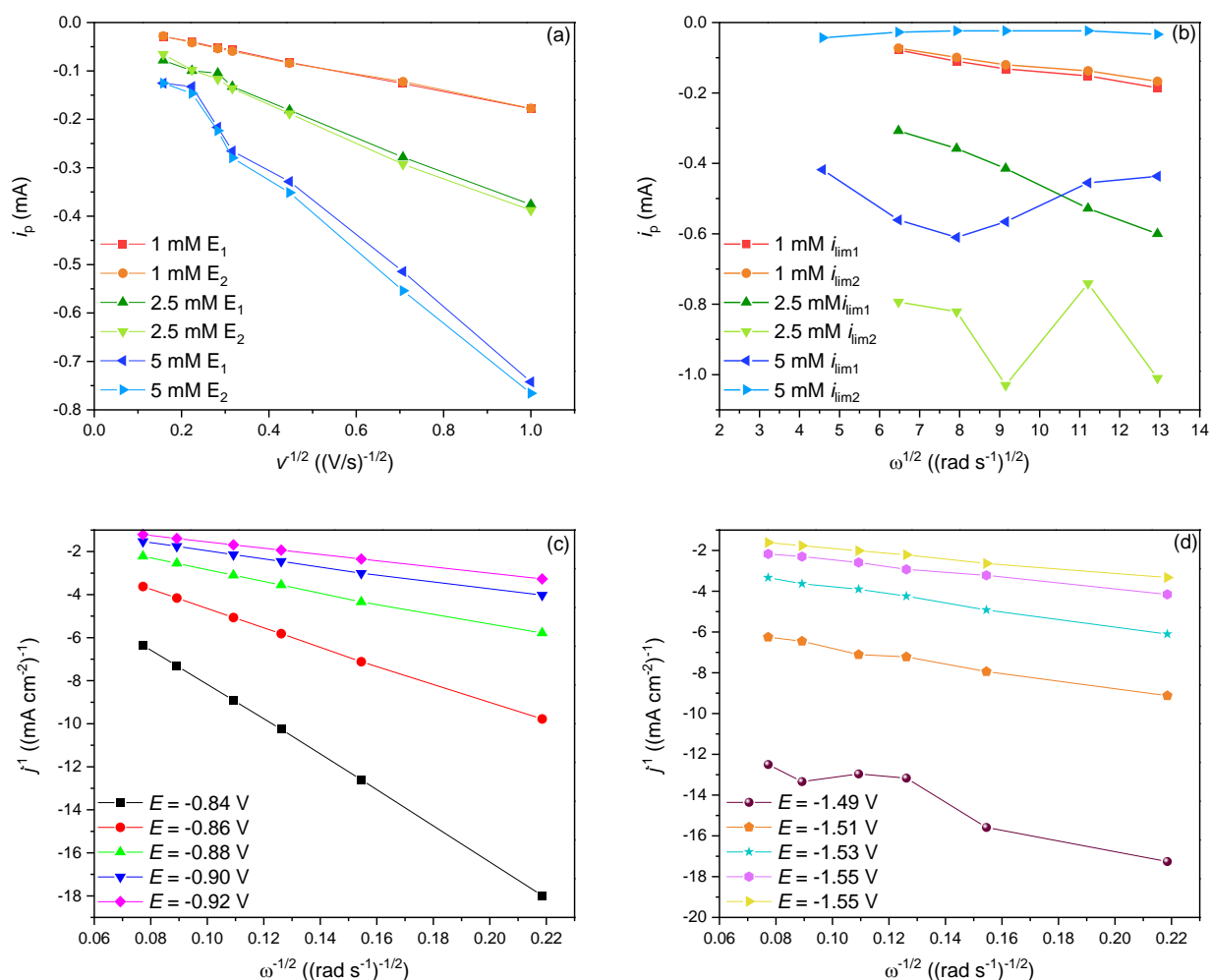
Figure 4.4. (a) Randles–Ševčík plots and (b) Levich plots for 1, 2.5, and 5 mM OFAQ in 0.1 M TBABF₄, ACN. (c) and (d) the Koutecký–Levich plots for 1 mM OFAQ in 0.1 M TBABF₄, ACN. All tests use a GC WE, Pt CE and Ag/Ag⁺ RE.

170

Table 4.2. Diffusion coefficients for 1, 2.5, and 5 mM OFAQ in 0.1 M TBABF$_4$, ACN calculated using Randles–Ševčík and Levich methods.

OFAQ Concentration (mM)	Randles–Ševčík D_o (cm^2 s^{-1})		Levich D_o (cm^2 s^{-1})	
	$E_{1,1/2}$ (−0.89 V) (vs Ag/Ag$^+$)	$E_{2,1/2}$ (−1.49 V) (vs Ag/Ag$^+$)	i_{lim1}	i_{lim2}
1	1.13×10^{-5}	1.09×10^{-5}	1.34×10^{-5}	1.07×10^{-5}
2.5	7.60×10^{-6}	8.53×10^{-6}	1.56×10^{-5}	-
5	7.85×10^{-6}	8.53×10^{-6}	7.98×10^{-6}	-

Table 4.3. Kinetic rate constant for 1 mM OFAQ in 0.1 M TBABF$_4$, ACN.

1 mM OFAQ	E_1	E_2
k_0 (cm s^{-1})	3.33×10^{-2}	2.20×10^{-3}

The D_o is almost equal for E_1 and E_2 for 2.5 and 5 mM OFAQ, both of which record slower rates of diffusion than the 1 mM electrolyte. This could be because the higher concentrations of the OFAQ molecule lead to enhanced intermolecular interactions between OFAQ molecules and thus slower mass transfer.

The reversibility of the system begins to break down upon increasing the residence time for the doubly charged species at higher concentrations. At the lowest concentration, 1 mM, the LSV shows two stable current plateaus, i_{lim1} and i_{lim2}, with Levich D_o values of 1.34×10^{-5} cm^2 s^{-1} and 1.07×10^{-5} cm^2 s^{-1}, respectively. These values correlate well with those using Randles–Ševčík analysis in Section 3.2.1. The system still achieves a linear i_{lim1} with respect to $\omega^{-1/2}$ after a 2.5-fold increase in OFAQ. This first step is still a reversible electrochemical reaction and has a D_o of 1.56×10^{-5} cm^2 s^{-1}. The i_{lim} values in Table 4.1. for Figure 4.3.(ii) are around 2.5-fold higher than in 4.3.(i), indicating the increase in OFAQ concentration does not affect the first reduction process.

The second electron transfer process in 2.5 mM OFAQ has a non-linear relationship between i_{lim2} and $\omega^{1/2}$ and no longer reaches a steady state current. Instead, after i_{lim1} the current increases at successively more negative potentials with increasing rotation rates. For

example, the onset of the second i increase is at −1.22 V (vs Ag/Ag$^+$) at 200 RPM and −1.36 V (vs Ag/Ag$^+$) for 1600 RPM. All scan rates show the second reduction step by the increasing i, but none of the rotation rates reach a steady state current limiting plateau.

Increasing OFAQ concentration to 5 mM further changes the LSV response. The E_1 process for OFAQ/OFAQ$^{\cdot-}$ still occurs at $E_{1,1/2}$ = −0.89 V (vs Ag/Ag$^+$) but only reaches an i_{lim} plateau at the relatively slow f of 200 RPM. A second i increase does not occur, instead i reaches an absolute maximum after the first plateau around the $E_{1,1/2}$ for OFAQ/OFAQ$^{\cdot-}$. The i subsequently drops to near zero at −1.42 V (vs Ag/Ag$^+$), which is near the OFAQ$^{\cdot-}$/OFAQ^{2-} potential in the CV ($E_{2,1/2}$ = −1.49 V (vs Ag/Ag$^+$)).

Faster rotation rates experience the same increase in i at −0.89 V (vs Ag/Ag$^+$) but the i subsequently peaks and then drops to near zero. A film is visible on the surface of the WE after the experiments where the current reaches 0 A.

Increasing the OFAQ concentration decreases the stability of the reduction products. Increasing the rotation speed increases the flux of material to the electrode surface and decreases the diffusion layer thickness. Hence, higher rotation rates generate more highly reactive anionic material at a given distance from the electrode surface. The higher concentration of charged OFAQ increases its likelihood of reacting with itself. This explains why the current drop at 5 mM OFAQ (Figure 4.3.(iii)) occurs at less negative potentials with increasing f.

At 5mM OFAQ, i drops to almost zero after the second reduction process ($E_{1/2}$ = −1.49 V (vs Ag/Ag$^+$)) when f = 200 RPM, but after the first reduction process ($E_{1/2}$ = −0.89 V (vs Ag/Ag$^+$)) when $f \geq$ 400 RPM in Figures 4.3.(ii) and 4.3.(b). The E of the i drop, E_{drop}, becomes less negative with increasing f. This is also consistent with the hypothesis that an increase in concentration of the reduced product near the electrode surface propagates the degradation.

Reports of similar quinone instability in aqueous RFBs conclude that the dimerisation of neutral quinones and hydroquinones occurs.[11] This is unlikely to be the case here, as direct dimerisation of OFAQ^{2-} and OFAQ (Equation 4.1.) would manifest as a less reversible E_2 in the CV which is not seen in Figures 4.3.(a) to (c).[12] Equation 4.1. shows the general dimerisation equation, which if occurring, must be at a slower rate than the timescale of the CV. Disregarding the exact pathway of the degradation process, it is certain that the degradation product fouls the electrode surface and blocks any further electrochemical process from occurring.

$$OFAQ^{2-} + OFAQ \rightarrow Dimer \qquad\qquad 4.1.$$

The onset potential for the current decay and electrode fouling in the 5 mM system at $f > 200$ RPM lies at a more positive potential than for OFAQ^{2-} formation. Therefore, dimerisation of the dianion and the neutral molecule cannot be the dominant degradation pathway. Previous reports on organic radical anions in non-aqueous media advocate the irreversible dimerisation of the semiquinone radical via pinacol coupling (Figure 4.5.).[13] The OFAQ$^{.-}$ will be somewhat stabilised through resonance, but this dimerisation may still occur to produce the octafluoro-9,10-anthrone dimer (OFAQ)$_2^{2-}$. The nucelophilicity of the dimer would be similar to the OFAQ^{2-} dianion. It would therefore be able to react with other OFAQ$^{.-}$ molecules in the solution to yield a large, insoluble, non-conductive oligomer that passivates the electrode surface.[12]

Other decomposition pathways may also occur concurrently. For example, disproportionation
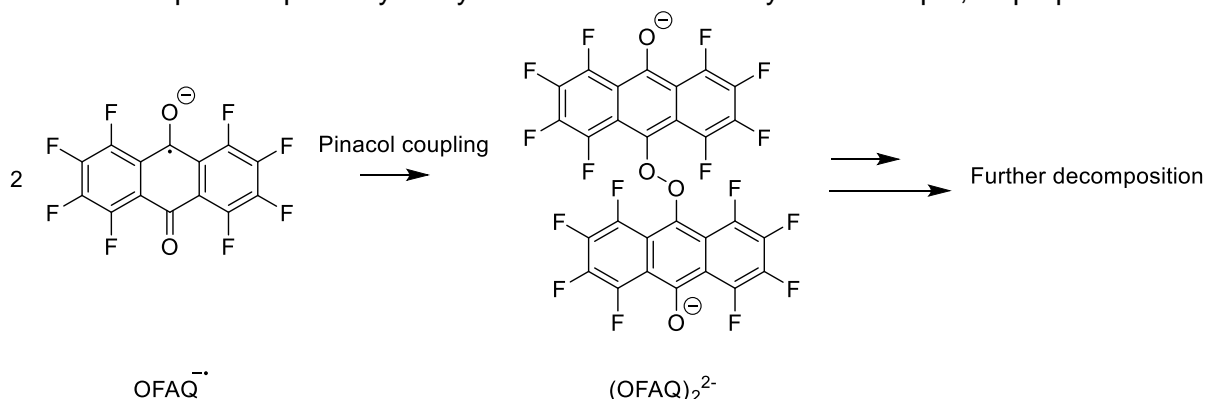
Figure 4.5. Irreversible OFAQ dimerisation decomposition pathway via pinacol coupling of OFAQ$^{.-}$ and OFAQ$^{.-}$ to yield (OFAQ)$_2^{2-}$.

of OFAQ$^{.-}$ to OFAQ and OFAQ^{2-} (Equation 4.2.) or degradation via nucleophilic attack on carbon and aromatic fluorine substitution.[12,14]

$$2OFAQ^{.-} \rightarrow OFAQ^{2-} + OFAQ \qquad\qquad 4.2.$$

XPS and XAFS show population overlap of the C-O and C-C orbitals at the LUMO level of the C-F antibonding orbital.[15] The overlap means that if electron density inserts into the orbital during reduction it can cleave the C-F bond and decompose the molecule near the dianionic reduction potential. This is possibly another contributing factor to the molecular instability in Figures 4.3.(ii) and 4.3.(iii).

The surface heterogeneity of the GC WE may also factor in the onset potential of the degradation process. It is challenging to maintain complete surface homogeneity over separate scans. Tests with higher electrode heterogeneity will have increased surface roughness, which can facilitate seeding of the dimer. This will influence the onset potential and vary the resulting E_{drop} values. Figures 4.6.(a) and (b) show the same degradation process occurs using a Pt WE. The CVs run before and after the LSV test on 5 mM OFAQ on a Pt WE in Figure 4.6.(c) show how the degradation produces an electrode passivating film: the

presence of this film prevents redox reactions from occurring. The process is therefore independent of the type of WE and is electrolyte related. The resulting film does not dissolve under acidic conditions and requires mechanical cleaning to remove.
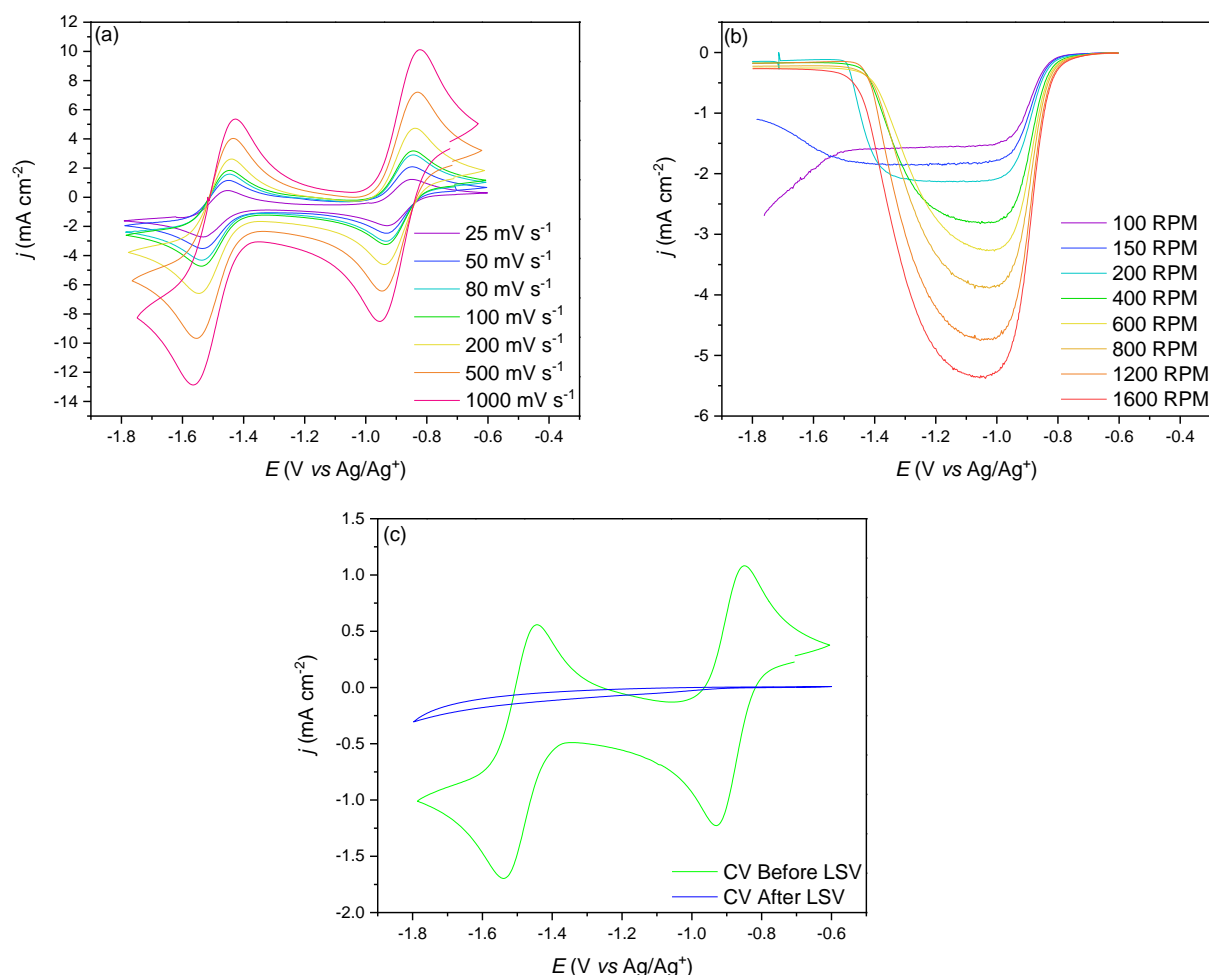
Figure 4.6. (a) CV data of 5 mM OFAQ, 100 mM TBABF₄, ACN over scan rates 25 ≤ v ≤ 1000 mV s⁻¹ with a Pt WE, Pt CE and Ag/Ag⁺ RE. (b) Corresponding LSV plots over rotation rates 100 ≤ f ≤ 1600 RPM at 2 mV s⁻¹ and (c) CVs at 100 mV s⁻¹ before and after reduction at 400 RPM.

4.1.2. Film Characterisation

Raman spectroscopy of the film (Figure 4.7.(a)) shows fluorescence using a 532 nm laser, whereas the OFAQ powder gives no response. The UV-Vis spectra in Figure 4.7.(b) shows the OFAQ powder does not have an absorbance peak at a wavelength long enough to extend into the remit of the Raman laser. There is only a main absorbance peak at 327 nm and another small absorbance around 488 nm, which means OFAQ should not give a Raman response. More conjugated systems absorb at higher wavelengths, which would likely extend

into that of the Raman laser. Therefore, the fluorescent response from the organic film in Figure 4.7.(a) indicates a much more highly conjugated system is present.
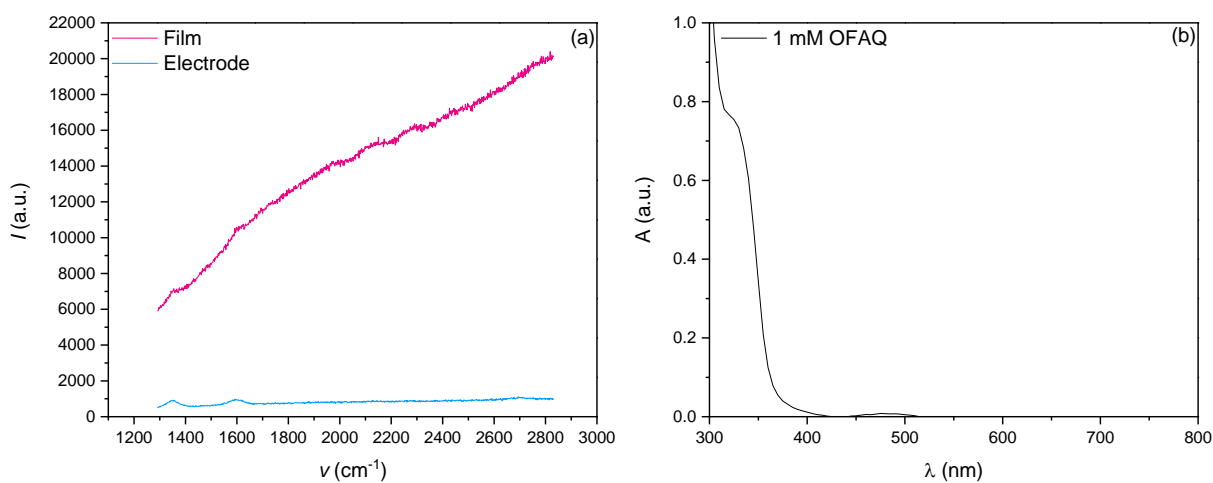
Figure 4.7. (a) Raman spectrum after 1600 RPM, 2 mV s $^{-1}$ LSV on 5 mM OFAQ, 0.1 M TBABF$_4$, ACN. (b) UV-Vis spectrum of 1 mM OFAQ, 0.1 M TBABF$_4$, ACN.
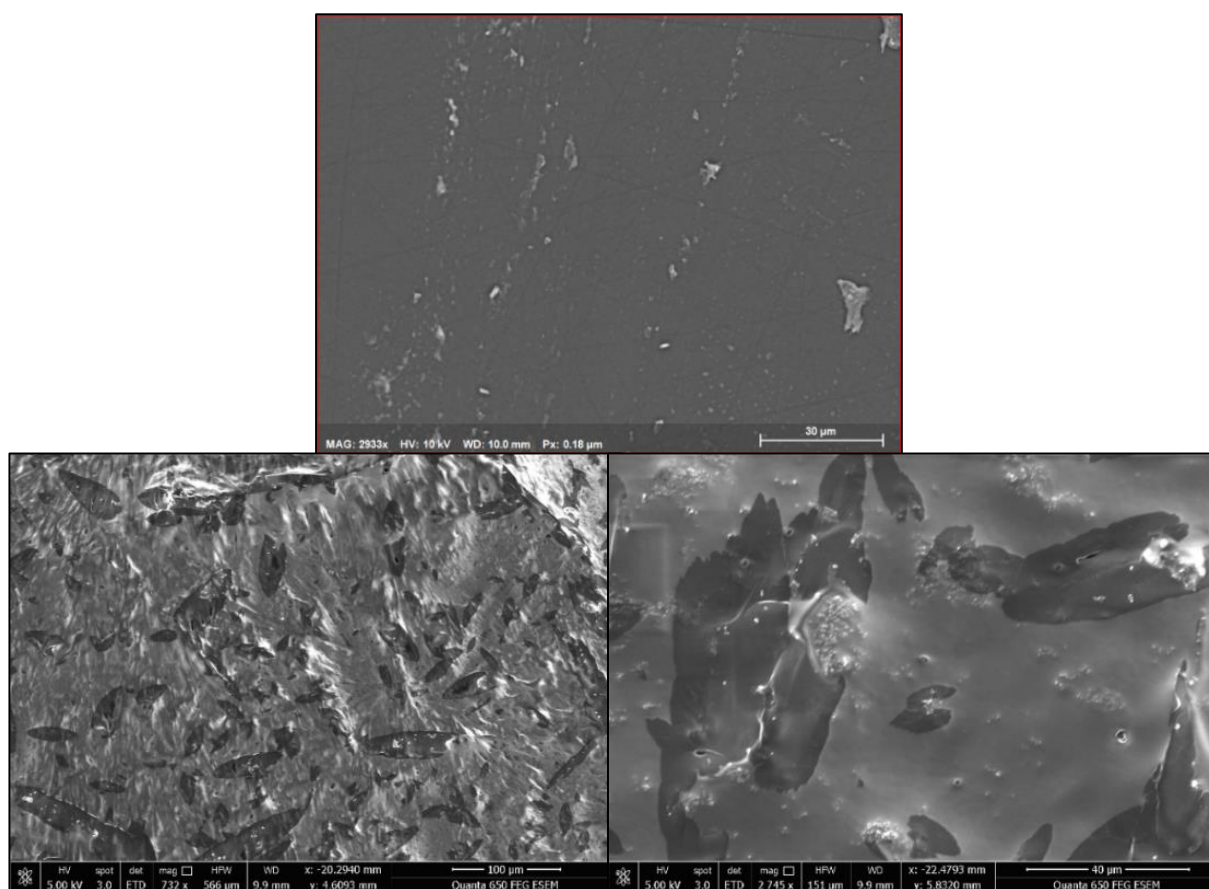
Figure 4.8. SEM images of (a) Bare GC WE, (b) and (c) the GC WE after 5 mM OFAQ, 0.1 M TBABF$_4$, ACN LSV at 1600 RPM, 2 mV s^{-1}.

The film is visible with the naked eye but has no features under atomic force microscopy (AFM), and so its thickness remains unknown. Comparing the SEM images of the bare GC before any reaction (Figure 4.8.(a)), and the GC after LSV at 1600 RPM, 2 mV s⁻¹ (Figures 4.8.(b) and (c)) shows the deposited homogeneous film on the surface. EDX analysis of Figure 4.8.(b) quantifies the film to have 59 % C, 31 % F, 7 % O, and only 3 % N by atomic percent. This corroborates with the OFAQ formula of $C_{14}F_8O_2$, which is 59 % C, 33 % F, and 8 % O. The low quantity of N alongside the lack of additional C and F signifies the supporting electrolyte and solvent are unlikely to be involved in forming the film and it is solely due to OFAQ. This contrasts with the FL⋅⁻ degradation pathways by Wei *et al.*, who show FL⋅⁻ radicals react via nucleophilic substitution with ACN and BF⁻.[13] OFAQ is a more conjugated system than FL⋅⁻. The higher conjugation may contribute better stability against the solvent and electrolyte environment.

X-Ray Photoelectron Spectroscopy (XPS) quantification is more surface sensitive than EDX. Figure 4.9. gives the XPS spectra over binding energies 677 – 695 eV for the GC WE after LSV at 1600 RPM at 2 mV s⁻¹ in 0.1 M TBABF₄, ACN with 5 mM OFAQ (black circles). The XPS data agrees with the EDX through the emergence of the characteristic F 1s peak at 689.8 eV in the 5 mM study, which records atomic percentages of 26 % F and only 3 % N and 3 % O.[16] The peak deconvolutes into three C-F systems, indicating a mix of C-F, C-F₂, and C-F₃ are present in the film. XPS analysis of the same electrolyte but with 1 mM OFAQ shows no C-F peak on the electrode surface.
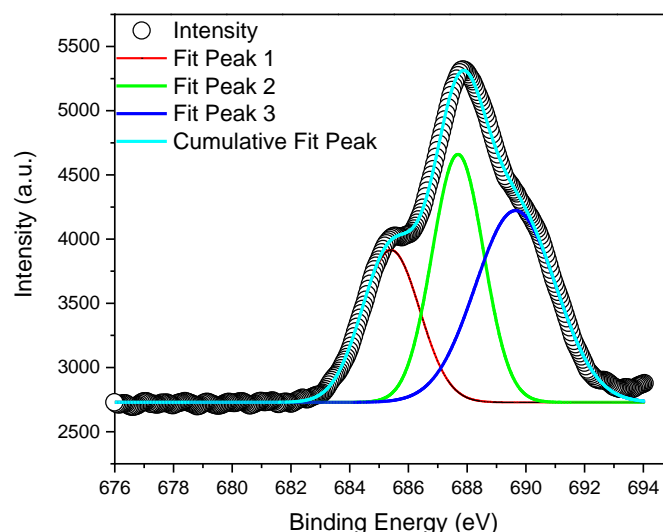
Figure 4.9. XPS spectra of the GC WE after 1600 RPM LSV at 2 mV s⁻¹ with 5 mM OFAQ in 0.1 M TBABF₄, ACN (black circles). The red, green, and dark blue peaks represent the different C-F bond types present.

The lack of the F peak in the tests with 1 mM OFAQ corroborates that the film does not form in low concentrations or via the supporting electrolyte or solvent. The slight discrepancy in

quantification percentages between EDX and XPS is possibly due to different degrees of degradation over different experiments, potentially due to the electrode surface heterogeneity effect discussed in section 4.1.1. Another cause may be the surface sensitivity of the XPS means that less of the underlying C is recorded, or that the surface of the film has a different composition to the bulk.

4.1.3. Relative Anionic Stability

The *ex-situ* analysis in section 4.1.2. supports the hypothesis that reduced OFAQ degrades into an insoluble polymer when at relatively high concentrations (5 mM). The characterisation shows the film is a non-conductive oligomeric layer that passivates the WE. The process onset potential of $E_{1/2}$ = −0.89 V (*vs* Ag/Ag$^+$) when $f \geq$ 400 RPM indicates the radical anion is likely causing the degradation, as the WE passivates before the onset potential for the dianion. To be applicable in an RFB an ORAM must be stable in its charged state over long periods. Therefore, the relative stability of the anionic and dianionic states of OFAQ are of keen interest when considering its applicability to the ORFB field. Understanding the relative stabilities will enable intelligent steps towards improving the anionic stability and preventing the degradation.

Chronoamperometry can be used to investigate the relative stability of the anionic states. To perform the experiment, one holds the electrolyte at potentials sufficiently negative to reduce OFAQ to either OFAQ$^{.-}$ or OFAQ^{2-} for 3600 s. The resulting i indicates the relative stability of the reduced states. A constant i indicates no further electrochemical changes occur after reduction and thus, the state is stable. Changes in i indicate an electrochemical reaction with the molecules at the electrode surface and advocate for side reactions or degradation.

Figure 4.10. shows the chronoamperometric data and Tables 4.4. and 4.5. detail i at t_0 (0 seconds), $t_{1/2}$ for each plateau, and t_{final} (3600 seconds) for the (a) and (c) 1 mM and (b) and (d) 5 mM tests, respectively, over WE rotation rates $0 \leq f \leq$ 3600 RPM. The step potentials of E = −1.1 V (*vs* Ag/Ag$^+$) and E = −1.7 V (*vs* Ag/Ag$^+$) are more negative than the E_{pc} values for the radical anion and dianion in the CV (see Figures 4.3.(a) to (c)) to ensure full conversion to OFAQ$^{.-}$ and OFAQ^{2-}, respectively. The systematic increase in WE rotation rate is used to observe the influence of increased production rate of charged species, as this has a noticeable effect in the LSV data (See Figures 4.3.(i) – (iii)).
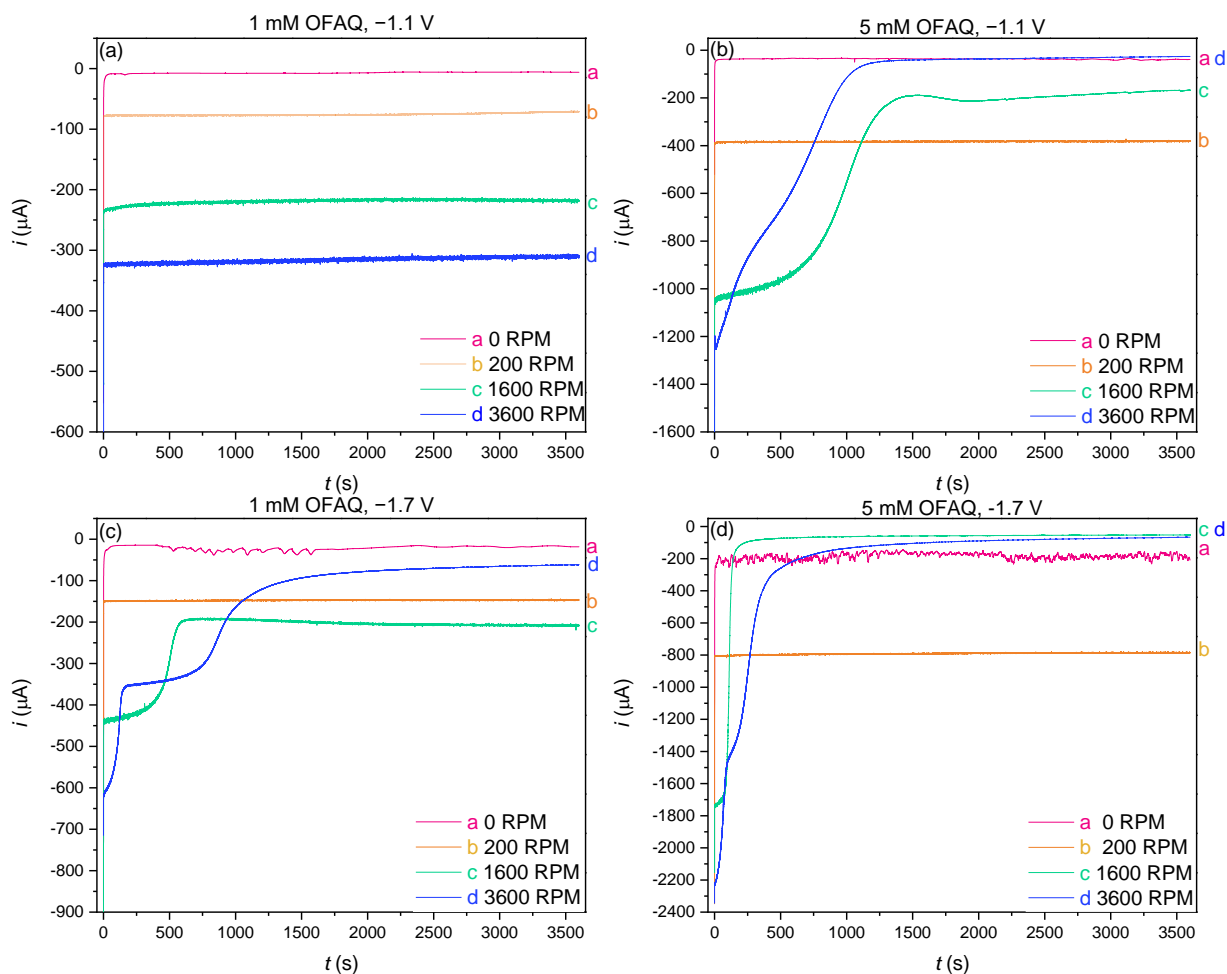
Figure 4.10. Chronoamperometry data at a range of rotation rates on (a) and (c) 1 mM OFAQ and (b) and (d) 5 mM OFAQ in 0.1 M TBABF₄, ACN with a GC WE, Ag/Ag⁺ RE and Pt CE. Each test is held for 3600 s at (a) and (b) −1.1 V and (c) and (d) −1.7 V to produce the radical anion and the dianion, respectively.

Table 4.4. Current values with respect to electrode rotation rate at t = 0, t = ½, and t = final for each plateau in 1 mM OFAQ, 0.1 M TBABF₄, ACN during chronoamperometry over 3600 s.

1 mM OFAQ 3600 s	$E = -1.1$ V (vs Ag/Ag⁺)			$E = -1.7$ V (vs Ag/Ag⁺)		
f (RPM)	$i_{t=0}$ (µA)	$i_{t=1/2}$ (µA)	$i_{t=final}$ (µA)	$i_{t=0}$ (µA)	$i_{t=1/2}$ (µA)	$i_{t=final}$ (µA)
0	−9	−8	−6	−14	−24	−17
200	−77	−76	−71	−149	−148	−148
1600	−233	−217	−218	−439	−409	−210
3600	−234	−315	−26	−613	−540, −84	−61

178

Table 4.5. Current values with respect to electrode rotation rate a t = 0, t = ½, and t = final for each plateau in 5 mM OFAQ, 0.1 M TBABF₄, ACN during choromamperometry over 3600 s.

5 mM OFAQ 3600 s	$E = -1.1$ V (*vs* Ag/Ag⁺)			$E = -1.7$ V (*vs* Ag/Ag⁺)		
f (RPM)	$i_{t=0}$ (µA)	$i_{t=1/2}$ (µA)	$i_{t=final}$ (µA)	$i_{t=0}$ (µA)	$i_{t=1/2}$ (µA)	$i_{t=final}$ (µA)
0	−39	−39	−39	−205	−172	−205
200	−384	−382	−382	−804	−788	−788
1600	−1046	−843	−170	−1743	−71	−53
3600	−1250	−750	−39	−2218	−1995, −94	−69

The constant i in Figure 4.10.(a) over all rotation rates suggests the radical anion is stable on at least a one-hour timescale at 1 mM. The $i_{t=0}$ value increases with increasing RPM as the amount of OFAQ drawn to the electrode at a given time is higher.

Increasing the OFAQ concentration from 1 mM to 5 mM results in a stable i when $f \leq 200$ RPM at $E = -1.1$ V (*vs* Ag/Ag⁺) (Figure 4.10.(b)). This agrees with the LSV data in Figure 4.3.(iii). Upon increasing f to 3600 RPM the system forms the radical anion and then undergoes a reaction that causes i to drop (i_{drop}) in one step over the first 1000 s, from $i_{t=0} = -1250$ µA to $i_{t=1/2} = -750$ µA before stabilising near 0 with $i_{final} = -39$ µA. There is a small bump in the current at $t = 236$ s $i = -870$ µA, which may be due to other concurrent decomposition pathways of lesser magnitude. The i_{final} value near zero indicates the main degradation process blocks the electrode as in the LSV. When $f = 1600$ RPM the i_{final} is −170 µA (Figure 4.10.(b) green line). The non-zero value indicates only some of the electrode is blocked as there is not a high enough concentration of OFAQ·⁻ present to react and completely block the surface.

Figure 4.10.(c) and (d) show the dianion is stable when $f \leq 200$ RPM upon applying the higher potential of $E = -1.7$ V (*vs* Ag/Ag⁺). Higher f rates show an unstable i even at the low concentration of 1 mM. For example, in Figure 4.10.(c) there is no i_{drop} when $f \leq 200$ RPM, but a one-step i_{drop} process at 1600 RPM that doesn't completely block the WE. At 3600 RPM there is a two-step decay that almost completely blocks the electrode surface. The trend is similar to the 5 mM OFAQ at the mono-anion potential of $E = -1.1$ V in Figure 4.10.(b). The similarity in behaviour between the lower concentration at the more negative potential and the

higher concentration at the less negative potential indicates a similar degradation mechanism operates in both cases. The one-step process likely involves the pinacol coupling mechanism between OFAQ$^{.-}$ molecules outlined in Figure 4.5. The two-step degradation process for the dianion possibly involves a comproportionation mechanism (Equation 4.3.) followed by the pinacol coupling.

$$OFAQ^{2-} + OFAQ \rightarrow 2OFAQ^{.-}$$ 4.3.

Appendix 4.A. shows both OFAQ$^{.-}$ and OFAQ^{2-} remain stable at 1600 RPM in 0.5 mM OFAQ, providing further evidence that concentration is a critical factor in this process.

The earlier $t_{1/2}$ in the dianion data sets in Figures 4.10.(c) and (d) compared to the $t_{1/2}$ for radical anion degradation in Figures 4.10.(a) and (b) indicates the lesser relative stability of OFAQ^{2-} over OFAQ$^{.-}$. The first i_{drop} in 1 mM and 5 mM OFAQ at $E = -1.1$ V (vs Ag/Ag$^+$), 3600 RPM is at $t_{1/2} = 1800$ s and 386 s, whereas the first i_{drop} when $E = -1.7$ V (vs Ag/Ag$^+$), 3600 RPM is at $t_{1/2} = 88$ s and 44 s. The earlier degradation onset t means less permanence of the doubly charged state, and hence less stability.

The solution changes from light orange/yellow (Figure 4.11.(a)) to red (Figure 4.11.(b)) over the course of the first reduction process. The initial colour is neutral OFAQ, and the red attributed to OFAQ$^{.-}$ or a subsequent degradation product. The red colour remains after
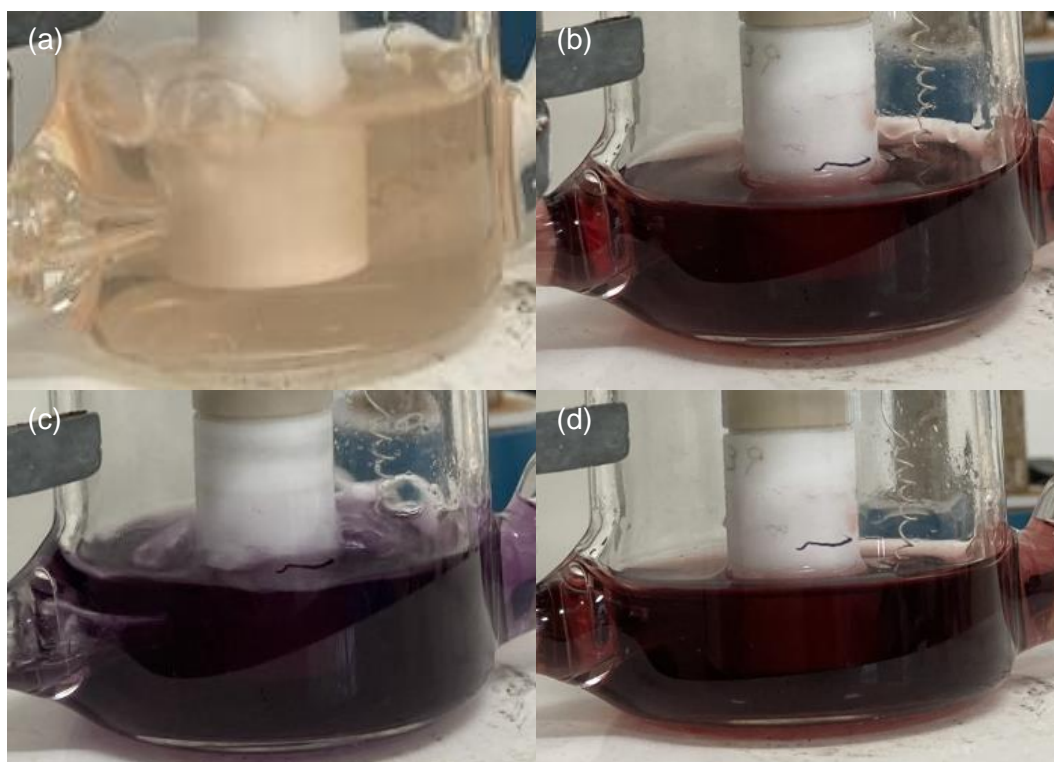
Figure 4.11. Photographs of 1 mM OFAQ, 0.1 M TBABF$_4$, ACN (a) prior to experiment, (b) after 3600 s at $E = -1.1$ V (vs Ag/Ag$^+$), (c) after 3600 s at $E = -1.7$ V (vs Ag/Ag$^+$), and (d) shows the solution in (c) after exposure to air.

removing of the applied potential and even after contact with air, indicating the high stability of this form.

The solution becomes deep purple (Figure 4.11.(c)) upon applying the more negative potential of $E = -1.7$ V (*vs* Ag/Ag$^+$) which is attributed to the dianion. The purple solution immediately changes to the same red colour as in Figure 4.11.(b) after contact with air (Figure 4.11.(d)), indicating an aerobically unstable dianion. Separating the solution from the CE with a PVDF membrane or with a porous glass frit led to the same results. This disregards CE side reactions as a source for the colour change.

The UV-Vis spectra in Figure 4.12. shows the change in absorbance between the initial 1 mM OFAQ, 0.1 M TBABF$_4$, ACN solution (orange line) and the red solution produced after one hour of chronoamperometry at $E = -1.7$ V (*vs* Ag/Ag$^+$) and exposure to air (purple line). The UV-Vis spectrum of the purple dianion in Figure 4.11.(c) could not be recorded due to experimental restrictions preventing UV-Vis studies without exposing the solution to air.
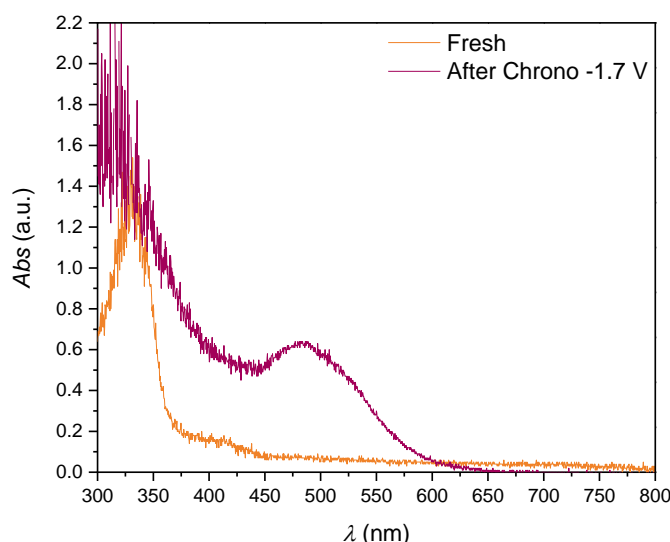
Figure 4.12. UV-Vis spectra of 1 mM OFAQ, 0.1 M TBABF$_4$, ACN when freshly prepared (orange line), and after chronoamperometry at E = −1.7 V (vs Ag/Ag$^+$) for 3600 s and exposure to air (purple line).

A new absorbance peak appears at 484 nm after chronoamperometry, alongside a general increase in absorption intensity of the 327 nm peak. The 327 nm peak associates with the benzenoid character of the molecule.[17] The large increase in intensity and broad nature of the absorption after charging compared to the fresh solution is indicative of a more conjugated system forming. The new peak indicates the presence a new functional group or molecule, likely the subsequent oligomer of (OFAQ)$_2^{2-}$, further corroborating the dimerisation/polymerisation hypothesis in Section 4.1.2. This is logical, as earlier sections in this chapter highlight how higher concentrations of OFAQ^{2-} lead to intermolecular attack, and

the electrolyte will have a high OFAQ^{2-} concentration after being held at $E = -1.7$ V (vs Ag/Ag$^+$) for such a long time.

The *in-situ* EPR spectroscopy data in Figure 4.13. further elucidates the redox and degradation processes. Previous reports use EPR spectroscopy to investigate VRFBs, as well as studying quinone radicals as intermediates in redox processes and estimating their stability.[18,19] The increase in the double integral (DI) of the EPR signal and the derivative of EPR signal intensity (S) at $t = 1416$ s in Figure 4.14.(a) parallels to $E = -0.62$ V (vs Pt) in Figure 4.13.(b) and corresponds to the production of the paramagnetic OFAQ^{-} ion. The arrows in Figure 4.13.(b) and (d) indicate the direction of the potential scans. The slowing in rate of increase in the EPR response from the paramagnetic species at $t = 2110$ s, $E = -1.29$ V (vs Pt) marks OFAQ^{2-} formation. The DI_{max} peak in Figure 4.13.(a) and (b) decreases after $t = 3500$ s because the reversal of the electrode potential causes re-oxidation of OFAQ^{2-} to OFAQ^{-} and subsequently OFAQ^{-} to neutral OFAQ over $3500 \leq t \leq 4750$ s where $-1.8 \leq E \leq 0$ V (vs Pt).

The second CV cycle, Scan 2 in Figure 4.13.(a) and (b), is almost identical to Scan 1, with OFAQ^{-} forming at $t = 6025$ s, $E = -0.62$ V (vs Pt), and OFAQ^{2-} at $t = 6770$ s, $E = -1.21$ V (vs Pt). The overlaying data indicates the reversibility and stability of the OFAQ reduction process at these low concentrations (1 mM). The experimental EPR hyperfine structure in Figures 4.14.(a) and (b) match the simulations in Figure 4.14.(c) and are consistent with the experimental data in Figure 4.13. Spectral simulations were performed using the EasySpin 5.2.25 simulation software by MATLAB. The hyperfine result is: AF1, 2.7G; Af2, 2.8G; AF3, 2.6G; AF4 2.8G. Figures 4.13.(c) and (d) show how this stable, reversible, process changes upon increasing the OFAQ concentration to 5 mM at 3 (purple line) and 5 (orange line) mV s^{-1}. Figure 4.13.(e) overlays the CV data for each concentration at each scan rate and shows around the expected five-fold increase in i_{pc} between the 1 and 5 mM tests.

Figures 4.13.(a) and 4.13.(b) show similar S and DI values for the reductions over both Scan 1 and Scan 2 at 1 mM OFAQ and 1 mV s^{-1}. Figure 4.13.(c) shows that upon a five-fold increase in OFAQ concentration Scan 2 gives an EPR DI much lower than Scan 1. Scan 1 reaches $DI_{max} = 22$ and $DI_{max} = 16$ at 3 and 5 mV s^{-1}, respectively, whereas Scan 2 only achieves $DI_{max} = 11$ for both scan rates. The second cycle for 3 mV s^{-1} in Figure 4.13.(c) and (d) is not a full CV scan, but this does not affect the conclusions.

The drop in DI for the second CV scan is further evidence of the degradation reaction wherein reduced OFAQ reacts with itself to form an electro-inactive species. This drop in current in the second scan is observable in the CVs using the EPR set up and not in the earlier CV in Figure 4. 3.(c) because of the much slower scan rate. Slower scan rates cause thicker diffusion layers

and longer residence times for the semiquinone state, meaning a relatively higher concentration of OFAQ·⁻ is present to react.
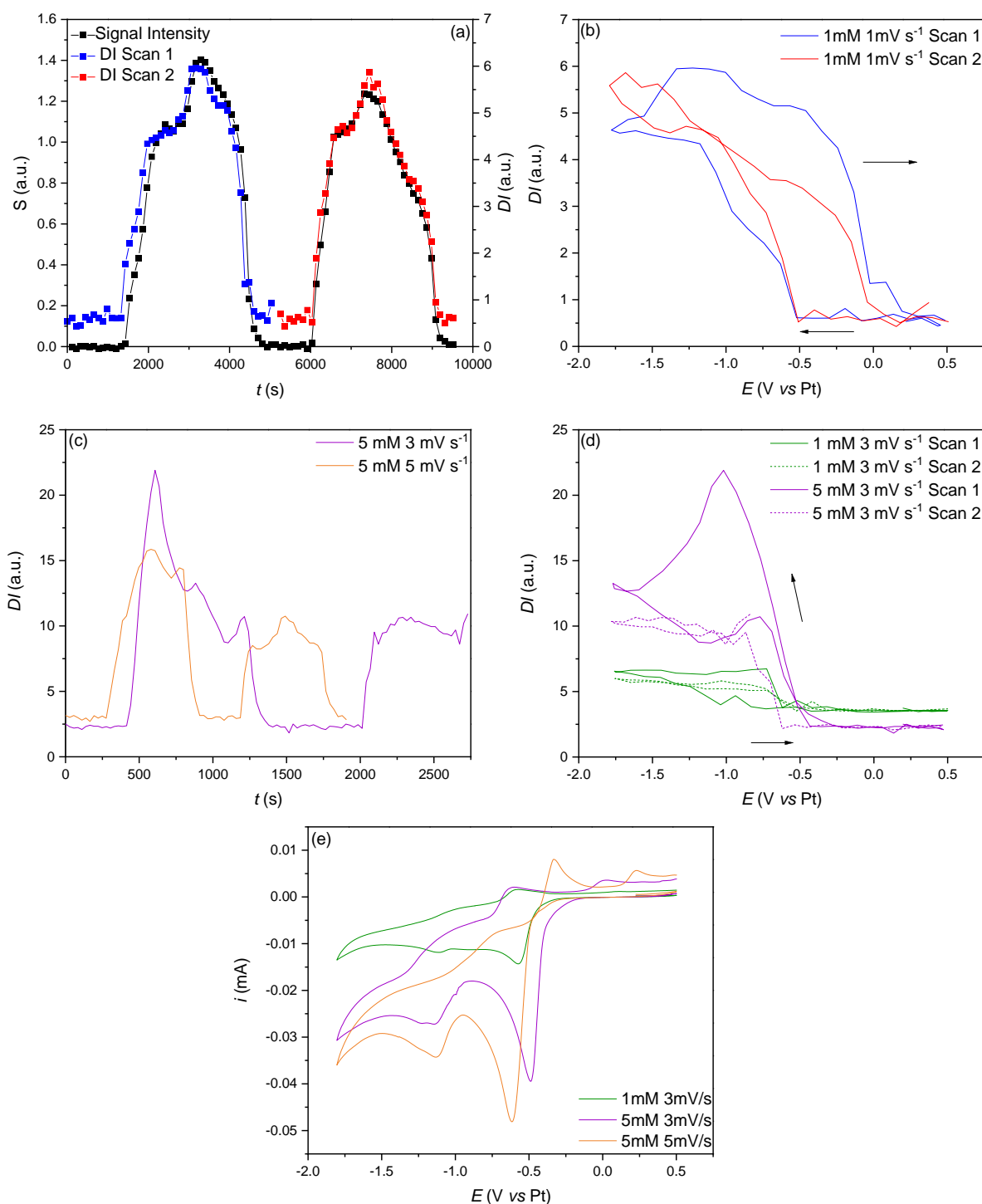
Figure 4.13. In-situ EPR spectra showing (a) the derivative of EPR signal intensity (S) and its double integral (DI) vs. time and (b) DI against potential for 1 mM OFAQ, 0.1 M TBABF₄, ACN at 1 mV s⁻¹. (c) The DI vs time for 5mM OFAQ, 0.1 M TBABF₄, ACN at 3 (purple line) and 5 (orange line) mV s⁻¹. (d) A comparison of 1 (green line) and 5 (purple line) mM OFAQ at 3 and 5 mV ⁻¹ with the solid and dotted lines representing the first and second CV scans, respectively. (e) The corresponding i vs E plots for the CVs using a Pt WE, Pt RE and Pt CE.
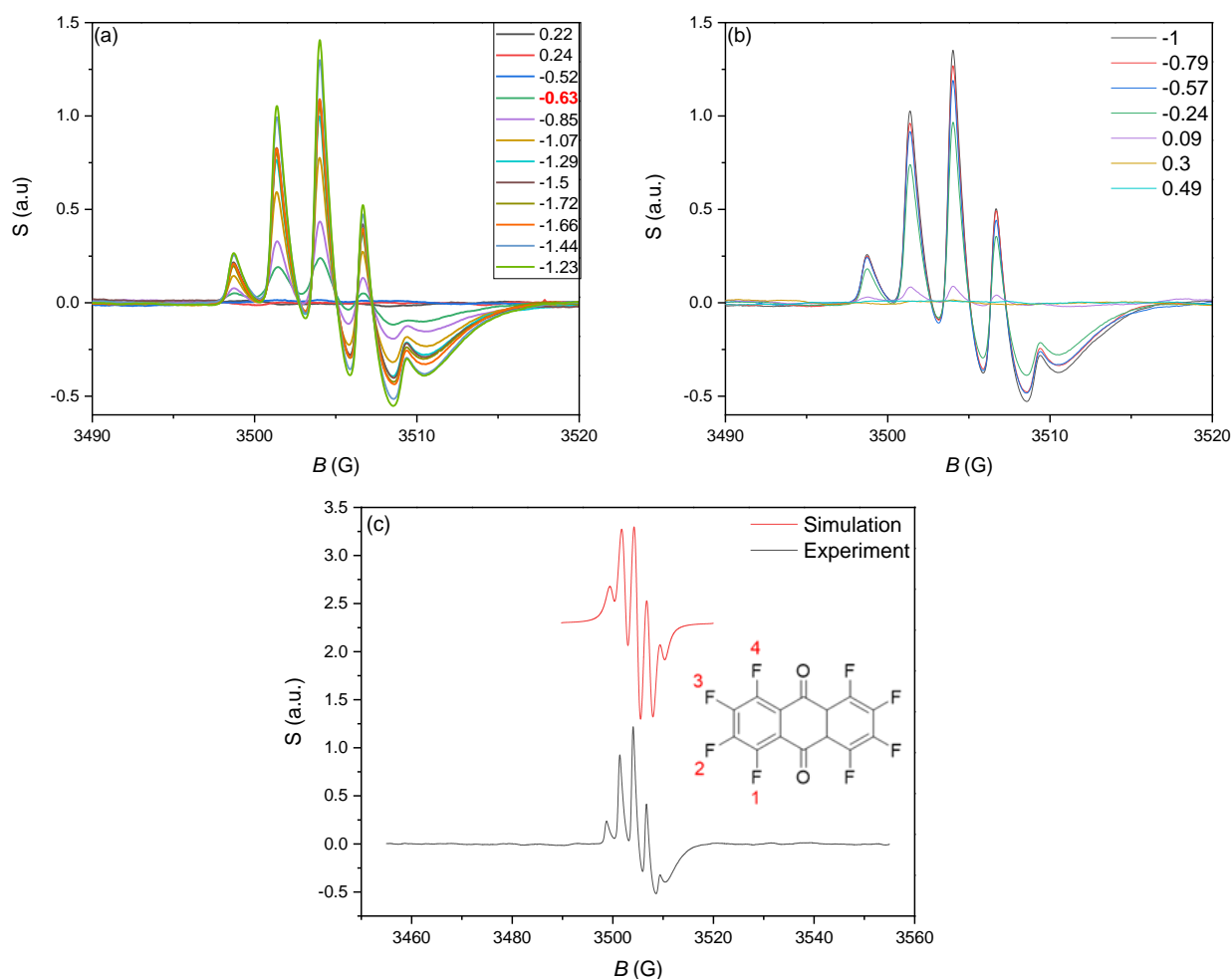
Figure 4.14. (a) EPR spectra for (a) the first reduction and (b) subsequent oxidation of OFAQ. (c) EPR hyperfine structure and simulation of OFAQ in a homemade in-situ EPR cell using a Pt wire WE, CE, and RE.

The smaller current magnitude for E_2 in Figure 4.13.(e) also corroborates the theory, as less OFAQ$^{\cdot-}$ to OFAQ^{2-} will occur relative to the amount of OFAQ to OFAQ$^{\cdot-}$ in E_1 as the radical anion degrades before reaching the second reduction potential.

In Figure 4.13.(d) Scan 1, the paramagnetic OFAQ$^{\cdot-}$ forms at $E = -0.44$ V (*vs* Pt) and increases the EPR *DI* intensity. The *DI* continues to increase up to $E = -1.02$ V (*vs* Pt) wherein it drops as the potential becomes increasingly negative. The decreasing *DI* is due to the OFAQ$^{\cdot-}$ converting to the EPR-silent OFAQ^{2-}. At the switching potential, the amount of paramagnetic species continues to decrease until $E = -1.13$ V (*vs* Pt), the potential where OFAQ$^{\cdot-}$ forms. At $E = -0.74$ V (*vs* Pt) the EPR signal intensity drops again, as all the OFAQ$^{\cdot-}$ oxidises to OFAQ.

Figure 4.13.(e) shows onset potentials for OFAQ$^{\cdot-}$ and OFAQ^{2-} at $E = -0.49$ V and $E = -1.13$ V (*vs* Pt) in 5 mM OFAQ at 3 mV s^{-1}. This mirrors the potentials in the EPR spectra for the 1 mM and 5 mM samples and suggests there is not any degradation. Additionally, these reduction potentials agree with the previous CV scans using an Ag/Ag$^+$ RE (Pt RE = +0.38 V (*vs* Ag/Ag$^+$).

However, Scan 2 (Figure 4.13.(d) purple dashed line) indicates a different process. The DI increase begins at $E = -0.63$ V (vs Pt) and reaches a plateau at $E = -0.86$ V (vs Pt). The DI plateau indicates the amount of paramagnetic species remains constant even though the potential is becoming increasingly negative. The onset of the DI plateau is prior to the reduction potential for forming $OFAQ^{2-}$. This corroborates with the earlier pinacol-coupling hypothesis in that for every two moles of $OFAQ^{\cdot-}$ produced at the electrode surface, one pinacol coupling occurs. This would equate to a net zero change in overall paramagnetic species concentration.

As the potential reaches the E_2 value ($E = -1.13$ V (vs Pt)) all forms of OFAQ at the surface will convert directly into $OFAQ^{2-}$. This should show as a decrease in the paramagnetic DI. Instead, the DI plateau continues past the E_2 up to the switching potential. This suggests another degradation reaction occurs when the dianion is present. This is possibly the comproportionation of the dianion to the radical anion and the neutral molecules (Equation 4.3.). The $OFAQ^{\cdot-}$ at the surface will reduce to $OFAQ^{2-}$. The dianion can then comproportionate with incoming OFAQ from the bulk to produce two moles of $OFAQ^{\cdot-}$ that rapidly reduces back to the dianion. This results in a net zero change in paramagnetic species concentration. The plateau continues on the reverse scan, which corroborates that the $OFAQ^{2-}$ has already reacted to yield the radical species.

It is useful to comprehend the in-$situ$ EPR data alongside the chronoamperometry tests in Figure 4.10. The pinacol coupling dimerisation attributed to the one-step degradation in Figure 4.10.(b) cannot be directly responsible for the two-step degradation process in the Figures 4.10.(c) and (d) chronoamperometry scans. This is because the electrode potential is sufficiently negative to convert any OFAQ into $OFAQ^{2-}$, so no $OFAQ^{\cdot-}$ forms and thus none is present to dimerise. The comproportionation of $OFAQ^{2-}$ as indicated by the EPR is likely the first step in this two-step process. This produces two moles of $OFAQ^{\cdot-}$, which at high concentrations favourably reacts via the pinacol coupling as the second step process (Figure 4.5.).

The timescale of the CV in Figure 4.3.(c) is too small to see any change in peak intensity from the OFAQ depletion. However, chronoamperometry and LSV timescales are much longer and allow identification of this reaction in Figures 4.3.(iii) and 4.10.(c) and (d).

A point to note is that comproportionation will not reduce the capacity of a battery but will reduce its energy density. During battery cycling, lowering the charging rate or increasing the RAM concentration can reduce the propensity for comproportionation. This is because all the OFAQ reduces to $OFAQ^{\cdot-}$ before any $OFAQ^{2-}$ forms. This means there is no neutral quinone present to comproportionate with $OFAQ^{2-}$.

To summarise, OFAQ undergoes a stable and reversible 2 × 1 e⁻ reduction process in 0.1 M TBABF$_4$, ACN at all concentrations under the timescale of the CV (Figures 4.3.(a) to (c)). Increasing the residency time for OFAQ in LSV (Figures 4.3.(i) to (iii)) shows molecular degradation of the anionic states at concentrations above 2.5 mM. At 5 mM OFAQ the radical anion degrades to form a non-conductive, oligomeric, passivating film on the electrode surface. The main hypothesis is that the radical anion dimerises with itself at high concentrations via pinacol coupling. The dimerisation produces (OFAQ)$_2^{2-}$, which subsequently oligomerises into a non-conductive, non-redox active polymer that blocks the WE surface. Section 4.1.2. characterises the film, confirming it comprises of solely OFAQ atoms and that the solvent and supporting electrolyte are not involved in the degradation process.

Chronoamperometric studies (Figure 4.10.) show a one-step degradation in the presence of the radical anion and a two-step process with the dianion. The rate for degradation is faster in the dianion tests, indicating lower stability of the OFAQ^{2-} form than the OFAQ$^{.-}$. The chronoamperometry and EPR data (Figure 4.13.) suggest the first step is comproportionation of OFAQ^{2-} and OFAQ to produce 2OFAQ$^{.-}$. The second step is the aforementioned pinacol coupling of the resulting radical anions.

4.2. Bulk Electrolysis and Symmetric Cell Tests

4.2.1. Bulk Electrolysis

BE and symmetric cell tests can delve more deeply into the ORAM stability. For BE, the 1 mM OFAQ, 0.1 M TBABF$_4$, ACN cell is held at E = −1.6 V (*vs* C felt) in the H-cell until it reaches a stable, capacitive current of near 0 A. Chapter 2.3.2. details the electrochemical cell and the experimental procedure. The reduction potential of −1.6 V (*vs* C) is sufficiently negative to produce the dianion, which has $E_{1/2}$ = −1.49 V (*vs* Ag/Ag⁺). The colour change of orange to purple indicates the conversion of OFAQ to OFAQ^{2-}. BE uses a larger WE surface area compared to chronoamperometry and so completely depletes the solution of neutral OFAQ leaving only OFAQ^{2-}, assuming no comproportionation. After exposing the purple solution to air, it becomes red as above in Figure 4.11.

Figures 4.15.(a) and (b) show the colour change between neutral OFAQ and fully charged OFAQ^{2-} in the left-hand side of the H-cell over the course of BE at −1.6 V (*vs* C). Raising the potential to E = −1.2 V (*vs* C) causes the purple solution to become red (Figure 4.15.(c)). The solution returns to purple upon returning the potential back to −1.6 V (Figure 4.15.(d)). The colour changes agree with those in Figure 4.11. and confirm the colours of the OFAQ oxidation states as: orange/yellow for neutral OFAQ, red for OFAQ$^{.-}$, and purple for OFAQ^{2-}. As before,

the purple solution becomes red as soon as it meets air and cannot be isolated for analysis. The bubbles in the images are due to the constant $Ar_{(g)}$ bubbling in the cell that maintains the degassed environment and facilitates a faster reaction through mixing. One should note that the observation of the same colour does not necessarily indicate a stable species throughout the whole solution. This is because one highly coloured species could persist but be a relatively minor component compared to the wider solution.
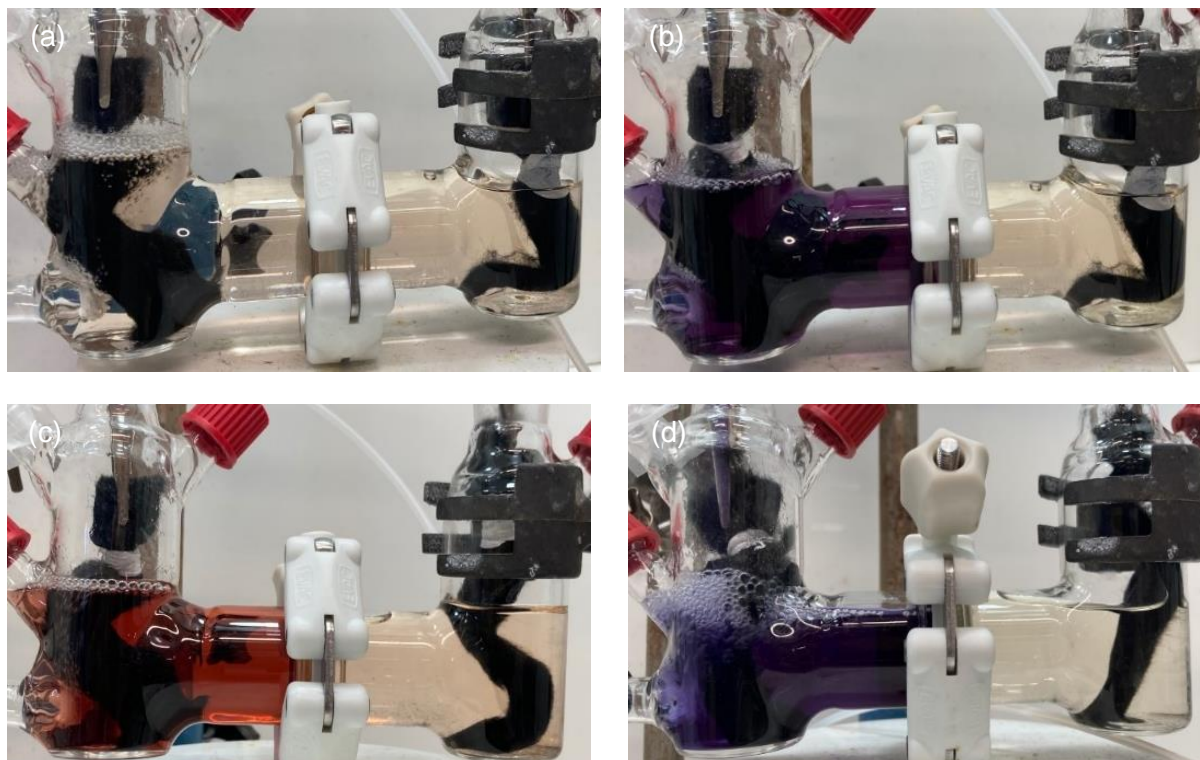
Figure 4.15. Photographs of the 1 mM OFAQ, 0.1 M TBABF₄, ACN electrolyte after successively holding the cell at the potentials (a) OCV, (b) −1.6 V, (c) −1.2 V, and (d) returning to −1.6 V.

Figure 4.16. compares the 100 mV s⁻¹ CV scans for the fresh (black line) and post-BE and post-air exposure (red line) electrolytes. Figure 4.17. shows the corresponding ¹⁹F-NMR analysis on the initial (top, black line) and post-BE (bottom, red line) solutions. See Appendix 4.B. for the tabulated NMR data. The inset in 4.17.(a) displays the low intensity OFAQ peak at −80.25 ppm.

The CV using the three-electrode cell set-up described in Chapter 2.3.1. for the electrolyte after BE taken and air exposure maintains two redox waves. The E_1 is at a similar potential as the initial solution, recording $E_{1,1/2}$ = −0.82 V (*vs* Ag/Ag⁺) and ΔE_p = 0.089 V at 100 mV s⁻¹. The E_2 shifts slightly positive with $E_{2,1/2}$ = −1.31 V (*vs* Ag/Ag⁺) and ΔE_p = 0.088 V in the post-BE compared to −1.49 V (*vs* Ag/Ag⁺) in the initial solution at 100 mV s⁻¹. Both redox events become less chemically reversible with decreasing scan rate, with no return oxidation for E_1 at 25 mV s⁻¹.
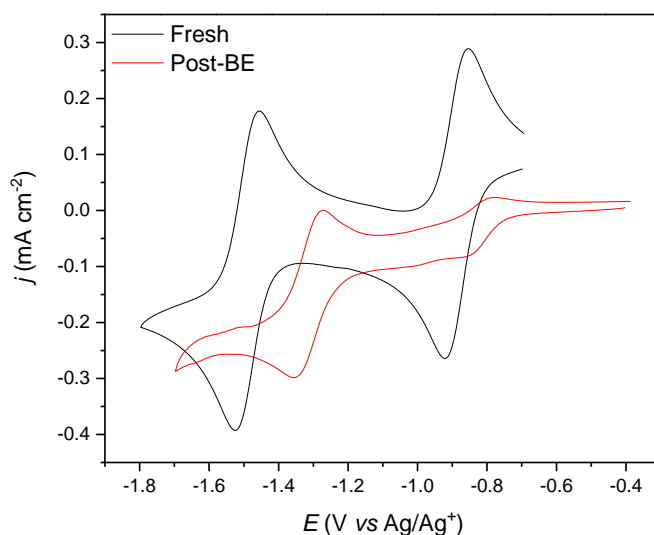
Figure 4.16. Overlay of CV plots for the initial (black line) and post-BE post-air exposure (red line) electrolytes at 100 mV s⁻¹.

In the post-BE CV, the E_1 reduction wave has lower i_p values than for E_2, with i_{pc} = −0.013 mA and i_{pc} = −0.032 mA for E_1 and E_2, respectively, at 100 mV s⁻¹. The i_{pa}/i_{pc} of 0.40 and 0.87 suggest a less reversible E_1 than E_2. However, this may be an artefact in measuring the baseline for E_1 oxidation resulting from the proximity of E_2 at fast scan rates.

The i_p values are higher in the initial solution compared to post-BE. This corroborates that side reactions and OFAQ degradation occurs when charging as a lower concentration is present in the post-BE CV.

The ¹⁹F-NMR data in Figure 4.17.(a) shows the spectrum for the initial OFAQ electrolyte. OFAQ gives peaks at −80.25, −140.77, −146.73, and −149.77 ppm. As with the ¹⁹F-NMR spectra for TFBQ in Section 3.1.1. Figures 3.5. and 3.6., the long-range coupling of F atoms complicates the spectra such that more than two F environments appear. The intensity of the −80.25 ppm peak is dependent on the electrolyte oxygen saturation and increases in intensity with degassing.

The peaks at −153.04 and −153.76 ppm are from the BF_4^- supporting electrolyte. The difference in ¹⁹F-NMR spectra between the fresh and post-BE species agree with the optical colour changes and different CVs in that the molecular nature of the electrolyte is different. The characteristic OFAQ F environments are not present in post-BE ¹⁹F-NMR spectra. Instead, many low intensity peaks populate the baseline and the BF_4^- peak shifts downfield to −151.45 and −151.50 ppm.

The absence of signals in the post-BE test may be evidence of the radical anion. Unpaired electrons have higher magnetic moments which promotes faster relaxation. This can mean

the nuclei may relax before the signal releases and result in a blank spectrum. The ^{19}F-NMR spectra in Figure 4.17. uses a 10° pulse width instead of the typical 90° pulse to overcome this limitation, but the OFAQ peaks are still not present. The unpaired electron in radical ions can displace the frequency of the nuclear resonance absorption so that it becomes non-observable.[20] The offset frequency (O1P) is the centre of the spectrum in ppm. Adjusting the O1P allows different areas of the ppm range to be viewed, which is useful if there have been large shifts in the chemical shifts of the peaks. However, adjusting the O1P over the range +200 − −800 ppm still finds no F environments, indicating the signals have not shifted these areas of the spectrum.
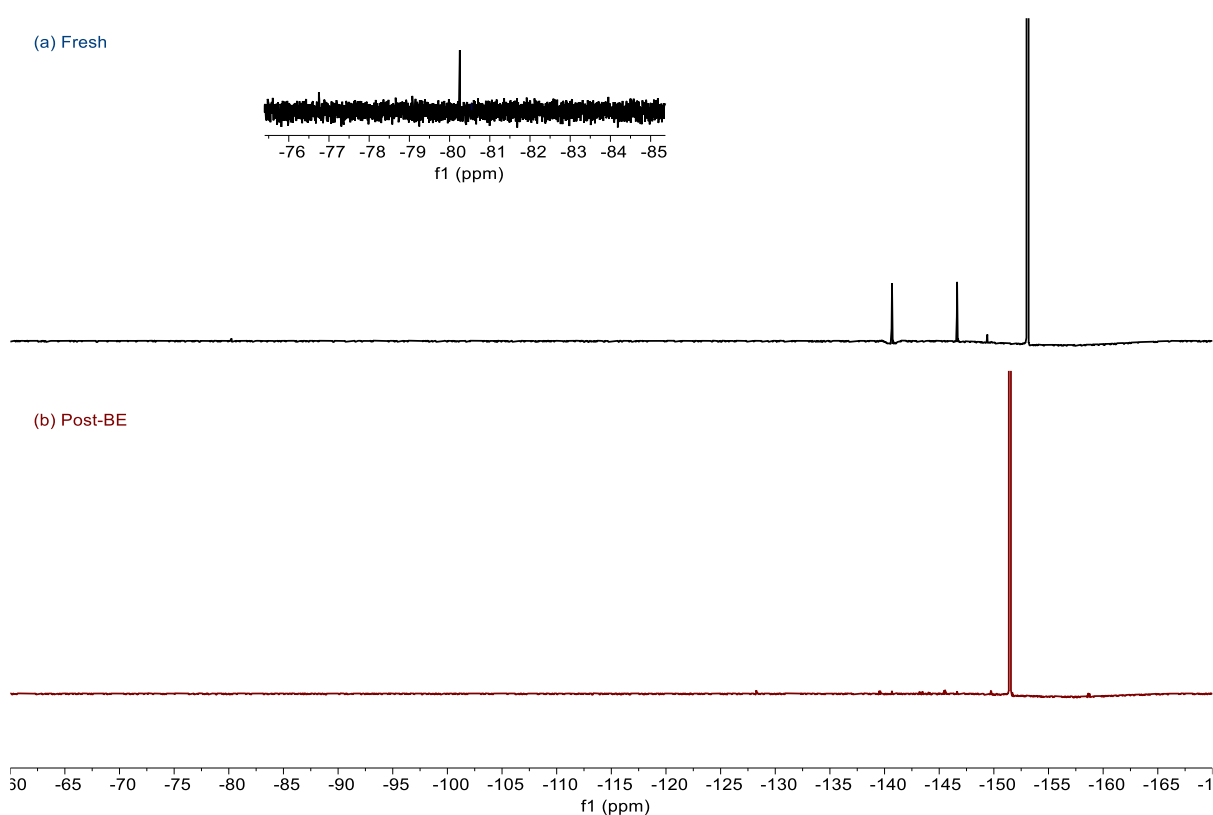
Figure 4.17. ^{19}F-NMR spectra of (a) fresh 1 mM OFAQ, 0.1 M TBABF4, ACN. The inset displays the low intensity −80.25 ppm peak (black line). (b) The spectra of the electrolyte after BE and exposure to air. NMR spectra run with a 10° pulse (red line).

Section 4.1.3. determines the radical anion to be more stable than the dianion. The colour change from purple (OFAQ^{2-}) to the same red as OFAQ$^{.-}$ indicates air exposure may cause the dianion to degrade to a stable radical anion. The lack of peaks in the ^{19}F-NMR agree with this hypothesis, however, the lack of paramagnetic signals in the EPR spectrum in Appendix 4.C. indicates this is not the case. One important difference between the NMR and EPR tests is that the EPR is performed *in-situ*, with reasonably O$_2$-free conditions. This may explain the

discrepancy in the radical stability. Future work should employ *in-situ* electrochemical NMR on the OFAQ over the charging cycling and after exposing to air to help locate the missing F environment peaks.

4.2.1. Symmetric Cell Tests

The post-BE half-cell without exposing to air should contain only $OFAQ^{2-}$ and possibly also degradation products. It can therefore act as the negative half-cell in a symmetric battery against fresh OFAQ electrolyte. The negative half-cell therefore consists of $OFAQ^{2-}$/OFAQ and the positive half-cell OFAQ/$OFAQ^{2-}$. Chapter 2.3.3. details the experimental procedure and electrochemical cells for the symmetric cell tests.

Symmetric cell cycling on the $OFAQ^{2-}$/OFAQ battery for 40 cycles with a charge and discharge time constraint of 120 s gives the data in Figure 4.18. Figure 4.18.(a) shows the galvanostatic charge-discharge profiles over the first six cycles, and Figure 4.18.(b) the profiles for Cycle 2, Cycle 20, and Cycle 40 with t normalised to 0 s. The corresponding change in overpotential as a function of cycle number is in Figure 4.18.(c). The overpotential is the potential difference between the charging and discharging plateaus at the end of each cycle. An increase in the overpotential with cycling suggests more energy is required than in previous cycles to drive the redox reaction.

Figure 4.18. shows the how the redox process changes within the first 6 cycles of the $OFAQ^{2-}$/OFAQ charge-discharge tests. The initial overpotential of 1.13 V in Cycle 2 increases to 1.52 V within 3 cycles. After the third cycle, a potential increase begins to appear after the initial voltage plateau, which results in an overpotential of 1.70 V by Cycle 6. A secondary voltage plateau appears at a higher potential after 10 cycles, recording an overpotential of 1.94 V. Figure 4.18.(b) shows how the initial voltage plateau becomes less observable with increasing cycle number. Cycle 6 has one charging plateau at −0.17 V (red line), Cycle 10 and 20 (dark blue and green lines) have two plateaus at 0.38 V and 0.65 V, and 0.37 V and 0.86 V, respectively. Cycle 40 only has one plateau at 1.07 V.

The discharge profile shows one voltage plateau for all tests, indicating side reactions occur during the charging process and yield an irreversible product. Figures 4.18.(b) and (c) suggest the side reactions exacerbate with increasing cycle number, ending in the final overpotential of 2.15 V after 40 cycles.
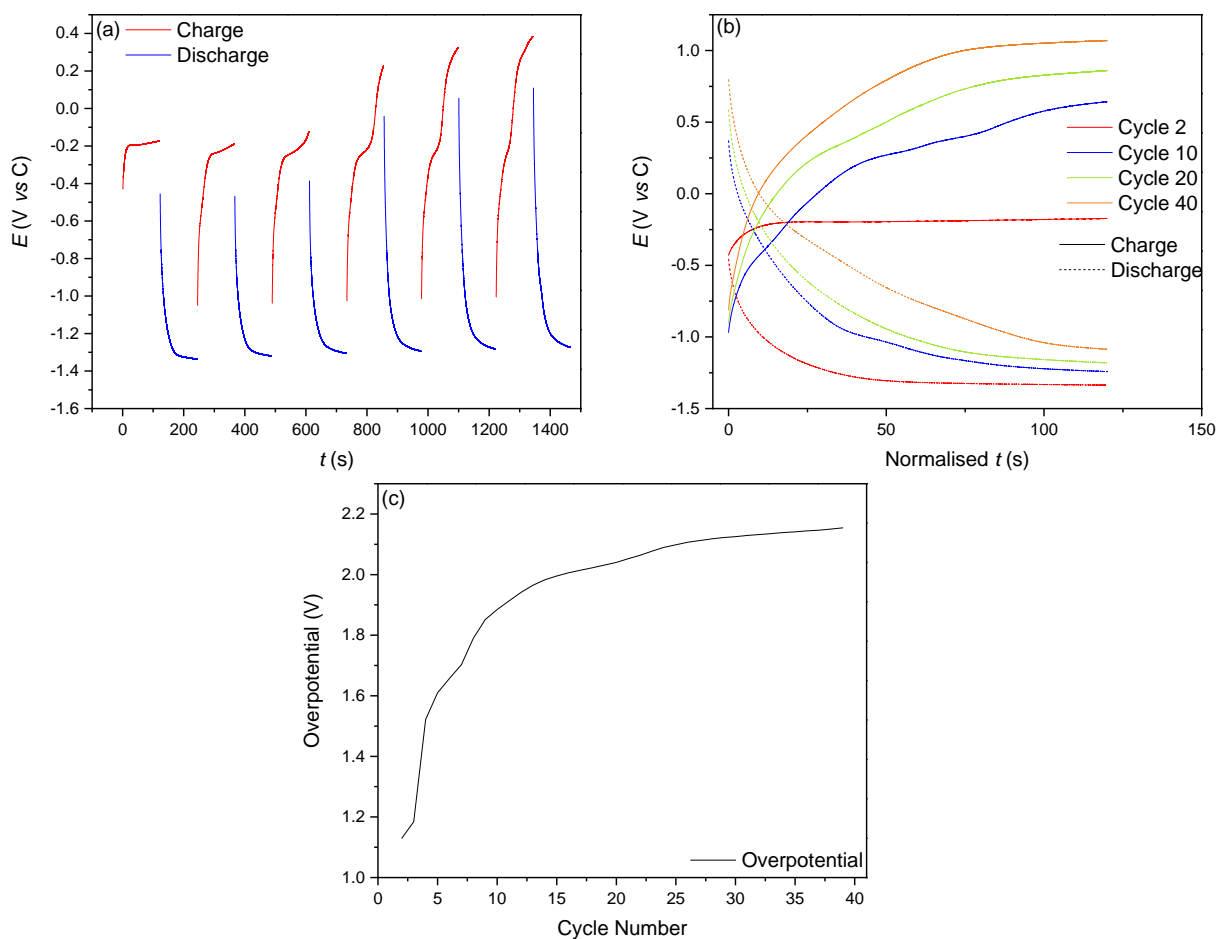
Figure 4.18. Symmetric battery cycling experiments of 1 mM OFAQ, 0.1 M TBABF₄, ACN. (a) The first six cycles of the OFAQ²⁻/OFAQ cell at 0.75 mA current for 120 s per charge and discharge cycle. (b) The time normalised charge-discharge profiles for Cycles 2, 10, 20, and 40. (c) The overpotential for each charge-discharge cycle.

The data so far in Chapter 4. show charged forms of OFAQ have insufficient stability for use in an ORFB without additional stabilising components. The promisingly negative reduction potential, two-electron charge storage mechanism at low concentrations or fast timescales, fast diffusion, fast kinetics, and electrochemical and chemical reversibility at low concentrations still maintain OFAQ as an interesting ORAM. If one can overcome the low stability and solubility, then these characteristics are promising for developing a competitive, high energy density ORFB. Therefore, it is of interest to investigate stabilising methods to improve the permanence of the charged states. The next section explores these aspects through varying supporting salt coordination strength, hydrogen bonding, and protonation.

4.3. Stabilisation Methods

In a complete ORFB, the ORAMs must be stable when fully charged for long periods. Chapter 4. determines reduced forms of OFAQ as unstable in higher concentrations over long-

timescales. Section 4.1.3. discovers $OFAQ^{2-}$ to be less stable than $OFAQ^{\cdot-}$ as it degrades at lower concentrations and over shorter timescales. $OFAQ^{\cdot-}$ is stable at low concentrations but also degrades at higher concentrations. Therefore, both reduction states require additional stabilising components to improve their permanence for an EESS.

Studies show many individual factors including solvent polarity, supporting electrolyte nature, intra- or intermolecular hydrogen bonding, presence of acidic or basic additives, ion pairing, and protonation-deprotonation equilibria can play decisive roles in stabilising reduced quinones.[19]

4.3.1. Strongly Coordinating Supporting Salts

Chapter 3.3. discusses the how a more strongly coordinating supporting cation, such as Li^+, changes the electrochemical pathway to a one-step process with a more positive $E_{1/2}$. Figure 3.20.(b) shows the $OFAQ/OFAQ^{2-}$ redox couple is chemically reversible on a voltammetry timescale at 1 mM concentration with a Li^+ supporting salt. The $LiBF_4$ supporting salt gives an $E_{1/2}$ of −0.73 V (vs Ag/Ag^+) with ΔE_p ranging 395 to 515 mV over scan rates $25 \leq v \leq 1000$ mV s^{-1}. The system becomes more chemically reversible with increasing v, with i_{pa}/i_{pc} values of 1.62 – 0.97. The positive shift in reduction potential is indicative of a lower energy LUMO level, which corresponds to improvements in anionic stability. The improvement comes from the more strongly coordinating cations forming ion pairs with the $OFAQ^{\cdot-}$ and $OFAQ^{2-}$.

Figure 4.19. gives the rotation rate dependent LSV scans on 1 mM OFAQ, 0.1 M $LiBF_4$, ACN over $200 \leq f \leq 1600$ RPM. The LSVs show a similar degradation into a non-conductive, passivating film on the electrode surface that occurs with high concentration OFAQ with $TBABF_4$. With a TBA^+ supporting salt, the degradation is only present when the OFAQ concentration surpasses 2.5 mM under rotating WE conditions. With Li^+ supporting cations, the passivation occurs at 1 mM OFAQ when under rotation. This is because even though the small size of the Li^+ cation allows it to form an ion pair with $OFAQ^{2-}$, it is too small to provide sufficient steric protection to prevent the anions from reacting with each other. TBA^+ is a much larger cation that only weakly interacts with the dianion. The large size causes steric protection, which means higher concentrations of anionic states are possible before degradation.

The E_{drop} in Figure 4.19. matches the E_{pc} in Figure 3.20.(b), indicating the reduction product is causing the electrode passivation. The unclear electron stoichiometry of the CV process indicates the transfer step is likely OFAQ to OFAQ^{2-} but with possible surface-adsorbed reactions occurring, *vide supra* Chapter 3.3. This evidences that LiBF$_4$ does not improve the anionic stability of OFAQ over TBABF$_4$.
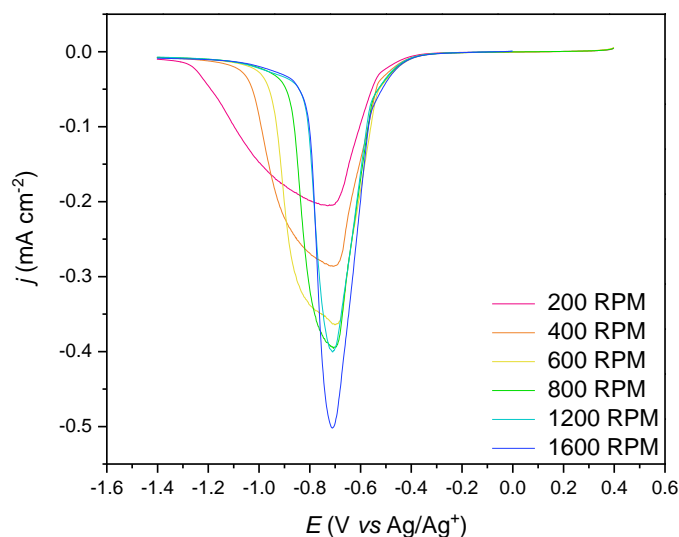
Figure 4.19. LSV data over rotation rates 200 ≤ f ≤ 1600 RPM at 2 mV s^{-1} for 1 mM OFAQ, 0.1 M LiBF$_4$, ACN using a GC WE, a Ag/Ag$^+$ RE, and a Pt CE.

Interestingly, the i_p in Figure 4.19. increase with f, which is not the case in the 5 mM OFAQ, 0.1 M TBABF$_4$ study in Figure 4.3.(iii). This is possibly due to the lower OFAQ concentration in the LiBF$_4$ study (1 mM), as raising the concentration exacerbates the degradation process. Additionally, the rate of the i_{drop} to 0 A increases with f. This corroborates that this is a concentration-led degradation process, as less OFAQ^{2-} is present at lower f rates. Therefore, less OFAQ^{2-} is reacting at a given time and hence there is a slower rate of film build up on the electrode surface.

4.3.2. Hydrogen Bonding and Protonation

Section 4.3.1. demonstrates more strongly coordinating electrolytes fail to improve the anionic stability of OFAQ^{2-} and do not inhibit the passivating film formation. Therefore, this study moves on to other stabilisation techniques.

Studies on similar quinones show hydrogen bonding or protonation between the quinone oxygen and solution additives stabilises the anionic states.[21] Weakly interacting quinone-hydrogen bond pairs positively shift the reduction waves with no loss in reversibility, thus

stabilising the mono- and dianionic reduction products. If the quinone-hydrogen bond pairs are moderately interacting, the reductive waves shift positive and the i_{pa} of E_1 increases whilst the E_2 broadens to an irreversible process. This occurs because the hydrogen bonding on the dianion assists radical anion disproportionation. If the pairs are strongly interacting, then hydrogen bonding or protonation of the initial neutral quinone becomes possible. This leads to one or two more positively shifted new cathodic waves and a new anodic wave.

The protonation of the neutral quinone can only occur if the added acid has a lower pK_a than the quinone.[21] The pK_a of OFAQ is unknown, and the competing inductive, mesomeric and steric effects make an accurate pK_a assumption challenging. Small changes in the attached functional groups can generate large changes in the pK_a. Estimates place the pK_a between 8 and 14, given that 1-aminoanthraquinone has a $pK_a = 8.01$, 1-(diethylamino)anthraquinone = 14.93, and that pK_a increases with the number of electronegative atoms and EWG groups, of which F is both.[17] Dianions are more basic than semiquinones, both of which are more basic than the parent neutral molecule and so will have more positive pK_a values.

The pK_a of water is 14. The positive shift in E_2 with increasing water concentration alongside the steady i_p in Chapter 3.2.1, Figure 3.16. shows H_2O does not protonate neutral OFAQ. Instead, water stabilises the reduced states through hydrogen bonding. The pK_a of all OFAQ states must therefore be below 14. The $E_{2,1/2}$ shifts positive from -1.49 V (vs Ag/Ag$^+$) with no H_2O to -1.05 V (vs Ag/Ag$^+$) after adding 20 % H_2O v/v. The higher charge delocalisation on OFAQ^{2-} compared to OFAQ$^{.-}$ means the hydrogen bonding stabilises the E_2 peak, causing E_2 to shift and not E_1. The improvement in stability is, however, in competition with the more positive reduction potential and so is not an ideal stabilising technique. This is a common dichotomy when stabilising the dianionic state, as improvements in stability come hand in hand with more positive reduction potentials.

Adding a strong, lipophilic acid (CF_3SO_3H) to the electrolyte probes the difference between hydrogen bonding and protonation on the OFAQ system. Protonation differs from hydrogen bonding through a much stronger interaction between the HBD and HBA. This means the hydrogen nuclei completely transfer rather than just associate. Generally, reactions involving protons have a slower k_0 than purely electron-transfer processes, which can lead to higher charge-transfer resistances in the RFB. Therefore, any improvements in stability will have to be substantial enough to compensate for the slower rate.

Figure 4.20.(a) shows the CV data and (b) the corresponding anionic stability chronoamperometry tests after increasing the acid concentration from 0.5 to 2-times the stoichiometric amount of hydrogen to oxygen atoms (1 mM acid:1 mM OFAQ to 4 mM acid:1mM OFAQ).
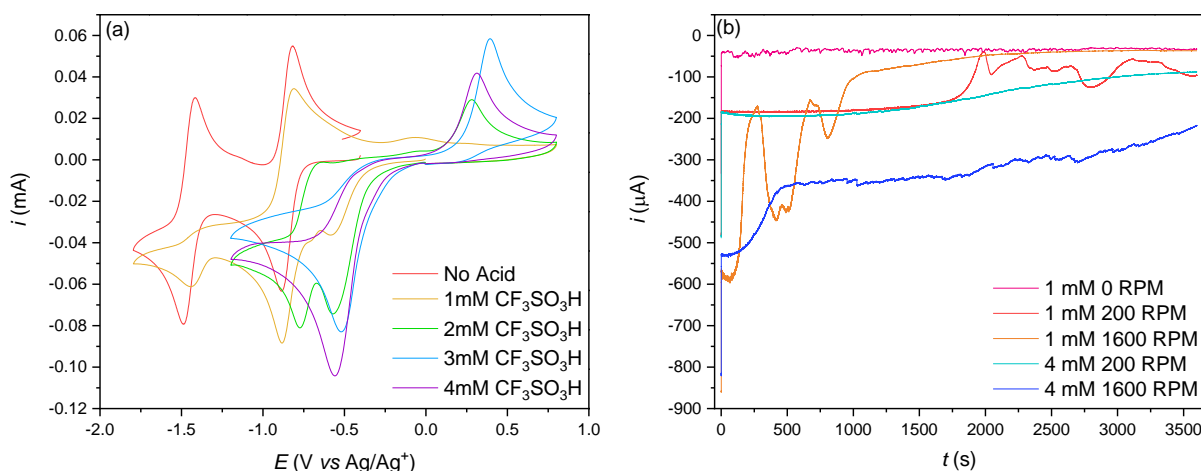
Figure 4.20. (a) CV data at 100 mV s⁻¹ for 1 mM OFAQ, 0.1 M TBABF₄, ACN with increasing CF₃SO₃H concentrations over scan rates 25 ≤ v ≤ 1000 mV s⁻¹. (b) Chronoamperometry of 1 mM OFAQ, 0.1 M TBABF₄, ACN with increasing CF₃SO₃H concentrations over rotation rates 0 ≤ f ≤ 1600 RPM. The 4 mM tests were held at −1.1 V and the 1 mM tests at −1.7 V to ensure OFAQ²⁻ is studied in both cases. All tests use a GC WE, Pt CE, and Ag/Ag⁺ RE.

The data in Figure 4.20.(a) is similar to literature studies on structurally related quinones, in that the 2 × 1e⁻ transfer converts into a singular step with a positively shifted $E_{1/2}$ upon adding acid.[19,21–23] As discussed above, when both an acid and a strongly coordinating electrolyte cation are absent, the process is 2 × 1e⁻ reduction at $E_{1,1/2}$ = −0.89 V and $E_{2,1/2}$ = −1.49 V (vs Ag/Ag⁺) (Figure 4.3.(a) and Figure 4.20.(a) red line). At 1 mM CF₃SO₃H (Figure 4.20.(a) yellow line), half the stoichiometric amount of H⁺ relative to the oxygen groups in the quinone, E_2 decreases in i_p, as does E_1 albeit to a lesser degree. A small new wave appears (E_3) with $E_{3,pa}$ and $E_{3,pc}$ of −0.07 V and −0.58 V, respectively ($\Delta E_{3,p}$ = 0.51 V, $E_{3,1/2}$ = −0.32 V (vs Ag/Ag⁺)). This indicates two reducible species are present in equilibrium and could be due to protonation of the quinone.

The pKa of CF₃SO₃H is 0.7 in ACN.[21] If the pKa of OFAQ lies above 0.7 then the CF₃SO₃H will protonate the quinone.[24] If protonation is occurring, there is not enough acid present to fully protonate both oxygen functional groups in the quinone at 1 mM CF₃SO₃H. This explains why there is still some of the first and second reduction waves visible in the yellow line in Figure 4.20.(a). The shift in $E_{1,pa}$ is from −0.89 V to −0.88 V (vs Ag/Ag⁺). The small shift in $E_{1,pa}$ suggests the acid is not fully protonating the semiquinone as this should display a large positive E_1 shift.[21]

This agrees with the data in Figure 4.21. which shows the ¹H NMR spectra of (a) (blue line) 2 mM OFAQ, 4 mM CF₃SO₃H, (b) (green line) 1 mM OFAQ, 4 mM CF₃SO₃H, and (c) (red line) 4 mM CF₃SO₃H, all with 0.1 M TBABF₄ supporting salt in ACN with a D₂O inner capillary reference. This gives a control reference for the acid, and compares the change in chemical

environment with proton concentration relative to the amount of O present in the solution. OFAQ contains no ^{1}H environments and so should not show in ^{1}H NMR spectra unless through an interaction with the acid. Appendix 4.D. tabulates the chemical shifts.
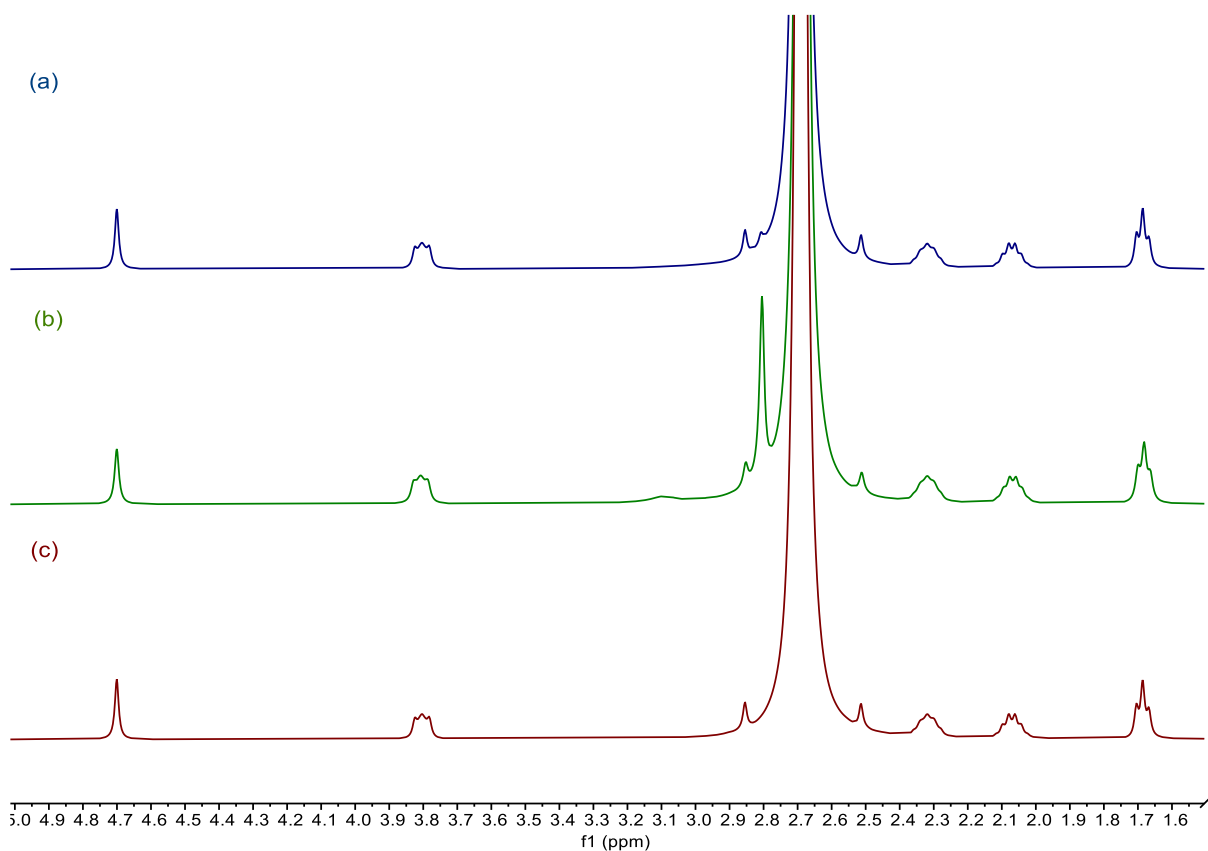
Figure 4.21. ^{1}H NMR spectra of 4mM CF$_3$SO$_3$H with (a) 2 mM OFAQ (blue line), (b) 1 mM OFAQ (green line), and (c) no OFAQ (red line) in 0.1 M TBABF$_4$, ACN, using a D$_2$O inner capillary reference.

The 4.70 ppm peak is due to residual water in the solvent. The TBABF$_4$ supporting electrolyte causes the peaks at the chemical shifts 3.80, 2.32, 2.07, and 1.69 ppm. The ACN solvent is responsible for the singlet peak at 2.69 ppm, with ^{13}C satellites either side. A new singlet peak appears at 2.80 ppm in Figures 4.21.(a) and (b) after adding OFAQ and indicates the presence of a new proton environment with no neighbouring protons. This would be the case in the protonated form of OFAQ, OFAQH$^+$.

The intensity of this new 2.80 ppm peak is higher when the relative proton concentration is above that of O in the molecule. Additionally, another new, small intensity, environment peak appears at 3.09 ppm in Figure 4.21.(b) when only 1 mM OFAQ is present. This peak is possibly a result of the ion pair of the CF$_3$SO$_3^-$ conjugate base and the OFAQH$^+$.

The relative ratio of OFAQ:H$^+$ in the 2 mM OFAQ, 4 mM CF$_3$SO$_3$H test is stoichiometric (1:1) and there should be full protonation of the quinone. The discrepancy between the 2 mM and 1 mM OFAQ spectra in Figures 4.21.(a) and (b) is likely because the system is only fully

protonated in the latter test. The higher acid concentration (relative to OFAQ concentration) in Figure 4.21.(b) (green line) leads to more OFAQH$^+$ being present and hence a higher intensity in the 2.80 ppm peak. The fuming nature of CF$_3$SO$_3$H makes it challenging to measure accurately the concentration when forming solutions. This means it is possible that less than 4 mM acid is present in (a), which would increase the relative OFAQ:H$^+$ ratios and yield less OFAQH$^+$ and hence yield a lower intensity peak.

In the CV Figure 4.20.(a), increasing the acid concentration to 2 mM (1:1 relative to O in the quinone) causes the more negative wave, E_2, to disappear and the E_1 to shift positive to $E_{1,pa}$ = −0.64 V and $E_{1,pc}$ = −0.77 V, with $E_{1,1/2}$ = −0.71 V (*vs* Ag/Ag$^+$). The new wave (E_3) that appears in the 1 mM test significantly increases in height at 2 mM , and the anodic peak shifts positive to become an irreversible process with $E_{3,pa}$ = 0.28 V and $E_{3,pc}$ = −0.57 V with E$_{3,1/2}$ = −0.15 V (*vs* Ag/Ag$^+$).

Increasing the acid concentration to 3 mM (i.e. 3:1 excess of acid:OFAQ), loses E_1 again, whilst E_3 increases in i_p and E_p, with $E_{3,pa}$ = 0.39 V, $E_{3,pc}$ = −0.52 V (ΔE_p = 0.91 V), and E$_{3,1/2}$ = −0.07 V (*vs* Ag/Ag$^+$). Increasing the acid concentration further to 4 mM does not alter the peak potentials. The corresponding ^{1}H-NMR spectra for this relative excess of acid to OFAQ is in Figure 4.21.(b) (green line). The increase in i_{pc} for the E_3 peak around $E_{3,pc}$ = −0.52 V (*vs* Ag/Ag$^+$) is likely due to the immediate reduction of the protonated OFAQ$^{.-}$.

To summarise, as the amount of strong acid increases relative to the amount of quinone, the process transforms from a 2 × 1e$^-$ process into a one-step electron transfer. The one-step process occurs when there is an excess of H$^+$. Given that OFAQ likely has a higher pK$_a$ than the acid, this is a 2H$^+$/2e$^-$ mechanism. The large change in ΔE_p, positive shift in $\Delta E_{2,1/2}$ from −1.49 V (*vs* Ag/Ag$^+$) with no acid (red line) to $\Delta E_{3,1/2}$ = −0.07 V (*vs* Ag/Ag$^+$) after adding over 3 mM CF$_3$SO$_3$H (blue line), alongside the increase in i in Figure 4.21.(a) advocates OFAQ protonation.

The redox waves are therefore likely due to the reduction and re-oxidation of the protonated neutral quinone (OFAQH$^+$) to the dihydroquinone (OFAQH$_2$) via the CECE pathway shown in blue in the square-scheme in Figure 4.22.
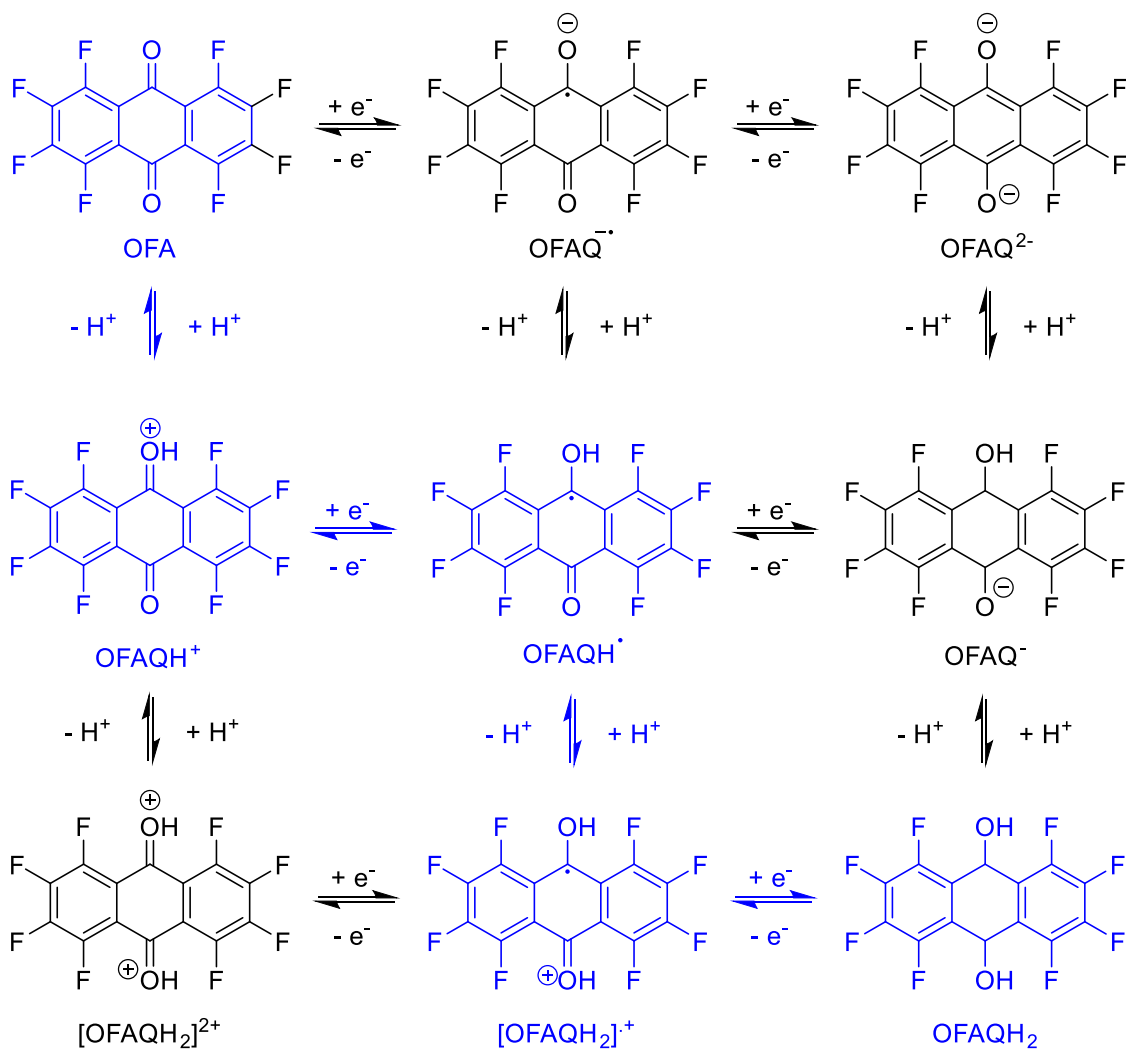
Figure 4.22. Electrochemical square-scheme for OFAQ involving protonation.
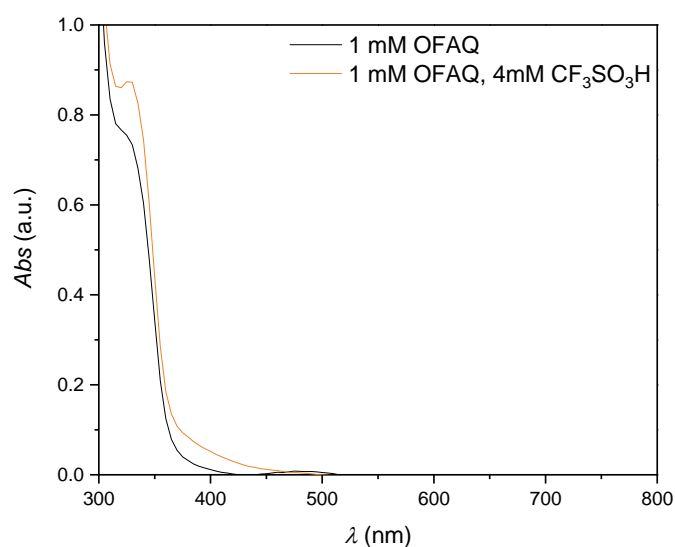
Figure 4.23. UV-Vis spectrum of (black line) 1 mM OFAQ, 0.1 M TBABF$_4$, ACN and (orange line) 1 mM OFAQ, 4 mM CF$_3$SO$_3$H, 0.1 M TBABF$_4$, ACN.

Acidification of the solution causes the colour change in shown in the UV-Vis data in Figure 4.23. The solution is light orange at (a) 0 mM acid and (b) a bright yellow solution after adding 4 mM CF_3SO_3H. The increase in peak intensity at 327 nm and a loss of the small 488 nm peak after acidification supports the hypothesis of a chemical change (i.e. protonation) of the neutral quinone.

Figure 4.24. shows the ^{19}F-NMR spectra for (a) (blue line) 1 mM OFAQ, 4 mM CF_3SO_3H, 0.1 M TBABF$_4$, ACN, (b) (green line) the acidified electrolyte solution without OFAQ (4 mM CF_3SO_3H, 0.1 M TBABF$_4$, ACN), and (c) (red line) 1mM OFAQ, 0.1 M TBABF$_4$, ACN. Appendix 4.E. gives the corresponding ^{19}F-NMR report. Figure 4.24.(c) shows the characteristic OFAQ peaks in the same regions as Figure 4.17., with peaks at −79.40, −139.88, and −145.79 ppm. The lower peak intensities in Figure 4.24. compared to Figure 4.17. is because this test uses a 90 ° pulse instead of 10 °. The larger pulse angle makes the peak at −149.77 non-observable. The spectrum in Figure 4.24.(b) contains no OFAQ and shows the CF_3SO_3H peaks at −79.18 ppm. The TBABF$_4$ is responsible for the two peaks in the −150.14 to −151.23 ppm region over all three spectra.
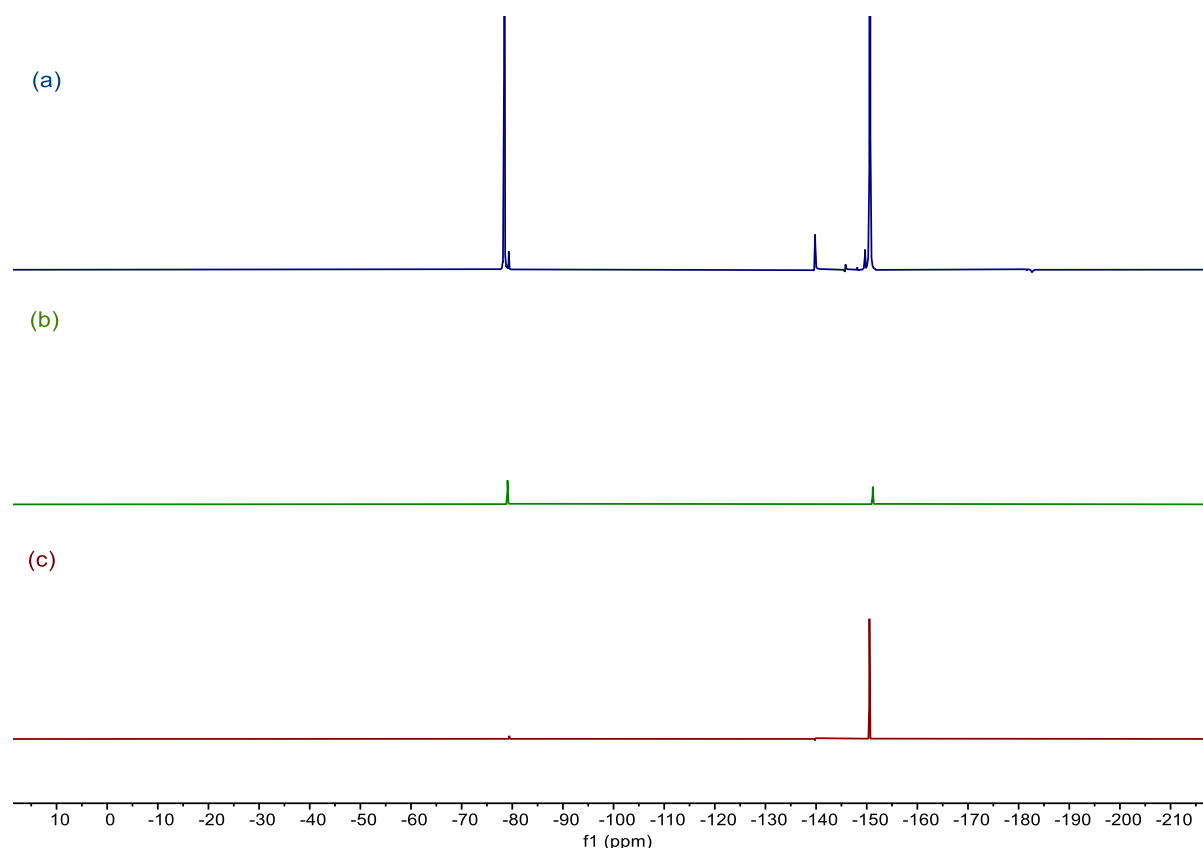
Figure 4.24. ^{19}F NMR spectra of (a) (blue line) 1 mM OFAQ, 4 mM CF$_3$SO$_3$H, 0.1 M TBABF$_4$, ACN, (b) (green line) 4 mM CF$_3$SO$_3$H, 0.1 M TBABF$_4$, ACN, and (c) (red line) 1 mM OFAQ, 0.1 M TBABF$_4$, ACN.

Adding OFAQ to the acid and supporting electrolyte solution in Figure 4.24.(a) shows peaks in the same regions as the separate OFAQ and CF_3SO_3H samples, with an additional peak at −149.67 ppm. The presence of a new peak is evidence of a structural change in the quinone.

The increase in intensity in the −78.61 ppm peak may be a result of ion-pair formation between $CF_3SO_3^-$ and OFAQH$^+$ discussed in context of the ^{1}H-NMR spectra in Figure 4.21. This evidences the source of the higher ppm peaks to be the protonated neutral quinone, OFAQH$^+$. The presence of the original OFAQ peaks indicates that some OFAQ molecules remain unprotonated in the solution. This could be due to a slow exchange with the CF_3SO_3H. The CV data in Figure 4.20.(a) (purple and blue lines) does not show the redox of this neutral OFAQ after adding acid because the semi-quinone and dianionic forms are more basic than the neutral OFAQ. This means they are completely protonated after forming via an CECE mechanism, which renders their aprotic electrochemistry unobservable. Peak intensities are also sensitive to the level of oxygen saturation in the sample, which may be affecting the data.

Hour-long chronoamperometry studies in Figure 4.20.(b) show the change in redox mechanism and quinone protonation that occurs upon adding the acid does improve the stability of the reduced quinones.

Adding 1 mM CF_3SO_3H shows a similar result to the OFAQ tests with no acid (Figures 4.10.(c) and (d)), being stable when $f \le 200$ RPM (pink and red lines), which is expected as some non-protonated quinone remains. Figure 4.10.(c) shows that in the absence of acid, 1mM OFAQ^{2-} degrades when $f \ge 1600$ RPM. Adding 1 mM (half the stoichiometric H:O amount) in Figure 4.20.(b) has the same trend and shows degradation when $f \ge 1600$ RPM.

Increasing the acid concentration to match the number of anions (Figure 4.20.(b) light blue and dark blue lines) also yields a current response indicating degradation. With no acid the i_{drop} is at $t_{1/2} = 309$ s, $i_{t1/2} = -410$ μA, and adding 4 mM CF_3SO_3H reduces this to $t_{1/2} = 94$ s, $i_{t1/2} = -480$ μA. This suggests, that even though the states are stabilised electrochemically by the presence of the acid, this does not improve the high-concentration degradation process that OFAQ displays throughout this study. The similarity in $i_{t1/2}$ and i_{final} for both neutral and acidic electrolyte indicates a similar level of degradation in both tests. This suggests the acid does not prevent the process. The trend of increasing f leading to faster decomposition remains concurrent over all tests, with and without acid.

4.4. Conclusions

To summarise, this chapter uncovers the fundamental electrochemistry of OFAQ and uses LSV and chronoamperometry to investigate its long-term stability in neutral, singly, and doubly charged forms.

Section 4.1. shows how higher concentrations of OFAQ degrade into a non-conductive film that passivates the WE surface and is visible by eye. A combination *in-situ* and *ex-situ* analysis techniques indicate this is most likely via a pinacol coupling mechanism of $2OFAQ^{-}$ to $(OFAQ)_2^{2-}$. The product subsequently degrades into larger polymers that are poorly-redox active and insoluble in ACN. This process passivates the electrode and prevents any further electrochemical response.

Hour-long chronoamperometric studies show the dianion to be less stable than the semiquinone radical. This agrees with previous literature computational studies that suggest the resonance structure of the radical anion can better stabilise the molecule than the delocalised charges on the dianion.[25] Chronoamperometry shows $OFAQ^{2-}$ undergoes a two-step degradation mechanism at the electrode surface, whereas $OFAQ^{-}$ follows a single step-degradation pathway. The single-step process is likely the aforementioned pinacol coupling. The two-step degradation possibly comprises a first comproportionation reaction step between $OFAQ^{2-}$ and OFAQ to produce $OFAQ^{-}$. The pinacol coupling of the resulting radical anions then follows.

Section 4.2. performs BE on the OFAQ electrolyte and confirms the colour change for the OFAQ redox process as orange/yellow for OFAQ, red for $OFAQ^{-}$, and purple for $OFAQ^{2-}$. The dianion is unstable upon contact with air and turns the same shade of red as the radical anion after exposure. Experimental limitations mean that the doubly charged state cannot be analysed in the present work.

Analysis on the electrolyte post-BE and after air exposure show no F environments in the ^{19}F-NMR, but still show two redox waves in the CV. The CV waves are less reversible than for the initial solution, with a similar E_1, a positively shifted E_2, and lower i_p values for both redox events compared to the fresh electrolyte. The lower currents indicate some of the ORAM has formed an insoluble or redox-inactive product. The lack of environments in the NMR and EPR spectra indicate a change in the F-environments in the electrolyte, but confirm this is not in the form of the paramagnetic species.

Symmetric cell cycling tests on the $OFAQ^{2-}$/OFAQ battery show evidence of side reactions within a couple of cycles. The initial cycle shows both a charge and discharge plateau, but

successive cycling leads to side reactions in the charging process and an increase in overpotential from 1.13 V to 2.15 V over 40 cycles.

Overall, the results from Section 4.1. and 4.2. indicate OFAQ is unstable in high concentrations in its charged state. It is therefore an unsuitable ORFB anolyte without sufficient stabilising components. Section 4.3. investigates various techniques to stabilise reduced OFAQ.

The more strongly coordinating salt, Li^+, did not stabilise the reduced states of OFAQ. Hydrodynamic voltammetry shows the reduced products degrade at even lower concentrations than when TBA^+ is the supporting cation. This is due to the small cationic radii of Li^+ providing less steric protection around $OFAQ^{\cdot-}$ and $OFAQ^{2-}$, such that is has a higher chance to react.

The dianion is more protophilic than the semiquinone radical. Therefore, adding a weak Brønsted acid, such as water, stabilises the dianion and pushes the E_2 value more positive. This improvement in stability reduces the reduction potential of OFAQ from $E_{2,1/2}$ = −1.49 V with no additives, to $E_{2,1/2}$ = −1.05 V (vs Ag/Ag$^+$). This is not ideal as it reduces the energy density battery of an OFAQ-based ORFB.

The pK_a of OFAQ is likely above that of the strong, lipophilic acid CF_3SO_3H, and the pK_a of reduced states will be even higher. Adding the acid stepwise up to a stoichiometric amount to match the electron concentration shows the successive protonation of the neutral OFAQ molecule. The electron transfer process changes from the aprotic 2 × 1e$^-$ process through to the one-step 2H$^+$/2e$^-$ redox of the protonated quinone. ^{19}F- and ^{1}H- NMR corroborate the protonation of the neutral quinone and show evidence of a $CF_3SO_3^-$-OFAQH$^+$ ion pair. The UV-Vis analysis provides further evidence of a change in molecular state upon acidification.

Unfortunately, chronoamperometry tests analogous to those in Section 4.1. on the acidified quinone show that protonation fails to improve the long-term stability. OFAQ degrades over one-step in similar timescales and with the same i_{final} values with the acid as without. This suggests the molecule degrades via a similar pathway, and by a similar amount, showing that the acid does not stabilise the system. The instability of charged oxidation states of ORAMs is an ever-present challenge in this area of research, and practically all literature ORAMs experience some level of capacity fade.

Chapters 3. and 4. find OFAQ unsuitable in its current form for an ORFB. However, its insolublility in aqueous media and particularly negative reduction potential make it useful for investigating the membrane-free ORFB concept. The following chapter therefore investigates OFAQ in the development of membrane-free RFBs.

4.5. References

1   J. Zhang, R. E. Corman, J. K. Schuh, R. H. Ewoldt, I. A. Shkrob and L. Zhang, Solution properties and practical limits of concentrated electrolytes for nonaqueous redox flow batteries, *J. Phys. Chem. C*, 2018, **122**, 8159–8172.

2   W. Wang, W. Xu, L. Cosimbescu, D. Choi, L. Li and Z. Yang, Anthraquinone with tailored structure for a nonaqueous metal-organic redox flow battery, *Chem. Commun.*, 2012, **48**, 6669–6671.

3   P. Geysens, Y. Li, I. Vankelecom, J. Fransaer and K. Binnemans, Highly soluble 1,4-diaminoanthraquinone derivative for nonaqueous symmetric redox flow batteries, *ACS Sustain. Chem. Eng.*, 2020, **8**, 3832–3843.

4   A. T. Bui, N. A. Hartley, A. J. W. Thom and A. C. Forse, Trade-off between redox potential and the strength of electrochemical CO2 capture in quinones, *J. Phys. Chem. C*, 2022, **126**, 14163–14172.

5   M. Li, Z. Rhodes, J. R. Cabrera-Pardo and S. D. Minteer, Recent advancements in rational design of non-aqueous organic redox flow batteries, *Sustain. Energy Fuels*, 2020, **4**, 4370–4389.

6   R. A. Potash, J. R. McKone, S. Conte and H. D. Abruña, On the benefits of a symmetric redox flow battery, *J. Electrochem. Soc.*, 2016, **163**, A338–A344.

7   K. Lin, Q. Chen, M. R. Gerhardt, L. Tong, S. B. Kim, L. Eisenach, A. W. Valle, D. Hardee, R. G. Gordon, M. J. Aziz and M. P. Marshak, Alkaline quinone flow battery, *Science*, 2015, **349**, 1529–1532.

8   Z. Li, S. Li, S. Liu, K. Huang, D. Fang, F. Wang and S. Peng, Electrochemical properties of an all-organic redox flow battery using 2,2,6,6-tetramethyl-1-piperidinyloxy and N-methylphthalimide, *Electrochem. Solid-State Lett.*, 2011, **14**, 171–173.

9   T. Liu, X. Wei, Z. Nie, V. Sprenkle and W. Wang, A total organic aqueous redox flow battery employing a low cost and sustainable methyl viologen anolyte and 4-HO-TEMPO catholyte, *Adv. Energy Mater.*, 2016, **6**, 1501449.

10   A. Z. Weber, M. M. Mench, J. P. Meyers, P. N. Ross, J. T. Gostick and Q. Liu, Redox flow batteries: A review, *J. Appl. Electrochem.*, 2011, **41**, 1137–1164.

11   L. Tong, Q. Chen, A. A. Wong, R. Gómez-Bombarelli, A. Aspuru-Guzik, R. G. Gordon and M. J. Aziz, UV-Vis spectrophotometry of quinone flow battery electrolyte for: In situ monitoring and improved electrochemical modeling of potential and quinhydrone formation, *Phys. Chem. Chem. Phys.*, 2017, **19**, 31684–31691.

12   A. René and D. H. Evans, Electrochemical reduction of some o-quinone anion radicals: Why is the current intensity so small?, *J. Phys. Chem. C*, 2012, **116**, 14454–14460.

13   X. Wei, W. Xu, J. Huang, L. Zhang, E. Walter, C. Lawrence, M. Vijayakumar, W. A. Henderson, T. Liu, L. Cosimbescu, B. Li, V. Sprenkle and W. Wang, Radical compatibility with nonaqueous electrolytes and its impact on an all-organic redox flow battery, *Angew. Chemie Int. Ed.*, 2015, **54**, 8684–8687.

14   M. Matsui, S. Taniguchi, M. Suzuki, M. Wang, K. Funabiki and H. Shiozaki, Dyes produced by the reaction of 1,2,3,4-tetrafluoro-9,10-anthraquinones with bifunctional nucleophiles, *Dye. Pigment.*, 2005, **65**, 211–220.

15   N. Nagamura, R. Taniki, Y. Kitada, A. Masuda, H. Kobayashi, N. Oka and I. Honma, Electronic states of quinones for organic energy devices: The effect of molecular structure on electrochemical characteristics, *ACS Appl. Energy Mater.*, 2018, **1**, 3084–3092.

16   G. Beamson and D. Briggs, *High resolution XPS of organic polymers: The Scienta ESCA300 database*, Wiley, New York, 1st Ed., 1992, vol. 73.

17   D. Zarzeczańska, P. Niedziałkowski, A. Wcisło, L. Chomicz, J. Rak and T. Ossowski, Synthesis, redox properties, and basicity of substituted 1-aminoanthraquinones: Spectroscopic, electrochemical, and computational studies in acetonitrile solutions, *Struct. Chem.*, 2014, **25**, 625–634.

18   J. S. Lawton, D. Aaron, T. Zhijiang and T. A. Zawodzinski, Electron spin resonance investigation of the effects of vanadium ions in ion exchange membranes for uses in vanadium redox flow batteries, *ECS Meet. Abstr.*, 2011, **MA2011-02**, 687–687.

19   P. S. Guin, S. Das and P. C. Mandal, Electrochemical reduction of quinones in different media: A review, *Int. J. Electrochem.*, 2011, **2011**, 1–22.

20   A. L. Buchachenko and N. A. Sysoeva, Nuclear magnetic resonance in radicals and in radical reactions, *Russ. Chem. Rev.*, 1968, **37**, 798–811.

21   N. Gupta and H. Linschitz, Hydrogen-bonding and protonation effects in electrochemistry of quinones in aprotic solvents, *J. Am. Chem. Soc.*, 1997, **119**, 6384–6391.

22   M. Gómez, I. González, F. J. González, R. Vargas and J. Garza, The association of neutral systems linked by hydrogen bond interactions: A quantitative electrochemical approach, *Electrochem. commun.*, 2003, **5**, 12–15.

23   M. Shamsipur, A. Siroueinejad, B. Hemmateenejad, A. Abbaspour, H. Sharghi, K. Alizadeh and S. Arshadi, Cyclic voltammetric, computational, and quantitative structure-electrochemistry relationship studies of the reduction of several 9,10-anthraquinone derivatives, *J. Electroanal. Chem.*, 2007, **600**, 345–358.

24   J. Bessard, G. Cauquis and D. Serve, Le comportement électrochemique des couples

quinone—hydroquinone a caractere basique en milieux organiques. Cas des dérivés polyméthoxyles, *Electrochim. Acta*, 1980, **25**, 1187–1197.

25   K. Izutsu, *Electrochemistry in nonaqueous solutions*, Wiley-VCH Verlag, Musashino, 2nd Ed., 2002.

5. Membrane-Free Battery

5.1. Membrane-Free Concept

The main factors hindering mass commercialisation of conventional RFBs are the (a) low energy density, (b) high electrolyte cost, and (c) high cost and limited lifetime of the IEMs. The electrolyte and membrane can account for up to 62 % and 20 – 40 % of the total cost of a 300 kW h VRFB.[1–3] Chapters 3. and 4. investigate methods of combatting the high electrolyte cost and low energy density. This includes utilising novel ORAMs to remove the reliance on expensive, scarce, V resources, and employing organic electrolytes to improve the energy density. The present chapter focusses on the other cost- and lifetime-limiting component, the IEM.

Many studies focus on improving upon the current Nafion membrane but none to date achieve comparable performances.[4] The most promising studies employ cheap, non-fluorinated polymer membranes or non-ionic separators, but these tend to have insufficient chemical or mechanical stability and high rates of crossover.[5–8]

Through rational electrolyte design, one can form a L/L ITIES and produce a membrane-free battery.[9–11] The concept is becoming more popular in the academic literature, but the lack of patents on the matter demonstrates the immaturity of the technology. One patent in the area is from Montes Gutierrez *et al.* for their immiscible electrolyte RFB design with a flow through electrode.[12] The design covers aqueous/non-aqueous biphasic and aqueous-biphasic electrolytes where one aqueous phase comprises a low concentration salt. Other key studies involve aqueous-biphasic systems or utilise organic solvents and RTILs.[9,10,13–15] The lab-scale demonstrations cover both metallic and organic redox components.[9,10] The best membrane-free battery utilising a non-aqueous half-cell to date is by Navalpotro *et al.* and comprises 4-OH-TEMPO, 0.5 M NaCl catholyte and BQ in an RTIL.[15] The battery achieves a *CE$_{ff}$* of 75 % over 300 cycles and a discharge capacity retention of 85 % under static conditions. An omnipresent problem with membrane-free devices is the thermodynamically driven cross-migration of active molecules over the interface. This leads to an imbalance in active material and eventual self-discharge of the battery. This is a key roadblock in their development.

The requirements for designing a membrane-free RFB are:

- Immiscible electrolytes in each half-cell.
- A common ion between both the anolyte and the catholyte that can migrate between the two and maintain charge balance.
- RAMs that are highly soluble in one phase and minimally soluble in the other, in both charged and discharged states to minimise crossover.

The previous chapters in this work find ACN to be the most promising organic electrolyte for an OFAQ-based battery. The miscibility of ACN with water means it will not form an ITIES for the proposed membrane-free device. Spontaneous phase separation occurs between water and ACN if the aqueous phase contains a sufficiently salt high concentration.[16,17] Theoretical models for the water-ACN-salt ternary system exist for a number of salt identities.[16] This phenomenon forms the basis for the common practice of salting-out assisted liquid-liquid extraction of chemicals, but is yet to be demonstrated for ORFB applications.[17]

Figure 5.1. shows photographs of mixtures containing 1mM OFAQ, 0.1 M LiBF$_4$, ACN (10 mL) and increasing concentrations of LiCl in H$_2$O of (a) 0.1 M, (b) 0.5 M, (c) 1 m, (d) 5 m, and (e) 10 m. The lower-case 'm' represents the molality, which is the number of moles per kilogram of solvent, whereas 'M' is the molality, which is the number of moles per solvent volume. At such high concentrations the molarity can become inaccurate. The phases are miscible when the LiCl concentrations are 0.1 M and 0.5 M (Figures 5.1.(a) and (b)), but two layers spontaneously separate when the LiCl concentration is >1 m (Figures 5.1.(c) to (e)). Above 1 m LiCl the phases separate into an organic layer on top of the denser aqueous layer. The layers are identifiable because the yellow OFAQ is not soluble in the colourless LiCl electrolyte. At 1 m LiCl, the volume of the non-aqueous layer is less than that of the aqueous layer, suggesting non-complete phase separation of ACN and H$_2$O. Above 5 m LiCl (Figures 5.1.(d) and (e)), the phases separate into two well-defined layers of equal volume. These self-stratifying layers remain stable after shaking. Additionally, ^{19}F-NMR analysis in Appendix 5.A. on the aqueous phase shows only noise and no F environments, indicating neutral OFAQ does not pass the interface. The phase separation also occurs when no LiBF$_4$ is present.
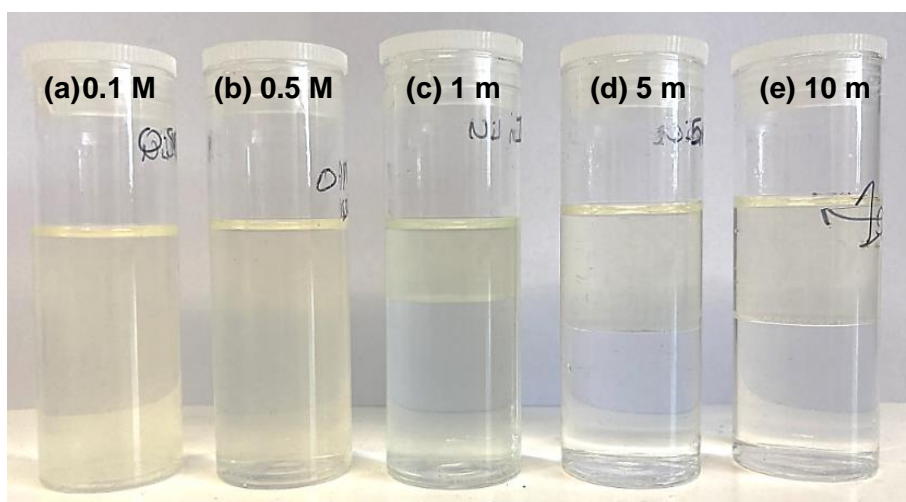
Figure 5.1. Photographs of mixtures comprising 1 mM OFAQ, 0.1 M LiBF$_4$, ACN (10 mL) with (a) 0.1 M, (b) 0.5 M, (c) 1 m, (d) 5 m, and (e) 10 m LiCl in H$_2$O (10 mL).

At 5 m LiCl the electrolyte is a 'water-in-salt' (WIS) electrolyte. This is when the amount of dissolved salt outnumbers the water molecules such that all the water molecules participate in the ion solvation shells. The lack of "free" water in these systems gives WIS electrolytes an advantageously wide ESW of up to 3 V.[18] This benefits the current system over previously reported membrane-free RFBs, which are inherently limited by the ESW of their aqueous phases. Using a WIS/ACN ITIES could therefore produce higher energy density batteries than the systems already in the literature.[19] Herein, the rest of this discussion refers to this WIS-electrolyte as the 'aqueous phase'.

Previous studies that discuss the ternary water-ACN-salt do not investigate the high concentration levels that exist in the WIS electrolyte.[17,20] Nor do these studies utilise these L/L interfaces for electrochemical means. Similar WIS/ACN concepts show promising performances for Zn-batteries and supercapacitors.[21,22] The concept is, however, yet to be reported in the RFB landscape. Therefore, employing the WIS/ACN L/L interface in a membrane-free RFB is a novel concept, and one of great interest for the progression of RFB technology. Regarding the applicability of WIS-electrolytes in an ORFB, one must consider the high cost of using such high salt concentrations. The high electrolyte cost may counteract the savings made from the energy density improvements and IEM removal.

A common ion must exist in both the aqueous and non-aqueous phases to maintain charge balance across the cell. Chapter 3.3. Figure 3.19.(b) shows 1 mM OFAQ has reversible electrochemistry with an $LiBF_4$ supporting salt. Applying $LiBF_4$ in the non-aqueous against a LiCl WIS aqueous phase would place Li^+ in both half-cells. $LiBF_4$ is not soluble in the WIS aqueous phase and so the cell can maintain charge-balance over the interface. The limited solubility and high concentration instability of OFAQ (Chapter 4.3.1) does, however, remain an issue for the future development of the system.

Figure 5.2. shows the CV plots for 1 mM OFAQ, 0.1M $LiBF_4$, ACN against 10 m LiCl in a three-electrode cell at scan rate 100 mV s^{-1}. The aqueous phase comprises 10 m LiCl to ensure full separation of the organic and aqueous media. During the tests, the CE is in either the organic (black line) or aqueous phase (red line) and the GC WE and Ag/Ag$^+$ RE are both in the organic phase. Placing the CE in each phase for respective tests identifies whether charge can pass the interface.

The CVs overlap almost exactly when the CE is in either phase, indicating successful charge transfer across the ITIES. Figure 5.2. records an $E_{1/2}$ = −0.76 V (*vs* Ag/Ag$^+$), ΔE_p = −0.11 V, and i_{pa}/i_{pc} = 0.94. The peak shape and separation compares closely to the CV in Chapter 3.3. Figure 3.20.(b) for 1 mM OFAQ, 0.1 M $LiBF_4$, ACN with no adjacent ACN phase. The i_{pa}/i_{pc} of near unity indicates chemical reversibility, and that contact with aqueous media does not

destroy the reduced OFAQ on the timescale of the CV. Additionally, the ITIES is stable over the CV scan and there is no visible mixing of the yellow organic phase into the colourless WIS phase.
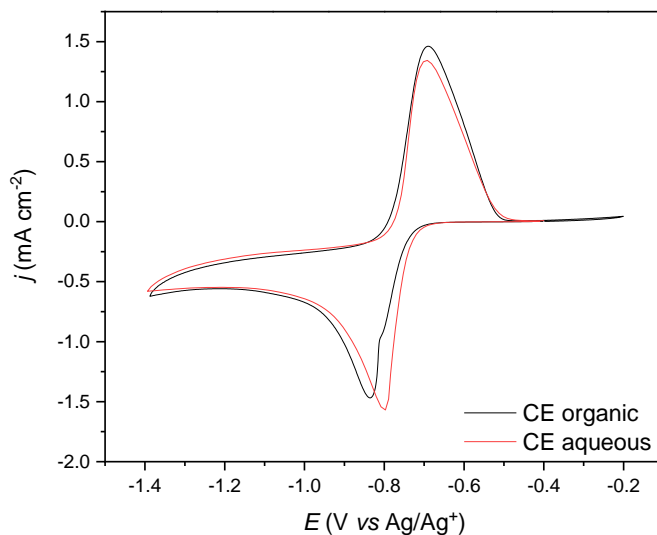
Figure 5.2. CV plots of 1 mM OFAQ, 0.1 M LiBF₄, ACN against 10 m LiCl where the CE is in the organic (black line) or the aqueous (red line) phase. Tests use a GC WE and an Ag/Ag⁺ RE in the organic phase and a scan rate 100 mV s⁻¹.

Neutral OFAQ is insoluble in the WIS and does not pass across the interface. The charged species will likely have a higher solubility in the aqueous phase than the neutral form. To function as an ORFB the ORAMs must remain in their respective phases in the charged and discharged forms. Chronoamperometry tests at −1.2 V (*vs* Ag/Ag⁺) for 6 hours using a three-electrode cell in the upper organic phase of the membrane-free system charges a large proportion of the OFAQ to its reduced state. Performing ¹⁹F-NMR studies on the aqueous phase after the test shows no F environments. This validates the robustness of the membraneless biphasic system in that the charged quinone does not pass into the aqueous phase.

SECM is a technique that studies ion transfer over L/L interfaces. This technique was applied to determine whether any OFAQ passes the interface into the aqueous phase after charging. If the product does not cross the interface, then the current recorded at the tip should increase upon approaching the surface, known as positive feedback. If the OFAQ²⁻ transfers into the aqueous phase then negative feedback is expected. Unfortunately, a degradation reaction involving OFAQ similar to that discussed in Chapter 4.3.1. occurs and passivates the WE. The UME WE in SECM has a large ratio of diffusion layer volume to electrode surface area. This effectively creates the high concentration conditions that increase the chance of OFAQ

degradation. Therefore, SECM cannot study whether ion-transfer occurs over this L/L interface.

5.2. Proof-of-Concept Water-in-Salt/Organic Membrane-Free Battery

5.2.1. Ferrocyanide/OFAQ

To function as a battery the aqueous phase requires a RAM to act as the catholyte to pair with the OFAQ anolyte. A common 'standard' catholyte in ORFB research used to compare the activity of novel ORAMs is the $K_3[Fe(CN)]_6/K_4[Fe(CN)]_6$ (ferri/ferrocyanide) reversible redox pair, with a redox potential of 0.36 V (*vs* SHE).[23–29] The solubility of ferrocyanide in ACN is <200 mM which makes it a good starting point for the membrane-free battery, as active material crossover should be minimal.[30] One should, however, consider the relatively low E^o, slow electron transfer kinetics on carbon, and propensity for follow-on reactions in the future feasibility of a $K_3[Fe(CN)]_6/K_4[Fe(CN)]_6$ based catholyte.

The CV plots in Figure 5.3.(a) for 2 mM $K_3[Fe(CN)_6]/K_4[Fe(CN)_6]$ in 10 m LiCl show how the high viscosity WIS results in quasi-reversible electrochemistry (ΔE_p = 0.09 V, $E_{1/2}$ = 0.44 V (*vs* Ag/AgCl)) and reversible chemistry (i_{pa}/i_{pc} = 0.97) at 100 mV s^{-1}. The RAM concentration is 2 mM to account for the two moles of electrons per OFAQ molecule, which is at a 1 mM concentration. The ΔE_p increases with scan rate from 0.079 to 0.145 V over 25 ≤ v ≤ 1000 mV s^{-1}. Figure 5.3.(b) gives the corresponding i_p *vs* $v^{1/2}$ plot for Randles-Ševčík analysis, which results in a D_o of 2.64 × 10^{-7} cm^2 s^{-1}.
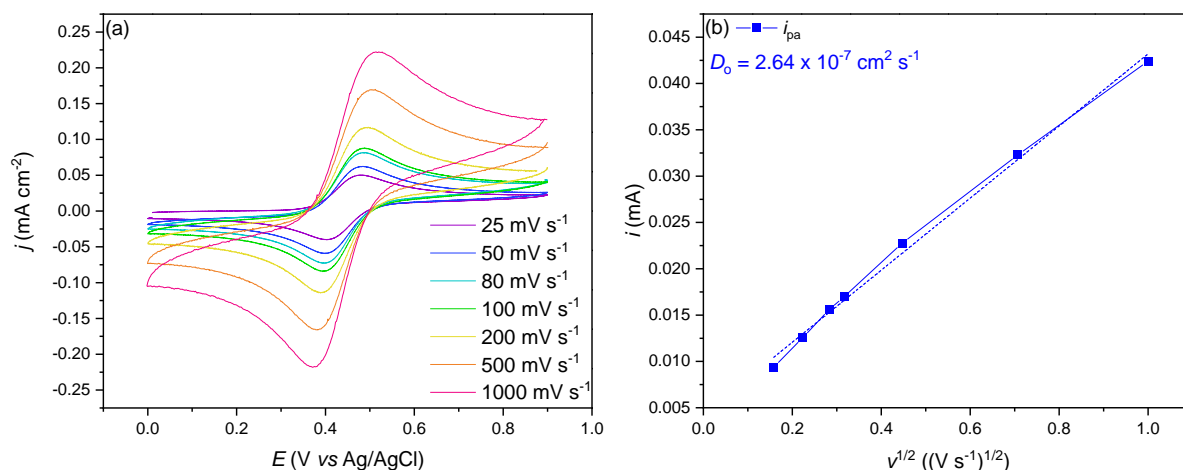
Figure 5.3. (a) CV plots and (b) corresponding i_p vs $v^{1/2}$ plot for 2 mM $K_4[Fe(CN)_6]$ in 10 m LiCl over scan rates 25 ≤ v ≤ 1000 mV s^{-1} using a GC WE, Ag/AgCl RE, and Pt CE.

The D_o value indicates slower mass transfer for $K_4[Fe(CN)_6]$ in the WIS than in conventional aqueous solvents (6.84 × 10^{-6} cm^2 s^{-1} in 1 M NH$_4$Cl$_{(aq)}$).[31] This suggests the higher viscosity of

the WIS electrolyte (2.52 mPa s at 293.15 K) may negatively affect the electrochemical performance of the positive half-cell.[32] The D_o is an order of magnitude slower than predicted from the difference in viscosities, but are similar to those for ferri/ferrocyanide in 10 m KF (1.94× 10^{-7} cm^2 s^{-1}).[33] This is because the Stokes- Einstein equation does not perfectly apply to highly viscous electrolytes. Thus, the viscosity attenuation on the D_o is much higher for very high concentration solutions.[33,34]

Figure 5.4.(a) shows notation for the full membrane-free cell, comprising a 2 mM K$_4$[Fe(CN)$_6$], 10 m LiCl catholyte and 1 mM OFAQ, 0.1 M LiBF$_4$, ACN anolyte. The double bar denotes the L/L interface. Figure 5.4.(b) calculates the theoretical OCV of the K$_4$[Fe(CN)$_6$]/OFAQ cell using the $E_{1/2}$ values of each individual half-cell at a scan rate of 100 mV s^{-1}. The theoretical OCV is 1.01 V. Each CV uses a three-electrode cell with a GC WE, Pt CE and an Ag/AgCl or Ag/Ag$^+$ RE for the aqueous and non-aqueous phases, respectively. For clarity, Figure 5.4.(b) converts both RE's to vs SHE (Ag/AgCl = +0.20 V, Ag/Ag$^+$ = +0.36 V (vs SHE)), which gives $E_{1/2}$ values of 0.64 V and −0.37 V (vs SHE) for K$_4$[Fe(CN)$_6$] and OFAQ, respectively. The electrode conversions were calculated from ferri/ferrocyanide blank tests in both aqueous and non-aqueous conditions. Figure 5.4.(c) shows the corresponding two-electrode cell CV at scan rate 5 mV s^{-1}. Figure 5.4.(d) gives the charge-discharge profiles for the second and sixtieth cycles, and Figure 5.4.(e) the cycling stability and performance over 60 cycles. The schematic in Chapter 2.3.4., Figure 2.7. describes the electrochemical cell for the static membrane-free tests in Figure 5.4.(c) and (d). The equation for calculating CE_{ff} is in Chapter 1.2.2., Equation 1.8.

The theoretical OCV of 1.01 V (Figure 5.4.(b)) does not improve over the benchmark VRFB cell voltage (1.25 V).[3] One should note that the K$_4$[Fe(CN)$_6$]/OFAQ cell is only a proof-of-concept system and utilising a catholyte with a more positive redox potential would improve the cell potential. Additionally, the benefits from removing the IEM may outweigh the loss in cell voltage.

The cell tests in Figures 5.4.(c) to (e) probe the viability of charge-transfer across the ITIES in a static system. Studying the static performance of the membrane-free system permits understanding of the electrochemistry without the additional complications created by flowing electrolytes. The two-electrode cell CV in Figure 5.4.(c) shows a reversible redox wave at $E_{1/2}$ = 0.41 V (vs C), with ΔE_p = 0.19 V and i_{pa}/i_{pc} = 1.05. The $E_{1/2}$ lies near the half-way point in the theoretical cell voltage, indicating the CV process is that for the K$_4$[Fe(CN)$_6$]/OFAQ redox reaction. The ΔE_p is larger than theoretical value of 30 mV for a reversible two-electron transfer from the Nernst Equation in (Chapter 2.2.1., Equation 2.5.). The quasi-reversibility is possibly an artefact of the high viscosity of the WIS electrolyte, or cell resistance from a combination

of factors, such as slow electron transfer kinetics. The i_{pa}/i_{pc} of near unity indicates chemical reversibility on the timescale of the CV.

(a) $C\ Felt_{(s)}|K_4[Fe(CN)_6]_{(aq)}, 10\ m\ LiCl_{(aq)}||1\ mM\ OFAQ_{(ACN)}, 0.1\ M\ LiBF_{4(ACN)}|C\ Felt_{(s)}$
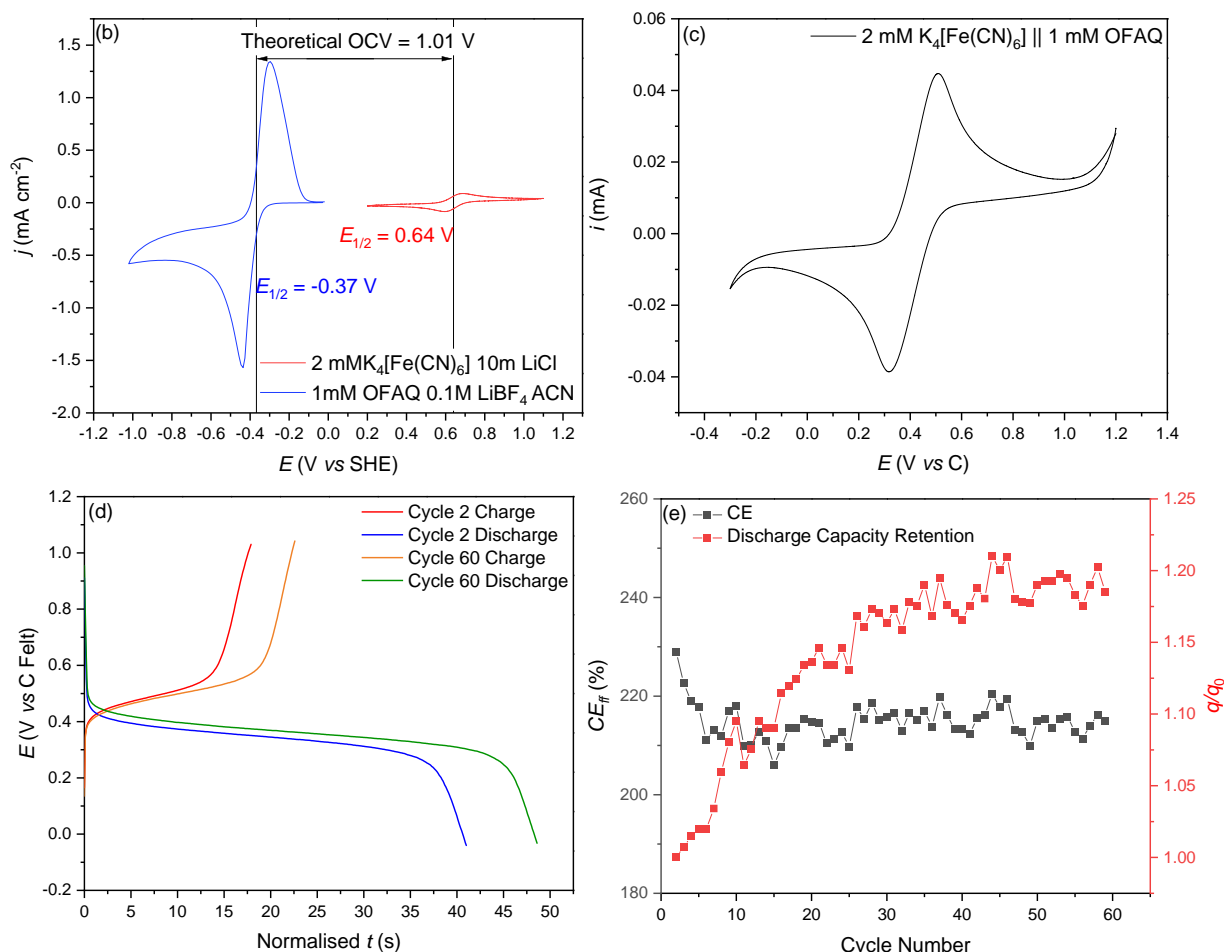
Figure 5.4. (a) Cell notation for the proof-of-concept WIS/ACN membrane-free battery, (b) separate three-electrode cell CV scans at 100 mV s⁻¹ on each half-cell using a GC WE, Pt CE, an Ag/Ag⁺ RE for the non-aqueous, and an Ag/AgCl RE for the aqueous systems. (c) The two-electrode cell CV plot for the $K_4[Fe(CN)_6]$/OFAQ system, using C felt electrodes at 5 mV s⁻¹. (d) Galvanostatic charge-discharge at 0.045 mA, showing cycle 2 (red and blue lines) and cycle 60 (orange and green lines) with potential cut-offs of 1.0 V and 0 V (vs C felt). (e) The corresponding CE_ff and discharge capacity retention for (d).

FRA potentiostatic impedance records a 110 Ω ohmic drop for the two-electrode system. This is similar to the R_u for the organic electrolyte with no adjacent aqueous phase. The ohmic resistance of the separated aqueous half-cell is only 8 Ω. The lower ionic conductivity of organic electrolyte likely causes it to be the more resistive phase (0.1 M LiPF₆, ACN σ = 50 mS cm⁻¹ whereas 10 m LiCl σ = 176 mS cm⁻¹).[35,36] Placing the electrodes as close together as possible should minimise this ohmic polarisation.

Reports on other membrane-free systems with organic electrolytes demonstrate large internal resistances.[14] However, one must consider that this is the total resistance for the entire system and that there are no further resistances from the inclusion of membranes. Reports suggest the interface itself is only responsible for around 5 % of the overall internal resistance of the cell.[15] This is important because in conventional RFB designs the membrane accounts for around 70 % of the total resistance.[13]

Figure 5.4.(d) gives the charge-discharge profiles of the $K_4[Fe(CN)_6]$/OFAQ cell using galvanostatic conditions defined by the i_p values in Figure 5.4.(c) of 0.045 mA. The battery voltage profile exhibits charging and discharging plateaus at 0.50 V and 0.34 V for the second cycle, which lie close to the $E_{1/2}$ of 0.41 V (V vs C) in the CV in Figure 5.4.(c) and the half-way point for the theoretical OCV (Figure 5.4.(b)).

The longer discharge plateau t in comparison to charge t for all cycles results in a CE_{ff} >100 % (Figure 5.4.(d)). Cycle 2 has a CE_{ff} of 229 %, which drops to 210 % over the first 11 cycles. The CE_{ff} then fluctuates between 210 and 220 % before ending at 215 % for Cycle 60. A CE_{ff} >100 % indicates side reactions in the electrolyte. These are possibly due to OFAQ degradation or a reaction between the anolyte and catholyte species when charged. These side reactions may also be causing the unusual increase in the discharge capacity retention (q/q_0) with cycle number. Wang et $al.$ observe a similar increase in discharge capacity in their membrane-free hybrid RFB, although it does not exceed 100 %.[30] The team attribute the increase to improved ionic conductivity of the organic electrolyte because of H_2O molecules transferring from the aqueous phase. The present system uses a WIS aqueous phase wherein there should be no "free" H_2O available to transfer, and thus this is unlikely to be causing the increase in discharge capacity in Figure 5.4.(e).

The j magnitude of the OFAQ redox wave in Figure 5.4.(b) is greater than for $K_4[Fe(CN)_6]$, despite having concentrations for an equal electron stoichiometry. This is possibly an artefact of the higher viscosity of the WIS electrolyte and suggests that higher catholyte concentrations are necessary to access the full OFAQ capacity. The ratio of difference between the OFAQ and $K_4[Fe(CN)_6]$ is 17.4 for both anodic and cathodic j values. The positive half-cell would therefore ideally contain 34.8 mM $K_4[Fe(CN)_6]$. However, $K_4[Fe(CN)_6]$ is not soluble to this concentration in 10 m LiCl which puts a limitation on the battery capacity.

Increasing the concentration of $K_4[Fe(CN)_6]$ to 20 mM causes additional problems. The $K_4[Fe(CN)_6]$ containing phase becomes increasing blue over galvanostatic charge-discharge experiments. A blue precipitate forms in the bottom of the cell after leaving the electrolyte to stand overnight. The blue precipitate is most likely Prussian Blue, a complex that forms via a reaction of ferric chloride and ferrocyanide.[37] Precipitation of the RAM is detrimental to the

battery capacity. Therefore, $K_4[Fe(CN)_6]$ is not suitable for the aqueous half-cell of the membrane-free RFB. The investigation consequently investigates other RAMs for the catholyte half-cell.

5.2.2. VOSO₄/OFAQ

Widening the identity of the catholyte RAM demonstrates the versatility of the membrane-free system. The archetypal VRFB uses the V^{4+}/V^{5+} redox couple in the form of acidic $VOSO_{4(aq)}$ as the positive half-cell. Pairing the non-aqueous OFAQ half-cell with a $VOSO_4$ WIS aqueous phase compares the membraneless design against the current market-leading chemistry.

Figure 5.5.(a) gives the full cell notation of the $VOSO_4$/OFAQ membrane-free cell. The aqueous, positive half-cell comprises 20 mM $VOSO_4$, 2 M HCl, 10 m LiCl and the non-aqueous, negative half-cell is as before. The catholyte concentration is a factor of twenty higher than the anolyte concentration to account for the discrepancy in j in Section 5.2.1. Figure 5.4.(b) between the 2 mM $K_4[Fe(CN)_6]$ and 1 mM OFAQ CVs. The $VOSO_4$ containing half-cell includes 2 M acid to stabilise the V^{4+}/V^{5+} process.[38] The acidification studies in Chapter 4.3.2. of this thesis confirm neutral OFAQ does not react with strong acids.

Figure 5.5.(b) images the $VOSO_4$/OFAQ interface, wherein the $VOSO_4$ WIS electrolyte populates the blue bottom phase and the OFAQ ACN electrolyte comprises the yellow top phase. The colour of the OFAQ solution becomes a brighter yellow after shaking with the $VOSO_4$ electrolyte but the interface remains stable. The new colour is similar to that seen when acidifying the OFAQ solution in Chapter 4.3.2. and may indicate some HCl crosses the interface to protonate the OFAQ. The cell tests used an equal electrolyte volume but only a small volume was transferred to the vial for the image. This did not affect the colours of the solutions.

The $E_{1/2}$ values of each individual half-cell ($VOSO_4$ $E_{1/2}$ = 1.35 V and OFAQ $E_{1/2}$ = −0.37 V (vs SHE)) at a scan rate of 100 mV s⁻¹ result in a theoretical OCV of 1.72 V (Figure 5.5.(c)). The theoretical OCV is wider than that of the archetypal VRFB. This demonstrates the improvements in energy density that can come from using ORAMs and alternate solvent systems. Figure 5.5.(d) shows the corresponding two-electrode cell CV at scan rate 5 mV s⁻¹ over potential ranges 0 – 2 V (purple line) and 0 – 1.6 V (red line) and the CV for the blank 10 m LiCl electrolyte (black dashed line). Figure 5.5.(e) gives the galvanostatic charge-discharge profile at 1.2 mA between the cut-off voltages 1.3 V and 0.6 V (vs C).

(a) $C\ Felt_{(s)}|20\ mM\ VOSO_{4(aq)}, 2\ M\ HCl_{(aq)}, 10\ m\ LiCl_{(aq)}||1\ mM\ OFAQ_{(ACN)}, 0.1\ M\ LiBF_{4(ACN)}|C\ Felt_{(s)}$
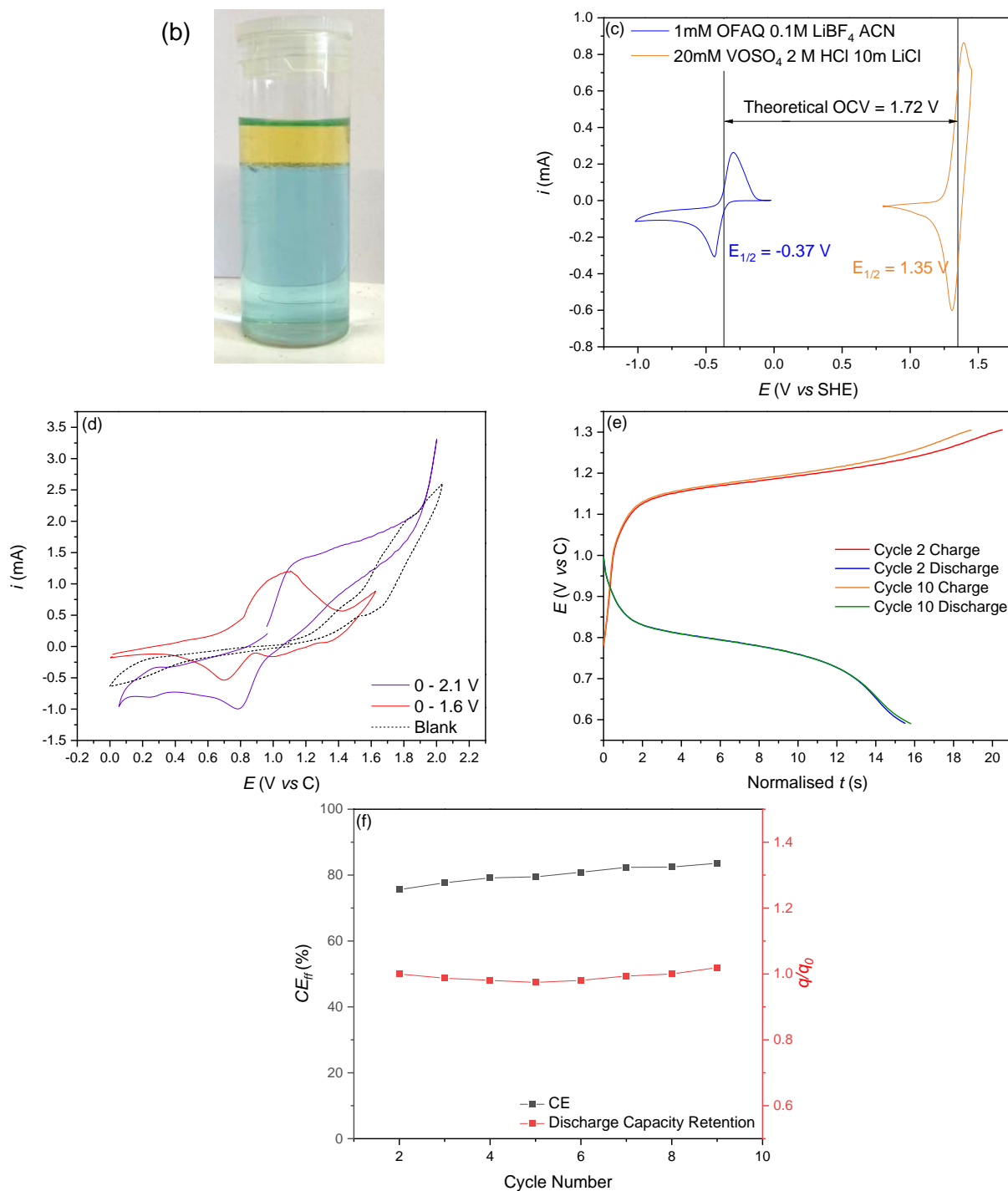
Figure 5.5. (a) Cell notation for the VOSO₄/OFAQ membrane-free battery, (b) a photograph of the VOSO₄/OFAQ ITIES, (c) the CV plots for the individual half-cells at 100 mV s⁻¹. The non-aqueous half-cell comprises 1 mM OFAQ, 0.1 M LiBF₄, ACN and uses a GC WE, Pt CE and Ag/Ag⁺ RE. The aqueous half-cell is 20 mM VOSO₄, 2 M HCl, 10 m LiCl, C Felt WE, Ag/AgCl RE, and Pt CE. (d) CV for the blank 10 m LiCl electrolyte (black dashed line) and VOSO₄/OFAQ cell (purple and red lines) using a two-electrode cell with C felt electrodes at 5 mV s⁻¹. (e) Galvanostatic charge-discharge profile of VOSO₄/OFAQ at 1.2 mA between 1.3 V and 0.6 V (vs C) and (f) the corresponding cycling stability.

The VOSO$_4$ i_p values in Figure 5.5.(c) are much higher than for the OFAQ. This is due to the higher surface area of the C felt WE in the VOSO$_4$ experiment compared to the GC WE for the OFAQ. Due to nature of felt electrodes, an accurate surface area of the C felt WE is unknown. A high surface area WE is necessary due to the sluggish kinetics of the V^{4+}/V^{5+} reaction on carbon electrodes. These sluggish kinetics place the V^{4+} oxidation potential close to that for chlorine evolution (E^o = 1.36 V (*vs* SHE) at 1 M HCl).[39] The potential must be kept beneath this value to prevent the evolution of Cl$_{2(g)}$. It is this Cl oxidation that causes the rising *i* towards the more positive potentials in the blank electrolyte and wider potential scan in Figure 5.5.(d) (black dashed line and purple line).

Keeping the upper potential range beneath 1.6 V (*vs* C) (Figure 5.5.(d) red line) avoids chlorine oxidation and produces a redox wave where $E_{1/2}$ = 0.90 V (*vs* C) and ΔE_p = 0.40 V. The $E_{1/2}$ lies near to the halfway potential for the theoretical OCV, confirming the electrochemical response is due to the VOSO$_4$/OFAQ redox reaction. The chemical reversibility is unfortunately rather poor, recording an i_{pa}/i_{pc} ratio of 2.23. However, the presence of both an oxidation and returning reduction wave indicates that charge-transfer is occurring over the interface. The wide ΔE_p and i_{pa}/i_{pc} over unity indicate the process is not completely reversible and there may be side reactions between the charged species. There is no visible reaction between the phases during testing. Additionally, the interface and respective half-cell colours appear stable even after long-charging times.

The galvanostatic charge-discharge profiles in Figure 5.5.(e) show charge and discharge voltage plateaus at 1.19 V and 0.78 V (*vs* C), respectively. These expectedly lie just above and below the $E_{1/2}$ of the full cell CV ($E_{1/2}$ = 0.90 V (*vs* C). The CE_{ff} values are 76 % and 84 % for Cycle 2 and Cycle 10, respectively, and the corresponding discharge capacities (*q*) are 5.16 × 10^{-5} mA h and 5.26 × 10^{-5} mA h. The discharge capacity retention over 10 cycles is around 100 %. The stable CE_{ff} and q/q_0 of the VOSO$_4$/OFAQ battery over the K$_4$[Fe(CN)$_6$]/OFAQ battery indicate a reduction in side reactions with the VOSO$_4$ catholyte. The plateau potential for the cell in Figure 5.5.(e) does not change over the 10 cycles, with charge and discharge plateau potentials of 1.19 V and 0.78 V (*vs* C). The lack of change in the overpotential indicates the side reactions causing the low CE_{ff} are not detrimental to the battery over 10 cycles.

The final CE_{ff} of 84 % and capacity retention near 100 % is above that of other reported non-aqueous membrane-free batteries. For example, the BQ/4-OH-TEMPO system by Navalpotro *et al.* records a CE_{ff} of 75 % and discharge capacity retention of 85 %.[9,15] Additionally, the ohmic drop, which is the drop in *E* at the start of the discharge curve, is around 310 mV which is near that reported for other membrane-free devices.[9]

The charge profile does not show the rapid rise in current near the potential cut-off (the concentration overpotential) that indicates a fully charged system. Increasing the cut-off potential to 1.6 V at a current of 1.5 mA in Figure 5.6.(a) reveals a secondary charging plateau at approximately 1.56 V (*vs* C).
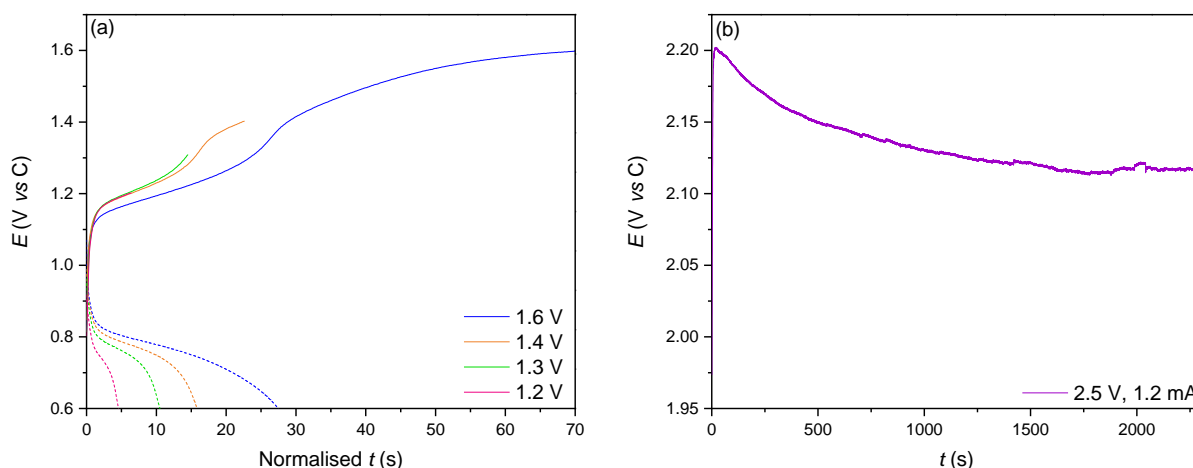
Figure 5.6. Galvanostatic charge-discharge profile of the $VOSO_4$/OFAQ membrane-free static battery at 1.5 mA with the upper potential cut-off's: 1.6 V (blue line), 1.4 V (orange line), 1.3 V (green line), and 1.2 V (pink line). The full and dashed lines represent charging and discharging profiles, respectively. (b) The charge profile for the $VOSO_4$/OFAQ system at 1.2 mA with the upper potential cut-off of 2.5 V (vs C).

When the upper cut-off potential is above >2 V with a 1.2 mA current (Figure 5.6.(b)) produces a current profile that peaks at 2.20 V (*vs* C) and then plateaus at 2.11 V (*vs* C) without reaching the upper cut-off voltage. These secondary plateaus are attributed to the aforementioned $Cl_{2(g)}$ evolution reaction and demonstrate the upper limit of this $VOSO_4$/OFAQ battery is 1.4 V (*vs* C).

Over the course of testing, the L/L interface remains stable to the eye and the electrolyte colours do not appear to mix. Chronoamperometry and ^{19}F-NMR tests similar to those described in Section 5.1. show no F environments in the aqueous phase after charging the OFAQ half-cell. This corroborates that charged forms of OFAQ do not pass through the interface to the aqueous phase in the static system. However, considering the small area of the L/L interface, the low ORAM concentration, and the relatively large volume of electrolyte, it is possible that the amount of crossover is small and easily missed in analysis. The high sensitivity of NMR means even small amounts of crossover should show evidence in the aqueous phase. However, the static nature of the system means that the sample area for the analysis solution may lie too far from the interface for crossover material to have reached yet via diffusion. Overall, the lack of F environments in the aqueous half-cell indicates the CE_{ff} of

<100 % is more likely a result of interfacial self-discharge rather than from active material cross-migration.

Galvanostatic charging and discharging of the VOSO$_4$/OFAQ battery at various currents, (1.5 mA, 1.2 mA, and 1.0 mA) between the cut-off voltages 1.3 V to 0.6 V (*vs* C) gives insight to the rate performance. Figure 5.7.(a) gives the charge-discharge profiles and Figure 5.7.(b) shows the trend in efficiencies as a function of *i*. The electrochemical data is in Table 5.1.

The *CE$_{ff}$* increases from 76.8 % to 77.9 % and the *VE$_{ff}$* decreases from 67.7 % to 62.1 % as the current rises. The increase in *CE$_{ff}$* is subtle and may be within the error of these values. Although the increase may also be due to the shorter cycling time for a given cell capacity at a higher current. The shorter cycling time means less self-discharge and side reactions can occur. The decrease in *VE$_{ff}$* is because the higher current leads to higher electrochemical and ohmic polarisation losses. The effect of the increased polarisation on the *VE$_{ff}$* is more detrimental than the reduction in self-discharge and side reaction rates of the *CE$_{ff}$*. This results in an overall decrease in the *EE$_{ff}$* with increasing current. The efficiencies in this cell are similar to those in the leading membrane-free static batteries.[14,15]

The discharge capacity of the VOSO$_4$/OFAQ cell decreases with increasing discharge current. This is evidence that self-discharge and ion-crossover are not detrimental to the function of the static battery at these currents. If self-discharge or diffusion of ions across the interface were occurring on a dominant level, then the discharge capacity would decrease with decreasing discharging current. This is because the effective residence time for charged materials in the cell is longer at lower currents. A longer residence time would amplify the detrimental effects of self-discharge or ion-crossover.

The theoretical gravimetric capacity of OFAQ is 152.21 mA h g^{-1}. The low OFAQ concentration means it is likely to be the capacity limiting half-cell for the membrane-free system. The uncertain electron stoichiometry for OFAQ with a LiBF$_4$ supporting salt (see Chapter 3.3.) makes accurate assumptions of the theoretical energy density and capacity challenging. Assuming an electron stoichiometry of two, the theoretical energy density ($E_{d,t}$) and theoretical capacity (q_t) for a 1 mM OFAQ half-cell are 9.22×10^{-2} W h L^{-1} and 5.36×10^{-1} mA h, respectively (Chapter 1.2.2., Equations 1.3. and 1.4.). This equates to a 53.6 mA h L^{-1} volumetric theoretical capacity ($q_{t,v}$) for the OFAQ half-cell. The current analysis in Chapter 3.3., Figure 3.21 concludes an average electron stoichiometry of 5 due to the possible ongoing electrodeposition mechanism. This would yield an $E_{d,t}$ of 2.30×10^{-1} W h L^{-1}, a q_t of 1.34 mA h, and a $q_{t,v}$ of 134 mA h L^{-1}.
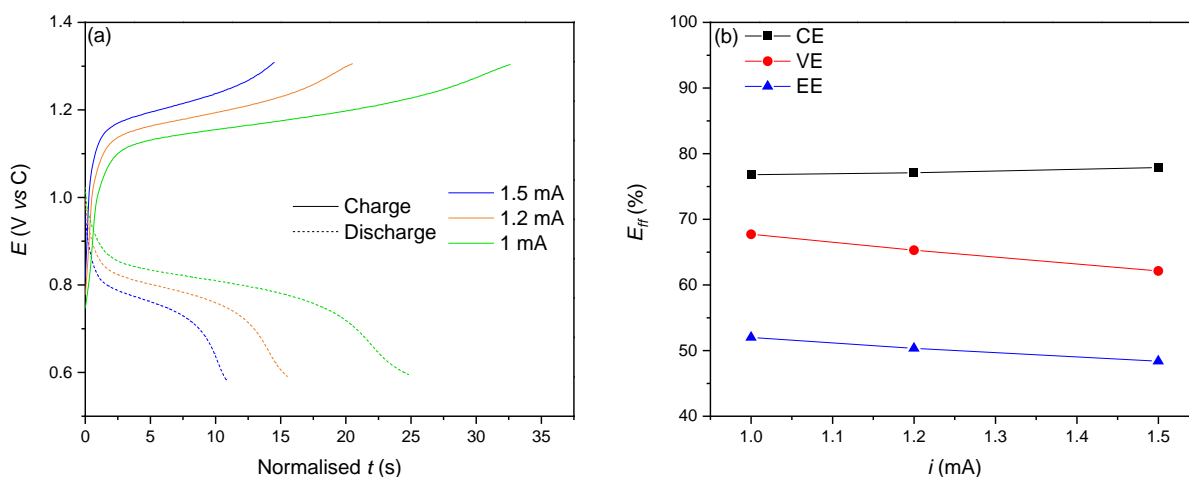
Figure 5.7. (a) Galvanostatic charge-discharge profiles for the VOSO₄/OFAQ static membrane-free battery at various currents and (b) the corresponding coulombic, voltage, and energy efficiencies.

Table 5.1. Cell performance for the VOSO₄/OFAQ membrane-free battery at various currents between the cut-off potentials 1.3 V and 0.6 V.

Discharge Current (mA)	Ohmic Drop (mV)	CE_{ff} (%)	VE_{ff} (%)	EE_{ff} (%)	Discharge Capacity (mA h)
1.0	274	76.8	67.7	52.0	6.75×10^{-3}
1.2	310	77.1	65.3	50.3	5.06×10^{-3}
1.5	322	77.9	62.1	48.4	4.38×10^{-3}

The experimental discharge capacity is much lower than the q_t for either value of *n*. For example, Cycle 2 of the VOSO₄/OFAQ battery at 1.2 mA only has discharge capacity of 5.06 × 10⁻³ mA h. Real systems will always have a lower q than q_t. This is due to several factors, such as the cell overpotential resulting in a <100 % RAM utilisation and side reactions.[40] The static nature of the cell will also contribute to the low capacity utilisation.

Thus far, the membrane-free cells in this Section demonstrate successful charge-transfer over the 10 m LiCl/ACN L/L interface with a Li⁺ common ion. The static systems do not show evidence of OFAQ passing the interface in either the neutral or charged states. The reversible CVs in Figures 5.4.(c) and 5.5.(d) alongside the charge-discharge plateaus in Figures 5.4.(d) and 5.5.(e) are evidence of the proof-of-concept membrane-free battery functioning. The poor CE_{ff} and discharge capacity retention of both cells suggest self-discharge and side reactions hinder the battery performance. These side reactions may be due to the OFAQ degradation discussed throughout Chapter 4., or possibly a chemical reaction between the oxidised catholyte and reduced anolyte. The side reactions decrease the durability of the membrane-free battery. Widening the identity of the RAMs may serve to improve the performance.

5.2.3. 4-OH-TEMPO/OFAQ

The cell demonstrations in Sections 5.2.1. and 5.2.2. combine the novel ORAM OFAQ with the inorganic RAMs $K_4[Fe(CN)_6]$ and $VOSO_4$. These systems improve over previous RFB designs through the removal of the high cost, resistance causing, and lifetime-limiting IEM. However, in using inorganic RAMs for the catholyte the batteries still rely on scarce and expensive metallic resources. Replacing the inorganic catholyte species with an ORAM removes this limitation and further improves the battery design. The investigation therefore moves to developing a fully ORAM-based membrane-free battery.

A common organic positive redox couple in the ORFB literature is TEMPO which has a redox potential of 0.75 V (*vs* SHE).[15] The 4-OH-TEMPO derivative has a higher water solubility (2.1 M) and a slightly more positive redox potential of 0.81 V (*vs* SHE).[41] These characteristics make it a more appealing catholyte for the proposed system.

Figure 5.8.(a) shows the CV plots for 2 mM 4-OH-TEMPO in the 10 m LiCl WIS over scan rates $25 \le v \le 1000$ mV s^{-1}. The corresponding i_p *vs* $v^{1/2}$ plot in Figure 5.8.(b) shows a linear relationship with a D_o of 2.89×10^{-7} cm^2 s^{-1}. As in Section 5.2.1. with $K_4[Fe(CN)_6]$, the low D_o indicates slower mass transport than in conventional aqueous solvents ($D_o = 3.14 \times 10^{-6}$ cm^2 s^{-1} in 0.5 M KCl).[42] The ΔE_p is near that of an electrochemically reversible process ($\Delta E_p = 0.071$ V at 100 mV s^{-1}) despite the low D_o. The rapid redox kinetics suggest the 4-OH-TEMPO performance in the WIS electrolyte is feasible for applications in an ORFB half- cell.
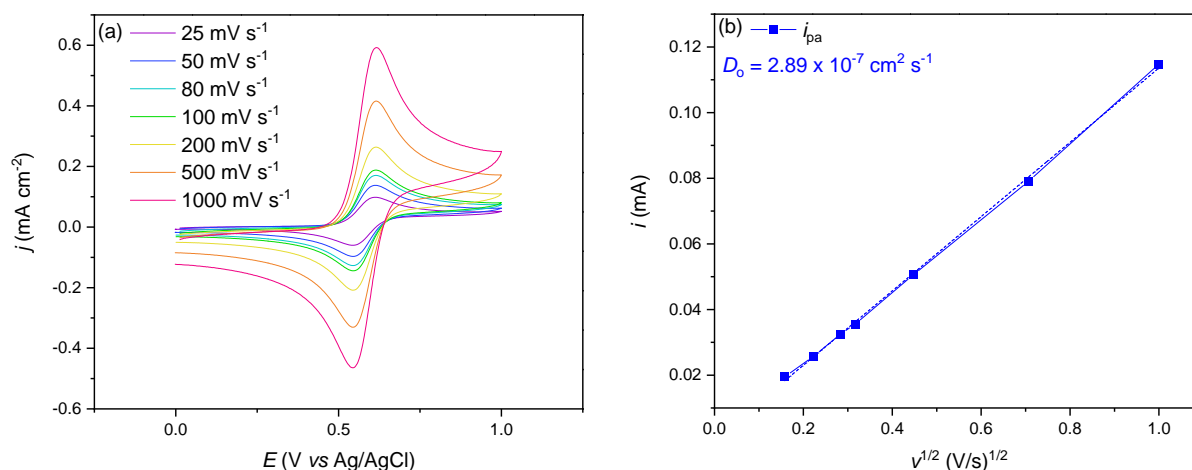
Figure 5.8. (a) The CV plot for 2 mM 4-OH-TEMPO in 10 m LiCl with (b) showing the corresponding i_p vs $v^{1/2}$ plot and resulting diffusion coefficient.

Figure 5.9.(a) gives the cell notation and (b) the theoretical OCV for the 4-OH-TEMPO/OFAQ battery. The theoretical OCV of 1.15 V is lower than the benchmark VRFB system (1.25 V)[3] and the $VOSO_4$/OFAQ cell in Section 5.2.2. (1.72 V). However, the 4-OH-TEMPO/OFAQ

membrane-free cell involves only organic redox couples and thus is free from the high costs and geopolitical complications that accompany inorganic RAMs.

(a) $C\ Felt_{(s)}|2\ mM\ 4-OH-TEMPO_{(aq)}, 10\ m\ LiCl_{(aq)}||1\ mM\ OFAQ_{(ACN)}, 0.1\ M\ LiBF_{4(ACN)}|C\ Felt_{(s)}$
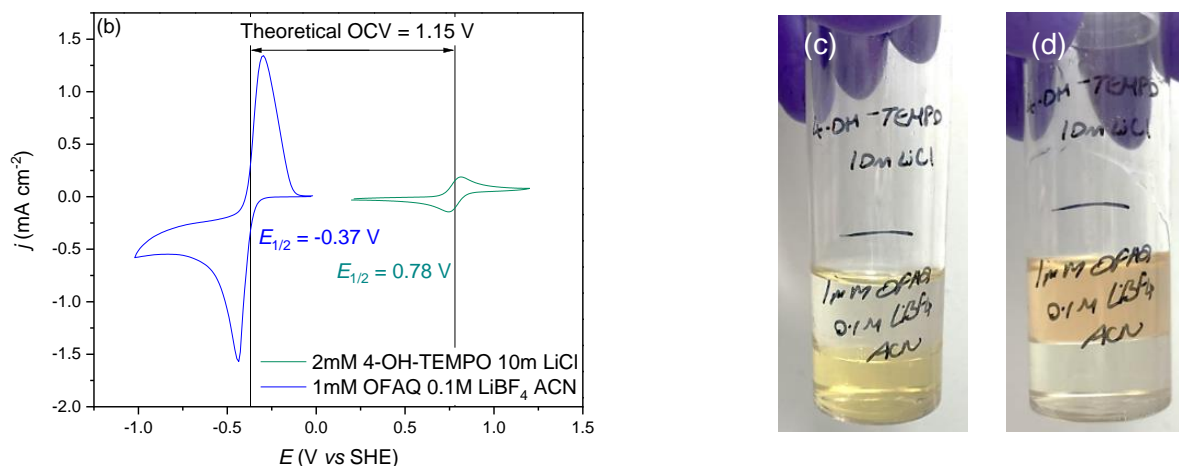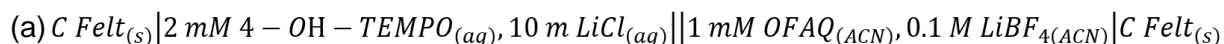
Figure 5.9. (a) Cell notation for the 4-OH-TEMPO/OFAQ WIS/ACN membrane-free battery. (b) Theoretical OCV from the three-electrode cell CV scans on the individual half-cells at 100 mV s⁻¹. The non-aqueous half-cell (blue line) uses a GC WE, Ag/Ag⁺ RE, and Pt CE. The aqueous half-cell (green line) uses a GC WE, Ag/AgCl RE, and Pt CE. (c) and (d) Photographs of the 4-OH-TEMPO/OFAQ L/L interface before (c) and after (d) shaking.

Figure 5.9.(c) shows the ITIES that forms when placing the OFAQ-containing ACN electrolyte on top of the 4-OH-TEMPO-containing WIS electrolyte. The 4-OH-TEMPO creates a bright yellow lower aqueous phase compared to the paler upper OFAQ-containing organic phase. After shaking, the yellow colour of the bottom phase becomes less intense, and the upper phase turns orange (Figure 5.9.(d)). This unfortunately indicates 4-OH-TEMPO is soluble in the ACN and passes the interface in its neutral form.

The propensity for the 4-OH-TEMPO to cross the interface means it is not a suitable ORAM for the WIS/ACN membrane-free ORFB. Interestingly, the CV tests in Figure 5.10.(a) on the undisturbed electrolyte (pictured in Figure 5.9.(c)) at 5 mV s⁻¹ show a redox wave centred at $E_{1/2} = 0.50$ V (vs C), with $\Delta E_p = 0.20$ V and $i_{pa}/i_{pc} = 1.17$. The $E_{1/2}$ lies near that for the halfway potential of the theoretical OCV, and the ΔE_p and i_{pa}/i_{pc} values indicate electrochemical and chemical quasi-reversibility or irreversibility.

Figure 5.10.(b) shows the first 10 cycles of the galvanostatic charge-discharge profiles using the cut-off voltages 0.8 V and 0.4 V (vs C) and charging current of 0.05 mA. Figure 5.10.(c) compares the profiles for the second, sixth, and hundredth cycles. The similarity in the charge discharge profiles over cycling indicates a stable system if the interface is not disturbed.
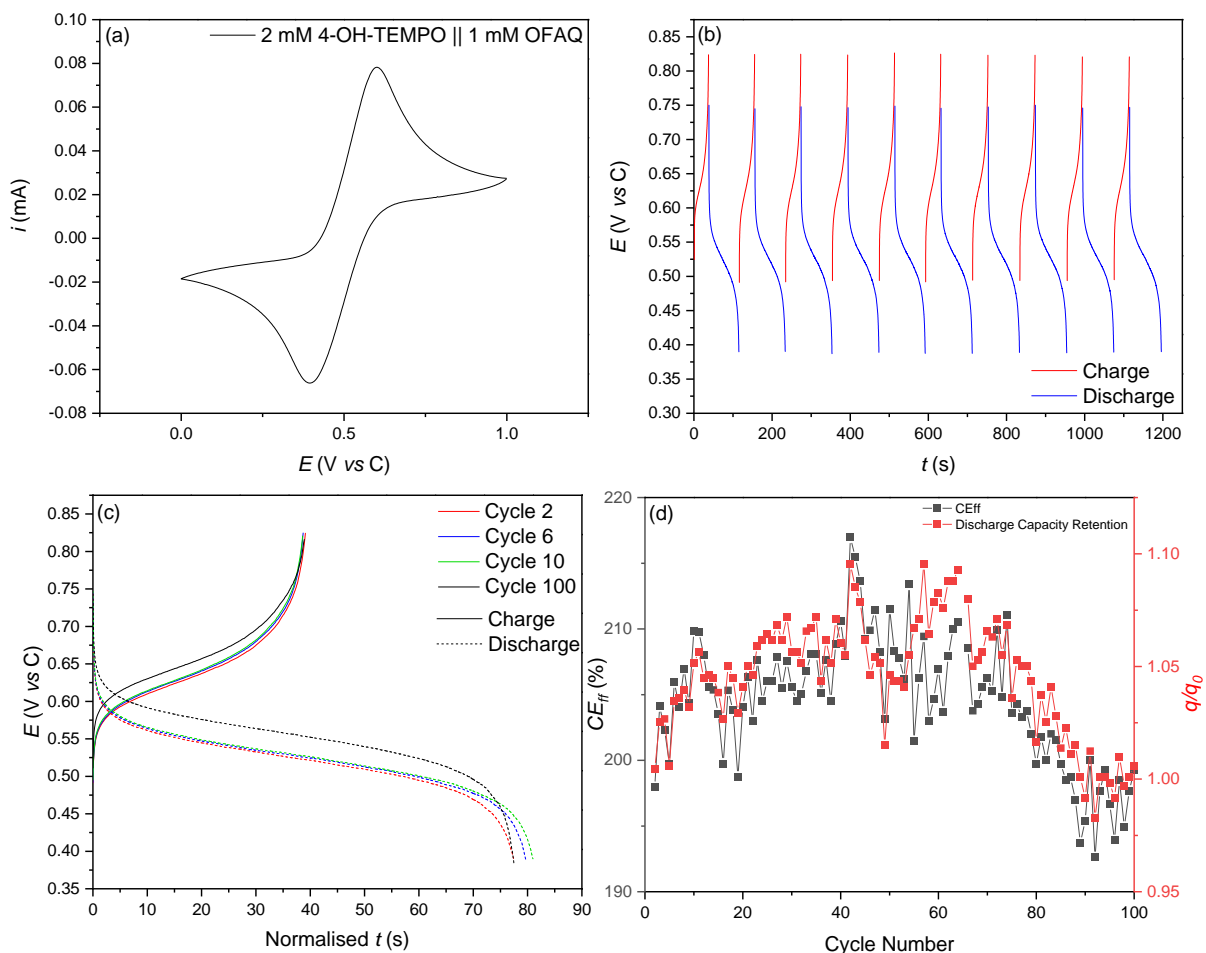
Figure 5.10. (a) CV scan for 4-OH-TEMPO/OFAQ before shaking, in a two-electrode cell comprising two C felt electrodes at 5 mV s⁻¹. (b) The first 10 cycles of the galvanostatic charge-discharge profiles with cut-off voltages 0.8 and 0.4 V (vs C) at a 0.05 mA current. (c) A comparison of the second, sixth, and hundredth cycle and (d) the cycling stability over 100 cycles.

The profiles in Figure 5.10.(c) show sloping curves for both charge and discharge processes, with the respective potentials at $t_{1/2}$ of 0.64 V and 0.52 V (*vs* C) for Cycle 2. Figure 5.10.(d) shows the CE_{ff} fluctuates in a curve over cycling but begins at 198 % and ends at 199 %. A CE_{ff} >100 % is indicative of side reactions, but the lack of overall change in the CE_{ff} suggests this is not detrimental to the battery performance. The discharge capacity retention follows a similar curved trend over cycling, but retains 100 % of its initial capacity in Cycle 100.

Despite the promising battery performance, the crossover of 4-OH-TEMPO to the non-aqueous phase after agitation means the ORAMs will not stay separate when under flow. Figure 5.11.(a) gives the CV on the 4-OH-TEMPO/OFAQ system after agitating and mixing the layers. Comparing the CV plots before (Figure 5.10.(a)) and after (Figure 5.11.(a)) mixing the electrolyte shows how the process changes from a quasi-reversible redox process to an irreversible oxidation at E_{pa} of 0.78 V (*vs* C) with no return reduction. There is also an additional oxidation peak at 0.05 V (*vs* C).

Figure 5.11.(b) shows the galvanostatic charge-discharge profiles performed at the same conditions as on the cell before mixing the electrolytes. None of the discharge profiles in the mixed system reaches a plateau, indicating the battery ceases to function. Interestingly, the first charging cycle does achieve a voltage plateau at around 0.47 V (*vs* C) and reaches the upper cut-off voltage after 267 s. The voltage reached in this charging cycle is slightly lower than the discharge voltage in the non-mixed electrolyte (0.52 V (*vs* C)).
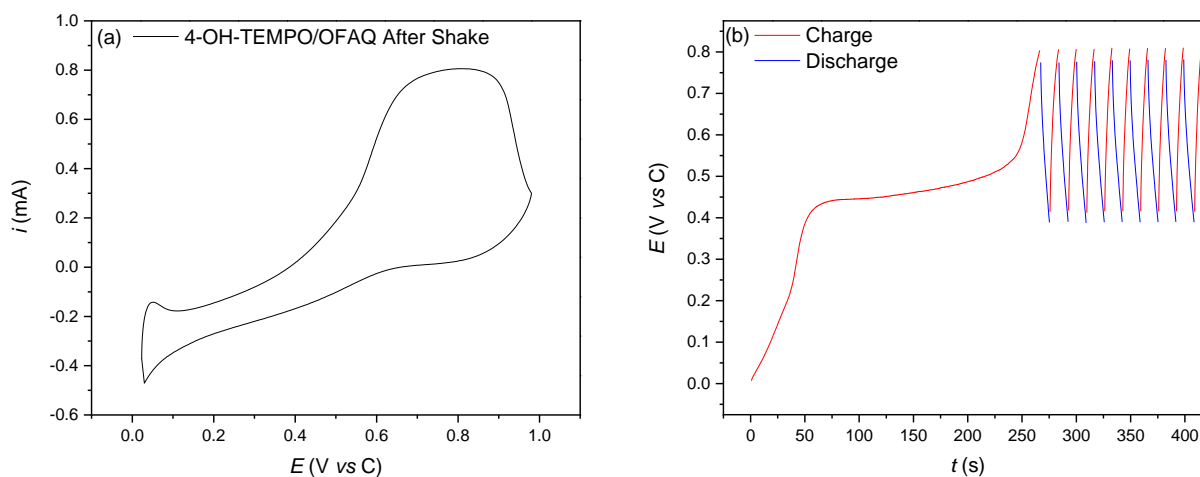
Figure 5.11. (a) The CV plot for the 4-OH-TEMPO/OFAQ membrane-free cell at 5 mV s^{-1} after agitation. (b) The corresponding galvanostatic charge-discharge profiles at the constant current off 0.05 mA and cut-off potentials of 0.8 V and 0.4 V over 10 cycles.

The presence of a voltage plateau in the first charging cycle and not in any subsequent profiles is indicative of self-discharge and cross-migration. The interface no longer separates the ORAMs and thus they immediately self-discharge after the initial charging process. Therefore, the battery does not hold charge or discharge during cycling after 4-OH-TEMPO populates the ACN half-cell. A similar phenomena occurs in the TEMPO/BQ membrane-free battery by Navalpotro *et al.*[15] This shows the 4-OH-TEMPO/OFAQ system is not useful for a WIS/ACN ITIES-based membrane-free ORFB.

5.3.   Water-in-Salt/Organic Membrane-Free Redox Flow Battery

Most literature on membrane-free devices only study the systems under static conditions and do not involve flowing electrolytes.[9] This makes conceptualising the static systems into full-scale ORFBs challenging, as incorporating flow has large effect on battery performance. Flowing the electrolytes perturbs the L/L interface and propagates the mixing of the anolyte and catholyte due to convective mass transport. This exacerbates self-discharge and active material crossover from one half-cell to the other. Previous literature that do involve flowing

electrolytes in membrane-free devices combat this by using low-concentration electrolytes, operating at relatively low flow rates, or using microfluidic devices.[10,43] However, this still makes envisioning scalable membrane-free ORFB systems difficult.

All the cells in this chapter so far are static membrane-free systems. Static cell cycling is useful for understanding the electrochemistry of the RAMs over the novel WIS/ACN L/L interface. However, as discussed, it is difficult to extrapolate this data for a flow device. Side reactions and self-discharge processes are ubiquitous in all the cells so far. These are, unfortunately an inherent issue in all membrane-free devices due to the thermodynamic driving force for cross-migration of charged species.[44] It is therefore useful to study the effect of electrolyte flow on the rate of these processes. Employing flow should reduce the propensity for self-discharge, as flow lowers the residence time for oxidised/reduced material at the interface where it reacts.

The $VOSO_4$/OFAQ battery shows the best performance of the cells in Section 5.2. The CE_{ff} of 84 % is better than the leading non-aqueous based static membrane-free device.[15] Therefore, this system is of most interest to study under flow. Chapter 2.3.4, Figure 2.8. describes the in-house designed flow-cell for studying membrane-free battery systems. Connecting the cell to a peristaltic pump at the flow rates 16.8, 32.4, and 37.2 ml min^{-1} and filling the chamber with an electrolyte analogous to that in Section 5.2.2. creates a flowing, membrane-free device. The upper layer consists of the yellow 1 mM OFAQ, 0.1 M $LiBF_4$, ACN and the lower layer the blue 20 mM $VOSO_4$, 2 M HCl, 10 m LiCl. Only the aqueous layer is subject to flow. Systematically stepping the study from static, to single-flow, to dual flow, should help understand the changes that occur from flowing electrolytes. The poor performance of the systems under a singularly flowing electrolyte mean this work does not extend to a dual flow system. Dual flow should be scope for future development of these membrane-free systems.

Chapter 2.3.4. discusses the cell design and experimental process for the flow tests in this section. The flow cell has a different geometry to the static membrane-free cell used in Section 5.2. The interfacial surface area of the static cell is 6.51 cm^2 and the flow cell is 3.41 cm^2. As the interface plays a critical role in the charge-transfer of the battery, a change in the interfacial surface is likely to affect the performance. Additionally, the flow cell holds less electrolyte and is open to air, which may also affect the results. The open nature of the cell presents challenges for long-term cycling studies due to the volatile nature of the upper ACN electrolyte. Repeating the static cell cycling tests in the flow cell allows for a fair comparison to the studies under flow.

Herein, tests comprise the same $VOSO_4$/OFAQ battery composition under a range of flow rates using the in-house designed flow cell discussed in Chapter 2.3.4. The galvanostatic

charge-discharge experiments use cut-off voltages of 1.4 V and 0.4 V (*vs* C) at a constant current of 1.2 mA for 10 cycles. The flow conditions are:

a) 0 mL min^{-1} (static cell)
b) 16.8 mL min^{-1}
c) 32.4 mL min^{-1}
d) 37.2 mL min^{-1}

The interface is stable under flowing conditions. Even the highest flow rates show no visible mixing of the blue and yellow layers. The layers remain their respective colours over cycling, and do not become the 'green' indicative of V^{5+} or red colour expected of $OFAQ^{2-}$. This indicates only small quantities of the RAMs are undergoing charge-discharge reactions.

Figure 5.12. gives the galvanostatic charge-discharge profiles for the $VOSO_4$/OFAQ cell under (a) static conditions, and under flow rates of (b) 16.8 mL min^{-1}, (c) 32.4 mL min^{-1}, and (d) 37.2 mL min^{-1}. Table 5.2. compares the charge and discharge times for the first, fifth and tenth cycles. The system maintains a stable cycling performance in the static test (Figure 5.12.(a)) and at the slowest flow rate (Figure 5.12.(b)).

Increasing the flow to >30 mL min^{-1} (Figures 5.12.(c) and (d)) changes the charge-discharge profile such that it goes through three distinct stages. Initially, the charge-discharge is similar to the systems with no, and low flow (Figures 5.12.(a) and (b)). Next, the faster pace systems demonstrate an extended charging *t* with a comparably short discharge *t*. After a few cycles of the longer charging *t*, the process enters a third phase wherein the charging step shortens again and the discharge remains rapid. The cycle at which each of these steps occurs is sooner at higher flow rates, indicating the increasing flow rate is causing the change. For example, the charge profile takes until Cycle 5 to extend in *t* at 32.4 mL min^{-1} but this occurs by Cycle 2 at 37.2 mL min^{-1}. The third phase in the charge-discharge profiles of Figures 5.12.(c) and (d) is likely due to side reactions of the RAMs. The products of these side reactions may not be redox active, or have higher solubility in adjacent phases. This will disrupt the redox pathway and prevent the system from holding charge.

Comparing the charge and discharge times for the first, fifth, and tenth cycles over the different flow rates demonstrates the change (Table 5.2.). At the slowest flow rate, 16.8 mL min^{-1}, Cycle 1 and Cycle 5 have charge and discharge times of 57 s and 26 s, and 43 s and 32 s, respectively. Stepping the flow rate to 32.4 mL min^{-1} maintains a similar response in Cycle 2, with 41 s and 16 s for charge and discharge, respectively. The fifth cycle, however, increases the charging *t* to 339 s, with only a 53 s discharge.
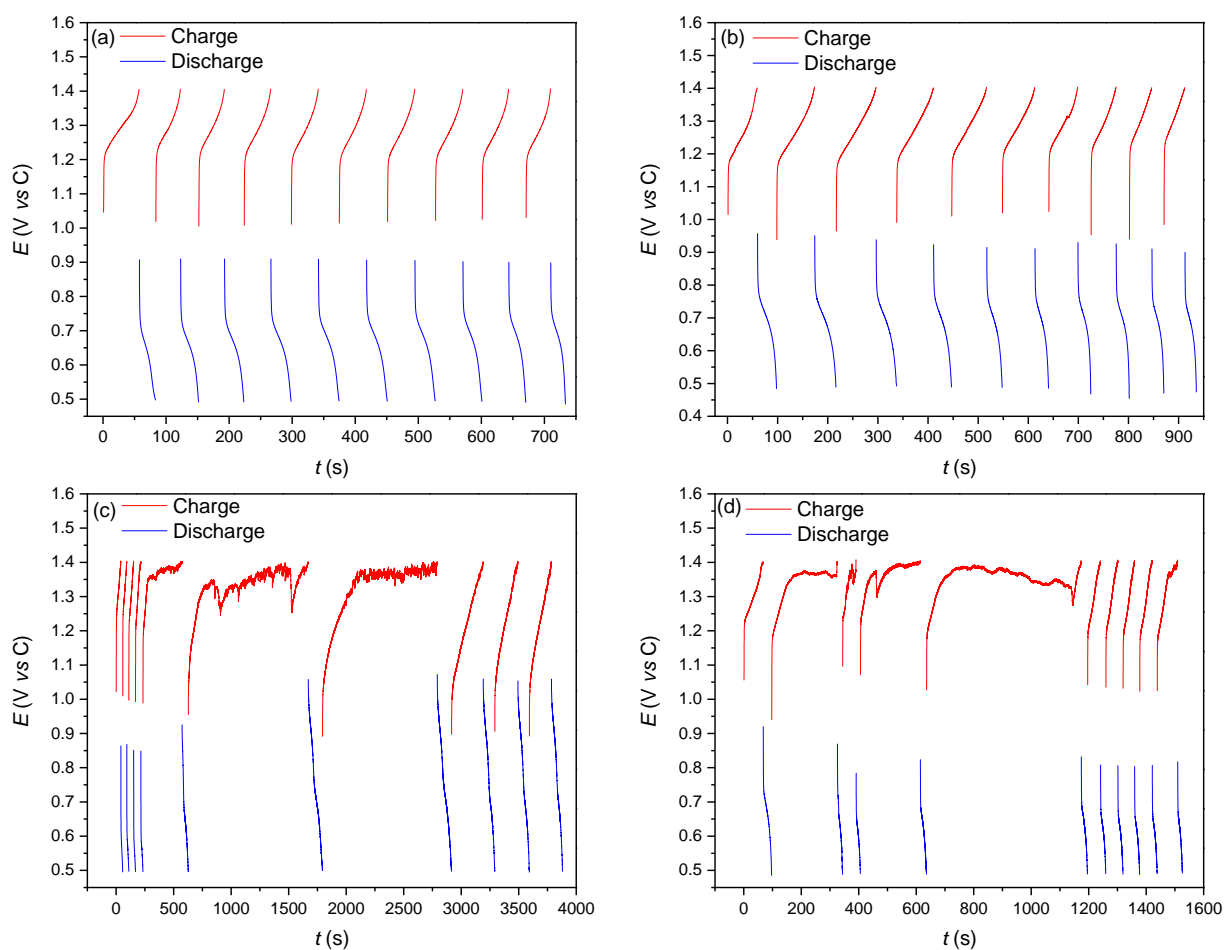
Figure 5.12. The galvanostatic charge-discharge profiles for the VOSO₄/OFAQ membrane-free cell under (a) 0 mL min⁻¹ (static conditions), (b) 16.8 mL min⁻¹, (c) 32.4 mL min⁻¹, and (d) 37.2 mL min⁻¹ using potential cut-offs of 1.4 V and 0.4 V at a constant current of 1.2 mA on C felt electrodes.

Table 5.2. Effect of cycle number on the charge and discharge times for the VOSO₄/OFAQ membrane-free battery under different flow rates.

Flow Rate (mL min⁻¹)	Normalised Charge t (s)			Normalised Discharge t (s)		
	Cycle 1	Cycle 5	Cycle 10	Cycle 1	Cycle 5	Cycle 10
0	57	43	39	26	32	23
16.8	59	69	41	38	31	23
32.4	41	339	191	16	53	96
37.2	67	537	71	30	21	16

226

Charging time should increase with increasing flow rate, which is what occurs over the first few cycles in Figures 5.12. For example, Cycle 5 in static conditions charges in 43 s, which increases to 69 s under 16.8 mL min^{-1} flow, and then to 339 s at 32.4 mL min^{-1}, and finally 537 s at 37.2 mL min^{-1}. However, the corresponding discharge profile for each long charging step is relatively short; for example, the Cycle 5 discharge at 37.2 mL min^{-1} is only 21 s. This indicates self-discharge at the interface after forming, such that there is no charged material present for the reverse process and hence the rapid discharge cycle.

The static and slowest flow tests show less of a discrepancy between the charge and discharge t, which indicates a lower rate of self-discharge. This suggests the perturbation of the interface from the faster flow causes more convective mixing of the charged species and increases the self-discharge rate.

Self-discharge determines the capacity fade rate in flow batteries. Monitoring the OCV is a method of studying the rate of self-discharge. Interestingly, the OCV at the beginning and end of the static and 37.2 mL min^{-1} flow tests was 0.90 V (vs C). However, charging the battery at the lower current density of 0.012 mA causes the OCV to drop from 0.90 V to 0 V (vs C). The drop in OCV is due to self-discharge. The higher self-discharge rate at lower currents is due to the increase in residence time for the charged material, and thus an increased chance for a reaction.

Figure 5.13. compares the difference in the charge profiles for the first and final cycles over all flow rates. None of the plots exactly overlay over the cycling process, corroborating the presence of self-discharge and side reactions. Interestingly, the test at the median flow rate (Figure 5.13.(c)) shows a vastly different profile over the two cycles, whereas the slowest and fastest flow rates have similar voltage plateaus and charging t for the first and last cycles.

One aspect that may contribute to the non-conformity of the data is the longer timescales in the 32.4 mL min^{-1} experiment compared to the rest. This means more of the electrolyte will have evaporated during testing than for the other samples. As OFAQ is less stable under higher concentration conditions, this may be contributing to the different charge-discharge profile in Figure 5.13.(c). This variation in electrolyte volume over time prevents an accurate calculation of the volumetric discharge capacity. The propensity for evaporation also limits the number of cycles possible to test and limits our understanding of the long-term effects of flow on the battery. Optimising the membrane-free flow cell should be a focus for future work, as this is a limiting factor in studying these systems.
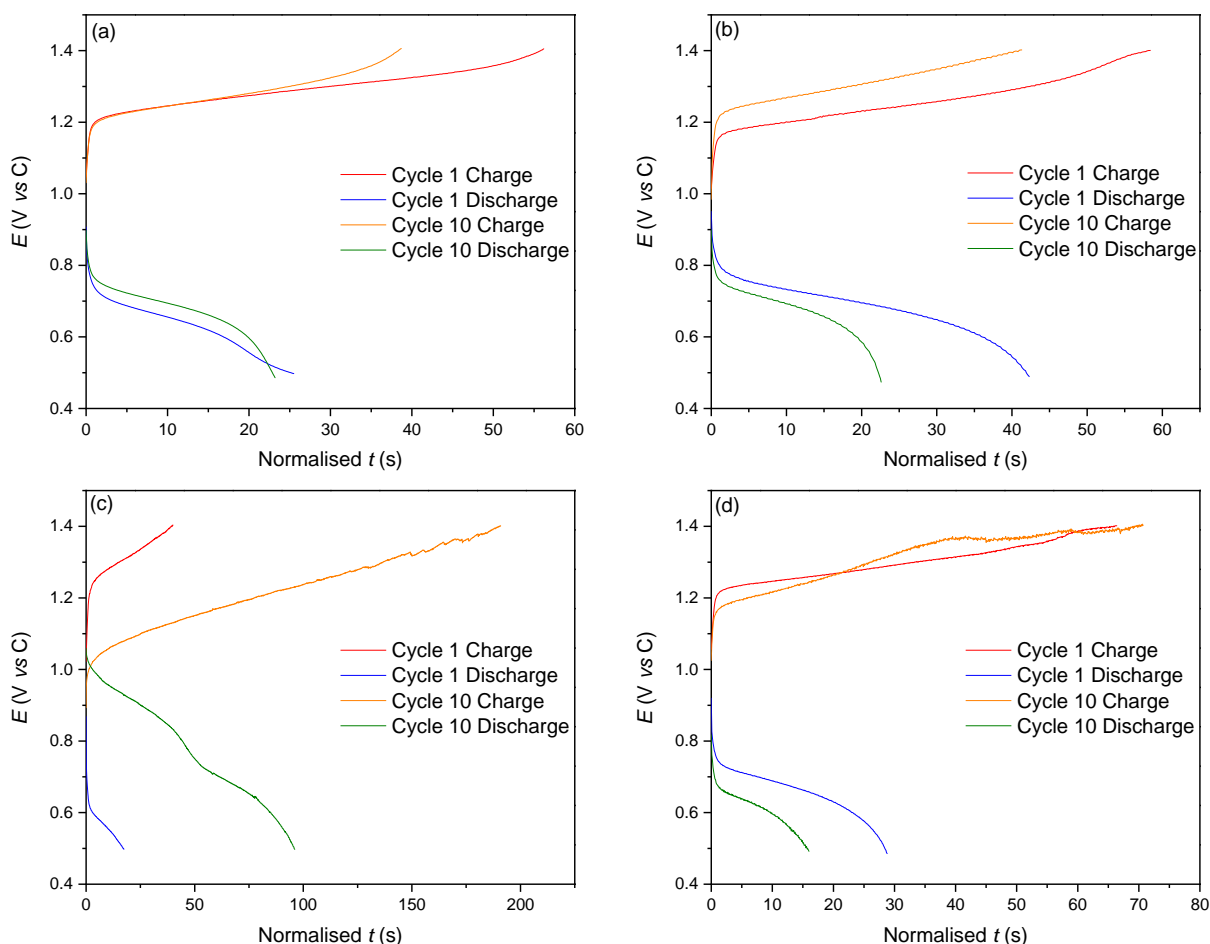
Figure 5.13. A comparison of the first and final cycles of the galvanostatic charge-discharge tests on the VOSO$_4$/OFAQ membrane-free battery under flow rates: (a) 0, (b) 16.8, (c) 32.4, and (d) 37.2 mL min^{-1}.

Figure 5.14. shows the trends in (a) CE_{ff}, (b) VE_{ff}, (c) EE_{ff} and (d) discharge capacity with cycle number. Table 5.3. compares the final efficiency values, charge and discharge capacities, and discharge capacity retention rates of the four flow conditions. The 32.4 mL min^{-1} (blue diamonds) test appears as an anomalous result when considering the trends of the other flow rates. The other three tests show the overall trends of decreasing CE_{ff}, VE_{ff}, EE_{ff}, and discharge capacity with increasing flow rate.

Increasing the flow rate increases the rate of self-discharge at the interface and causes the CE_{ff} to fluctuate. At 32.4 mL min^{-1} (blue diamonds), the CE_{ff} fluctuates between 40 %, 16 %, and 50 % in Cycles 2, 5, and 10, respectively. The faster flow rate, 37.2 mL min^{-1} (green triangles) shows a similar trend, fluctuating between 24 %, 4 %, and 23 % for Cycles 2, 5, and 10, respectively. The similarity in VE_{ff} indicates a similar overpotential in each test, and thus the EE_{ff} values follow a similar trend to the CE_{ff}. The final EE_{ff} of the fastest flow rate remarkably lower than the others, at 10 % as opposed to around 30 %. This is a direct result of the increase in the rate of self-discharge.
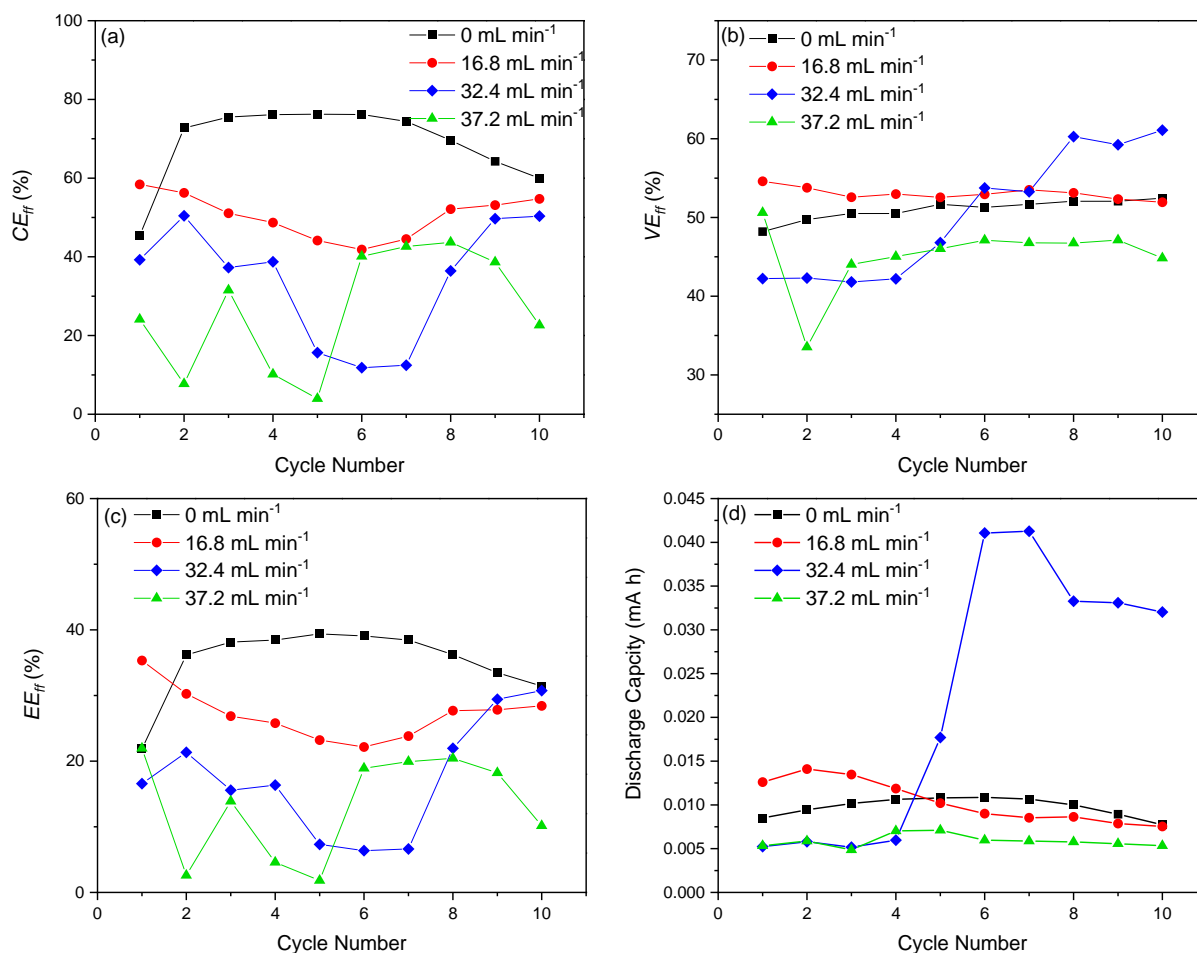
Figure 5.14. The trends in the (a) coulombic, (b) voltage, and (c) energy efficiencies, and (d) discharge capacity for the VOSO$_4$/OFAQ membrane-free battery and flow rates: 0 (black squares), 16.8 (red circles), 32.4 (blue diamonds), and 37.2 mL min^{-1} (green triangles).

Table 5.3. Cycling performance of the VOSO$_4$/OFAQ membrane-free battery under different flow rates after 10 cycles.

Flow Rate (mL min^{-1})	CE_{ff} (%)	EE_{ff} (%)	Charge Capacity (mA h)	Discharge Capacity (mA h)	Discharge Capacity Retention (%)
0	60	31	1.29×10^{-2}	7.73×10^{-3}	91
16.8	55	28	1.38×10^{-2}	7.53×10^{-3}	60
32.4	50	30	6.36×10^{-2}	3.20×10^{-2}	612
37.2	23	10	2.36×10^{-2}	5.33×10^{-3}	56

The large fluctuations in charging and discharge times leads to the rise in discharge capacity seen in the 32.4 mL min^{-1} test at Cycle 6. Cycle 2 discharges in 16 s, whereas Cycle 6 takes 123 s to reach the cut-off potential. The discharge capacity should increase with flow at a given j due to consistently refreshing the electrodes with unreacted material. However, the data in Table 5.3. shows that incorporation of flow to the device decreases the discharge capacity. This is likely a result of the aforementioned self-discharge. If one considers the charge capacity, then this does increase from 1.29 × 10^{-2} mA h in the static system to 6.36 × 10^{-2} mA h when at 32.4 mL min^{-1}. The capacity lowers for the fastest flow rate, but still remains above the values for the static and slowest flow tests.

(a) 1 mM OFAQ, 0.1 M LiBF$_4$CN, After Flow

(b) 20 mM VOSO$_4$, 2 M HCl, 10 m LiCl, After Flow
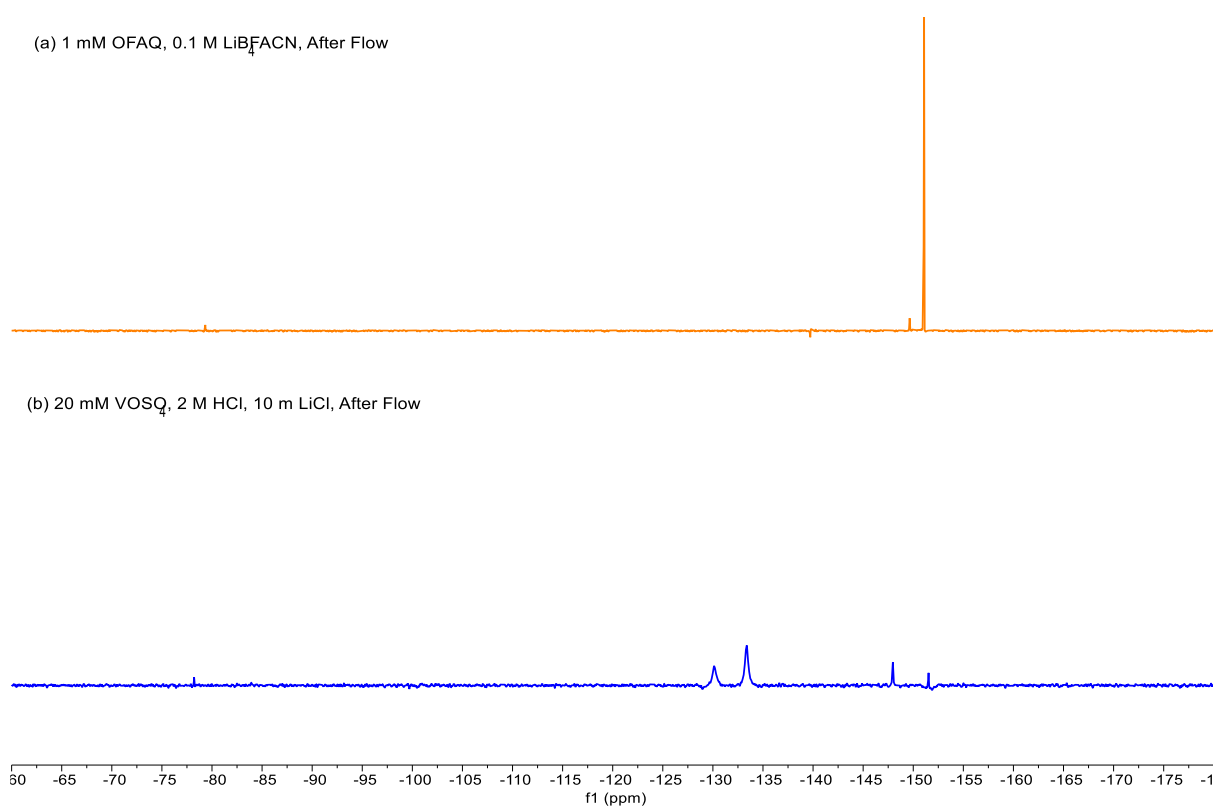
Figure 5.15. ^{19}F-NMR spectra for the (a) organic phase (orange line) and (b) aqueous (blue line) phase after 10 cycles at a flow rate of 37.2 mL min^{-1} in the VOSO$_4$/OFAQ membrane-free cell.

Figure 5.15. gives the ^{19}F-NMR analysis for the (a) organic (orange line), and (b) aqueous (blue line) phases of the membrane-free device after cycling at 37.2 mL min^{-1}. Appendix 5.B. tabulates the ^{19}F-NMR data.

The interface appears stable over the course of cycling to the eye and no colour change occurs during the test. The organic phase (Figure 5.15.(a)) shows the similar characteristic OFAQ peaks as in the spectra in Chapter 4.2.1. Figure 4.17. The OFAQ gives the peaks at −79.34, −140.23 and −149.64 ppm, with BF$_4^-$ is responsible for those at −151.03, −151.09 ppm. The aqueous phase (Figure 5.15.(b)) should show no F environments if there is no crossover. The

aqueous phase gives a peak at −151.53 ppm, which is likely the BF_4^- anion. Two F environments occur at resonances similar to OFAQ, at −78.22 and −147.97 ppm, and two new resonances appear at chemical shifts not seen in the OFAQ spectra. These lie at −130.12 and −133.38 ppm and are evidence of a side reaction involving the quinone that produces something other than OFAQ. The new product is soluble in the aqueous phase. This means the concentration of active material in the organic phase is lower than at the start of the test. These side reactions are therefore detrimental to the battery capacity.

To summarise, the data in this section shows that the $VOSO_4$/OFAQ membrane-free battery holds charge and discharge under static and slow flow rates. The CE_{ff} remains relatively stable up to 16.8 mL min^{-1} electrolyte flow but decreases and fluctuates when the flow rate rises above 30 mL min^{-1}. The CE_{ff} values are always <100 %, which indicates self-discharge and side reactions are prevalent in all modes of function. The application of flow should decrease the amount of self-discharge at the interface, as any charged RAMs flow away from the interface after formation. This is likely occurring in the 16.8 mL min^{-1} study and is the cause for the stable CE_{ff}.

Faster flow rates likely disrupt the interface more than the slow rates, which increases the amount of electrolyte mixing and increases the chance of self-discharge and side reactions. The increased mixing counteracts the improvements made in the slow flow case from reduced self-discharge and results in a lower CE_{ff} and discharge capacity. The ^{19}F-NMR confirms the side reactions through evidencing F-containing compounds in the aqueous phase at different chemical shifts to OFAQ. This suggests there is an optimum flow rate that balances reducing the rate of discharge and maintaining a stable interface.

The increasing charge capacity with increasing flow demonstrate the benefits of a flow system over a static cell. However, in the present design, the decreasing CE_{ff} and discharge capacity indicate that any flow reduces the battery's performance. It is imperative that research discovers RAMs with a lower propensity to react for the membrane-free flow device to function optimally. Once found, future work should also focus on optimising the flow rate to maximise the capacity, but minimise the convective mixing and self-discharge. Additionally, one needs to consider the higher energy requirements for faster flow rates and how this will affect the overall cost of the system.

5.4. Conclusions

This chapter proposes and demonstrates the novel concept of a membrane-free RFB wherein one half-cell comprises a non-aqueous electrolyte (ACN), and the other is a WIS electrolyte

(10 m LiCl). The non-aqueous phase takes the form of the electrolyte developed in Chapters 3. and 4. of this thesis, which uses the ORAM OFAQ (1 mM) in an ACN solvent. The miscibility of ACN and water suggests it is not suitable for a membrane-free device against an aqueous electrolyte. A ternary water-ACN-salt system forms with sufficiently high salt concentrations. The present study extends this idea to using WIS electrolytes, wherein the ESW is wider than in conventional high concentration aqueous media.

Salt-induced L/L phase separation occurs for the ACN and LiCl WIS electrolyte into phases of equal volume at 5 m LiCl (Figure 5.1.). The devices in this chapter use a 10 m LiCl aqueous electrolyte to ensure full phase separation. Lower LiCl concentrations would decrease the overall device cost. Future work should investigate lower salt concentrations and the affects this has on the robustness of the interface alongside its influence on RAM cross-migration.

Chapter 3.3. indicates that TBABF$_4$ is the best supporting salt for OFAQ reduction. The large TBA$^+$ cation stabilises the anions through steric crowding and results in the most negative redox potential ($E_{2,1/2}$ = −1.49 V (vs Ag/Ag$^+$)) of the salts tested. TBABF$_4$ is not suitable for the WIS/ACN membrane-free device, as the system requires a common ion between the half-cells. LiBF$_4$ is insoluble in the WIS electrolyte and yields a stable OFAQ redox reaction ($E_{1/2}$ = −0.79 V (vs Ag/Ag$^+$)) at low concentrations (Chapter 3.3.) and so is the supporting salt in this study. The overlapping CVs in Section 5.1. on the OFAQ, 0.1 M LiBF$_4$, ACN/10 m LiCl self-stratified system (Figure 5.2.) indicate charge can transfer over the interface via the Li$^+$ common ion.

Section 5.2. demonstrates several proof-of-concept membrane-free WIS-based batteries by populating the WIS phase with various RAMs. Both the K$_4$[Fe(CN)$_6$]/OFAQ and VOSO$_4$/OFAQ systems shows a stable L/L interface. Additionally, both cells yield CVs with reduction and oxidation processes, indicating charge-transfer occurs over the interface.

Galvanostatic charge-discharge tests show the K$_4$[Fe(CN)$_6$]/OFAQ has a CE_{ff} of 215 % and a discharge capacity retention of 120 % after 60 cycles. The CE_{ff} and discharge capacity retention of >100 % is indicative of side reactions. These are possibly due to RAM degradation or a side reaction between the anolyte and catholyte during charging and discharging processes. Additionally, the tendency for K$_4$[Fe(CN)$_6$] to form a precipitate means it is not useful for the catholyte half-cell.

The VOSO$_4$/OFAQ system yields a promisingly high theoretical OCV of 1.72 V, which is above that for the VRFB. The static battery presents a CE_{ff} of 84 % and a discharge capacity retention of near 100 % after 10 cycles. The potentials for the charge and discharge plateaus are 1.19 V and 0.78 V (vs C) with a 1.2 mA current and do not change over 10 cycles. This suggests that the side reactions are not detrimental to the performance over this timescale under static

conditions. The CE_{ff} and discharge capacity retention of the VOSO$_4$/OFAQ WIS/ACN system is higher than the leading non-aqueous based membrane-free static battery, which has a CE_{ff} of 75 % and a capacity retention of 85 % over 300 cycles.[15]

Whilst confirming the concept, one should note that the EE_{ff} values of the membrane-free RFBs are only around 50 %. This is far below that of the state-of-the-art aqueous RFBs, which record EE_{ff} values around 80 % for a kW-scale system at 100 mA cm^{-1}.[45]

Section 5.2.3. proposes a novel all-organic WIS/ACN membrane-free battery with a theoretical OCV of 1.15 V. The aqueous ORAM is a 4-OH-TEMPO catholyte and the non-aqueous phase comprises the same OFAQ electrolyte as previous tests. If carefully assembled, the electrolytes do not mix and a L/L interface forms that demonstrates feasible charge-transfer. The CV of the full-cell has a CE_{ff} of 199 % and a discharge capacity retention of near 100 % over 60 cycles. This indicates there is degradation and side reactions even in the static device and not a useful system. Additionally, 4-OH-TEMPO is soluble in the ACN phase and crosses the interface after agitation. This destroys the battery performance, resulting in an irreversible CV and charge-discharge tests that show the system does not hold charge. This is likely a result of a reaction between the 4-OH-TEMPO and the OFAQ upon applying charge and is unavoidable. Further work should consider the relative partition coefficients of ORAMs to find catholyte and anolyte molecules that are less soluble in the adjacent media.

Investigating the WIS/ACN interface under flowing conditions with the VOSO$_4$/OFAQ membrane-free cell demonstrates the interface is stable under a range of flow rates and the electrolytes remain separate. Section 5.3. shows charge capacity increases with flow rate. However, the RAMs immediately self-discharge, resulting in poor discharge capacities and unstable CE_{ff} values. This study only flows one half-cell. Future work should investigate dual-phase flow and the effects this has on rates of self-discharge and capacity fade.

ORAM crossover was negligible in the static system, with no F-containing compounds found in the aqueous phase after cycling. Raising the flow rate to 37.2 mL min^{-1} reveals F-environments in the VOSO$_4$ half-cell, and evidences new molecular structures other than OFAQ. This corroborates that high flow rates disrupt the interface and increase the propensity for electrolyte mixing. Upon mixing, the OFAQ undergoes a side reaction that forms a species that is soluble in the adjacent half-cell. This is detrimental to the battery capacity.

The flow cell in this study is not optimal for the electrolytes involved. The cell is open to air and covered with an Ar$_{(g)}$ blanket, thus ACN evaporation is an omnipresent issue during testing. This means that cycling performances >10 cycles are not accessible without further cell development. The blanket of Ar$_{(g)}$ should prevent decomposition of any reduction products, but this cannot be certified. Future iterations should seal the flow cell to reduce evaporation,

as in the cells by Gong *et al.* and Bamgbopa *et al.*[10,14] The next-generation device should also hold the electrodes as close to the interface as possible to minimise solution resistance. Additionally, as self-discharge at the interface is the likely the dominate cause for capacity decay; one should consider alternate flow cell designs that minimise the residence time for the species at the interface.[11,20,46]

The low solubility and instability of OFAQ inherently limit the batteries in this chapter. The low concentration limits the capacity and makes it challenging to compare the membrane-free systems with other literature devices. Future work should consider widening the anolyte identity to more stable ORAMs, such as BzNSN ($E_{1/2}$ = −1.58 V (*vs* Ag/Ag$^+$), and solubility of 5.7 M in ACN).[47] Nevertheless, the present work demonstrates a novel membrane-free device based on a WIS/ACN ITIES. The device maintains a stable interface under flowing conditions. However, applying flow proliferates electrolyte mixing and propagates self-discharge and side reactions.

At the time of writing, no previous work has been published using a WIS electrolyte as the aqueous half-cell against an ACN electrolyte in a membrane-free RFB. The wide ESW of WIS electrolytes means the possible energy density of the design is far above previous aqueous-based membrane-free batteries. Appropriate selection of more soluble and stable ORAMs alongside cell optimisation could lead to a membrane-free ORFB that answers our low cost, high energy density desires.

5.5.   References

1   V. Viswanathan, A. Crawford, D. Stephenson, S. Kim, W. Wang, B. Li, G. Coffey, E. Thomsen, G. Graff, P. Balducci, M. Kintner-Meyer and V. Sprenkle, Cost and performance model for redox flow batteries, *J. Power Sources*, 2014, **247**, 1040–1051.

2   G. Kear, A. A. Shah and F. C. Walsh, Development of the all-vanadium redox flow battery for energy storage: a review of technological, financial and policy aspects, *Int. J. energy Res.*, 2012, **36**, 1105–1120.

3   E. Sánchez-Díez, E. Ventosa, M. Guarnieri, A. Trovò, C. Flox, R. Marcilla, F. Soavi, P. Mazur, E. Aranzabe and R. Ferret, Redox flow batteries: Status and perspective towards sustainable stationary energy storage, *J. Power Sources*, 2021, **481**, 228804.

4   H. Chen, G. Cong and Y. C. Lu, Recent progress in organic redox flow batteries: Active materials, electrolytes and membranes, *J. Energy Chem.*, 2018, **27**, 1304–1325.

5   J. Xi, Z. Wu, X. Teng, Y. Zhao, L. Chen and X. Qiu, Self-assembled polyelectrolyte multilayer modified Nafion membrane with suppressed vanadium ion crossover for

vanadium redox flow batteries, *J. Mater. Chem.*, 2008, **18**, 1232–1238.

6   Q. Luo, H. Zhang, J. Chen, D. You, C. Sun and Y. Zhang, Preparation and characterization of Nafion/SPEEK layered composite membrane and its application in vanadium redox flow battery, *J. Memb. Sci.*, 2008, **325**, 553–558.

7   D. Xing, S. Zhang, C. Yin, B. Zhang and X. Jian, Effect of amination agent on the properties of quaternized poly(phthalazinone ether sulfone) anion exchange membrane for vanadium redox flow battery application, *J. Memb. Sci.*, 2010, **354**, 68–73.

8   S. C. Chieng, M. Kazacos and M. Skyllas-Kazacos, Modification of Daramic, microporous separator, for redox flow battery applications, *J. Memb. Sci.*, 1992, **75**, 81–91.

9   P. Navalpotro, C. Trujillo, I. Montes, C. M. S. S. Neves, J. Palma, M. G. Freire, J. A. P. Coutinho and R. Marcilla, Critical aspects of membrane-free aqueous battery based on two immiscible neutral electrolytes, *Energy Storage Mater.*, 2020, **26**, 400–407.

10   M. O. Bamgbopa, Y. Shao-Horn, R. Hashaikeh and S. Almheiri, Cyclable membraneless redox flow batteries based on immiscible liquid electrolytes: Demonstration with all-iron redox chemistry, *Electrochim. Acta*, 2018, **267**, 41–50.

11   M. O. Bamgbopa, S. Almheiri and H. Sun, Prospects of recently developed membraneless cell designs for redox flow batteries, *Renew. Sustain. Energy Rev.*, 2017, **70**, 506–518.

12   WO2021209585A1, 2021.

13   P. Navalpotro, C. M. S. S. Nevers, J. Palma, R. Marcilla, M. G. Freire, J. A. P. Coutinho and R. Marcilla, Pioneering use of ionic liquid-based aqueous biphasic systems as membrane-free batteries, *Adv. Sci.*, 2018, **5**, 1800576.

14   K. Gong, F. Xu, M. G. Lehrich, X. Ma, S. Gu and Y. Yan, Exploiting immiscible aqueous-nonaqueous electrolyte interface toward a membraneless redox-flow battery concept, *J. Electrochem. Soc.*, 2017, **164**, A2590–A2593.

15   P. Navalpotro, N. Sierra, C. Trujillo, I. Montes, J. Palma and R. Marcilla, Exploring the versatility of membrane-free battery concept using different combinations of immiscible redox electrolytes, *ACS Appl. Mater. Interfaces*, 2018, **10**, 41246–41256.

16   J. A. Renard and H. R. Heichelheim, Ternary systems, *J. Chem. Eng. Data*, 1965, **10**, 485–488.

17   M. Li, B. Zhuang, Y. Lu, L. An and Z. G. Wang, Salt-induced liquid-liquid phase separation: Combined experimental and theoretical investigation of water-acetonitrile-salt mixtures, *J. Am. Chem. Soc.*, 2021, **143**, 773–784.

18   Y. Wang, X. Meng, J. Sun, Y. Liu and L. Hou, Recent progress in "water-in-salt"

electrolytes toward non-lithium based rechargeable batteries, *Front. Chem.*, 2020, **8**, 1–8.

19   L. Droguet, A. Grimaud, O. Fontaine and J. M. Tarascon, Water-in-salt electrolyte (WiSE) for aqueous batteries: A long way to practicality, *Adv. Energy Mater.*, 2020, **10**, 1–14.

20   J. D. Watkins, S. M. MacDonald, P. S. Fordred, S. D. Bull, Y. Gu, K. Yunus, A. C. Fisher, P. C. Bulman-Page and F. Marken, High-yield acetonitrile | water triple phase boundary electrolysis at platinised Teflon electrodes, *Electrochim. Acta*, 2009, **54**, 6908–6912.

21   X. Song, H. He, M. H. Aboonasr Shiraz, H. Zhu, A. Khosrozadeh and J. Liu, Enhanced reversibility and electrochemical window of Zn-ion batteries with an acetonitrile/water-in-salt electrolyte, *Chem. Commun.*, 2021, **57**, 1246–1249.

22   Q. Dou, S. Lei, D. W. Wang, Q. Zhang, D. Xiao, H. Guo, A. Wang, H. Yang, Y. Li, S. Shi and X. Yan, Safe and high-rate supercapacitors based on an 'acetonitrile/water in salt' hybrid electrolyte, *Energy Environ. Sci.*, 2018, **11**, 3212–3219.

23   J. Luo, A. Sam, B. Hu, C. DeBruler, X. Wei, W. Wang and T. L. Liu, Unraveling pH dependent cycling stability of ferricyanide/ferrocyanide in redox flow batteries, *Nano Energy*, 2017, **42**, 215–221.

24   Z. Yang, L. Tong, D. P. Tabor, E. S. Beh, M. A. Goulet, D. De Porcellinis, A. Aspuru-Guzik, R. G. Gordon and M. J. Aziz, Alkaline benzoquinone aqueous flow battery for large-scale storage of electrical energy, *Adv. Energy Mater.*, 2018, **8**, 1–9.

25   C. Wang, Z. Yang, Y. Wang, P. Zhao, W. Yan, G. Zhu, L. Ma, B. Yu, L. Wang, G. Li, J. Liu and Z. Jin, High-performance alkaline organic redox flow batteries based on 2-hydroxy-3-carboxy-1,4-naphthoquinone, *ACS Energy Lett.*, 2018, **3**, 2404–2409.

26   X. Zu, L. Zhang, Y. Qian, C. Zhang and G. Yu, Molecular engineering of azobenzene-based anolytes towards high-capacity aqueous redox flow batteries, *Angew. Chemie Int. Ed.*, 2020, **59**, 22163–22170.

27   R. Feng, X. Zhang, V. Murugesan, A. Hollas, Y. Chen, Y. Shao, E. Walter, N. P. N. Wellala, L. Yan, K. M. Rosso and W. Wang, Reversible ketone hydrogenation and dehydrogenation for aqueous organic redox flow batteries, *Science*, 2021, **372**, 836–840.

28   K. Wedege, E. Draževič, D. Konya and A. Bentien, Organic redox species in aqueous flow batteries: Redox potentials, solubility and chemical stability, *Sci. Rep.*, 2016, **6**, 1–13.

29   C. Wang, Z. Yang, B. Yu, H. Wang, K. Zhang, G. Li, Z. Tie and Z. Jin, Alkaline soluble 1,3,5,7-tetrahydroxyanthraquinone with high reversibility as anolyte for aqueous redox

flow battery, *J. Power Sources*, 2022, **524**, 3–9.

30   X. Wang, A. Lashgari, J. Chai and J. Jiang, A membrane-free, aqueous/nonaqueous hybrid redox flow battery, *Energy Storage Mater.*, 2022, **45**, 1100–1108.

31   J. Luo, B. Hu, C. Debruler, Y. Bi, Y. Zhao, B. Yuan, M. Hu, W. Wu and T. L. Liu, Unprecedented capacity and stability of ammonium ferrocyanide catholyte in pH neutral aqueous redox flow batteries, *Joule*, 2019, **3**, 149–163.

32   K. Tanaka and R. Tamamushi, A physico-chemical study of concentrated aqueous solutions of lithium chloride, *Zeitschrift fur Naturforsch. A*, 1991, **46**, 141–147.

33   P. Iamprasertkun, A. Ejigu and R. A. W. Dryfe, Understanding the electrochemistry of 'water-in-salt' electrolytes: Basal plane highly ordered pyrolytic graphite as a model system, *Chem. Sci.*, 2020, **11**, 6978–6989.

34   S. Prasad, C. Chakravarty and H. K. Kashyap, Concentration-dependent structure and dynamics of aqueous LiCl solutions: A molecular dynamics study, *J. Mol. Liq.*, 2017, **225**, 240–250.

35   X. Wu, Y. Gong, S. Xu, Z. Yan, X. Zhang and S. Yang, Electrical conductivity of lithium chloride, lithium bromide, and lithium iodide electrolytes in methanol, water, and their binary mixtures, *J. Chem. Eng. Data*, 2019, **64**, 4319–4329.

36   S. Creager, in *Handbook of Electrochemistry*, ed. C. G. Zoski, Elsevier B.V., Las Cruces, 1st Ed., 2007, pp. 57–72.

37   H. D. Graham, Stabilization of the prussian blue color in the determination of polyphenols, *J. Agric. Food Chem.*, 1992, **40**, 801–805.

38   C. Choi, S. Kim, R. Kim, Y. Choi, S. Kim, H. young Jung, J. H. Yang and H. T. Kim, A review of vanadium electrolytes for vanadium redox flow batteries, *Renew. Sustain. Energy Rev.*, 2017, **69**, 263–274.

39   M. Pourbaix, *Atlas electrochemical equilibria aqueous solutions*, National Association of Corrosion Engineers, Houston, 2nd Ed., 1974.

40   W. Wang, X. Wei, D. Choi, X. Lu, G. Yang and C. Sun, Electrochemical cells for medium-and large-scale energy storage: Fundamentals, *Adv. Batter. Mediu. Large-Scale Energy Storage Types Appl.*, 2014, 3–28.

41   W. Zhou, W. Liu, M. Qin, Z. Chen, J. Xu, J. Cao and J. Li, Fundamental properties of TEMPO-based catholytes for aqueous redox flow batteries: Effects of substituent groups and electrolytes on electrochemical properties, solubilities and battery performance, *RSC Adv.*, 2020, **10**, 21839–21844.

42   Y. Liu, M. A. Goulet, L. Tong, Y. Liu, Y. Ji, L. Wu, R. G. Gordon, M. J. Aziz, Z. Yang and T. Xu, A long-lifetime all-organic aqueous flow battery utilizing TMAP-TEMPO

radical, *Chem*, 2019, **5**, 1861–1870.

43   H. Park, G. Kwon, H. Lee, K. Lee, S. Y. Park, J. E. Kwon, K. Kang and S. J. Kim, In operando visualization of redox flow battery in membrane-free microfluidic platform, *Proc. Natl. Acad. Sci. U. S. A.*, 2022, **119**, 1–9.

44   M. Li, Z. Rhodes, J. R. Cabrera-Pardo and S. D. Minteer, Recent advancements in rational design of non-aqueous organic redox flow batteries, *Sustain. Energy Fuels*, 2020, **4**, 4370–4389.

45   M. Kapoor and A. Verma, Technical benchmarking and challenges of kilowatt scale vanadium redox flow battery, *Wiley Interdiscip. Rev. Energy Environ.*, 2022, **11**, 1–17.

46   J. H. Atherton, in *The Investigation of Organic Reactions and Their Mechanisms*, ed. H. Maskill, Blackwell Publishing, Newcastle-upon-Tyne, 1st Ed., 2006, p. 122.

47   J. Zhang, J. Huang, L. A. Robertson, R. S. Assary, I. A. Shkrob and L. Zhang, Elucidating factors controlling long-term stability of radical anions for negative charge storage in nonaqueous redox flow batteries, *J. Phys. Chem. C*, 2018, **122**, 8116–8127.

6. Deep Eutectic Solvents for Organic Redox Flow Batteries

Section 1.4. outlines the concepts and benefits of DES electrolytes in ORFBs and reviews the state-of-the-art literature surrounding ORFB-DES systems. DES benefits include wide ESWs; low volatility; low flammability; low cost; environmental biodegradability; and simple preparation. The DES role in an ORFB can be as the solvent in which the ORAMs dissolve, or as the electroactive compound itself. The latter method removes the requirement of additional solvents and the dependency on solubility, which could lead to significantly concentrated electrolytes compared to current systems. High concentration electrolytes can create significantly more energy dense ORFBs.

This section serves to research ORAMs for a DES-based RFB device using only easily produced or widely available materials for facile scale-up. The basic material requirements are a) simple synthesis or ease of attainment, b) safety, c) low cost, d) electrochemical reversibility, and e) low molecular weight. Section 1.3.2. shows the vast array of possible ORAMs for RFBs. One example includes the OFAQ molecule from the previous chapters of this thesis. Unfortunately, the large size, low solubility, and high cost of OFAQ make it unsuitable for scaling up into an RFB device. Additionally, many promising state-of-the-art ORAMs in the literature require complex synthesis with small yields and are not commercially available.[1,2]

A low molecular weight ORAM is even more critical in DES-systems than in conventional-electrolyte-based ORFBs. This is because of the high viscosity of the DES constrain the mass transfer. A fast D_o of the molecules is therefore essential, which typically follows the trend of increasing D_o with decreasing molecular size. Other factors such as the strength of intermolecular interactions with the solvent also contribute to the rate of transfer. This can be especially critical in DES-electrolytes as the solvent forms via intermolecular interactions and thus has a high capacity to interact strongly with ORAMs.

The narrow time window available for researching this chapter limits the number of molecules available for study to a select few. Figure 1.6. in Section 1.4.2. provides an assortment of possible organic DES components for future studies. One should note, however, that the possible number of DES-forming components is only limited by one's imagination. Table 6.1. presents the ORAMs in this study along with their prices (Sigma-Aldrich, September 2022) scaled to 1 kg. The price is essential in understanding the accessibility and scalability of each ORAM. Table 6.1. also describes the reversible electrochemistry and/or evidence of the ORAM in an existing DES, along with the DES driving force if known. From this information, one can appreciate the functional group combinations that form room temperature DESs and how to adapt these systems for an ORFB.
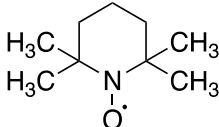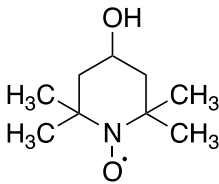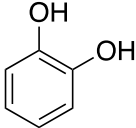
The route of this work for identifying a new redox-active DES system is as follows:
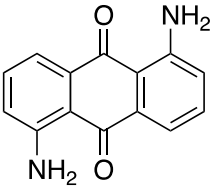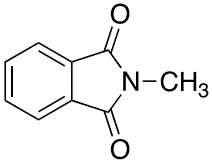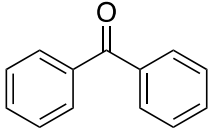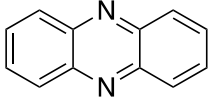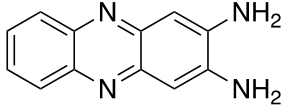
a) Test similar DES structures to those from existing literature
b) Extrapolate the HBD/HBA functional groups responsible for the DES driving force
c) Employ ORAMs with these functional groups to identify new redox active DESs

For example: The driving force behind the known DES 2:1 H_2Q:ChCl is the HBD of the Q backbone and the HBA ChCl.[3] One can then extrapolate the driving force of the hydrogen bonding network to similar molecules with more negative redox potentials or higher electrochemical stabilities, such as phenazine or AQ (H_2Q $E = 0.7$, phenazine $E = -0.76$ V, and AQ $E = 0.10$ V (vs SHE) at pH 7).[4,5] Phenazine shows reversible electrochemistry in aqueous and non-aqueous media, has a similar aromatic HBA moiety, but no reports cover its use in a DES.

This chapter discusses the electrochemistry of the novel systems and their possible application in future flowing EESSs. Appendix 6.A. reports the room temperature physical state all of the ORAM compositions tested during this study, which may aid future research.

Table 6.1. ORAM candidates for DES−based ORFBs with price, literature redox potential, and reported related DES systems with their driving forces.

ORAM	Structure	Price ($£\ kg^{-1}$)	Reversible Electrochemistry E^o (RE) (V)	Reported DES (T_m)	DES Driving Force	Ref / Year
TEMPO		4120	0.58 (*vs* SHE)	([Quaternium TEMPO]$^+$Br$^-$):Urea 2:1 (333 K) 0.17 M solubility in 2:1 ChCl:EG (Reversible redox)	NH$_3$ and [Quaternium]$^+$ group on TEMPO	[6–8] / 2014, 2014, 2020
4-OH-TEMPO		1620	0.80 (*vs* SHE) 0.64 (vs Ag/AgCl)	1.93 M solubility in 2:1 ChCl:EG 8:1:1 EG:4-OH-TEMPO:Benzylviologen 2:1:4 4-OH-TEMPO:TEACl:H$_2$O	4-OH-TEMPO disrupts ChCl:EG HB network	[8–10] / 2020, 2016, 2021
Catechol		49	0.24 (vs Ag/AgCl) in pH 3	Catechol:ChCl 2:1 (325 K) (Irreversible redox)	Cl$^-$ and C=O	[11,12] / 2019, 2017

1,5-Diaminoanthraquinone (1,5-DAAQ)		2170	1,4-DAAQ = −1.51, −1.98 (*vs* Ag/Ag⁺)			[13] / 2015
NMePh		5100	−1.79 (*vs* Ag/Ag⁺)	NMePh:LiTFSI:Urea 1:2:3	C=O and Li⁺ TFSI⁻ improves plasticity	[14] / 2018
BP		34.55	−2.16 (*vs* Ag/Ag⁺)	BP:alkalki metal – TFSI⁻ 2:1 – 4:1	C=O and alkali metal cation	[15,16] / 2017, 2021
Phenazine		7710	−1.50 (*vs* Ag/Ag⁺, non-aqueous) −0.56 (*vs* Ag/AgCl, aqueous)			[4] / 2021
2,3-Diaminophenazine		9240	−0.20 (*vs* Ag/Ag⁺)			[17] (2013)

6.1. Organic Redox Active Materials in Deep Eutectic Solvents

There are over 10^{18} possible DES systems, many of which can comprise of ORAMs.[18] The vast number of available combinations means boundaries and requirements must be set to focus the study and intelligently design a system. To streamline the work, this study begins focussing on one of the most well-known DES systems: ethaline. Ethaline comprises a 1:2 molar ratio of ChCl and EG and is one of the most well studied DES systems for RFB applications. This is due to its relatively low room temperature viscosity and density alongside its intrinsic conductivity (42 mPa s, 1.11 g cm^{-3}, and 7.61 mS cm^{-1}, respectively).[19]

The ORAMs in Table 6.1. show reversible electrochemistry in traditional-electrolyte ORFBs alongside evidence of forming or being soluble in DESs. However, as discussed in Chapter 3.2., the solvent environment significantly affects the ORAM electrochemistry. Figure 6.1.(a) – (g) shows the CV and (i) – (vii) the LSV data from an initial screening of the molecules in Table 6.1. in ethaline. The CVs are over scan rates $25 \leq v \leq 1000$ mV s^{-1} and the LSVs over rotation rates $500 \leq f \leq 6000$ RPM. Table 6.2. gives the solubility and electrochemical data for the ORAM CVs in Figure 6.1. at 100 mV s^{-1}. Appendix 6.B. gives the corresponding Levich graphs and D_o values (using Equation 2.10. in Section 2.2.2.). The CVs are normalised to 1 mM concentrations for easier comparison between the ORAMs. Different concentrations are used to probe the performance the highest achievable ORAM concentrations in ethaline. The irreversibility of many of the ethaline-based CVs compared to reversible systems in conventional solvents indeed indicates the nature of the DES greatly affects the electrochemistry.

Figure 6.1.(a), (b), (c), and (f) show 4-OH-TEMPO, 1,5-DAAQ, catechol, and phenazine give both oxidation and reduction electrochemical events at millimolar concentrations in ethaline. BP and NMePh display irreversible electrochemistry in ethaline despite their reversibility in conventional non-aqueous electrolytes, such as ACN. Drying and degassing did not improve the reversibility. Typically, studies on these ORAMs use a glove box environment, but a glove box was not accessible during this study. Using a glove box may improve the reversibility, as the highly charged states are likely to be oxygen sensitive.[14] A point to note is that absolute oxygen exclusion is not ideal for an industrial scale device. A system that demands a completely deoxygenated environment is more costly than if it were more tolerant to air.

None of the systems in Figure 6.1. has an i_{pa}/i_{pc} of unity, indicating none of the ORAMs are completely chemically reversible in ethaline. The causes of the irreversibility differ depending on the ORAM in question. For example, catechol is most reversible in acidic media (0.2 V (*vs* Ag/AgCl), pH 3), which explains its poor behaviour in the nearly neutral ethaline.[20] Meanwhile,

BP and NMePh have such highly reactive charged states that require completely O_2 and H^+ free environments to remain stable and so chemical degradation is likely.

The ORAMs with the best chemical reversibility in Figure 6.1. are 4-OH-TEMPO and 1,5-DAAQ, both with i_{pa}/i_{pc} values of 1.28. Additionally, their ΔE_p values of 0.077 and 0.042 V (*vs* Ag/Ag$^+$) are similar to that for electrochemically reversible 1- and 2-electron processes, as described by the Nernst Equation (Chapter 2.2.1. Equation 2.5.). Based on the CV and LSV data in Figure 6.1., 4-OH-TEMPO/1,5-DAAQ is the most appropriate pair for an ORFB system with a theoretical cell voltage of 1.46 V (4-OH-TEMPO $E_{1/2}$ = 0.65 V (*vs* Ag/Ag$^+$), 1,5-DAAQ $E_{1/2}$ = −0.81 V (*vs* Ag/Ag$^+$)). This improves over the VRFB OCV of 1.26 V and negates the need for extreme pH's or non-environmentally friendly and toxic non-aqueous solvents.[21]

Chemically and electrochemically reversible redox events are not the only requirement for acceptable electrolyte systems. The insufficient long-term stability of 4-OH-TEMPO in ethaline and low solubility limit of 1,5-DAAQ in ethaline (<2.7 mM) are flaws in the proposed 4-OH-TEMPO/1,5-DAAQ system.[8] Most of the ORAMs in Figure 6.1. have solubilities of <10 mM in ethaline. This restricts the viable energy densities and means these ethaline-based systems are not useful in ESS. Additives, such as ACN or water, improve the solubilities but the concentrations remain in the millimolar range. Additionally, even though high concentrations are sometimes achievable, such as with 4-OH-TEMPO, the high viscosity of the resulting system poses an issue for a flow device.

4-OH-TEMPO is soluble up to 2.1 M in aqueous environments and has a redox potential of E^o = 0.81 V (*vs* SHE).[22] The high solubility of 4-OH-TEMPO in ethaline (1.93 M) and the low saturation limits of the less polar, larger size ORAMs indicates ethaline is exhibiting 'aqueous'-like solvent behaviour on the ORAMs. The CVs of 1,5-DAAQ corroborate this by showing a 1 × 2e$^-$ process at $E_{1/2}$ rather than the 2 × 1e$^-$ pathway that is expected in non-aqueous media. The phenazine $E_{1/2}$ = −0.53 V (*vs* Ag/Ag$^+$) in ethaline concurs this behaviour, which has a non-aqueous $E_{1/2}$ of −1.50 V and an aqueous $E_{1/2}$ of −1.10 to −0.56 V depending on the environment. The different reduction potentials of NMePh and BP further demonstrate the different behaviour of ethaline to conventional solvents. In ethaline, NMePh and BP have the respective E_{pc} values of E_{pc} = −1.20 V and −1.42 V (*vs* Ag/Ag$^+$). In conventional non-aqueous electrolytes, the respective redox potentials are $E_{1/2}$ = −1.79 V (*vs* Ag/Ag$^+$) for NMePh, and $E_{1/2}$ = −2.16 V (*vs* Ag/Ag$^+$) for BP.[14,15] The positive shifts in E are likely due to hydrogen bonding of the active species with ethaline facilitating reduction. A similar effect is seen in the study of PTIO in ChCl:EG 1:4.[23] The reduced states, even with the additional hydrogen bonding, are not stable in ethaline and degrade upon formation. This likely occurs via attack of the high

energy ORAMs from dissolved water that is responsible for the 'aqueous' appearing electrochemistry.

The D_o values in Table 6.2. are in the range $1 \times 10^{-6} - 1 \times 10^{-7}$ cm^2 s^{-1}. These are above those for ORAMs in conventional non-aqueous solvents (OFAQ = 1.13×10^{-5} cm^2 s^{-1} in ACN, Chapter 4.1.1. Table 4.2.) and are similar to RTILs (OFAQ = 2.85×10^{-7} cm^2 s^{-1} in [BMPyrr][TFSI] (Chapter 3.2.3. Table 3.3.)). The higher value represents the higher viscosity of ethaline over conventional organic solvents. Table 6.2. shows D_o slows with increasing molecular size, with 4-OH-TEMPO recording the fastest D_o. This is likely because of its small size and lack of charge preventing strong associations with ethaline. The D_o of 4-OH-TEMPO in ethaline (1.44×10^{-6} cm^2 s^{-1}) is still much slower than that in ACN (2.95×10^{-5} cm^2 s^{-1})[24], which demonstrates the technical challenges posed by DES electrolytes.

The limited solubilities and electrochemical reversibility's in Figure 6.1. show ethaline to be an inappropriate solvent for these ORAMs. Extending the DES electrolyte to other common binary systems, such as reline, does not improve the electrochemistry. The high viscosity (750 mPa s at 298 K)[19] leads to such sluggish mass transport that results in unobservable electrochemistry. Most DES systems have viscosities >100 mPa s.[25] Techno-economic analysis suggests electrolytes must have viscosities <10 mPa s to minimise hydrodynamic resistance in the battery.[26] Therefore, most reported DESs are too viscous for flow systems. This propels the search towards designing new DESs with better physicochemical properties.[19]
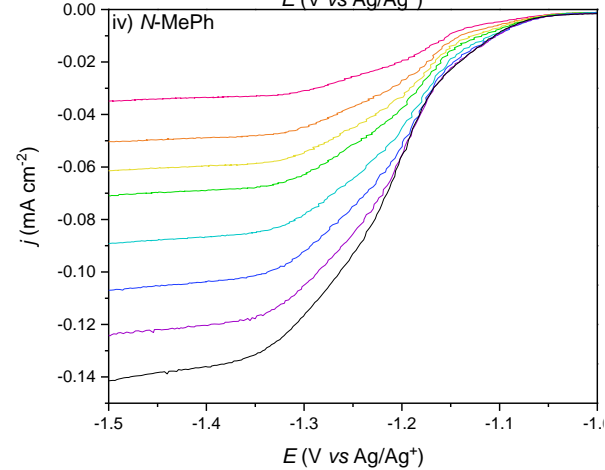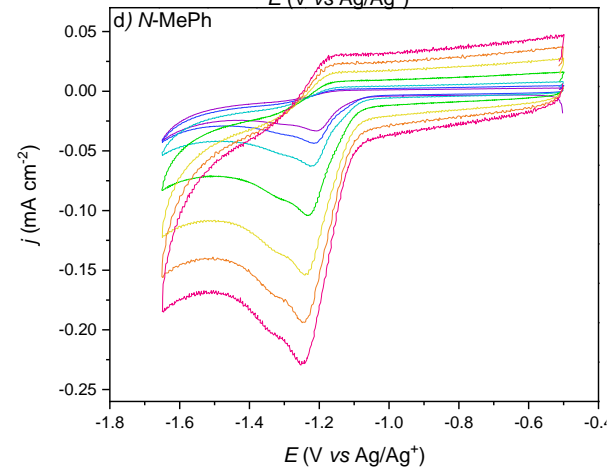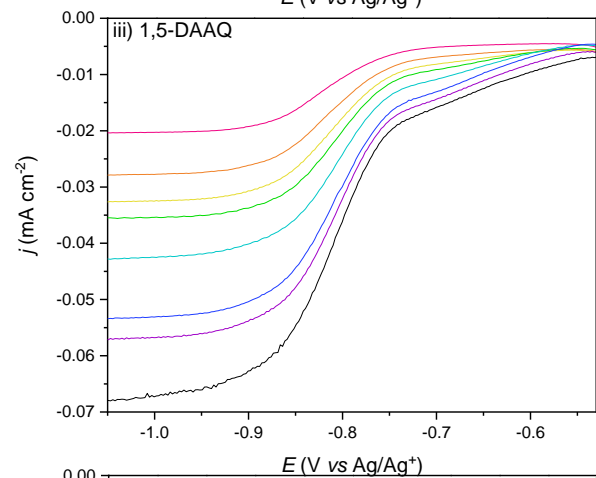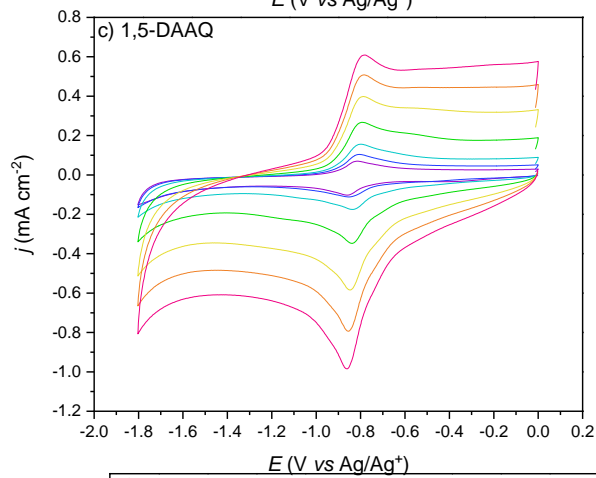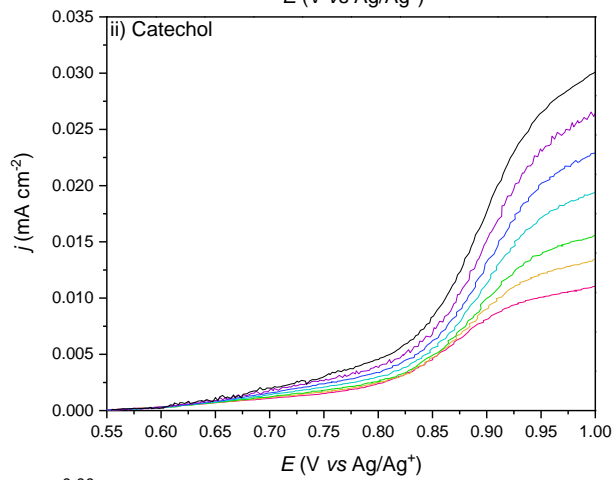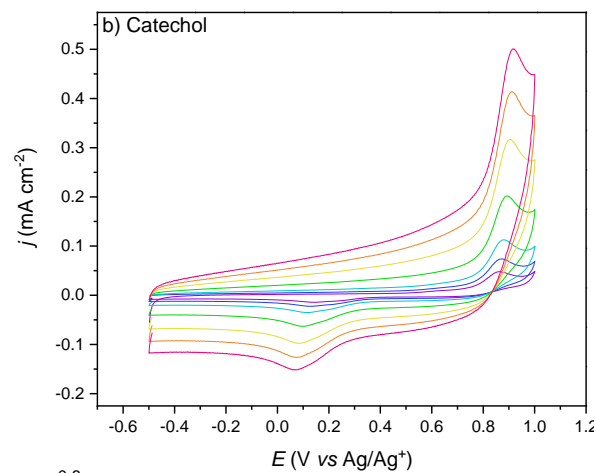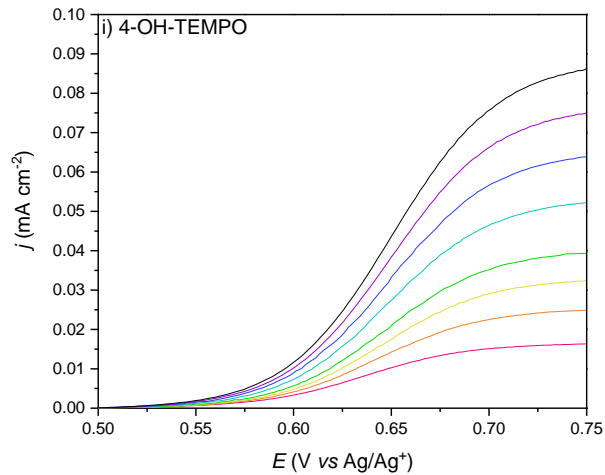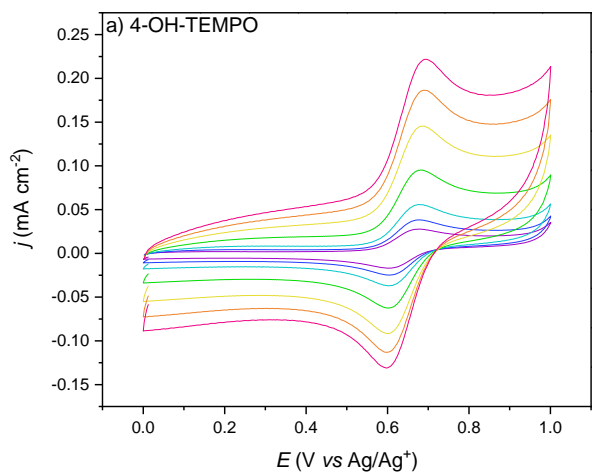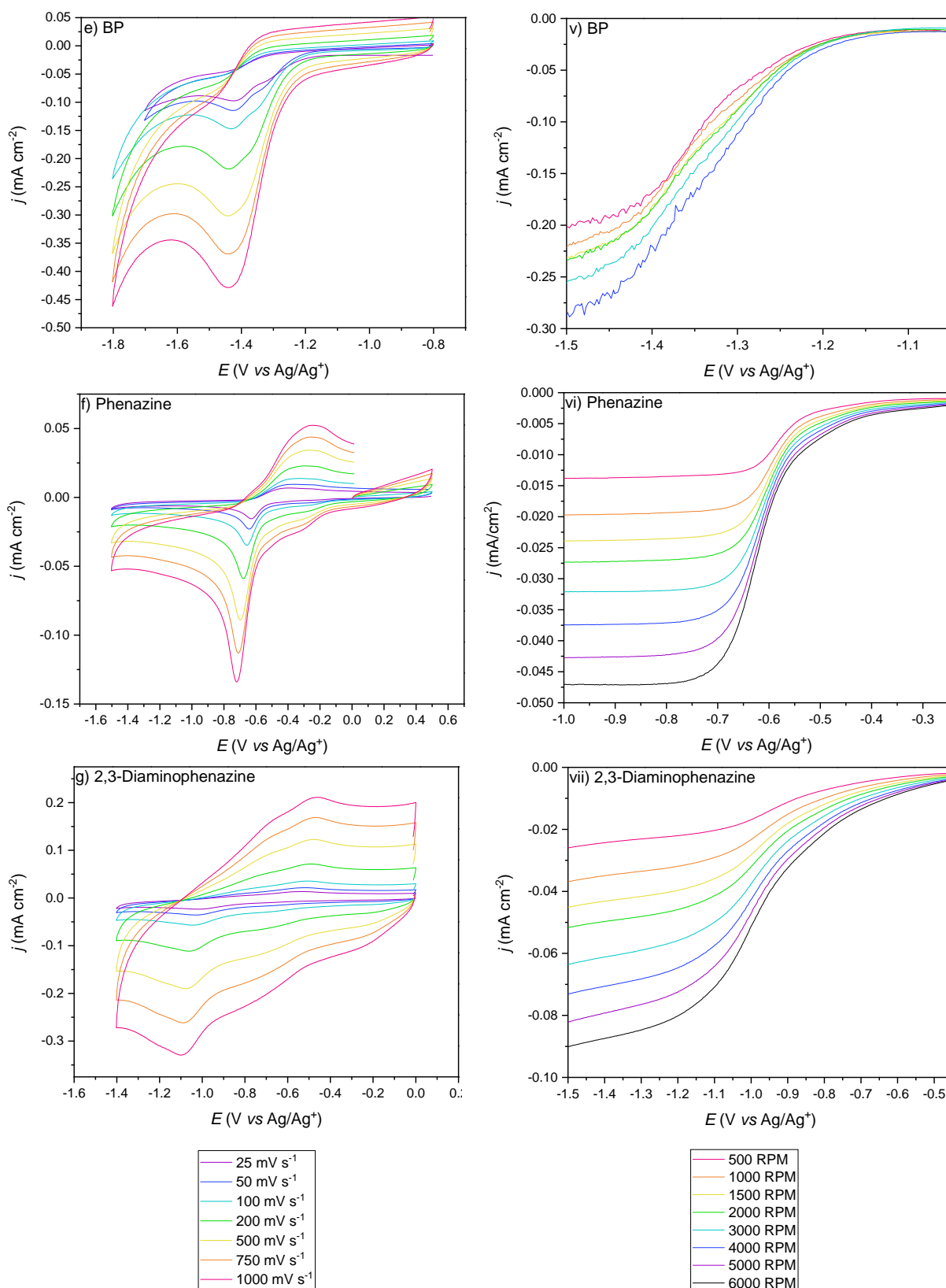
Figure 6.1. (a) – (g) CV data and (i) – (vii) corresponding LSV plots for 1mM 4-OH-TEMPO, 0.9 mM catechol, 2.7 mM 1,5-diaminoanthraquinone, 1.6 mM N-MePh, 1.4 mM benzophenone, 10.0 mM phenazine, and 2.6 mM 2,3-diaminophenazine. Scan rates are $25 \leq v \leq 1000$ mV s^{-1} and rotation rates $500 \leq f \leq 6000$ RPM and tests use a GC WE, Ag/Ag$^+$ RE, and Pt CE. All concentrations are normalised to 1 mM.

Table 6.2. Solubility and electrochemical data from the CVs at scan rate v = 100 mV s^{-1} of the ORAMs in ethaline in Figure 6.1.

ORAM	Maximum solubility in ethaline (M)	E_{pa} (V vs Ag/Ag$^+$)	E_{pc} (V vs Ag/Ag$^+$)	ΔE_p (V vs Ag/Ag$^+$)	$E_{1/2}$ (V vs Ag/Ag$^+$)	i_{pa} (mA)	i_{pc} (mA)	i_{pa}/i_{pc}	D_o (cm^2 s^{-1})
4-OH-TEMPO	1.93	0.68	0.61	0.071	0.65	9.27 × 10^{-3}	−7.36 × 10^{-3}	1.28	1.44 × 10^{-6} (n = 1)
Catechol	1.5 × 10^{-3}	0.88	0.12	0.762	0.50	1.50 × 10^{-2}	−4.15 × 10^{-3}	3.62	9.79 × 10^{-7} (n = 2)
1,5-DAAQ	2.7 × 10^{-3}	−0.79	−0.83	0.042	−0.81	9.27 × 10^{-3}	−7.26 × 10^{-3}	1.28	2.54 × 10^{-7} (n = 2)
NMePh	1.6 × 10^{-3}	−1.15	−1.20	0.059	−1.17	2.19 × 10^{-3}	−1.26 × 10^{-3}	0.17	1.62 × 10^{-6} (n = 1)
BP	1 × 10^{-3}	-	−1.42	-	-	-	−2.76 × 10^{-2}	-	3.83 × 10^{-6} (n = 1)
Phenazine	1 × 10^{-2}	−0.39	−0.66	0.268	−0.53	2.51 × 10^{-2}	−5.22 × 10^{-2}	0.40	1.54 × 10^{-7} (n = 2)
2,3-Diaminophenazine	2.6 × 10^{-3}	−0.49	−1.05	0.555	−0.77	5.47 × 10^{-3}	−1.22 × 10^{-2}	0.45	4.25 × 10^{-7} (n = 2)

6.2. Organic Redox Active Materials as One Deep Eutectic Solvent Component

ORAM solubility is an issue in ethaline-based DES systems. One approach around this is to design the DES with a redox active component. Metal-based DES systems already demonstrate this, and recently the concept has been studied from an organic perspective.[14,16,25–36] The infancy of both ORFB and DES fields limit the extent of the existing literature. However, the wide range of ORAMs and possible DES systems mean the possibility for high-energy electrolytes is promising.

Little theoretical methodology covers which combination of components form a DES, as the systems do not always follow general trends or rules.[30] Therefore, to determine new DES systems this work takes ideas from existing literature containing a redox active DES component and applies them to the ORAMs in Figure 6.1.

Previous studies show 2:1 and 1:1 ratios of H_2Q:ChCl form DES systems with T_m above room temperature.[37,38] H_2Q dissolves to around 6 M in ethaline and its small molecular weight lends well to RFB systems. However, the relative solubilities of the reduced/oxidised states are an issue, as BQ is only soluble to 0.3 M.[39] Catechol is similar in structure to BQ and has reversible electrochemistry in acidic media.[40] Smith *et al.* show a 2:1 ratio of catechol and ChCl forms a DES with a T_m of 325 K. The catechol concentration reaches 6.6 M in this media, but the T_m is too high for a room temperature electrolyte and the electrochemistry is irreversible.[20]

Using the above system as inspiration, this study finds a previously unreported room temperature DES by combining oxalic acid (OA), ChCl, and catechol in a 1:1:2 molar ratio. A 1:1 mixture of ChCl:OA has a T_m of 307 K, hence including OA should improve both electrochemical reversibility and reduce the T_m. The mixture has a catechol concentration of 5.78 M and carries inherent conductivity due to the OA and the ChCl. Figure 6.2.(a) shows an observable oxidation and a less visible reduction of catechol when in 1:1 ChCl:OA at low concentrations (1.51 mM).

Increasing the catechol concentration so that it becomes the tertiary component in the 1:1:2 DES (Figure 6.2.(b)) renders the electrochemistry unobservable. The 1:1:2 DES has a high viscosity and barely flows at room temperature. The high viscosity reduces the rate of catechol mass transport to such a degree that there is no visible redox on the timescale of the CV.

The small geometric area of microelectrodes draws smaller currents and decreases the ohmic drop whilst enhancing the rate of mass transport.[41] Performing the CV analysis of 1:1:2 ChCl:OA:Catechol with a microelectrode results in a similar CV with no observable peaks indicating that the mass transport issue is not easily overcome.
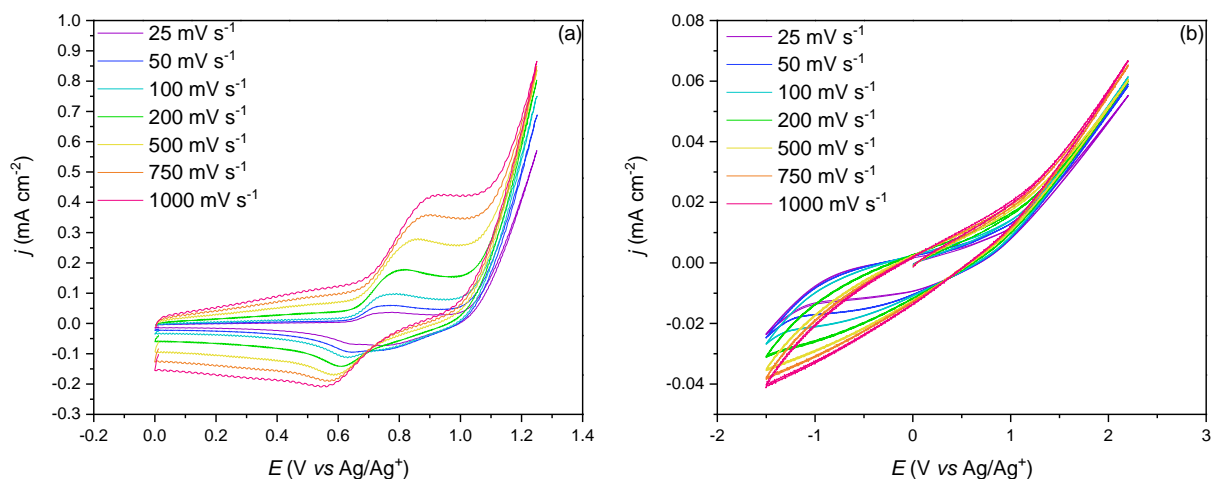
Figure 6.2. CV plots of (a) 1.5 mM catechol in 1:1 ChCl:OA at 328 K and (b) 1:1:2 ChCl:OA:Catechol DES at room temperature over scan rates 25 ≤ v ≤ 1000 mV s⁻¹ using a GC WE, Ag/Ag⁺ RE, and Pt CE.

1,5-DAAQ also gives reversible electrochemistry in ethaline (Figure 6.1.(c)) but suffers from low solubility (<10 mM). Despite the similar quinone backbone to catechol, 1,5-DAAQ does not form a room temperature DES with ChCl at any ratio, even after adding oxalic acid. The 1,5-DAAQ has a larger size and higher number of hydrogen bonding sites. These likely create a stronger intermolecular bonding network that results in the room temperature solid.

A 2:1 ratio of glycerol and ChCl forms a room temperature DES.[19] Using this as inspiration, the present study finds adding 4 molar equivalents of glycerol to the 1:2 1,5-DAAQ:ChCl solid mixture yields a viscous room temperature liquid. The final composition is 1:2:4 1,5-DAAQ:ChCl:glycerol, which has an active material of 1.41 M 1,5-DAAQ. Again, the high viscosity of the system leads to poor mass transport and results in almost unobservable redox for 1,5-DAAQ (Figure 6.3.(a)). Figure 6.3.(b) highlights the effect of the viscous media on the electrochemistry by overlaying the CV for the 1:2:4 1,5-DAAQ:ChCl:glycerol DES (black line) with that for the less viscous 2.7 mM 1,5-DAAQ in ethaline (red line) at 25 mV s⁻¹. Table 6.3. compares the electrochemical data.

The oxidative and reductive peaks at 1.13 V and -2.21 V in the 1:2:4 DES in Figure 6.3.(b) are due to degradation of the ChCl:Glycerol components. The redox of 1,5-DAAQ is at $E_{1/2}$ = −0.71 V (*vs* Ag/Ag⁺). The higher viscosity of the tertiary systems causes the wider ΔE_p in the 1:2:4 DES (0.95 V) compared to 1,5-DAAQ in ethaline (0.049 V). Interestingly, the peak currents in Figure 6.3.(b) between the two electrolytes are similar even though the 1,5-DAAQ concentrations are vastly different, at 1.42 M and 2.7 × 10⁻³ M, respectively. This indicates low material utilisation in the highly concentrated system, which is potentially due to the 1,5-DAAQ being 'trapped' in the DES network and not diffusing to the electrode for reaction. Increasing

the molar ratio of glycerol decreases the viscosity of the system but fails to improve the electrochemical properties.
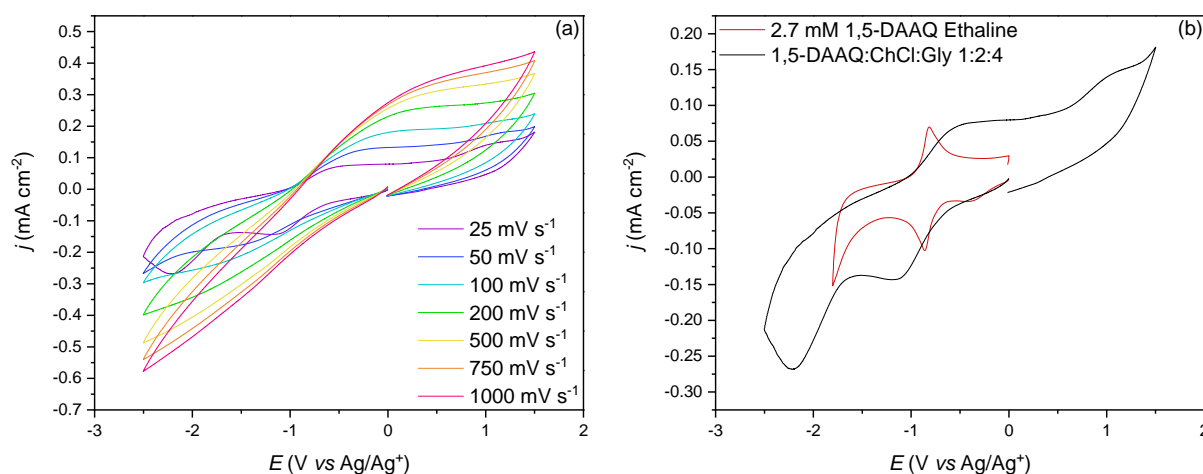
Figure 6.3. CVs of 1:2:4 1,5-DAAQ:ChCl:Glycerol DES over scan rates $25 \leq v \leq 1000$ mV s^{-1}, and (b) overlay of CVs for 1:2:4 1,5-DAAQ:ChCl:Glycerol and 2.7 mM 1,5-DAAQ in ethaline at 25 mV s^{-1}. CVs taken using a GC WE, Ag/Ag$^+$ RE, and Pt CE.

Table 6.3. Solubility and electrochemical data for different 1,5-DAAQ DES systems at 25 mV s^{-1} .

DES	1,5-DAAQ (M)	E_{pa} (V vs Ag/Ag$^+$)	E_{pc} (V vs Ag/Ag$^+$)	ΔE_p (V vs Ag/Ag$^+$)	$E_{1/2}$ (V vs Ag/Ag$^+$)	i_{pa} (mA)	i_{pa} (mA)	i_{pa}/i_{pc}
1:2:4 1,5-DAAQ:ChCl:Gly	1.42	−0.23	−1.18	0.950	−0.71	7.48×10^{-3}	-1.29×10^{-2}	0.60
1,5-DAAQ Ethaline	2.7×10^{-3}	−0.80	−0.86	0.049	−0.83	1.32×10^{-2}	-1.36×10^{-2}	0.97

TEMPO is a promising ORFB catholyte in aqueous and non-aqueous systems.[6,9,22,42–47] Some studies already cover TEMPO in DES-RFB applications due to its HBA-containing structure.[7,8,23] The promising electrochemical activity in ethaline in Figures 6.1.(a) and (i), and in the existing literature, guides this study towards a TEMPO-based DES.

Goeltz *et al.* form a DES comprising 2:1:4 4-OH-TEMPO:TEACl:H_2O with a T_m of 302 K and TEMPO redox at $E_{1/2}$ = 0.64 V (*vs* Ag/AgCl) with ΔE_p = 0.15 V at 323.15 K.[10] The team did not study at lower temperatures, but such high temperature systems will require large energy inputs and are hence not ideal for RFB devices.

Understanding the room temperature behaviour is pivotal for a feasible EESS. Figure 6.4. gives the CV for 2:1:4 4-OH-TEMPO:TEACl:H_2O at a T just above the T_m of 303 K. The ever-increasing oxidation and irreversible reduction at 0.5 V (*vs* Ag/Ag$^+$) demonstrate that the reversible 4-OH-TEMPO (3.5 M) redox is inaccessible in this DES at lower temperatures. The mixture is almost solid at this temperature, so the poor electrochemistry is likely a result of high viscosity. Therefore, the 2:1:4 system is not feasible for a DES-RFB.
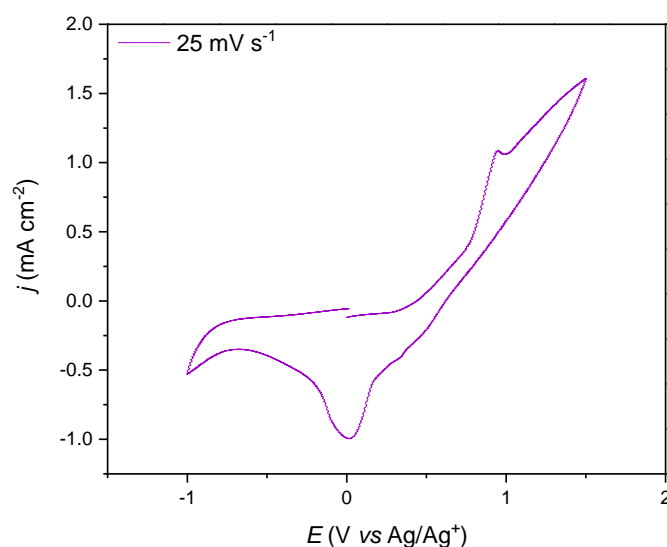
Figure 6.4. CV plot for 1:1 4-OH-TEMPO:LiTFSI with 15 wt% ACN at 25 mV s⁻¹ using a GC WE, Ag/Ag⁺ RE, and Pt CE.

High viscosity is an issue in other TEMPO-DESs, such as in MeO-TEMPO:LiTFSI 1:1.[48] The inventors of this DES note vast improvements in the electrochemistry with up to 17 wt% of water or ACN additives. The additives decrease the viscosity from 20000 mPa s to 72 mPa s. The team did not expand the test to other TEMPO derivatives. Taking inspiration from this MeO-TEMPO:LiTFSI system, the present study finds pairing 4-OH-TEMPO with LiTFSI in a similar 1:1 ratio yields a viscous room-temperature liquid. Interestingly, the 4-OH-TEMPO system forms a liquid at room temperature, whereas the MeO-TEMPO equivalent forms a super cooled liquid that crystallises upon seeding.

Figure 6.5. shows the CV for 1:1 4-OH-TEMPO:LiTFSI after adding a 15 wt% ACN co-solvent. The final 4-OH-TEMPO concentration is 2.36 M. The additional ACN reduces the room temperature viscosity enough for electrochemical analysis. The redox wave centred at $E_{1/2}$ = 0.47 V with ΔE_p = 0.94 V (*vs* Ag/Ag$^+$) indicates vast ohmic overpotentials compared to 4-OH-TEMPO in conventional solvents. The redox process in 4-OH-TEMPO:LiTFSI also has wider

separation than the literature MeO-TEMPO:LiTFSI system. This is possibly because 4-OH-TEMPO has more hydrogen bond forming moieties (2 HBA, 1 HBD) than MeO-TEMPO (2 HBA). This may create a stronger hydrogen bonding network between 4-OH-TEMPO, LiTFSI and the co-solvent. A stronger network will hinder ORAM diffusion to the electrode alongside stabilising the 4-OH-TEMPO neutral radical, meaning it will require more extreme potentials to react.
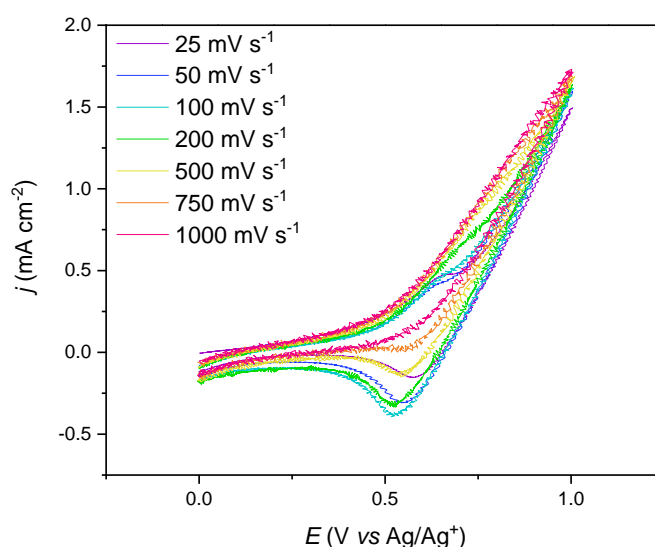
Figure 6.5. CV for 2:1:4 4-OH-TEMPO:TEACl:H_2O over scan rates $25 \leq v \leq 1000$ mV s^{-1} at 303 K using a GC WE, Ag/Ag+ RE, and Pt CE.

Further expanding the TEMPO:LiTFSI DES finds the similar system of 4-NH$_2$-TEMPO in 1:1 LiTFSI and H_2O to be solid at all temperatures. 4-NH$_2$-TEMPO has the same number of HBA and HBD groups as 4-OH-TEMPO, so this cannot be the only factor defining the room-temperature physical state. The state and viscosity of TEMPO:LiTFSI DESs follows the trend in melting point for each individual TEMPO derivative (MeO-TEMPO < 4-OH-TEMPO < 4-NH$_2$-TEMPO). The higher number of hydrogen bonding moieties in 4-NH$_2$-TEMPO and 4-OH-TEMPO will also create stronger interactions with the LiTFSI. Therefore, in designing a TEMPO-based LiTFSI-DES with a low viscosity, one should use TEMPO derivatives with low melting points and weaker or less HBD moieties. Utilising a higher percentage of hydrogen bonding disruptors such as ACN or H_2O, and paying attention to steric affects will also improve the fluid properties.

The DES driving force for the TEMPO:LiTFSI systems involves coordination of the nitroxyl radical (N–O·) and the Li+ as well as the large disruptive anion size of TFSI−.[14,16] Similarly, electrophilic carbonyl (C=O) groups also coordinate with Li+ to yield DESs, for example 1:2:3 NMePh:LiTFSI:Urea.[14] This system has the most negative reversible redox potential (−1.79 V (*vs* Ag/Ag+)) of any ORAM-DES to date. BP has an even more negative redox potential of

253

−2.16 V (*vs* Ag/Ag⁺) and also contains the carbonyl moiety, but literature is yet to demonsrate an BP containing-DES.[49]

Mixing a 1:2:3 molar ratio of BP:LiTFSI:Urea forms a previously unreported room temperature DES with a BP concentration of 1.37 M. The DES driving force is likely between C=O on BP and Li⁺, as in 1:2:3 NMePh:LiTFSI:Urea. Unfortunately, the black line in Figure 6.6. shows the viscosity of the system is too high to observe redox in the CV. The red line in Figure 6.6. shows how adding a 10 % ACN co-solvent (new BP concentration = 1.24 M), reduces the viscosity enough to observe BP reduction, with E_{pc} = −2.38 V (*vs* Ag/Ag⁺) at 25 mV s⁻¹. The process is irreversible and becomes unobservable when v > 100 mV s⁻¹ and hence is not useful for an EESS. The irreversibility of BPs electrochemistry is not a surprise, as literature shows the nature of the solvent and supporting electrolyte system is pivotal to the reversibility of the redox process.[15]
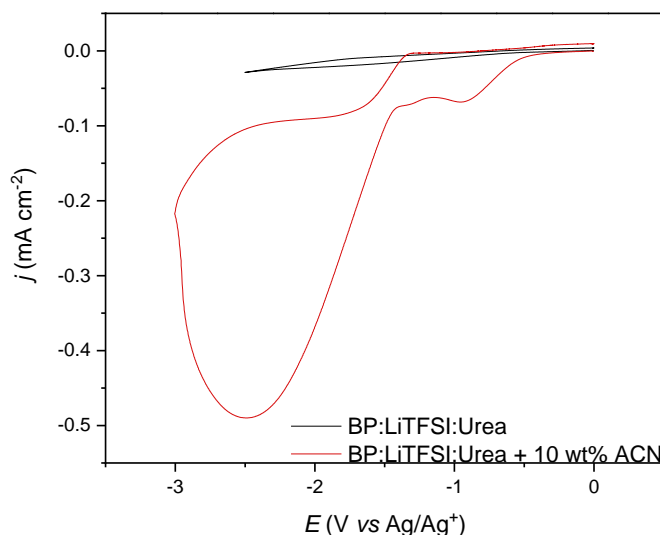
Figure 6.6. CV data of (black line) 1:2:3 BP:LiTFSI:Urea and (red line) 1:2:3 BP:LiTFSI:Urea + 10 wt% ACN at 25 mV s⁻¹ using a GC WE, Ag/Ag⁺ RE, and Pt CE.

LiTFSI is expensive and toxic and would ideally not be in a RFB. However, the coordination interactions between the ORAM carbonyl and the Li⁺ cation, alongside the plasticising effects from the Lewis basic properties of [TFSI]⁻ are critical to the DES driving force. Moreover, the ORAMs show better radical stability with [TFSI]⁻ than with other supporting anions. This makes it difficult to replace [TFSI]⁻ with other cheaper or safer materials.[14] The reliance on both components of LiTFSI in forming the DES presents a challenge with the NMePh and BP systems, as environmental benignity and low cost are two key aspects behind the DES-electrolyte concept.

To summarise, this section extrapolates from previous literature and reports the discovery and electrochemical analysis of the following room-temperature DES systems: 1:1:2 ChCl:OA: catechol, 1:2:4 1,5-DAAQ:ChCl:Glycerol, 1:1 4-OH-TEMPO:LiTFSI, and 1:2:3 BP:LiTFSI:Urea. High viscosities, irreversible electrochemistry, or slow redox kinetics hamper the new systems such that they are not feasible for ORFB devices.

6.3.   Organic Redox Active Materials as Both DES Components

6.3.1. Theorising a Novel BP:TEMPO Deep Eutectic Solvent

The systems discussed thus far comprise either a) ORAMs dissolved in a DES solvent (Section 6.1.) or b) ORAMs forming one component of the DES system (Section 6.2.). The benefit of the former is in the safety, affordability, wide ESW, and ease of preparation of DESs like ethaline. Nonetheless, solubility limitations obstruct the development of competitive ORFBs. The latter systems benefit from high ORAM concentrations and hence promisingly high energy densities, but suffer from high viscosities and sluggish mass transfer. Furthermore, these systems are difficult to develop as they rarely follow structured theory to determine trends.

None of the DES electrolyte compositions in this chapter so far a feasible for an ORFB due to insufficient electrochemical, chemical, or physicochemical properties. Additionally, each of these systems have at least one electrochemically inactive DES component. This section therefore searches for a new DES system based on solely RAMs with a low viscosity and reasonable electrochemical activity. This ensures a maximum active material concentration and reasonable pumping costs.

As previously discussed, BP has one of the most negative redox potentials amongst organic anolyte materials, at −2.16 V (*vs* Ag/Ag⁺) in 0.1 M TEAPF$_6$, ACN and is soluble up to 4.3 M.[15] Xing *et al.* pair BP with TEMPO to give a non-aqueous RFB with a cell voltage of 2.41 V and a theoretical energy density of 139 Wh L^{-1}.[15] Figure 6.7. shows the CVs for BP and TEMPO in 0.1 M TBAPF$_6$, ACN at 100 mV s^{-1} to have redox potentials of $E_{1/2}$ = −1.87 V and 0.71 V (*vs* Ag/Ag⁺), respectively. This gives a theoretical cell voltage of 2.58 V for a BP/TEMPO cell, which is a lower OCV than literature predicts. This may be due the different supporting salts shifting the BP redox potential positive.
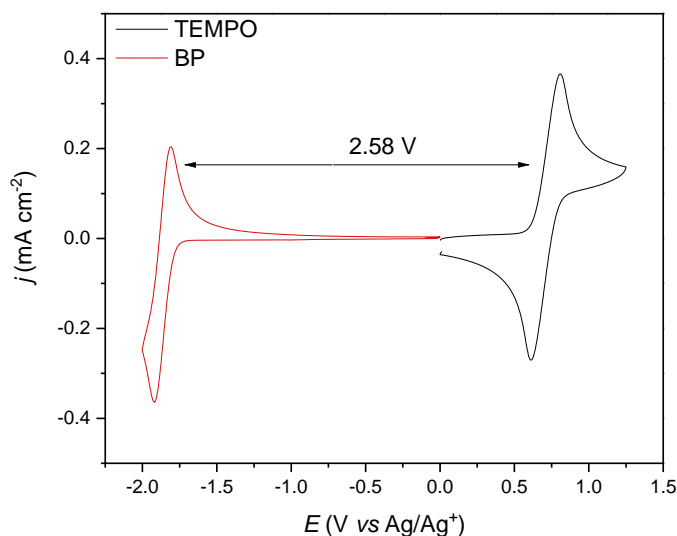
Figure 6.7. CVs at 100 mV s⁻¹ for 1 mM (black line) TEMPO and (red line) BP in 0.1 M TBAPF₆, ACN showing the theoretical cell voltage.

Zhang *et al.* form a low viscosity eutectic electrolyte using a biredox molecule of BuPh and DMFc.[50] The electrolyte has active concentrations of 3.5 M, a room temperature viscosity of 4.5 mPa s, and a working voltage of 1.8 V. The DES driving force is the interaction between the carbonyl moiety on BuPh and the methyl groups on DMFc. Extrapolating this concept to the theoretical BP/TEMPO system results in a previously unreported, low viscosity, room temperature, dark brown DES of 1:1 BP:TEMPO. This system is key interest given its high ORAM concentration and low observational viscosity. The DES driving force is not hydrogen bonding as in ethaline or reline, as both BP and TEMPO only contain one HBA moiety and no HBDs. Instead the driving force is likely similar to that in BuPh-DMFc and a result of C=O and C-CH₃ interactions (Figure 6.8.).
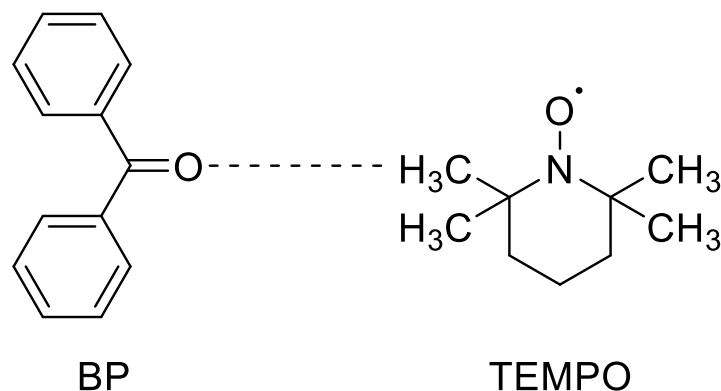
Figure 6.8. Schematic of the most likely driving force interactions for the room temperature 1:1 BP:TEMPO DES

The driving force poses an issue in applying the BP:TEMPO DES for EESSs. The DES driving force involves the redox active centre of the BP ORAM. During charge the C=O functional group reduces to the radical anion, which may alter the BP-TEMPO interaction. This could lead to salting out of the ORAM, as with H_2Q and BQ, or to a stronger coordination network that raises the T_m and changes the physicochemical properties.[16,39]

It is imperative to understand the physicochemical properties of a system if it is to find use as a flowing electrolyte. The next section therefore examines the effects of TEMPO mole fraction and temperature on the physicochemical properties and investigates the electrochemical capabilities of this new DES system with different supporting electrolytes and co-solvents.

6.3.2. Physicochemical Properties of BP:TEMPO

Understanding the physicochemical properties of an electrolyte is pivotal for a successful RFB. High viscosity and density lead to sluggish mass transport, which then requires large over potentials and higher pumping power. Low ionic conductivity prevents complete ORAM utilisation and adds additional complications with supporting electrolytes. Together, high viscosities and low ionic conductivities lead to low operational current densities (<1 mA cm^{-2}).[51] Other characteristics such as a low T_m are important for a wide the operational temperature range. The ideal RFB electrolyte has low viscosity, density and T_m alongside high ionic conductivity and reversible electrochemistry. Appendix 6.D. tabulates the physicochemical data of BP:TEMPO in Section 6.3.2.

6.3.2.1. Phase Behaviour

Figure 6.9. shows photographs of BP:TEMPO mixtures with molar ratios ranging 2:1 – 1:10. Molar ratios 1:1, 1:2, 1:3, 1:4 yield room temperature liquids, and crystals appear when the TEMPO molar fraction is <5 or the BP molar fraction is higher than TEMPO (2:1). Table 6.4. shows the ORAM concentration and T_m for each room-temperature liquid system. The DESs experience a depression in T_m compared to the parent molecules, which have melting points of 321 and 309 K for BP and TEMPO, respectively. The 1:1, 1:3, and 1:4 DESs have a T_m of 290 K, and the 1:2 system is the eutectic composition with a T_m of 273 K.

Figure 6.9. Image of BP:TEMPO mixtures with molar ratios from left to right of: 2:1, 1:2, 1:3, 1:4, 1:5, 1:6, and 1:10

Table 6.4. BP and TEMPO concentrations and T_m data for each room-temperature liquid DES in Figure 6.9.

DES	1:1	1:2	1:3	1:4
BP/TEMPO Concentration (M)	2.78/2.78	1.78/3.56	1.56/4.69	1.47/5.88
T_m (K)	290	273	290	290

Xing *et al*. report the maximum solubilities of BP and TEMPO in ACN without supporting electrolytes as 4.3 M and 6.1 M, which is higher than the DESs in Table 6.4.[15] The DESs in Table 6.4. are, however, higher in concentration than the aqueous solubilities wherein BP is insoluble, and TEMPO achieves 2.1 M.

Nevertheless, when Xing *et al*. apply the BP and TEMPO ORAMs for RFB testing they do not utilise the maximum concentrations. The team use low concentrations of 0.003 M with a 0.5 M TEAPF$_6$ supporting salt and do not give a reason for the low concentration. The advantage of the DES systems in Table 6.4. over the previous non-aqueous studies is the full utilisation of high ORAM concentration. Other advantages involve cost reductions, as further co-solvents are not necessary, alongside simpler electrolyte preparation as the DES involves less individual components.

Interestingly, combining BP with 4-OH-TEMPO fails to produce a room temperature liquid at any ratio. This is likely because the extra hydrogen bonding moieties from the additional -OH group form a hydrogen bonding network with BP and other OH-TEMPO molecules that is strong enough to facilitate crystallisation.

6.3.2.2. pH

Figure 6.10. shows the relationship of pH with temperature over 293.15 – 323.15 K for BP:TEMPO molar ratios 1:1 – 1:4. At room temperature the lower mole fraction DESs (1:1 and 1:2) are close to neutral pH. A higher TEMPO content (1:3, 1:4) leads to a more acidic DES. Overall, increasing the TEMPO content decreases the pH and each DES and becomes more acidic with increasing T.
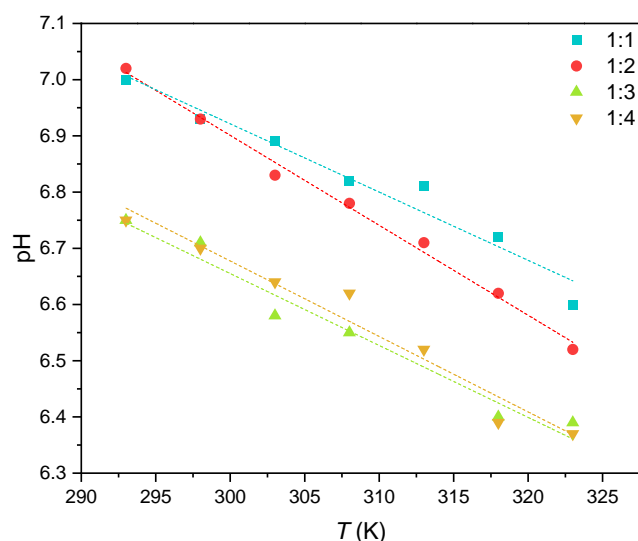
Figure 6.10. Relationship of pH vs temperature over BP:TEMPO molar ratios 1:1, 1:2, 1:3, and 1:4.

The acidic nature of the DES likely comes from the hygroscopicity of TEMPO. TEMPO absorbs atmospheric H_2O and creates a degree of water content in the DES. This dissolved water can split into H^+ causing a decrease in pH. Higher TEMPO molar fractions absorb more water and thus result in a lower pH DES.

6.3.2.3. Density

Density (ρ) is an important physical property that affects the design and operation of processes. A low ρ is desirable for flow devices. Most DES systems exhibit higher densities than water. Hole-theory explains this phenomenon in that the DES comprises large ionic species and smaller holes.[27] Combining the relatively large DES components into a liquid network results in a smaller hole radius and thus an increase in ρ.

Figure 6.11. shows the BP:TEMPO ρ at different molar ratios with respect to T, as well as the effect of adding 1.25 M TBABF$_4$ supporting electrolyte (purple diamonds) to the eutectic composition (1:2). The BP:TEMPO DES has no inherent conductivity, and so its physicochemical response to additional supporting salts is of interest. The ρ decreases with

increasing TEMPO mole fraction and increasing T. Appendix 6.E. shows the linear regression of the experimental ρ as a function of T have a linear relationship with an R^2 value of almost one.

The BP:TEMPO DESs have a lower ρ than previous DES systems (TEMPO in ethaline $\rho =$
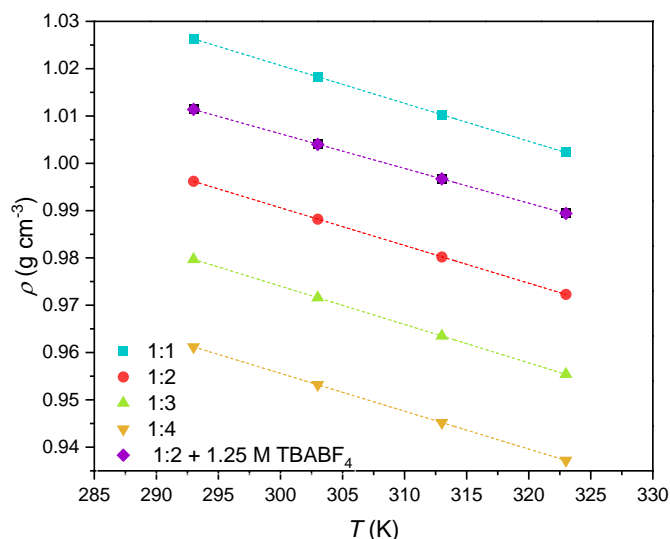
Figure 6.11. The density of different molar ratios of BP:TEMPO with respect to temperature, and the effect of 1.25 M TBABF4 supporting electrolyte on the eutectic DES composition (purple diamonds).

1.12 g cm^{-3})[8] and even have a similar density to water (ρ = 0.9982 g cm^{-3} at 298 K).[52,53] The 1:1 ratio has the highest ρ of the BP:TEMPO systems (1.0263 g cm^{-3} at 293.15 K) and 1:4 the lowest (0.9372 g cm^{-3} at 323.15 K). The ρ values for the DESs fall between the respective values for the parent molecules, which 0.912 g cm^{-3} for TEMPO at 313 K, and 1.11 g cm^{-3} for BP at 291 K. Including a supporting salt raises the 1:2 BP:TEMPO ρ from 0.9962 g cm^{-3} to1.0114 g cm^{-3} at 293.15 K, but its value remains below that of the 1:1 system.

Increasing T improves molecular mobility in the DES, which then increases the volume. This leads to the inverse relationship of ρ as a function of T. Increasing TEMPO molar fraction decreases ρ due to hole-theory and the relative molar volumes (V_m) of the components. Table 6.5. gives the V_m of BP and TEMPO in the DES mixtures at different molar ratios at 293.15 K (See Chapter 2.4.6., Equation 2.27.).

TEMPO has a smaller V_m at all DES compositions. Increasing its molar fraction with respect to BP increases the free volume in the DES network and reduces the overall ρ of the system. Additionally, there is likely a higher degree of interaction between the two components when the molar ratio is more similar. A 1:1 ratio DES will have a higher number of interactions between C=O and C-CH$_3$. This creates a more tightly bound structure, and hence a higher ρ, than when the TEMPO mole fraction exceeds the BP.

Table 6.5. Corresponding V_m values for BP and TEMPO in each molar fraction of BP:TEMPO at 293.15 K.

	1:1	1:2	1:3	1:4
ρ (g cm^{-3})	1.0263	0.9962	0.9797	0.9612
BP V_m (Mr = 182.22 g mol^{-1})	177.55	182.91	185.99	189.57
TEMPO V_m (Mr = 122.25 g mol^{-1})	152.25	156.85	159.49	162.56

6.3.2.4. Viscosity

The viscosity (η) is the resistance to flow of a fluid and is dependent on the interactions between the residing species. It has a strong effect on mass transport properties as it affects the ionic conductivity, ion diffusion rates, and electrode wettability.[51] Most DESs exhibit higher viscosities (<100 mPa s at room temperature)[27] than their aqueous and non-aqueous counterparts (1.043 mPa s for 0.5 M NaCl, 0.334 mPa s for ACN)[54] because of the larger influence of intermolecular interactions. This is not good for RFBs, as high η electrolytes create larger pressure drops in the stack during the charge and discharge process. This necessitates more pumping energy and results in low system efficiency and capacity. It is therefore essential to have a thorough understanding of an electrolytes η to for reduce the energy requirements in flow applications.[52]

Figure 6.12. compares the variation of η and T on the 1:2 BP:TEMPO DES (red circles), and the effect of adding a 1.25 M TBABF$_4$ supporting electrolyte (purple diamonds). Figure 6.12.(a) shows the relationship between η and T, and Figure 6.12.(b) the natural log of η against the reciprocal of T wherein the linear regressions have an R^2 of almost 1. There is no data for the other DES compositions as they have viscosities above the limits of the viscometer. This is

not surprising, as the eutectic composition (1:2) is likely to have a lower η than other molar fractions.
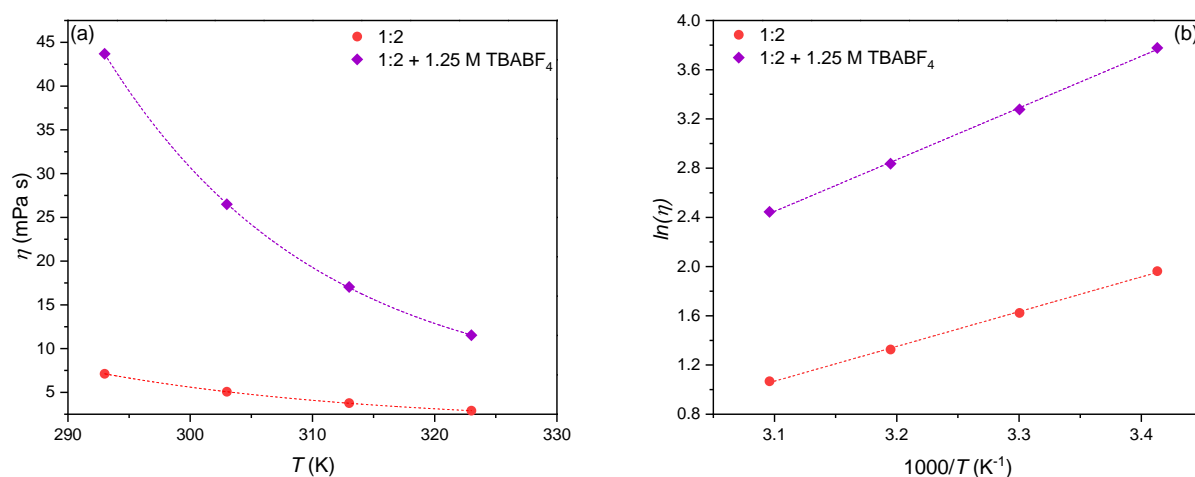
Figure 6.12. (a) The dynamic viscosity against temperature, (b) the natural logarithm of dynamic viscosity against the reciprocal temperature for the 1:2 BP:TEMPO DES (red circles) and 1:2 BP:TEMPO DES with + 1.25 M TBABF$_4$ (purple diamonds).

The binary eutectic mixtures in Figure 6.12.(a) have exponentially decaying η-T relationship profiles. The trend is similar to literature reports of other RTIL and DES systems. The η values are much lower than in previous systems, and similar to those in the BuPh-DMFc DES (4.5 mPa s).[50,52,55,56] Including the supporting electrolyte has a 6-fold increase on the room-temperature η of 1:2 BP:TEMPO from 7.123 mPa s to 43.697 mPa s. The increase seems large but the densities are still low relative to other DESs, for example the room-temperature η of TEMPO in ethaline is 60 mPa s.[8] This highlights the potential for the BP:TEMPO DES for a flow device.

The plots of log η as a function of reciprocal absolute T (Figure 6.12.(b)) show the linear profiles align well with the η-T relationship described by the Arrhenius equation (Chapter 2.4.7., Equation 2.30). Table 6.7. tabulates the η and v values and subsequent E_a values for the DESs in Figure 6.12. A lower E_a is more desirable. A high-energy barrier of the fluid to shear stress indicates it is more difficult for the molecules to move past each other due to a combination of stronger inter- and intramolecular interactions in the fluid and the size/entanglement of the molecules.

E_a values for the 1:2 DES increase from 23.50 kJ mol^{-1} to 34.96 kJ mol^{-1} after adding the supporting salt. This indicates a higher energy barrier for mass transport in the salt-supported solution. E_a increases because the supporting salt molecules take up space in the DES holes and reduces their radius. This makes it more difficult for the DES molecules to move. The non-ionic nature of the BP and TEMPO components demand the inclusion of supporting salts, but

the inclusion of supporting salts impairs the physicochemical properties. This is not ideal for RFB applications. Different supporting salts identities and concentrations will have different degrees of interaction with the DES molecules and different effects on the hole radii. This may reduce the E_a of the salt containing DES. Therefore, future work should consider the physicochemistry of a wider range of supporting salts and concentration.

Table 6.6. Dynamic and kinematic viscosities and activation energy data for 1:2 BP:TEMPO and 1:2 BP:TEMPO with a 1.25 M TBABF₄ supporting salt.

BP:TEMPO	η (mPa s)	v (mm² s⁻¹)	E_a (kJ mol⁻¹)
1:2	7.123	7.150	23.50
1:2 + 1.25 M TBABF₄	43.697	43.206	34.96

6.3.2.5.   Conductivity

Ionic conductivity (σ) is another crucial parameter in EESSs. The high η of most DES systems leads to poor σ of less than 2 mS cm⁻¹ at room temperature.[27] Techno-economic analysis suggests an electrochemical device requires an a η <10 mPa s with an σ >5 mS cm⁻¹ to minimise hydrodynamic resistance for battery applications.[26] Some DES systems do achieve this, such as TEMPO in ethaline which has σ of 6 mS cm⁻¹.[8] Figure 6.13. shows how σ varies with T in (a) BP:TEMPO DESs over a range of mole fractions and (b) 1:2 BP:TEMPO with 1.25 M TBABF₄. Figures 6.13.(c) and (d) show the corresponding ln σ versus T^{-1} to fit the Arrhenius-like equation (Chapter 2.4.8., Equation 2.31) which predicts the σ behaviour of the DES. Table 6.7. gives the conductivity-temperature parameters and R^2 coefficients for the linear regressions.

Figure 6.13.(a) shows the DES without any supporting salts has σ in the µS cm⁻¹ range. The low values due to non-ionicity of the DES molecules. The σ for the pure DESs are in a similar region to pure non-aqueous (10^{-8} – 10^{-10} S cm⁻¹) and pure water electrolytes (6×10^{-8} S cm⁻¹).[57] The large increase in σ from 0.712 to 405.7 µS cm⁻¹ upon including TBABF₄ demonstrates the necessity of supporting electrolytes. However, the conductivity is still an order of magnitude below that required for a feasible electrolyte.

The presence of any conductivity in the pure DES is interesting as there should be no ions in the media to carry charge. The likely cause for the small conductivity is water absorbed by the hygroscopic TEMPO, *vide supra* Section 6.3.2.2. The conductivity increases with increasing TEMPO molar fraction (0.439 µS cm⁻¹ and for 1.200 µS cm⁻¹ for 1:1 and 1:4 BP:TEMPO at

293.15 K, respectively) because the presence of more TEMPO means the absorption of more water. Additionally, the smaller dimension of TEMPO compared to BP means that at a higher TEMPO molar fraction there are larger holes in the DES network. These holes facilitate atomic movement and improve the conductivity.
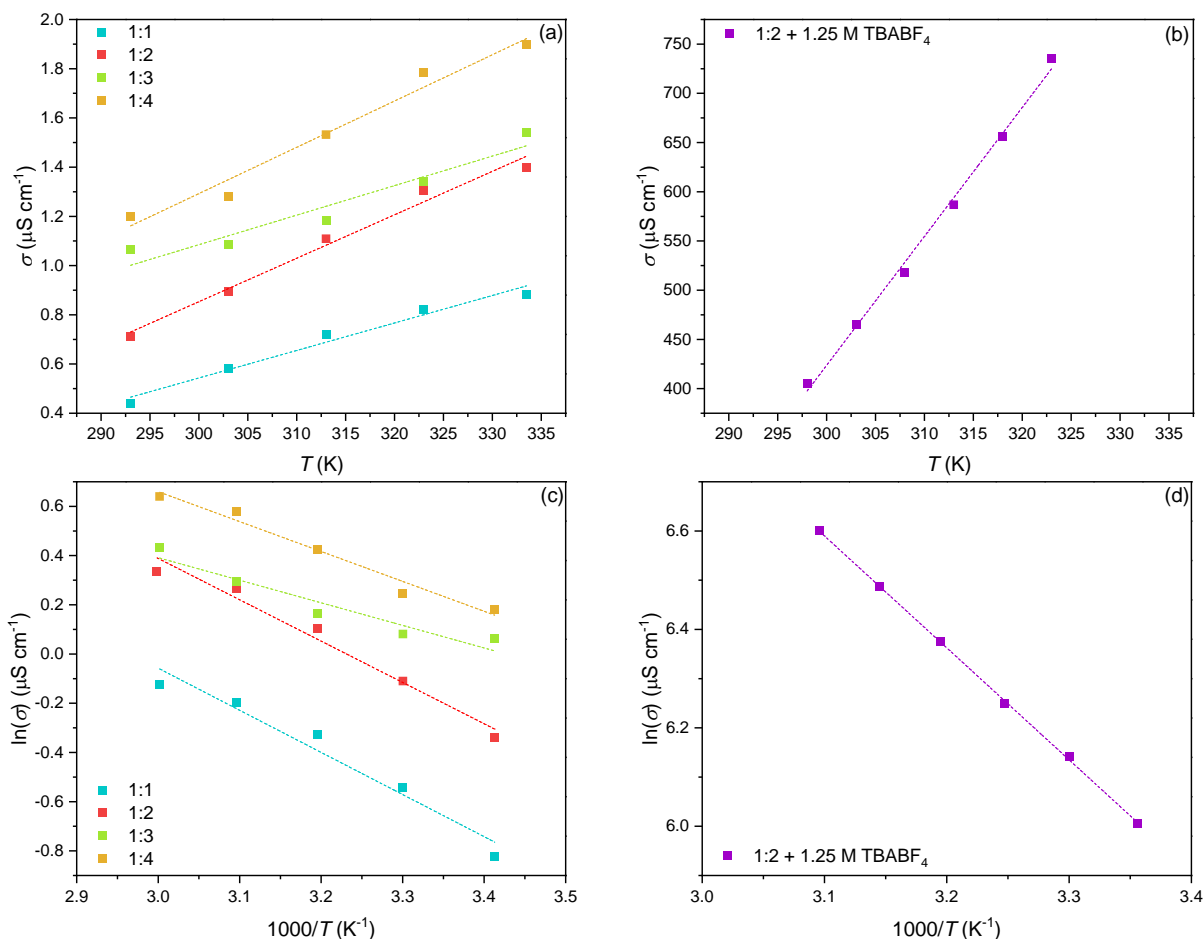
Figure 6.13. Plots of the variation of conductivity with temperature for (a) pure BP:TEMPO DESs at a range of molar ratios and (b) 1:2 BP:TEMPO + 1.25 M TBABF₄. Graphs (c) and (d) show the corresponding plots of ln(conductivity) against the reciprocal temperature.

Table 6.7. Conductivity-temperature parameters for BP:TEMPO DESs.

BP:TEMPO	σ^o ($\mu S\ cm^{-1}$)	E_σ ($kJ\ mol^{-1}$)	R^2
1:1	160	−14.23	0.959
1:2	137	−14.06	0.977
1:3	23	−7.63	0.920
1:4	74	−10.10	0.972
1:2 + 1.25 M TBABF₄	0.75	−18.30	0.999

The σ increases with T in a linear behaviour that follows the prediction of the Arrhenius-type equation (Chapter 2.4.8., Equation 2.31). The trend is due to an increase in kinetic energy with T increasing the frequency of collision between molecules. The decreasing η with T will also have an effect, in that the molecules will have faster transport through the media.

Generally, E_σ decreases with increasing TEMPO content, ranging $-14.23 - -10.10$ kJ mol^{-1} from 1:1 – 1:4 BP:TEMPO. The 1:3 sample does not follow the trend and the lower R^2 reflects this. These conductivity values are comparable to other non-ionic DES analogues in the literature.[53] Adding a supporting electrolyte expectedly improves the E_σ to -18.30 kJ mol^{-1}. A higher E_σ indicates the σ changes more rapidly than in systems with a lower E_σ over a given T range. Therefore, the effect of T on σ is greater at lower TEMPO molar fractions and with a supporting electrolyte. The E_σ values relate to the energy requirement for the formation and expansion of the vacancies responsible for mass transport, similarly to E_a in Section 6.3.2.4. The lower E_σ in the higher molar fraction TEMPO solutions is reflective of the lesser amount of intermolecular interactions present in the DES than in equal ratios of BP and TEMPO.

6.3.3. Electrochemical Properties of BP:TEMPO

The near neutral pH, low T_m, low ρ and low η of the BP:TEMPO DESs in Section 6.3.2. are promising fluid properties for ORFB applications. The DES σ is low because neither BP nor TEMPO are ionic species, and so a charge carrying supporting salt must be included to form a viable EESS.

Chapter 3.3. discusses how the identity of the supporting electrolyte plays a large role in the redox activity of the molecules. Hence, great care should be taken in selecting the optimum supporting salt for the BP:TEMPO DES. Electrochemical devices demand at least a 1:1 ratio of charge carrier to RAM for single electron transfer processes. Typically, CV experiments use supporting salt concentrations that exceed the RAM by a factor of one hundred. The high concentrations in the DES means a large quantity of supporting electrolyte would have to be soluble to access 100 % of the active material. For example, to supply ionic conductivity to every TEMPO molecule in the 1:2 BP:TEMPO DES (3.56 M TEMPO) the supporting salt would need to be soluble to over 3.5 M. A limiting factor in these high concentration DESs is therefore the solubility of the supporting salt, which in such large quantities will vastly increase the cost.[50] Additionally, the supporting salt may negatively affect some of the physicochemical properties such as increasing ρ and η as in Figures 6.11. and 6.12.

This section investigates the difference in electrochemical performance of the BP:TEMPO DES with different co-solvents (H$_2$O, EG, and ACN) and supporting salts (TBAPF$_6$, TBABF$_4$,

and TEACl). The physicochemical responses of the 1:2 BP:TEMPO system to a 1.25 M TBABF$_4$ supporting salt are above in Section 6.3.2.

The supporting electrolytes in this study were selected for the following reasons:

- TBAPF$_6$: Both BP and TEMPO show reversible electrochemistry with a TBABF$_6$ supporting salt (See Figure 6.8.).
- TEACl: TEA$^+$ has higher conductivity than TBA$^+$ in non-aqueous media.[58] TEACl is similar to the DES system that inspired the BP:TEMPO DES by Zhang *et al.*, who show TEABF$_4$ is soluble to >1 M with a 1:1 ratio of ACN in their BuPh-DMFc system.[50] TEABF$_4$ was not available for this study and so a supporting salt containing the same TEA$^+$ cation was selected. Additionally, TEACl uses the Cl$^-$ ion for charge balancing across the IEM in an RFB. This makes for facile membrane selection in full battery tests because the small Cl$^-$ ion is commonly used.
- TBABF$_4$: TBABF$_4$ is a common supporting salt with one of the widest ESWs.[59] A wide ESW is beneficial in overcoming the large overpotentials resulting from the sluggish mass transport in these high concentration systems.

The maximum supporting salt concentrations in the pure DES are <0.1 M, 0.1 M, and nearly 2 M for TEACl, TBAPF$_6$, and TBABF$_4$, respectively. The solubilities did not noticeably change with different TEMPO molar fractions. The blank supporting electrolyte CV scans in Appendix 6.F. give the ESWs of TEACl, TBABF$_4$, and TBAPF$_6$ as 3.75 V (1.4 – –2.75 V (*vs* Ag/Ag$^+$)), 6 V (3 V – –3 V (*vs* Ag/Ag$^+$)), and 7.3 V (4.5 – –2.8 V (*vs* Ag/Ag$^+$)), respectively. The wide ESW and high solubility of TBABF$_4$ make it the most useful supporting salt for this DES.

6.3.3.1. Full-Cell Studies

The 1:1 BP:TEMPO DES has the highest concentration of both ORAMs (2.78 M) and would result in the highest energy density ORFB. Figure 6.14. shows the CV for 1:1 BP:TEMPO with 2 M TBABF$_4$ and a 20 wt% ACN co-solvent. Table 6.8. gives the corresponding electrochemical data. The ACN co-solvent is necessary to improve the diffusion characteristics enough to visualise the full redox process of both ORAMs. Figure 6.14. shows four redox peaks, two oxidation peaks at 1.46 V (I$_a$) and 0.18 V (II$_a$) (*vs* Ag/Ag$^+$) and two reduction peaks at −0.33 V (I$_c$) and −2.42 V (II$_c$) (*vs* Ag/Ag$^+$). Figures 6.15.(a) and (b) suggests the possible electrochemical processes responsible for the redox waves in Figure 6.14.
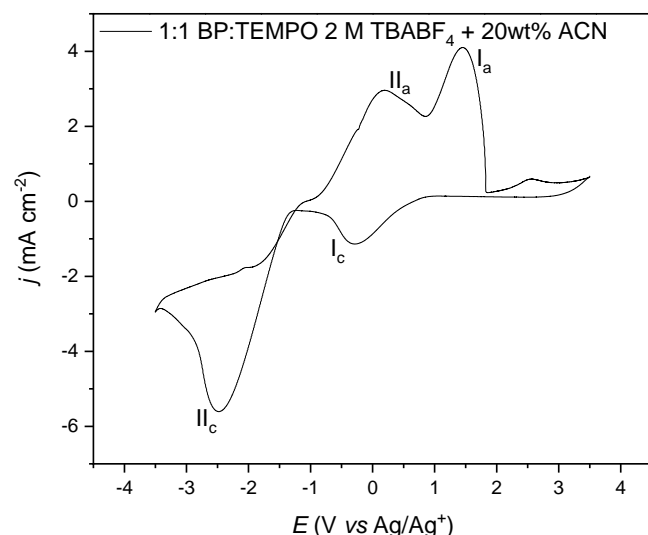
Figure 6.14. CV of 1:1 BP:TEMPO with 2 M TBABF$_4$ and 20 wt% ACN at 25 mV s^{-1}. I$_a$ and II$_a$ represent the anodic and I$_c$ and II$_c$ the cathodic peaks. All tests use a GC WE, Ag/Ag$^+$ RE, and Pt CE.

Table 6.8. Electrochemical data for 1:1 BP:TEMPO, 2 M TBABF$_4$, 20 wt% ACN.

Peaks	E_{pa} (V) (*vs* Ag/Ag$^+$)	E_{pc} (V) (*vs* Ag/Ag$^+$)	ΔE_p (V) (*vs* Ag/Ag$^+$)	$E_{1/2}$ (V) (*vs* Ag/Ag$^+$)	i_{pa} (mA)	i_{pc} (mA)	i_{pa}/i_{pc}
I$_a$, I$_c$	1.45	−0.29	1.74	1.16	5.40×10^{-1}	-2.4×10^{-1}	2.14
II$_a$, II$_c$	0.20	−2.47	2.67	−1.13	4.60×10^{-1}	−1.05	0.43

Peaks I$_a$ and I$_c$ are likely the oxidation and subsequent reduction of TEMPO (Figure 6.15.(a)). The $E_{1/2}$ of the I$_a$/I$_c$ wave at 1.15 V does, however, lie more positive than that of TEMPO in ACN (see Figure 6.7.), which is 0.71 V (*vs* Ag/Ag$^+$).

Peak II$_c$ and II$_a$ are possibly the reduction and return oxidation of BP (Figure 6.15.(b)). BP reduction in ACN has an $E_{1/2}$ of −1.87 V (*vs* Ag/Ag$^+$). The more negative wave in Figure 6.14. (II$_a$/II$_c$) has an $E_{1/2}$ = −1.13 V (*vs* Ag/Ag$^+$), which is also more positive than non-aqueous BP reduction should lie.

Another possible explanation for the more negative redox wave may be the reduction of TEMPO shown in Figure 6.15.(c). This process is usually a rapid irreversible proton transfer of the aminoxy anion to TEMPOH which occurs at −0.9 V in aqueous media, and between −1 and −1.8 V in non-aqueous and RTIL environments.[44] There is a positive shift of 0.74 V in E_{pa} for TEMPO oxidation in the DES in Figure 6.14 (I$_a$ = 1.45 V (*vs* Ag/Ag$^+$)) compared to conventional non-aqueous electrolytes (0.71 V (*vs* Ag/Ag$^+$)). If this irreversible reduction step

were also shifted by a similar value it would appear between −1.75 V to −2.55 V (vs Ag/Ag⁺), which is near the potential of II$_c$ (E_{pc} = −2.47 V (vs Ag/Ag⁺)).
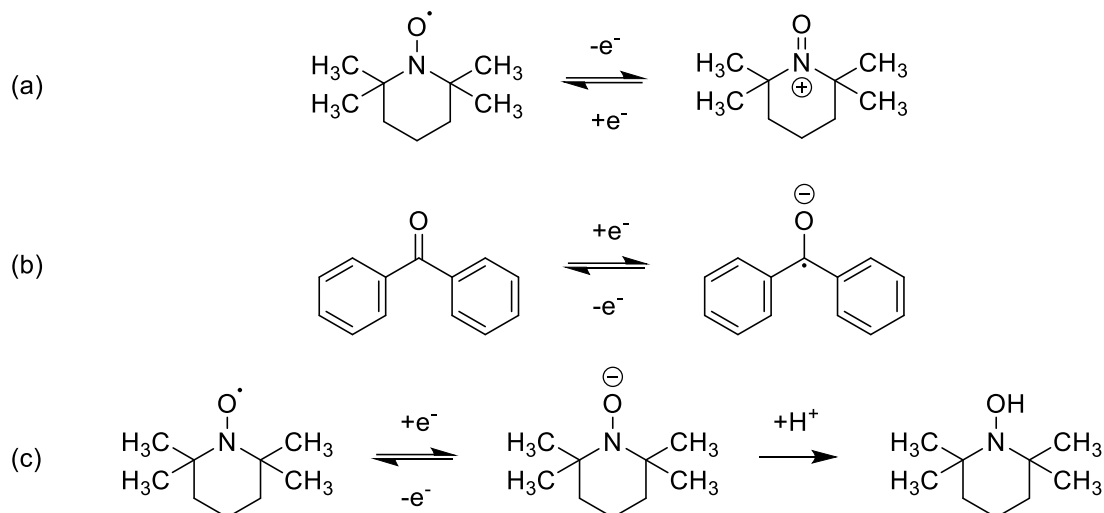
Figure 6.15. Schemes showing the proposed electrochemical pathways for the redox peaks in Figure 6.14. (a) TEMPO oxidation, (b) BP reduction, and (c) irreversible TEMPO reduction.

Literature studies show that this irreversible reduction becomes reversible in some RTIL environments. Wylie *et al.* use the BF$_4^-$ anion to stabilise TEMPO⁻ to yield reversible TEMPO/TEMPO⁻ redox peaks with an redox potential of −1.5 V (vs Ag/Ag⁺) and an overall potential of 2.5 V.[44] The BF$_4^-$ supporting salt may contribute to the stability of the reduced product in the DES, agreeing with the TEMPO/TEMPO⁻ theory. The DES likely has a low proton concentration, as the only H⁺ will come from ambient H$_2$O absorbed by the hygroscopic TEMPO. Therefore, the propensity for the irreversible TEMPO⁻ to TEMPOH step is low.

If II$_a$/II$_c$ is quasi-reversible reduction of TEMPO/TEMPO⁻, then the DES could be an interesting method of accessing the full range of TEMPO oxidation states. Accessing the four different oxidation states of TEMPO could present a symmetric cell RFB with a theoretical OCV of 2.29 V (vs Ag/Ag⁺). This system would not face the same crossover issues that occur in the archetypal VRFB. The high theoretical cell potential would mean the DES battery could compete with the VRFB (1.25 V).[21] However, the low reversibility (i_{pa}/i_{pc} = 0.43) would remain an issue.

The CV data in Figure 6.14. alone is not sufficient to draw a conclusion on the chemical origin of the redox waves, and the mechanism may be more complex than that given above. This may involve chemical steps after electron transfer, or both TEMPO and BP reductive processes occurring simultaneously, or a combination of both phenomena. Studying the change in paramagnetic species in the solution with *in-situ* EPR spectroscopy may identify the process. The *in-situ* EPR spectra should show the TEMPO radical species disappearing on the anodic scan as it is oxidised. Reversing the scan in the cathodic direction should

demonstrate the reappearance of the neutral TEMPO radical species. A further increase in paramagnetic signal intensity would indicate the presence of the BP/BP$^{.-}$ process, whereas if the TEMPO/TEMPO$^-$ is occurring then the paramagnetic signal intensity will decrease as the TEMPO reduces. Unfortunately, EPR spectroscopy was not available during this secondment.

The i_{pa}/i_{pc} values for each respective wave fall far from unity and the ΔE_p values are wide, indicating chemical and electrochemical irreversibility. However, supporting electrolyte and co-solvent optimisation may improve these factors. One should note that merely observing both an oxidation and reduction peak for the two processes is encouraging, especially when comparing to the lack of reversibility in the DES systems in Sections 6.1. and 6.2.

A larger issue with the electrochemistry in Figure 6.14. is the overlap of the two individual redox processes. The return oxidation for the more negative wave (II$_a$) is more positive than the reduction of the more positive wave (I$_c$). A potential separation in the half-reaction redox processes is necessary to store charge in a battery. Wider separations between the respective $E_{1/2}$ values yield higher operational voltages. The overlap of the two processes under these conditions renders this system inadequate for charge storage using both redox events. With proper supporting salt and co-solvent optimisation, the two processes may be separable and the full system accessible and is scope for future work.

The following section isolates the more positive redox wave, attributed to the TEMPO/TEMPO$^+$ redox couple. In focussing only on this half of the redox cell one also avoids the issues discussed in Section 6.3.2. regarding the change in coordination network upon reducing BP. The next part of the investigation covers the effects of supporting salts and co-solvents on the electrochemistry on this process.

6.3.3.2.   Half-Cell Studies

The E_{pa} of TEMPO in the 2 M TBABF$_4$, 20% ACN system (E_{pa} = 1.45 V (*vs* Ag/Ag$^+$)) is more positive than the anodic end of the ESW for a TEACl supporting salt. Therefore, TEACl is unsuitable as a supporting electrolyte for TEMPO redox in this DES.

As the TEMPO/TEMPO$^+$ redox couple is the focus of this study, a DES with higher TEMPO concentration is of more interest. The 1:2 BP:TEMPO DES contains a higher TEMPO concentration and is also the eutectic composition. This makes it the most favourable composition for understanding the DES properties and its prospective use in a flow device.

Figure 6.16. shows the CVs for 1:2 BP:TEMPO with 0.1 M $TBAPF_6$ (black line) and $TBABF_4$ (red line) supporting salts at 25 mV s^{-1}. Table 6.9. gives the corresponding electrochemical data. The concentrations are at the maximum solubility limit for $TBAPF_6$ for direct comparison of the two supports. The smaller ΔE_p with $TBABF_4$ compared to $TBAPF_6$ (2.71 V and 5.09 V (*vs* Ag/Ag$^+$), respectively) suggest $TBABF_4$ is better at supporting TEMPO redox in the DES than $TBAPF_6$. It is possible the larger size of the PF_6^- anion (3.58 Å *vs* 3.37 Å)[60] causes a weaker interaction with the small TEMPO. This may result in less support and more sluggish kinetics. The proximity of the E_{pa} peak with the anodic end of the ESW for $TBAPF_6$ is also a cause for concern.
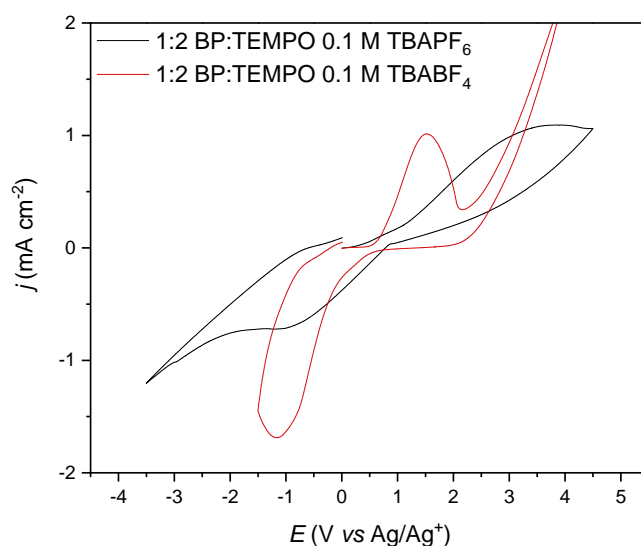
Figure 6.16. CV data for 1:2 BP:TEMPO with 0.1 M TBAPF$_6$ (black line) and 0.1 M TBABF$_4$ (red line) at 25 mV s^{-1}. All tests use a GC WE, Ag/Ag$^+$ RE, and Pt CE.

Table 6.9. Electrochemical data for 1:2 BP:TEMPO with 0.1 M TBAPF$_6$ and 0.1 M TBABF$_4$.

Supporting Salt	E_{pa} (V) (*vs* Ag/Ag$^+$)	E_{pc} (V) (*vs* Ag/Ag$^+$)	ΔE_p (V) (*vs* Ag/Ag$^+$)	$E_{1/2}$ (V) (*vs* Ag/Ag$^+$)	i_{pa} (mA)	i_{pc} (mA)	i_{pa}/i_{pc}
TBAPF$_6$	3.82	−1.17	4.99	1.33	1.90×10^{-1}	-9.49×10^{-2}	2
TBABF$_4$	1.55	−1.16	2.71	0.19	1.99×10^{-1}	-3.16×10^{-1}	0.63

The i_{pa} values are similar for both supporting salts at around 1.90×10^{-1} mA, indicating a similar oxidation process. The reduction process reaches a much higher i_{pc} with BF_4^- than with PF_6^-, at -3.16×10^{-1} mA against -9.49×10^{-2} mA. If the salts were sufficiently supporting the

reaction they would record equal i_p values as the concentrations are the same. The higher i_{pc} with TBABF$_4$ may be an artefact from the large i increase towards the positive end of the scan creating an overlapping response with the reduction.

The low TBAPF$_6$ solubility means co-solvents are necessary to increase supporting salt concentration to sufficiently to fully access the high concentration of RAM in the DES. H$_2$O or EG are non-volatile, cheap, and safe co-solvent candidates. Unfortunately, both are immiscible with the BP:TEMPO DES and so are not useful in this system. ACN is miscible and has a lower η and ρ than the DES. ACN is also permits higher concentrations of TBAPF$_6$ and TBABF$_4$ supporting salts so should improve the electrochemical performance over the pure DES.

Figure 6.17. gives the CV and Table 6.10. the corresponding electrochemical data for (a) 1:2 BP:TEMPO and (b) 1:4 BP:TEMPO with 0.1 M TBAPF$_6$ and increasing wt% ACN co-solvent from 0 wt% (black line), 1 wt% (red line), and 5 wt% (blue line) at 25 mV s^{-1}. The low conductivity, and hence high solution resistance result in the wide ΔE_p in these tests
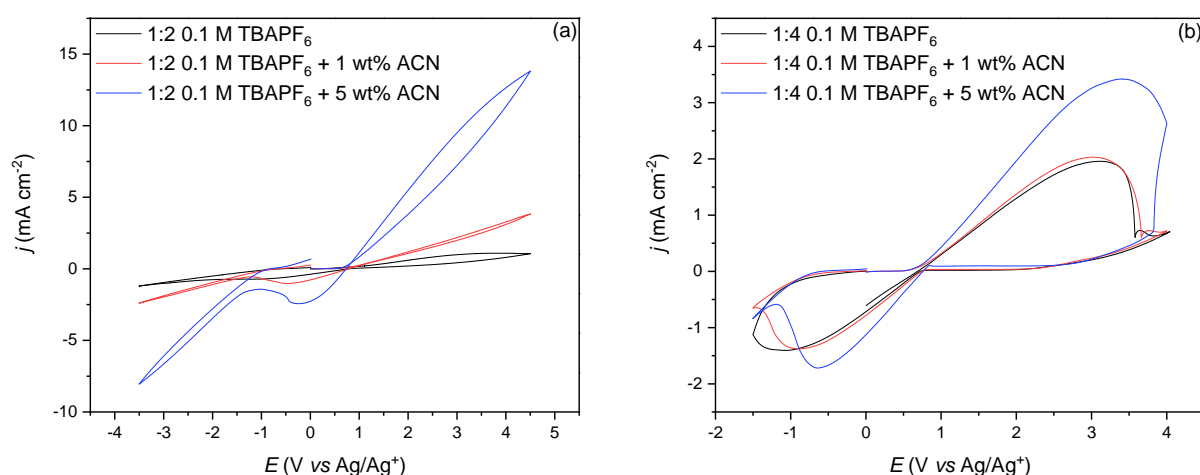
Figure 6.17. CV data for (a) 1:2 BP:TEMPO and (b) 1:4 BP:TEMPO with 0.1 M TBAPF$_6$ with 0 (black line), 1 (red line), and 5 (blue line) wt% ACN co-solvent at 25 mV s^{-1}. All tests use a GC WE, Ag/Ag$^+$ RE, and Pt CE.

Increasing the TEMPO concentration from the 1:2 to the 1:4 DES makes E_{pa} become observable. An E_{pa} is present over all tests in 1:4 BP:TEMPO but only when no supporting salt is present in the 1:2 system. There is, however, no obvious trend in the E_{pa} values with salt concentration. The E_{pc} moves positive with increasing co-solvent wt%, from −1.17 V to −0.25 V (*vs* Ag/Ag$^+$) in 1:2 BP:TEMPO, and from −1.06 V to −0.64 V (*vs* Ag/Ag$^+$) in 1:4 BP:TEMPO. This indicates the co-solvent is stabilising the TEMPO and that the effect increases with supporting electrolyte concentration.

Table 6.10. Electrochemical data for 1:2 BP:TEMPO and 1:4 BP:TEMPO 0.1 M TBAPF$_6$ with increasing wt % ACN co-solvent.

DES + 0.1 M TBAPF$_6$	wt% ACN	E_{pa} (V) (*vs* Ag/Ag$^+$)	E_{pc} (V) (*vs* Ag/Ag$^+$)	ΔE_p (V) (*vs* Ag/Ag$^+$)	$E_{1/2}$ (V) (*vs* Ag/Ag$^+$)	i_{pa} (mA)	i_{pc} (mA)	i_{pa}/i_{pc}
1:2	0	3.82	−1.17	4.99	1.33	1.90×10^{-1}	-9.49×10^{-2}	2
	1	-	−0.45	-	-	-	-2.03×10^{-1}	-
	5	-	−0.25	-	-	-	-4.78×10^{-1}	-
1:4	0	3.12	−1.06	4.18	1.02	3.87×10^{-1}	-3.42×10^{-1}	1.13
	1	3.02	−0.90	3.92	1.06	3.97×10^{-1}	-2.80×10^{-1}	1.42
	5	3.40	−0.64	4.04	1.38	6.69×10^{-1}	-1.81×10^{-1}	1.88

The i_{pc} values are comparable for both DESs other than the outlying 1:2 + 5 wt% ACN system which has much higher peak currents. Disregarding the outlier, the trend agrees that the limiting factor in the system's conductivity is the supporting salt. The salt concentration is 0.1 M for all tests, which is much lower than that for TEMPO. Therefore, the salts should provide the same level of support to each DES, which would result in similar peak currents.

Generally, the i_p values increase and ΔE_p values decrease with increasing co-solvent wt%. This is because adding a co-solvent decreases the η and therefore improves the diffusion of the molecules. Higher co-solvent concentrations allow more TEMPO to reach the electrode surface within the timeframe of the CV, thus resulting in the higher i_p values. This faster rate of TEMPO mass transport also decreases the ΔE_p. Overall, the smaller ΔE_p and presence of both E_{pa} and E_{pc} in the 1:4 DES indicate this molar composition as more beneficial for accessing higher TEMPO concentrations.

TBAPF$_6$ solubility increases from 0.1 M to nearly 2 M after adding 5 wt% ACN to the 1:2 DES. Figure 6.18. compares the CV data for 1:2 BP:TEMPO, 0.1 M TBAPF$_6$ (black line), 1:2 BP:TEMPO, 2 M TBAPF$_6$, 5 wt% ACN (red line) against the conventional cell conditions of 1 mM TEMPO, 0.1 M TBAPF$_6$, ACN. Table 6.11. compiles the electrochemical data.
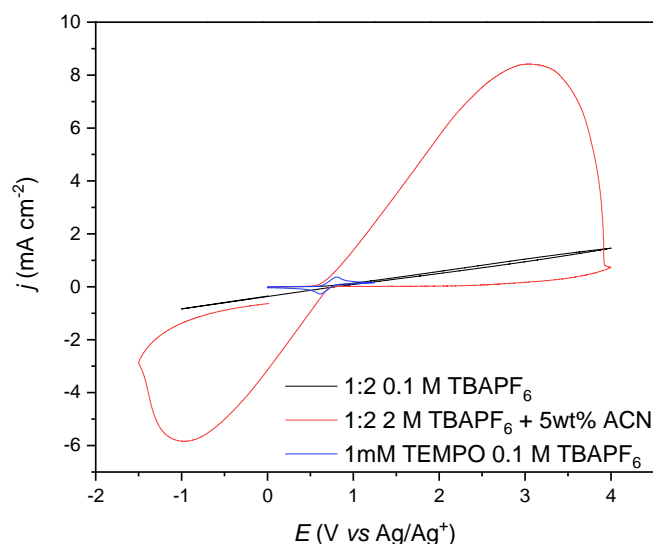
Figure 6.18. CV data for 1:2 BP:TEMPO DES with maximum solubility TBAPF$_6$ at 0 wt% (black line) and 5 wt% (red line) ACN co-solvent overlaid with the CV data for 1 mM TEMPO, 0.1 M TBAPF$_6$ in ACN (blue line) at 100 mV s^{-1}. All tests use a GC WE, Ag/Ag$^+$ RE, and Pt CE.

Table 6.11. Electrochemical data for 1 mM TEMPO, 0.1 M TBAPF$_6$ in ACN and 1:2 BP:TEMPO with 2 M TBAPF$_6$, 5 wt% ACN at 100 mV s^{-1}.

DES	E_{pa} (V) (*vs* Ag/Ag$^+$)	E_{pc} (V) (*vs* Ag/Ag$^+$)	ΔE_p (V) (*vs* Ag/Ag$^+$)	$E_{1/2}$ (V) (*vs* Ag/Ag$^+$)	i_{pa} (mA)	i_{pc} (mA)	i_{pa}/i_{pc}
1:2 BP:TEMPO 0.1 M TBAPF$_6$	-	-	-	-	-	-	-
1:2 BP:TEMPO, 2 M TBAPF$_6$, 5 wt% ACN	3.05	−0.98	0.404	1.03	1.66	−1.44	1.46
1 mM TEMPO, 0.1 M TBAPF$_6$, ACN	0.81	0.61	0.20	0.71	7.62 × 10^{-2}	−7.42 × 10^{-2}	0.98

With 0.1 M TBAPF$_6$, no redox is observable in the 1:2 DES CV (Figure 6.18. black line). Increasing the TBAPF$_6$ and co-solvent concentrations improves the charge carrying capabilities of the DES to yield a widely separated redox wave of $E_{1/2}$ = 1.03 V and ΔE_p = 4.04 V (*vs* Ag/Ag$^+$).

The $E_{1/2}$ values and gradients of the redox waves are similar in 1:2 BP:TEMPO, 2 M TBAPF$_6$ 5 wt% ACN (red line) and 1 mM TEMPO, 0.1 M TBABF$_4$, ACN (blue line). The similarity in peak location and shape indicates a comparable redox process is likely occurring in both

media. The wider ΔE_p is a result of the increased η. The increase in i_p with the TEMPO concentration from 1 mM to 3.56 M corroborates that both processes involve TEMPO. There is a 22.9-fold increase in i_{pa} and 15.4-fold increase in i_{pc} in the 1:2 DES compared to the 1 mM TEMPO. The i_{pa} increase is in line with the relative increase in supporting salt concentration, which is 20-times higher in the DES test. This indicates the supporting salt is the limiting factor in active material utilisation and the resulting j for the high concentration systems. The insufficient supporting salt solubility means that electromigration is an issue, which makes analysis on the cell more challenging.

The lower i_{pa}/i_{pc} in the DES compared to ACN (1.46 and 1, respectively) suggests lower chemical reversibility in the high concentration system. A higher proportion of TEMPO$^+$ forms on the positive scan than reduces back to TEMPO in the reverse (i_{pa} is higher than i_{pc}). Therefore, some TEMPO$^+$ must degrade in the DES where it does not in the conventional low concentration electrolyte.

The large overpotential in charging the electrolyte is something to take into consideration if applying this system to EES. The system would need a long charging time at a low current density, but the resulting amount of charge stored would be vast. Future work should focus on improving the conductivity and liquidity of the DES to reduce the overpotential and eliminate electromigration from the system.

Figures 6.17. and 6.18. show that co-solvents are necessary to reduce η and improve σ sufficiently with a TBAPF$_6$ supporting salt to yield observable electrochemistry. A disadvantage of co-solvents is that they dilute the ORAM concentration. Therefore, it is of interest to study the DES electrochemistry with a supporting electrolyte that does not require any additional co-solvents, such as TBABF$_4$ (see Figure 6.16.)

Figure 6.19.(a) gives the CVs for 1:2 BP:TEMPO with increasing TBABF$_4$ concentrations from 0.1 M (black line), 0.5 M (red line), and 1 M (blue line) at 25 mV s^{-1}. Table 6.12. tabulates the electrochemical data and Figure 6.19.(b) displays the LSV plot for 1:2 BP:TEMPO DES with 1 M TBABF$_4$ over rotation rates $500 \leq f \leq 2000$ RPM at 2 mV s^{-1} and the corresponding Levich plot is in Appendix 6.G.

Increasing the TBABF$_4$ concentration from 0.1 M to 1 M decreases ΔE_p from 2.71 V to 1.71 V (*vs* Ag/Ag$^+$). The positive shift in the cathodic peak is greater than the magnitude of negative shift in the anodic peak. The $E_{1/2}$ is similar with 0.1 M and 0.5 M TBABF$_4$ at around 0.2 V (*vs* Ag/Ag$^+$), but shifts positive by 0.3 V with 1 M TBABF$_4$. The increase in i around −0.5 V on the anodic scan in the 0.5 M test is a result of the more negative potential in this test and is the same II$_a$ peak seen in Figure 6.14.

Increasing the supporting electrolyte concentration by a factor of 10 improves the reversibility (i_{pa}/i_{pc} goes from 0.63 to unity) with a relative increase in i_p of 1.69- and 1.18-times, for i_{pc} and i_{pa}, respectively.
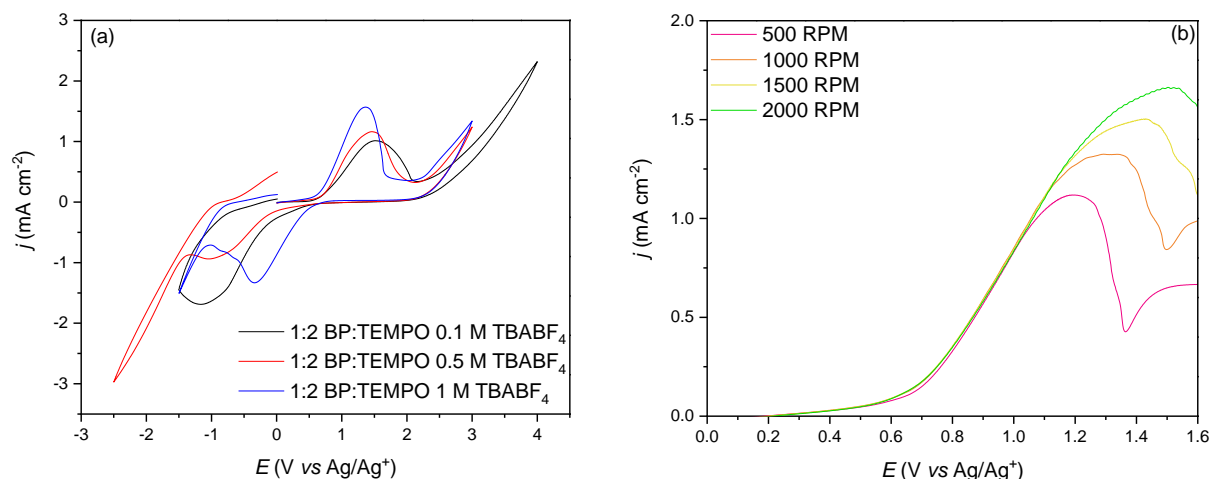

Figure 6.19. (a) CV data for 1:2 BP:TEMPO with TBABF$_4$ concentrations of 0.1 M (black line), 0.5 M (red line) and 1 M (blue line) at 25 mV s^{-1}, and (b) hydrodynamic data for 1:2 BP:TEMPO 1 M TBABF$_4$ over rotation rates 500 ≤ f ≤ 2000 RP at 2 mV s^{-1}. All tests use a GC WE, Ag/Ag$^+$ RE, and Pt CE.

Table 6.12. Electrochemical data for 1:2 BP:TEMPO and increasing concentrations of TBABF$_4$.

DES	E_{pa} (V) (vs Ag/Ag$^+$)	E_{pc} (V) (vs Ag/Ag$^+$)	ΔE_p (V) (vs Ag/Ag$^+$)	$E_{1/2}$ (V) (vs Ag/Ag$^+$)	i_{pa} (mA)	i_{pc} (mA)	i_{pa}/i_{pc}
0.1	1.55	−1.16	2.71	0.20	1.99×10^{-1}	-3.16×10^{-1}	0.63
0.5	1.47	−1.04	2.51	0.21	2.03×10^{-1}	-1.87×10^{-1}	1.09
1	1.37	−0.34	1.71	0.51	2.71×10^{-1}	-2.68×10^{-1}	1

The LSV data in Figure 6.19.(b) does not show the typical i_{lim} for hydrodynamic voltammetry, but instead each test reaches a maximum i which subsequently drops as E becomes more positive. Interestingly, each f rate has the same onset potential and a similar gradient of increasing i, but with a more positive i_p at faster f rates. The current peak indicates the mass transport limited current, but the decrease in i may indicate degradation of the oxidised product. The more positive E of the plateau in the higher RPM tests is a result of the sluggish kinetics causing a large overpotential. The LSV data has also not been iR-corrected and the

high resistances in the DES (R_u = 1.52 kΩ in 1:2 BP:TEMPO 1 M TBABF$_4$) will somewhat distort the E.

Using the i_p in Figure 6.19.(b) and the Levich equation (taking v as the value for 1:2 BP:TEMPO, 1.25 M TBABF$_4$, 0.43 cm^2 s^{-1}, in Section 6.3.3.4.) gives a linear relationship of i_p vs $\omega^{1/2}$ with a D_o value of 1.13 × 10^{-5} cm^2 s^{-1}. This indicates a fast D_o for the TEMPO oxidation reaction despite the poor conductivity and relatively high viscosity of the DES.

Resistance remains an issue in the DES at even the highest concentration supporting electrolyte test. Using i-interrupt the 1:2 BP:TEMPO DES with no supporting electrolyte records an uncompensated resistance of 19.83 kΩ which drops to 1.52 kΩ after adding 1 M TBABF$_4$. This is much higher than the R_u of near 100 Ω in 0.1 M TBABF$_4$ ACN and shows how comparably resistive these DES's are to conventional non-aqueous electrolytes. These high resistances contribute to the large overpotential for TEMPO oxidation and further work should focus on reducing resistance as much as possible.

To summarise, this section demonstrates an observable TEMPO redox process is accessible in the BP:TEMPO DES. Section 6.3.3.1 performs a potential sweep covering the full cell and shows two overlapping redox processes comprising TEMPO/TEMPO$^+$ and either BP/BP$^{.-}$ or TEMPO/TEMPO$^-$. The overlapping nature of the events means both redox events cannot store charge in the same battery without further electrolyte optimisation to separate them.

Section 6.3.3.2. narrows the study to solely the TEMPO/TEMPO$^+$ redox process. The electrochemical characteristics improve when in the company of supporting electrolytes and co-solvents. A TBABF$_4$ salt has the highest solubility in the DES and at 1 M in 1:2 BP:TEMPO achieves the smallest ΔE_p (ΔE_p = 1.71 V) and highest i_p (2.71 × 10^{-1} mA and −2.68 x 10^{-1} mA for i_{pa} and i_{pc}, respectively) of all the conditions tested, alongside good chemical reversibility (i_{pa}/i_{pc} = 1) for the TEMPO redox reaction. Optimising the combination of TBABF$_4$ and co-solvents may improve these attributes even more.

6.4.   Conclusions

Chapter 6. investigates the applicability of DES electrolytes for ORFBs. Section 6.1. outlines a selection of promising ORAMs in the non-aqueous literature and tests them in ethaline, the 'benchmark' DES. The data shows the reversible non-aqueous electrochemistry of ORAMs may not directly correlate to a reversible system in a DES electrolyte. Despite observing both oxidation and reduction events in 4-OH-TEMPO, 1,5-DAAQ, catechol, and phenazine, the low solubilities (typically <10 mM) are too low for a feasible ORFB.

Section 6.2. moves on to design several novel DES electrolytes wherein one component is redox active. The novel DES systems discovered comprise:

- 1:1:2 OA, ChCl, catechol
- 1:2:4 1,5-DAAQ:ChCl:glycerol
- 1:1 4-OH-TEMPO:LiTFSI
- 1:2:3 BP:LiTFSI:Urea

The high ORAM concentrations in these systems is encouraging, for example 5.78 M for catechol in 2:1:1 catechol:oxalic acid:ChCl. Unfortunately, the unfavourable physicochemical properties mean the mixtures are difficult to handle. High viscosities and T_m values near room temperature result in unobservable redox in CV measurements. Such high viscosity systems will lead to pumping and ohmic losses on a magnitude likely too challenging and costly to overcome.

Section 6.3. designs a novel DES wherein both components are redox active. Section 6.3.2. investigates the physicochemical properties of the BP:TEMPO DES. The eutectic composition (T_m = 273 K) is 1:2 BP:TEMPO and the low ρ and η of ρ = 0.9962 g cm^{-3} and η = 7.123 mPa s. These values are much lower than previously reported DES systems, and similar to those in the BuPh-DMFc DES.[50,52,55,56] These values increase to ρ = 1.0114 g cm^{-3} and η = 42.697 mPa s upon inclusion of a supporting electrolyte, but remain beneath previously reported DESs. The non-ionicity of BP:TEMPO means it carries the inherently low σ of 0.712 µS cm^{-1}, which is far below below the estimated requirement for an ORFB (>5 mS cm^{-1}).[26]

Section 6.3.3. investigates the effects of supporting salts and co-solvents on the σ and resulting electrochemistry of the BP:TEMPO DES. The theoretical OCV of the BP:TEMPO DES is impressive, at 2.58 V. A wide potential scan shows two overlapping redox processes in the DES (I$_a$/I$_c$ at 1.45 V and −0.29 V, and II$_a$/II$_c$ at 0.20 V and −2.47 V). The identity of these peaks is unknown, but likely TEMPO/TEMPO$^+$ and either BP/BP$^{·-}$ or TEMPO/TEMPO$^-$. Future work should optimise the supporting salt and co-solvent environment to separate the waves and utilise EPR spectroscopy to identify the peaks. The $E_{1/2}$ values of I$_a$/I$_c$ ($E_{1/2}$ = 1.16 V) and II$_a$/II$_c$ ($E_{1/2}$ = −1.13 V) suggest fully separating the redox processes would yield a theoretical OCV of 2.29 V. A device with such a high redox potential could likely compete with commercially available VRFBs.

The supporting salt with the highest solubility and most favourable electrochemical characteristics is TBABF$_4$. Including co-solvents reduces E_p, with ACN showing as suitable co-solvent for the system.

The best half-cell in the study is the 1:2 BP:TEMPO DES with 1 M TBABF$_4$ which has $E_{1/2}$ = 0.51 V, ΔE_p 1.71 V (*vs* Ag/Ag$^+$) at 100 mV s^{-1} and a rapid D_o of 1.13 × 10^{-5} cm^2 s^{-1}. Despite the relatively low η of the DES and the enhancements in σ with the supporting salt, the high overpotentials for TEMPO oxidation and the limited supporting salt solubility remain limiting factors in the system.

If the salt solubility were not limiting and the full TEMPO concentration achievable, certain experimental complications would hinder further study. For example, 15 mL of 1:1 BP:TEMPO (2.78 M TEMPO) would take nearly 224 hours to reach 100 % SoC at a 5 mA charging current. A full charge and discharge cycle would therefore take over 18 days. This may not be an issue in commercial systems, where long charging times may be a viable compromise for storing such high amounts of energy. However, the long cycle life poses a challenge in developing high concentration electrolytes on the laboratory scale. Literature studies avoid this by using small electrolyte volumes (20 µL) or diluting the ORAM concentration (4 M to 0.5 M).[14,48]

The inherent low volatility, thermostability, η, and ρ, alongside the facile preparation and lack of necessary purification mean the DES could find use in other applications. An example of this is in aiding facile product separation in TEMPO catalysis reactions.[7,61–63] The toxicity of BP must also be taken into consideration for applications of the BP:TEMPO DES.

6.5. References

1   M. Park, E. S. Beh, E. M. Fell, Y. Jing, E. F. Kerr, D. De Porcellinis, M. A. Goulet, J. Ryu, A. A. Wong, R. G. Gordon, J. Cho and M. J. Aziz, A high voltage aqueous zinc–organic hybrid flow battery, *Adv. Energy Mater.*, 2019, **9**, 1–8.

2   C. S. Sevov, S. K. Samaroo and M. S. Sanford, Cyclopropenium salts as cyclable, high-potential catholytes in nonaqueous media, *Adv. Energy Mater.*, 2017, **7**, 1602027.

3   M. R. Afshar Mogaddam, M. A. Farajzadeh, M. Tuzen, A. Jouyban and J. Khandaghi, Organic solvent-free elevated temperature liquid–liquid extraction combined with a new switchable deep eutectic solvent-based dispersive liquid–liquid microextraction of three phenolic antioxidants from oil samples, *Microchem. J.*, 2021, **168**, 106433.

4   E. I. Romadina, D. S. Komarov, K. J. Stevenson and P. A. Troshin, New phenazine based anolyte material for high voltage organic redox flow batteries, *Chem. Commun.*, 2021, **57**, 2986–2989.

5   S. Er, C. Suh, M. P. Marshak and A. Aspuru-Guzik, Computational design of molecules for an all-quinone redox flow battery, *Chem. Sci.*, 2015, **6**, 885–893.

6   X. Wei, W. Xu, M. Vijayakumar, L. Cosimbescu, T. Liu, V. Sprenkle and W. Wang,

TEMPO-based catholyte for high-energy density nonaqueous redox flow batteries, *Adv. Mater.*, 2014, **26**, 7649–7653.

7   Y. Zhang, F. Lü, X. Cao and J. Zhao, Deep eutectic solvent supported TEMPO for oxidation of alcohols, *RSC Adv.*, 2014, **4**, 40161–40169.

8   B. Chen, S. Mitchell, N. Sinclair, J. Wainright, E. Pentzer and B. Gurkan, Feasibility of TEMPO-functionalized imidazolium, ammonium and pyridinium salts as redox-active carriers in ethaline deep eutectic solvent for energy storage, *Mol. Syst. Des. Eng.*, 2020, **5**, 1147–1157.

9   T. Liu, X. Wei, Z. Nie, V. Sprenkle and W. Wang, A total organic aqueous redox flow battery employing a low cost and sustainable methyl viologen anolyte and 4-HO-TEMPO catholyte, *Adv. Energy Mater.*, 2016, **6**, 1501449.

10   J. C. Goeltz and J. M. Carter, Finding balance with deep eutectic solvents: High concentrations and improved conductivities for the off-the-shelf nitroxide TEMPOL, *J. Mol. Liq.*, 2021, **338**, 116556.

11   A. Pasadakis-Kavounis, V. Baj and J. Hjelm, Electrochemical characterization of aromatic molecules with 1,4-diaza groups for flow battery applications, *Molecules*, 2021, **26**, 1–13.

12   W. Kangro and H. Pieper, Zur frage der speicherung von elektrischer energie in flüssigkeiten, *Electrochim. Acta*, 1962, **7**, 435–448.

13   R. A. Potash, J. R. McKone, S. Conte and H. D. Abruña, On the benefits of a symmetric redox flow battery, *J. Electrochem. Soc.*, 2016, **163**, A338–A344.

14   C. Zhang, Z. Niu, Y. Ding, L. Zhang, Y. Zhou, X. Guo, X. Zhang, Y. Zhao and G. Yu, Highly concentrated phthalimide-based anolytes for organic redox flow batteries with enhanced reversibility, *Chem*, 2018, **4**, 2814–2825.

15   X. Xing, Y. Huo, X. Wang, Y. Zhao and Y. Li, A benzophenone-based anolyte for high energy density all-organic redox flow battery, *Int. J. Hydrogen Energy*, 2017, **42**, 17488–17494.

16   C. Zhang, H. Chen, Y. Qian, G. Dai, Y. Zhao and G. Yu, General design methodology for organic eutectic electrolytes toward high-energy-density redox flow batteries, *Adv. Mater.*, 2021, **33**, 1–8.

17   S. Y. Kishioka, Redox properties of 2,3-diaminophenazine and its electropolymerized product in aqueous and acetonitrile solutions, *Electrochemistry*, 2013, **81**, 343–346.

18   J. Rodriguez, M. Politi, S. Adler, D. Beck and L. Pozzo, High-throughput and data driven strategies for the design of deep-eutectic solvent electrolytes, *Mol. Syst. Des. Eng.*, 2022, **7**, 933–949.

19   Y. Marcus, *Deep Eutectic Solvents*, 2019.

20   P. J. Smith and J. C. Goeltz, Proton-coupled electron transfer and substituent effects in catechol-based deep eutectic solvents: Gross and fine tuning of redox activity, *J. Phys. Chem. B*, 2017, **121**, 10974–10978.

21   E. Sánchez-Díez, E. Ventosa, M. Guarnieri, A. Trovò, C. Flox, R. Marcilla, F. Soavi, P. Mazur, E. Aranzabe and R. Ferret, Redox flow batteries: Status and perspective towards sustainable stationary energy storage, *J. Power Sources*, 2021, **481**, 228804.

22   W. Zhou, W. Liu, M. Qin, Z. Chen, J. Xu, J. Cao and J. Li, Fundamental properties of TEMPO-based catholytes for aqueous redox flow batteries: Effects of substituent groups and electrolytes on electrochemical properties, solubilities and battery performance, *RSC Adv.*, 2020, **10**, 21839–21844.

23   N. S. Sinclair, D. Poe, R. F. Savinell, E. J. Maginn and J. S. Wainright, A nitroxide containing organic molecule in a deep eutectic solvent for flow battery applications, *J. Electrochem. Soc.*, 2021, **168**, 020527.

24   Y. Liu, M. A. Goulet, L. Tong, Y. Liu, Y. Ji, L. Wu, R. G. Gordon, M. J. Aziz, Z. Yang and T. Xu, A long-lifetime all-organic aqueous flow battery utilizing TMAP-TEMPO radical, *Chem*, 2019, **5**, 1861–1870.

25   M. E. Di Pietro and A. Mele, Deep eutectics and analogues as electrolytes in batteries, *J. Mol. Liq.*, 2021, **338**, 116597.

26   J. Zhang, R. E. Corman, J. K. Schuh, R. H. Ewoldt, I. A. Shkrob and L. Zhang, Solution properties and practical limits of concentrated electrolytes for nonaqueous redox flow batteries, *J. Phys. Chem. C*, 2018, **122**, 8159–8172.

27   Q. Zhang, K. De Oliveira Vigier, S. Royer and F. Jérôme, Deep eutectic solvents: Syntheses, properties and applications, *Chem. Soc. Rev.*, 2012, **41**, 7108–7146.

28   Y. Wang, Z. Niu, Q. Zheng, C. Zhang, J. Ye, G. Dai, Y. Zhao and X. Zhang, Zn-based eutectic mixture as anolyte for hybrid redox flow batteries, *Sci. Rep.*, 2018, **8**, 8–15.

29   J. C. Goeltz and L. N. Matsushima, Metal-free redox active deep eutectic solvents, *Chem. Commun.*, 2017, **53**, 9983–9985.

30   B. B. Hansen, S. Spittle, B. Chen, D. Poe, Y. Zhang, J. M. Klein, A. Horton, L. Adhikari, T. Zelovich, B. W. Doherty, B. Gurkan, E. J. Maginn, A. Ragauskas, M. Dadmun, T. A. Zawodzinski, G. A. Baker, M. E. Tuckerman, R. F. Savinell and J. R. Sangoro, Deep eutectic solvents: A review of fundamentals and applications, *Chem. Rev.*, 2021, **121**, 1232–1285.

31   C. W. Lien, B. Vedhanarayanan, J. H. Chen, J. Y. Lin, H. H. Tsai, L. D. Shao and T. W. Lin, Optimization of acetonitrile/water content in hybrid deep eutectic solvent for

graphene/MoS2 hydrogel-based supercapacitors, *Chem. Eng. J.*, 2021, **405**, 126706.

32   L. Zhang, C. Zhang, Y. Ding, K. Ramirez-Meyers and G. Yu, A low-cost and high-energy hybrid iron-aluminum liquid battery achieved by deep eutectic solvents, *Joule*, 2017, **1**, 623–633.

33   Y. Wang and H. Zhou, A green and cost-effective rechargeable battery with high energy density based on a deep eutectic catholyte, *Energy Environ. Sci.*, 2016, **9**, 2267–2272.

34   C. Zhang, Y. Ding, L. Zhang, X. Wang, Y. Zhao, X. Zhang and G. Yu, A sustainable redox-flow battery with an aluminum-based, deep-eutectic-solvent anolyte, *Angew. Chemie Int. Ed.*, 2017, **56**, 7454–7459.

35   D. R. Macfarlane, N. Tachikawa, M. Forsyth, J. M. Pringle, P. C. Howlett, G. D. Elliott, J. H. Davis, M. Watanabe, P. Simon and C. A. Angell, Energy applications of ionic liquids, *Energy Environ. Sci.*, 2014, **7**, 232–250.

36   T. T. A. Dinh, T. T. K. Huynh, L. T. M. Le, T. T. T. Truong, O. H. Nguyen, K. T. T. Tran, M. V. Tran, P. H. Tran, W. Kaveevivitchai and P. M. L. Le, Deep eutectic solvent based on lithium bis[(trifluoromethyl)sulfonyl] imide (LiTFSI) and 2,2,2-trifluoroacetamide (TFA) as a promising electrolyte for a high voltage lithium-ion battery with a LiMn2O4 cathode, *ACS Omega*, 2020, **5**, 23843–23853.

37   S. Sandhu, N. Kumar, V. V. P. Singh and V. V. P. Singh, Synthesis of reactive faceted nanosized titania with enhanced photocatalytic performance under fluorine free conditions using deep eutectic solvent, *Vacuum*, 2021, **184**, 109896.

38   A. Alhadid, C. Jandl, L. Mokrushina and M. Minceva, Cocrystal formation in choline chloride deep eutectic solvents, *Cryst. Growth Des.*, 2022, **22**, 1933–1942.

39   H. Squire, Case Western Reserve University, 2020.

40   Y. Fang, B. Suganthan and R. P. Ramasamy, Electrochemical characterization of aromatic corrosion inhibitors from plant extracts, *J. Electroanal. Chem.*, 2019, **840**, 74–83.

41   M. C. Henstridge and R. G. Compton, Mass transport to micro- and nanoelectrodes and their arrays: A review, *Chem. Rec.*, 2012, **12**, 63–71.

42   J. Winsberg, C. Stolze, A. Schwenke, S. Muench, M. D. Hager and U. S. Schubert, Aqueous 2,2,6,6-tetramethylpiperidine-N-oxyl catholytes for a high-capacity and high current density oxygen-insensitive hybrid-flow battery, *ACS Energy Lett.*, 2017, **2**, 411–416.

43   B. Hu, Y. Tang, J. Luo, G. Grove, Y. Guo and T. L. Liu, Improved radical stability of viologen anolytes in aqueous organic redox flow batteries, *Chem. Commun.*, 2018, **54**, 6871–6874.

44   L. Wylie, T. Blesch, R. Freeman, K. Hatakeyama-Sato, K. Oyaizu, M. Yoshizawa-Fujita and E. I. Izgorodina, Reversible reduction of the TEMPO radical: One step closer to an all-organic redox flow battery, *ACS Sustain. Chem. Eng.*, 2020, **8**, 17988–17996.

45   U. S. Schubert, P. Rohland, O. Nolte, K. Schreyer, H. Görls and M. D. Hager, Structural alterations on the TEMPO scaffold and their impact on the performance as active materials for redox flow batteries, *Mater. Adv.*, 2022, **3**, 4278–4288.

46   S. K. Park, J. Shim, J. H. Yang, K. H. Shin, C. S. Jin, B. S. Lee, Y. S. Lee, J. D. Jeon, B. Suk, Y. S. Lee and J. D. Jeon, Electrochemical properties of a non-aqueous redox battery with all-organic redox couples, *Electrochem. commun.*, 2015, **59**, 68–71.

47   J. D. Milshtein, J. L. Barton, R. M. Darling and F. R. Brushett, 4-Acetamido-2,2,6,6-tetramethylpiperidine-1-oxyl as a model organic redox active compound for nonaqueous flow batteries, *J. Power Sources*, 2016, **327**, 151–159.

48   K. Takechi, Y. Kato and Y. Hase, A highly concentrated catholyte based on a solvate ionic liquid for rechargeable flow batteries, *Adv. Mater.*, 2015, **27**, 2501–2506.

49   Y. Huo, X. Xing, C. Zhang, X. Wang and Y. Li, An all organic redox flow battery with high cell voltage, *RSC Adv.*, 2019, **9**, 13128–13132.

50   C. Zhang, Y. Qian, Y. Ding, L. Zhang, X. Guo, Y. Zhao and G. Yu, Biredox eutectic electrolytes derived from organic redox-active molecules: High-energy storage systems, *Angew. Chemie Int. Ed.*, 2019, **58**, 7045–7050.

51   T. Xuan and L. Wang, Eutectic electrolyte and interface engineering for redox flow batteries, *Energy Storage Mater.*, 2022, **48**, 263–282.

52   F. S. Mjalli, J. Naser, B. Jibril, V. Alizadeh and Z. Gano, Tetrabutylammonium chloride based ionic liquid analogues and their physical properties, *J. Chem. Eng. Data*, 2014, **59**, 2242–2251.

53   F. Cardellini, M. Tiecco, R. Germani, G. Cardinali, L. Corte, L. Roscini and N. Spreti, Novel zwitterionic deep eutectic solvents from trimethylglycine and carboxylic acids: Characterization of their properties and their toxicity, *RSC Adv.*, 2014, **4**, 55990–56002.

54   J. Kestin, H. E. Khalifa and R. J. Correia, Tables of the dynamic and kinematic viscosity of aqueous NaCl solutions in the temperature range 20-150 °C and the pressure range 0.1-35 MPa, *J. Phys. Chem. Ref. Data*, 1981, **10**, 71–88.

55   M. H. Ghatee, M. Zare, F. Moosavi and A. R. Zolghadr, Temperature-dependent density and viscosity of the ionic liquids 1-alkyl-3-methylimidazolium iodides: Experiment and molecular dynamics simulation, *J. Chem. Eng. Data*, 2010, **55**, 3084–3088.

56   M. A. Kareem, F. S. Mjalli, M. A. Hashim and I. M. Alnashef, Phosphonium-based ionic liquids analogues and their physical properties, *J. Chem. Eng. Data*, 2010, **55**, 4632–

4637.

57   R. Dmello, J. D. Milshtein, F. R. Brushett and K. C. Smith, Cost-driven materials selection criteria for redox flow battery electrolytes, *J. Power Sources*, 2016, **330**, 261–272.

58   K. Gong, Q. Fang, S. Gu, S. F. Y. Li and Y. Yan, Nonaqueous redox-flow batteries: Organic solvents, supporting electrolytes, and redox pairs, *Energy Environ. Sci.*, 2015, **8**, 3515–3530.

59   V. M. Ortiz-Martínez, L. Gómez-Coma, G. Pérez, A. Ortiz and I. Ortiz, The roles of ionic liquids as new electrolytes in redox flow batteries, *Sep. Purif. Technol.*, 2020, **252**, 117436.

60   S. Kazemiabnavi, Z. Zhang, K. Thornton and S. Banerjee, Electrochemical stability window of imidazolium-based ionic liquids as electrolytes for lithium batteries, *J. Phys. Chem. B*, 2016, **120**, 5691–5702.

61   Z. Ma, K. T. Mahmudov, V. A. Aliyeva, A. V. Gurbanov and A. J. L. Pombeiro, TEMPO in metal complex catalysis, *Coord. Chem. Rev.*, 2020, **423**, 213482.

62   X. Lang and J. Zhao, Integrating TEMPO and its analogues with visible-light photocatalysis, *Chem. Asian J.*, 2018, **13**, 599–613.

63   J. E. Nutting, M. Rafiee and S. S. Stahl, Tetramethylpiperidine n-oxyl (TEMPO), phthalimide n-oxyl (PINO), and related n-oxyl species: Electrochemical properties and their use in electrocatalytic reactions, *Chem. Rev.*, 2018, **118**, 4834–4885.

7. Conclusions and Future Work

7.1. Conclusions

To summarise, the decoupling of energy capacity and power makes RFBs attractive for fulfilling our large-scale stationary energy storage needs. The high costs of the RAMs and IEMs, alongside the relatively low energy density impede their commercial development.[1] The application of non-aqueous electrolytes in combination with ORAMs address these challenges by enhancing the cell potential and reducing the cost.

Herein, a novel organic species was studied for the application in novel non-aqueous ORFBs. An initial screening of quinoid species demonstrated the redox potential for OFAQ was particularly negative in comparison to other literature anolytes.[2–4] Additionally, it improves over previous ORAMs with more negative redox potentials by storing two moles of electrons per mole of compound.[5] Chapter 3. focusses on optimising the solvent and supporting electrolyte system. The optimum system has the most negative redox potential with the best chemical and electrochemical reversibility for OFAQ. This was determined as an ACN solvent with a 0.1 M TBABF$_4$ supporting electrolyte. Large cations (TBA$^+$, [EMIm]$^+$) do not interact strongly with the quinone and direct the pathway into a $2 \times 1e^-$ process. Smaller cations (Li$^+$) form ion pairs with the reduced states and cause a 1-step electrochemical pathway that may involve Li electrodeposition.

Investigations into the fundamental electrochemistry of the novel OFAQ ORAM demonstrate instability of the charged states under higher concentrations. The maximum solubility of OFAQ in ACN is <10 mM. Low solubilities are common in AQ ORAMs and limit their use in flow battery applications without molecular tailoring.[6] After charging for less than one hour there is a reaction in the electrolyte that results in an electrode passivating film. A combination of Raman spectroscopy, SEM, and XPS determine the film to comprise a polymeric form of OFAQ. Comparing the degradation process to previous literature studies indicates this may be a result of pinacol coupling of the radical anion species. Chronoamperometry and EPR spectroscopy tests indicate the dianionic species is less stable than the radical anion. The study deduces the degradation pathway of the OFAQ^{2-} to be via a comproportionation reaction with neutral OFAQ, yielding the radical anion. The radical anion then subsequently degrades by the aforementioned pinacol pathway. Hydrogen bonding, protonation, or utilising more strongly supporting cations did not improve the stability of the charged oxidation states. Symmetric cell testing demonstrate these side reactions are detrimental to the battery's function through an increasing overpotential with each cycle. Bulk electrolysis reveals the specific colour changes of the OFAQ reduction process as: yellow (neutral OFAQ), red (the radical anion, OFAQ$^{.-}$), and purple (the dianion, OFAQ^{2-}).

The purple dianion is unstable to air, and could not be analysed with the techniques available in this work. Upon contact with air, the purple media becomes red and shows no peaks in the ^{19}F-NMR. A lack of signals in the spectrum can indicate presence of a radical anion. However, EPR spectroscopy shows no radicals are present in the post-BE solution, suggesting this is not the case.

Given the attractive electrochemical characteristics of OFAQ in low concentrations, it was used as a model anolyte in the proof-of-concept membrane-free RFB device. Chapter 5. forms an ITIES using a high concentration WIS electrolyte and ACN for a self-stratifying battery. Three membrane-free static cells were realised, comprising $K_4[Fe(CN)_6]$/OFAQ, $VOSO_4$/OFAQ, and 4-OH-TEMPO/OFAQ. The latter of these is the first demonstration of a fully organic membrane-free WIS/ACN battery. All three systems demonstrated the ability to hold charge under static conditions. The instability of $K_4[Fe(CN)_6]$ and the high non-aqueous solubility of 4-OH-TEMPO prevent further development of these systems. The $VOSO_4$/OFAQ battery gave the best performance, with a theoretical OCV of 1.72 V, a CE_{ff} of 83 %, and a discharge capacity retention of nearly 100 % over 10 cycles. The theoretical cell voltage and CE_{ff} are 0.72 V and 12 % higher than the leading non-aqueous membrane-free static battery.[7] An additional advantage of the present system over previous work is the avoidance of expensive RTIL electrolytes.

Each battery showed evidence of side reactions and self-discharge, which are an inevitable aspect of the membrane-free design. The impact of these processes worsens with increasing flow rate. The $VOSO_4$/OFAQ battery demonstrated a stable cycling performance over 10 cycles with a CE_{ff} of 55 % and a discharge capacity of 7.53×10^{-3} mA h at a flow rate of 16.8 mL min^{-1}. Increasing the flow rate to 37.2 mL min^{-1} reduced the CE_{ff} to 23 % and the discharge capacity to 5.33×10^{-3} mA h. The drop in performance is due to the increased perturbation of the interface under faster flow rates. This causes more mixing of the charged species and thus propagates the self-discharge processes that ultimately reduce the capacity.

Analysis on the aqueous half-cell after cell cycling evidences F-containing molecules cross the interface. The presence of F environments that differ from the characteristic OFAQ ^{19}F-NMR spectrum indicates the side reactions produce a different product to the parent molecule. This product is soluble in the aqueous phase, which means the active material concentration in the organic phase is reduced. Therefore, these side reactions are permanently detrimental to the battery capacity.

Chapter 6. comprises a separate secondment study in collaboration with TNO, Nederlandse Organisatie voor Toegepast Natuurwetenschappelijk Onderzoek. The work exploits the environmental benignity, low cost, facile preparation, and wide ESWs of DESs in search of a

high-concentration redox active organic-based DES for application in an ORFB. Screening of known electrochemically reversible ORAMs in the common DES electrolyte, ethaline, demonstrated low ORAM reversibility and solubility. Establishing the ORAM as part of the DES electrolyte itself led to the discovery of four new redox-active room-temperature DES electrolytes:

- 1:1:2 OA, ChCl, catechol
- 1:2:4 1,5-DAAQ:ChCl:glycerol
- 1:1 4-OH-TEMPO:LiTFSI
- 1:2:3 BP:LiTFSI:Urea

None of the newly designed systems was feasible for a flow battery due to high viscosities that compounded into irreversible electrochemistry and slow redox kinetics. These challenges are prevalent throughout research on highly concentrated electrolytes.[1] This chapter discovers a novel redox-active room temperature DES with a eutectic composition of 1:2 BP:TEMPO. If both redox processes were to be accessed, this DES would offer a solvent-free ORFB with a theoretical OCV of 2.58 V. The viscosity and density is lower than previously reported DES systems, even after including a 1.25 M TBABF$_4$ supporting salt. Electrochemical studies show evidence of two redox processes in the DES. These are attributed to TEMPO/TEMPO$^+$, and either BP/BP$^{\cdot-}$, or TEMPO/TEMPO$^-$. The overlapping nature of the redox pairs means only the TEMPO/TEMPO$^+$ half-reaction is accessible in the present conditions. Despite the low viscosity of the DES and the enhancements in σ with supporting salts, the overpotentials for TEMPO oxidation remain high and the supporting salt solubility low. This limits the applicability of the DES in ORFBs. The promising attributes of the novel DES may mean it finds use in other areas of chemistry. For example, in aiding facile product separation in TEMPO catalysis reactions.[8,9–11]

Analysis via EPR spectroscopy would elucidate which molecules are responsible for the redox peaks. Additionally, further optimisation of the supporting electrolyte may separate the redox potentials of the two half-reactions such that the DES can comprise the full cell. This could result in an electrolyte wherein all four TEMPO redox are accessible. The resulting system carries a theoretical OCV of 2.26 V, which could potentially compete with the commercially available VRFBs.[12]

7.2. Retrospectives

The full capabilities of organic, non-aqueous RFBs is yet to be demonstrated, and almost all development remains within the academic landscape. Since their original conception in 2011,

there has been a great deal of research on ORFBs. A wide array of ORAMs have been screened, but generally poor electrochemical performance means this has culminated in only one demonstration unit for an aqueous ORFB (Jena Batteries, 100 kW h, the Netherlands) by the time of writing.[13,14] Designs confined to solely non-aqueous ORFBs are yet to leave the laboratory and have only been demonstrated in single cell experiments.

Research has been positive in utilising non-aqueous ORFBs to overcome the limited cell potential of aqueous counterparts. Many reports state full cells with potentials far above the limitations created by water.[2,3,5,15–20] It is the wide ESW of ACN that allows access to the second reduction step in OFAQ in Chapter 3, which carries the redox potential of −1.49 V (vs Ag/Ag$^+$). Studies are yet to develop a system that utilises the full ESW of the non-aqueous electrolytes, with the highest non-aqueous ORFB achieving a cell voltage of 2.97 V.[5] The experimental energy density of 4 Wh L^{-1} compared to the 223 Wh L^{-1} theoretical energy density represents the challenges in this area of research. Despite the promising advancements in energy density, the best non-aqueous ORFBs still show experimental values beneath the archetypal VRFB, at around 17 Wh L^{-1}.[21]

Theoretically, a combination of the ORAMs with the most negative and positive redox potentials from the literature, BP (−3.17 (vs Fc/Fc$^+$)) and cyclopropenium (1.33 V (vs Fc/Fc$^+$)) would yield a OCV of 4.5 V.[5,22,23] Such high redox potentials would provide vast improvements in energy density over the aqueous systems. This would also mean the concentration of electrolytes could be reduced, which may offset the increased cost of the non-aqueous solvents and supporting salts.[24]

DES electrolytes demonstrate an interesting route around the limiting ESW of water and benefit over conventional non-aqueous solvents by being environmentally benign. If the DES comprises redox active components within its network, then we can obtain electrolytes with concentrations far above those in conventional non-aqueous solvents. However, these systems face inherent challenges from the unfavourable physicochemical characteristics that such high concentration materials provide. The typically high viscosities would require large energy requirements for a flow device, and the high concentrations would mean lengthy charging cycles. One must also consider the effect on the electrolyte if the redox active moiety is part of the DES network. As oxidising or reducing a key component of the DES driving force may result in salting out of the RAM and a dysfunctional battery.

Unfortunately, increasing the cell potential is not enough to develop a suitable flow battery. The ORAMs that exhibit highly positive and negative redox potentials tend to present inadequate stability due to their highly reactive radical states. Rational design of the

substituent groups has worked to improve the stability of the charged species, but there is yet to be an organic redox material that does not exhibit capacity fade.[25,26]

Beyond the remit of the ORAMs lie other challenges specific to the non-aqueous ORFB. The electrolytes have low conductivities that necessitate the inclusion of expensive supporting salts.[27] The low conductivities result in high area specific resistances, which causes high overpotentials and thus low VE_{ff} and a limited power density. Furthermore, the lack of progress in designing efficient IEMs for non-aqueous electrolytes means active material crossover and low CE_{ff} values are frequent issues.[23] The membrane-free concept tries to tackle this problem by separating the half-cell using an ITIES. Removing the membrane would reduce the cost of the full system improve the performance by decreasing the internal resistance. Despite promising performances, cross-migration of the active materials and self-discharge at the interface obstruct progress.[28,29]

The membrane-free concept has the added complexity of species having different solubilities in each phase when in charged and discharged states. This makes is particularly difficult to highlight feasible RAMs that will not cross-migrate or self-discharge during cycling. Investigations into relative partition coefficients of ORAMs may narrow the search, but studies covering this area rarely study the systems under flow.[28] It is critical for the future development of these systems for RFBs that the performance under flow is fully understood.

7.3.   Future Work

The opportunities awarded to the RFB field from using ORAMs have been widely demonstrated. Much of the present work focusses on determining ORAMs with impressively high or low redox potentials for high energy density systems. However, the stability of the reported materials is often dissatisfactory, especially given that techno-economic analyses shows that materials with lifetimes <5 years are unsuitable for EESS. Therefore, the attractive qualities of the ORAMs with more extreme redox potentials, such as the OFAQ from this work, must become second player to the long-term stability of the molecules themselves. Researchers should instead focus on isolating the ORAMs in their charged states and studying the half-lives via NMR or EPR spectroscopy techniques.[3,30]

Computational advancements have streamlined the ORAM screening process. Through quantitative structure-property relationships we are able to predict highly stable, highly soluble, and high potential molecules.[26,31] However, a large proportion of experimental work in this field relies on short-timescale electrochemical techniques, such as CV, to screen ORAMs. These voltammetry techniques only study small concentrations over fast timescales, which gives an

insufficient description of the ORAMs performance in a full-cell battery. As demonstrated in Chapter 4, solely relying on CV can miss the critical degradation pathways that are only observable under longer timescales or higher concentrations. Future work should focus on combining both high-throughput computational screening with long-term cycling studies to evaluate the applicability of an ORAM.

Regarding the OFAQ ORAM presented in this work, there are a number key issues to consider for future studies. Improvements in the non-aqueous solubility of the quinone are critical so that the capacity of the device is not inherently limited. Previous studies show improvements in AQ solubilities through the introduction of long chain ether groups into the molecular backbone.[32,33] This may provide a route to high concentrations of the fluorinated quinone. These large sterically hindering chains may also improve upon the instability of the charged states of OFAQ by inhibiting the intermolecular degradation reported in Chapter 4.

Even if molecular tailoring improves the stability and solubility of OFAQ it is unlikely to be useful in a commercially applicable ORFB. The high molecular weight results in an active molecule equivalent weight of 176 g mol^{-1} e^{-1}, which is far about the target set by the DoE. The DoE target of 150 g mol^{-1} e^{-1} is inclusive of both the active molecule and the electrolyte, which is an impossibility with OFAQ. Therefore, future work should consider ORAMs with smaller molecular backbones to align with these goals. A starting point should be the promising BzNSN anolyte, which has an equivalent weight of 136 g mol^{-1} e^{-1}, high solubility, (5.7 M in ACN), and a low redox potential (−1.58 V (*vs* Ag/Ag$^+$)).[34]

In terms of the prospects for the membrane-free device, optimisation should ideally continue through widening the identity of the ORAMs in both the anolyte and catholyte phases. Focussing on the relative partition coefficients of the individual species is an effective technique for reducing ion crossover.[28] However, as Chapter 5 shows, an understanding of the partition coefficients of the materials in both their neutral and charged states is critical to developing a functioning system. Studies should fully charge each half-cell and monitor the propensity of crossover alongside the neutral systems. The WIS/ACN membrane-free concept could also benefit from investigations reducing the WIS concentration to reduce the electrolyte cost. The electrolytes stratify into layers of equal volume at 5 m LiCl. Future work should evaluate the effects of the lower WIS concentration on the battery performance.

Optimising the design of the membrane-free flow cell will also rapidly progress research. Most researches in this area do not study under flow conditions, and there is yet to be a standardised membrane-free flow cell to allow accurate comparison of the literature.[7,35,36] The electrochemical performance of an RFB depends on balancing the extrinsic flow rate and the

intrinsic charge-transfer kinetics of the RAMs. It is naïve to predict the applicability of a system to an RFB without understanding the mechanisms in combination with flow.

Future cell iterations should consider sealing the cell from ambient atmosphere with a lid, and fixing the electrode positions in the cell such that the active area and inter-electrode distance is constant. Furthermore, studies should evaluate the effects different flow rates on the battery performance, and open the study to test dual electrolyte flow. Understanding the effects of flow is critical for any future application of membrane-free devices in ORFBs.

One must also consider the high-cost and toxicity of the ACN solvent used throughout this thesis. Chapter 6 discusses the possibilities of high concentration DES electrolytes, which may be a route to non-aqueous ORFBs that avoids such media. The toxicity of BP is also a concern in the BP:TEMPO DES proposed in Chapter 6, and future work should consider more environmentally benign ORAMs with similar functional groups. Additionally, the immiscibility of the BP:TEMPO DES with water could make it a possible non-aqueous half-cell for the proposed membrane-free device.

7.4.　References

1　C. Zhang, L. Zhang, Y. Ding, S. Peng, X. Guo, Y. Zhao, G. He and G. Yu, Progress and prospects of next-generation redox flow batteries, *Energy Storage Mater.*, 2018, **15**, 324–350.

2　X. Wei, W. Duan, J. Huang, L. Zhang, B. Li, D. Reed, W. Xu, V. Sprenkle and W. Wang, A high-current, stable nonaqueous organic redox flow battery, *ACS Energy Lett.*, 2016, **1**, 705–711.

3　X. Wei, W. Xu, J. Huang, L. Zhang, E. Walter, C. Lawrence, M. Vijayakumar, W. A. Henderson, T. Liu, L. Cosimbescu, B. Li, V. Sprenkle and W. Wang, Radical compatibility with nonaqueous electrolytes and its impact on an all-organic redox flow battery, *Angew. Chemie Int. Ed.*, 2015, **54**, 8684–8687.

4　X. Xing, Q. Liu, W. Xu, W. Liang, J. Liu, B. Wang and J. P. Lemmon, All-liquid electroactive materials for high energy density organic flow battery, *ACS Appl. Energy Mater.*, 2019, **2**, 2364–2369.

5　X. Xing, Y. Huo, X. Wang, Y. Zhao and Y. Li, A benzophenone-based anolyte for high energy density all-organic redox flow battery, *Int. J. Hydrogen Energy*, 2017, **42**, 17488–17494.

6　P. Symons, Quinones for redox flow batteries, *Curr. Opin. Electrochem.*, 2021, **29**,

100759.

7   P. Navalpotro, N. Sierra, C. Trujillo, I. Montes, J. Palma and R. Marcilla, Exploring the versatility of membrane-free battery concept using different combinations of immiscible redox electrolytes, *ACS Appl. Mater. Interfaces*, 2018, **10**, 41246–41256.

8   Y. Zhang, F. Lü, X. Cao and J. Zhao, Deep eutectic solvent supported TEMPO for oxidation of alcohols, *RSC Adv.*, 2014, **4**, 40161–40169.

9   Z. Ma, K. T. Mahmudov, V. A. Aliyeva, A. V. Gurbanov and A. J. L. Pombeiro, TEMPO in metal complex catalysis, *Coord. Chem. Rev.*, 2020, **423**, 213482.

10   X. Lang and J. Zhao, Integrating TEMPO and its analogues with visible-light photocatalysis, *Chem. Asian J.*, 2018, **13**, 599–613.

11   J. E. Nutting, M. Rafiee and S. S. Stahl, Tetramethylpiperidine n-oxyl (TEMPO), phthalimide n-oxyl (PINO), and related n-oxyl species: Electrochemical properties and their use in electrocatalytic reactions, *Chem. Rev.*, 2018, **118**, 4834–4885.

12   L. F. Arenas, C. Ponce de León and F. C. Walsh, Redox flow batteries for energy storage: their promise, achievements and challenges, *Curr. Opin. Electrochem.*, 2019, **16**, 117–126.

13   Z. Li, S. Li, S. Liu, K. Huang, D. Fang, F. Wang and S. Peng, Electrochemical properties of an all-organic redox flow battery using 2,2,6,6-tetramethyl-1-piperidinyloxy and N-methylphthalimide, *Electrochem. Solid-State Lett.*, 2011, **14**, 171–173.

14   JenaBatteries GmbH, Jena Batteries, https://jenabatteries.de/en/, (accessed 21 January 2022).

15   J. Yu, Y. S. Hu, F. Pan, Z. Zhang, Q. Wang, H. Li, X. Huang and L. Chen, A class of liquid anode for rechargeable batteries with ultralong cycle life, *Nat. Commun.*, 2017, **8**, 1–7.

16   C. S. Sevov, R. E. M. Brooner, E. Chénard, R. S. Assary, J. S. Moore, J. Rodríguez-López and M. S. Sanford, Evolutionary design of low molecular weight organic anolyte materials for applications in nonaqueous redox flow batteries, *J. Am. Chem. Soc.*, 2015, **137**, 14465–14472.

17   B. Hu and T. L. Liu, Two electron utilization of methyl viologen anolyte in nonaqueous organic redox flow battery, *J. Energy Chem.*, 2018, **27**, 1326–1332.

18   J. Huang, W. Duan, J. Zhang, I. A. Shkrob, R. S. Assary, B. Pan, C. Liao, Z. Zhang, X. Wei and L. Zhang, Substituted thiadiazoles as energy-rich anolytes for nonaqueous

redox flow cells, *J. Mater. Chem. A*, 2018, **6**, 6251–6254.

19   C. N. Gannett, B. M. Peterson, L. Shen, J. Seok, B. P. Fors and H. D. Abruña, Cross-linking effects on performance metrics of phenazine-based polymer cathodes, *ChemSusChem*, 2020, **13**, 2428–2435.

20   D. Xu, C. Zhang, Y. Zhen, Y. Zhao and Y. Li, A high-rate nonaqueous organic redox flow battery, *J. Power Sources*, 2021, **495**, 229819.

21   G. Kwon, S. Lee, J. Hwang, H. S. Shim, B. Lee, M. H. Lee, Y. Ko, S. K. Jung, K. Ku, J. Hong and K. Kang, Multi-redox molecule for high-energy redox flow batteries, *Joule*, 2018, **2**, 1771–1782.

22   A. Shrestha, K. H. Hendriks, M. S. Sigman, S. D. Minteer and M. S. Sanford, Realization of an asymmetric non-aqueous redox flow battery through molecular design to minimize active species crossover and decomposition, *Chem. Eur. J.*, 2020, **26**, 5369–5373.

23   M. Li, Z. Rhodes, J. R. Cabrera-Pardo and S. D. Minteer, Recent advancements in rational design of non-aqueous organic redox flow batteries, *Sustain. Energy Fuels*, 2020, **4**, 4370–4389.

24   R. Dmello, J. D. Milshtein, F. R. Brushett and K. C. Smith, Cost-driven materials selection criteria for redox flow battery electrolytes, *J. Power Sources*, 2016, **330**, 261–272.

25   J. Zhang, J. Huang, L. A. Robertson, R. S. Assary, I. A. Shkrob and L. Zhang, Elucidating factors controlling long-term stability of radical anions for negative charge storage in nonaqueous redox flow batteries, *J. Phys. Chem. C*, 2018, **122**, 8116–8127.

26   C. S. Sevov, D. P. Hickey, M. E. Cook, S. G. Robinson, S. Barnett, S. D. Minteer, M. S. Sigman and M. S. Sanford, Physical organic approach to persistent, cyclable, low-potential electrolytes for flow battery applications, *J. Am. Chem. Soc.*, 2017, **139**, 2924–2927.

27   K. Wedege, E. Dražević, D. Konya and A. Bentien, Organic redox species in aqueous flow batteries: Redox potentials, solubility and chemical stability, *Sci. Rep.*, 2016, **6**, 1–13.

28   P. Navalpotro, C. Trujillo, I. Montes, C. M. S. S. Neves, J. Palma, M. G. Freire, J. A. P. Coutinho and R. Marcilla, Critical aspects of membrane-free aqueous battery based on two immiscible neutral electrolytes, *Energy Storage Mater.*, 2020, **26**, 400–407.

29   X. Wang, A. Lashgari, J. Chai and J. Jiang, A membrane-free, aqueous/nonaqueous

hybrid redox flow battery, *Energy Storage Mater.*, 2022, **45**, 1100–1108.

30   E. W. Zhao, E. Jónsson, R. B. Jethwa, D. Hey, D. Lyu, A. Brookfield, P. A. A. Klusener, D. Collison and C. P. Grey, Coupled in Situ NMR and EPR Studies Reveal the Electron Transfer Rate and Electrolyte Decomposition in Redox Flow Batteries, *J. Am. Chem. Soc.*, 2021, **143**, 1885–1895.

31   D. P. Tabor, R. Gómez-Bombarelli, L. Tong, R. G. Gordon, M. J. Aziz and A. Aspuru-Guzik, Mapping the frontiers of quinone stability in aqueous media: implications for organic aqueous redox flow batteries, *J. Mater. Chem. A*, 2019, **7**, 12833–12841.

32   W. Wang, W. Xu, L. Cosimbescu, D. Choi, L. Li and Z. Yang, Anthraquinone with tailored structure for a nonaqueous metal-organic redox flow battery, *Chem. Commun.*, 2012, **48**, 6669–6671.

33   P. Geysens, Y. Li, I. Vankelecom, J. Fransaer and K. Binnemans, Highly soluble 1,4-diaminoanthraquinone derivative for nonaqueous symmetric redox flow batteries, *ACS Sustain. Chem. Eng.*, 2020, **8**, 3832–3843.

34   Y. Zhao, Z. Yu, L. A. Robertson, J. Zhang, Z. Shi, S. R. Bheemireddy, I. A. Shkrob, Y Z, T. Li, Z. Zhang, L. Cheng and L. Zhang, Unexpected electrochemical behavior of an anolyte redoxmer in flow battery electrolytes: Solvating cations help to fight against the thermodynamic-kinetic dilemma, *J. Mater. Chem. A*, 2020, **8**, 13470–13479.

35   M. O. Bamgbopa, S. Almheiri and H. Sun, Prospects of recently developed membraneless cell designs for redox flow batteries, *Renew. Sustain. Energy Rev.*, 2017, **70**, 506–518.

36   S. A. M. Shaegh, N. T. Nguyen and S. H. Chan, A review on membraneless laminar flow-based fuel cells, *Int. J. Hydrogen Energy*, 2011, **36**, 5675–5694.

8. Appendix

Fresh	^{19}F NMR (376 MHz, D_2O) δ −79.20, −130.17, −139.95, −144.68
4 Days Old	^{19}F NMR (376 MHz, D_2O) δ −79.20, −129.35, −130.18
7 Days Old	^{19}F NMR (376 MHz, D_2O) δ −79.42, −79.42, −130.26, −130.26, −130.27

Appendix 3. A. ^{19}F-NMR of 20 mM TFBQ in (a) fresh (b) 4 day old, and (c) 7 day old 20 mM TFBQ in D_2O.

Fresh	^{19}F NMR (376 MHz, CF_3CO_2D) δ −11.70, −11.70, −77.45, −77.99, −78.50, −144.27
7 Days Old	^{19}F NMR (376 MHz, CF_3CO_2D) δ −11.81, −11.82, −77.82, −78.82, −78.06, −78.57, −144.30

Appendix 3. B. ^{19}F-NMR spectra showing non-aqueous stability of (a) fresh and (b) week-old 20 mM TFBQ in CF_3CO_2D.

(a)

(b)

(c)
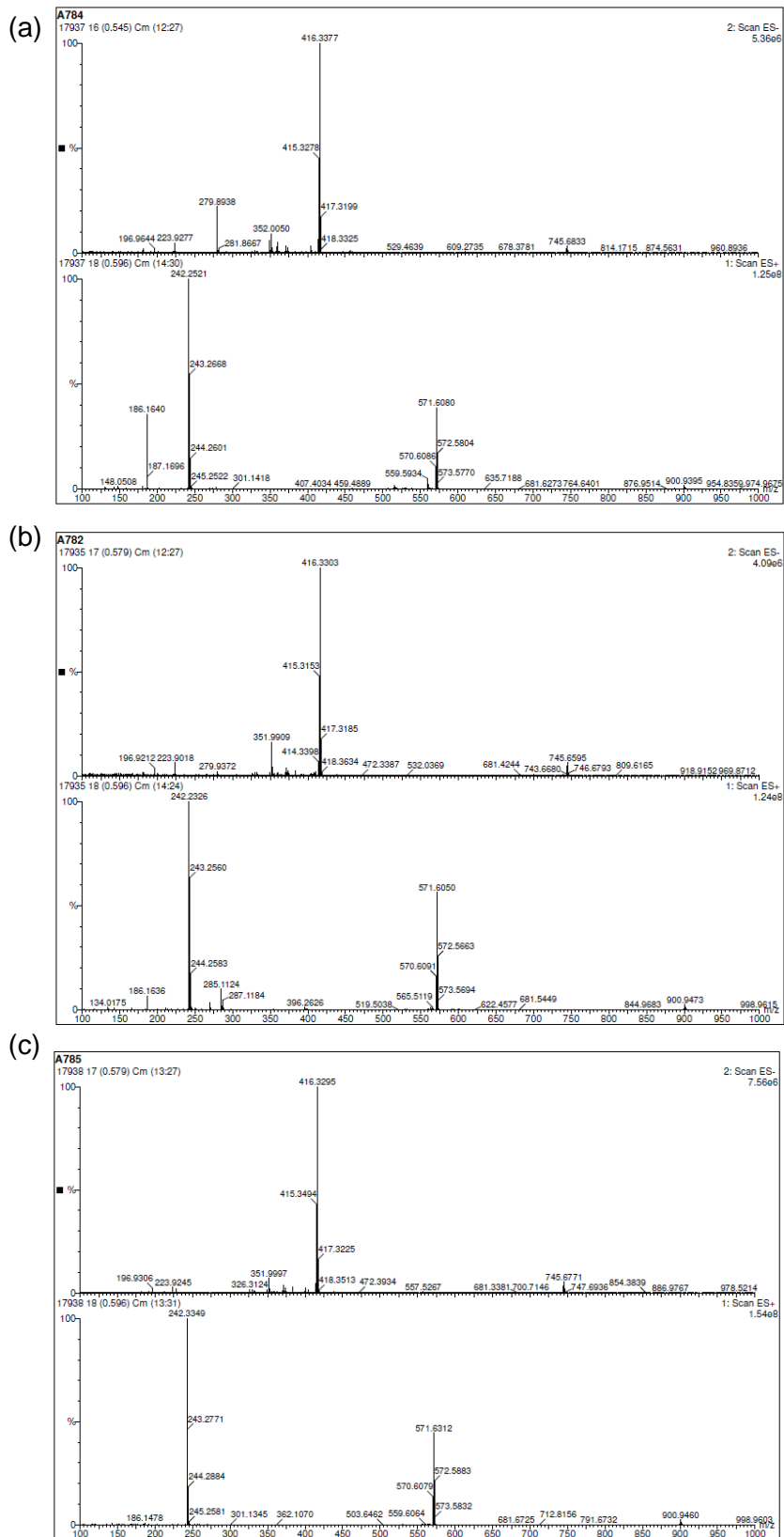
Appendix 3. C. Mass spectrometry data for 1 mM OFAQ in (a) valeronitrile, (b) heptanenitrile, and (c) caprylonitrile after 10 months.
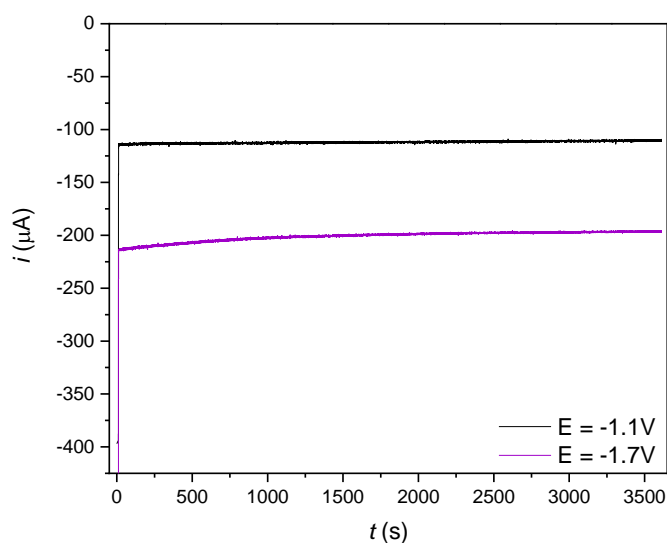
Appendix 4. A. Chronoamperometry at 1600 RPM on 0.5 mM OFAQ, 0.1 M TBABF$_4$, ACN at step potentials E = −1.1 V (vs Ag/Ag$^+$) (black line) and E = −1.7 V (vs Ag/Ag$^+$) (purple line) over 3600 s. Tests are run using a GC WE, Ag/Ag$^+$ RE, and Pt CE.

Fresh **1 mM OFAQ, 0.1 M TBABF$_4$, ACN**	^{19}F NMR (376 MHz, No Deuterated Solvent) δ −80.25, −140.77, −146.73, −149.77, −153.04, −153.76.
After BE at −1.6 V (*vs* C) **1 mM OFAQ, 0.1 M TBABF$_4$, ACN**	^{19}F NMR (376 MHz, No Deuterated Solvent) δ −151.45, −151.50

Appendix 4. B. ^{19}F-NMR of 1 mM OFAQ, 0.1 M TBABF$_4$, ACN when (a) fresh, (b) after BE at -1.6 V (vs Ag/Ag$^+$).

Appendix 4. C. EPR spectrum of 1 mM OFAQ, 0.1 M TBABF₄, ACN after BE at −1.6 V (vs Ag/Ag⁺) and exposure to air (blue line) against the glass capillary control (orange line).

2 mM OFAQ, 4 mM CF₃SO₃H, 0.1 M TBABF₄, ACN	^{1}H NMR (400 MHz, D₂O) δ 4.70 (s, residual solvent), 3.80 (dd, 9.0 Hz), 2.81 (s), 2.69 (s), 2.32 (m), 2.07 (m), 1.69 (t, 7.8 Hz).
1 mM OFAQ, 4 mM CF₃SO₃H, 0.1 M TBABF₄, ACN	^{1}H NMR (400 MHz, D₂O) δ 4.70 (s, residual solvent), 3.80 (dd, 9.0 Hz), 2.80 (s), 2.69 (s), 2.36 (m), 2.07 (m), 1.70 (t, 7.8 Hz).
4 mM CF₃SO₃H, 0.1 M TBABF₄, ACN	^{1}H NMR (400 MHz, D₂O) δ 4.70 (s, residual solvent), 3.80 (dd, 9.0 Hz), 2.69 (s), 2.36 (m), 2.07 (m), 1.69 (t, 7.8 Hz).

Appendix 4. D. ^{1}H-NMR chemical shifts for OFAQ in 4 mM CF₃SO₃H, 0.1 M TBABF₄, ACN with a D₂O inner-capillary reference.

Appendix 4. C. EPR spectrum of 1 mM OFAQ, 0.1 M $TBABF_4$, ACN after BE at −1.6 V (vs Ag/Ag^+) and exposure to air (blue line) against the glass capillary control (orange line).

2 mM OFAQ, 4 mM CF_3SO_3H, 0.1 M $TBABF_4$, ACN	^{1}H NMR (400 MHz, D_2O) δ 4.70 (s, residual solvent), 3.80 (dd, 9.0 Hz), 2.81 (s), 2.69 (s), 2.32 (m), 2.07 (m), 1.69 (t, 7.8 Hz).
1 mM OFAQ, 4 mM CF_3SO_3H, 0.1 M $TBABF_4$, ACN	^{1}H NMR (400 MHz, D_2O) δ 4.70 (s, residual solvent), 3.80 (dd, 9.0 Hz), 2.80 (s), 2.69 (s), 2.36 (m), 2.07 (m), 1.70 (t, 7.8 Hz).
4 mM CF_3SO_3H, 0.1 M $TBABF_4$, ACN	^{1}H NMR (400 MHz, D_2O) δ 4.70 (s, residual solvent), 3.80 (dd, 9.0 Hz), 2.69 (s), 2.36 (m), 2.07 (m), 1.69 (t, 7.8 Hz).

Appendix 4. D. ^{1}H-NMR chemical shifts for OFAQ in 4 mM CF_3SO_3H, 0.1 M $TBABF_4$, ACN with a D_2O inner-capillary reference.

1 mM OFAQ, 4 mM CF₃SO₃H, 0.1 M TBABF₄, ACN	^{19}F NMR (376 MHz, No Deuterated Solvent) δ −78.42, −79.31, −139.81, −145.82, −149.67, 150.95, −150.64.
4 mM CF₃SO₃H, 0.1 M TBABF₄, ACN	^{19}F NMR (376 MHz, No Deuterated Solvent) δ −79.18, −150.14, −151.23
1 mM OFAQ, 0.1 M TBABF₄, ACN	^{19}F NMR (376 MHz, No Deuterated Solvent) δ −79.40, −139.88, −145.79, −150.48, −150.54.

Appendix 4. E. ^{19}F-NMR chemical shifts for 1 mM OFAQ, 4 mM CF₃SO₃H and 1 mM OFAQ, 4 mM CF₃SO₃H, in 0.1 M TBABF₄, ACN.
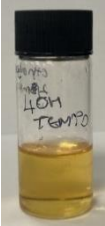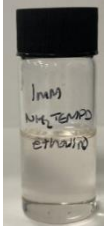
5.A. 10m LiCl ‖ 1 mM OFAQ 0.1 M LiBF₄ ACN


```
  10    0   -10  -20  -30  -40  -50  -60  -70  -80  -90  -100 -110 -120 -130 -140 -150 -160 -170 -180 -190 -200 -210
                                              f1 (ppm)
```
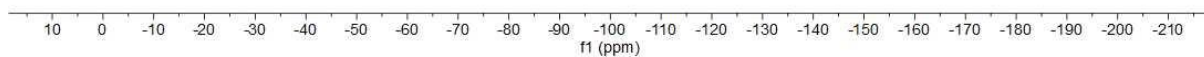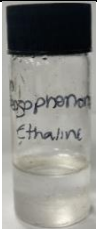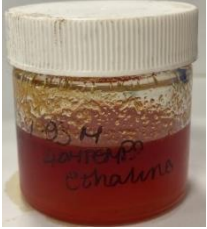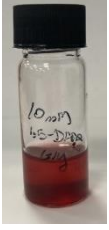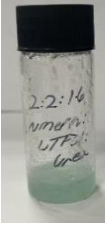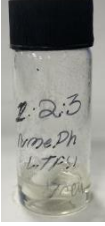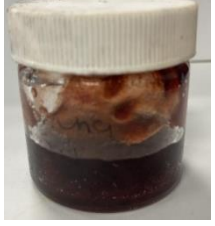
Appendix 5. A. ^{19}F-NMR spectrum for 10 m LiCl after shaking with 1 mM OFAQ, 0.1 M LiBF₄, ACN.
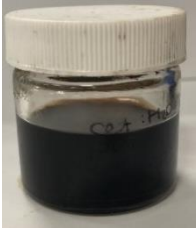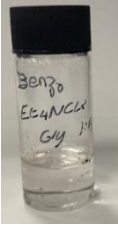
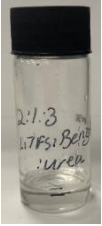|	^{19}F NMR (376 MHz, No Deuterated Solvent)
1 mM OFAQ, 0.1 M LiBF₄, ACN	δ −79.34, −140.23, −149.64, −151.03, −151.09.
20 mM VOSO₄, 2 M HCl, 10 m LiCl	^{19}F NMR (376 MHz, No Deuterated Solvent) δ −78.22, −130.12, −133.38, −147.97, −151.53

Appendix 5. B. ^{19}F-NMR chemical shifts for 1 mM OFAQ, 0.1 M LiBF₄, ACN and 20 mM VOSO₄, 2 M HCl, 10 m LiCl after 10 cycles in the membrane-free device at 1.2 mA under flow at 37.2 mL min^{-1}.
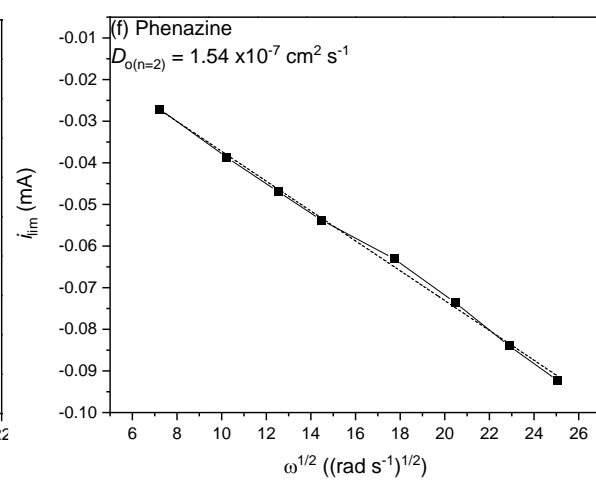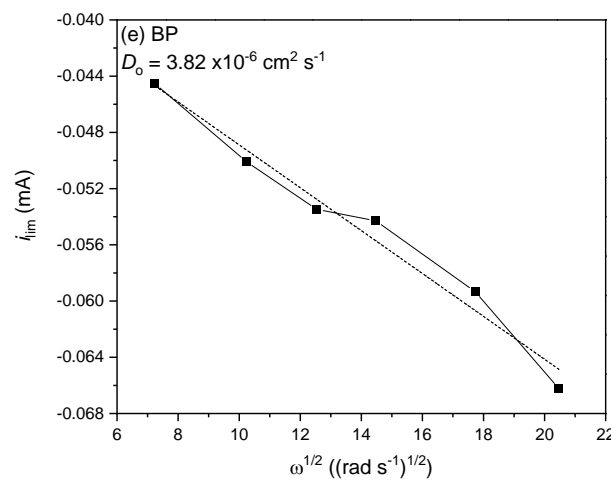
299

ORAM	ORAM Concentration (M)	DES	Phase	Photo
4-OH-TEMPO	4×10^{-3}	Ethaline	Liquid	
NH$_2$-TEMPO	1×10^{-3}	Ethaline	Liquid	
NMePh	1×10^{-3}	Ethaline (Dry)	Liquid	
Phenazine	$<1 \times 10^{-2}$ (Max saturation)	Ethaline	Liquid	
1,3-Diaminophenazine	2.6×10^{-3}	Ethaline	Liquid	
1,5-DAAQ	1×10^{-2}	EthalineCM2	Liquid	

BP	1×10^{-3}	Ethaline	Liquid	
4-OH-TEMPO	1.93	Ethaline	Viscous liquid	
1,5-DAAQ	1.41	2:1:4 ChCl:DAAQ:Gly	Viscous liquid	
1,5-DAAQ	4.01	2:1:1 DAAQ:ChCl:OA	Solid	
1,5-DAAQ	$<1 \times 10^{-2}$ (Max saturation)	ChCl:Gly	Thick liquid	
1,5-DAAQ	$<1 \times 10^{-2}$ (Max saturation)	Gly	Thick liquid	
NMePh:4-OH-TEMPO	3.61	1:1	Solid	

NMePh:TEMPO	3.40	1:1	Solid	
NMePh:NH$_2$-TEMPO	3.47	1:1	Solid	
NMePh	2.65	2:2:1.6 NMePh:LiTFSI:Urea	Solid	
NMePh	2.45	1:2:3 NMePh:LiTFSI:Urea	Very viscous liquid	
4-OH-TEMPO	3.77	2:1:4 4-OH-TEMPO :TEACl:H2O	Solid	
NH$_2$-TEMPO	2.20	1:1:4 NH$_2$-TEMPO:TEACl:H2O	Solid	
Catechol	6.80	2:1 Catechol:ChCl	Solid	

Catechol	1.40	2:1:4 Catechol:urea:H_2O + NaCl	Liquid (Similar viscosity to water)	
Catechol	5.78	2:1:1 Catechol ChCl:Oxalic Acid	Very viscous liquid	
BP	1×10^{-3}	1:4 TEACl:Gly	Low viscosity liquid	
BP	1.37	2:1:3 LiTFSI:BP:Urea	Viscous liquid	

Appendix 6. A. Table of compositions tested during DES development.

(a) 4-OH-TEMPO
D_o = 1.44 x10^{-6} cm^2 s^{-1}

(b) Catechol
$D_{o(n=2)}$ = 9.78 x10^{-7} cm^2 s^{-1}

(c) 1,5-DAAQ
$D_{o(n=2)}$ = 2.54 x10^{-7} cm^2 s^{-1}

(d) N-MePh
D_o = 1.63 x10^{-6} cm^2 s^{-1}

(e) BP
D_o = 3.82 x10^{-6} cm^2 s^{-1}

(f) Phenazine
$D_{o(n=2)}$ = 1.54 x10^{-7} cm^2 s^{-1}

i_{lim} (mA)

$\omega^{1/2}$ ((rad s^{-1})$^{1/2}$)

304
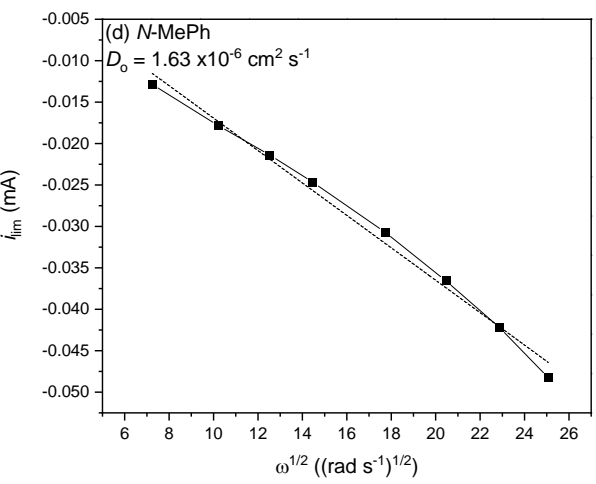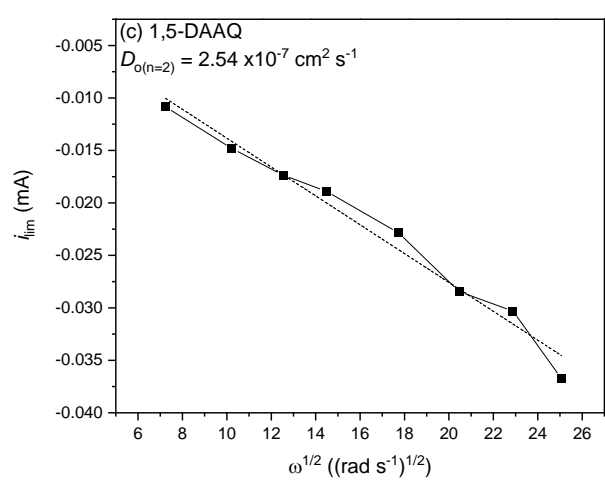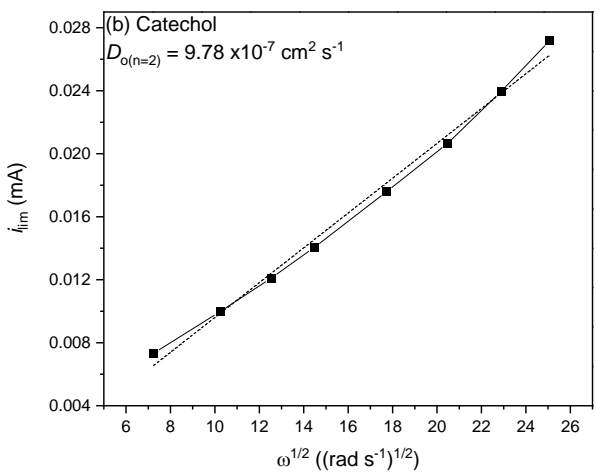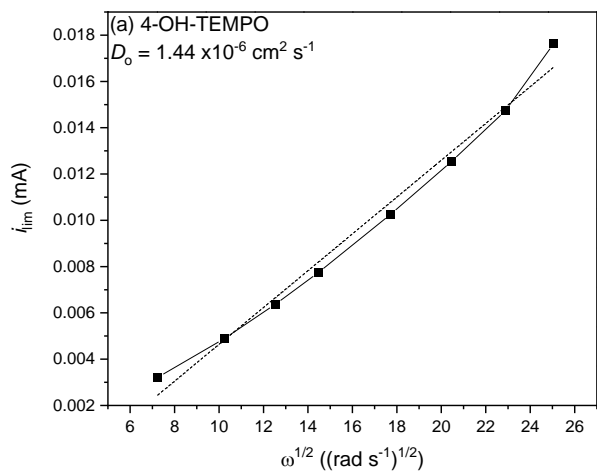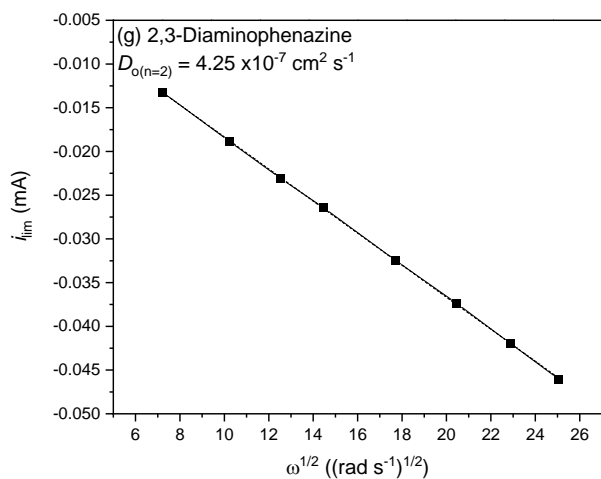
Appendix 6. B. Levich plots and corresponding D_o values calculated using the Levich equation for the LSV data in Figure 6.1. D_o calculations use n = 1 unless otherwise specified.
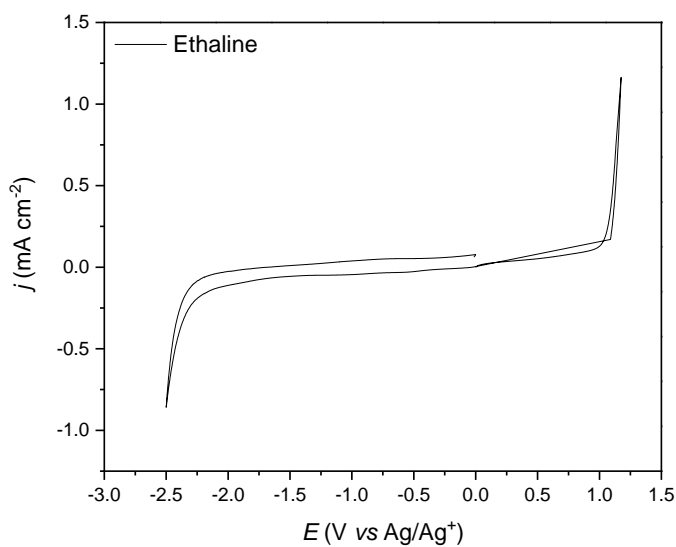
Appendix 6. C. Ethaline blank CV at 100 mV s^{-1} taken using a GC WE, Ag/Ag$^+$ RE, and Pt CE.

Appendix 6. D. Physicochemical Properties of the BP:TEMPO DES at different molar ratios

BP:TEMPO	T (K)	σ (μS cm s⁻¹)	Ph	ρ (g cm⁻³)	η (mPa s)	v (mm² s⁻¹)
	293.15	0.439	7.02	1.0263	-	-
	303.15	0.582	6.83	1.0183	-	-
01:01	313.15	0.722	6.71	1.0102	-	-
	323.15	0.822	6.52	1.0023	-	-
	333.15	0.884	-	-	-	-
	293.15	0.712	7.02	0.9962	7.1233	7.1504
	303.15	0.896	6.83	0.9882	5.0714	5.1319
01:02	313.15	1.109	6.71	0.9802	3.7676	3.8436
	323.15	1.307	6.52	0.9723	2.9096	2.9927
	333.15	1.399	-	-	-	-
	293.15	1.064	6.75	0.9797	-	-
	303.15	1.085	6.58	0.9716	-	-
01:03	313.15	1.181	-	0.9635	-	-
	323.15	1.340	6.39	0.9554	-	-
	333.15	1.541	-	-	-	-
01:04	293.15	1.200	6.75	0.9612	-	-

	303.15	1.280	6.64	0.9532	-	-
	313.15	1.532	6.52	0.9452	-	-
	323.15	1.786	6.37	0.9372	-	-
	333.15	1.897	-	-	-	-
1:02 + 1.25 M TBABF$_4$	293.15	-	-	1.0114	43.697	43.206
	298.15	405.7	-	-	-	-
	303.15	465.3	-	1.0040	26.502	26.396
	313.15	586.8	-	0.9967	17.046	17.102
	323.15	735.5	-	0.9894	11.527	11.651